



THE UNIVERSITY *of* EDINBURGH

Title	Proton magnetic resonance spectroscopic imaging of the human brain
Author	Wild, James Michael
Qualification	PhD
Year	1998

This thesis scanned from best copy available: may contain faint or blurred text, and/or cropped or missing pages.

Digitisation Notes:

- pag 186 instead of 188 in original numeration; content unaffected by mistake.

**Proton Magnetic Resonance
Spectroscopic Imaging of the Human
Brain**

James Michael Wild

PhD
Department of Medical Physics
University of Edinburgh
1998



Abstract

Over the last ten years proton MR spectroscopy has been performed on clinical MRI scanners using single voxel localisation and spectroscopic imaging sequences. In this work inner volume excitation of a transverse imaging plane within the brain has been used to obtain single slice spectroscopic images of proton metabolites.

The existing image processing protocols used to construct the metabolite images were improved and optimised so as to give as accurate a picture of metabolite distribution as possible. Inaccuracy in these images can be introduced by the excitation profile of the radio frequency pulses used in inner volume excitation. A new normalisation technique is proposed which will remove these inaccuracies enabling more reliable quantification of metabolite concentrations.

Of particular importance in stroke is the metabolite lactate, elevated levels of which are symptomatic with the conditions of anaerobic glycolysis that are thought to precede infarction. The signal from lactate is often obscured by lipid and macro-molecule resonances in the same frequency range. Lactate editing sequences compatible with the hardware capabilities of the scanner and spectroscopic imaging sequences were investigated for viability in-vivo. Using two different editing sequences, lactate editing was performed successfully in-vitro and in-vivo

In-vivo results are presented from a study of 23 acute stroke patients and a smaller pilot study of 8 closed head injury patients. These patients were drawn from the Lothian Stroke Register as part of the Clinical Research Initiative (CRI) in stroke and head injury being co-ordinated at the Western General Hospital, Edinburgh. To our knowledge this is the largest spectroscopic imaging study of stroke and the first spectroscopic imaging study of head injury. As such these findings could have a significant bearing in analysing the physiological implications of these conditions.

Contents

	Page No.
List of symbols	9
List of abbreviations	10
1. Introduction	11
1.1 Background to the project	12
1.1.1 Summary of the work described in subsequent chapters	13
1.2 Historical development of NMR, MRI and in-vivo spectroscopy	16
1.3 Alternative methods of imaging metabolism and physiology	16
1.3.1 Metabolic imaging	16
1.3.2 Physiological imaging	17
1.4 The metabolites imaged with ^1H MR spectroscopy	20
1.4.1 Amino acids	21
1.4.2 Choline	22
1.4.3 Creatine	22
1.4.4 Lactate	23
1.4.5 Lipids and macro-molecules	23
1.5 Summary	23
2. Physical principles of NMR and MRI	
2.1 Introduction	24
2.2 Behaviour of a spin in an applied B_0 field	24
2.3 The chemical shift effect	28
2.4 Classical behaviour of the net magnetisation vector	28
2.5 Evolution of the net magnetisation in the absence of r.f. fields - the Bloch equations	31
2.6 Spin manipulation based on the Bloch equations	33
2.6.1 Averaging -repetitive r.f. pulses	34
2.6.2 Inversion recovery	35

2.6.3 The Hahn spin echo	36
2.6.4 The stimulated echo	37
2.7 Localisation using B_0 gradients	39
2.7.1 Slice selection	39
2.7.2 Frequency encoding in the readout direction	39
2.7.3 Phase encoding	40
2.8 R.F. pulses	42
2.9 Spectroscopic localisation	44
2.9.1 Single voxel localisation sequences	44
2.9.2 Multi-shot methods	44
2.9.3 Single-shot methods	46
2.9.3.1 STEAM	46
2.9.3.2 PRESS	47
2.9.4 SI sequences	47
2.9.4.1 Single slice SI	48
2.9.4.2 Multiple slice SI	50
2.10 Summary	52
3. Data Acquisition	
3.1 Introduction	54
3.1.1 The main B_0 and gradient fields	55
3.1.2 The R.F. (B_1) coil	56
3.1.3 The shim coils	57
3.1.4 The computer operating system	57
3.2 Acquisition protocols	58
3.2.1 Preparation	58
3.2.2 Acquisition	59
3.2.3 Specification of the SI grid	59
3.3 B_0 field inhomogeneity - Shimming	61
3.3.1 Consequences of a good and bad shim	61
3.3.2. The shimming procedure	64
3.3.3 Automated shimming	66
3.3.4 Field mapping	67

3.3.5 Shim current optimisation	68
3.3.6 Shimming on the Magnetom SP 63	68
3.3.7 In-vitro examples of the effects of shimming	70
3.3.8 Conclusions	71
3.4 Water suppression	
3.4.1 Introduction	72
3.4.2 Pre-saturation	72
3.4.3 Inversion recovery	73
3.4.4 Selective excitation	73
3.5 Conclusions	74
4. Data Processing	
4.1 Importing data from the scanner	75
4.2 Raw data processing -overview	76
4.2.1 Reading the data- water reference data set	
4.2.2 Zero-filling of k-space	
4.2.3 k-space windowing	
4.2.4 Voxel shifting	
4.2.5 k-space to real space FFT	
4.2.6 Calculating the zero order phase correction	
4.3 Water suppressed data set	78
4.3.1 Applying the zero order phase correction	
4.3.2 Line broadening	
4.3.3 Save FIDs for time domain modelling-water removal	
4.3.4 Spectral transform	
4.3.5 Automatic integration	
4.4 Post acquisition water removal	78
4.5 Individual data processing steps implemented by the program <code>centrefill12.c</code>	81
4.6 Zero-filling	81
4.7 Voxel shifting	83
4.8 Spatial filtering	86
4.8.1 Artefacts introduced by the discrete to real space FFT	86
4.8.2 Spatial windowing	88

4.8.3 Window functions in one spatial dimension	90
4.8.4 2D simulations of the effects of windowing functions	91
4.8.5 In-vivo comparisons of window functions	94
4.9 Phase correction	97
4.7.1 Introduction	97
4.7.2 Implementing zero order phase corrections	98
4.7.3 Using a zero-filled water reference data set to reduce acquisition time	99
4.7.4 First order phase corrections	101
4.7.5 Artefacts introduced by the zero order phase correction process	103
4.7.6 Source of artefacts	105
4.10 Time domain windowing -line broadening	107
4.11 Signal interpretation-FFT and alternative models	109
4.11.1 Introduction	109
4.11.2 The Fourier transform	109
4.11.3 Artefacts of the discrete Fourier transform	111
4.11.4 Implementation of the discrete FFT on a SI data set	113
4.12 Fitting	115
4.12.1 Non-parametric methods	116
4.12.2 Parametric modelling	119
4.12.3 Non linear methods -time domain	119
4.12.4 Non linear methods -frequency domain	120
4.12.5 Linear methods	121
4.12.6 Summary	122
4.13 Spectroscopic image construction	123
5. VOI profile correction	
5.1 Introduction	127
5.2 Background	127
5.3 VOI localisation -excitation profiles	128
5.3.1 Methods	130
5.3.2 Results and discussion	131
5.4 Chemical shift artefact and normalisation	132
5.4.1 Spatial shift of the VOI	132

5.4.2 Cross correlation technique	133
5.5 The effect of T_R and T_I on the profile of the VOI	135
5.5.1 Experimental evidence	135
5.5.2 Computer simulations	136
5.6 In-vivo image normalisation	138
5.7 Lipid contamination	140
5.8 Conclusions	141
6. Lactate editing	144
6.1 Introduction	144
6.1.2 Lactate	146
6.1.3 Lipids and their characteristic spectra	147
6.1.4 In-vitro lipid spectra at a high B_0 field strength	148
6.2 Homonuclear polarisation transfer in double spin echo spectroscopy	150
6.2.1 Background	150
6.2.2 AX_3 doublet signal modulation in a double spin echo system	150
- experimental evidence	
6.2.3 Theoretical predictions of the signal	151
6.2.4 Calculation of the lactate signal in a double spin echo	151
6.2.5 Experimental verification of the T_E modulation of the HOPE signal	154
-determination of δ	
6.2.6 Polarisation transfer editing	156
6.2.7 Single voxel edited spectra	157
6.2.8 In vivo tests	158
6.2.9 HOPE SI editing	160
6.2.10 In-vivo tests	162
6.2.11 Discussion	163
6.3 Zero quantum coherence editing with a STEAM sequence	
6.3.1 Introduction	165
6.3.2 Coherence transfer	166
6.3.3 Calculation of the lactate signal for STEAM	167
6.3.4. Simulations	168
6.3.5 Experimental verification of the T_m modulation of the signal	170

6.3.6. Quantum Coherence Editing	172
6.3.7. Editing methods	173
6.3.8. Editing with an interleaved sequence	174
6.3.9. Editing lactate from lipids	175
6.4 Discussion - comparison of HOPE and STEAM techniques	178
7. In-vivo SI studies	
7.1 Introduction	180
7.2 Accuracy of in-vivo SI	181
7.2.1.1 Background	182
7.2.1.2 Methods	182
7.2.1.3 Analysis (<i>I</i>).	183
7.2.1.4 Analysis (<i>ii</i>).	184
7.2.1.5 Discussion	184
7.2.2 Errors introduced by image construction	186
7.3 Patient studies	189
7.3.1 Healthy volunteer study	190
7.3.1.1 Methods	190
7.3.1.2 Results	191
7.3.1.3 Discussion	191
7.3.2 Stroke patient study	191
7.3.2.1 Review of metabolite changes in stroke	191
7.3.2.2 Stroke study	196
7.3.2.3 Methods	197
7.3.2.4 Results	198
7.3.2.5 Conclusions	202
7.3.3 Ischaemic penumbra study	203
7.3.3.1 Introduction	203
7.3.3.2 Methods	203
7.3.3.3 Results	204
7.3.3.4 Discussion	204
7.3.4 Acute head injury study	205
7.3.4.1 Review of proton spectroscopy in head injury	206

7.3.4.2 SI acute head injury study -methods	208
7.3.4.3 Statistical analysis and results	210
7.3.4.4 Discussion	210
8. Conclusions	
8.1 Introduction	211
8.2 Pulse sequences and acquisition protocols	211
8.2.1 Hardware limitations	211
8.2.2 The SI pulse sequence and how it can be optimised	212
8.3 Data processing aspects	214
8.4 In-vivo findings with SI	215
8.5 Summary	216
A1 Quantum mechanical description of NMR using density operators and product operators	
A 1.1 Introduction	218
A 1.2 The density operator	218
A 1.2.1 Time evolution of the density operator	220
A 1.2.3 Expectation value of a measurable quantity	220
A 1.2.4 Density operator of a single spin 1/2	221
A 1.2.4.1 Time evolution	222
A 1.2.4.2 Evolution under r.f. pulses	223
A 1.3 Product operator expansion of the density operator	224
A 1.3.1 Application to a weakly coupled system of two spin 1/2 protons(<i>AX</i>) system	225
A 1.3.2 Classes of the <i>AX</i> product operator	226
A 1.3.3 Time evolution and r.f. pulses	226
A1.3.4 Free precession	228
A1.3.5 R.F. pulses	230
A2 Computer source code and pulse sequence listings	232

A3 Publications	273
References	275
Acknowledgements	286
Declaration	288

Symbols

B_0	static external magnetic field
B_1	applied radio frequency magnetic field
\mathbf{M}	magnetisation vector
ω_0	Larmor frequency of free precession
γ	proton nuclear magnetogyroscopic ratio
\hbar	Plancks constant
k	Boltzmann constant
σ	chemical shift of a metabolite
μ	proton nuclear magnetic moment (Bohr magneton)
T_1	longitudinal relaxation time (spin-lattice)
T_2	transverse relaxation time (spin-spin)
T_R	repetition time
T_E	echo time
J	spin-spin coupling constant of the lactate molecule (~7 Hz)
δ	chemical shift difference of the CH and CH ₃ spins of lactate (~183 Hz)
ϕ	phase angle of an FID
\hat{H}	Hamiltonian operator
$\hat{\rho}$	spin density operator
\hat{I}	spin product operator
ψ	nuclear wave function

Abbreviations

General abbreviations

NMR	Nuclear Magnetic Resonance
MRI	Magnetic Resonance Imaging
SI	Spectroscopic Imaging
CSI	Chemical Shift Imaging
FID	Free Induction Decay
RF	Radio Frequency
FFT	Fast Fourier Transform
VOI	Volume Of Interest
FOV	Field Of View
MEM	Maximum Entropy Method
PSF	Point Spread Function
PSD	Power Spectral Density
CT	Computed Tomography
PET	Positron Emission Tomography
SPECT	Single Photon Emission Computed Tomography
QC	Quantum Coherence

Pulse sequences

PRESS	Point Resolved Echo Selective Spectroscopy
STEAM	Stimulated Echo Acquisition Mode
HOPE	HOmonuclear Polarisation transfer Editing
ISIS	Image Selected In vivo Spectroscopy
EPI	Echo Planar Imaging
PEPSI	Proton Echo Planar Spectroscopic Imaging
FLASH	Fast Low Angle Shot
PRESTO	Point Resolved Echo Shifted Train
CHESS	Chemical Shift SElective Saturation

Chapter 1.

Introduction

1.1 Background to the project

The work described in this thesis is concerned with the implementation of proton (^1H) magnetic resonance spectroscopic imaging (SI) techniques, using a routine clinical magnetic resonance imaging (MRI) scanner. The project was funded by the Medical Research Council of Great Britain, with the aim of studying the metabolic changes that accompany ischaemic brain injury, in particular stroke and closed head trauma. The work was carried out in the Department of Clinical Neurosciences of the University of Edinburgh, based at the Western General Hospital, Edinburgh. Prior to the author joining the group, a pilot study of brain metabolism in stroke had been instigated using single voxel ^1H proton spectroscopy. The technical aspects of this initial work were done by the author's supervisor Dr Ian Marshall, (Senior Lecturer in MRI, Department of Medical Physics, University of Edinburgh) whilst the clinical impetus came from Dr Joanna Wardlaw (Consultant Research Neuro-radiologist, Department of Clinical Neurosciences, University of Edinburgh). In late 1994, a spectroscopic imaging pulse sequence (PRESS -SI) was made available to the group by the manufacturers (Siemens, Erlangen, Germany). With the potential to show metabolite distribution throughout a whole slice of the brain as opposed to specific single voxel locations, the clinical advantages of the technique were obvious. As such the technical direction of the work moved towards transforming the raw data acquired from a SI acquisition into clinically meaningful images of metabolite distribution. In February 1995, the author joined the MRI Physics group, and the work carried out herein has been concerned with optimisation of the SI acquisition and processing methods in an attempt to gain accurate metabolic data from ischaemic brain disorders.

1.1.1 Summary of the work described in subsequent chapters

The theory that underpins MRI and NMR spectroscopy is complicated, a rigorous explanation of the physical principles involved requires a good deal of advanced physics and an understanding of atomic chemistry. In Chapter 2, this background theory is outlined for future reference in subsequent chapters.

In chapter 3, the equipment used (the Siemens Magnetom SP63 1.5 T MRI scanner) is described. An account of the methods for acquiring spectroscopic data using this machine are also given in this chapter with particular reference to the r.f. pulse sequences used. The additional preparational steps that are essential for a successful spectroscopic scan using this clinical machine are emphasised.

As the MRI scanner was used for routine clinical scanning for twelve hours a day, five days of the week, all the developmental and experimental work using the machine was performed out of hours. Therefore a large part of the work described in the thesis (roughly 50%) is concerned with optimisation and development of the data and image processing techniques - which do not rely on constant access to the MRI scanner. The bulk of the computer software used to process the data and construct the metabolite images was written in house. Chapter 4 describes these data processing methods in detail, giving critical comparisons with the techniques used by other groups working on SI in-vivo.

In chapter 5, a novel post acquisition data processing technique is proposed which removes sources of error from a volume selective (PRESS localised) spectroscopic image by normalisation with uniform phantom data. The need for such a normalisation is emphasised with quantitative in-vivo metabolite image measurements.

Using the acquisition and data processing methods described in Chapters 3, 4 and 5, the study of stroke patients with SI progressed. During the course of the study it became obvious that the signal from lactate (an important indicator of impaired oxygenation in the brain), was obscured by a lipid signal in many patients studied. The bulk of the work carried out in the last year and a half of the study was therefore focused on developing pulse sequences that are capable of editing lactate from lipids. The two techniques developed are

both based on the J coupling property of spins in the lactate molecule. The first sequence (a variant on the PRESS double spin echo sequence) utilises the transfer of polarisation between lactate spins. In the first part of Chapter 6, this technique is described in detail and the first in-vivo and spectroscopic imaging examples of spectra obtained using this technique are presented. The second technique uses a stimulated echo (STEAM) sequence to exploit the transfer of zero quantum coherence between the lactate spins.

In Chapter 7, the quantitative results of the in-vivo stroke and head injury studies are presented. The stroke study of 23 patients scanned within 72 hours of ischaemic onset constitutes one of the largest spectroscopic studies of stroke to date. A further smaller serial study of 9 patients scanned on 2-3 occasions is included. Finally the results from a pilot study (nine patients) of SI in acute closed head injury are given, this represents the first application of spectroscopic imaging techniques in head injury

In the final chapter the conclusions drawn from this work are discussed, with recommendations of how the techniques could be improved in further work

1.2 Historical development of NMR, MRI and in-vivo spectroscopy.

The first observations of Nuclear Magnetic Resonance (NMR) were made in the USA in 1945 by two independent groups based at Stanford (Bloch et al) and MIT (Purcell et al). When water molecules were irradiated with radio frequency (r.f.) electromagnetic radiation in the presence of a strong static magnetic field, it was noticed that a certain frequency of radiation was absorbed. It was later discovered that this radiation was subsequently re-emitted as spins returned to their ground state energy level corresponding to an alignment of the spin parallel with the applied magnetic field. In 1949 two independent groups, (Proctor and Yu) and (Dickinson et al) discovered that the frequency of absorption and re-emission of r.f. radiation by the proton spins, varied microscopically depending upon the chemical structure of the molecule to which the proton was bound. This effect, was called the *chemical shift* of the nucleus and gave chemists a tool with which to identify the composition and structure of molecules by analysing the characteristic frequencies present in the NMR spectra. To distinguish one species of proton from another the spectra must be very well resolved so as to identify different resonant frequencies (i.e. chemical shifts are very small). This meant that very homogeneous static magnetic fields were needed (1 part in

10⁹) and a good deal of effort went in to spectrometer design technology. In 1950 Hahn discovered the spin echo, which plays an integral part in modern day MRI and spectroscopy. A further important discovery made in the 1950's which had huge implications for MRI was that field gradients could give spatial mapping within the coil - Gabillard 1951. By 1953, commercial NMR spectrometers were available and the technique became universally adopted by chemists studying the resonance spectra of a variety of nuclei with integer and half integer spins (e.g. ¹H, ¹³C, ¹⁵N).

The extension of the technique as a method of determining the composition of biological tissue was a logical one and in 1956 Odelblad and Lindstrom published the first NMR data from excised biological samples. With technological advances, more homogeneous fields were achievable across wider bore spectrometers and by the late 1960's/early 1970's spectra had been collected from living rodents and human limbs and digits. Damadian et al in 1971, observed different relaxation times in the signal from healthy and cancerous tissue in the human arm. This finding was the basis of the T_1 and T_2 weighting used to produce contrast in subsequent MR images. Meanwhile high-resolution in-vivo studies of proton spectra were hampered by the "drowning out" of the small metabolite resonances by the abundant water signal. Consequently in-vivo spectral studies at the time focused on the ³¹P resonance, Hoult et al 1974.

In order to use the technique accurately in-vivo some form of spatial localisation of the collected signal was needed, this came about by using linear gradients in the static magnetic field to produce linear position dependent shifts in the resonant frequency and phase of the excited spins. Using such gradients, Lauterbur et al 1973, published the first NMR image of two test tubes, which was constructed using a back projection reconstruction algorithm. In 1976, Mansfield's group at Nottingham produced the first human anatomical image of the fingers. In 1978 Damadian et al produced the first whole body image of the human thorax using the FONAR technique. Mansfield et al 1978, produced images of even better spatial resolution using a line-scan technique. Around this time commercial medical imaging manufacturers became interested in the technique and by 1983 the first commercial instruments were on sale in the USA. The majority of these and subsequent machines being used today base their MRI sequences on the spin-warp phase encoding techniques developed by Edelstein et al in 1980 at Aberdeen. Frequency and phase encoding of the signal is conducive to Fourier image reconstruction (Kumar et al 1975) based on a two

dimensional fast Fourier transform (2D-FFT). As such virtually all MR images are nowadays constructed using Fourier methods.

With stronger fields being used in commercial MRI scanners (1.5 T) by the early eighties, and water suppression techniques being adapted from the solvent suppression pulses used in small bore NMR (Hore 1983, Patt and Sykes 1972), proton spectroscopy in-vivo became more realistic. In 1983 new MRI scanners were being produced with an in-built proton spectroscopic capability (Bottomley et al 1983). Previously any in-vivo spectroscopy had been carried out on research machines with purpose written pulse sequences.

Around this time the first spectroscopic imaging sequences were being used (Brown et al 1982, Maudsley et al 1983). These combined the volume selective localisation techniques of in-vivo spectroscopy with spatial phase encoding (previously employed in one dimension in spin-warp imaging techniques). The result was an array of spectra from a planar grid of voxels which with one acquisition gave spectroscopic data from a much larger spatial region than the previous single voxel techniques. From these spectral arrays, images corresponding to metabolite distribution were built up, the intensity from a given voxel being proportional to the concentration of the metabolite found in that voxel. The spatial resolution in these images was typically quite coarse as field strengths imposed a lower limit on the voxel size needed to collect a spectrum in which the metabolite peaks are distinguishable from noise. A further limitation is the need for sequence repetition with different phase encodings in two spatial dimensions. As such the majority of SI studies to date have been single slice images with a matrix size of 16×16 (Luyten et al 1989) or in cases where high fields were available 32×32 voxels (e.g. Hetherington et al 1995, at 4.1 T).

The coarse appearance of the SI together with the need for user involvement in constructing the images probably explains in part why the technique has been slow in becoming accepted by radiologists. There is also some doubt in neuro-radiological circles as to the general clinical usefulness of MR spectroscopy as a routine diagnostic imaging sequence. As a result the bulk of SI studies to date have been carried out in research hospitals and institutes with MRI physicist support. For the same reasons many MRI scanner manufacturers have regarded SI as an expensive side line. Indeed many of the top of the range scanners currently on the market in 1998 have yet to include SI sequences in the package (e.g. Elscint, Picker) despite the fact that the scanners are perfectly capable of supporting the sequences.

The need for phase encoding in two directions also constrained most SI sequences used in the late eighties/early nineties to one plane. With the advent of multi-slice/multi-echo SI sequences (Duyn and Moonen 1994) and echo planar (EPI -after Mansfield 1977) SI sequences (PEPSI -Posse et al 1995, Adalsteinsson et al 1995) a multi-slice SI data set can be acquired in the time taken to acquire a single slice with 2D phase encoding. With many of the new scanners having the hardware capabilities needed to run such sequences, hopefully 3D SI will begin to become accepted as a viable and useful imaging modality with its unique ability to provide comprehensive spatial information on the distribution of metabolites within tissue.

1.3 Alternative methods of imaging brain metabolism and physiology

Before describing the metabolites that can be detected using proton spectroscopy, alternative metabolic and physiological imaging techniques will be reviewed with particular attention being paid to hypoxic injuries such as ischaemia and head injury. The advantages and disadvantages of these techniques when compared with spectroscopy will be emphasised as will possible ways in which they can complement a spectroscopic examination.

1.3.1 Metabolic imaging

Using positron emitting isotopes (generated in a particle accelerator), Ter-Pogossian et al 1975 pioneered the technique of Positron Emission Tomography (PET). The range of positron emitting nuclides that can be used with a PET scanner (e.g. ^{18}F , ^{14}C , ^{15}O and ^{13}N) is greater than with Single Photon Emission Computed Tomography (SPECT). Many of them are less harmful as a result of their short half lives. This allows the use of higher activities than with SPECT and also makes repeated measurements possible. PET has increased the metabolic capability of nuclear medicine. In particular the nuclide ^{14}C -deoxyglucose allowed Sokoloff et al 1977, to study cerebral glucose metabolism. Furthermore the isotope ^{15}O allows monitoring of cerebral oxygen uptake and offers an alternative method of monitoring cerebral metabolism and tissue oxygenation (Broich et al 1992). As such PET has enabled regions of hypoxia and reduced glucose metabolism to be imaged, as well as enabling maps of regional cerebral blood flow (rCBF) to be computed whereas SPECT is more suited to regional cerebral blood volume (rCBV) images. Much

work has been done more recently on PET/SPECT tracers for CNS receptors such as dopamine and serotonin. Variations in the levels of these receptors is established in nervous disorders such as Alzheimer's disease and Huntington's disease, their involvement in ischaemia appears to be less significant. The ability of PET/SPECT to monitor such receptors may have a role in functional imaging of neuro-activity but is less useful in metabolic imaging.

Modern PET scanners are capable of achieving a finer spatial resolution (5-6 mm). The major disadvantage of PET systems is that they are very expensive (£2m+ in 1997). The short half-life of the radio-nuclides requires an on site particle accelerator and chemical synthesis laboratory. As a result PET facilities are currently restricted to large hospitals with major research programmes.

1.3.2 Physiological imaging

Whilst PET and MR spectroscopy are the only imaging modalities that give an indication of metabolic activity, other techniques such as Single Photon Emission Computed Tomography (SPECT-Kuhl and Edwards 1963), Computed Tomography (CT - Hounsfield 1973), Trans-Cranial Doppler Ultrasound (TCD-Aaslid et al 1982) and MRI (after Lauterbur et al 1973) may provide complementary physiological information on blood perfusion, oedema and cell wall viability. Routine anatomical brain imaging at present amounts to CT and to a lesser extent T_1 and T_2 weighted MRI. These modalities are excellent indicators of brain anatomy, however they may be less effective in highlighting ischaemic injury in the acute stage and in particular areas of potentially salvageable tissue. The advantage of CT is its acquisition speed (a few minutes) compared to fifteen minutes for a typical MRI examination. CT does however rely on the use of ionising radiation and as such is potentially harmful, whereas no known side effects of non-invasive MR techniques have been found to date. A typical CT head scan delivers 2.0 mSv of radiation (the equivalent of 100 chest X-ray scans or 1 years background radiation) and has a risk of 1 in 10 000 of inducing a fatal cancer. In a clinical MRI - CT comparative study of acute cerebral infarction, Bryan et al 1991, found that in the first 24 hours following the insult that 82 % of the study group had MR visible infarction whilst only 58 % were CT visible.

These findings indicate that conventional MRI is more sensitive than CT in picking up changes in the early stages of ischaemic injury. In a T_2 weighted MRI, there is a hyper intensity caused by the swelling of cerebral oedema. In the early stages of ischaemia,

oedema may not be very severe and as such no abnormality may be apparent in the image. With more advanced MR imaging strategies such as MR angiography, diffusion weighted MRI and perfusion MRI, the physiological processes that precede oedema and infarction could be highlighted.

Conventional MR angiography techniques use arterial spin-tagging or the injection of a bolus of paramagnetic contrast agent into the blood stream, to provide image contrast. If the brain is imaged quickly using a fast imaging sequence (e.g. EPI Mansfield 1977) then the contrast agent will have largely remained in the major blood vessels within the brain. The images will therefore highlight the major arterial and venous structure. As such the technique is effective at indicating macro-perfusion abnormalities such as aneurysms and major vessel occlusions which could cause the onset of ischaemia. An alternative/complementary method of studying large scale cerebral blood flow is TCD, which can register turbulent blood flow in partially occluded vessels. This technique was used in conjunction with the SI study of stroke patients discussed in more detail in Chapter 7. The technique has the advantage of being relatively cheap as the apparatus costs tens of thousands of pounds compared to hundreds of thousands for an MRI scanner.

Blood perfusion deficits on a microscopic scale can be imaged with PET and SPECT to give estimates of rCBF and rCBV. The first technique to be used to produce tomographic images of the brain was Single Photon Emission Computed Tomography (SPECT) (after Kuhl and Edwards 1963), which detects the signal from gamma emitting radio-nuclides injected into the patient, using a gamma camera. Rotation of the camera allows a series of planar images to be obtained. A tomographic image is then constructed from the planar images using a back projection technique. The radio-nuclides normally used in SPECT are Technetium-99m and Iodine-123, which can be attached to various ligands. When administered intravenously these radio-pharmaceuticals are distributed in proportion to blood flow. SPECT images of the brain can therefore give a good indication of rCBV. The resolution of a modern SPECT gamma camera is a pixel of nominal width 12 mm (at full width half maximum). This compares favourably with state of the art NMR spectroscopic imaging techniques, but is much less well resolved than MRI/CT images. There is a relatively high radiation dose associated with the radio-pharmaceuticals used which limits the levels administered (8 mSv - 4 in 10 000 risk of inducing a fatal cancer). This in turn limits the precision of rCBV measurements from small anatomical regions. In addition the relatively long effective half-life of the radio-pharmaceuticals makes interventional studies (e.g. reperfusion drug tests) difficult to perform. Parallel SPECT - SI studies have been

conducted using stroke patients Graham et al 1994, and the results are promising showing a strong correlation between reduced rCBV and elevated lactate. The development of perfusion MRI as an alternative to PET/SPECT could reduce the chances of further PET/SPECT - NMR spectroscopic imaging parallel studies. This is because it is more convenient to carry out metabolic imaging and physiological imaging in a single scanning process. As such there is the possibility that the two fields will diverge further apart. If both facilities are available to the radiologist then it makes sense to try and correlate the metabolic and physiological information available with MRI/SI and that gained from SPECT/PET.

Work on MRI perfusion imaging in animals shows promising results (Rosen et al 1990). The methods used can be split into two categories according to the mechanism used for contrasting perfusion abnormalities. Arterial spin tagging methods (Edelman et al 1994) use successive fast imaging sequences (EPI) with spin inversion pulses applied and omitted alternately. Subtraction of the images from one another can give quantifiable rCBF estimates.

Alternatively the contrast in the abnormal region of perfusion can be achieved by monitoring localised changes in magnetic susceptibility (T_2^* changes). The degree of oxygen saturation of deoxy-haemoglobin in the blood plays a large part in determining the T_2^* in the adjacent area. Thus endogenous decreases in blood oxygenation levels will register as a deficit in hypo-perfused tissue imaged with a T_2^* weighted imaging sequence. This is the basis of Blood Oxygenation Level Determination (BOLD) image contrast, which has shown significant signal reductions in ischaemia and hypoxia (De Crespigny et al 1992, Turner et al 1991).

Paramagnetic contrast agents can be used as an alternative method of obtaining localised T_2^* contrast, following intravenous administration of a bolus. Fast T_2^* weighted imaging sequences (e.g. EPI Rosen et al 1991, BURST Duyn et al 1994) allow the determination of rCBF, rCBV and time of flight of the bolus. These techniques are currently more accurate than the other two contrast methods but do require invasive administration of contrast. Perfusion MRI can therefore give information on regions which may be in danger of infarction as a result of their impaired perfusion.

Diffusion weighted imaging has been shown to pinpoint areas that have already succumbed to the ischaemic process (Moseley et al 1990, Moonen et al 1991) where cells have undergone some degree of metabolic energy failure and are unable to regulate the normal concentrations of intra-cellular and extra-cellular water. These sequences use additional

strong “diffusion” gradients applied separately in three orthogonal directions to provide image contrast. Spin signals from regions of abnormally high diffusion will be more severely attenuated by the dephasing action of these gradients than will those from spins present in areas of abnormally low diffusion. Therefore impaired diffusion as might be expected in regions in which oedema has caused cell swelling and a decrease in extracellular space, will register as hyper intensity (reduced apparent diffusion coefficient ADC) on a diffusion image, (van Gelderen et al 1994). The technique also has a role in monitoring the late stages of stroke, as cell walls breakdown following infarction, water molecule mobility could increase causing the ADC to rise again (Szafer et al 1995).

With fast spectroscopic, diffusion weighted and perfusion sequences it is conceivable that all three scanning techniques could be integrated in one MRI examination, giving comprehensive information on brain metabolism and physiology. With the possibility of detecting ischaemia at a much earlier stage, such an integrated scan could be of great use in deciding upon the prescription of reperfusing neuro-protecting drugs (Minnematsu et al 1993, Peruche and Krieglstein 1993).

1.4 The metabolites imaged with ^1H MR spectroscopy

Proton spectroscopy has to date found most in-vivo applications in the human brain, where the spectroscopic volume of interest (VOI) can be strategically positioned so as to avoid excitation of sub-cutaneous lipids (Chapter 6). Having said this, ^1H spectroscopy of the prostate gland has been pursued giving unique information on the distribution of the metabolite citrate (Schick et al 1996). The brain is less prone to the motion artefacts found in the thorax and is probably the most stationary of all parts of the human body, prone to a slight respiratory and cardiac pulsatility and the inevitable patient movement. As such the brain presents an ideal site from which to collect ^1H spectra. In this section the proton metabolites found in healthy and diseased cerebral tissue will be described. Particular reference is made to the methyl spin resonances (methyl groups highlighted in bold) of metabolites that are visible at the long echo times (135 ms and above) used in this study. The primary methyl resonances of the metabolites choline, creatine, N-acetyl aspartate and lactate are illustrated in the spectrum of fig. 2.7. A much more detailed discussion of the distributions of these metabolites in ischaemic tissue and head injured brain is given later in Chapter 7.

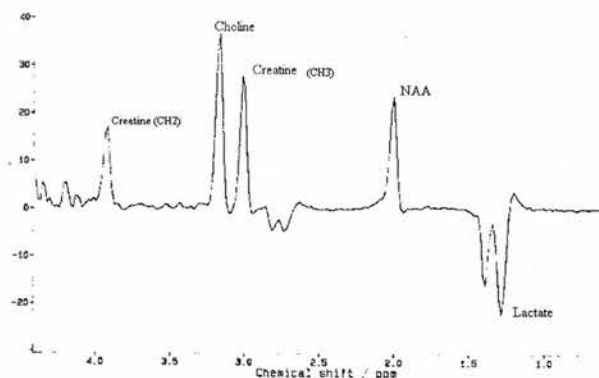


Fig. 1.1 The four main metabolites found in-vivo in ischaemic tissue, acquired using in-vitro samples.

1.4.1 Amino acids

Amino acids are the building blocks of proteins found throughout the body, in the brain and CNS they also participate in physiological neurotransmitter mechanisms.

N-acetylaspartate NAA (2.0 ppm) $\text{CH}_3\text{CO}\cdot\text{COO}\cdot\text{CHNH}_2\cdot\text{CH}_2\cdot\text{COOH}$

NAA is found in relatively high concentrations (5-10 mM) in normal adult brain tissue and is evident at short and long echo times as a well defined single spectral resonance. The fact that the NAA resonance is easily identifiable as a singlet (i.e. its lineshape is not complicated by J coupling) at long echo times explains in part why it is one of the most studied metabolites in ^1H MRS to date. NAA is an amino acid associated with neurones, being absent in oligodendrocytes and astrocytes in adult tissue extracts, (Williams et al 1995). In the infant brain, NAA concentration increases with age and is found in both neurones and oligodendrocytes, (Bachelard et al 1993). In NMR spectroscopy studies of degenerative neurological disorders other than stroke, e.g. brain tumours, Alzheimer's disease, MS, AIDS and epilepsy, reductions in NAA concentration were found (Christiansen et al 1995, Luyten et al 1993, Hugg et al 1993, Meyerhoff et al 1994). The fact that it is found only in neurones in adult brain and shows significant decreases in neurodegenerative disorders studied with spectroscopy has meant that NAA has become accepted as a marker of neuronal viability.

Amino acids with strongly coupled spins: glutamate, glutamine, GABA, aspartate.

(2.1-2.5ppm)

An additional set of resonances (not present in the sample of fig 1.1) is evident in the ^1H spectrum of brain tissue when short T_E (<50 ms) acquisitions are made. These species, all

amino acids, have strongly coupled spins and as such their peaks are J modulated. This makes their detection at longer echo times more complex as signals tend to cancel one another out. Blamire et al 1994, made spin echo acquisitions at $T_E=30$ ms & 270 ms and subtracted the first set of spectra from the second so as to remove the contribution from these spin-coupled resonances from the NAA peak. Similarly, Frahm et al 1989 attribute the apparent overestimate of the concentration of NAA, when compared to in vitro methods, to these resonances.

Despite being difficult to detect quantitatively, knowledge of the distribution of these amino acids could give vital metabolic information in diseased tissue. For instance, glutamate is an excitatory neurotransmitter and has been linked to the initiation of ischaemic neuronal damage. Studies of alterations in concentration of these metabolites in-vivo have been made (Frahm et al 1990, Kreis 1994). Their study is likely to become more popular as high field strength scanners (>1.5 T) become more common. At higher fields the frequency spacing of these metabolites becomes greater and the resolution of individual peaks is better.

Furthermore, stronger, quicker, actively shielded gradients will help in the detection of these metabolites as eddy currents will be reduced (thus minimising line broadening due to field inhomogeneity) and shorter echo times can be attained.

1.4.2 Choline (3.2 ppm) $\text{HO.CH}_2\text{CH}_2.\text{N}(\text{CH}_3)_3$

The choline resonance (3.2 ppm) arises from the methyl groups of choline containing intermediate compounds formed in phospholipid metabolism. Raised levels of choline might be interpreted as an indication of increased phospholipid turnover, (Luyten et al 1990). One possible source of phospholipid release is the breakdown of cell membranes in decaying tissue. In ^1H MRS studies of carcinogenic tissue in-vivo and in-vitro, choline levels have been found to rise.

1.4.3 Creatine (3.0ppm) $\text{NH}_2\text{CNH.NCH}_3.\text{CH}_2.\text{COOH}$

The creatine resonance encompasses two species; creatine (Cr) and phospho-creatine (PCr), which together are found in fairly constant concentrations of around 10 mM in human brain. Two distinct resonances are found, due to the N-CH_2 (3.9 ppm) and N-CH_3 (3.0 ppm) protons respectively. Creatine is found both in neurones and glial cells and has been proposed as an intermediary mechanism for phosphate transfer, acting as an energy buffer. The interplay between Cr and PCr in this metabolic reaction means that the total creatine resonance remains constant in healthy tissue. For this reason, the creatine resonance has been adopted as a constant internal reference for quantification of the other metabolites in

terms of ratios. Whether creatine remains constant in diseased tissue is uncertain and this method is open to flaws.

1.4.4 Lactate (1.3-1.5)ppm; $\text{CH}_3\text{CHOH.COO}^-$

Lactate is present in low concentrations in healthy brain tissue (less than 0.5 mM) and not normally detectable. The lactate resonance shows *J* modulation from a weak spin-spin coupling of the CH (4.1-4.3 ppm) and CH₃ (1.3-1.5 ppm) protons, as such its lineshape varies with changing echo time (see Chapter 6).

As a by-product of anaerobic glycolysis, that is induced by states of hypo-perfusion, lactate elevation might be expected in regions where there is an imbalance between glucose uptake and blood flow clearance. As lactate levels can rise dramatically over a short period of time in oxygen deprived tissue, lactate spectroscopy has received a lot of attention as an indicator of ischaemic and hypoxic pathologies (Chapters 6 and 9). Conditions of anaerobic glycolysis are not associated with brain pathology alone, lactate has been found in elevated levels using ¹H NMR spectroscopy in the visual cortex following optical stimulation (Sappier-Marinier et al 1992). Lactate spectroscopy is discussed in much greater detail in Chapter 6.

1.4.5 Lipids and macro-molecules (0.9-1.3 ppm);

Sometimes present in an ill defined broad resonance these signals were first thought to originate from fatty deposits within membranes. The immobility of membrane bound lipid molecules, severely restricts their *T*₁ and *T*₂^{*}. The observation of a large lipid signal therefore suggests an increase in molecular mobility. This was attributed to membrane degradation by Williams et al 1989. Recent work by Behar et al 1993 and 1994, suggests that the resonances found in this chemical shift range are not only due to lipids but macro-molecular proteins as well. Lipids and methods of distinguishing their peaks from lactate are covered in more depth in Chapter 6.

1.5 Summary

In this first chapter the historical evolution of MR spectroscopic imaging was described, and alternative/complementary imaging strategies were discussed. The chemicals (metabolites) that can be detected with the technique were also introduced. In the next chapter the background theory of NMR spectroscopy and MR imaging is treated in some depth as the principles are fundamental to understanding the work described in later chapters.

Chapter 2.

Physical principles of NMR and MRI

2.1 Introduction

In this chapter the physical principles behind an NMR experiment are discussed in terms of the intrinsic spin of the protons and the quantum energy levels available to the protons when an external magnetic field (B_0) is applied. The magnetisation that results from the occupation of these energy levels is then described classically and the Bloch equations which account for the effects of a B_1 r.f. perturbation are described. Using the Bloch equations, the response of a spin sample to simple r.f. pulse sequences are predicted. A more rigorous quantum mechanical description that uses density operators and product operators is given in Appendix 1, this is needed to understand the response of a coupled spin system to the pulse sequences described in chapter 6.

In the second half of this chapter the physical aspects of performing NMR localised spectroscopy and MRI in vivo are dealt with, namely localisation using orthogonal gradients. A brief summary of MRI imaging methods is given before dealing with NMR spectroscopic localisation and imaging techniques. The background NMR theory discussed in this chapter can be found in more detail in texts such as Canet 1996 and Callaghan 1995, the imaging aspects are well documented in books such as Morris 1986 and Brown and Semelka 1995.

2.2 Behaviour of a spin in an applied B_0 field

Nuclei consist of protons and neutrons, each of which has an intrinsic spin. Using quantum mechanics, the total spin of an arbitrary nucleus can be calculated by taking the vector sum of the component nucleon spins, I . When an external direction of measurement is imposed on this spin system (by the application of an external magnetic field for example), then quantum mechanics stipulates that only certain allowed quantum states or axes of rotation are available to the total nuclear angular momentum J .

This process of measurement is expressed in quantum mechanics as the application of an operator to the spin wave function of the nucleus. Defining the spin operator $\hat{I} = \frac{\hat{J}}{\hbar}$ and the nuclear spin wave function $|\psi\rangle$ then the following eigenvalue equation applies:

$$\hat{I}|\psi\rangle = \sqrt{I(I+1)}|\psi\rangle \quad (2.1)$$

This eigenvalue equation means in physical terms that if the total spin of the nucleus is measured it will have a value of $\sqrt{I(I+1)}$ where the total spin quantum number I can take integer or half integer values. If the axis of the direction of measurement (the external field) is set at z then the eigenvalue equation for the z component of the spin angular momentum is:

$$\hat{I}_z|\psi\rangle = m|\psi\rangle \quad (2.2)$$

The spin quantum number, m can take $(2I+1)$ individual integer or semi-integer values given by $-I \leq m \leq I$ providing that $\Delta m=1$.

In nuclei which have only a single unpaired nucleon such as ^1H , ^{13}C , ^{19}F and ^{31}P , then

$I = \frac{1}{2}$ and m can take only two values, $\pm \frac{1}{2}$ corresponding to the two eigenfunctions,

parallel (up) $|\uparrow\rangle$ and antiparallel (down) $|\downarrow\rangle$. Nuclei such as ^2H with two unpaired nucleons

(a proton and a neutron) have $I=1$, with $m=0, -1, +1$ and have three possible axes of rotation.

These individual spin states correspond to different alignments of the total nuclear magnetic moment of the nucleus with respect to the direction of the external field.

As this work deals with the NMR signals from proton containing species, then the analysis for a single proton is described. In chapter 6 and Appendix I, the interaction of spins from different protons in the same molecule are dealt with when the process of spin-spin coupling is discussed.

Now the total angular momentum of the single proton spin (of gyromagnetic ratio γ) has a classical magnetic moment μ . The energy of interaction of this moment with an applied field \mathbf{B}_0 along the z axis is given by:

$$E = -\mu \cdot \mathbf{B}_0 = -\gamma J_z B_0 \quad (2.3)$$

In quantum mechanical terms this energy of interaction is given by the eigenvalues of the Hamiltonian:

$$\hat{H} = -\gamma\hbar\hat{I}_z B_0 \quad (2.4)$$

The eigenfunctions of this Hamiltonian are again the up and down spin states $|\uparrow\rangle$ and $|\downarrow\rangle$ with respective eigenvalues corresponding to the of either state of ;

$$\begin{aligned} E_{\uparrow} &= -\frac{\gamma\hbar B_0}{2} \\ E_{\downarrow} &= +\frac{\gamma\hbar B_0}{2} \end{aligned} \quad (2.5)$$

The difference in energy between the two possible states is called the Zeeman splitting. Transitions between the ground state $|\uparrow\rangle$ and the excited state, $|\downarrow\rangle$ can be induced by irradiation of the system with a quantum of energy of frequency ω :

$$\Delta E = \hbar\omega = \gamma\hbar B_0 \quad (2.6)$$

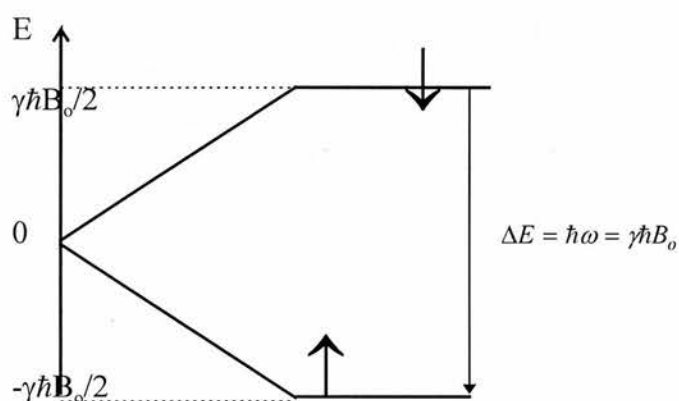


Figure 2.1. Splitting in energy levels of the two spin states of a proton

Now as this frequency of absorption is identical to the Larmor frequency (ω_0) of precession then it follows that a spin should interact with a magnetic field which cyclically rotates at the Larmor frequency. If any bulk effect following the irradiation of a sample containing protons is to be observed then there must exist an imbalance in the population of the two

energy levels. This is the case when the spin system is in a state of thermal equilibrium with the surrounding lattice and the population imbalance can be predicted from the Boltzmann distribution:

$$\frac{n_{\downarrow}}{n_{\uparrow}} = e^{-\frac{\Delta E}{kT}} = e^{-\frac{\gamma \hbar B_0}{kT}} \quad (2.7)$$

The total number of spins is given by:

$$n = n_{\downarrow} + n_{\uparrow} \quad (2.8)$$

And the difference in population of the up and down spin energy states is

$$n_{\uparrow} - n_{\downarrow} = n \left[\frac{1 - e^{-\frac{\gamma \hbar B_0}{kT}}}{1 + e^{-\frac{\gamma \hbar B_0}{kT}}} \right] = n \tanh\left(\frac{\gamma \hbar B_0}{2kT}\right) \quad (2.9)$$

At a field strength of $B_0 = 1.5\text{T}$ and at room temperature this fraction is equal to 7×10^{-7} , as such when performing NMR experiments under such conditions the tanh function in eq. (2.9) can be approximated $\tanh(x) \approx x$ for small x and (2.9) becomes

$$(n_{\uparrow} - n_{\downarrow}) / n = \left(\frac{\gamma \hbar B_0}{2kT}\right) \quad (2.10)$$

So at moderate temperatures and field strengths attainable in practice the fractional imbalance in populations of the two spin states is directly proportional to the strength of the external magnetic field B_0 . This imbalance gives rise to a net magnetisation M pointing in the positive z direction:

$$M_0 = (n_{\uparrow} - n_{\downarrow}) \gamma \hbar m = \gamma^2 \hbar^2 B_0 n / 4kT \quad (2.11)$$

As the majority of spins have a z component that is parallel rather than anti-parallel with B_0 there is a net magnetisation of the sample in the z direction given by M_0 in eq.(2.11). With no field applied parallel to x and y the spins are distributed in random directions within the xy plane i.e. they have random phases. This situation is represented pictorially in fig. 2.2.

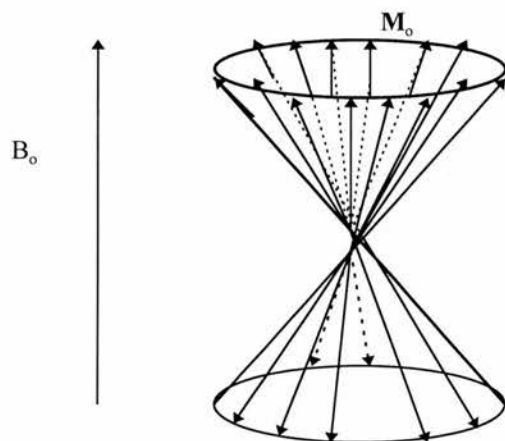


Fig. 2.2 Diagram illustrating how a fractional majority of the spins in a sample align parallel with the direction of an applied B_0 field rather than anti-parallel. (The direction of alignment of the spins is represented by their vector isochromats)

2.3 The chemical shift effect

So far in this treatment it has been assumed that the field felt by each proton spin is equal to the static B_0 field. In reality the localised field felt at a nucleus is perturbed by the precession of the molecular electron cloud's angular momentum in the B_0 field. The electronic shielding effect causes the perturbation in the field felt by the nucleus and consequently causes a change in the Larmor frequency of that nuclear spin. The offset of the resonant frequency due to the localised electron shielding is therefore directly related to the electron wavefunctions of the molecule. As such Larmor frequency offsets can be used as a method of classifying the chemical environment of the proton in resonance. The degree of offset from a reference proton spin (e.g. water) is quantified in terms of the chemical shift (σ) which can be incorporated in to the equation for the Larmor frequency (eq. 2.6)), as a perturbation to the gyromagnetic ratio:

$$\omega = \gamma(1 - \sigma)B_0 \quad (2.12)$$

This property is the basis of NMR spectroscopy, in that it allows the identification of a chemically distinct proton from its resonant frequency.

2.4 Classical behaviour of the net magnetisation vector

Staying with the treatment of the net magnetisation and disregarding chemical shift perturbations, the net magnetisation can be represented as a net magnetic moment \mathbf{M} . Were it possible to somehow displace the alignment of \mathbf{J} away from the z axis by an angle θ , then

the action of the B_0 field on the net magnetic moment, \mathbf{M} ($=\gamma\mathbf{J}$), is to exert a couple. The magnitude and direction of this couple is given by Γ :

$$\Gamma = \mathbf{M} \times \mathbf{B}_0 \quad (2.13)$$

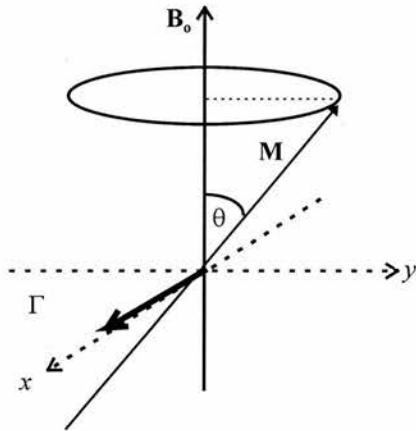


Fig. 2.3 The couple set up by displacing the magnetisation away from the z axis

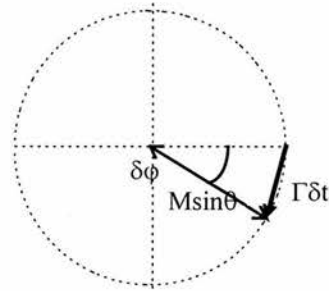


Fig. 2.4 Plan view in the -z direction

The effect of the couple Γ , is to increase the angular momentum according to the relation:

$$\Gamma = d\mathbf{J}/dt = (1/\gamma)d\mathbf{M}/dt \quad (2.14)$$

Therefore:

$$d\mathbf{M}/dt = \gamma \mathbf{M} \times \mathbf{B}_0 \quad (2.15)$$

The magnetisation therefore has an equation of motion (2.15) which describes a gyroscopic precession about the z axis with a frequency ω given by the resonant Larmor frequency;

$$\omega_o = \gamma B_o \quad (2.16)$$

In the previous paragraph it was mentioned that some mechanism of tipping the magnetisation, so that it has a component in the xy plane is required to initiate this precession. If a second time varying magnetic field \mathbf{B}_1 is applied rotating in the xy plane at frequency ω_1 , then (2.15) becomes;

$$d\mathbf{M}/dt = \gamma \mathbf{M} \times (\mathbf{B}_0 + \mathbf{B}_1) \quad (2.17)$$

where;

$$\mathbf{B}_1 = B_1 \cos(\omega_1 t + \psi) \mathbf{i} - B_1 \sin(\omega_1 t + \psi) \mathbf{j} \quad (2.18)$$

and \mathbf{i} and \mathbf{j} represent the unit vectors in the x and y directions of the transverse plane.

The B_1 field induces precessional motion of the bulk magnetisation in the yz and xz planes in a similar way that the individual spins precess about the z axis in the presence of B_0 . This compound motion is best considered by viewing the system in a frame of reference (x' , y' , z') rotating at angular frequency ω . With a rotating reference frame:

$$\frac{d\mathbf{M}}{dt} = \left(\mathbf{i} \frac{\partial M_{x'}}{\partial t} + \mathbf{j} \frac{\partial M_{y'}}{\partial t} + \mathbf{k} \frac{\partial M_{z'}}{\partial t} \right) + \left(M_{x'} \frac{\partial \mathbf{i}}{\partial t} + M_{y'} \frac{\partial \mathbf{j}}{\partial t} + M_{z'} \frac{\partial \mathbf{k}}{\partial t} \right) \quad (2.19)$$

The rate of change of the (x' , y' , z') position vectors (\mathbf{i} , \mathbf{j} , \mathbf{k}) for a frame rotating at an angular frequency ω is given by :

$$\frac{\partial \mathbf{i}}{\partial t} = \omega \times \mathbf{i} \quad (2.20)$$

Similarly $\frac{\partial \mathbf{j}}{\partial t} = \omega \times \mathbf{j}$ and $\frac{\partial \mathbf{k}}{\partial t} = \omega \times \mathbf{k}$, so (2.19) becomes;

$$\frac{d\mathbf{M}}{dt} = \frac{\partial \mathbf{M}}{\partial t} + (\omega \times \mathbf{M}) \quad (2.21)$$

Equating (2.17) and (2.21);

$$\frac{\partial \mathbf{M}}{\partial t} + (\omega \times \mathbf{M}) = \gamma \mathbf{M} \times (\mathbf{B}_0 + \mathbf{B}_1) \quad (2.22)$$

At resonance $\omega = \gamma B_0$ so (2.22) becomes;

$$\frac{\partial \mathbf{M}}{\partial t} = \gamma \mathbf{M} \times \mathbf{B}_1 \quad (2.23)$$

Equation (2.23) describes the torque action of the \mathbf{B}_1 field on the magnetisation vector, tipping it in to the xy plane. Now as the frequency of precession of the net magnetisation about \mathbf{B}_0 equals the frequency of rotation of \mathbf{B}_1 , i.e. $\omega_1 = \omega_0 = \gamma B_0$, then the magnetisation remains perpendicular to rotating \mathbf{B}_1 field. Therefore the magnetisation precesses about the \mathbf{B}_1 field at an angular frequency γB_1 whilst precessing about \mathbf{B}_0 at frequency γB_0 . The compound motion of simultaneous precession about two axes is called a nutation and is analogous to the nutational motion of a gyroscope spinning in a gravitational field.

So application of a pulse of radio frequency radiation in the form of a \mathbf{B}_1 field, will tip the magnetisation in to the xy plane. To apply such a \mathbf{B}_1 field requires a secondary r.f. coil aligned with its axis perpendicular to \mathbf{B}_0 through which a sinusoidally varying current of radio frequency $\omega_0 = \gamma B_0$ is applied. The duration of the radio frequency pulse t_p determines the degree of tipping (the flip angle θ) of the magnetisation vector from the z axis;

$$\theta = \gamma B_1 t_p \quad (2.24)$$

Having been tipped such that it now has a component in the xy plane, the precession of the magnetisation vector \mathbf{M} constitutes an alternating magnetic flux. This induces a current in the \mathbf{B}_1 conducting coils that are arranged perpendicular to \mathbf{B}_0 . These currents can be detected using phase sensitive receivers enabling the measurement of the magnetisation response of a bulk sample of protons resonating at their Larmor frequency. Thus the response of a sample containing protons, to an arbitrary sequence of r.f. pulses can be detected as an induced current in the receiver coils, this signal is called the free induction decay (FID).

2.5 Evolution of the net magnetisation in the absence of r-f fields - the Bloch equations

Supposing a radio frequency pulse has rotated the magnetisation through 90° in to alignment with the x axis (a 90°_y pulse). The time evolution of the magnetisation in the absence of any further r.f. pulses can then be predicted classically by considering the damping effects of relaxation on the free precession. In a similar way that the equations of motion of a damped pendulum are obtained, this analysis leads to the Bloch equations of

magnetisation evolution (Callaghan 1996). Alternatively a quantum mechanical treatment can be used by considering the Hamiltonian of a single spin in free precession starting from a spin state I_x , i.e. alignment with the x axis (Appendix 1).

In the transverse (xy) plane the net magnetisation is attenuated by spin-spin interactions leading to a transverse relaxation time of T_2 . However inhomogeneity in the B_0 field has an additional contribution to spin-spin dephasing and as such the transverse relaxation time constant can be separated in to two parts; the contribution from natural spin-spin effects

$$(T_2) \text{ and a } B_0 \text{ inhomogeneity effect } (k); \quad \frac{1}{T_2^*} = \frac{1}{T_2} + k$$

The longitudinal magnetisation relaxation undergoes a spin-lattice relaxation following the initial excitation to a value M_0 , this is quantified by the longitudinal relaxation time T_1 . T_1 relaxation is attributed to spin-lattice dephasing between the spin dipole itself and fluctuating induced dipole fields in the lattice (the lattice being the liquid in a phantom or the mobile liquids within an in-vivo sample).

If equation (2.22) is considered at resonance for a field $\mathbf{B}=\mathbf{B}_0+\mathbf{B}_1$, then the individual x,y and z components can be considered and the transverse and longitudinal relaxation incorporated so that in the laboratory frame equation (2.22) becomes:

$$\frac{dM_{x,y}}{dt} = \gamma(\mathbf{M} \times \mathbf{B})_{x,y} - \frac{M_{x,y}}{T_2^*} \quad (2.25a)$$

$$\frac{dM_z}{dt} = \gamma(\mathbf{M} \times \mathbf{B})_z - \frac{M_0 - M_z}{T_1} \quad (2.25 b)$$

If these equations are now considered immediately after the application of a 90°_y pulse which has rotated the magnetisation from alignment with the z axis in to alignment with the x axis, with no further r.f. pulses being applied (i.e. $\mathbf{B}=\mathbf{B}_0$), then;

$$\frac{dM_x}{dt} = (\gamma B_0 - \omega_r) M_y - \frac{M_x}{T_2^*} \quad (2.26a)$$

$$\frac{dM_y}{dt} = -(\gamma B_0 - \omega_r) M_x - \frac{M_y}{T_2^*} \quad (2.26b)$$

$$\frac{dM_z}{dt} = \frac{(M_0 - M_z)}{T_1} \quad (2.26c)$$

These differential equations can now be solved. When solving for the components of the magnetisation in the transverse plane it helps to define the complex transverse magnetisation as $M_t = M_x + iM_y$. The first and second differential equations can then be combined;

$$\frac{dM_t}{dt} = -\frac{dM_t}{dt} = -\left(\frac{1}{T_2^*} - 2\pi i\nu'\right)M_t \quad (2.26d)$$

Where the precessional frequency in the rotating frame ν' is defined as $\nu' = \nu_r - \nu_0$ where the Larmor frequency is ν_0 (in Hz) and the rotational frequency of the frame of reference is ν_r . Solving for the transverse and longitudinal components with the starting conditions of $M_t(0) = M_0$ and $M_z(0) = 0$ (magnetisation aligned with x axis) gives;

$$M_t = M_0 e^{\left(\frac{-1}{T_2^*} + 2\pi i\nu'\right)t} \quad (2.27a)$$

$$M_z = M_0 \left(1 - e^{\frac{-t}{T_1}}\right) \quad (2.27b)$$

These are the Bloch equations. With these and the vector equations from which they are derived [eq.(2.25)] the behaviour of a bulk macroscopic magnetisation resulting from an ensemble of spins can be described in terms of the magnetisation vectors M_x , M_y and M_z . For individual spins this classical analysis may also be applicable providing the magnetisation of the individual spin system can be described in terms of the three vector components. Such an example is an uncoupled single spin. When dealing with a system in which there is an interaction between more than one spin this approach fails and a quantum mechanical approach is necessary to predict the time evolution of a spin signal. This approach utilises spin density operators and is discussed in more detail in Appendix 1.

2.6 Spin manipulation based on the Bloch equations.

Having derived the classical Bloch equations, they can be used to predict the time evolution response of a single spin to various sequences of applied r.f. pulses that are used in spectroscopy. In the following examples the classical vector approach gives a more pictorial insight in to the evolution of the spin signal than the equivalent quantum mechanical approach which relies on the mathematical tools of Hamiltonians and spin density operators.

2.6.1 Averaging -repetitive r.f. pulses

In order to obtain a signal of sufficient strength in spectroscopy it is quite often necessary to repeat a given r.f. pulse sequence and average the successive acquisitions as the signal to noise ratio of a series of N averaged acquisitions is proportional to \sqrt{N} . Also in imaging sequences, repetitive excitations are needed with different amounts of phase encoding so as to provide spatial resolution. In a B_0 field aligned with the z axis, an individual spin magnetisation lies in equilibrium precessing about the z axis. Following the application of a B_1 r.f. pulse the spin magnetisation will tend to return to its equilibrium position. Ideally the subsequent excitation in the sequence should not proceed until this state of full relaxation has been reached, otherwise the strength of the signal from this and subsequent acquisitions will never be optimal. The time interval allowed between application of successive r.f. pulse sequences is the repetition time T_R . In order to obtain full relaxation T_R needs to be set at several times the longitudinal relaxation time T_1 . In certain NMR sequences, T_R is deliberately shortened so as not to allow the longitudinal magnetisation of the chosen spin (with its own characteristic T_1) to recover. This procedure is called partial saturation and is often used in imaging to provide contrast between the signals from species such as water and lipids. Returning to the role of the Bloch equations, the longitudinal magnetisation immediately before the next repetition of a single r.f. pulse of angle θ_y , after a time T_R is predicted as follows. An initial assumption is made, that the transverse magnetisation is negligible upon application of the successive r.f. pulse. This is achieved in practice by either choosing $T_R \gg T_2$ or by spoiling the residual transverse magnetisation with spoiler gradients. The z magnetisation residual just before the next r.f. pulse application is then equated to the magnetisation immediately after:

$$M_z(\theta_+) = M_z(\theta_-) \cos \theta \quad (2.28)$$

$$M_z(T_R) = M_z(\theta_+) e^{-T_R/T_1} + M_0(1 - e^{-T_R/T_1}) \quad (2.29)$$

Equating $M_z(\theta_-)$ with $M_z(T_R)$ gives an expression for the z component of the magnetisation immediately after the application of the r.f. pulse;

$$M_z(0_+) = \frac{M_o \cos \theta (1 - e^{-\frac{T_R}{T_I}})}{1 - e^{-\frac{T_R}{T_I}} \cos \theta} \quad (2.30)$$

Resolving this magnetisation in to the transverse plane along the x axis

$$M_x(0_+) = \frac{M_o \sin \theta (1 - e^{-\frac{T_R}{T_I}})}{1 - e^{-\frac{T_R}{T_I}} \cos \theta} \quad (2.31)$$

Eq. (2.30) allows the optimum flip angle (the Ernst angle) to be calculated corresponding to the maximum partial saturation signal. For values of $T_R/T_I > 3$, this angle is approximately 90° . In experiments where $T_R < T_I$, a smaller θ can give an optimum partial saturation signal, the residual transverse magnetisation in such cases can be dephased using spoiler gradients. The FLASH imaging sequence which is based on a repetition of a series of small θ flip angles uses such spoilers. These two relations can also be used to calculate the longitudinal and transverse magnetisation as a function of T_R and T_I and the flip angle θ . This treatment is utilised in chapter (5) where the spatial distribution of θ is non-ideal and as such the spatial distribution of the magnetisation that prescribes the volume of interest deviates from an oblong shape.

2.6.2 Inversion recovery

Equation (2.25c) can be applied to the situation of a 180°_x pulse at time equals zero, which inverts the magnetisation, this is then allowed to undergo T_I relaxation until a time t . At this point a 90°_x pulse is applied so as to sample the magnetisation in the transverse plane.

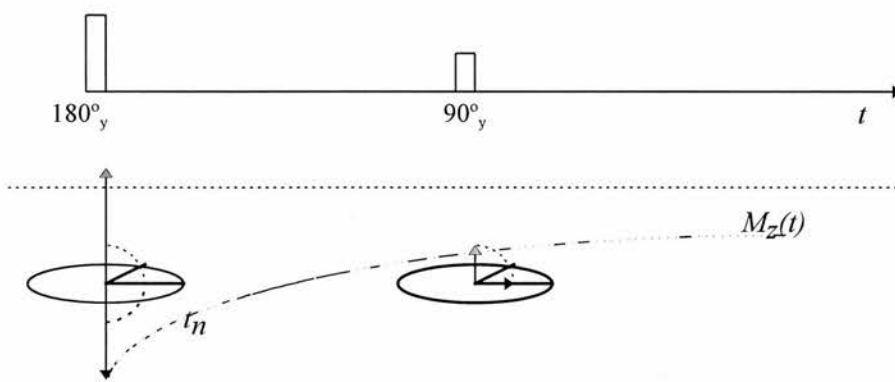


Fig. 2.5 The inversion

recovery r.f. pulse sequence, showing a null point at time t_n .

At a time t the sampled magnetisation is given by;

$$M(t) = M_0 \left[1 - 2e^{-\frac{t}{T_1}} \right] \quad (2.32)$$

From eq. 2.31 it can be seen that sampling the longitudinal magnetisation as it passes through the null point at a time $t_n = \ln 2 \cdot T_1$ will yield zero magnetisation (fig. 2.5). This forms the basis of a simple mode of signal suppression in imaging and spectroscopy. An ensuing imaging sequence commences after a time t_n , the null time of longitudinal inversion recovery of the resonance that requires suppression. This sequence also enables the calculation of T_1 with just one measurement.

2.6.3 The Hahn spin echo

In this experiment a 90°_x pulse is used to bring the longitudinal equilibrium magnetisation in to the transverse plane. Once in the transverse plane the net transverse magnetisation undergoes a T_2^* dephasing as a result of field inhomogeneities. The result is a splaying out of the spin isochromats in the rotational frame. If at a time τ later a 180°_y pulse is applied the direction of precession of the individual isochromats will be reversed in the transverse plane. Thus after a further time τ the individual isochromats will become rephased in alignment with the y axis and form an echo in the signal intensity. This is the principle of the spin echo and is represented pictorially in fig.2.6. The behaviour of the individual isochromats under the T_2^* dephasing effect can be described more rigorously by the spin operator formalism (Appendix 1).

The spin echo refocuses all dephasing due to field inhomogeneities and chemical shift (see section 2.4 for the T_2^* definition) as such all transverse attenuation is due to true T_2 alone. Conventionally the timing parameters are expressed in terms of T_E ($2\tau = T_E$). Hence the spin echo sequence is used for T_2 determination;

$$M(2\tau) = M_0 e^{(-2\tau/T_2)} \quad (2.33)$$

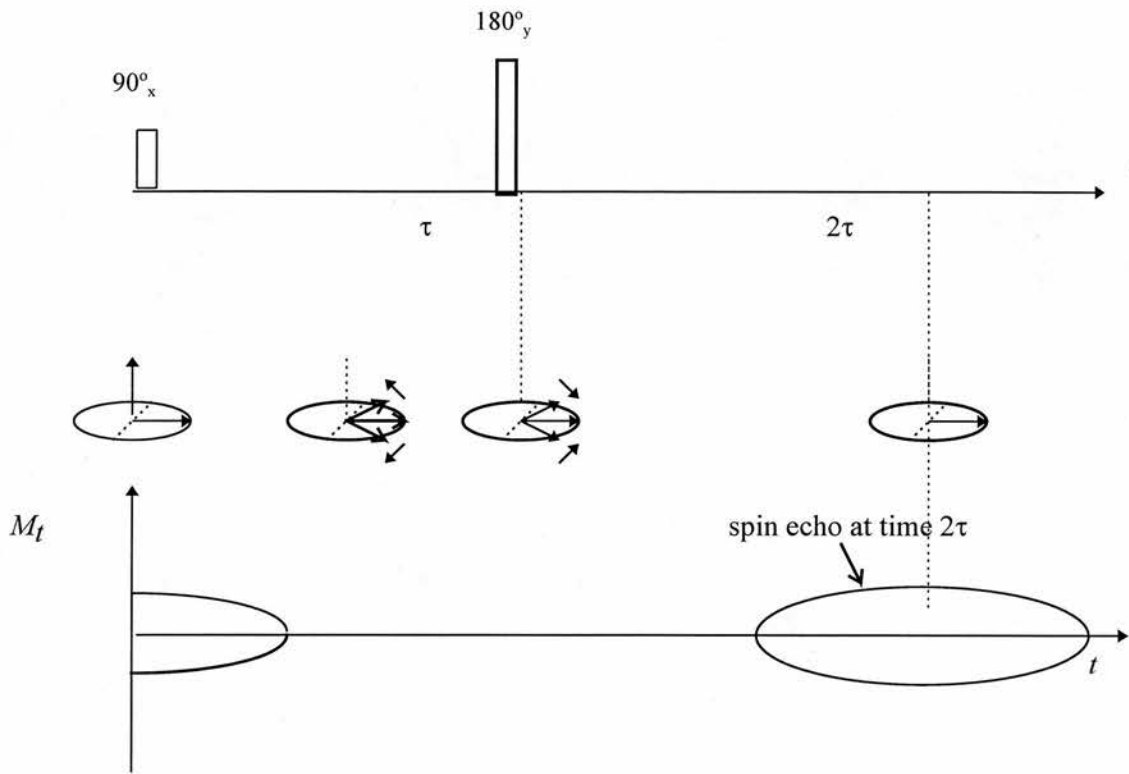


Fig. 2.6 The spin-echo r.f. pulse sequence, with a diagrammatic representation of the magnetisation evolution that leads to echo formation.

2.6.4 The stimulated echo

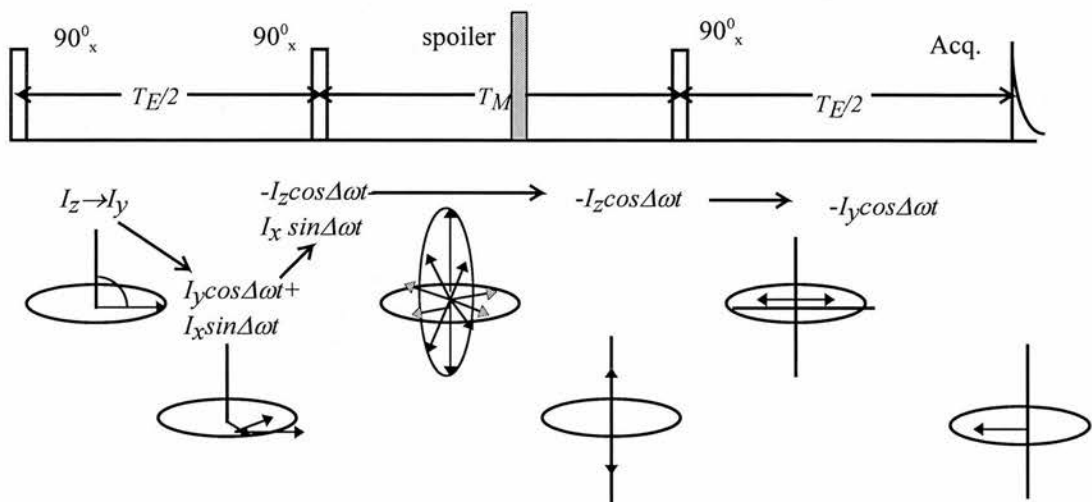


Fig. 2.7 The stimulated echo pulse sequence, indicating the evolution of the spin isochromats.

A 90^0_x pulse flips the longitudinal magnetisation in to alignment with the y axis ($I_z \rightarrow I_y$). A second 90^0_x pulse applied at a time $T_E/2$ later flips only the y component of the transverse magnetisation back into the z direction, the x component is unaffected. Half of the transverse magnetisation can thus be stored in the longitudinal direction during the mixing time T_m . A third 90^0_x pulse applied at the end of the mixing time flips the magnetisation back along the y axis which leads to the formation of a stimulated echo at a time of $T_E/2$ later as illustrated in fig. 2.7). The sequence also gives rise to two spin echoes - due to the refocusing of the first pulse's FID by the second pulse and the second pulse's FID by the third pulse. These are dephased by the homospoil gradient applied during the mixing time which dephases all transverse magnetisation whilst not affecting the longitudinal stored magnetisation needed to form the stimulated echo. The fact that the magnetisation is stored longitudinally during the mixing time means that it is possible to curtail T_2^* decay during this period. The stimulated echo will be discussed in more detail in the section on zero quantum coherence editing of lactate, where a STEAM (STimulated Echo Acquisition Mode) spectroscopy sequence is used.

2.7 Localisation using B_0 gradients

Localisation in both MRI and in-vivo MR spectroscopy is achieved by applying spatial gradient pulses in conjunction with the r.f pulses used for excitation (Lauterbur 1973 after Gabillard 1951). These gradients are perturbations to the main B_0 field and are typically less than 1% of the B_0 field strength.

The presence of a gradient (\mathbf{G}) within the magnet leads to a position (\mathbf{r}_i) dependent variation in the resonant frequency ω_i of a given spin i ;

$$\omega_i = \gamma(B_0 + \mathbf{G} \cdot \mathbf{r}_i) \quad (2.34)$$

These gradients are used to encode the x , y and z directions by means of frequency, phase and longitudinal position. The type of encoding used for a given direction is flexible and varies from sequence to sequence. As such a given point in space within the volume of excitation can be defined and Fourier transforms used to decipher these respective encodings.

2.7.1 Slice selection

A slice within the magnet is selectively magnetised by simultaneously applying a gradient pulse in the direction perpendicular to the slice and a frequency selective r.f. pulse with a given central resonant frequency and narrow bandwidth of typically 1-2 kHz. The presence of the linear gradient \mathbf{G}_s in the slice select direction will mean that only a certain spatial distribution of spins will match the Larmor frequency in eq.(2.34). The position of the slice is determined by the central frequency of the r.f pulse used. Further slices perpendicular to the slice select direction can be excited by applying further pulses centred about a different frequency in the presence of the same gradient. The size of \mathbf{G}_s dictates the thickness of the slices by the condition;

$$\Delta\omega = \gamma G_s \Delta z \quad (2.35)$$

Where $\Delta\omega$ is the frequency bandwidth of the r.f. pulse and Δz is the thickness of the slice in the slice select direction. Using fixed bandwidth pulses, the slice thickness can be increased by decreasing the amplitude G_s .

2.7.2 Frequency encoding in the readout direction.

The concept of frequency encoding is used in MRI to achieve spatial resolution in one of the directions within the plane selected by the slice select gradient. As an echo starts to form in the plane perpendicular to \mathbf{B}_0 (fig. 2.6) a linear gradient is applied in one of the directions

orthogonal to the slice select direction, (this is known as the readout direction). From eq. (2.34), spins distributed along this spatial direction will have their resonant frequencies modified in the acquired spin echo according to the size of the gradient at that point. As such the array of spins in k-space (the reciprocal space) is said to be frequency encoded in this direction. The range of frequencies ($\Delta\omega_R$) swept out by the readout gradient is set such that spins at the edges of the field of view (FOV) correspond to the Nyquist frequency, ω_N . This avoids aliasing and wrap around artefacts in the read direction providing that the object does not extend beyond the FOV.

$$\Delta\omega_R = 2\omega_N = \gamma\Delta\mathbf{G}_R \times FOV \quad (2.34)$$

The Nyquist frequency is in turn given by $\omega_N = \frac{N}{2\Delta k}$ where N is the number of points sampled and Δk is the sampling interval.

2.7.3 Phase encoding

The second in plane direction in an MRI slice (the phase direction) is spatially encoded using the technique of phase encoding (Edelstein et al 1982). In spectroscopic imaging (SI) phase encoding is often applied in both the in-plane directions (read and phase) as frequency encoding is pointless in spectroscopic imaging. The phase encoding gradient \mathbf{G}_p is varied between successive repetitions of the sequence. For a given value of \mathbf{G}_p the resonant frequency of spins along the phase direction is encoded according to eq.(2.33). When \mathbf{G}_p is subsequently turned off, the spin resonant frequency returns to its previous unencoded value. The increase in resonant frequency during application of \mathbf{G}_p adds a phase angle to the spin vector precession in the transverse plane orthogonal to \mathbf{B}_0 . During the subsequent repetition of the sequence the phase encoding gradient is stepped up such that the phase incurred upon cessation of \mathbf{G}_p is increased. Spins found at the edge of the FOV in the phase encoding direction will experience larger changes in phase for any given value of \mathbf{G}_p as a direct result of eq. (2.33). Spins at opposite ends of the FOV have phase angles differing by 2π . The number of phase encoding steps used is determined by the desired spatial resolution in the phase encode direction. Thus the voxel size can be reduced by increasing the number of phase encoding steps, whilst the FOV is reduced by increasing the range of \mathbf{G}_p . Fourier transforms can be used after acquisition to convert the phase encoded k-space data in to an array of voxels segmented in space.

The three gradient methods outlined above when used with selective r.f. pulses provide the spatial delineation in a conventional MRI. As an example, application of these three gradient methods to the simple spin-echo excitation pulse sequence of fig. 2.6, gives a standard spin-echo MRI sequence;

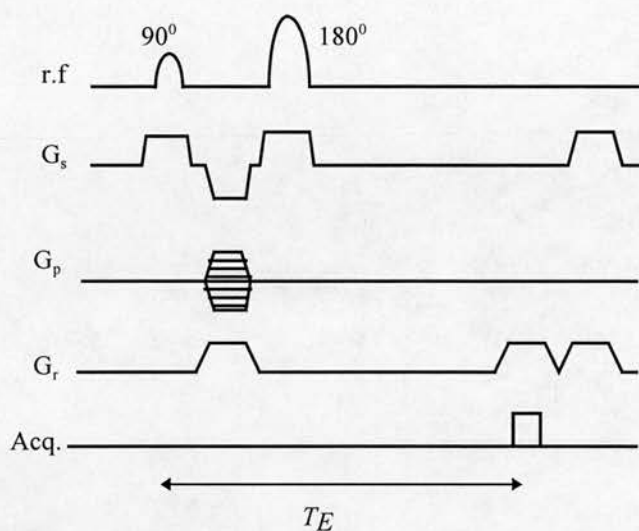


Fig. 2.8 A spin echo imaging sequence, the stepped values of G_p between phase encoding steps are represented schematically by the horizontal hatching of the gradient envelope. The ADC is switched on for a relatively short period around the point at which the echo has reached its peak amplitude. The echo does not persist for a long time as it is dephased by the read gradient. (In spectroscopy acquisitions (discussed in Section 2.8), there is no read gradient and the whole of the second half of the echo is sampled to gain the necessary frequency spectrum resolution).

Each of these gradient techniques have certain applications in both single voxel and SI localisation, particularly the use of phase encode and slice select gradients. Spectroscopic localisation methods are dealt with in the following section, before this the r.f. pulses used for excitation are discussed.

2.8 R.F. pulses

The shape of an arbitrary r.f. pulse in the frequency domain can be approximated for small flip angles ($<30^\circ$) by the Fourier transform (FT) of its time varying r.f. envelope. Thus a rectangular pulse will yield a sinc shaped profile in the frequency domain with a central frequency equal to the radio transmitter frequency and side lobes at either side. The bandwidth of the pulse is determined by the duration of the r.f. pulse, short sharp pulses or “hard” pulses give rise to broad band excitation at all frequencies. Conversely, elongated “soft” pulses give rise to a narrower bandwidth in the frequency domain, which when selected using gradients implies a narrower spatial range of excitation. The problem with the rectangular profile of a soft pulse is that the side bands become more significant in amplitude as the amplitude of the pulse is decreased and its duration increased. This will give rise to significant excitation at frequencies well away from the central transmitter r.f.

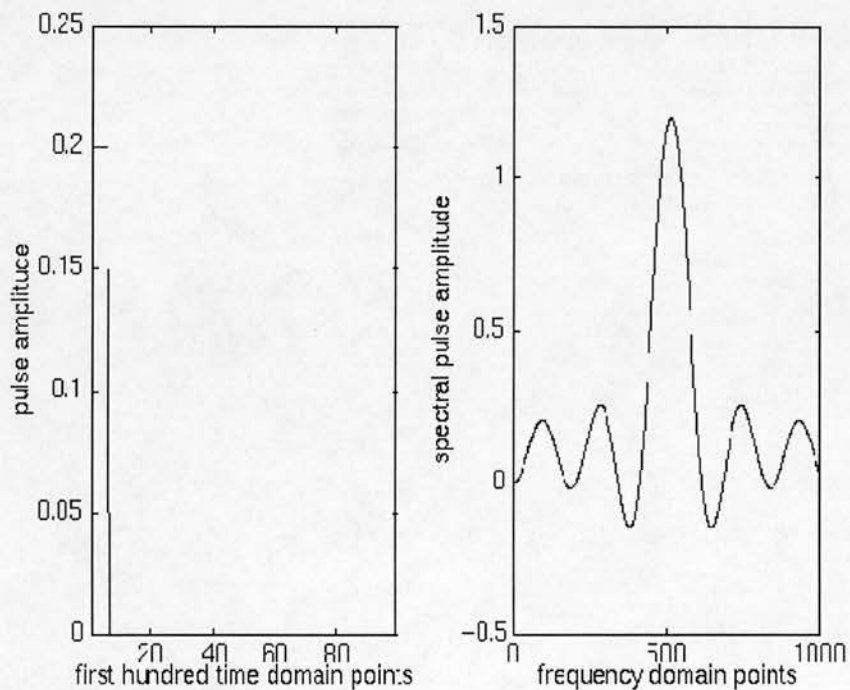


Fig 2.9 A simulated small flip angle short duration “hard” pulse, with a corresponding broad frequency bandwidth and significant sidelobes at all frequencies.

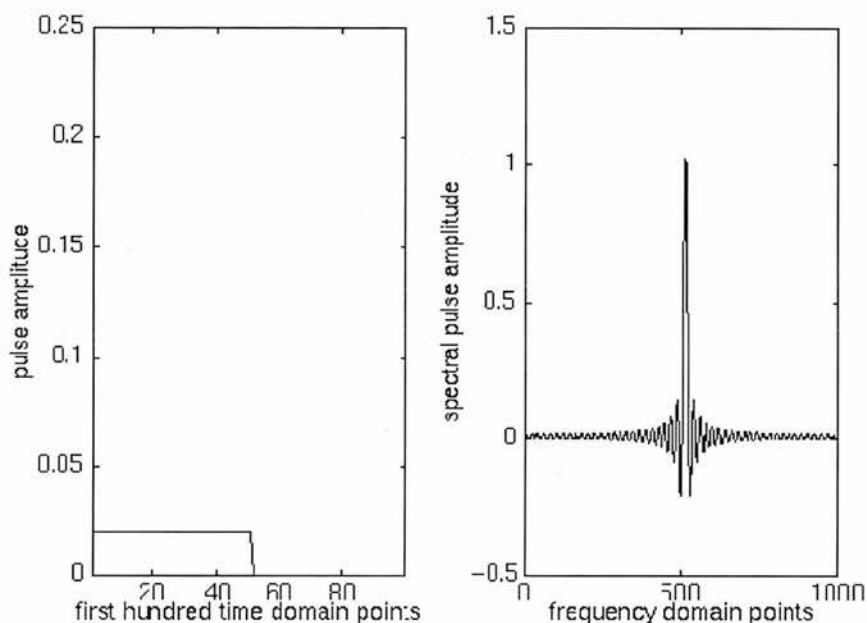


Fig. 2.10 A small flip angle “soft” pulse was simulated using a smaller amplitude and longer duration (area under pulse the same as in 2.9). The frequency response is much sharper with a narrower bandwidth and less excitation in the sidelobes away from the central frequency.

Complications arise from using the FT of the r.f. profile in that it assumes linearity in the Bloch equations. This approximation becomes particularly poor for large flip angles where non linearity in the Bloch equations becomes significant (Matson 1994). In practice selective uniform excitation over a given frequency range is achieved by using shaped pulse profiles with time varying pulse angle distributions numerically optimised using the Shinnar-le Roux algorithm (Matson 1994, Pauly et al 1991). If a rectangular frequency domain profile is sought then approximately speaking, a sinc modulated time domain profile is needed. The parameters needed to create such a pulse can be derived from numerical solution of the Bloch equations eqs. (2.25). Pulse shape optimisation for selective excitation is a branch of NMR in its own right and will not be dealt with in great depth here. It is worth mentioning one method of deriving the frequency response of an arbitrary time domain flip angle distribution, the Shinnar-le Roux algorithm. This uses digital filter theory to derive the frequency response of a time varying pulse angle distribution. This is done by numerical solution of the Cayley-Klein parameters (Pauly et al 1991).

From now on it will be accepted that different shapes of r.f. envelope give rise to specific frequency domain excitation responses. Hence different combinations of shaped pulses can give rise to excitation profiles that can be used to selectively excite and suppress individual

resonances. In chapter 5, the r.f. pulse shapes used to define the SI volume of interest (VOI) are discussed with particular reference to the non-linearity of the Bloch equations, whilst in the section on water suppression some of the spectral-spatial specialised pulse shapes are reviewed. Finally it is worth mentioning that there is a limitation on r.f. power delivered by a given r.f. pulse set by the maximum output of the transmitter amplifier. This imposes a restriction on both the amplitude and duration (and hence the minimum frequency bandwidth) of the r.f. pulse train used.

2.9 Spectroscopic localisation

In both single voxel MRS and multi-voxel SI, B_0 field gradients set up within the main coil are utilised in spatially locating the site from which a time varying FID or echo is collected. In single voxel MRS, the three gradient directions are used to slice select the corresponding r.f. pulses (i.e. no readout or phase encoding) and thereby localise the volume of intersection of the three slice select planes (fig. 2.11). This mode of spatial selection has a lot in common with the methods of slice selection employed in constructing MR images. In SI the field gradients are used to phase encode the magnetisation of free precession in one, two or three of the spatial dimensions. These two methods can also be combined to produce phase encoded spectra within a region of space defined by single voxel acquisition procedures (fig. 2.12). The useful minimum size of the voxels delineated by either mode of localisation, is dictated by the signal : noise ratio of the signals from metabolites within the volume of interest. At a typical clinical field strength of 1.5 T the smallest voxel size that will give a reliable in-vivo peak resolution, is around 1 cm^3 . This minimum voxel size scales in inverse proportion to the B_0 field strength as a consequence of the population imbalance described by eq. 2.10.

2.9.1 Single voxel localisation sequences

Since most volume selection techniques used for single voxel spectroscopy with clinical coils, employ the same principles as slice selection in 2D FT imaging then the selection of a spectroscopic VOI using imaging gradients is relatively straightforward.

2.9.2 Multi-shot methods

In multi-shot Image Selected In vivo Spectroscopy, ISIS, (Ordidge et al 1986, i), a series of eight (2^3) signals is added and subtracted in alternation to define a cube as the volume of

intersection of three planes. The ISIS sequence has largely been superseded by the more elegant single shot methods which give better outer volume suppression. Nevertheless, it still has the advantages that FID acquisition follows excitation immediately, minimising T_2 relaxation effects and more intricate signal combinations allow the definition of non cubical volumes.

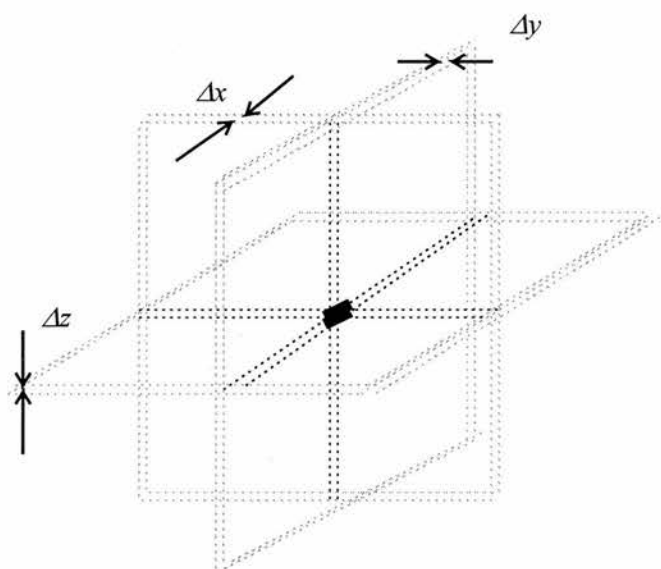


Fig. 2.11 Definition of a volume of interest by the intersection of three orthogonal slices of thickness Δx , Δy and Δz .

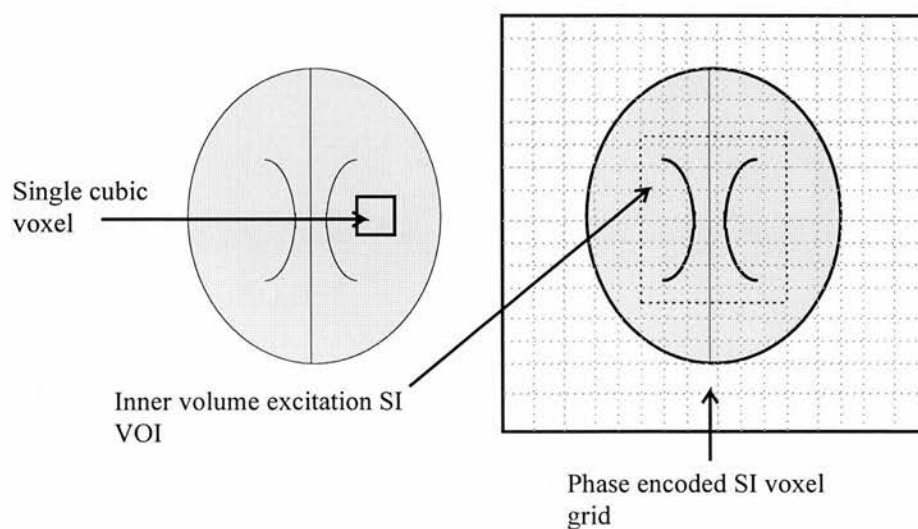


Fig. 2.12 Graphical representation of a single voxel and an inner volume SI VOI. Note how a SI localisation incorporates much more of the transverse section of the brain.

2.9.3 Single-shot methods

The modes of single shot spatial localisation (STEAM and PRESS) both rely on the sequential application of three orthogonal, slice selective r.f. pulses whereby an echo from the voxel of plane intersection is acquired. The size of this voxel is dictated by the bandwidth of the radio frequency combined with the strength of the pulsed gradients (eq.(2.34)) and its position by the central radio frequency.

2.9.3.1 STEAM

In Stimulated Echo Acquisition Mode (STEAM) -Frahm et al 1987, (see Section 2.5.4 for the definition of a stimulated echo), three frequency selective 90° r.f. pulses are applied in the presence of the orthogonal field gradients (fig 6.19). The transverse magnetisation is set up by the first pulse and is then transformed into a longitudinal magnetisation by the second pulse, which is then refocused as a transverse stimulated echo by the third pulse;

$$90_x^\circ - T_E/2 - 90_x^\circ - T_M - 90_x^\circ - T_E/2 - Acq.$$

During the first $T_E/2$ period a spoiler gradient pulse is applied to de-phase the transverse component of the FID of the previous r.f. pulse and prevent the formation of an echo upon application of the second pulse. Similarly, an identical gradient is applied in the second $T_E/2$ period to refocus the spins of interest in a stimulated echo and prevent the formation of an echo upon application of the third pulse. The period between the second and third pulse is known as the mixing time T_M , during which no transverse decay takes place as the magnetisation is stored in the z direction. The mixing time duration can be varied in order to observe longitudinal T_1 relaxation effects. During this period the longitudinal magnetisation is unperturbed by the transverse magnetic field gradients, and spoiler gradients can be applied to implement water suppression (CHESS - Frahm et al 1990, Moonen et al 1990) and to exclude echoes from outside the region of interest. The STEAM localisation sequence is based on the STEAM imaging sequence with the phase encoding and read gradients replaced with x and y slice select pulses with a slice selection pulse in the z direction. The second 90° pulse rotates only half of the transverse magnetisation (the y component) out of the transverse plane, the residual transverse magnetisation is spoiled. This results in a signal roughly half that of the equivalent spin echo (Payne et al 1994).

2.9.3.2 PRESS

The second method, PRESS (Bottomley 1989), stands for Point Resolved Spectroscopy which was developed from the Depth Resolved localisation sequence (DRESS), used with surface coils (Bottomley et al 1984). PRESS employs a double spin echo sequence consisting of a 90° excitation pulse followed by two 180° refocusing pulses.

$$90^\circ - T_{E1} - 180^\circ - (T_{E1} + T_{E2}) - 180^\circ - T_{E2} - Acq.$$

Each of these pulses is slice selected in one of the three orthogonal directions as with STEAM. The resulting signal should, being a double spin echo have twice the signal of an acquisition from a STEAM localised VOI. However the 180° pulses give a less well defined edge to a volume of interest than do 90° pulses (section 5.3) and so there is potential for some signal loss at the edge of a PRESS VOI. In order to reduce quantum coherence evolution, the first echo interval (T_{E1}), is made as small as possible ($T_{E1} < T_{E2}$). Spoiler gradients are again used to dephase spin signals from regions common to two of the slices, but outside of the cube defined by the intersection of all three slices. Water suppression can also be incorporated in to PRESS localisation using CHESS sequences but the suppression factors are less than with STEAM. The echo time of PRESS is generally greater than in STEAM and as such is suited to lactate detection in the presence of lipids of short T_2 .

2.9.4 SI sequences

In conventional SI, phase encoding gradients are applied in one, two or three orthogonal directions during the free induction decay. Acquisition then takes place in the absence of any gradients. When imaging an array of voxels, a different configuration of the x, y and z phase encoding gradients will be needed for each voxel acquisition. Thus the number of voxels imaged (different combinations of phase encode gradients), combined with the repetition time between acquisitions (which is in turn largely dictated by the acquisition time and T_1 decay), determines the overall acquisition time. The type of excitation pulses used varies from sequence to sequence, and depends upon whether the T_1 , T_2 , and J modulation effects of the spins of interest are to be enhanced or not. The basic SI localisation procedure consisted of a single excitation pulse with phase encoding applied during the free precession decay (Maudsley et al 1983). The main advantage of this simple sequence is its fast speed, resulting from the use of small angle excitation pulses, enabling the imaging of short T_2 metabolites. Single voxel localisation sequences (PRESS, STEAM)

using slice selection of the r.f. pulses can be used in conjunction with phase encoding to define a VOI limitation of the SI (Duyn et al 1992). This is particularly useful in brain imaging as a large cubic region of the brain can be excited without exciting the lipids in the skull and scalp. Using such inner volume excitation techniques there is a greater chance of achieving a good shim (see section 3.3.1) as regions of high B_0 inhomogeneity, such as the skull boundary can be excluded. These inner volume excitation techniques do suffer the drawback of exclusion of a large part of the FOV through the cuboidal limitation on the shape of the VOI. Alternatively the whole FOV can be excited and outer volume suppression (OVS) techniques can be employed to suppress signals from the scalp. This technique (Spielman et al 1991, Duyn and Moonen 1993, Posse et al 1994) makes use of user positioned spatial suppression pulses (inversion recovery pulses -see Section 2.5.2) to block out the signal from the skull. A combination of 8 overlapping pulses will define an inner volume of an octagon shape. The magnetisation excited by these pulses is subsequently dephased using spoiler gradients prior to the excitation and phase encoded acquisition that follows. Unfortunately not all clinical scanners are equipped with such user defined positioning of OVS pulses.

2.9.4.1 Single slice SI

If a single slice is selected with gradient pulses (e.g. STEAM or PRESS) and in plane 2-D phase encoding is applied, then a SI of the slice can be obtained (Roebuck et al 1993, Duyn et al 1992, Graham et al 1995). This is the imaging strategy used in this work (Chapter 3), where $n_x = 16$ and $n_y = 16$ in plane phase encodings were used (16^2 separate acquisitions). All 1024 data points of the spin echo are sampled for each phase encoding step with a repetition time of 1600 ms, allowing a single slice SI acquisition in 7 minutes. If the scanner is equipped with Echo Planar Imaging (EPI-Mansfield 1977) capabilities (i.e. fast switching gradients) then a time oscillating readout (x) gradient combined with a phase encoding gradient (y) allows the acquisition of $n_x \times N_t$ points per excitation ($N(t)$ is the number of time domain samples). The oscillation of the readout gradient with a constant phase encoding gradient leads to a non uniform sampling interval in the phase encode direction i.e. a zig-zag k_x - k_y space trajectory (fig.2.14) as opposed to the sequential line raster trajectory (fig.2.13) corresponding to 2D phase encoded sampling of k-space. Special 2D gridded reconstruction algorithms are needed to assist with Fourier transformation of the non-uniformly sampled data. The result is that only n_x independently phase encoded acquisitions are needed and for

a given repetition time. The overall acquisition time of a single slice Proton Echo Planar Spectroscopic Image (PEPSI) is a factor of n_x less than the equivalent 2D phase encoded sequence. Alternatively the phase encode gradient can be blipped on and off in time with the readout gradient, this gives a spiral k-space trajectory (fig .2.15) that samples two k_x planes per acquisition (Webb et al 1989). The size of n_x is determined by how many cycles of the readout gradient can be incorporated in to the period during which the echo is being acquired (i.e. the switching speed of the gradients is the limiting factor). If fast switching gradients are not available an alternative strategy is to acquire all the phase encodings for each time domain data point ($n=1...N_t$). This would require N_t separate acquisitions and as such a fast low flip angle imaging sequence is needed (e.g. U-FLARE Norris and Dreher 1993, FLASH Haase 1990). This strategy is only faster than traditional 2D phase encoding if $N_t < n_x \times n_y$. Consequently it may have useful applications in an experiment at very high field strengths (e.g. 4.1 T) which would facilitate a large number of spectroscopic voxels of small volume say an array of 64×64 . Similarly if only a limited spectral bandwidth is required for the imaging of a small ppm range, then N_t could be reduced and these methods would be faster.

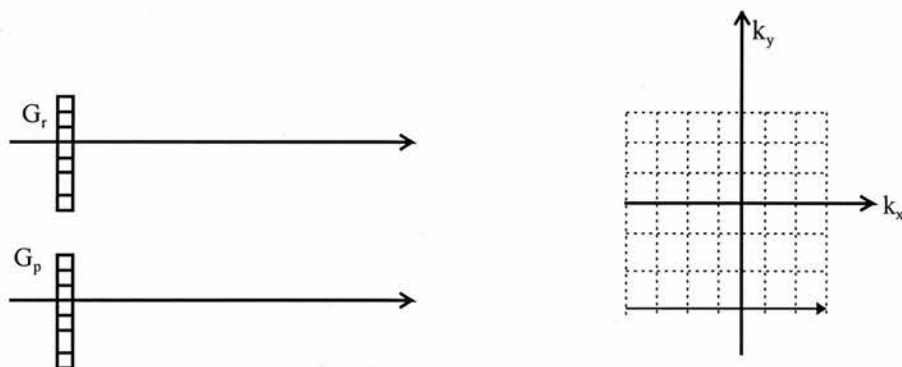


Fig.2.13. "Readout" gradient and "phase encode" gradient for single slice SI with phase encoding in both directions. Also shown is the k-space trajectory swept out during one cycle of the phase encode gradient (n_x separate acquisitions- readout phase encoding fixed). Successive repetitions with n_y different values of the readout (y) phase encode gradient are needed to sample the rest of k-space.

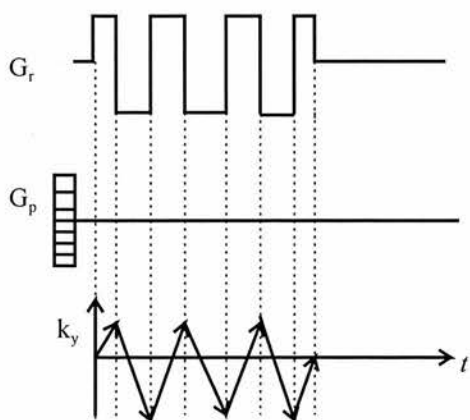


Fig. 2.14 Readout gradient and phase encode gradient for single slice PEPSI, the ramp time of the switched readout gradient was neglected. If it was included the zig-zag appearance of the k_y trajectory would be more rounded at the turning points due to the non-constant gradients. A total of n_x separate acquisitions is needed to cover the k_x dimension.

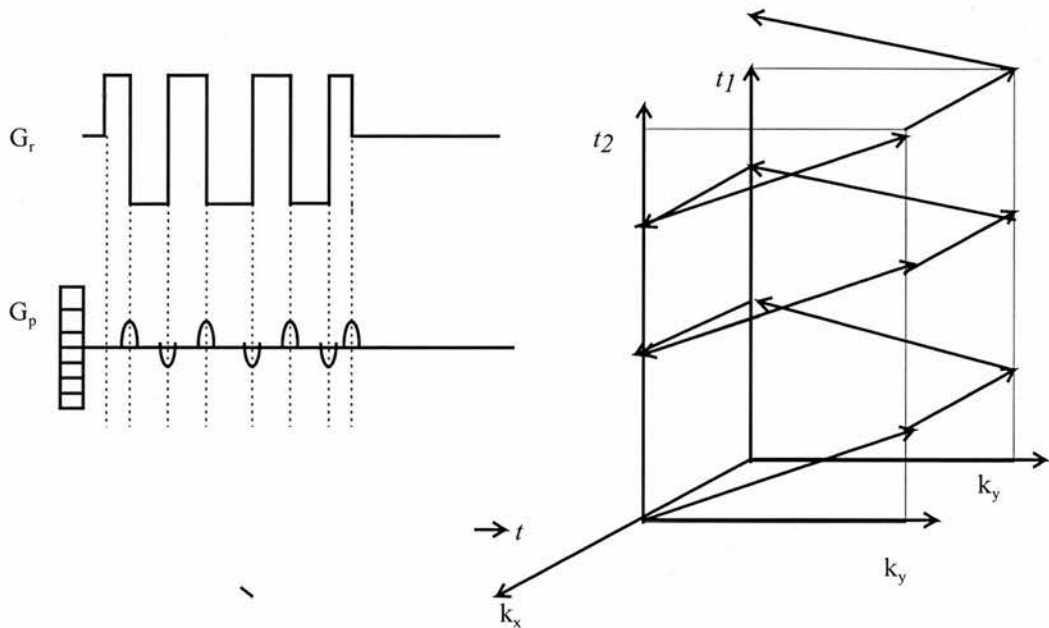


Fig.2.15 The blipped phase encode gradient of Webb, that gives a dual k_x plane spiral trajectory.

2.9.4.2 Multiple slice SI

The application of phase encoding in the x , y and z directions is the obvious way of acquiring a 3D spectroscopic image. Time limitations impose the constraint that $N_z < N_x$ and N_y . A further problem arises when a small number of phase encodings are applied in one direction, as the k space-real space FFT used to decode the information in this direction is more prone to inter voxel leakage (chapter 4). A more effective method of achieving 3D coverage is to interleave between N_z sequential multiple slices using N_z different frequency excitations in the presence of a slice select gradient (Duyn et al 1993, Spielman et al 1991). Duyn and Moonen 1993, increased the efficiency of this technique by acquiring multiple echoes ($n=3$) per excitation cycle, each of which is individually slice selected and sequentially phase encoded. The overall measurement time of a multi-slice, multi-echo sequence is a third of that of the equivalent multi-slice single echo version. There is however a slight decrease in spectral resolution as the total acquisition time (echo time \times no. of echoes) is limited by T_2 decay. If the individual effective acquisition time is less than the T_2^* of a given voxel then the spectrum from that voxel will have a reduced resolution

(Section 3.3). As such the technique is not suited to short T_E (as required for short T_2 metabolites e.g. glutamate) but is particularly effective if the T_2^* of the voxel is relatively short (poor B_0 homogeneity) as might arise when shimming across the SI VOI is poor. Hadamard encoding has also been used in the slice selection direction (Gonen et al 1995) combined with 2-D phase encoded in slice SI. This has the advantage that a smaller number of voxels can be applied in one of the dimensions without the compromise to spectral isolation caused by Fourier 'bleed' between voxels with a small number (e.g. $N_z = 4$) of phase encoding steps. As the Hadamard encoding can be acquired simultaneously to the phase encoding in an excitation of the whole VOI a reduction by a factor of $\sqrt{N_z}$ in the overall acquisition time is made over the equivalent single-echo multi-slice technique. If the scanner has fast gradient capabilities then a time varying read-out gradient can be used in one of the three spatial directions (z say) with phase encoding in the other two (an extension of single slice PEPSI to 3D) (Adalsteinsson et al 1995, Posse et al 1994). This allows a multiple number (n_z) of points in k-space to be sampled per phase encode acquisition and enables a 3D image to be built up in an equivalent acquisition time to a conventional 2D single slice SI.

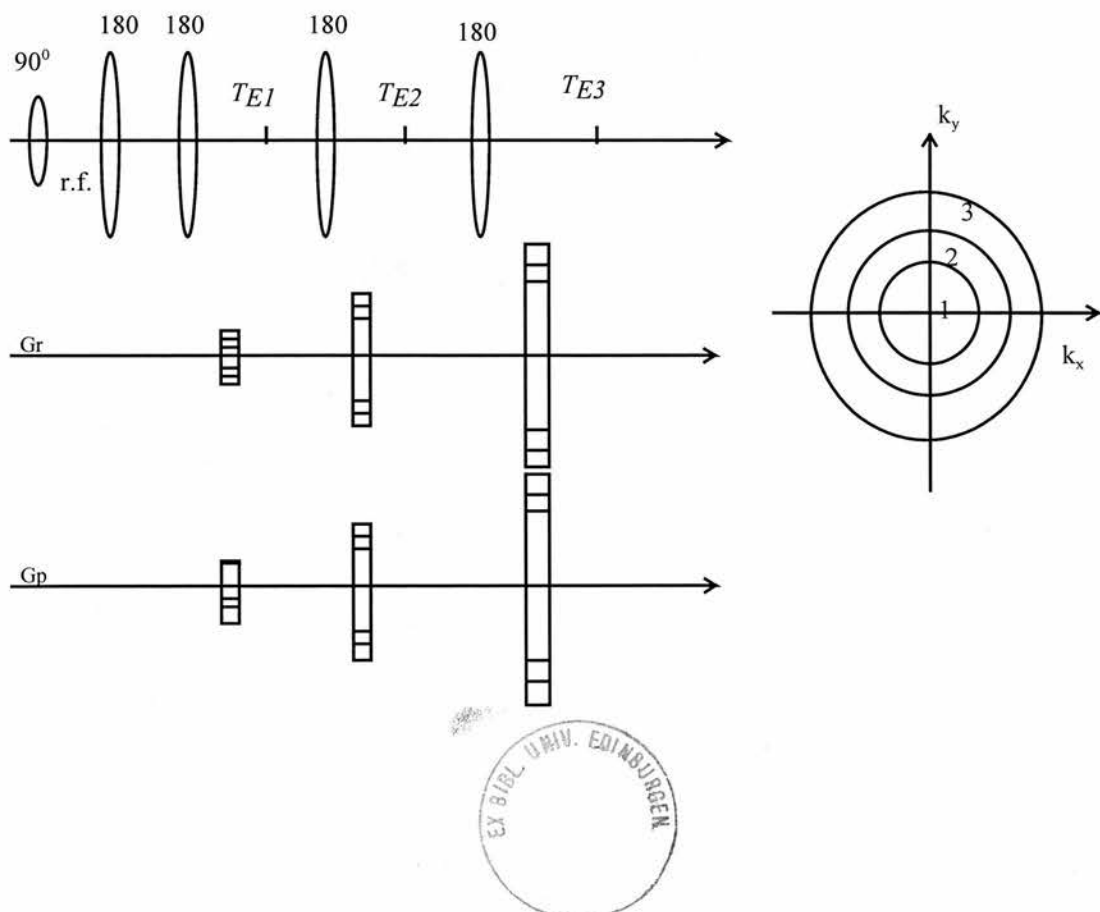


Fig. 2.16 The multi-slice, multi-spin echo SI sequence of Duyn and Moonen, each of the r.f. pulses is single slice selected. The sequence is then repeated with different r.f. frequencies. The k-space trajectory of the successive echoes is also shown with its concentric circle pattern.

2.10 Summary

Water suppression can be incorporated into these SI and single voxel sequences using CHESS, WEFT and frequency selective excitation pulses (see Section 3.4). Lipid suppression based upon the same principles as water suppression i.e. frequency selective excitation and selective inversion have been used to reduce Fourier leakage of unwanted lipid signals with the additional option of spatial selectivity (OVS). Similarly methods of outer volume suppression have been implemented allowing water suppression in the mixing time period of STEAM localised 3-D SI to reduce lipid and water Fourier bleed, from the scalp region (Duyn et al 1992, Posse et al 1994).

When comparing a SI with anatomical features it is important to remember that the SI plane of interest may have an axial voxel resolution that is greater than the separation of the adjacent MR image. In which case a mean MR image corresponding to the average of the contiguous MR images present in the SI slice ought to be considered (Maudsley et al 1994). An edge detected version of such an image is often used to overlay the SI to match chemical distribution with anatomy, but in so doing some visual bias is introduced in to the combined image. This can lead to further confusion as the edge detected image (and for that matter the SI VOI) corresponds to the water chemical shift and not that of the metabolite in the SI. Chemical shift dependent corrections can be implemented to account for this mis-registration (Chapter 5, Wild and Marshall 1997).

Inherent to all techniques of SI localisation is the Fourier artefact resulting from the oscillation of the sinc behaviour of the point spread function, however measures to minimise this artefact will be discussed in Chapter 4 dealing with post acquisition processing measures.

In summary, the smaller volume of interest used in single voxel acquisitions enables more precise shimming and consequently better water suppression than in SI. Finally much less post acquisition processing is needed. SI has the advantage that the volume of interest is much larger, meaning that the metabolite distribution over a much larger region of space

can be compared. With refinements in localisation, shimming and water suppression sequences, the signal to noise ratio of a spectrum from a SI voxel should be equal to that from a single voxel of the same size. However Fourier bleed from adjacent voxels, means that a SI voxel will have a noisier spectrum than the equivalent single voxel spectrum. In this chapter the physical principles that underpin spectroscopic excitation and gradient localisation methods used in present day in-vivo spectroscopy were outlined . Chapter 3 will go onto cover the equipment, preparatory methods and pulse sequences used in the course this study to acquire spectroscopic data.

Chapter 3.

Data Acquisition

3.1 Introduction

In this chapter the protocols for acquisition of single voxel and SI data sets will be discussed, with reference to the MRI scanner used to run the pulse sequences and the protocols followed. As a clinical scanner was used throughout the study, the flexibility of the hardware capabilities of the system was restricted. As such, any optimisations made to the acquisition procedure (e.g. pulse sequence design, shimming procedures and water suppression techniques) need to be compatible with the hardware and software capabilities of the machine used. In section 3.1 a description of the MRI hardware is given, followed by an outline of acquisition protocols (including pulse sequences) used when performing SI on this machine - Section 3.2. In Section 3.3 a detailed account of the shimming procedure, which is crucial to in-vivo spectroscopy, is given and similarly a detailed description of water suppression techniques is found in section 3.4.

3.1 The Siemens SP63 Magnetom MRI scanner -hardware and software descriptions

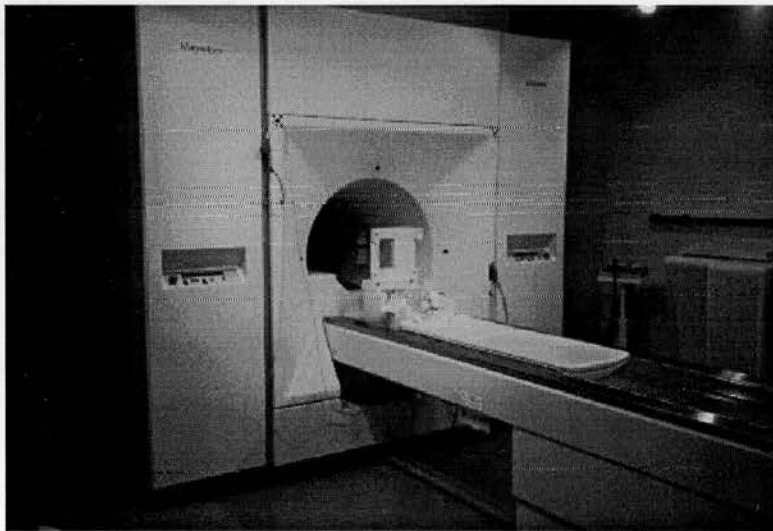


Fig. 3.1 The Siemens SP63 Magnetom MRI scanner used throughout this study.

3.1.1 The main B_0 and gradient fields

All of the work was performed using a clinical MRI scanner Siemens 63 SP 1.5 T Magnetom (Erlangen, Germany). This operates at a B_0 field strength of 1.5 T which gives a proton resonant frequency of 63.63 MHz. Such a high field strength is achieved by the passage of a large current through an axial arrangement of multiple closed loops of superconducting material (Niobium-titanium alloy). The superconducting coil needs to be maintained at temperatures below the critical superconducting temperature (4 K) and so requires a liquid helium/nitrogen cryogenic cooling system. As such much of the bulk that surrounds the B_0 coil is devoted to its cooling. The B_0 gradients of the scanner used for localisation and spoiling have a maximum output of 10 mT/m which when compared to the current state of the art scanners (30mT/m) is relatively weak. Perhaps more important is the rise time of the gradients i.e. the time taken for the gradients to reach their peak values. The Magnetom has relatively slow gradient performance (10 mT/m/ms) when compared to state of the art clinical scanners (up to 120 mT/m/ms). This means that pulse sequences that rely on rapid switching of the gradients (e.g. EPI) are not practically attainable on this system. Furthermore the gradient coils which are located within the main B_0 field coil are not actively shielded. This means that imaging sequences are prone to eddy current inhomogeneities due to the fluctuation of currents within the gradient coils. In order to perform localised excitation the orientation of these coils inside the bore of the B_0 coils is important. The G_x and G_y gradients are produced by a Golay arrangement of 4 saddle coils (fig. 3.2) whilst the G_z gradient is produced by an arrangement of axial loops in which the current direction is opposed (fig 3.2).

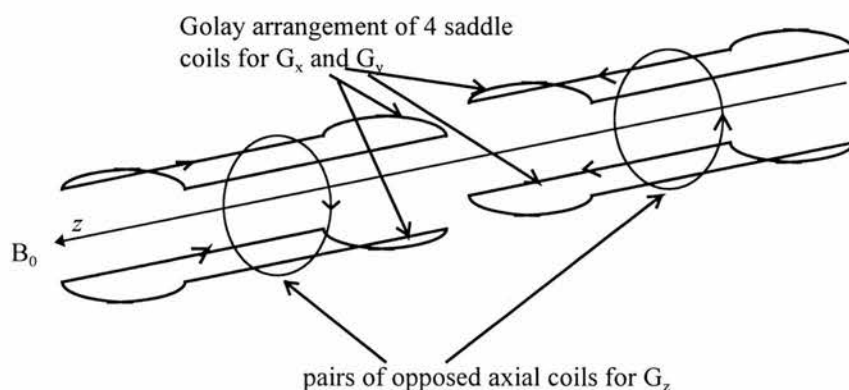


Fig.3.2 Gradient coil configuration, the arrows indicate direction of current flow.

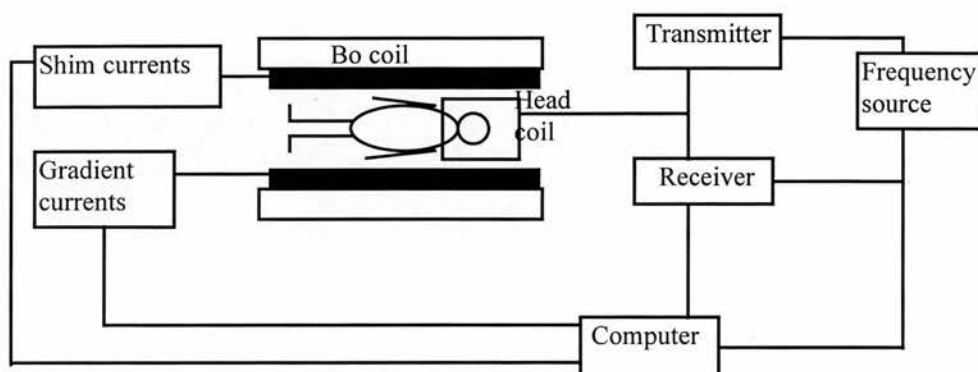


Fig. 3.3 Schematic diagram of the layout of a clinical MRI scanner (adapted from de Certaines et al 1992).

3.1.2 The R.F. (B_1) coil

The r.f. coil used throughout was a circularly polarised head coil (see fig. 3.4) which acts both as a transmitter (antennae) for the B_1 r.f. excitation pulses and as a receiver to detect the FID. Applying the principle of reciprocity, the stronger the B_1 field produced whilst transmitting implies a better sensitivity when receiving. The design criteria for a transmit-receive coil are therefore a large r.f. field for a given excitation power with a simultaneous small resistance, which means coils with high receiver quality (Q) factors. In practice it is often easier to have separate transmitter and receiver coils. A further point worth noting which is of equal importance in the design of the gradient coils is the stability of the current amplifiers. These deal with a wide range of input currents, depending upon the sequence being run and as such need to have a predictable output. R.f. coil design and the amplification and circuit impedance matching of the transmit-receive system is an engineering subject in its own right. As the head coil used here is of a standard clinical design without modifications, these aspects will not be discussed in detail here. It is worth noting however that the receiver coil detects two channels of data; the real and imaginary components of the sampled FID. These are 90° out of phase with each other hence the terminologies circularly polarised or quadrature detection. Furthermore the frequency of the signal received deviates from the transmitter frequency by only a few kHz. It therefore makes sense to de-modulate the transmitter frequency using the technique of phase sensitive detection which essentially amounts to the multiplication of successive points in the FID by ± 1 . The frequency of this sign change is the reference (Larmor) frequency ω_0 . This process

converts the frequency to a much more computer friendly figure of a few kHz as opposed to 60 Mhz.

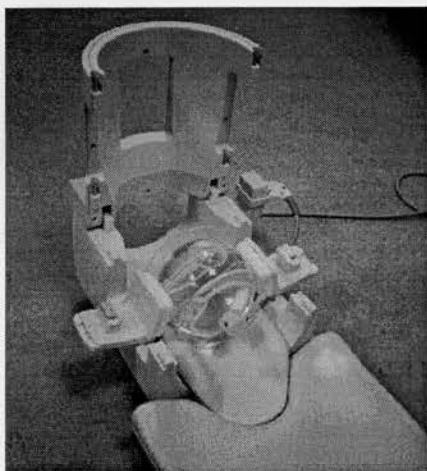


Fig. 3.4 The r.f. head coil used for brain imaging and proton spectroscopy, shown in the open position. In position is the Siemens acetate-lactate spectroscopy phantom.

3.1.3 The shim coils

From fig. 3.2 it can be seen that a set of shim coils are aligned concentric with the z axis (head to toe) of the magnet. These are positioned between the main B_0 coil and the gradient coils. The purpose of the shim coils is to attain as homogeneous field as is possible within the centre of the magnet. This is done by adjusting the currents within the coils either automatically or manually (Section 3.3) using the microprocessor control of the computer system. The shim process is essentially a fine tuning of the magnetic field and as such the currents used are typically less than 10 A. A detailed description of shimming is given later in section 3.3.

3.1.4 The computer operating system

The transmitter, receiver, shim coils and gradient coils depicted in fig.3.3 are all controlled by means of microprocessors driven by the computer operating system of the Siemens Magnetom - Numaris. This computer is also responsible for processing the raw sampled data in to MR Images or in the case of spectroscopy, spectra. The r.f. pulse sequences that are used to acquire data are written in a listed format indicating pulse duration and timing within the sequence. The code used for pulse sequences is known as PARGEN and is a Siemens language. PARGEN sequence files are compiled in a file appended with .UDB and are run in Numaris upon acquisition.

3.2 Acquisition protocols

3.2.1 Preparation

The acquisition of single voxel spectroscopy data and SI data follow the same preparation steps, the main difference lies in the pulse sequence used to acquire the data. Having placed the subject/phantom in the head coil, the coil is automatically tuned in the magnet room. The remainder of the preparation and acquisition programming takes place in the console room. The first step is to acquire localiser images using a turbo-spin echo imaging sequence (acq. time 15 seconds) with a square field of view (FOV) of 300 mm. When imaging human subjects it is also necessary to acquire more detailed images using a T_2 weighted spin echo sequence (acq. time 3 minutes, FOV 240 mm). The MR images can then be used to place the VOI. In single voxel spectroscopy this is done using the PRESS localisation program PRESS.UDB. In SI the program VOI.UDB is used to localise the VOI. A single voxel's dimensions are typically a cube of edge 20-24 mm, a SI VOI typically covers a cuboid of in plane dimensions 75×75 or 90×90 and thickness 15 mm. The gradients used for selective excitation of the r.f. pulses 2mT/m in all directions for single voxel localisation and 0.8 mT/m in plane and 3mT/m orthogonal in the case of SI. The size of the r.f. voltages needed to excite the VOI in a given subject are calculated by the Siemens program WORK_SRF_1HCSI_A27. Transmitter amplifier limitations restrict the maximum size of any one of the r.f. pulses to less than 292 V. This explains why the gradient strengths used for localisation are relatively weak when compared with the maximum output (10mT/m). The r.f pulses are at their maximum amplitude so as to allow a minimum time duration of the pulse thus facilitating a large frequency bandwidth which in turn needs weak gradients (- see Section 2.6). Having positioned the VOI and calculated the r.f. voltage needed the next procedure is to shim the magnet over the prescribed VOI and having done this, adjust the transmitter frequency back to ω_0 (63.63 MHz). The shimming process is crucial in spectroscopy if well resolved spectra are to be obtained, as such it is described in more detail in section 3.3. For the time being it is assumed that the magnet has been shimmed over the VOI.

Both the single voxel and SI PRESS sequences incorporate a preliminary single water suppression pulse (CHESS) of a 60 Hz bandwidth. This is used to excite the water signal which is subsequently dephased by spoiler gradients. The size of the water suppression pulse is optimised so as to give as small a water signal as possible. This process is carried out interactively by a trial and error procedure of setting the voltage and acquiring a

subsequent FID (acq. time 3s). On more sophisticated scanners this process could presumably be automated. A more detailed review of water suppression is given in section (3.4).

3.2.2 Acquisition

Having carried out these preparatory steps all that remains is to run the sequence. The single voxel PRESS sequence as supplied by Siemens has a total echo time of 135 ms, a repetition time of 1600 ms and 4096 time domain samples over a frequency bandwidth of 4000 Hz.

The PRESS SI sequence supplied by Siemens again has $T_E=135$ ms, $T_R=1600$ ms but only 1024 data points sampled per phase encoding step (frequency bandwidth 1000 Hz). In SI, phase encoding was applied in the x and y directions before the acquisition of the spin echo.

The number of phase encoding steps applied in human studies was generally restricted to 16×16 giving an acquisition time of 7 minutes. When performing SI on phantoms, a much smaller voxel can be used as metabolite concentrations can be made much greater than those found in vivo, and there is no restriction on acquisition time. Consequently 32×32

acquisitions were used with a smaller FOV (160 mm), with the specific aim of achieving a finer spatial resolution (0.5 cm square) across the VOI of excitation.

Two sets of data are acquired; one with water suppression and the other without so as to enable a zero order phase correction for the effects of eddy currents and field inhomogeneities (Ordidge and Cresshull 1986). The size of the signal must be small enough to fall within the dynamic range of the ADC of ± 10 V, to ensure this is the case, the receiver gain is set at 90 dB for a water reference acquisition and at 103 dB (the maximum possible) for a water suppressed acquisition in-vivo. In single voxel spectroscopy, the data is saved in a Siemens image file format (.IMA) whilst in SI the data is saved as raw files (.RAW).

3.2.3 Specification of the SI grid

Having collected the two raw SI data files and a set of transverse T_2 weighted and proton density images, a pictorial representation of the VOI and grid matrix was generated using the Siemens program WORK_CSI. The T_2 image coincident with the centre of the transverse spectroscopic image plane was taken and upon it was superimposed the VOI outline using the positions and dimensions chosen at acquisition. The voxel grid was then drawn in, if the edges of the voxels and the VOI are not coincident the grid mesh can be shifted by a fraction of a voxel in the coronal and sagittal directions (Section 4.9). This image is then saved as a Siemens .IMA file for SI display purposes (section 4.12).

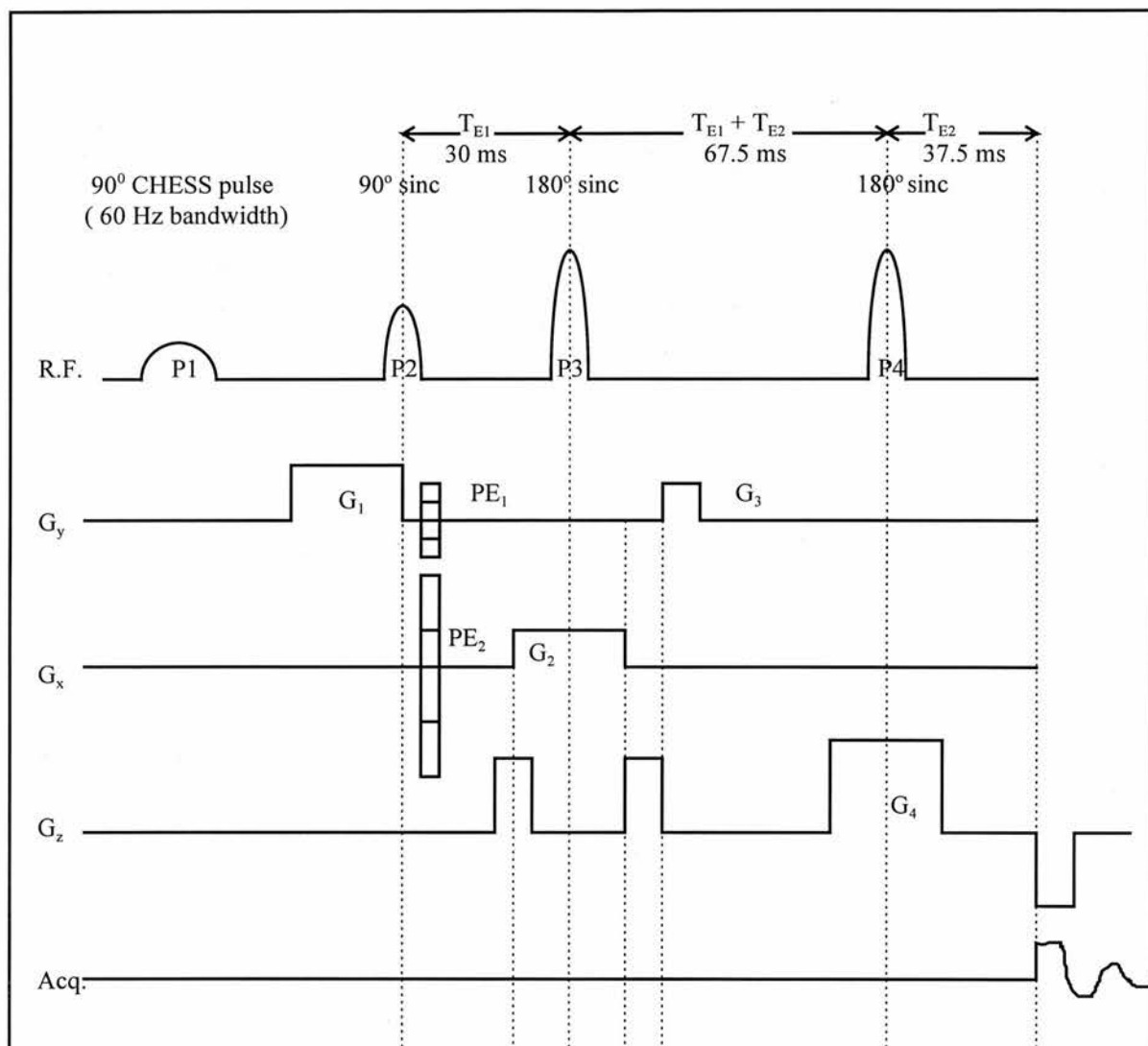


Fig. 3.5 The PRESS SI sequence

Water suppression is achieved by exciting water protons with a narrow bandwidth (60 Hz) water selective 90° CHESS pulse (P1), this magnetisation is subsequently dephased by the spoiling action of gradient pulse G_1 . The trailing end of G_1 also serves as a slice select pulse for the 90° pulse P2. Phase encoding (PE_1) in 16 steps provides the spatial partition of the VOI in the y (coronal) direction. The gradient pulse G_2 is centred on the 2nd 180° r.f. pulse (P3) and as such serves to slice select it. This pulse is also phase encoded by the action of pulse PE_2 in the x (sagittal) direction and it serves the further purpose of dephasing any unwanted magnetisation. Pulse G_3 refocuses the magnetisation of the 90° pulse (P2) following its inversion under the effect of P3. The final gradient pulse G_4 is centred about the final 180° sinc pulse (P4) and as such slice selects this pulse in the z direction, whilst it also dephases unwanted signals. Acquisition of the second half of the final echo takes place at a time T_{E2} after the midpoint of P4. A total echo time of $T_E = 135$ ms was used with a repetition time $T_R = 1600$ ms.

3.3 B₀ field inhomogeneity - Shimming

In order to detect well resolved metabolite peaks in a spectrum it is essential to minimise the inhomogeneity in the B₀ field. A spatial variation in B₀ will cause a shifting of the k-space origin leading to a spatially dependent phase shift of the spectra and an uncertainty in voxel localisation. Of equal importance in proton spectroscopy is maximum homogeneity within a voxel. This will ensure that all chemically similar spins within the voxel have the same Larmor frequency. As a consequence, spectra from a voxel with a homogeneous field will be well resolved i.e. sharp peaks centred at frequencies corresponding to the true resonant frequency of the metabolite of interest. In the interest of effective water suppression, the line width of the water resonance should be a minimum so as to facilitate optimum water suppression at the central water frequency. With single voxel techniques, shimming of the B₀ field throughout the voxel is more straightforward than in SI, where the volume of space used is larger and consequently contains more imperfections and variations in object susceptibility.

Prior to describing the mechanism of the shimming process, the consequences of a poorly shimmed FID in spectral terms are discussed.

3.3.1 Consequences of a good and bad shim

In spin echo spectroscopy such as PRESS, the magnetisation vector precesses in the transverse plane for the bulk of its evolution time following excitation and prior to acquisition. As such the signal is prone to T_2^* transverse relaxation which can be separated in to two parts; the contribution from natural spin-spin effects (T_2) and a B₀ inhomogeneity effect (k) - see Section 2.4.

$$\frac{1}{T_2^*} = \frac{1}{T_2} + k \quad (3.1)$$

In a spin-echo/double spin-echo imaging sequence, the effect of a short T_2^* due to in plane dephasing is not important as the acquisition occurs over a short period of time commencing at the instant the echo is refocused when all dephased spins are again back in phase. In spin-echo spectroscopy, in order to gain sufficient frequency resolution in the spectrum to detect metabolites, it is necessary to collect an FID over a longer period of time. This is illustrated by the relation for the frequency resolution $\Delta f = 1/T_{acq.}$ where $T_{acq.}$ is the overall acquisition time. As such the effect of dephasing needs to be minimised so that the time

duration of the echo is drawn out for as long as possible. Therefore a well shimmed FID corresponding to a long T_2^* is a priority in spin-echo spectroscopy. Figure 3.6 illustrates this point, with the FID and spectrum corresponding to a homogeneous field (long T_2^*) and in Figure 3.7 an inhomogeneous field (short T_2^*).

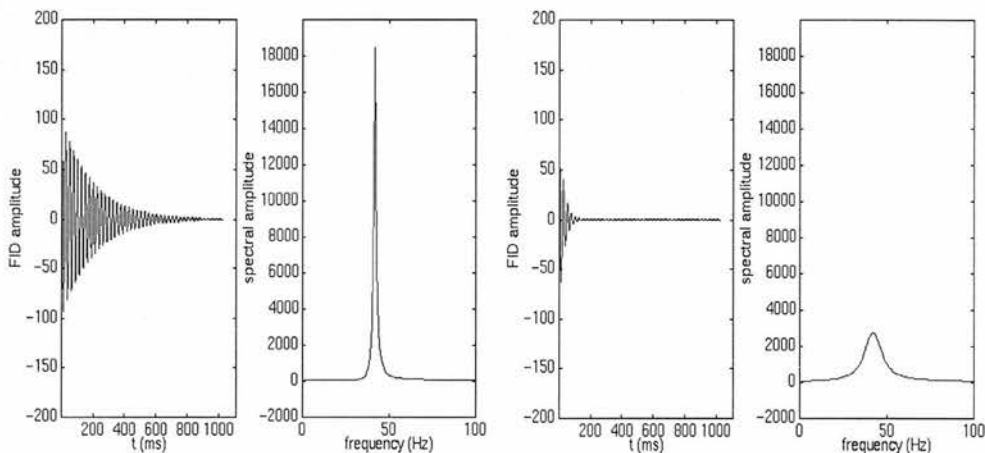


Fig. 3.6 A well shimmed FID and spectrum

Fig. 3.7 A poorly shimmed FID and spectrum

The decay of the envelope of the FID gives a good indication of the size of T_2^* . An initially strong signal that decays to noise level just before the end of sampling is ideal. If the signal is somehow truncated at the end of the sampling period before it has decayed to noise level then a phase artefact can be introduced in to the spectrum by the FFT. This is apparent when the acquisition time does not represent a complete number of cycles of the resonant frequency of the peak of interest i.e. $\omega_j T_{acq} \neq n\pi$. The amplitude of this phase distortion is determined by the size of the FID upon truncation which is in turn determined by the size of T_2^* relative to T_{acq} . Such a phase distortion is evident in the simulated spectrum of the FID in fig. 3.8. For comparison the spectrum of an apodised FID (i.e. one that has decayed to noise level by the time the sampling acquisition time is complete), is shown in figure 3.9. The apodised FID (Fig. 3.9) has a spectrum with broader lines as a result of the shorter T_2^* used for relaxation damping in the simulations.

If an FID is truncated as in figure 3.8, its shape can be forced to one resembling the FID in fig's 3.6 and 3.9, by apodising the FID with a "line broadening" filter. This adds an additional weighting to the exponential decay of T_2^* , the use of such apodisation filters is described in more detail in section 4.10.

An FID may have an envelope that is essentially a smooth decay upon which there is superimposed "beating" modulation. This phenomenon is described in more detail in the

section on phase correction (section 4.7), but is basically due to the presence of two volumes of spins resonating at slightly different frequencies. Such a situation might arise when there is an abrupt change in the B_0 field within a voxel. A sudden change in field could occur across an interface of two tissue types with significantly different magnetic susceptibilities (e.g. air in the sinuses and brain matter). The “beating” in the FID (Fig. 3.10) manifests itself as a frequency splitting in the spectrum as is shown in Fig. 3.10. By shimming the VOI prior to acquisition all of these potential artefacts can be minimised.

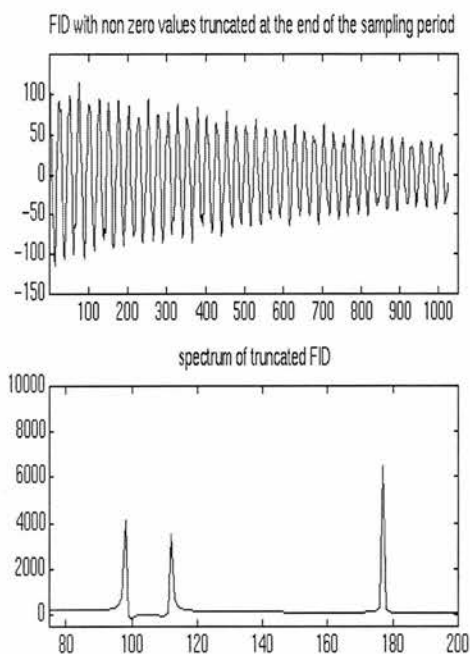


Fig. 3.8 Truncated FID and spectrum with baseline distortion

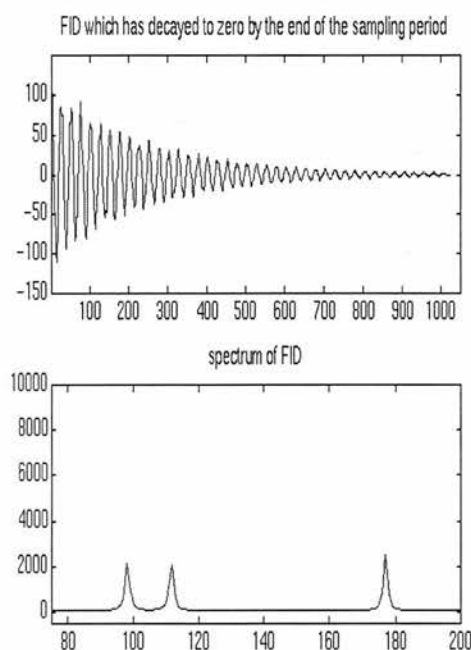


Fig. 3.9 Apodised FID and spectrum

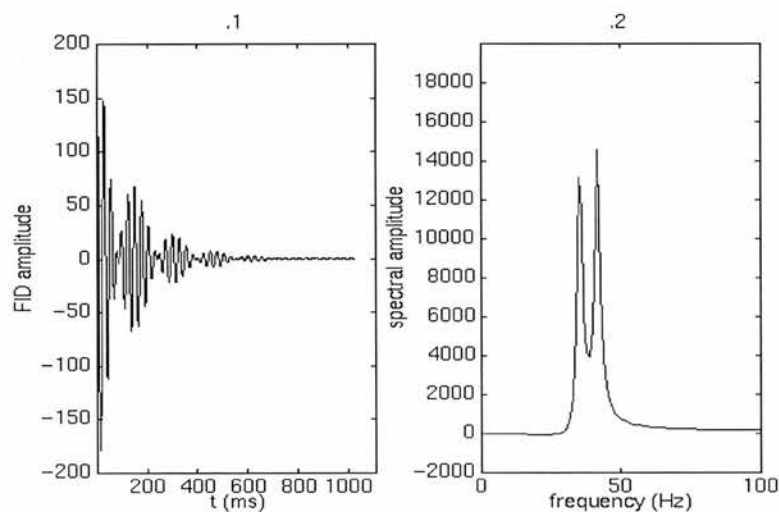


Fig. 3.10. The beating effect in the FID (3.10.1) and as a frequency splitting in the spectrum (3.10.2)

3.3.2. The shimming procedure

The adjustment of the currents in the shim coils (predominantly the linear, x, y and z components) to achieve as homogeneous B_0 field as possible is the basis of the shimming procedure. The shim coils are complementary to the main B_0 coil with the specific purpose of providing a means of fine tuning the B_0 field set up by the main coil. The orientation of the coils with respect to the iso-centre of the magnet is influenced by the fact that the field within the bore of the coil (providing it contains no conducting bodies) satisfies Laplace's equation:

$$\nabla^2 V = 0 \quad (3.2)$$

Where the field \mathbf{B} is derived using Maxwell's equations, as the gradient of the scalar potential (V);

$$\mathbf{B} = \text{grad } V \quad (3.3)$$

The solution of Laplace's equation (3.2) is based on the set of spherical harmonics

$Y_l^m(\theta, \phi)$:

$$V = \sum_{lm} A_{lm} r^l Y_l^m(\theta, \phi) \quad (3.4)$$

where

$$Y_l^m(\theta, \phi) = (-1)^m \left[\frac{2l+1}{4\pi} \frac{(l-m)!}{(l+m)!} \right]^{\frac{1}{2}} e^{im\phi} P_l^m(\cos\theta) \quad (3.5)$$

with $P_l^m(\cos\theta)$ the l, m^{th} Legendre polynomial (expressed in terms of $\cos\theta$ (or alternatively in terms of $\sin\theta$), where l and m are integer and $l \geq m \geq 0$). If $\text{grad } V$ is calculated from (3.3) and (3.4) using spherical polar co-ordinates then the field can be expressed in spherical polars as a sum of the *zonal* (symmetrical about the z axis - no variation in ϕ , $m=0$) spherical harmonics and the *tesseral* (variation with ϕ positioning) spherical harmonics (Gruetter et al 1992)

$$B(r, \theta, \phi) = \sum_l [c_l r^l P_l(\cos \theta) + \sum_m b_{lm} r^l P_{lm}(\sin \theta) \sin m\phi + a_{lm} r^l P_{lm}(\sin \theta) \cos m\phi] \quad (3.6)$$

where c_l , b_{lm} and a_{lm} are constants determined by the values of l and m .

These solutions for B , form an orthonormal set (a consequence of Laplace's equation), the 15 lowest order solutions are tabulated below in Table 3.1;

l	m	Spherical spatial dependence	Cartesian representation	Shorthand notation	Coefficient (c_l, b_{lm}, a_{lm})
1	0	$r \cos \theta$	z	z	c_1
1	1	$r \sin \theta \cos \phi$	x	x	a_{11}
1	1	$r \sin \theta \sin \phi$	y	y	b_{11}
2	0	$r^2(3 \cos^2 \theta - 1)/2$	$z^2 - (x^2 + y^2)/2$	z^2	c_2
2	1	$r^2 \sin \theta \cos \theta \cos \phi$	xz	xz	$3a_{21}$
2	1	$r^2 \sin \theta \cos \theta \sin \phi$	yz	yz	$3b_{21}$
2	2	$r^2 \sin^2 \theta \cos 2\phi$	$x^2 - y^2$	$x^2 - y^2$	$3a_{22}$
2	2	$r^2 \sin^2 \theta \sin 2\phi$	$2xy$	$2xy$	$3b_{22}$
3	0	$r^3(5 \cos^3 \theta - 3 \cos \theta)/2$	$z(z^2 - 3(x^2 + y^2)/2)$	z^3	c_3
3	1	$r^3 \sin \theta (5 \cos^2 \theta - 1) \cos \phi$	$x(4z^2 - x^2 - y^2)$	xz^2	$3/2a_{31}$
3	1	$r^3 \sin \theta (5 \cos^2 \theta - 1) \sin \phi$	$y(4z^2 - x^2 - y^2)$	yz^2	$3/2b_{31}$
3	2	$r^3 \sin^2 \theta \cos \theta \cos 2\phi$	$z(x^2 - y^2)$	$z(x^2 - y^2)$	$15a_{32}$
3	2	$r^3 \sin^2 \theta \cos \theta \sin 2\phi$	$2xyz$	xyz	$15b_{32}$
3	3	$r^3 \sin^3 \theta \cos 3\phi$	$x^3 - 3xy^2$	x^3	$15a_{33}$
3	3	$r^3 \sin^3 \theta \sin 3\phi$	$3x^2y - y^3$	y^3	$15b_{33}$

Table 3.1. The lowest order spherical harmonics which are solutions to Laplace's equation

The orthonormality of the solutions means that specific shim coils can be shaped and orientated so as to generate one of these spherical harmonics, without influencing the field due to any of the other harmonics. The field can then be modified by adjustment of the current in this coil alone without altering the components due to the other harmonics. Thus tuning of currents in each of the shim coils will allow an increasingly homogeneous field to be built up. In practice the clinical scanner has 12 coils corresponding to an alignment with the basis spherical harmonics which are solutions to (3.6) centred at the magnets isocentre. These are namely the $x, y, z, z^2, z^3, z^4, zx, zy, xy, x^2 - y^2, z^2x$, and z^2y solutions described above. The zonal harmonics (z, z^2, z^3) can be implemented by passing current through circular axial coil arrangements whilst the tesseral harmonics require coils that are oblique to the xy plane. The orientation and configuration of these tesseral coils can be theoretically predicted by rotating zonal harmonics out of the xy plane (Romeo and Hoult 1984). The

resulting tesseral harmonics correspond to oblique elliptical arcs of current in the specially shaped shim coils and have $m \neq 0$ and an m -fold symmetry about the z axis.

With a comprehensive basis set of spherical harmonics corresponding to individual shim coils, shimming can proceed. A manual interactive process is adopted whereby the currents in each of the coils are adjusted individually whilst the shape and magnitude of the water FID and spectrum are monitored as an indication of homogeneity. The FID and spectrum shapes corresponding to good and bad shims are discussed in sections 3.3.1 and 3.3.7. With a choice of 12 coils, only the 4 main coils can be practically used in this manual shimming. If a comprehensive shim that utilises all of the coils is to be performed then some form of automatic shim current optimisation algorithm is required.

3.3.3 Automated shimming

The process of automated shimming is most practically useful when the currents in the shim coils can be controlled by microprocessors linked up to the network on which the shim optimisation algorithm is computed. On many new machines such algorithms can be implemented internally allowing a user friendly automated shim. On older machines (eg SP 63 Magnetom) both the computing power and network links to the shim coils are not available and automated shimming is more time consuming.

Various different optimisation algorithms have been reported, the first works on the principle of maximising the energy contained in the FID envelope. The iterative alteration of shim currents is performed in accordance with an optimisation algorithm such as the simplex (Press et al 1992). Such a method requires computer feedback to the shim coils and as such is not possible on many clinical scanners currently in use. An inferior method based on the same principles is used on the current Siemens Magnetom and is performed by the `Autoshim` command. This changes the current in the four fundamental x, y, z and z^2 coils in cyclic steps and retains the values corresponding to an increase in the integrated area of the FID. The problem is that poor shim shapes with large integrals may be retained. Making use of only the four basic coils, the method shows little advantage over a manual shim, where operator knowledge can be used to find an optimum FID shape.

The second method of automated shimming utilises preliminary field measurements of the unshimmed volume of interest. These measure the initial field values across the VOI, which equate to the static field of the magnet and sample (B_0) plus the field contributions from the various shim coils that correspond to the starting value currents in those coils. Two

methods of field mapping prevail, the first uses SI and the second uses imaging sequences that reveal phase information.

3.3.4. Field Mapping

A SI field map is based on calculation of the frequency of the water resonance at all voxels in the VOI (Hu et al 1995, Ericsson et al 1995). Being frequency specific this SI method avoids the possibility of signal contamination with lipids, which can be a problem when using phase images to calculate the field distribution. The drawback is the long scan time for a large SI data set of say 64×64 in plane phase encodings. This can be reduced substantially from that of a water suppressed acquisition by using less time domain samples to acquire a narrow bandwidth around the water resonance only.

The second method calculates the local field distribution from phase sensitised imaging sequences (Bailles et al 1988, Spielman et al 1989, Schneider and Glover 1991, Webb and Macovski 1991, Gruetter and Boesch 1992, Wen et al 1995). These imaging sequences are used to calculate the local B distribution from the phase difference $d\phi$ of two images taken at slightly different spin evolution times. From the definition of the Larmor frequency, ω :

$$\omega = \frac{d\phi}{dt} = \gamma B_0 \quad (3.7)$$

Using two gradient recalled echos of different echo times a spatially localised phase difference can be obtained as a function of time, from which the B_0 field can be calculated using equation (3.7) (Bailles et al 1988, Spielman et al 1989 and Webb et al 1992):

$$\Delta\phi = \gamma B(x, y, z) \Delta T_E \quad (3.8)$$

These phase difference imaging methods require phase unwrapping to remove the steps that occur as $\Delta\phi$ passes through increments of 2π (Axel and Morton 1995). A further complication with the technique is the interference of lipids with the phase of the water resonance. To get around this problem Webb and Macovski 1991, used spatial-spectral water frequency selective excitation pulses. The volume of interest over which shimming is intended is then specified in matrix form from this field image.

3.3.5. Shim current optimisation

The field is then optimised with respect to the currents flowing in all the shim coils. With say 12 individual coils and the same number of corresponding field contributions, algorithms using matrix methods are the most practical way of performing such an optimisation. The target function to be optimised is a measure of the homogeneity of the field, the majority of methods described (Hu et al 1995, Gruetter and Boesch 1992, Wen et al 1995) minimise a target function based on the least squares equation (3.9)

$$G = \int_{\text{voi}} (B(\mathbf{r}) - B_0)^2 d\mathbf{r} \quad (3.9)$$

Where the position dependent field $B(\mathbf{r})$ (evaluated at the position of all pixels, \mathbf{r} in the VOI) is a function of the static field distribution of the magnet, the shape/position of the shim coil and the current flowing in that coil:

$$B(\mathbf{r}) = B_{\text{st}}(\mathbf{r}) + \sum_{i=1}^N I_i F_i(\mathbf{r}) \quad (3.10)$$

Where $B_{\text{st}}(\mathbf{r})$ is the static position dependent field of the magnet, I_i is the current in the i^{th} coil and $F_i(\mathbf{r})$ is the field per unit of current due to the i^{th} shim coil.

3.3.6 Shimming on the Magnetom SP 63

Initial spectroscopic studies on this machine were carried out with a preliminary `autoshim` across the transverse imaging plane followed by a manual shim over the rectangular VOI of excitation. These measures often require up to seven minutes of operator time to achieve a shim of sufficient quality to go on and acquire spectra and only employ the four shim coils; x, y, z and z^2 . Consequently, a more effective and reliable mode of automated shimming was sought. The technique used by Wen et al 1995, utilises all the shim coil and optimises the shim currents in each subject to the current carrying constraint of each. This method was implemented with the aim of being incorporated routinely in to spectroscopic examinations on the Magnetom. This work was carried out by Ian Marshall and Carlo Götz and utilises gradient echo phase images (Fig. 3.11) to map out the B_0 field. These phase

images are unwrapped to yield the field dependent phase difference $\Delta\phi$ (equation 3.8) from which the starting value of the field in the spectroscopic VOI can be expressed in matrix form in terms of the basis shim currents. The matrix optimisation methods for minimisation of the target function (equation 3.11) are discussed in more detail in the paper by Wen and the project report of Götz.

Having specified the VOI and collected the phase images from the same transverse plane, the starting values of the shim currents are noted for use in the computation of equation 3.10. The data is then processed remotely on a Sun workstation, the whole data processing routine lasts about 5 minutes. For in-vivo examinations this should not delay the overall examination time as the T_2 weighted images can be collected in the meantime. The drawback is that a second operator is needed on hand to execute the shim algorithm on a remote workstation. The only additional acquisition time is that needed to collect the phase images (2 minutes), which is comparable to the time taken to conduct a rudimentary manual shim with just three coils.

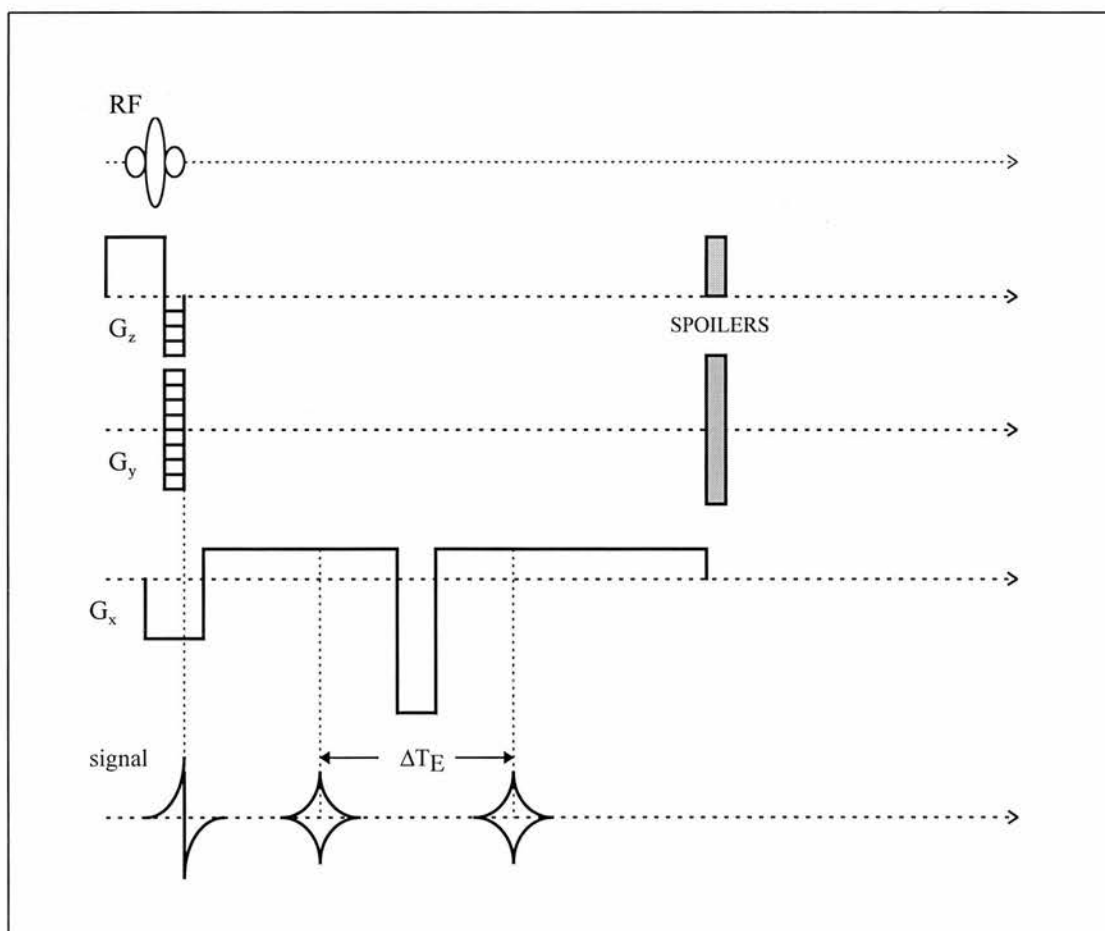


Fig. 3.11 Gradient recalled echo sequence for phase imaging.

3.3.7 In vitro examples of the effects of shimming

Having developed an automated shimming routine, Götz was keen to visualise the resulting shims in spectral terms. With respect to this work, an evaluation of the practicality of the technique for routine spectroscopy was felt to be needed. As such SI acquisitions were made on the standard Siemens acetate-lactate phantom. The HOPE SI localisation sequence was used (Chapter 6) at an echo time of 292 ms with a square VOI (centred at the magnets isocentre) of 75mm×75 mm and 8×8 phase encodings were applied in the sagittal and coronal directions. In addition to SI, field contour maps were collected using the sequence FIELD_MAPPING.UDB, a spin-echo / stimulated echo sequence. These give a good graphical representation of the field homogeneity, with a contour separation of 0.1 ppm corresponding to an echo time of 157 ms (see eq. 3.8). An initial data set and contour map was collected without shimming followed by automatic shimming using the three lowest order coils and finally automatic shimming with the five lowest order coils. When trying to perform shimming with more than five coils, the algorithm encountered problems owing to truncation of the shim currents. Götz recognised this as a problem with the method of constrained optimisation and found that the algorithm works most reliably when only the first five coils are utilised.

The results of the in-vitro tests are shown in figure 3.12, the corresponding field contour maps are shown in figures 3.13. There is a noticeable decrease in the line width of the acetate singlet and lactate doublet when the 3 coil shim is compared to the unshimmed data. This reflects the increase in T_2^* as the field is made more homogeneous. The lactate line width is now sufficiently narrow to allow resolution of the doublet in the lactate peak (a separation of 7 Hz). Progressing to 5 coils there seems to be little improvement in the appearance of the spectra and similarly the field appears to be only marginally more homogeneous from examination of the contour maps (Fig. 3.13).

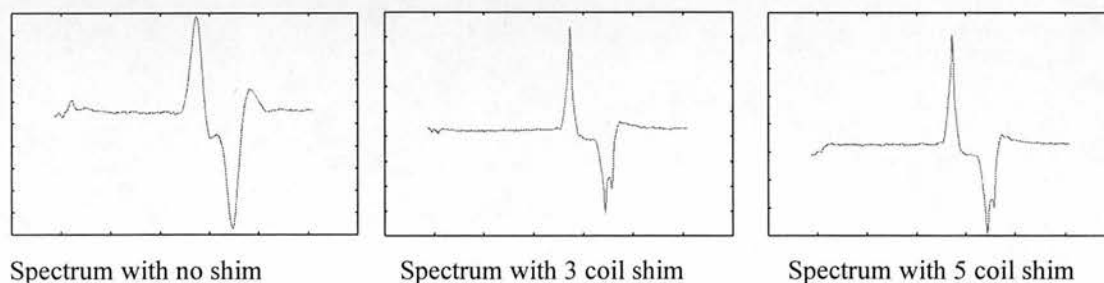
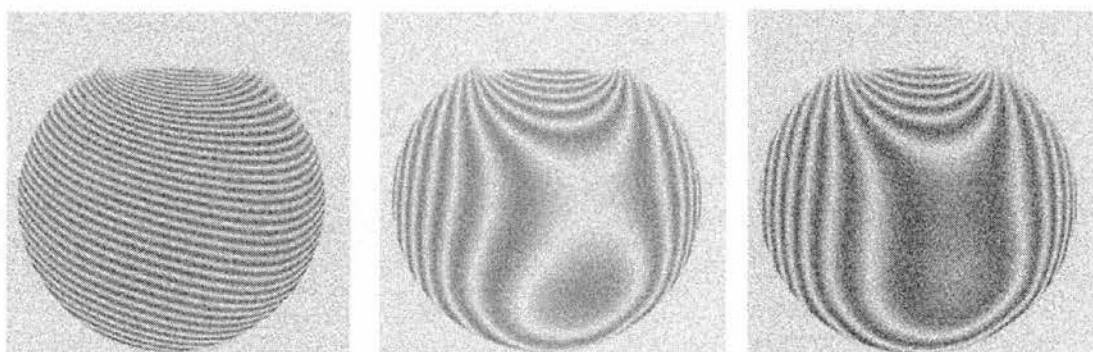


Fig. 3.12



Field map with no shim

Field map with 3 coil shim

Field map with 5 coil shim

Fig. 3.13 (Contour separation 0.1 ppm)

3.3.8 Conclusions

From the in-vitro examples of spectra given above it can be seen that the algorithm is effective. When tested further in-vitro more complications arose, the first problem is caused by the fact that the algorithm uses a basis of spherical harmonics centred at the iso-centre of the magnet. When a VOI was positioned at a point well away from the iso-centre the algorithm produced shim currents which were associated with poor shims. The second drawback of the technique as a routine shimming method is the need for the second operator on hand during the shimming process, to run the algorithm and compute the shim currents. Bearing these factors in mind it was decided that this automated shimming technique was too complicated to be incorporated in to the routine in-vivo acquisition protocols.

With a more robust constrained optimisation that accounts for both the current carrying capacity of individual coils and the overall power supply, then perhaps all twelve coils could be used effectively. Similarly a spatial transformation of the origin would allow universal VOI positioning within the coil. Finally if the shim current values could be set automatically by reading the output of the algorithm, then the technique would be less labour intensive, cutting down the need for a second person on hand. If these improvements were to be effectively incorporated then routine use would be beneficial.

3.4 Water Suppression

3.4.1 Introduction

The presence of a water resonance of up to three orders of magnitude the size of the resonances of metabolites of interest, presents the problem of obscuring the metabolite signal. Post acquisition spectral modelling of the water signal can be used to counter this effect prior to spectral interpretation. However if metabolite spectra are to be detected at all in the post acquisition stage then water suppression needs to be incorporated in to the excitation/acquisition sequence. If the bit resolution of the ADC (16 for this ADC) of the FID is lower than the ratio of the metabolite and water signals then the metabolite contributions to the FID will be omitted altogether. Consequently a variety of techniques of water suppression have been used in conjunction with SI and single-voxel pulse sequences. A significant number of these have been adapted from the field of NMR spectroscopy of dilute solutions of solutes in water.

Water suppression techniques used in practice generally use one of, or a combination of, two strategies : those that make acquisitions at a point in time when the water signal is at a minimum - inversion recovery/ partial saturation - and those that do not excite the water resonance - selective excitation.

3.4.2 Pre-saturation

In *pre-saturation*, the water resonance is irradiated with chemical shift selective pulses for a period long enough to produce equal population of the two spin states (\uparrow and \downarrow) and then acquisition commences. In Chemical Shift Selective Suppression or CHESS (Haase et al 1985), a $\pi/2$ water selective pulse is used to produce a transverse magnetisation. This is subsequently crushed by a spoiler gradient which dephases the transverse magnetisation leaving metabolite signals unchanged in the z direction. Moonen et al (1990) when using CHESS in conjunction with STEAM localisation (one CHESS cycle in the preparation period and one during the mixing period, T_M) report on improvements made in the dispersal of any non-stimulated water echoes, having predicted the optimum crusher gradient configuration by using the coherence of the spin evolution. The residual water peak was smaller than that of a 5 mM concentration of NAA, implying 10,000 fold water suppression. In addition they point out that CHESS water suppression has the advantage over selective excitation in that the phase and intensity are unaltered across the spectrum. As the residual z component of water relaxes with T_1 relaxation, then by altering the pulse angle so as to give a zero magnetisation at the end of each CHESS sequence, water suppression can be tailored to the individual T_1 environment.

The total number of CHESS sequences employed has been varied and cycles of three have been found to be the most effective in excluding unwanted echoes. Frahm et al (1990) using three pulses, altered

experimentally, the flip angle of each pulse together with the time interval between successive saturation pulses (and the acquisition) so as to give the optimum water suppression (1000 fold) for their system.

Ernst et al (1995) sought to find the optimum three cycle CHESS sequence that gave effective water suppression for short echo times by minimising the residual z magnetisation with respect to the three flip angles θ_i , the three time intervals τ_i and the localised T_1 . They use the notation $(\alpha, \beta, \gamma, \tau_1 \tau_2 \tau_3)$ to denote the three successive pulse angle sizes and their separation in time, finding the sequence $(\tau, \tau, \tau, \theta, \theta, 2\theta)$ was five times as effective (1000:1 cf 200:1 suppression) as the conventional equidistant sequence $(\tau, \tau, \tau, \theta, \theta, \theta)$ of equal flip angles.

3.4.3 Inversion recovery

Inversion recovery or selective T_1 relaxation (Section 2.5.2) is based upon inversion of the water signal using a frequency selective π pulse, the aim being to perform localisation at the instant the longitudinal water magnetisation crosses through zero. In Water Eliminated Fourier Transform water suppression (WEFT -Patt & Sykes 1972) the following pulse sequence is used;

$$\pi \text{ H}_2\text{O} - t_H - \pi/2 \text{ -Localisation.}$$

Where the interval $t_H = T_1(\text{H}_2\text{O}) \cdot \ln 2$ for a π water inversion pulse (see section 2.5.2).

Hugg et al 1992, report an improvement in water suppression by using a double WEFT sequence prior to localisation, with the two t_H intervals empirically varied to minimise the longitudinal water signal. They attribute the advantage of two pulses to the non-mono exponential decay of the water T_1 . A double WEFT sequence was again found to give effective suppression prior to PRESS localisation by Duyn et al 1992(ii). In both cases of Double WEFT a gradient spoiler pulse after the inversion pulse was found to be effective in dispersing unwanted transverse magnetisations caused by imperfect longitudinal inversions. The use of spoilers allows the use of a $\pi/2$ selective excitation pulse which has an associated t_H of zero thus minimising the time taken before localisation commences.

3.4.4 Selective excitation

Selective excitation aims to excite resonances of interest whilst leaving the unwanted water resonance unexcited. As such a pulse sequence is needed whose frequency response is zero at and near to the water resonance. If a rectangular small flip angle excitation pulse is used its Fourier transform yields a sinc function, the zeros of which can be aligned with the resonant frequency of water, purely by altering the pulse width. The nulls in such a function are relatively narrow and as such, do not allow for any spread in ω_0 of the water resonance arising from B_0 inhomogeneities. More widespread suppression may be achieved with an excitation pulse with broader nulls and peaks (both 1st and 2nd derivatives = 0) which

can be constructed from the superposition of the Fourier transforms of a series of hard rectangular pulses of different durations. Hore (1983) devised pulse sequences by considering the Fourier transformation of analytical functions of frequency which met the excitation profile requirements for water suppression. The set of delta functions of alternating sign, whose amplitudes are given by the binomial coefficients were one such solution. In particular the four pulse sequence or $\overline{1331}$ sequence has the advantage of being relatively simple (4 pulses) and gives good broad band selective suppression (1000 fold in aqueous solution NMR spectroscopy):

$$\alpha(x) - \tau - 3\alpha(-x) - \tau - 3\alpha(x) - \tau - \alpha(-x)$$

where α is a unit of pulse height that meets the condition that the total energy gives a 90° excitation and τ is the time interval between pulses.

The non uniformity of the excitation profile makes this form of water suppression more suitable, if a specific resonance is of interest, whereby one of the broad peaks of the excitation profile could be aligned with the resonant frequency. Quantification of resonances either side of this frequency would be more difficult as frequency dependent suppression factors would need to be calculated. Hetherington et al (1985) and Pan et al (1991) compensated for this spectral inhomogeneity by applying such corrections. More recently a lot of work has been done on producing optimum frequency responses for a given r.f. pulse envelope by using digital filter theory (Matson 1995, Star-lack et al 1996 -BASING pulses). With such pulses effective suppression can be achieved over a narrow or broad spectral range.

3.5 Conclusions

Having described the acquisition protocols and reviewed the techniques used for shimming and water suppression optimisation, from here on it will be assumed that the optimum set of data has been acquired.

In the next chapter the techniques used to convert this data into clinically meaningful spectra and metabolite images will be discussed in detail.

Chapter 4.

Data processing

In this chapter the techniques used to convert the raw data in to frequency spectra are discussed. These techniques are described in detail, largely because they were all implemented using specially written software. As such this chapter represents the bulk of the work carried out in the preliminary stage of the project. The stages in the data processing procedure are probably best summarised in flow chart form;

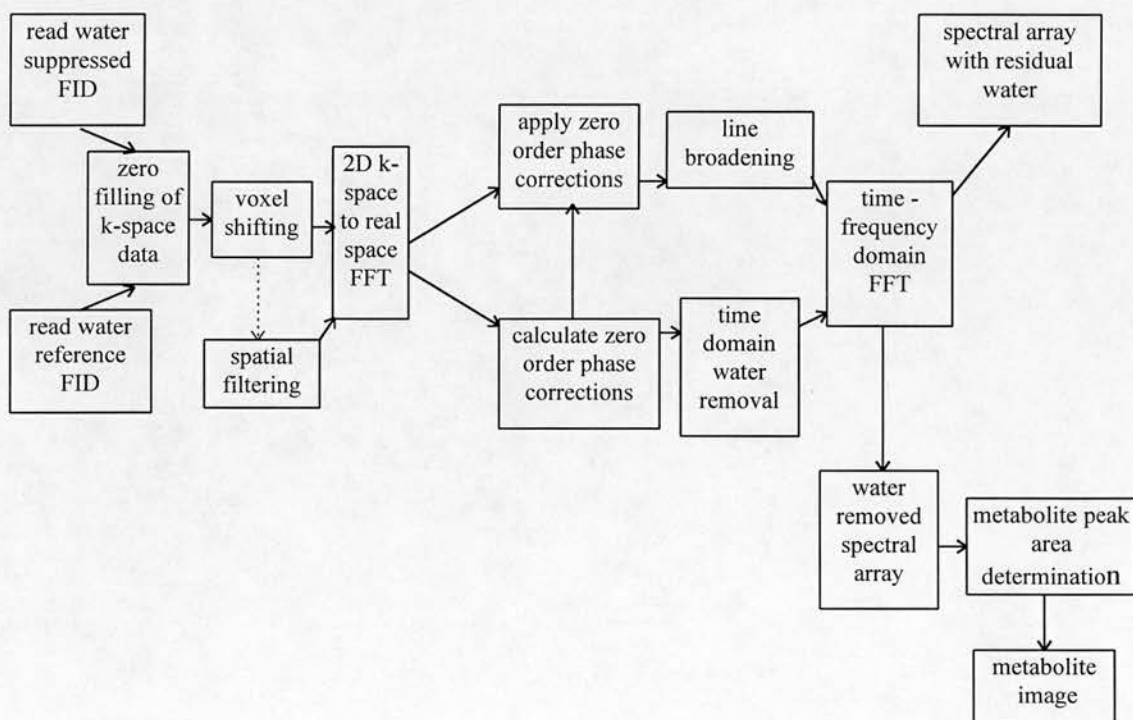


Fig. 4.1 Flow chart summarising the data processing steps used to produce spectra from raw data files.

4.1 Importing the data from the scanner

The raw data and images collected as described in the data acquisition section, were imported from the VAX operating system of the Siemens Magnetom to the UNIX mainframe of Sun Sparc (UNIX) systems, upon which the post acquisition data processing was performed. This transfer was done using the UNIX batch files `dcn-transfer` and `dcn-raw transfer` written by Martin Connell. The `image+grid` image file generated by `WORK_CSI`, was then converted from ACRNEMA format to an ANALYZE™(CNS, Rochester, MN) compatible format using the program `conv_analyze_acrnema` which was also written by Martin Connell.

4.2 Raw Data Processing- overview

The raw data was then processed using programs written in house in C. Significant adaptations to the initial software `csi.c` (written by Ian Marshall) have been made by the author since the SI study was started. The version which incorporates all the modifications discussed later in this chapter is `centrefill12.c`. The code listing of `centrefill12.c` is found in Appendix II. A brief overview of the steps implemented by this program is now given. Each step will be dealt with in greater depth in individual sections appearing later on in this chapter.

4.2.1 Reading the data - water reference data set

The water reference raw data files are read first, their processing proceeds as follows. The files are first converted from the Siemens format in to an ASCII format suitable for C processing. The function `read_data_file(void)` performs this task, by first stripping the Siemens raw data header and then converting the data from the VAX VMS floating point format to C floating point format. The function then performs a byte reversal on the integer numbers in the header. The data is then allocated to a three dimensional (2 spatial and one time) array, `FID[row][col][i]` using three pointers. The indices `row` and `col` represent the n_y and n_x coronal and sagittal voxel co-ordinates; with $1 \leq n_x \leq N_x$ and $1 \leq n_y \leq N_y$, (N_x and N_y are the number of coronal and sagittal k-space phase encodings). The index `i` represents the data sampling point in the time domain with a sample interval of 1 ms and 1024 samples of complex data. The real and imaginary components of each sample are saved in an interleaved format for `i=1:2048`.

4.2.2 Zero-filling of k-space

The data can then be zero padded in k-space (the reciprocal of real space) to increase the number of voxels from $N_x \times N_y$ to $2N_x \times 2N_y$ (section 4.6).

4.2.3 k-space windowing

Windowing functions can be applied to the FID prior to the transforms to provide a spatial filter to reduce Fourier leakage between voxels, this technique is discussed in detail in section 4.8.

4.2.4 Voxel shifting

Voxel shifting can be applied in the x and y directions using the functions `voxshiftx(void)` and `voxshifty(void)` see section 4.9.

4.2.5 k-space to real space FFT

A k_x space - x spatial discrete FFT is then performed using the function `column_transform(void)` which implements a one dimensional real FFT in N_x steps to decode the FID in the x direction. Similarly the k_y space - y spatial transform is then implemented in the same way by `row_transform(void)`.

The FFT algorithm used here was taken from Numerical Recipes in C (Press et al 1992) and replaces the interleaved complex FID data with its discrete Fourier transform. This FFT algorithm is performed by the Numerical Recipes function `four1(double data[], int nn, int isign)`. The mechanics of the FFT is described in much more depth in section 4.11. The spatially decoded data is then rearranged to account for the fact that the origin in k-space corresponds to the central voxel ($N_x/2, N_y/2$) of the grid ie. the magnet isocentre. The function `rearrange_FIDs(void)` performs this operation.

4.2.6 Calculating zero order phase correction

The spatially decoded water reference FID is then used to calculate the phase correction angle needed to remove the phase offsets induced by B_0 field inhomogeneities and eddy currents. The function `calc_phase_corrections(void)` performs this calculation and is described in section 4.7.

4.3 Water suppressed data set

The water suppressed FID was then processed in an identical way (steps 4.2.1 - 4.2.6) with the exceptions that;

4.3.1 Applying zero order phase correction

The phase correction angles calculated from the reference data were now applied to the suppressed data by the function `apply_phase_corrections` (see section 4.7).

4.3.2 Line broadening

The water suppressed data was also multiplied with a Gaussian window by the function `line_broadening(void)` before the frequency domain spectral transform was carried out (see section 4.10).

4.3.3 Save FIDs for time domain modelling - water removal

The spatially resolved time domain FIDs were then saved as individual FIDs by the function `save_FIDs_for_Delft(void)` in the files `csi_nx_ny` (section 4.4).

4.3.4 Spectral transform

A 1D FFT which replaces the complex FID with its complex FFT was performed by the function `spectral_transform(void)`

4.3.5 Automatic integration

The area under the spectrum corresponding to a ppm range of $f_1 - f_2$ is calculated for the spectrum from each voxel and saved in a 2D array by the function `save_areas(void)`. This algorithm algebraically sums successive data point values, for all data points in the range $f_1 - f_2$.

4.4 Post Acquisition Water Removal

Every effort is taken to reduce the contribution of the water resonance to the water suppressed FID by optimising the amplitude of the CHESS pulse voltage (section 3.2.1). However the residual water signal will be comparable in size if not larger than the peaks of the metabolites of interest. Fig. 4.2 illustrates this point with a suppressed water signal which conceals some of the signals from choline and creatine.

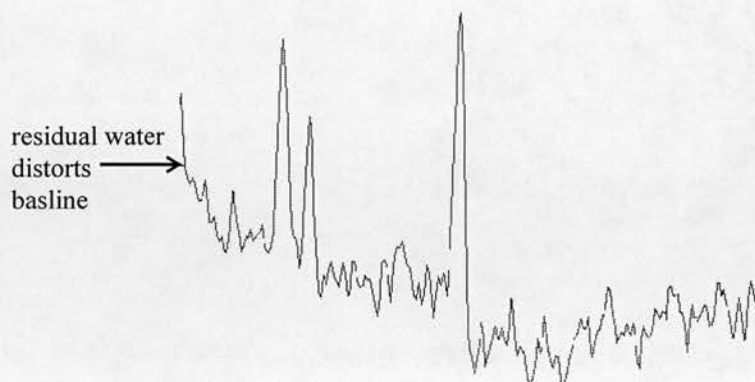


Fig 4.2 Spectrum with residual baseline distortion due to incomplete water suppression (ppm range 4-0)

Such spectra are virtually useless for quantitative studies as their baselines are severely distorted by the residual water. Mathematical modelling of the water FID or spectrum can be performed, whereby the signal from the residual water is modelled. The fitted signal is then subtracted from the water suppressed FID leaving a signal which predominantly contains frequency and phase information specific to the metabolites and not the water. The reader is referred to section (4.11.4), reviewing modelling techniques, for a more detailed review of the options available.

For the sole purpose of water removal from an FID, a linear parametric time domain fitting procedure was used, which was developed in 1994 by Aad van den Boogart at the University of Delft, Netherlands. This software uses linear prediction to express the n th data point in of the water signal as a sum of the previous data points.

$$x_n = a_1 x_{n-1} + a_2 x_{n-2} + \dots + a_m x_{n-m} \quad (4.1)$$

Hankel-Lanczos singular value decomposition (HLSVD) matrices are then used to fit this prediction of the water signal to the raw data. This procedure effectively amounts to a fitting of the residual water signal with a combination of Lorentzian damped sinusoids. The technique does not incorporate a-priori information, instead it fits the largest component first followed by the next largest etc. As the residual water signal is inevitably larger than the metabolite signal, the technique is well suited to water removal. The technique was found to be less reliable when fitting metabolite signals, the methods described in Section 4.11 are more well suited to metabolite peak fitting.

The function `hlmain` performs the HLSVD, on the water suppressed FID ASCII files (`csi_n_x_ny.asc`) storing the metabolite FID after subtraction of the water signal in files

`csi_nx_ny.freres.dat`. The program `hlmain` can be operated interactively using the command `hlmain`, or in batch file mode using the program `batch_csi_realimag`. This batch application is useful when processing an array of FIDs from a SI experiment. The program invokes parameter files stored in the same directory. The threshold frequency in Hz, is set as the frequency offset from the water resonance at which the removal ceases and is specified in the file `threshold.par`. For FIDs containing signals from choline and creatine (offsets from water of 95 Hz and 108 Hz respectively) this threshold was set at 50 Hz. The threshold can be set at a higher value (e.g. 100 Hz) if the signal is known to contain only the signals from species with a larger offset in resonance from that of water e.g. acetate, NAA and lactate.

The number of iterative steps performed by `hlmain` is dictated by the parameter file `hl_main.par`. As a rule of thumb this was set at 10 times the number of different metabolites expected in the signal (≈ 50). This file also contains information on the size (`n_samples`) of the incoming data set, either 1024 samples or 4096 samples. The dimensions of the HLSVD matrices are then set in accordance at $(n_samples/2 + 1)$ (513 and 2049 respectively). Having performed the HLSVD removal of water, the data is FFTd and saved in its real frequency domain form in a file `csi_nx_ny.mets`, whilst the complex data is stored in the files `csi_nx_ny.freres.dat`.

To illustrate the effect of post acquisition water removal, the FFT of the same data in the spectrum of fig. 4.2, following HLSVD water removal is shown in figure 4.3.

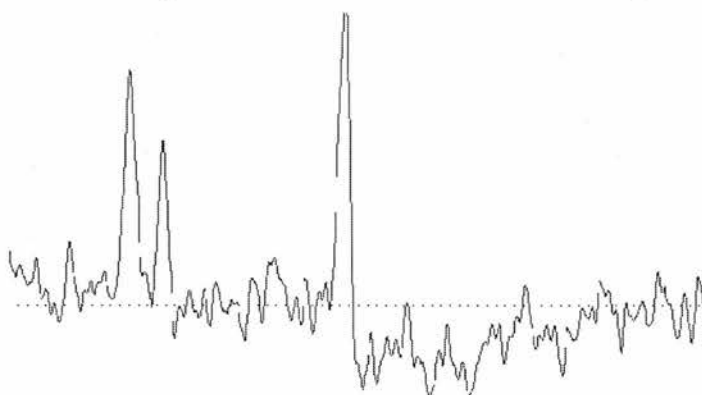


Fig. 4.3 The spectral model of fig.4.2 after HLSVD water removal - note how the baseline is less distorted.

The `.mets` files can then be combined into a spatial array using the C program `mets2gnu.c`, (written by Ian Marshall) which allows the array of spectra to be viewed using the Gnuplot graphics facility. The complex frequency domain representations

(`nx_ny.freres.dat`. files) are similarly combined for a spatial SI array by the UNIX batch file `realimag_dcsi`. This array is in a format compatible with the X-Windows SI display software `display_csi_phase` written by Martin Connell (section 4.13)

4.5 Individual data processing steps implemented by the program `centrefi112.c`

The steps outlined in sections 4.2 and 4.3 will now be covered in more detail including theoretical and experimental factors that need to be considered when implementing the techniques using computer software.

4.6 Zero filling

At a field strength of 1.5 T the signal to noise ratio of metabolite resonances imposes a lower limit on the voxel size of approximately 1 cm^3 . This produces a coarse spatial resolution in the resulting spectroscopic images. In the time domain the time limitations imposed by overall acquisition time and sampling speed of the receiver restrict the number of data points sampled in each FID.

The images can be smoothed following the k-space to real space 2D FFT using a suitable interpolation algorithm. The program `display_csi_phase` applies such a bilinear interpolation to the grid of voxel intensities to smooth the SI. An alternative mode of smoothing is to apply zero filling prior to the 2D FFT. This technique is equally useful in smoothing the frequency spectra of a time domain FID by the insertion of extra data points between the sampled data points in the spectrum.

In the time domain a series of extra data points of zero intensity can be appended to the sampled data. Upon FFT the additional data points are added as interpolated points between the points produced by FFT of the sampled data alone. Addition of a multiple of $N \times 2^n$ zeros at the end of the time domain signal of N sampled data points will add an additional 2^n interpolated points between adjacent points in the FFT.

When performing zero filling on k-space data, zeros must be appended in all four quadrants as both positive and negative k-space is sampled. This is done prior to the 2D spatial FFT by superimposing the k-space phase encoded data on a k-space array of zeros of extent $N \times 2^n$ in both the x and y directions. See (fig 4.4). This will increase the number of voxels by a factor of 2^{n+1} . Application of zero filling does not add any additional spatial detail to the end product, it does however serve as an effective method of visual smoothing. An array of water spectra zero filled from 16×16 to 32×32 is illustrated in fig. 4.5.

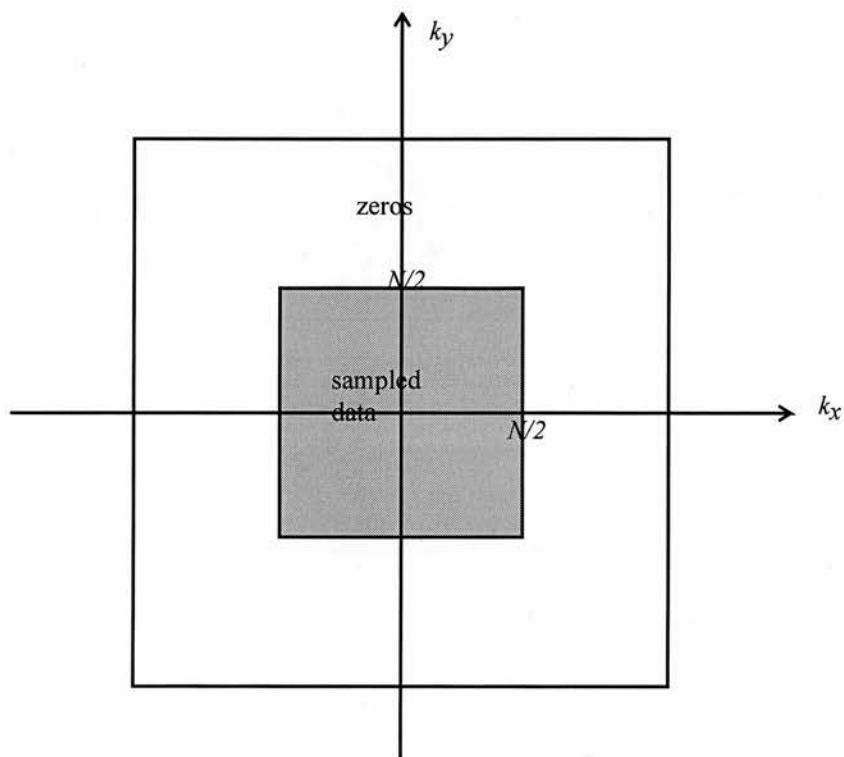


Fig. 4.4 Graphical illustration of the zero filling of outer k-space using zeros prior to the 2D k-space-real space FFT. The acquired data with $N \times N$ phase encodings in k-space is superimposed at the origin of a grid in k-space of dimensions $2N \times 2N$ and the remaining points in the grid are set to zero prior to the 2D-FFT.

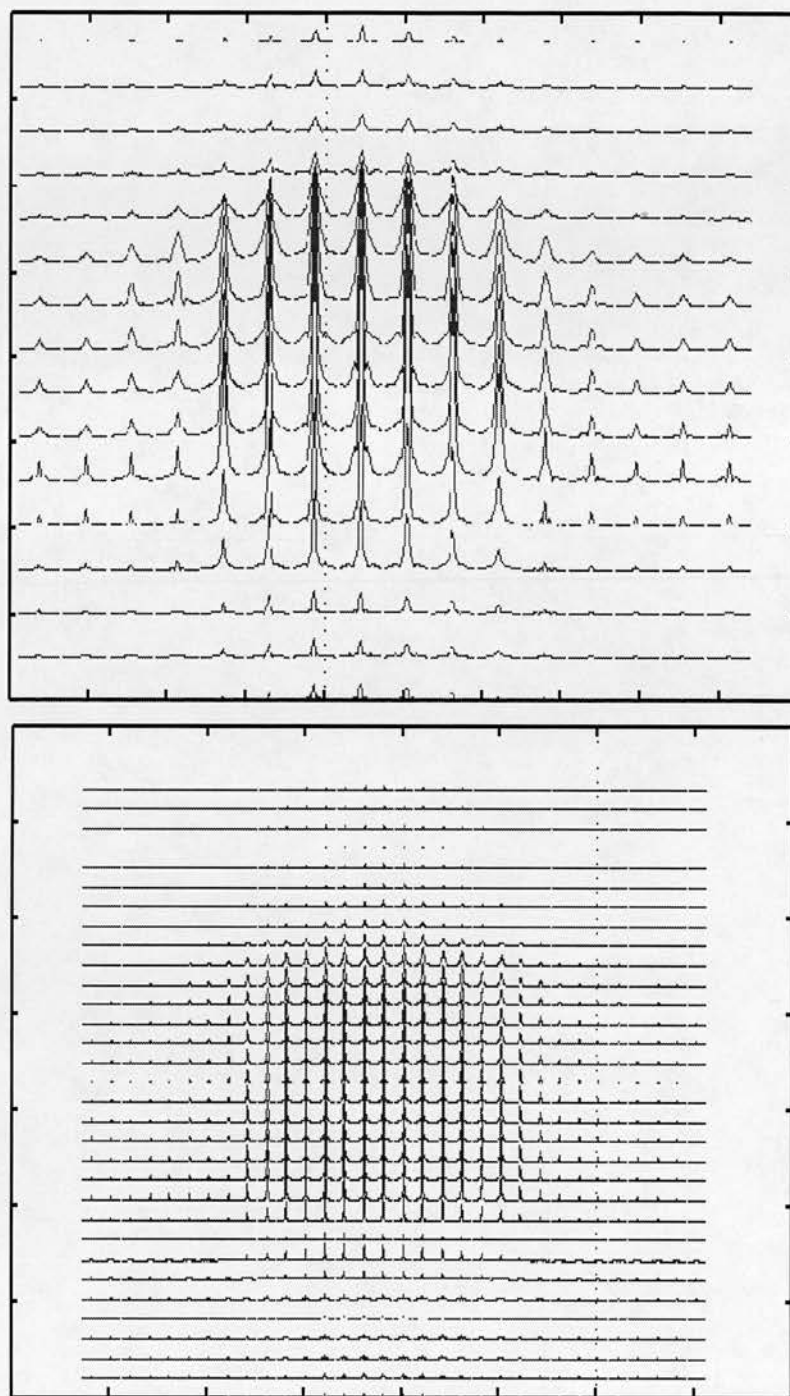


Fig. 4.5 An array of 16×16 water resonances and the same data zero filled to 32×32 spatial resolution. The spectral scale is the same, the reduced signal strength in the zero-filled array is due to the fact that the voxels are effectively four times smaller.

4.7 Voxel shifting

With selective excitation SI localisation such as PRESS, the VOI needs to be strategically positioned to avoid excitation of lipids in the scalp and marrow of the skull. Anatomic features within the brain dictate the positioning of the VOI of excitation. As such the edges of the VOI may not coincide with the edges of the SI voxels in the grid. Providing the VOI dimensions in the coronal and sagittal directions are integral numbers of the voxel width, then a post acquisition voxel shift can be implemented to align the grid and VOI retrospectively.

To do this a k-space (as opposed to time related) phase angle was added to the FID after spatial filtering but before the implementation of the spatial 2D-FFT. This procedure is entirely analogous to the addition of a phase correction angle prior to the time-frequency domain FFT. An angle of $2n\pi/16$ added in either of the sagittal or coronal directions will shift the FID by an integral number of voxels (n), with respect to the grid. This procedure is performed by the functions `voxelshiftx(void)` and `voxelshifty(void)` in the program `centrefill2.c`. The voxel shifting of the SI grid is shown in fig. 4.6 and in fig. 4.7 the corresponding effect on the spectral array is illustrated.

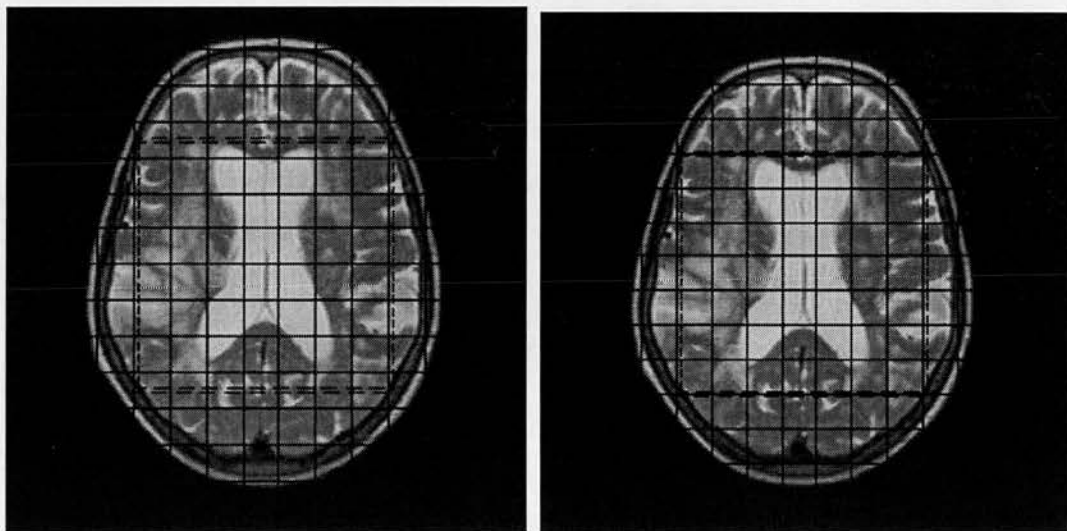


Fig. 4.6 Illustrates this process, where the grid is misaligned with the positioning of the VOI within the brain. In the second image the grid has been shifted by half a voxel in the coronal direction in to alignment with the VOI.

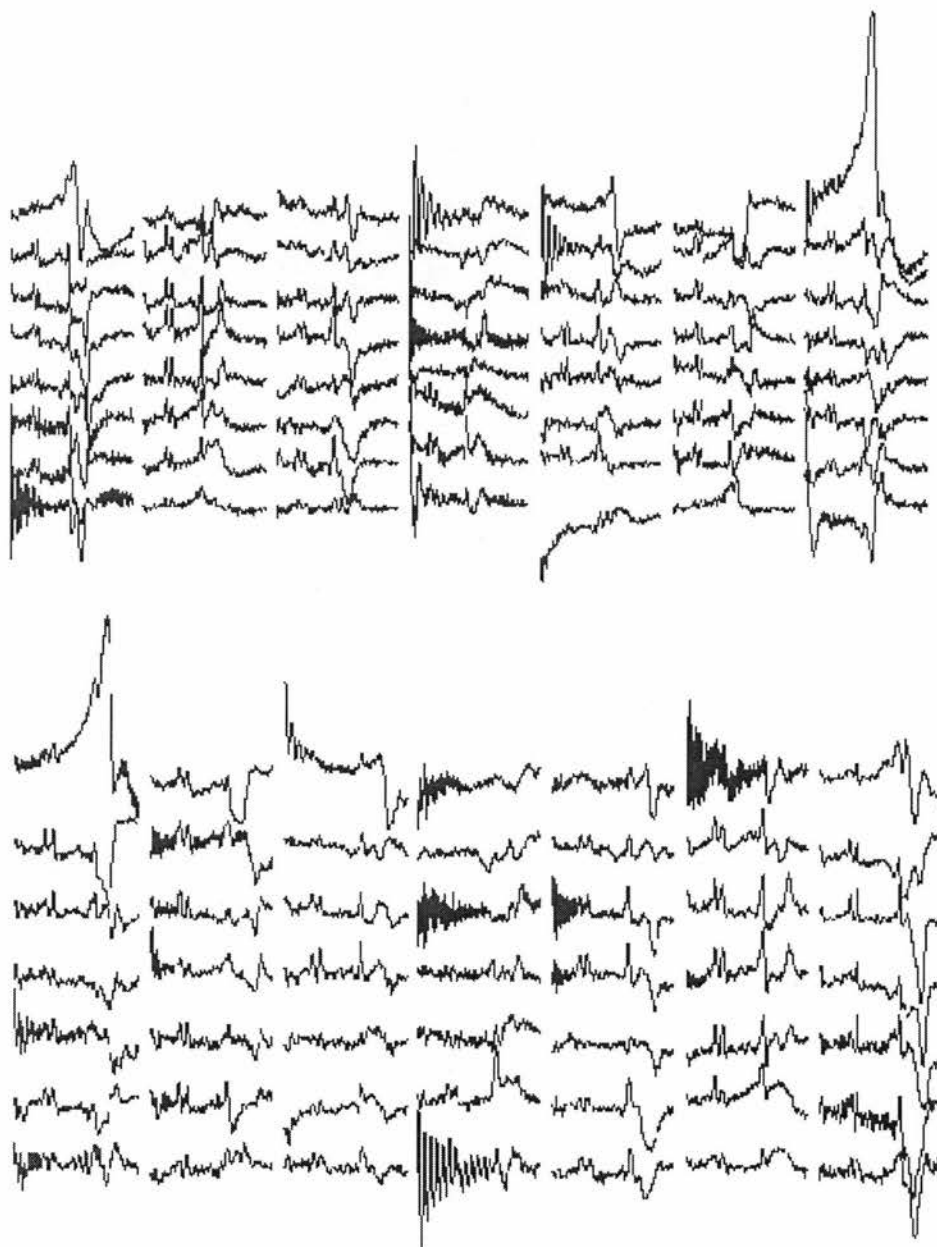


Figure 4.7 Shows the spectra obtained from this VOI prior to the voxel shifting process (upper) and afterwards (lower).

The first spectral array contains 8 rows as the bottom and top rows are partially excited by the VOI. In the second array only 7 rows are present as the VOI now covers an integral number of *whole* voxels. The voxel shifted spectra resemble a *mean* representation of the spectra from the two voxels which constitute the spatially shifted voxel.

4.8 Spatial Filtering

In this section some of the artefacts introduced to the SI by the 2D k-space to real space discrete FFT are examined and methods of filtering are reviewed to minimise such artefacts. The actual algorithm used to implement the FFT is entirely analogous to the time - frequency domain 1D-FFT. The difference being that the two *real* k-space dimensions (k_x and k_y) replace that of time and the two *real* space dimensions (x and y) replace the frequency domain.

4.8.1 Artefacts introduced by the discrete k-space to real space FFT

In common with MR imaging, SI is prone to the artefacts induced by the discrete sampling of k-space and the time domain. If the object being imaged is considered as a continuum within a finite field of view, then the corresponding reciprocal k-space is discrete but infinite. As only a finite region of k-space can be sampled, truncation artefacts are introduced when the data is Fourier transformed in to real space. In MR imaging this truncation artefact is referred to as the Gibbs phenomenon, whereby the signal obtained for one position in real space is contaminated with contributions from other positions. In this discrete analysis of k-space and real space, the total spin magnetisation within the voxel is considered and the distribution of spins within the voxel is unaccounted for. In SI a smaller number of discrete k-space samplings (phase encoding steps) are performed than in imaging, with a typical voxel grid of 16×16 compared to a 256×256 image array. As such the potential for inter voxel contamination due to the truncation of k-space sampling is greater in SI (Wang et al, 1991). In section 4.8.2, details of how this effect may be minimised are given and tests using simulations and SI data are performed.

With reference to sections 2.6.3 and 2.8.4.1, the k-space phase encoding effect of gradient \mathbf{G} on the time domain spin-echo signal, gives a SI signal, $S(k, t)$:

$$S(k, t) = \iint e^{i(\gamma \mathbf{G} \cdot \mathbf{X} \tau - \omega t)} P(\mathbf{X}, \omega) d\mathbf{X} d\omega \quad (4.2)$$

where \mathbf{X} is the 2D position vector, $P(\mathbf{X}, \omega)$ is the spin distribution function and τ is the duration of a phase encoding step. The gradient steps through N values corresponding to the segmentation of the volume of interest (width L in real space) in the m^{th} k-space direction:

$$G = \frac{2m\pi}{\gamma L N \tau} \quad (m = -N/2, \dots, N/2 - 1). \quad (4.3)$$

The spin distribution function can then be described in terms of the n square voxels which are centred at position \mathbf{X}_n

$$P_n(\mathbf{X} - \mathbf{X}_n, \omega) = P(\mathbf{X}, \omega) \quad (4.4)$$

Which when substituted in (4.2), gives the signal from each of n voxels;

$$S(k, t) = \sum_n \int e^{i(\gamma \mathbf{G} \cdot \mathbf{X}_n \tau - \omega t)} P_n(\mathbf{X} - \mathbf{X}_n, \omega) d\mathbf{X} d\omega \quad (4.5)$$

Now the discrete analysis of k-space uses the approximation that all spins are located at the voxel centre, as such (4.4) simplifies to;

$$P_n(\mathbf{X} - \mathbf{X}_n, \omega) = \delta(\mathbf{X} - \mathbf{X}_n) P_n(\omega) \quad (4.6)$$

This gives a discrete representation of (4.2);

$$S(k, t) = \sum_n \int e^{i(\gamma \mathbf{G} \cdot \mathbf{X}_n \tau - \omega t)} P_n(\omega) d\omega \quad (4.7)$$

The spectral intensity of the n th voxel P_n is then given by the time to frequency domain Fourier transform ;

$$P_n(\omega) = \sum_{\mathbf{G}} \int e^{-i(\gamma \mathbf{G} \cdot \mathbf{X}_n \tau - \omega t)} S(k, t) dt \quad (4.8)$$

The inaccuracy introduced by the assumption made in (4.6), can be investigated by considering instead, an even distribution of spins throughout each voxel rather than point sources at the centre. These effects are physically attributable to intra voxel dephasing between spins. So for a voxel centred at X_n whose width is L , (4.5) gives;

$$\begin{aligned} S(k, t) &= \sum_n \int_{X_n - L/2}^{X_n + L/2} \int e^{i(\gamma G X \tau - \omega t)} P_n(\omega) dX d\omega \\ &= \sum_n \int_{X_n - L/2}^{X_n + L/2} e^{i\gamma G X \tau} dX \int e^{-i\omega t} P_n(\omega) d\omega = L \operatorname{sinc}\left(\frac{\gamma G L \tau}{2\pi}\right) \sum_n e^{i\gamma G X_n \tau} \int e^{-i\omega t} P_n(\omega) d\omega \end{aligned} \quad (4.9)$$

This description of $S(k,t)$ given in (4.9) is a sinc modulated version of that in (4.7) where G is related to the number of the phase encoding step, m by the relation of eq (4.3)

So the k-space Fourier transformed time domain signal is left with a sinc modulation artefact as a direct result of the discrete nature of the Fourier transform, which cannot account for the distribution of spins within the voxel. In reality spins are rarely distributed evenly throughout an in-vivo voxel. As such the distribution of spins within the voxel will add a further source of inaccuracy in localisation. This effect is often referred to as the partial volume effect and is independent of the truncation artefact of the Fourier transform, just discussed. If the distribution of spins within the voxel can be predicted, by using information gained from high resolution MR images say, then this effect can be compensated (Wang et al 1991). In vivo implementation of such a technique is impractical as it involves defining the SI voxels around morphological features within which spin distributions are homogeneous. As such, corrections to reduce inter voxel contamination due to the Fourier leakage introduced by the sinc truncation artefact are the only practical form of artefact limitation and are best implemented by spatial windowing.

4.8.2 Spatial windowing

Prior to performance of the k-space to real space fast Fourier transform (FFT), a windowing function can be applied to the spatially encoded data so as to minimise Fourier leakage between adjacent spatial elements (voxels) upon transformation. This procedure is analogous to the application of a line broadening filter function (section 4.11) to the time domain FID prior to the time-frequency domain transformation (section 4.12) (Although line broadening is used for a different reason).

Multiplication of the k-space encoded FID $S(k,t)$, with a window function $w(k)$ will give a signal whose k-space to real space FT is equal to the convolution of the FTs of $S(k,t)$ and $w(k)$, (the Convolution Theorem):

$$\overline{w(k) \times S(k,t)} = \overline{w(k)} \otimes \overline{S(k,t)} = w(x) \otimes S(x,t) \quad (4.10)$$

Where $\overline{w(k)}$ and $\overline{S(k,t)}$ represent the Fourier transforms of the k-space window function and the FID, represented in real space as $w(x)$ and $S(x,t)$. The FT of the window function in

the spatial domain $w(x)$, is called the point spread function (PSF) as such the windowing process gives us a signal equal to the convolution of the spatially decoded FID with the PSF.

Data that is not windowed (i.e. windowed with a square window) has a $\text{sinc}(x)$ PSF (arising from the truncation of the Fourier transform -section 4.8.1) which has side lobes of 20 % of the magnitude of the centre lobe maximum. Effective windowing of the data prior to the 2D k-space to real space FFT will require a PSF with attenuated side lobes to reduce the inter-voxel Fourier leakage. Various filter functions are recognised as being effective, they all share the common features of being zero at either edge and rise to a maximum at the centre. The effect of such a filter is to apodise the PSF to attenuate the oscillations off axis. This is complemented by weighting each signal with a function which gradually decays to zero with distance from the centre of 2-D k-space. With an attenuation of the side lobes there is a corresponding broadening of the central lobe of the PSF. This is a result of the conservation of spectral power density whereby the integral of the square of the PSF is a constant. The broadening of the central lobe will increase the effective extent of the boundaries of a given voxel in the same way that windowing in the time domain produces line broadening in the frequency domain. Luyten et al 1990, report a two fold increase in nominal 2D SI voxel area using a cosine squared window.

For a transformation in say the x direction in to N voxels, the n th voxel (working from an origin in k-space of $N/2$) will be windowed by multiplying the data by the window function $W(n)$, prior to the FFT.

The following window functions (found in Press et al 1989) were tested, their PSF calculated and their effects on in-vivo 16×16 data compared to data filtered with a square window:

$$\text{Square window:} \quad W(n) = 1, \quad \forall n \quad (4.11)$$

$$\text{Bartlett (triangular) window:} \quad W(n) = 1 - \left| \frac{n - \frac{N}{2}}{\frac{N}{2}} \right| \quad (4.12)$$

$$\text{Hann window:} \quad W(n) = \frac{1}{2} \left(1 - \cos\left(\frac{2\pi n}{N}\right) \right) \quad (4.13)$$

Welch window:

$$W(n) = 1 - \left(\frac{n - \frac{N}{2}}{\frac{N}{2}} \right)^2 \quad (4.14)$$

4.8.3 Window functions in one spatial dimension

The window functions described above, were plotted in k-space over the range $0 \leftrightarrow n \leftrightarrow 256$ - using Matlab. A normalised FFT was then implemented on each window function to give the corresponding PSF in real space.

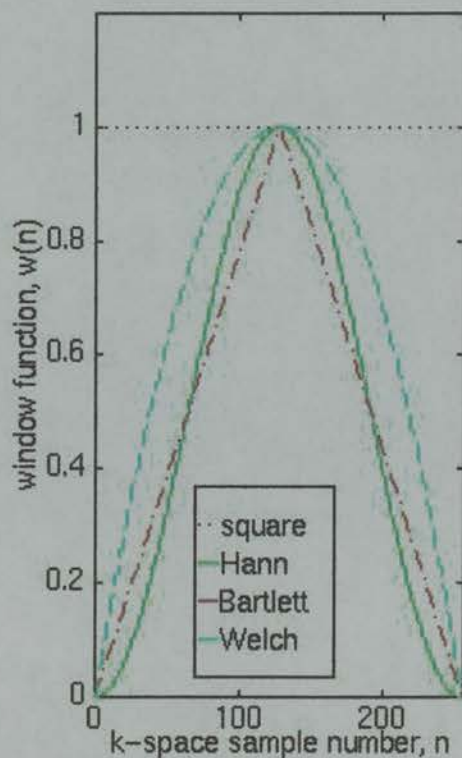


Fig. 4.8.

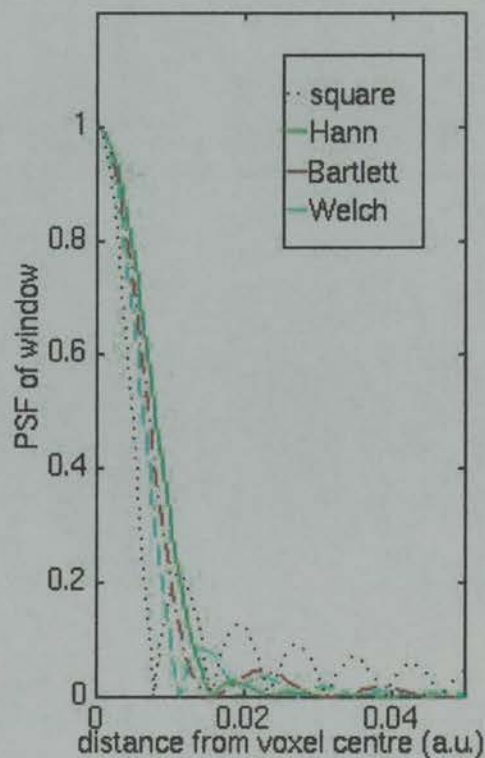


Fig. 4.9.

Fig. 4.8. The window functions plotted over the range $0 \leftrightarrow n \leftrightarrow 256$ in k-space

Fig. 4.9. The Point Spread Functions of the window functions plotted in real space. It can be seen that the square window has the narrowest centre lobe with larger side lobes, whereas the window functions have broader centre lobes with attenuated side lobes.

The full width at half maximum (FWHM) of each PSF was measured, enabling a comparison of nominal voxel width to be made. The nominal voxel width will therefore be enlarged by a factor proportional to the FWHM, whilst in 2D the voxel area will be enlarged by a factor proportional to $(FWHM)^2$.

The size of the largest subsidiary maximum is also given as an indication of the size of off axis oscillation in the PSF. These are tabulated below in table 4.1.

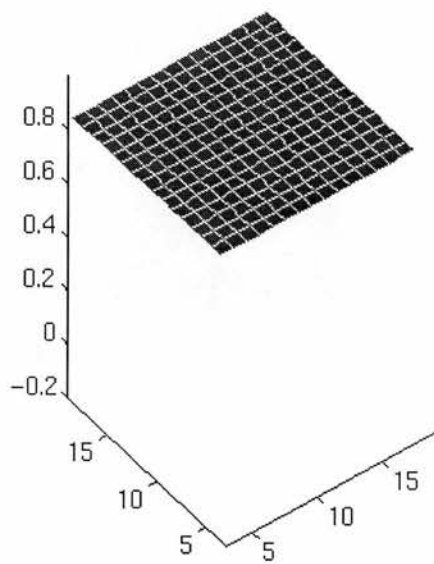
Window	FWHM of PSF	$(FWHM)^2$ - Nominal voxel area	Amplitude of 1st subsidiary maximum
Square	1	1	0.2
Hann	1.3	1.69	0.09
Bartlett	1.46	2.13	0.05
Welch	1.62	2.62	0.03

Table 4.1 Summary of the features of the respective windows illustrated in fig. 4.9.

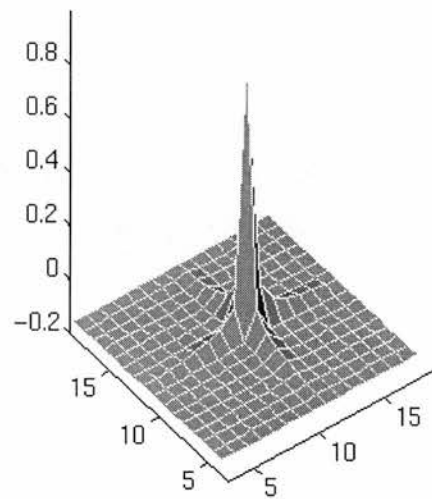
4.8.4 2D simulations of the effects of windowing functions.

To analyse the effect of a 2D window function on a 2D k-space SI data set, simulations were again performed in Matlab. A 16×16 real space array of zeros was first initialised, the central element (9,9) of this array was then set at an arbitrary value of 1000, giving a blank array with a central spike in intensity. This array was then inverse FFTd and interpolated to 256×256 points in k-space using the function `ifft2(array, 256, 256)`. The central 16×16 elements centred on the k-space origin, were then extracted and multiplied by the 2D windowing functions on a voxel by voxel basis. Extraction of the central region of k-space simulates the truncation effect imposed by the discrete nature of the k-space to real space Fourier transform. This windowed k-space data was then transformed back in to 16×16 real space array using the function `fft2(array, 16, 16)`. Each of the data sets was then normalised by dividing through by the maximum intensities located in the central voxel. This removes discrepancies in amplitude introduced by the difference in volume enclosed by the different window functions. The amplitude of the real space array - the 2D PSF, was then plotted for each window - see fig. 4.10.

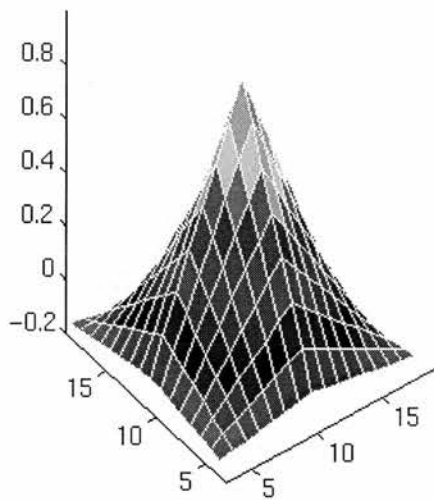
square window



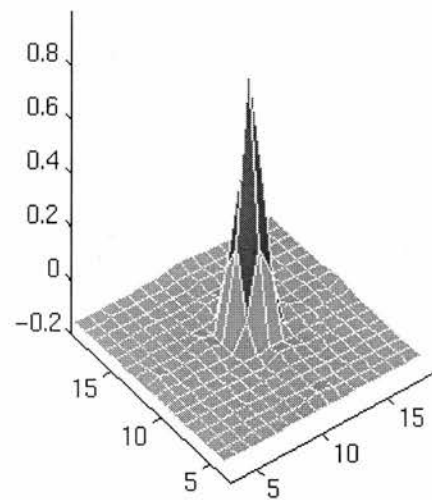
Fourier leakage from a spike in the central voxel



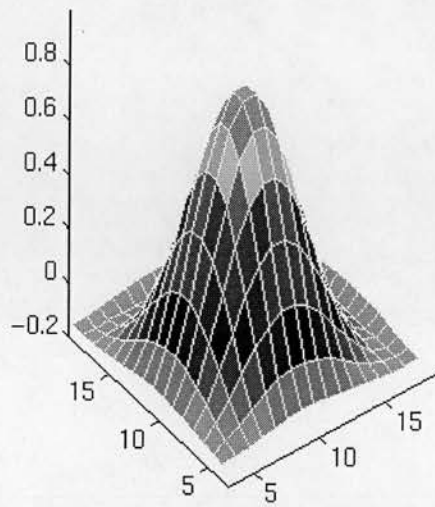
Bartlett window



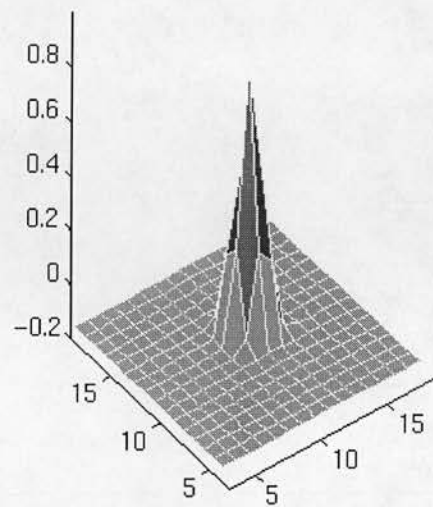
Fourier leakage from a spike in the central voxel



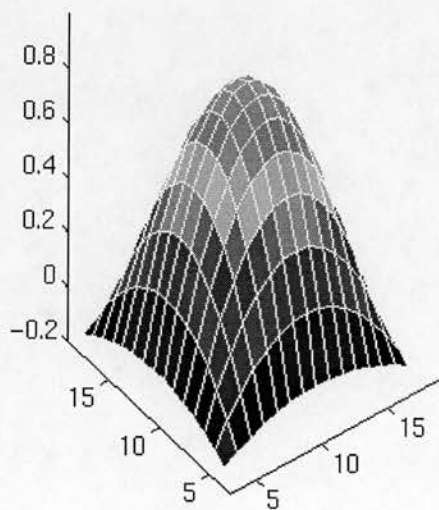
Hann window



Fourier leakage from a spike in the central voxel



Welch window



Fourier leakage from a spike in the central voxel

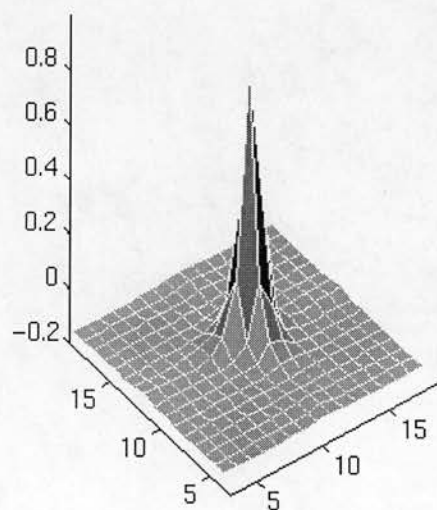


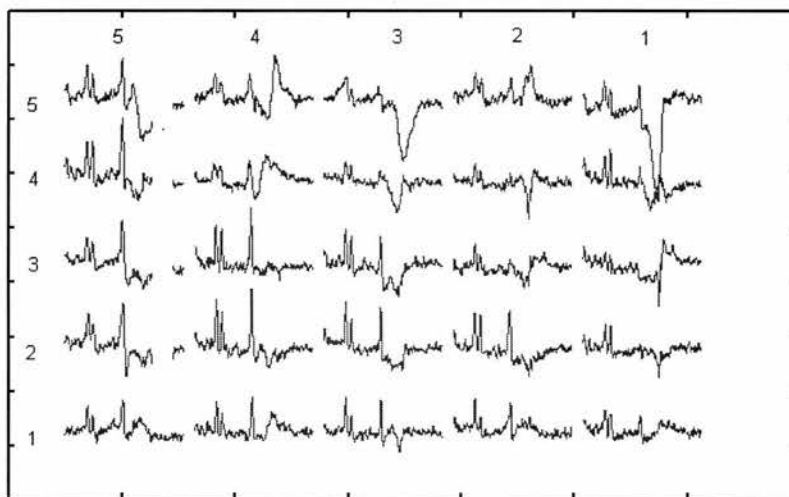
Fig. 4.10.

2D representations of the window functions over a 16x16 array

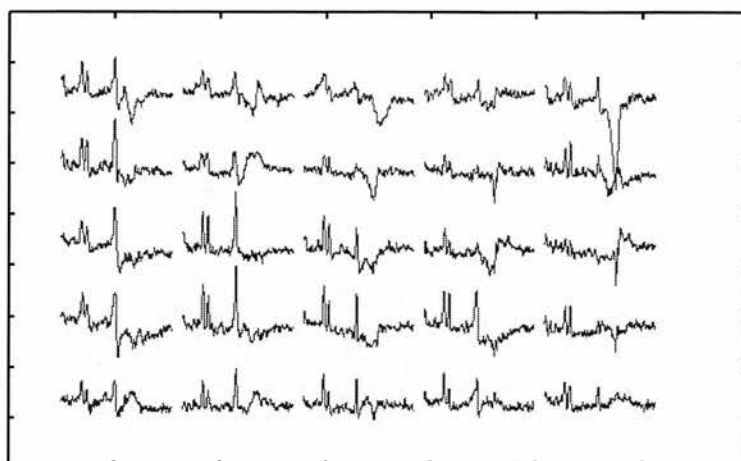
Figure 4.19 shows the Fourier leakage from a central point source signal when the FFT is filtered with the various window functions. Note that the shaped windows cause a greater attenuation in signal at large off axis distances, a consequence of the diminished PSF side lobe intensity. However there is a marked spreading of the central signal in to adjacent voxels, consistent with the larger nominal voxel size (Table 4.1).

4.8.5 In-vivo comparisons of window functions.

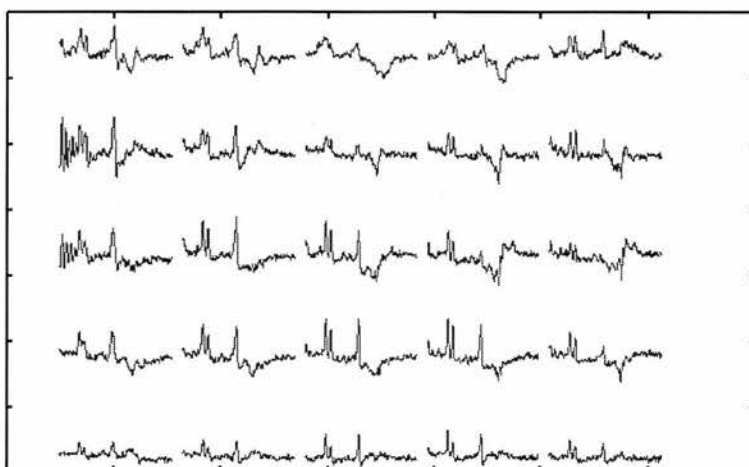
The need for k-space-real space windowing is highlighted when one of the voxels contains an abnormally large signal from a given resonance. Fourier leakage of this signal between voxels may obscure the smaller signals from the same metabolite or others with similar resonant frequencies, from adjacent voxels. With in-vivo SI studies quite often subcutaneous lipid is excited in the peripheral voxels of the grid. At concentrations greater than those of the metabolites of interest, the leakage of the lipid signal from the side lobes of the PSF in to adjacent voxels, can be significant. To investigate this, in-vivo data that was contaminated with outer volume lipid signals was taken and processed with each of the four window functions. The results are presented in fig 4.11.



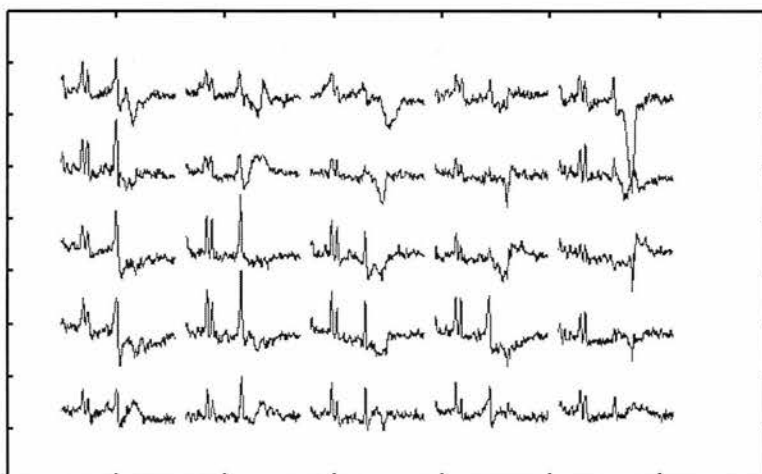
Square window



Bartlett



Hann



Welch

Fig. 4.11 The effects of different spatial window functions on the same in-vivo data.

In the example chosen from a 90mm×90mm VOI of 5×5 voxels, the spectrum from the upper left voxel (5,1) shows lipid excitation which is propagated in to the adjacent voxels by the k-space - real space FFT. Voxel (5,3) in particular shows substantial lipid leakage with a square window. The Hann window seems to be most effective in reducing the bleed of signal from this voxel. The drawback of this window is it has the widest centre lobe and as such the resolution of choline from creatine in voxels (2,5) and (5,2) is compromised. This can be explained by considering the leakage introduced by the spreading of the centre lobe of a windowed PSF from a voxel at the edge of the VOI into regions outside the shimmed VOI. Regions outside the VOI are not specifically shimmed and as such the resonant frequency of metabolites found here may be significantly different. Summarising the results of these simulations and experimental tests it seems fair to say that if attenuation of a contaminating signal from a distant voxel is required then the use of a shaped window is advisable. This will however compromise the spatial resolution of the spectral array with a greater amount of contamination between adjacent voxels. As such when processing data taken from a VOI whose edges are well away from any potentially contaminating signal, then in the interest of a more reliable spatial resolution of spectra it is best not to use a shaped window.

4.9 Phase Correction

4.9.1 Introduction

If spectra produced by ^1H SI are to be systematically viewed in the absorption mode (the real part of the spectrum) across a 2D spatial array, then phase correction is needed. This is to account for the zero order phase changes caused by spatial inhomogeneities in the B_0 field and eddy currents set up in the magnet by the fluctuating gradients of the sequence. Methods of lineshape correction rely on the deconvolution of individual signals with a single defined resonance known to be subject to identical lineshape distortions. A well defined peak in a given localised spectrum may be used as an internal reference (Maudsley 1994) providing that the same peak is discernible in all of the spatially resolved spectra. Alternatively, a separate reference can be used to correct for field induced phase discrepancies. This requires a separate acquisition of a well defined reference signal (water). As the water reference signal will be much larger than the suppressed signal, then the majority of any time evolving phase shift incurred by the signal will be due to field distortions rather than metabolite resonances. Thus the phase angle of a given data point of the water reference signal from a given voxel represents to a good approximation the zero order phase distortions. By subtracting the phase of the water component from the metabolites FID on a data point by data point basis, then any remaining phase angle will be due to metabolite chemical shifts alone. Ordidge & Cresshull 1986, pioneered this technique in applying phase corrections to non-localised spectra following the application of pulsed gradients. Klose 1990, went on to use the same method in correcting for eddy currents after shimming in a STEAM localisation experiment. The drawback of this form of lineshape correction is the extra time taken to acquire a reference signal. Roebuck et al (1993) in a 1D SI experiment tried a reduced number of phase encoding steps for the water reference, followed by zero filling to the same size as the array of metabolite spectra, and reduced the length of T_R , as a possible method of saving time. Additional frequency dependent first order adjustments may be required to phase spectra. This is more likely in SI than single voxel spectroscopy because the VOI is typically larger and as such is more prone to the field inhomogeneities produced by the spatial distributions in eddy currents and in the static field. These can be performed manually by interactive phase angle adjustment or by using an automatic phase correction algorithm (Siegel 1981).

In this work, the zero order phase correction algorithm was implemented on all FIDs (Section 4.9.2). As a potential means of reducing the acquisition time, the effect of using a reduced number of phase encodings in the water reference data was investigated (Section 4.9.3). Additional first order phase corrections were also performed when needed, either interactively (section 4.12) or automatically using a simple auto-phasing algorithm written by the author -section (4.9.4). In practice these phase correction algorithms may introduce artefacts in to the spectra, in Section 4.9.5 these artefacts are studied and their origin is explained.

4.9.2 Implementing zero order phase corrections

In both single voxel and SI PRESS localised spectroscopy, the zero order eddy current phase correction method of Ordidge and Cresshull was implemented. Having acquired phase sensitive data from the acquisition in the form of an FID, the time varying signal can be represented as:

$$S(t) = s(t)e^{i\phi(t)} \quad (4.15)$$

Where $\phi(t)$ is the time varying phase angle. If the contribution of the metabolite signal to the water reference FID is regarded as negligible then the water reference FID (collected at the transmitter frequency of the water resonance), can be represented by the time dependent water signal:

$$S_w(t) = s_w(t)e^{i\phi_w(t)} \quad (4.16)$$

Where the time varying phase of water on resonance is due to eddy currents alone i.e.

$$\phi_w = \phi_{ed}$$

The water suppressed FID will in addition to the phase changes caused by eddy currents, contain a time dependent component which bears spectral information of resonances at other frequencies, the metabolites. The water suppressed FID can therefore be represented as:

$$S_s(t) = s_s(t)e^{i\phi_s(t)} \quad (4.17)$$

Where $\phi_s(t) = \phi_{met}(t) + \phi_{ed}(t)$

Division of the suppressed signal by the reference signal phase factor should remove any time varying phase effects of eddy currents, to give a corrected signal:

$$S_c(t) = \frac{s_s(t)e^{i\phi_s(t)}}{e^{i\phi_w(t)}} = s_s(t)e^{i\phi_{met}(t)} \quad (4.18)$$

In practice the phase factor ϕ_w , was calculated by taking the arctangent of the ratio of the imaginary and real parts of the reference signal for all sampled points in time (1024 data points), by the function `calc_phase_corrections(void)`. The water suppressed signal was then corrected on a data point by data point basis by the function `apply_phase_corrections(void)` which implements the division of eq. (4.18). An example of two sets of data acquired using the STEAM single voxel sequence (Chapter 6) with an acetate-lactate phantom, with and without the phase correction process is given below, in figs. 4.12 and 4.13.

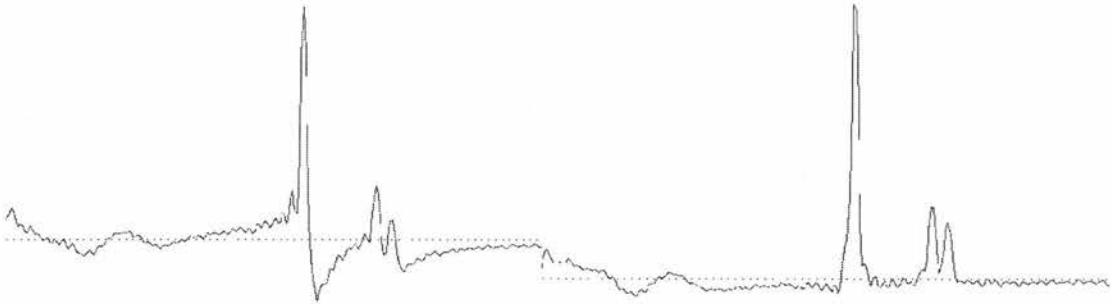


Fig.4.12. Spectrum without zero order corrections. Fig. 4.13. Spectrum after zero order correction

Note how the baseline is less distorted and the individual peaks are better resolved in the absorption mode following phase correction.

4.9.3 Using a zero-filled water reference data to reduce acquisition time

This mode of phase correction is based upon the acquisition of a second water reference data set, which for SI data sets of 16×16 phase encodings will add an additional 7 minutes to the overall scan time. When studying patients this additional time may well prove to be intolerable for a subject who has already been lying still in the scanner for 25 minutes. One method of reducing the acquisition time is to acquire a water reference SI data set with a reduced number of phase encode steps. This is then zero filled (section 4.6) to the same spatial resolution after acquisition. This technique has been reported to give effective phase

correction of 1D ^1H SI spectra of phantom data (Roebuck et al 1993). The concern with 2D in-vivo SI is that with a larger field of view there is a greater prospect of inhomogeneous fields at tissue interfaces. The technique may fail to correct for phase changes caused by field inhomogeneities that are confined to one of the voxels. To test this hypothesis a 2D SI study was conducted on a set of 6 volunteers whereby the 16×16 phase encoded water suppressed data was phase corrected with a 16×16 water reference and a zero filled 8×8 water reference. The standard PRESS SI acquisition protocols were followed (Chapter 3) with $T_R=1600$ s and $T_E=135$ ms. The data processing techniques discussed in this chapter were also adhered to with the exception that the 8×8 set was zero filled (to 16×16) prior to the 2D spatial FFT using the program `centrefill2.c`. (Section 4.6)

Areas under the spectrum corresponding to peaks of the metabolites choline, creatine and NAA were then calculated using `display_csi_phase` (Section 4.12). This is done either by fitting a Gaussian lineshape or integration between user defined limits. The area under a given peak from a given voxel for the two sets (8×8 and 16×16) of phase corrected data were then tested for statistical agreement (Bland and Altman 1986). For each of the three metabolites in all subjects, a plot of the difference between the two sets of area measurements was made against their average, for all voxels in the grid. In all cases the mean difference of the measurements from the same voxel for the same metabolite, was found to be much closer to zero than it was to the mean ± 2 s.d. limits of agreement. (Fig. 4.14). The coefficient of variation (CV) was then calculated for each metabolite and each subject, it being the s.d. of the mean of the difference measurements divided by the average of the two sets of readings. For all metabolite peaks in all subjects the CV was less than 20%, i.e. the difference was not statistically different from zero. The day-day error in reproducibility from a PRESS SI voxel of 3.375 cm^3 was found to be in the range 11%-27% (Chapter 7). With a variability of size comparable to the error in reproducibility, it can be concluded that zero filling of a reduced water reference data set will not compromise the spectral accuracy. Zero filling of the water reference data will therefore reduce the overall acquisition time without significantly reducing the accuracy of the technique and should be used as a means of reducing patient scan time.

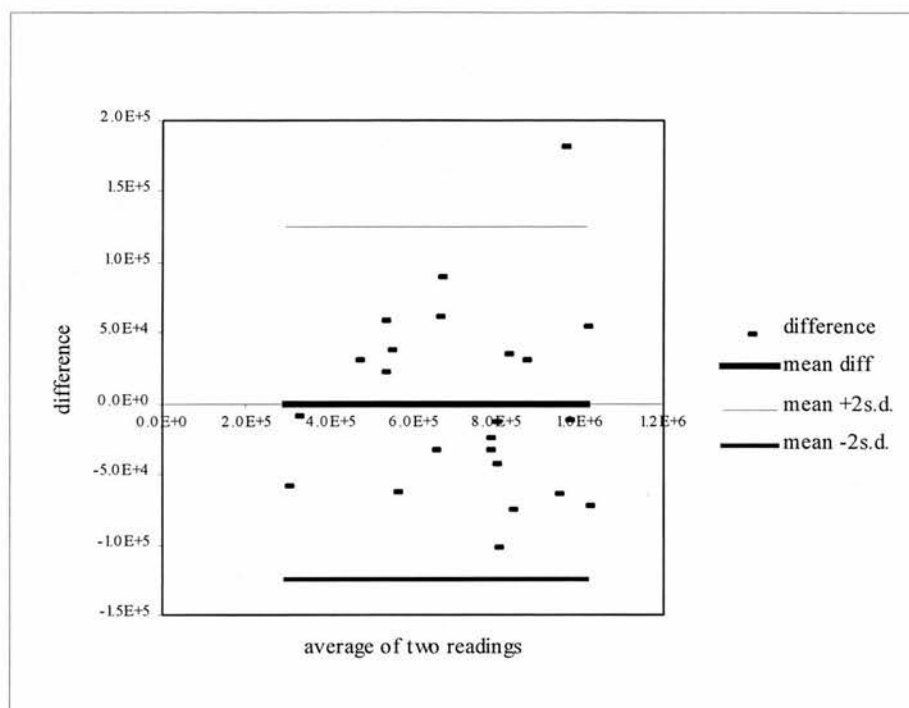


Fig. 4.14 Scatter diagram illustrating the distribution of the difference in the readings from the same voxel measured using the two different reference data set for phase correction. The confidence limits of ± 2 s.d. are drawn in.

4.9.4 First order phase corrections

Following zero order phase correction of the FID, the individual peaks in the spectrum produced by the subsequent FFT should all appear reasonably well phased. If there is a delay between the top of the echo and the start of acquisition, all of the peaks within the spectrum will have a frequency dependent phase offset. Hence an additional frequency dependent phase correction may be required to bring a peak of a given frequency into the absorption mode. This can be done retrospectively (provided that the complex frequency domain data are available), by trial and error adjustment of an additional phase angle. This mode of fine tuning of spectrum phase is available in the SI display facility `display_csi_phase` whereby an individual peak can be interactively manually phased. Alternatively the optimum first order phase angle can be calculated for a given frequency using an iterative algorithm.

The algorithm used here (written by the author) calculates the central resonant frequency for each peak by finding the point at which the magnitude of the spectrum is greatest (See fig. 4.15), using a sorting routine `sort2.c` (Numerical Recipes). It then evaluates the

phase angle of the uncorrected spectrum (fig.4.16) and subsequently phases the spectrum using this angle.

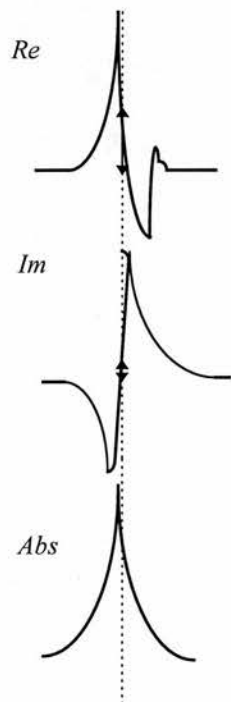


Fig. 4.15 A spectrum requiring additional first order phase correction.

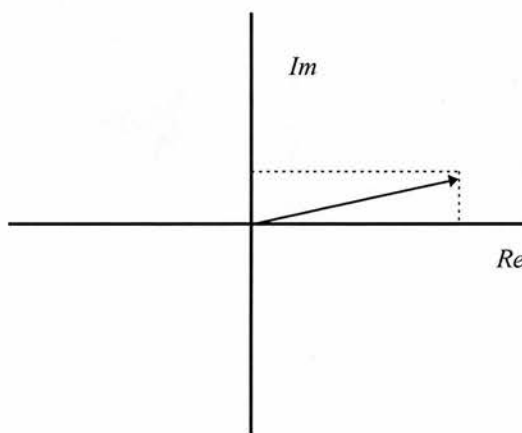


Fig. 4.16 The necessary phase angle ϕ is calculated from the phasor Argand diagram.

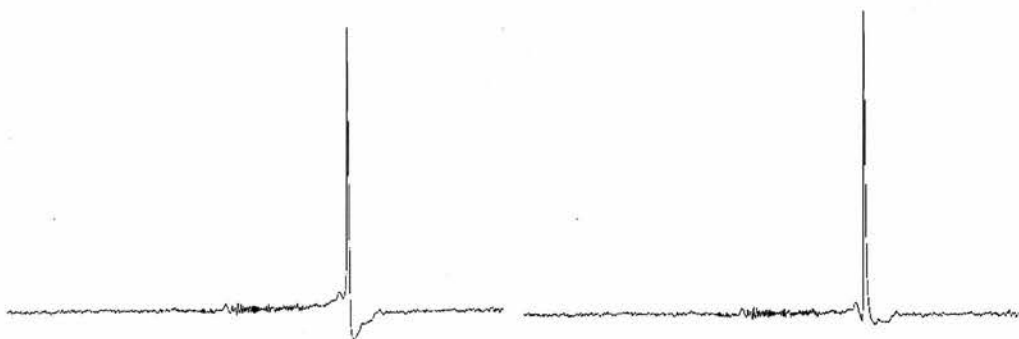


Fig. 4.17 Acetate peak before 1st order correction. Fig. 4.18 Acetate peak after 1st order phase correction.

An example of a real acetate spectrum which is in need of an additional frequency dependent phase correction is shown in fig 4.17., fig 4.18. shows the same spectrum following correction using this algorithm. More elaborate algorithms (Siegel 1981) will be needed for phasing more complicated multiplet peaks e.g. lactate.

4.9.5 Artefacts introduced by the zero order phase correction process

Examination of a number of the spectral arrays produced by the spectral FFT of the phase corrected FIDs reveals the presence of a significant number of individual spectra whose shape is distorted by a superimposed oscillatory or “ringing” artefact (see fig. 4.19)

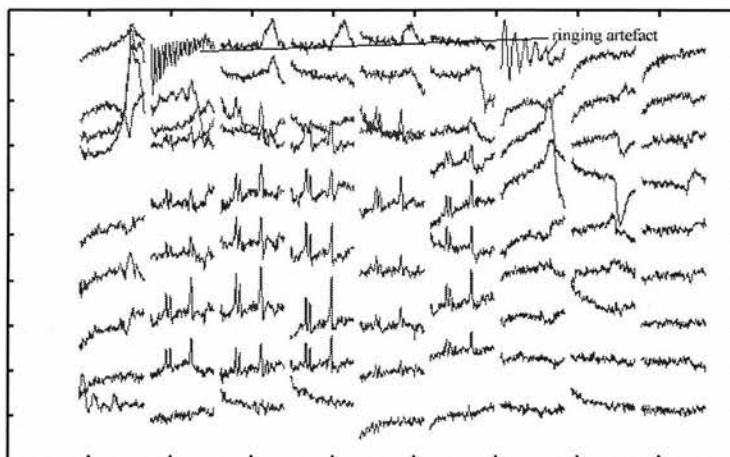


Fig.4.19. An in-vivo array of spectra, two of which are contaminated by ringing artefacts.

In order to investigate the cause of this distortion the spectral signals were examined prior to each stage of post-processing (k-space transformation in to rows and columns, phase correction and spectral transformation). It was found that the so called ‘ringing’ effect was introduced by the implementation of the first order phase correction algorithm of Ordidge and Cresshull.

The algorithm calculates the phase angle for a given data point by calculating the arctangent of the real and imaginary values of the FID for that data point. The *atan2* algorithm used in the C language to calculate such arctangents, returns an angle in the range $\pm\pi$. Thus a graph of phase angle versus data point might be expected to give a relatively smoothly evolving function with abrupt steps from $-\pi$ to $+\pi$. The phase angles of the water reference FIDs of uncontaminated spectra do in fact show such a trend.

However the plots of phase correction angle in data corresponding to contaminated spectra usually display additional jumps in phase angle at values well within the range of $\pm\pi$.

Figure 4.20 shows the plot of phase correction angle for all 1024 data points of the FID corresponding to the marked spectrum in the top right hand corner (patients left) of the array in fig. 4.19. The height of the unexpected jump in phase angle has been measured as π . Such

a jump of π in phase angle will make itself evident in the phase corrected, water suppressed FID as a step that passes through zero. The real and imaginary parts of the FID will assume the negative values of the FID that would occur if a phase flip had not taken place.

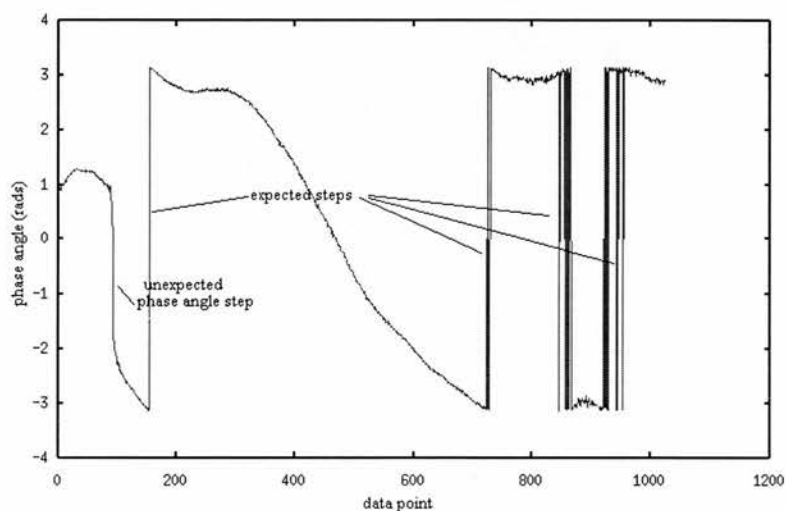


Fig. 4.20. The phase correction angle of an FID contaminated by the ringing artefact in the frequency domain.

To check that such a flip in the sign of the FID does in fact propagate the ringing artefact, simulations were performed using Matlab™. A simplified artificial FID, $F(t)$, was made from a sum of damped sinusoids consisting of a water peak off resonance by 4 Hz and the three resonances of Choline, Creatine and NAA that are consistently present in healthy volunteer spectra. The relative amplitudes, T_2 's, frequencies and phases are tabulated below. The frequencies were calculated from the chemical shift of the respective metabolite relative to a water resonance of 63.63 MHz.

j^{th} metabolite	Amplitude, a	$1/T_2^*$ (s) ⁻¹	Phase, ϕ (rad)	Frequency, ω (rad/s)
Water	100	7	0	25
NAA	2	5	0	1080
Choline	1	5	0	597
Creatine	1	5	0	679

Table 4.2. Parameters used in Matlab simulations of eq. (4.19).

$$F(t) = \sum_j a_j e^{i(\omega_j t + \phi_j) - \frac{t}{T_{2j}}} \quad (4.19)$$

When the sum of these damped sinusoids is FFTd the result is a spectrum of four definite peaks (Fig. 4.21). The model FID was then taken and at a data point of 100, was sign flipped such that the new function $F'(t)$ is represented in terms of the old model function $F(t)$:

$$\begin{aligned} F'(t) &= F(t); t \leq 100 \\ F'(t) &= -F(t); t > 100 \end{aligned} \quad (4.20)$$

When FFTd this flipped FID does show the ringing artefact found in actual patient/phantom data. Therefore it is the steps in the water suppressed, phase corrected FID that are responsible for the ringing effect.

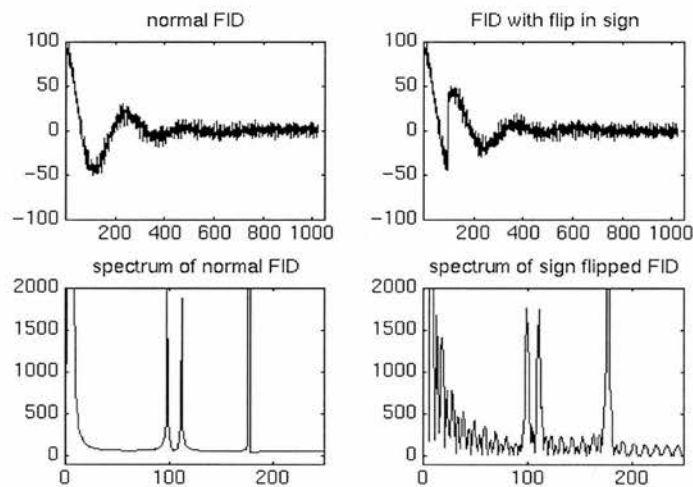


Fig. 4.21. Matlab simulations involving a step in the FID.

4.9.6 Source of artefact

The next question is why are the steps produced, i.e. why does the phase correction angle undergo unexpected jumps. In order to investigate this the water suppressed and water reference FIDs need to be looked at prior to implementation of the phase correction algorithm. Examination of the magnitude of the complex FID at data points close to the step in phase angle, reveal a node in the magnitude of the water reference FID which is reminiscent of the nodes observed in the beats effect of harmonic interference.

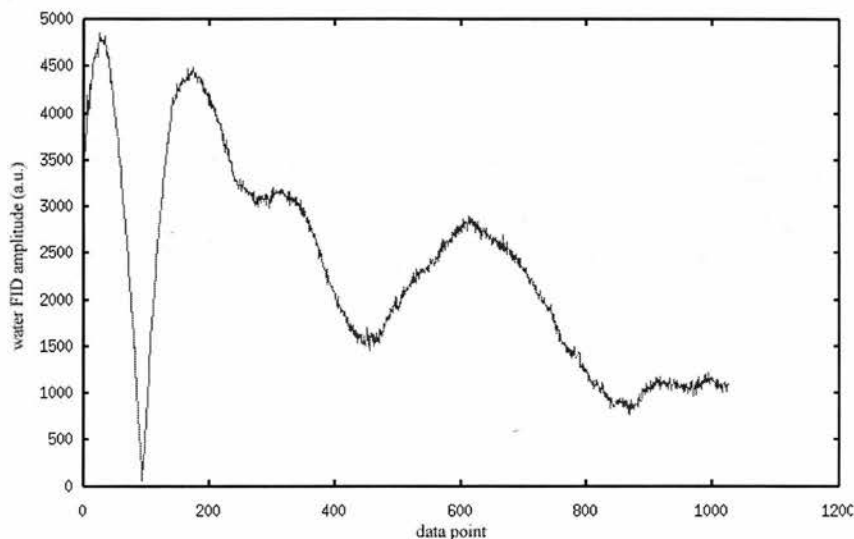


Fig. 4.22. The amplitude of the water reference FID used to phase correct the spectrum discussed in fig. 4.19.

This effect is produced by the interference of two sources whose frequencies differ by a small amount. Such a situation might arise in the field of NMR if separate regions within a volume of excitation were resonating at slightly different frequencies i.e. the B_0 field is poorly shimmed. Such a situation will often arise in a region in which there is a rapid change in susceptibility such as at a tissue/fat interface in-vivo or at a fluid-air boundary in-vitro.

To simulate such a condition, Matlab™ simulations were done using a signal consisting of the sum of two damped sinusoids whose magnitudes are comparable but whose resonant frequency differ slightly. In section 3.3 on shimming, the function $f(t)$ was plotted (fig.3.10.1), and the beating effect of interference is evident as a modulation of the e^{-t} decay envelope. The spectrum produced by FFT does indeed illustrate the splitting in resonant frequency fig.(3.10.2).

So in conclusion, if the oscillatory phase correction artefact is to be avoided then a well shimmed B_0 field throughout the VOI must be sought. Automatic shimming algorithms (Section 3.3.3) may help as will avoiding obvious regions of differential susceptibility. If the artefact persists, the individual spectra can be corrected using an algorithm that reverses the flip in sign of the atan2 function whenever the water reference FID approaches a node in its magnitude. Such an algorithm was tested but was not found to be very robust, working in some cases and producing additional artefacts of its own in others.

4.10 Time domain windowing- line broadening

The time domain FID can be filtered by multiplication with a time domain window function, $w(t)$, prior to spectral transformation. The effect of this window is to apodise the FID to ensure that it decays towards zero within the period of the acquisition time. Otherwise the FID will be truncated (Fig. 3.9) and the spectrum will be subject to baseline distortions. In-vivo, this effect is not such a problem as the FID has generally decayed to noise level by the end on the acquisition time. Forcing the FID to decay to zero amounts to an apparent decrease in the T_2^* and causes an increase in the line width of individual peaks. As such the contribution from minor peaks (noise) can be smoothed out. A variety of time decay functions can be used for $w(t)$. In this analysis a Gaussian line broadening function was used

$$w(t) = e^{-\ln b^2 t^2} \quad (4.21)$$

This Gaussian window gives a frequency domain line broadening equal to b Hz. In the examples shown in fig. 4.23. a range of line broadenings from $b=0-8$ Hz, were applied to in-vivo data.

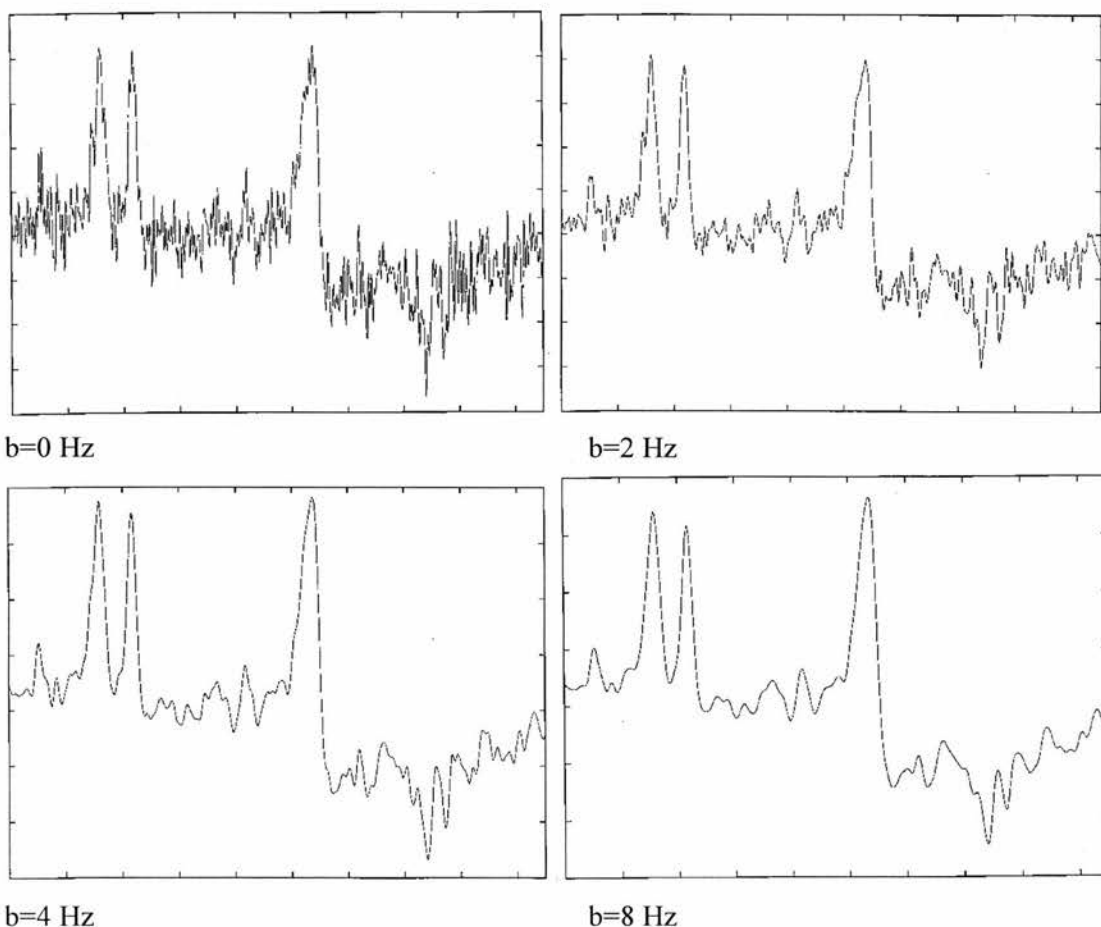


Fig.4.23 The effects of degrees of line broadening in in-vivo data.

The smoothing effect of line broadening is quite clear, with no line broadening the noise in the spectrum is well resolved. Conversely with a drastic line broadening $b=8$ Hz, the noise has been attenuated at the expense of a broadening of the choline and creatine peaks. This effect is analogous to the k -space-spatial filter which broadens the central lobe of the PSF to a range greater than one voxel, in this t - f domain case there is an increased smearing between adjacent points which leads to a broader f -domain signal. For routine data processing in vivo a line broadening of $b=4$ Hz was used throughout the study.

4.11 Signal Interpretation - FFT and alternative models

4.11.1 Introduction

The classical way of determining the frequency components of an oscillatory time domain signal is to use Fourier methods. Ideally the Fourier transformation of FIDs will yield spectra with well defined peaks, the area under which can be integrated to give a direct measurement of individual metabolite concentration. In practice however, the peak of interest may have incurred a B_0 frequency shift and lineshape distortion. These effects may be reduced by deconvolution with a reference signal. Nevertheless the baseline of the spectrum may still contain some water distortion, and furthermore some peaks will inevitably overlap (e.g. choline and creatine). However if water suppression has left a flat baseline and the aforementioned frequency shift corrections have left specific metabolite peaks aligned at the same frequency for all voxels, then it may be possible to proceed directly to automated integration of certain well defined peaks (section 4.3.5). For long echo time acquisitions, only metabolites with long T_2 's will be pronounced (cho, cr, NAA and lactate) and as such, peaks should be well discerned with respect to the baseline. However at short echo times, short T_2 resonances will be evident and the definition of individual peak frequency limits may well be impossible (Frahm et al 1989) especially if baseline distortions are persistent. In such circumstances the signal may have to be broken down in to its components using a fitting procedure in order to isolate a desired resonance from baseline distortions and background noise.

4.11.2 The Fourier transform

With a continuous function, a continuous Fourier transform integral can be performed. With a physically realistic signal that consists of discrete sampled data points, a discrete Fourier transform is needed. Various algorithms have been used to perform such a discrete Fourier transform, most notably the Fast Fourier transform (FFT) first described by Cooley and Tukey (Press et al 1992). In this section the process of performing a FFT on a sampled FID is discussed and the various artefacts that can arise as a result of the FFT are considered. In chapter 2 the time varying response of a spin system to an applied r.f. pulse was obtained from the Bloch equations (2.26a) for the time evolution of the transverse magnetisation. Applying this equation to a discretely sampled signal gives:

$$S(t) = \sum_j a_j e^{-(i\omega_j + 1/T_{2j}^*)t} \text{ for } t \geq 0 \quad (4.22)$$

$$S(t) = 0 \quad \text{for } t < 0$$

Where the amplitude, chemical shift and relaxation time are given for the j^{th} resonance by; a_j , ω_j and T_{2j}^* . Detection of a complex signal is made possible by the quadrature arrangement of the receiver coil (section 3.1.2). To achieve a frequency representation of this signal a complex Fourier transform $\hat{S}(\omega)$, can be performed to give:

$$\hat{S}(\omega) = \int_{-\infty}^{\infty} S(t)e^{-i\omega t} dt = \sum_j \frac{a_j}{1/T_{2j}^* - i\Delta\omega_j} \quad -\infty < \omega < \infty \quad (4.23)$$

Where $\Delta\omega_j = \omega - \omega_j$. Equation (4.23) expresses the Fourier transform as a sum of complex Lorentzians. Separating the expression in to its real and imaginary parts gives:

$$\hat{S}(\omega) = \sum_j \frac{a_j}{(1/T_{2j}^*)^2 + (\Delta\omega_j)^2} [1/T_{2j}^* + i\Delta\omega_j] \quad (4.24)$$

The real part of this expression corresponds to the classical absorption spectrum whilst the imaginary part refers to the dispersion spectrum. In reality NMR spectra are very rarely purely in the absorption mode as the detection process adds a phase angle φ to the exponential in equation (4.22). This phase angle has two components, a frequency independent, zero-order angle (φ_0) due to the demodulation with the reference signal during detection (see section 3.1.2) and a first order frequency dependent component ($\omega_j\varphi_1$).

$$\varphi_j = \varphi_0 + \omega_j\varphi_1 \quad (4.25)$$

The first order term arises from the effect of the low-pass filter of the detection mode (Tang 1994) and in addition there is a time lag τ between the top of the echo and the start of acquisition, this is a result of the finite ramp times of the ADC switching.

The fact that a physical time domain signal is not continuous but instead consists of discrete data points implies that the Fourier transform must also be discrete in nature rather than a continuous integral. The sampled signal is now expressed as a function of $t = k\Delta t + \tau$. The sampling interval is Δt , the number of the sampled data point is an integer k and the time lag between the centre of the r.f. pulse and the start of acquisition is τ .

$$S(k) = \sum_j a_j e^{-(i\omega_j + 1/T_{2j}^*)(k\Delta t + \tau)} \quad \text{for } t = k\Delta t, k = 0, 1, 2, \dots, N-1. \quad (4.26)$$

Using the relation $A_j = a_j e^{(i\omega_j - 1/T_{2j}^*)\tau}$, the exponential of the first order phase term due to the acquisition time lag can be incorporated. The discrete Fourier transform can then be calculated by performing a summation as opposed to the continuous integral of eq. (4.23), for all values of k . The derivation of the discrete Fourier transform as a finite sum of a geometrical progression is given by Gesmar et al 1994. It is quoted here:

$$\hat{S}(\omega) = \sum_j \frac{A_j (1 - e^{-(1/T_{2j}^* + i\omega_j)N\Delta t})}{1 - e^{-(1/T_{2j}^* - i\Delta\omega_j)\Delta t}} \quad -\pi w \leq \omega < \pi w \quad (4.27)$$

Where the angular frequency ω , takes on all the N discrete values within the bandwidth of the spectrum ($2\pi w$). This is in turn dictated by the reciprocal of the sampling interval, $w = 1/\Delta t$. Unlike the continuous Fourier transform of eq. (4.23), this discrete version is no longer a sum of Lorentzians. Equation (4.27) can, however be simplified. The numerator approximates to unity as the exponential term [the value of the FID at the end of acquisition ($t=N\Delta t$)] approaches zero, either through the natural effect of T_2^* decay or by a post processing apodisation (line broadening) of the FID. If we let $(i\Delta\omega_j - 1/T_{2j}^*)\Delta t = x$, then the expression $\lim_{x \rightarrow 0} \left(\frac{1}{1 - e^x} + \frac{1}{x} \right) = \frac{1}{2}$ can be used to reduce equation (4.27) to:

$$\hat{S}(\omega) = \sum_j A_j \left[\frac{1}{2} - \frac{1}{(i\Delta\omega_j - 1/T_{2j}^*)\Delta t} \right] \quad (4.28)$$

4.11.3 Artefacts of the discrete Fourier transform

The expression in eq. (4.28) for the discrete Fourier transform can now be analysed in more detail. First of all there is an additional time lag induced, first order phase shift that is

intrinsic to $A_j = a_j e^{(i\omega_j - 1/T_{2j}^*)\tau}$. With a time lag of τ the j^{th} spectral line incurs a phase of $\omega_j \tau$. The simulations shown in Fig. 4.24, illustrate this point with a lag of one data point in 1024 causing the distortion in the baseline of the second spectrum (ii) compared to the pure absorption spectrum of the first spectrum (i) which corresponds to a signal acquisition

commencing at $t=0$. A lag of one data point in a SI signal corresponds to a time lag of 1ms between the start of a 1024 ms acquisition and the application of the r.f pulse (i.e. the top of the echo).

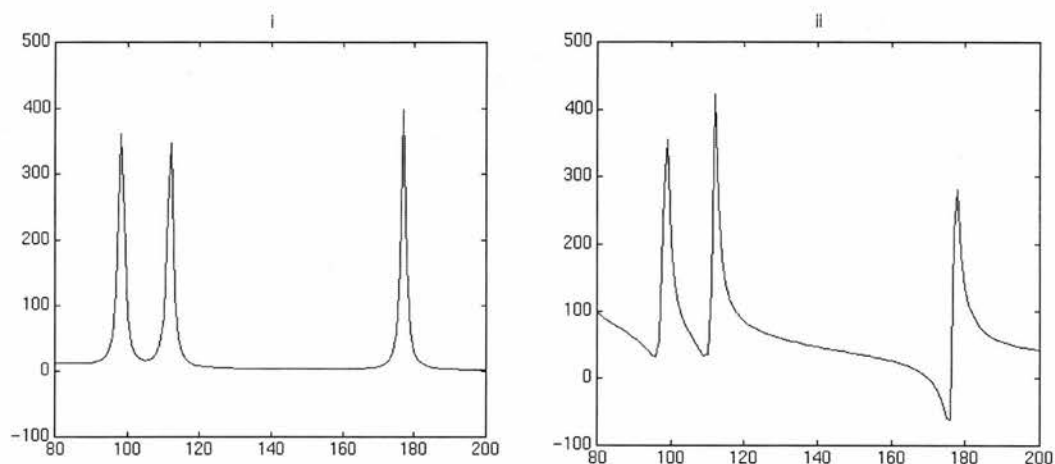


Figure 4.24. Baseline distortions introduced by a time lag between the onset of sampling and the maximum ($t=0$) signal of the FID/echo.

The term of $1/2$ in equation 4.28, also gives rise to an artefact in the form of a baseline offset to each data point equal to $\frac{A_j}{2}$. This is a direct result of the discrete nature of the Fourier transform, in that there is a discontinuity in the function at $t=0$ (because the function $S(t)$ only exists for $t>0$ and as such $S(t)$ cannot be evaluated either side of the point $t = 0$).

Now the coefficient $\frac{A_j}{2}$ is equal to half the value of the first data point of the acquisition ($S(0)/2$) - see eq.(4.26). Consequently, if half the value of the first data point is subtracted from the remaining sum of $N (=1024)$ data points, this offset can be removed. Figure 4.25. shows the FFT (iii) of an FID(i) without the factor of $S(0)/2$ removed and the FFT(iv) of the same FID (ii) with this factor removed.

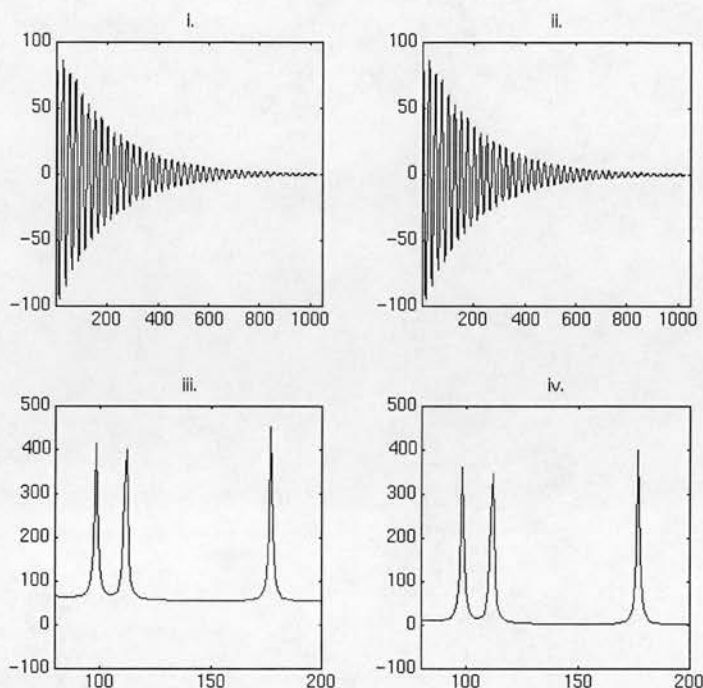


Fig 4.25. Baseline offsets introduced by the discontinuity in the sampling of the FID at $t=0$.

4.11.4 Implementation of the discrete fast Fourier transform (FFT) on a SI data set.

In section 2.1 the relation between bandwidth of the spectrum and sampling interval was given; ($w = 1/\Delta t$). Nyquist's theorem, states that the minimum sampling frequency (the Nyquist frequency) required to extract all the frequency information from a sinusoidally time varying signal is twice that of the highest frequency component. If the signal being sampled is not bandwidth limited (i.e. contains frequencies greater than the Nyquist frequency $>1/2\Delta t$) then the high frequency components will be aliased and combined with the frequencies actually sampled in the chosen bandwidth. In ^1H spectroscopy the metabolites of interest lie within a range of 0-500 Hz away from the water resonant frequency (the carrier frequency of the transmitter). As such a minimum sampling frequency of 1000 Hz corresponding to a sampling interval of 1 ms is used. With a quadrature detection system both the real and imaginary parts of the time domain signal can be sampled. The Magnetom collects the real part of the signal followed by the imaginary part in an interleaved sample giving 1024 real data points and 1024 imaginary data points. With a discrete time domain signal, the Fourier transform integral of eq. (4.23) can be approximated by a summation. If the magnitude of the discrete value of the sampled signal

at the k^{th} data point (corresponding to time $t = kT_{\text{a/q}}/N$) is given by $s_k (= u_k + iv_k)$, then the discrete Fourier transform can be approximated for the j^{th} frequency by the series:

$$\widehat{S}(f_j) = \int_{-\infty}^{\infty} S(t) e^{-f_j t} dt = \sum_{k=0}^{N-1} s_k e^{(-2i\pi f_j k \Delta t)} \Delta t = \Delta t \sum_{k=0}^{N-1} s_k e^{(-2i\pi k j / N)} \quad (4.28)$$

The summation in the above expression is the definition of the discrete Fourier transform (\widehat{S}_j) which is related to the continuous Fourier transform by the relation $\widehat{S}(f_j) \approx \Delta t \widehat{S}_j$ (eq. 4.28). Where the frequency f_j is given by; $f_j = j/N\Delta t$ and j takes values in the range $-N/2$ to $N/2 - 1$. The FT in the negative frequency range ($-N/2$ to -1) is replicated by the positive range ($N/2$ to $N-1$). Since it is physically meaningful to think in terms of positive frequencies then it is simpler to express \widehat{S}_j for the range $j=0, 1, 2, \dots, N-1$. The second half of the frequency domain data then needs to be displayed prior to the first half to maintain consistency with the defining range of $-N/2$ to $N/2 - 1$. This is done in practice by the last part of the function `spectral_transform(void)`, the routine that implements the FFT. The expression for \widehat{S}_j can now be split up into two components corresponding to even and odd data points:

$$\begin{aligned} \widehat{S}_j &= \sum_{k=0}^{N-1} s_k e^{(-2i\pi k j / N)} = \sum_{k=0}^{N/2-1} s_{2k} e^{(-2i\pi j(2k) / N)} + \sum_{k=0}^{N/2-1} s_{2k+1} e^{(-2i\pi j(2k+1) / N)} \\ &= \sum_{k=0}^{N/2-1} s_{2k} e^{(-2i\pi j k / (N/2))} + e^{(-2i\pi j / N)} \sum_{k=0}^{N/2-1} s_{2k+1} e^{(-2i\pi j k / (N/2))} \end{aligned} \quad (4.29)$$

Let $W = e^{-2\pi i / N}$ then;

$$\begin{aligned} \widehat{S}_j &= \sum_{k=0}^{N/2-1} s_{2k} W^{2jk} + W^j \sum_{k=0}^{N/2-1} s_{2k+1} W^{2jk} \\ \widehat{S}_j &= \widehat{S}_{jk}^e + W^j \widehat{S}_{jk}^o \end{aligned} \quad (4.30)$$

Equation (4.30) illustrates how the discrete Fourier transform of length N can be split in to a sum of separate even and odd Fourier transforms of length $N/2$, which are formed from the even and odd numbered points of the original N respectively. A recursive application of this reduction allows \widehat{S}_{jk}^e and \widehat{S}_{jk}^o to be broken down in the same way in to odd and even components of length $N/4$ (e.g. $\widehat{S}_{jk}^e \rightarrow \widehat{S}_{jk}^{ee}$ and \widehat{S}_{jk}^o). Providing that the length N of the input array is an integer power of 2, then repetition of this process leads to the point where a transform of length 1 is left, the value of which corresponds to one of the original s_k input

numbers. A process of bit reversal is then used to order the end products of the FFT with respect to the even and odd ordering of the breakdown. The arrival of the algorithm at an end value equal to one of the input (s_k) values means that the computer algorithm can directly replace the array of input s_k 's with the corresponding discrete value of the FT (\hat{S}_{jk}). This is the FFT algorithm of Danielsen and Lanczos (Press et al 1992) performed by the routine `four1(spec_FT_temp, n_samples, 1)`. This is a complex FFT routine taken from Numerical Recipes in C, and incorporated as part of the subroutine `spectral_transforms(void)` in the program `centrefill12.c`. Following implementation of the FFT the complex array (N real points interleaved with N imaginary points) of data is replaced by its complex FFT which is again interleaved.

4.12 Fitting

As described in section 4.11.3, the FFT process can quite often introduce spurious artefacts in to the frequency domain representation of a time domain signal. Measures to curtail these effects are also discussed in section 4.11.3. Despite these measures, individual peaks in a FFTd spectrum may be difficult to discern, either through low signal to noise, poor shimming or incomplete water/lipid suppression. In such cases a mathematical fitting of either the time domain signal or the frequency domain spectrum (FFT) may well reveal metabolite information not apparent from a visual inspection of the spectrum alone. Fitting procedures can be implemented on the spectrum itself or alternatively on the time domain signals. They can be based upon a parametric model of the signal which yields estimates of the parameters in eq.(4.26). Alternatively a modelling procedure that does not use the parameters of (4.26) but instead some other physical property of the signal, (e.g. its entropy) can be used. Such techniques are termed *non-parametric* even though they involve the prediction of parameters relating to some physical property which is representative of the signal/spectrum. In either case, prior knowledge of the experimental spectrum, such as metabolite chemical shifts, line width and multiplicity can be used to facilitate the fitting. As the Fourier transformation of an FID into the frequency domain can, introduce sources of error then fitting in the time domain may be more reliable as such effects are circumvented. Frequency domain fitting procedures are however, still valid and have been used. In many respects it seems more logical to model in the frequency domain as specific resonances are more clearly visible as peaks in the frequency domain than as minor oscillations in the FID.

Whether calculations are performed in the time or frequency domain, it is still necessary to visualise the model as a set of peaks in the frequency domain.

4.12.1 Non-parametric methods

Maximum entropy /Auto-regressive spectral estimation

The maximum entropy method (MEM) uses an approximation that is the most probable representation of the true power spectrum density (PSD) of the original FID and its inherent noise, as opposed to its Fourier transform. Eq. 4.29. gives an expression for the discrete FFT from which an estimate of the power spectrum is obtained by taking the square of the FFT:

$$P(f) = \left| \sum_{k=-N/2}^{N/2-1} s_k z^k \right|^2 \quad (4.32)$$

Where $z = e^{2\pi i f \Delta t}$. This estimate is subject to inaccuracies as a result of its finite nature, a consequence of the finite number of time domain samples. An analytical expression of the true PSD is given by :

$$P(f) = \left| \sum_{k=-\infty}^{\infty} s_k z^k \right|^2 \quad (4.33)$$

In the MEM, an alternative estimate to the analytical function of eq.(4.33) is used which has a summation in k in its denominator;

$$P(f) \approx \frac{a_0}{\left| 1 + \sum_{k=1}^M a_k z^k \right|^2} \quad (4.34)$$

Zero values of this denominator will give rise to poles in eq. (4.34), these correspond to an infinite power spectral density i.e. very sharp spectral peaks (delta functions). This suggests that the MEM method will be good at resolving fine detail in the frequency domain. A measure of the amount of such detail contained in an estimate of a signal is the entropy of the signal, as such coefficients a_0 and a_k are sought in eq.4.34 which maximise this entropy. The entropy of an NMR signal has been dealt with on a more statistical basis (Daniell and Hore 1989) than the z function definition given in (4.34) which has its foundations in digital filter theory.

The program used to perform the MEM estimate of the PSD is called `armatd.c` and reads the real part of the time domain signal which is saved by the `save_td(void)` routine of the SI program. The coefficients a_0 and a_k are then calculated using a linear prediction

(LP) technique (see section 4.11.10) whereby the user specifies the number of linear prediction coefficients (M). This in turn dictates the total number of poles (spikes) in the PSD estimate. The linear prediction routine used here, is taken from Numerical Recipes in C; `memcof(float data[], int n, int m, float *xms, float d[])`, which for a vector of data $s[k]$ of length n , and a specified number M , of LP coefficients will return the coefficients of eq. (4.34) as $a_k=d[1..m]$ and a_0 as $*xms$. This routine uses Burg's algorithm (Kay 1988, Marple 1988) to calculate the LP coefficients. Having determined a_0 and a_k for a given M , the routine `evlmem(float fdt, float d[], int m, float xms)` calculates the PSD estimate as a function of $f\Delta t$. The computational operations count of the `memcof.c` routine scales as the product of N (the no. of data points) and M , the desired order of the MEM approximation. In comparison the computing time required to implement the FFT on a data set of length N , is scaled according to $N\log N$. In practice the number chosen for M is usually one order of magnitude larger than the number of peaks expected in the spectrum. If say 4 metabolite peaks plus a water peak are anticipated then M would be set at 50 giving an overall computation time of around 50000 (a.u.). This is approximately one order of magnitude longer than the equivalent FFT (6000 a.u.). If a smaller M is chosen, the MEM has a tendency to smooth out the broader peaks in the spectrum. Conversely if too large a value of M is used then the MEM can give rise to spurious additional peaks in the PSD estimate of the spectrum. To test the viability of the MEM in fitting in-vivo data, the PSD of the real part of an in-vivo time domain signal was calculated over a frequency range of $50 \text{ Hz} < f < 300 \text{ hz}$ for a Δt of 1ms (the fixed sampling interval). Values of M ranging from 20 to 200 were used and the square root of the MEM PSD was calculated and compared to the N point real FFT of the same time domain data. The results are shown below in Fig. 4.26.

With $M=20$, the NAA peak has been well resolved whilst the overlapping choline and creatine peaks are smoothed together. At $M=35$, the choline and creatine peaks start showing some resolution, but it is not until $M=40$ that the MEM estimate bears a noticeable resemblance to the FFT. One good feature of the MEM model at low M is the absence of significant spikes of noise, present in the FFT. A more drastic line broadening of the FID prior to FFT (section 4.10) will have a similar effect on the FFT spectral estimate. At large M (80), noise peaks become more pronounced and the metabolite peaks become sharper. At very large M (200), the metabolite peaks start to show additional spurious peaks. From the

results of these tests it seems that an $M=80$ is optimum, in that it gives well defined peaks without excessive noise and spurious peaks. The computation time of the MEM algorithm for $M=80$, is approximately 11 times that of the FFT and as such is less well suited to the processing of an array of say 25 spectra.

(i) FFT

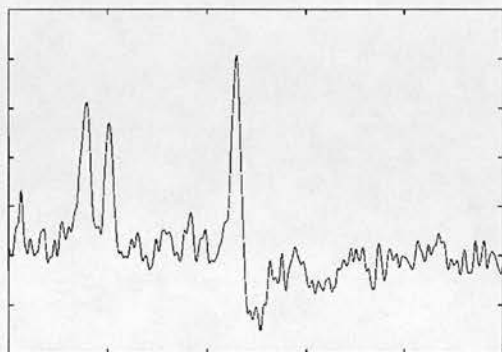
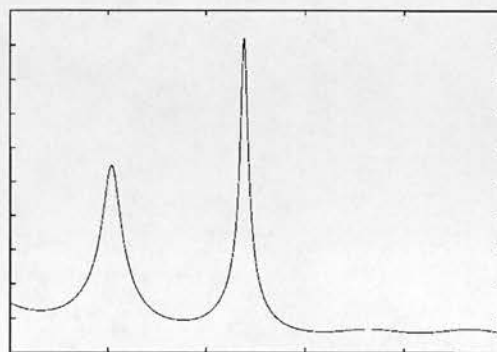
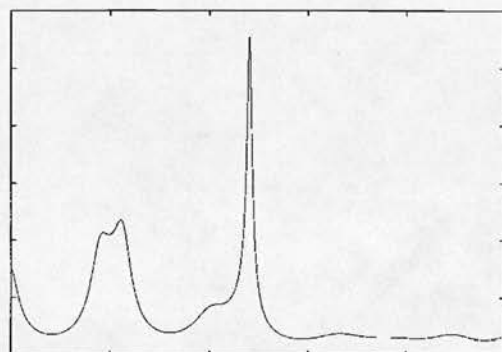
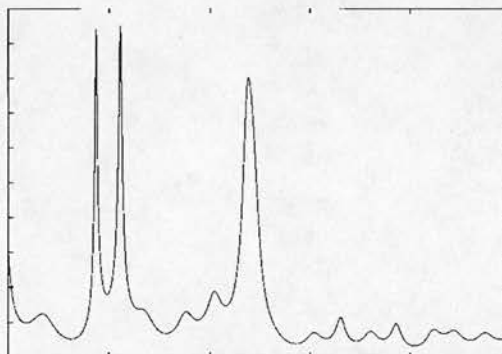
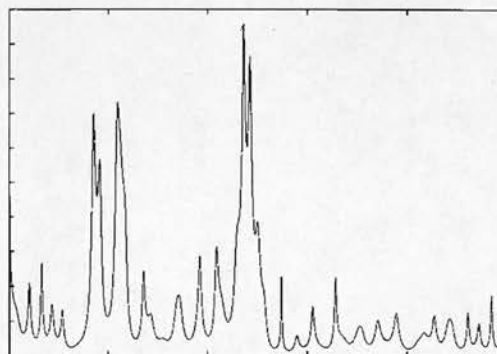
(ii) MEM ($M=20$)(iii) $M=35$ (iv) $M=40$ (v) $M=80$ (vi) $M=200$ 

Fig. 4.26. MEM models of an in-vivo spectrum for various values of M

The potential of the MEM fitting technique as an alternative to the FFT could be explored more thoroughly in further work. Firstly the complex time domain signal could be utilised as opposed to the real data alone allowing the effects of phasing to be incorporated in to the MEM fit. When fitting synthetic complex NMR data using a different MEM algorithm,

Daniell and Hore 1989, noticed an over estimate in the real part of the spectrum and a corresponding underestimate in the imaginary part. It would be interesting to see whether this algorithm produces the same effects when fitting complex in-vivo data. Secondly a statistical analysis (e.g. χ^2) could be used to compare the difference in peak area between the MEM fit and the FFT results. Using this analysis the M values that give the best approximation to an FFT spectral estimate could be predicted.

4.12.2 Parametric modelling

Parametric modelling procedures use combinations of Lorentzians/Gaussians in the frequency domain and exponentially/Gaussian damped sinusoids in the time domain (eq.4.26) to achieve a fit. In the frequency domain non linear algorithms are needed whilst in the time domain both linear and non linear routines can be used.

4.12.3 Non Linear methods-time domain

These use non linear, least squares fitting techniques to minimise the difference between a calculated model, $S_m(t)$ and the experimental spectrum / FID. In these iterative methods the exponential in eq.(4.26) is replaced by a model function f_j

$$S_m(t) = \sum_{j=1}^N A_j f_j(\gamma_j, t) \quad (4.35)$$

where γ_j are the model parameters (ω_j, T_{2j}^* etc.), t is the sampling interval which may be uniform or variable. These parameters are then altered iteratively so as to minimise the difference between the experimental and calculated signal. Certain parameters; frequency, amplitude and decay constant T_{2j}^* , are used non linearly in the exponential during the iteration and as such need to be specified with starting values. The need for starting values prior to fitting means that a-priori information concerning frequency and decay rates (estimated from either the Fourier transformed spectrum or linear prediction methods - see section 4.11.10) can be incorporated in to the iterative procedure, (de Beer et al 1988 - VARPRO).

The presence of non-linear combinations of frequencies and decay constants in the exponent may lead to model functions which are by no means similar to the physically real, and mathematically manageable damped sinusoid. Linear prediction methods can be used to constrain these parameters to linear combinations (Barkhuijsen et al 1985, 1986) with the

drawback that the chance to incorporate prior knowledge of the signal via starting values is lost.

Computational algorithms that minimise the difference between experimental and calculated time domain signals, by optimisation of these parameters, are usually based on a least squares minimisation. The Levenburg-Marquardt algorithm (as published in Press et al 1992), seems particularly popular, it is used in the Variation Projection (VARPRO) method, (van der Veen et al 1988).

If the experimental spectrum is very noisy such that exact resonant frequencies are not clear, then Simulated Annealing optimisation has been found to give accurate estimates of the amplitudes of spectral components of an FID. Variation of frequency, phase, decay rate etc. take place within a range of limits deduced from the experimental signal. Sekihara et al 1990, report the error in amplitude and frequency of the computed function as being low for low S:N ratios, with the drawback that 13 minutes of computer time is needed to fit a single FID. Hoffman et al 1989, again found an accurate fit of a noisy spectrum but needed 30 minutes of time on a super computer and several hours using a Sun work station.

4.12.4 Non-linear frequency domain methods

Iterative fitting can also take place in the frequency domain, whereby a non-linear fit of the spectrum is made to a sum of line shapes. This is analogous to fitting an FID with a sum of damped sinusoids. The FITPLA method of Hiltunen et al 1991, uses a set of Lorentzian line shapes (corresponding to exponentially damped sinusoids in the time domain). All four parameters which define the individual Lorentzian; amplitude, frequency, phase and decay rate are non linearly optimised. The starting values can contain prior knowledge from the FFT spectrum. In a comparison of the FITPLA method with the VARPRO time domain method, van den Boogart et al 1994, report equally accurate fits of strongly overlapping ^1H lipid resonances. Imperfect shimming within a VOI gives rise to a Gaussian line broadening of the underlying Lorentzian shape of a spectral peak. Marshall et al 1997(ii) found that a non-linear fit that was based on a combination of Lorentzian and Gaussian lineshapes (Voigt lineshape) was more effective at fitting both in-vitro and in-vivo data in the frequency domain.

4.12.5 Linear Methods

These fitting methods use sums of damped sinusoids to model the FID in the time domain. The presence of frequency and decay rate in the exponential of eq.(4.26), imply non linear dependence, which would require iterative procedures to achieve a fit. To overcome this, Linear Prediction (LP) techniques (Barkhuijsen et al 1986), can be used to express the n th data point in an FID as a weighted sum of m previous data points, a technique of backward projection;

$$x_n = a_1 x_{n-1} + a_2 x_{n-2} + \dots + a_m x_{n-m} \quad (4.36)$$

Standard linear least squares estimation methods are then used to fit the above to the raw data. Alternatively Singular Value Decomposition SVD methods have been used, (LPSVD - Barkhuijsen et al 1985 after Kumaresan et al 1982), to express the sum in a diagonalised matrix. For a hypothetical noiseless signal consisting of N damped sinusoids, this matrix would then have N non-singular values i.e. a rank of N . These solutions are computer intensive when compared with the traditional approach to signal analysis - the FFT. They do however, have the advantage that calculation of all the quantitative descriptors of the signal are made at once meaning further quantification is unnecessary.

Having solved for x_n , the frequency and decay rate (damping) can be determined by solving eq. (4.26) for $t = n\Delta t$, using the x_n coefficients of eq.(4.36). If these frequencies are then substituted back in to eq.(4.36) which is then expressed for all N data points, the time dependent values for amplitude and phase can be extracted. These are then fitted to the raw data using standard non-iterative, linear least squares fitting.

In a modification to the standard LP technique (Barkhuijsen et al 1985), Desluc et al 1987, used the m previous data points in forward projection but in addition used the m following data points (backward projection) to perform linear prediction with SVD, and found a more accurate fit to the experimental spectrum than with forward projection LP alone. Gesmar et al 1994 use Toeplitz matrix methods different to those of SVD to decompose the linear prediction coefficients, of a noisy, ^{13}C spectrum and report a speeding up in computational time - Fast Linear Prediction.

More recent refinements use the Hankel matrix structure (HSVD) which cuts down computing time, requires less user interaction and reportedly gives a better statistical description of a noisy FID than LPSVD methods, (Barkhuijsen et al 1985, Pijnappel et al 1992 and de Beer et al 1993). Diop et al 1994, suggest an enhancement procedure for SVD

linear prediction processing of noisy signals - EPLPSVD, whereby the N largest non singular values in the SVD matrix (corresponding to resonances) are retained whilst the remainder (noise related) are set to zero. Statistical tests of fit accuracy, for the various hybrid techniques combining LP and SVD have been performed by Koehl et al 1994 using Monte Carlo methods. They suggest that whilst frequency estimates are excellent the estimates of amplitude and linewidth are less accurate. A quicker routine which uses a lot less singular data points is Hankel-Lanczos SVD, used by van den Boogart et al (1994), to quickly fit the messy water signal, that is residual from suppression. This takes a few seconds per FID on a typical SUN work station and significantly improves baseline flatness. Whilst achieving a good fit of the residual water, this technique is not as effective in fitting metabolite resonances. This HLSVD software was made available to our group by the authors and is now used routinely in removing residual water from in-vivo data. The mechanics of the algorithm are not discussed in detail here but an outline of the steps involved is discussed in the section on water suppression (section 4.4).

4.12.6 Summary of modelling techniques

In summary the advantages of non-iterative and iterative modelling routines are compared, (from de Beer et al 1988);

Non-iterative routines do not rely on the provision of starting values and hence are well suited to automated signal fitting. At the same time the potential for prior knowledge incorporation is restricted to fixing the number of model functions as equal to the number of resonances seen in the spectrum. As the input of starting values is not implicit in these methods, then they are well suited to the fitting of the residual water signal, for which the input of starting values would be difficult. They have the additional disadvantage that the model functions are restricted to exponentially damped sinusoids.

Iterative routines may take any physically meaningful function as a model, use an arbitrary choice of sampling time, utilise prior knowledge in deciphering awkward signals (e.g. overlapping resonances) and in general tend to give more precise quantification of signals especially noisy ones. The drawbacks are firstly the computational expense, which is reduced if model functions are restricted to damped sinusoids and a uniform sampling interval is maintained. Secondly the input of starting values requires operator involvement and is not conducive to automation. By sacrificing the input of prior knowledge the only real advantage these techniques have over non-iterative procedures is that of precision. However if starting value estimates are taken from inspection of the individual metabolite

peaks then such routines may well provide the most accurate fits of the actual metabolite signals.

4.13 Spectroscopic Image construction.

The array of signals from the voxel grid can be used to produce an image representing metabolite distribution. As mentioned in chapter 1, the area under a given peak is proportional to the concentration of spins found in the voxel. By integrating the peak area present in spectra from all voxels, the image is built up. Accurate integration is only possible if the baseline is not distorted. As such the HLSVD water removed FID was FFTd and used to produce the metabolite images instead of the direct FFT of the same time domain data.

The image display facility was developed by Martin Connell in 1994, and is X windows driven, which enables user interaction. The program calls up the complex (real and imaginary) spectra following HLSVD water removal. The individual `csi_nx_ny.freres.dat` files are first combined for all 16x16 voxels, the batch file `realimag_dcsi` performs this operation saving the data in a file `.realimag`. The display program `display_csi_phase` is then run in the directory in which the image and raw data are being stored. To assist with visualisation, the T_2 image with the SI grid superimposed is used as a background (fig.4.27). This image is invoked by entering its file number. The user then proceeds to construct the image by clicking the selected voxel within the grid. This calls up the corresponding spectrum, the frequency range can be adjusted using a sliding scale as can the amplitude of the spectrum. The real data is initially displayed and, individual peaks can then be first order phase corrected by adjustment of the phase angle in the range 0-360°. To quantify the chosen peak the user has the option of a manual integration between user defined frequency limits or fitting a Gaussian lineshape to the peak. The fitting procedure is useful in separating the peaks of choline and creatine whose bases overlap. The manual integration was found to be more useful when the baseline is particularly distorted. Using such a process, inevitably introduces some user dependent bias in to the measurement. These sources of error are discussed further in Chapter 7. With more robust fitting procedures for in-vivo data (Marshall et al 1997, ii), the need for user involvement in the peak integration process should hopefully be minimised.

Having calculated the peak integrals for all voxels covered by the VOI (figure 4.28) the image is stored as an ASCII file using the function `store_mets`. The B_1 inhomogeneity must then

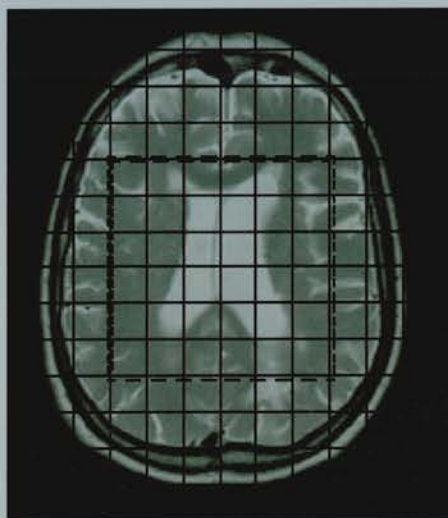


Fig. 4.27 Background T_2 image

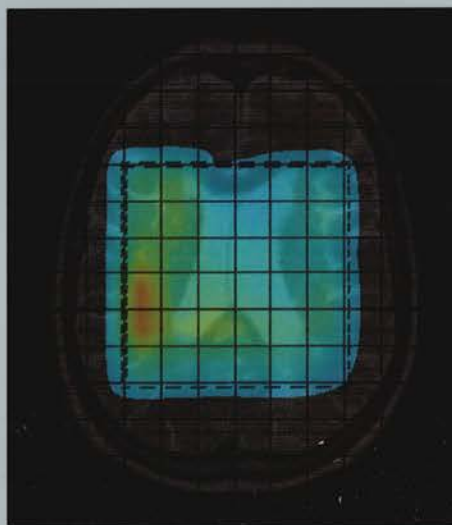


Fig. 4.29 Interpolated version of the coarse image of fig. 4.28

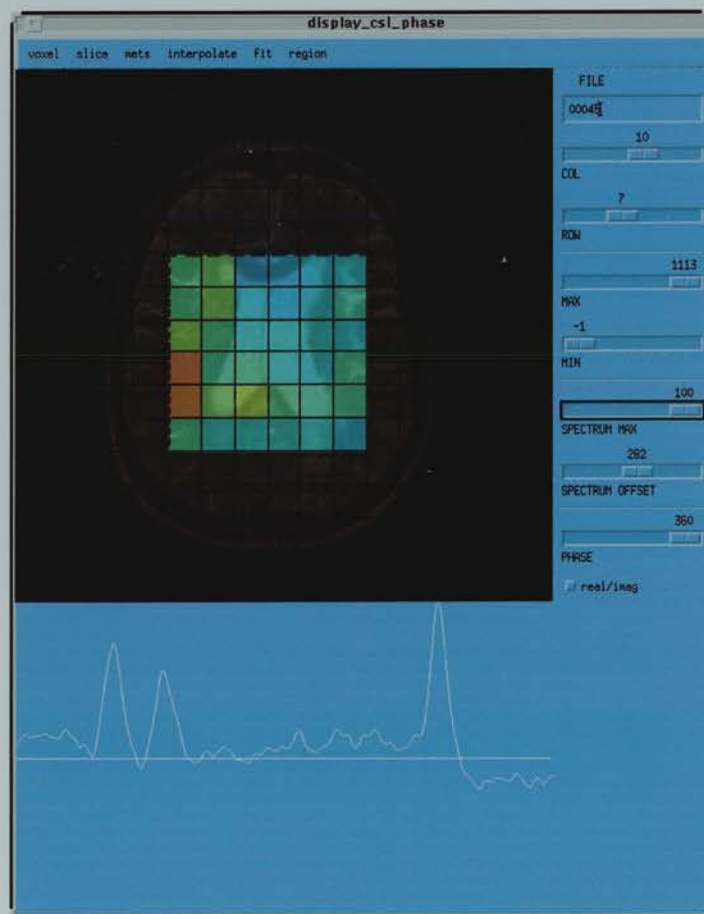


Fig. 4.28 The `display_csi_phase` Xwindow, showing a completed coarse NAA image grid and one of the spectra used to interactively build up this image.

be removed (Chapter 5) before quantitative measurements are made. In practice this is done using the program `normalise.c` which divides the metabolite image by a uniform phantom

water image, which is spatially voxel shifted to account for the chemical shift of the metabolite.

Having normalised the coarse image matrix, the image can be smoothed by application of a bilinear interpolation (fig. 4.29). The smoothing process leaves a more visually attractive image, however the user should proceed with caution. This is because the SI matrix is particularly coarse (16×16) and as such the interpolation process is liable to introduce a mean weighting to regions found at voxel boundaries, which may be significantly different in terms of actual spatial metabolite distribution. This possible pitfall is discussed in more detail in Chapter 7 with respect to identifying the ischaemic “penumbra” from the metabolite images.

The smoothed image can then be used to make quantitative measurements using an interactive region of interest (ROI). This tool returns the mean intensity of the image from the ROI and its standard deviation. The background T_2 image is useful in helping define anatomical guidelines (e.g. visible infarcts and ventricles). It must be remembered that the metabolite image is chemical shifted with respect to the T_2 image. A spatial mapping to shift the image by the desired amount corresponding to the chemical shift of the metabolite could help avoid confusion.

4.14 Summary

In this chapter the bulk of the data processing methods used throughout the course of the work have been described in detail. Where the theory behind the methods used was felt to be instructive it was covered in some detail e.g. the FFT of section 4.11. Emphasis throughout this chapter has however been focused on novel work done by the author. Refinements made by the author to the basic data processing routine (implemented by `centrefill12.c`) include:

- A k-space zero filling algorithm, used to increase the visual smoothness of the images - section 4.6
- A voxel shifting routine for post acquisition of the SI grid with anatomical features - detailed in section 4.7.
- An investigation in to the effect of spatial windowing of the k-space data prior to the 2D FFT -section 4.8. It was concluded that in the interest of optimum spatial resolution, windowing was only advantageous in SI data with severe subcutaneous lipid contamination.

In addition to these data processing refinements, in section 4.9 the source of a spectral artefact introduced by the common method of zero order phase correction has been elucidated. In section 4.12 alternative spectral models to the commonly used FFT were reviewed and in section 4.12.1 preliminary investigations were made using the Maximum Entropy Method to model in-vivo spectral data.

Chapter 5.

VOI profile correction

5.1 Introduction

In this chapter the methods used to study the PRESS SI excitation profile of water and metabolite resonances will be discussed. A method of removing the effect of the inhomogeneous B_1 excitation profile of the metabolite image using a water phantom normalisation image is then proposed (5.3). An account of the basis of this work has already been published (Wild and Marshall 1997). In this chapter a more complete analysis will be given.

The normalisation procedure is described with the chemical shift dependent precautions that need to be considered when normalising a specific metabolite resonance spectroscopic image (5.4). Using experimental phantom acquisitions (5.5) and computer simulations, the effects of different T_R and T_I on the VOI profile are discussed and compared with experimental results.

A protocol used to routinely normalise in-vivo chemical shift images is then described (5.6). The possibility of excitation of subcutaneous lipids when imaging in-vivo with a grid close to the skull is also emphasised (5.7). Finally in the conclusions, the limitations of the normalisation process are discussed with possible reasons for the remaining variation in a normalised uniform phantom image.

5.2 Background

Many implementations of SI use selective excitation of a volume of interest (VOI) inside the skull to avoid lipid contamination (PRESS-Bottomley et al 1984, STEAM-Frahm et al). The r.f. pulse shapes used to define a VOI often lead to non-uniformities in the excitation profile of this VOI, and as such within plane correction for x and y position is necessary. Reviewing the literature concerning excitation of an inner volume within the skull, no mention of in plane image correction has been found. Duyn et al 1992, recognise a 10% variation in intensity of their PRESS VOI but do not report any corrections performed to remove this source of error. In these studies a variation of 50 % in intensity between the

edges and centre of the VOI was found (fig.5.3) and as such a normalisation procedure to remove this source of error was thought to be essential.

Such corrections were found to be best implemented by using a uniformity correction image from a phantom VOI of the same physical dimensions as that used in in vivo SI.

Phantom replacement techniques have been reported (Soher et al 1996) which use phantom measurements to get an absolute quantification of spectroscopic images in conjunction with T_1 and T_2 relaxation measurements. These methods will implicitly remove B_1 inhomogeneities but do not account for spatial offsets in the VOI introduced by the specific chemical shift of the metabolite of interest. In this chapter an explicit method for removing the chemical shift dependent, B_1 inhomogeneity from a PRESS localised SI is proposed and its validity checked by testing on in-vivo SI's.

5.3 VOI Localisation - Excitation Profiles

Ideally the VOI prescribed should be a cuboid of uniform magnetisation with in plane dimensions of n_x by n_y voxels and a thickness of one voxel. The pulses used by the standard manufacturers SI pulse sequences, (in this case PRESS- 90° - 180° - 180° r.f. pulses), have windowed sinc waveforms. The theoretical spatial pulse shape due to slice selection of the frequency distribution of these pulses can be investigated by numerical solution of the Cayley-Klein (C-K) parameters for the chosen pulses (Pauly et al 1991, Chapter 2.7). The method used here uses the algorithm of Shinnar-le Roux to calculate the C-K coefficients of the time varying pulse angle distributions of the 90° and 180° pulses used by the Siemens SI sequence. The program used to calculate the Cayley-Kein parameters of a Siemens pulse angle file (`cayleyklein.m`) was written by Ian Marshall in 1995 using Matlab. The program `profile.m` then uses these C-K parameters to generate the frequency magnetisation response to the r.f. pulse envelope. In the presence of linear slice select gradients this gives a linear mapping to the spatial magnetisation response. Similar programs with graphical interfaces have been reported and are freely available (Matpulse, Matson 1994). The theoretical spatial pulse angle distributions in the coronal (90° pulse) and sagittal (180°) directions are given below in fig 5.1.

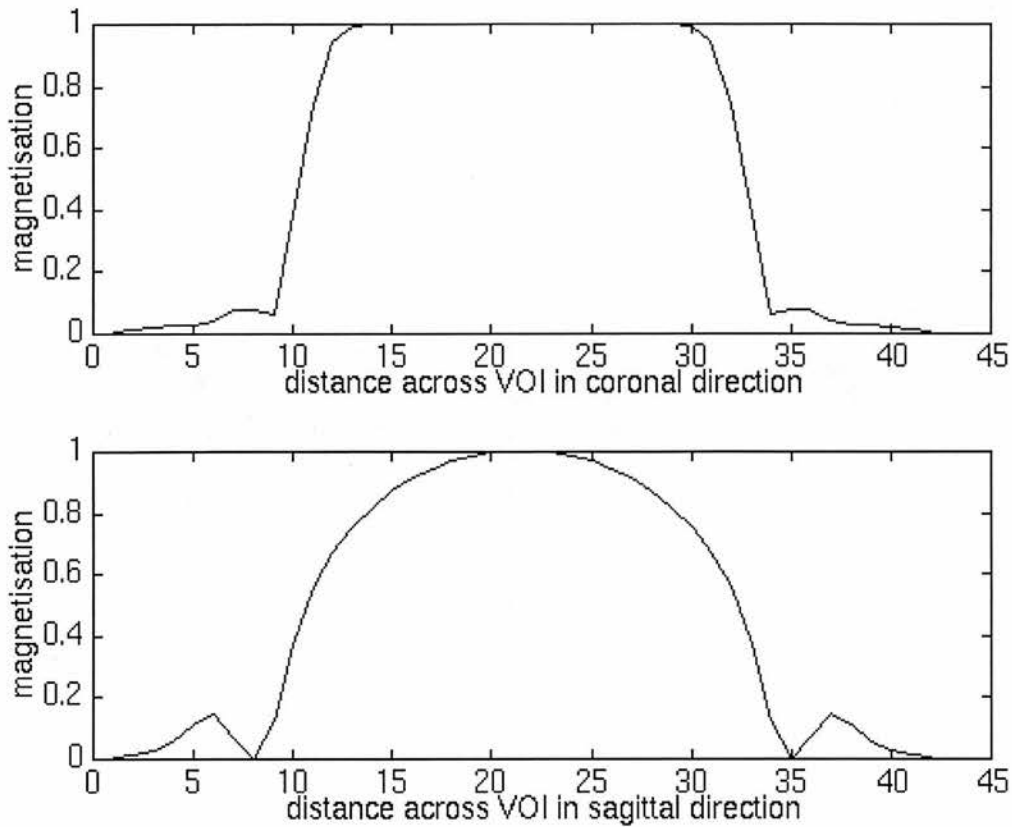


Fig. 5.1 Theoretical 90° and 180° pulse profiles

Despite the 90° and 180° pulses having the same time domain envelope, their profiles are markedly different. The 90° pulse has sharper edges and less pronounced sidebands compared to the broader less well defined 180° pulse. This can be attributed to the non-linearity of the Bloch equations in that the factor of 2 increase in rf energy between a 90° and a 180° pulse does not manifest itself as a corresponding scaling of the pulse in the frequency domain. A more uniform VOI might be expected if STEAM localisation employing three slice selective 90° pulses is used (rather than 90° - 180° - 180° in PRESS). In recent work carried out on a Magnetom SP63, Kwok et al 1997, claim that a single voxel STEAM VOI is less well defined than the corresponding PRESS VOI. This seems suspect as theoretical pulse calculations using the corresponding single voxel PRESS pulse angle files reveals a similar pattern to that found in fig. 5.1.

5.3.1 Methods

To investigate the effective spatial magnetisation distribution resulting from such pulses in practice, a water proton density, double spin echo image of the PRESS localised VOI within the phantom (nominal size 75 mm square) was collected. The phantom contained 20mM sodium acetate and 50mM sodium lactate doped with 0.1 mM Gd-DTPA . A 256×256 image matrix was collected with frequency and phase encoding with an echo time of 135 ms and a repetition time of 1600 ms. From this water map, excitation profiles were measured along user defined lines using the `evaluate` function in the Numaris operating system of the scanner, (see fig. 5.2). In addition a 75 mm square spectroscopic imaging PRESS VOI was set up using a background image with a 160 mm FOV. The acquisition protocols of PRESS SI were as outlined in Chapter 3, and included shimming, optimisation of CHESS water suppression voltages and collection of both water suppressed and reference signals. Application of 32×32 phase encoding gave a nominal voxel size of 0.5×0.5×1.0 cm³. Data processing proceeded as described in Chapter 4, in addition the area under the water resonance in the water reference spectrum, was automatically integrated for each voxel over the spectral limits of 4.3 ppm - 5.1 ppm. The 3D excitation profile was constructed as a 32×32 array of water peak integrals and is shown in fig. 5.3. The same procedure was used to produce acetate and lactate SIs of the VOI and its immediate surroundings. The integrals for metabolites were calculated by either fitting a Gaussian or by automatic integration between user defined limits. The lactate metabolite image from the 32×32 acquisition is given in fig. 5.4.1 together with the corresponding water image (fig. 5.4.2), and the ratio of the two images is given in fig. 5.4.3.

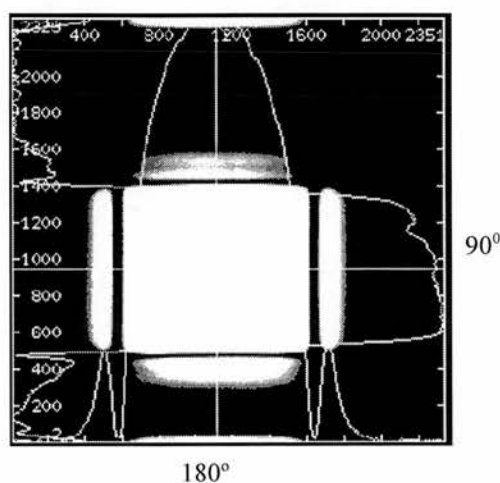


Fig. 5.2 The PRESS localised water image

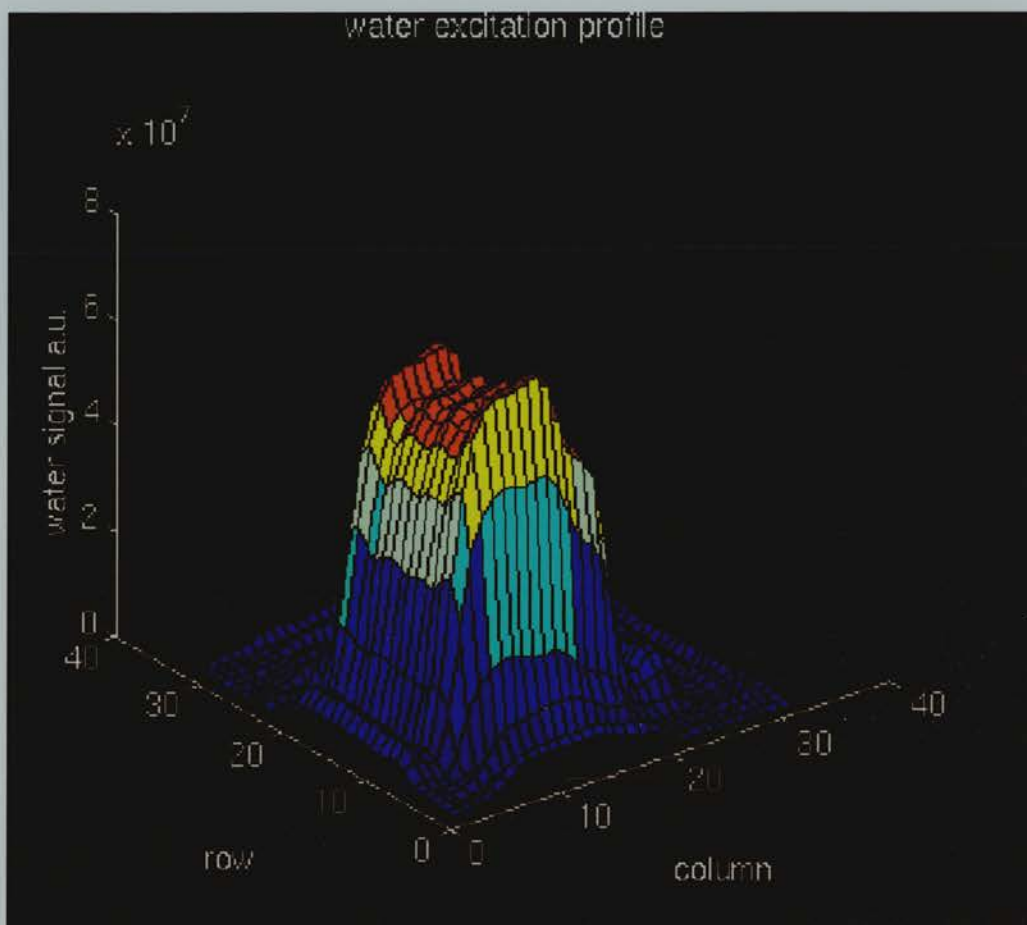
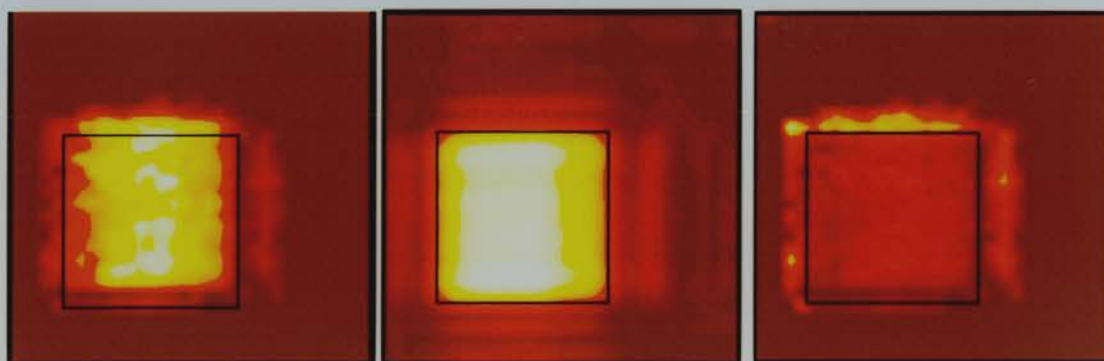


Figure 5.3. The water excitation profile for a 32×32 phase encoded SI with a 75mm square VOI and a 160 mm FOV.



5.4.1

5.4.2

5.4.3

Fig. 5.4.1 shows the image of the lactate resonance. This was obtained by direct integration of the lactate peaks from the 32×32 data sets. Shown in Fig. 5.4.2, is the corresponding water image calculated by integrating the area under the spectrum of the SI water reference signal (i.e. a 2D representation of fig. 5.3). On first appearance the water data seems to be in good agreement with the metabolite data despite its much greater signal to noise ratio. Figure 5.4.3 shows the ratio of the lactate image and the water image. It is worth noting that the 32×32 data sets have been smoothed for visual purposes using a bilinear interpolation.

5.4. Chemical Shift Artefact and Normalisation

5.4.1 Spatial shift of the VOI

The non uniformity of figs. 5.3, 5.4.1 and 5.4.2 show that within-plane normalisation of metabolite peak areas is required if misleading conclusions are to be avoided. Normalisation of the metabolite image grid using the water spectroscopic image was implemented by dividing on a voxel by voxel basis, see Fig. 5.4.3. These normalisation corrections reveal the problem of chemical shift artefact in SI, with dark and bright fringes at the edge of an otherwise uniform VOI. The effect is most pronounced in the coronal (up-down) (90°) direction, which is to be expected considering the sharper edges of the profile in that direction. Figure 5.4.3. illustrates this effect with the ratio images of the lactate : water profiles.

The theoretical chemical shift artefact can be calculated from the expression for the Larmor frequency ω of a metabolite i , of chemical shift relative to water σ_i , in the presence of a field gradient \mathbf{G} , at a position \mathbf{r} :

$$\begin{aligned}\omega_i &= \gamma(1 - \sigma_i)(B_0 + \mathbf{G} \cdot \mathbf{r}) \\ \omega_i &= \gamma(1 - \sigma_i)\left(B_0 + \frac{\partial B_0}{\partial x} \cdot \mathbf{r}\right)\end{aligned}\quad (5.1)$$

Equation 5.1 yields an expression for the relative spatial misregistration in the x direction between the resonance i and water;

$$\Delta x_i = \left(\frac{B_0 \sigma_i}{\frac{\partial B_0}{\partial x} (1 - \sigma_i)} \right) \approx \frac{\Delta \omega_i}{\gamma \frac{\partial B_0}{\partial x}} \quad (5.2)$$

So with a field strength of $B_0=1.5$ T, gradient strength $G=\frac{dB}{dx}=0.8$ mT/m and $\Delta\omega_{lac}/2\pi=223$

Hz -as used in this SI sequence, eq.(5.2) gives $\Delta x_{lac}=6.5$ mm.

With a voxel resolution of 5 mm in the 160 mm FOV ratio image, the positioning of the bright and dark fringes in figure 5.4.3. appear consistent with this predicted chemical shift artefact misregistration. By using stronger gradients this chemical shift offset in the VOI could be reeduced, unfortunately stronger gradients correspond to wider bandwidths and hence shorter duration pulses. As the r.f. amplitude of a pulse is limited by the transmitter amplifier, there is as a consequence a lower limit on the pulse duration. This in turn limits the gradient strength compatible with the SI r.f. pulses to 0.8mT/m in plane.

5.4.2 Cross-correlation technique

To check the direction and size of the chemical shift misregistration in the coronal and sagittal directions, a cross correlation of the water image, $W(x,y)$ and the metabolite image $M(x,y)$ was performed. The resulting cross correlation function $r(\xi, \psi)$ should be centred about a point equal to the chemical shift misregistration of the metabolite as a result of the sagittal and coronal gradients.

The cross correlation function is given by:

$$r(\xi, \psi) = \int_{-\infty}^{\infty} \int_{-\infty}^{\infty} W(x, y) \cdot M(x + \xi, y + \psi) \cdot dy \cdot dx \quad (5.3)$$

This integral was implemented on pairs of water and metabolite image matrices using the `xcorr2` function in Matlab. A plot of $r(\xi, \psi)$ for a water lactate cross-correlation is illustrated in figure 5.5.

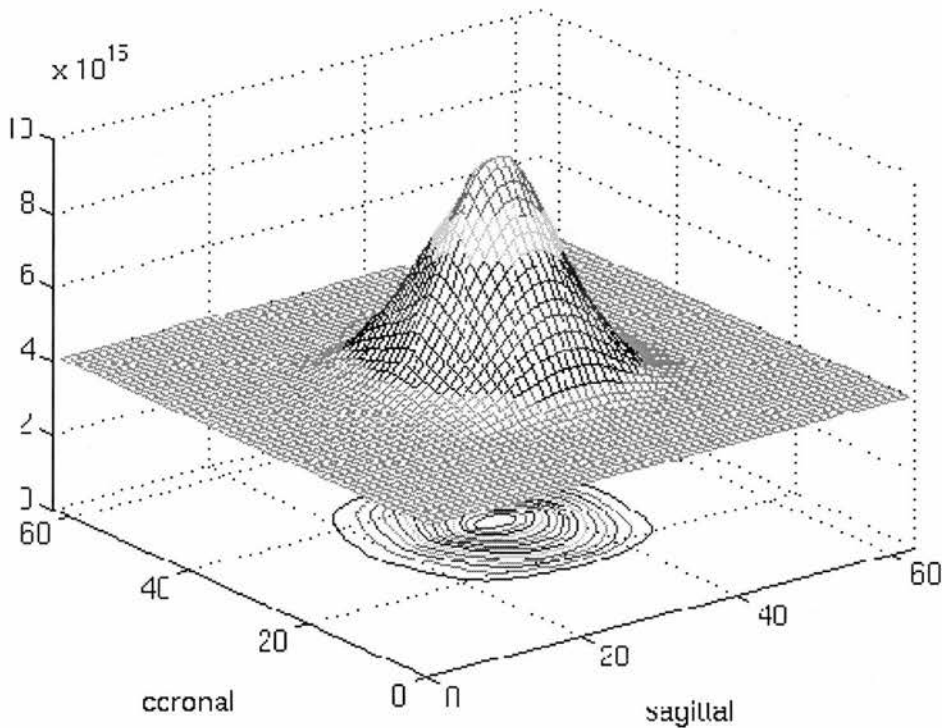


Figure 5.5. The cross correlation function of the lactate and water image matrices.

A 63×63 $[(2n_x - 1) \times (2n_y - 1)]$ matrix grid was formed by the cross correlation of a 32×32 lactate matrix with a 32×32 water matrix. The position of the maximum of this grid

indicates the point at which the two data sets overlapped the most. As such the displacement of the maximum from the centre of the 63×63 array indicates the size and direction of the chemical shift of lactate with respect to water. In this example the maximum was found to be displaced by one voxel from the centre in both the sagittal and coronal directions. The centre of the contour map indicates the position of this maximum, to confirm its position the maximum was found using the Matlab function $\max(\max(\text{xcorr2}(M,W)))$. With a voxel size of 5mm this chemical shift is consistent with that of 6.5 mm predicted by theory. Having accounted for the chemical shift of the metabolite, a normalised image of a VOI from phantom acquisitions has a remaining variation in intensity of less than 20 % across its entirety, (fig. 5.6.2). The remaining discrepancies are found in isolated voxels, usually at the edge of the VOI.

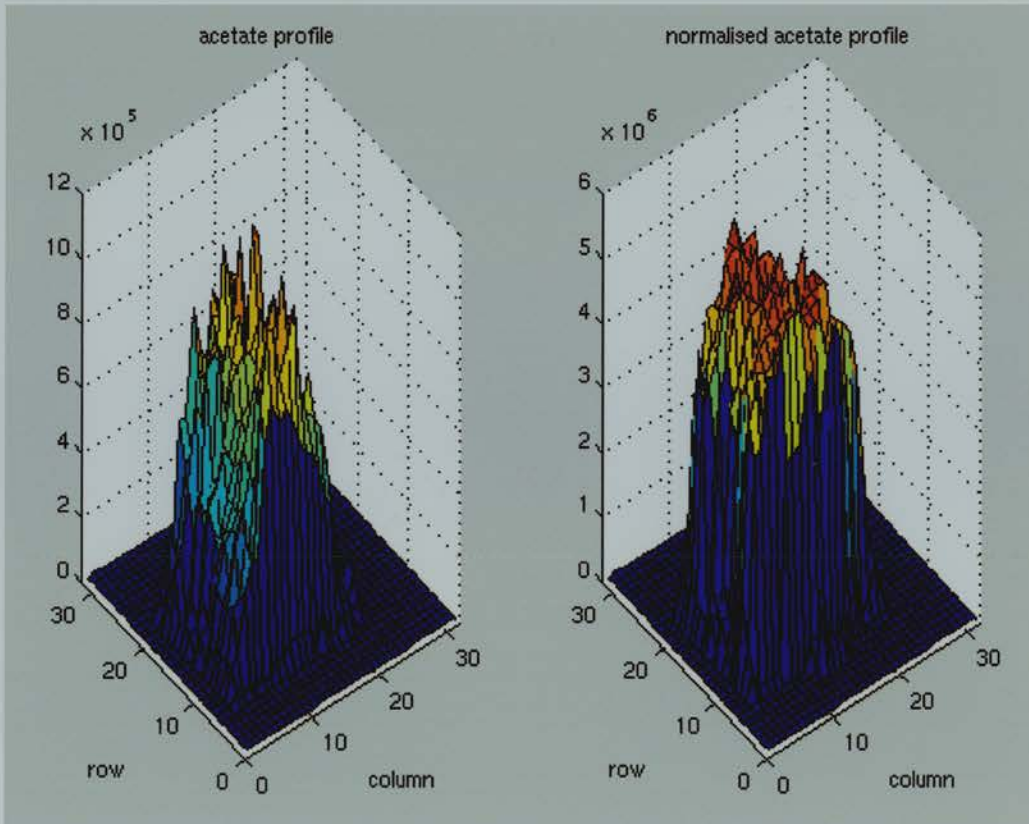


Fig. 5.6.1

Fig. 5.6.2

Fig. 5.6. A raw acetate image from a uniform phantom and the normalised version.

5.5 The effect of T_R and T_1 on the profile of the VOI

5.5.1 Experimental evidence

A further possible cause of discrepancy in the excitation profile between metabolites arises from the differences in T_1 relaxation times. This may lead to differential degrees of saturation upon application of the subsequent r.f. pulse after a time T_R . Different degrees of saturation will lead to different signal intensities at the edge of the VOI. As a consequence the amplitude and shape of the VOI may well change between metabolites. For these phantom studies the metabolite solutions were heavily doped to ensure that the T_1 of the lactate and acetate were at least five times less than T_R . As such this effect should be minimal and *should not* be the cause of the remaining 20 % variation in VOI uniformity. Possible explanations for the residual variation are offered in Sections 5.6 and 5.8.

This effect should however be considered when normalising in vivo data as the T_1 's found in vivo are typically of the order of 1000-2000 ms (Wilkinson et al 1994, Kamada et al 1994) which will lead to incomplete saturation with a repetition time of 1600 ms. The effect was investigated experimentally by plotting sagittal and coronal profiles of water images of a PRESS localised VOI (see section 5.3) for a range of different T_R s. (See fig. 5.7). The individual profiles were normalised by dividing through by the maximum that the profile reached at its plateau, this enables a direct comparison of profile shape rather than magnitude.

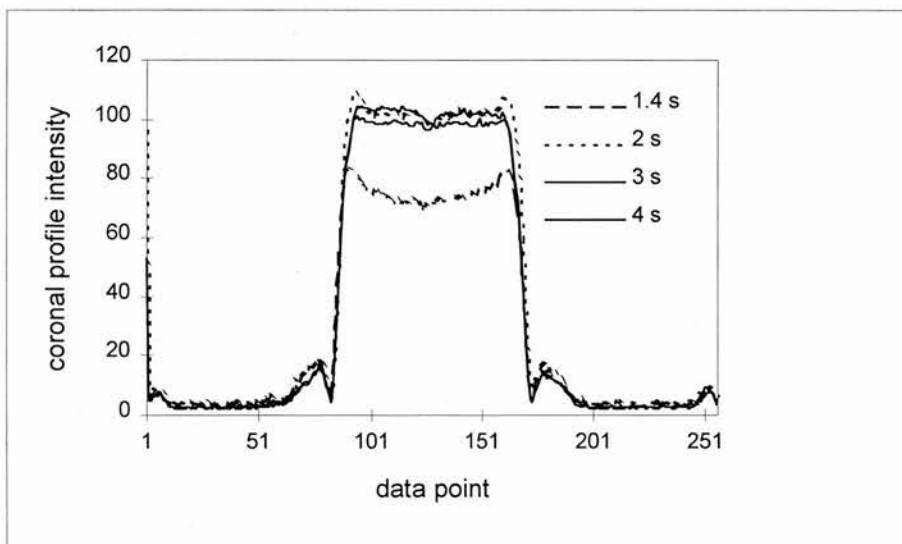
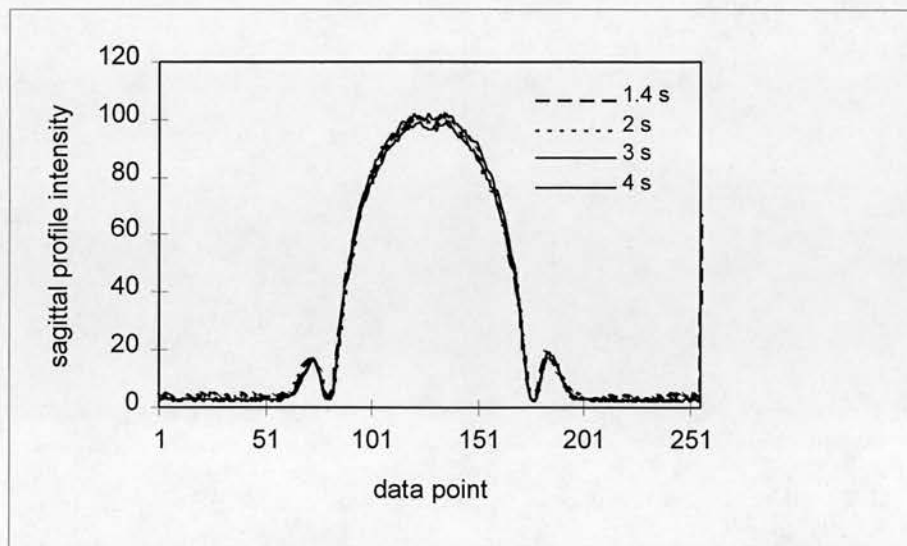


Fig. 5.7. 1. The coronal water excitation profile of a PRESS VOI for different T_R Fig. 5.7.2 The sagittal water excitation profile of a PRESS VOI for different T_R

The sagittal (180°) profile shows no noticeable change in shape for T_R 's in the range 1400 - 4000 ms, however the coronal profile (90°) does exhibit a marked T_R dependence. The fact that there is variation with a 90° pulse is because this pulse is applied first and is responsible for flipping the longitudinal magnetisation into the transverse plane. The 180° pulses act to refocus the transverse magnetisation and as such play no part in the excitation process and are therefore T_R independent.

5.5.2 Computer simulations

The distribution of flip angles across a VOI edge depends upon the shape of the excitation pulse and is represented in a given direction by the flip angle distribution θ . The shape of the VOI is predicted, from the Bloch equations as a function of θ , T_R and T_I ;

$$S(\theta) = \frac{(1 - e^{-T_R/T_I}) \sin \theta}{1 - e^{-T_R/T_I} \cos \theta} \quad (5.4)$$

Matlab simulations were performed using the spatial distribution of θ across the edges of the coronal and sagittal sinc pulses (calculated from the time dependence of the sinc pulses using the Cayley-Klein parameters (Matson 1994)) see section 5.3. With T_I fixed at 1500 ms ($\approx T_I$ H₂O) and T_R varied - see fig. 5.8.1 and in fig. 5.8.2, T_R fixed at 1600 ms, T_I

ranging from 1500 to 3000 ms (Kamada et al 1994). A T_R of 1600 ms was used for consistency with in-vivo work with T_I values of 1500 ms (representing water) and 3000 ms (representing the metabolite acetate). These T_I values were calculated by integrating the area under the metabolite and water resonances from single voxel PRESS localised spectra at T_R 's of 1500 ms, 1800 ms and 3000 ms. These integrals were then fitted to an exponential decay of the form $(1-\exp(-T_R/T_I))$.

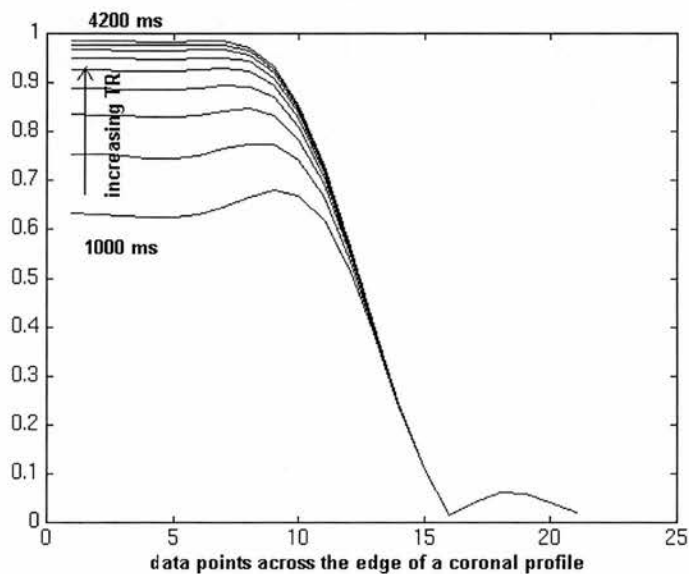


Fig. 5.8.1. Simulation of the edge of a 90° pulse for a fixed $T_I=1500$ ms and variable T_R

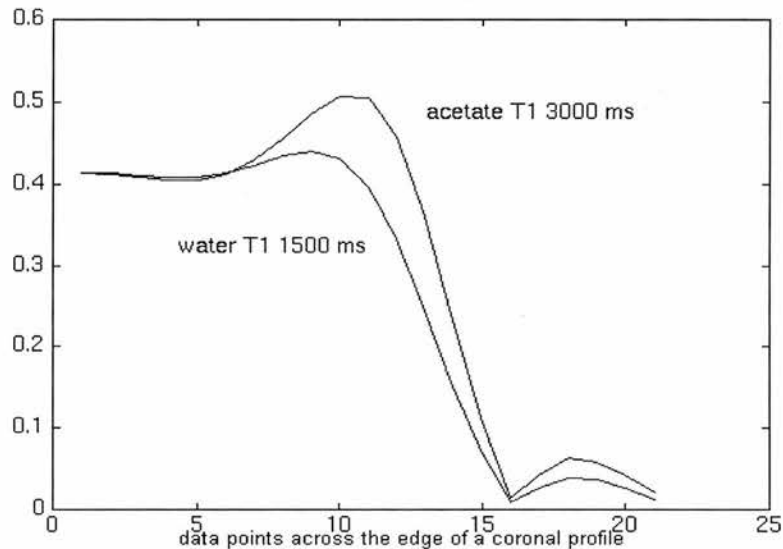


Fig. 5.8.2 Simulation of the edge of a 90° pulse for a fixed $T_R=1600$ ms and two different T_I 's representing water and acetate in-vitro.

Figure 5.8. Simulation of the distribution of magnetisation across the edge of a PRESS VOI

localised with a 90° sinc pulse. The amplitudes of the plateaux of the profiles have been normalised to the same intensity to enable quantification of the relative overpulsing at the profile edge.

Figure 5.8.1 shows the results of the fixed T_I simulations, it is clear that there is an “over pulsing” effect due to incomplete relaxation at the edges of the plateaux of the shorter T_R profiles. This is consistent with the experimental results of fig. 5.7.1. Figure 5.8.2 shows the results of the fixed T_R (1600 ms), variable T_I simulations. Again there is a distinct “over pulsing” effect due to incomplete relaxation at the edges of the plateaux of the longer T_I profile. Having normalised the plateaux of these two profile simulations to the same intensity then the magnitude of the “over pulsing” in this region can be quantified. The result is a water profile that is 25% less intense than the metabolite profile. As such the inconsistencies at the VOI edge can be attributed to differences in T_I . As a consequence, when normalising in vivo data, a water phantom of T_I comparable to the T_I 's of metabolites found in-vivo (≈ 2000 ms Kamada et al 1994) should be used. A further final possible contribution to non-uniformity in a normalised lactate image results from the J-coupling of the lactate protons. At the edge of a PRESS VOI the distribution of flip angles is found to be non ideal (equation 5.4 (Hoult 1974)), as a result the signal from a coupled species, whose signal depends upon protons resonating at different frequencies, will vary in shape at the edges of the VOI. Non symmetrical doublets will result in the case of lactate, which upon integration may well result in an asymmetric excitation profile. This aspect of asymmetry of the lactate doublet is explored in greater detail in chapter 6 and in the paper (Marshall and Wild 1997).

5.6 In-vivo image normalisation

To implement image normalisation a 16×16 water reference data set (voxel 1.5 cm cube) was taken from a doped phantom acquisition, the VOI was of the same dimensions as that of the SI to be normalised. The phantom was doped with Gd-DTPA at a concentration of 0.1 mM, to give a water T_I of 2000 ms, comparable with those of metabolites in healthy tissue at 1.5 T (Kamada et al 1994, Wilkinson et al 1994). A user defined voxel shift was then implemented so as to align the corners of the two VOIs within the spatial framework of the FOV. This voxel shift is implemented by adding a phase angle in the x and y phase encoding directions prior to the 2D spatial FFT. By prescribing an additional fractional shift to account for the chemical shift misregistration of the specific metabolite (eq. 5.2) then images from any of the metabolites can be normalised effectively using a single water image from a VOI

of the same size as that used in-vivo. An example of the NAA image from a stroke patient with an infarct in the right cerebral hemisphere is given in fig. 5.9, before and after the normalisation procedure. Such images were made for a group of 14 acute stroke patients (Chapter 7). Using an interactive ROI (section 4.13), intensities of the signals from NAA, choline and creatine were calculated from the region covered by the infarct on the T_2 image and from a contra-lateral (opposite hemisphere) region. This procedure was implemented on both the normalised and non-normalised images and the mean intensity in either region calculated. The 2-tailed paired students t -test for significant difference between these means, together with the mean ratio of the means is tabulated below in Table 5.1.

	Non- normalised images		Normalised images	
	infarct:contra	t-test (p)	infarct:contra	t-test (p)
NAA	0.592	<0.001	0.455	<0.001
Cho	0.984	>0.1	0.757	<0.001
Cr	1.006	>0.1	0.691	<0.001

Table 5.1 Statistical comparisons of metabolite ratios found in infarcted and contralateral regions for non-normalised and normalised sets of metabolite images taken from a group of $n=14$ stroke patients. The mean ratios of the metabolite concentrations in the infarcted and contra-lateral regions are presented together with the t -test for significance of difference between the mean intensity found in the regions.

The metabolite data pre and post normalisation differs significantly, confirming that normalisation has a significant bearing on quantitative SI measurements.

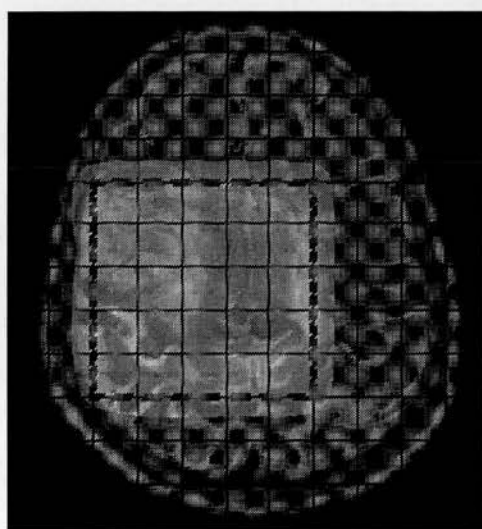


Figure 5.9.1 In vivo transverse NAA prior to normalisation

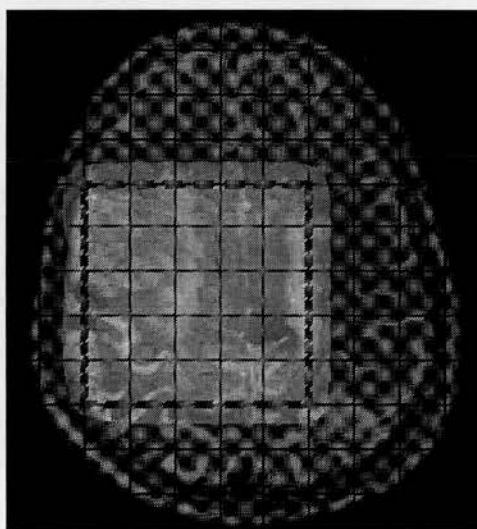


Figure 5.9.2 In vivo transverse NAA image after normalisation

5.7 Lipid Contamination

A further consequence of the chemical shift artefact is inadvertent excitation of lipid in the marrow of the skull and subcutaneous layer of the scalp, when placing the VOI. Figure 6.4 shows the ^1H spectrum of a FID obtained from a sample of animal fat using a high field Bruker small bore spectrometer. With the main lipid resonances found in the range 1.5 - 0.9 ppm (203-242 Hz at 1.5 T), a chemical shift of 0.9 ppm gives $\sigma_{lip} = 3.8 \times 10^{-6}$. When substituted in to equation (5.2) with the gradient strength of 0.8 mT/m, used on the Magnetom, gives $\Delta x_{lip} = 7.1$ mm. Consequently any lipid visible on the transverse MRI scan used to localise the VOI must be at least 7.1 mm (1/2 a voxel) away from the VOI in the anterior and right hand side directions of the patient. This is because the VOI is positioned assuming it contains only water.

This effect of inadvertent lipid contamination was investigated by SI of the phantom shown graphically in fig. 5.10, which contained doped acetate solution which was compartmented by two horizontal bands of solid lard (bovine lipid). The phantom was first imaged with VOIs almost overlapping the vertical left and right planes of fat. The phantom was then rotated through 90° and imaged upright with VOIs almost touching the anterior and posterior planes of fat. The arrays of spectra in figure 5.11, illustrate the direction of the chemical shift artefact and the extent of contamination by lipids on an acetate spectrum from a solution of 20 mM concentration.

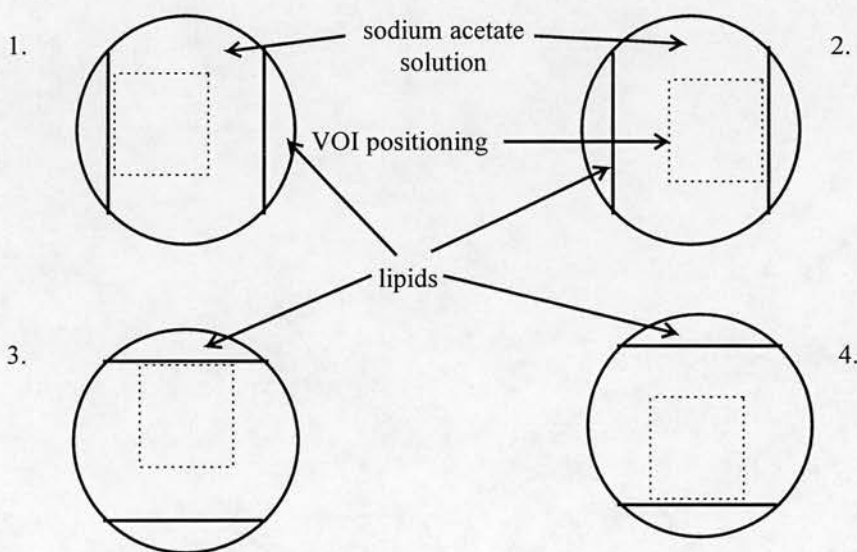


Fig. 5.10. The lipid phantom showing the four SI VOI orientations. The spectra from these four sets of acquisitions are given in fig. 5.11 to indicate the degree of lipid contamination introduced by the chemical shift dependent spatial shift of the VOI due to the localisation gradients.

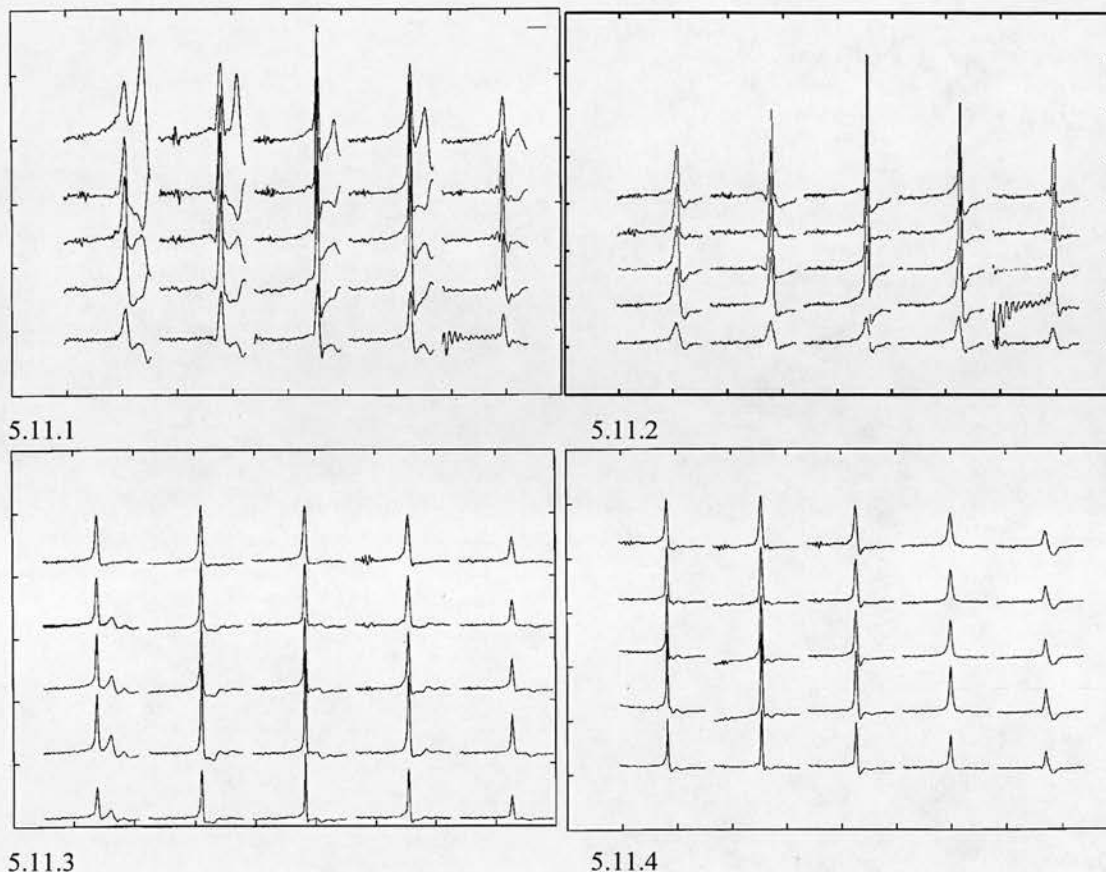


Figure 5.11

Lipid leakage spectra, 5×5 array of spectra from a 75 mm square PRESS VOI with 1.5cm square nominal voxel size. The ppm range is 4.0-0.0 from left to right, the acetate resonance is present at 2.15 ppm.

5.11.1) VOI nearly touching leftwards lipid band, significant lipid contributions around 1-1.5 ppm

5.11.2) VOI nearly touching rightwards lipid band

5.11.3) VOI nearly touching the upper lipid band, significant lipid contributions around 1-1.5 ppm

5.11.4) VOI nearly touching lower lipid band

5.8 Conclusions

With a PRESS localisation sequence it is inevitable that spectroscopic images will have an intensity proportional to the spatial magnetisation distribution. Corrections for a non uniform slice excitation will be needed before spectroscopic images of metabolites can be quantified accurately. Such normalisation procedures will need to be chemical shift dependent to

account for the differences in spatial positioning of a SI VOI as calculated from the magnetisation profiles of different metabolites.

Performing such normalisation procedures removes to a large part the spatial variation across the VOI, with a normalised image uniformity of less than 20% as compared to 50% prior to normalisation. The existing non uniformities were mainly found to persist at the edges of the VOI and may be explained by the fact that the shape as well as the position of the VOI profile can differ between metabolites. At the edge of a PRESS VOI the distribution of flip angles is found to be non ideal (Marshall and Wild 1997), as a result the signal from a coupled species, whose signal depends upon protons resonating at different frequencies, will vary in shape at the edges of the VOI. Non symmetrical doublets will result in the case of lactate, which upon integration may well result in an asymmetric excitation profile.

Singlet signals will not be prone to this effect only the obvious chemical shift dependent displacement of the VOI. A further possible cause of discrepancy in excitation profile between metabolites arises from the differences in T_1 relaxation times which may lead to differential degrees of saturation upon application of the subsequent r.f. pulse after a time T_R . Different degrees of saturation will lead to different signal intensities and distribution of flip angles at the edge of the VOI. As a consequence the amplitude and shape of the VOI may well change between metabolites. For these phantom studies the metabolite solutions were heavily doped to ensure that the T_1 of the lactate and acetate were at least five times less than T_R . As such this effect should be minimal and therefore should not be the cause of the remaining 20 % variation in VOI uniformity. This effect should however be considered when normalising in vivo data as the T_1 's found in vivo are typically of the order of 1000-2000 ms, which will lead to incomplete saturation with a repetition time of 1600 ms.

Having discounted these possible explanations, the only obvious explanation left is that of peak area accuracy. With a SI VOI, the shim quality inevitably drifts across the VOI (section 3.3) and as a result some spectra are better resolved than others. This could lead to over/under estimation of the area of a given peak in the presence of noise and explains why fig. 5.6.1 is much noisier than the water resonance profile of fig. 5.3. With an in-vivo error of reproducibility of around 20% for choline, creatine and NAA (Chapter 7), the error introduced by normalisation of in-vivo images should be negligible.

Measurements made on the lipid phantom reveal that inadvertent excitation of subcutaneous fat takes place despite the apparent positioning of the VOI being up to 7mm away in the anterior and right directions from any MRI visible lipid. Precautions should be taken when positioning a PRESS volume within the brain, so as not to contaminate the spectral array with the lipid signal, particularly if the presence of lactate, (which has a chemical shift similar to lipids), needs to be detected.

Chapter 6.

Lactate editing

6.1 Introduction

In preliminary studies, PRESS localised spectroscopic images of stroke patients have been acquired at an echo time of 135 ms. In a study of 14 acute stroke patients a significant depression in the levels of the metabolites NAA, choline and creatine in infarcted regions when compared to contra-lateral regions was observed (Wild and Marshall 1997). The metabolite lactate was visible as a well defined doublet at 1.3 ppm in only 5 of the 14 cases, usually in voxels coincident with the T_2 visible infarcted region. In other proton spectroscopic studies of stroke (Prichard 1993, Graham et al 1993, Gideon et al 1992 and 1994) a well defined lactate doublet would appear to be expected in and around an infarct. In this study, a signal in the ppm range 1.0 - 1.5 was often observed (Fig 6.1), which is most likely that of lipids and macromolecules. These lipid signals can be very large and as they are found at around the same frequency as lactate, any lactate present could be obscured by the lipid signal.

These lipids/macromolecules are thought to be liberated by the process of cell wall necrosis in the advanced stages of infarction (Behar 1993, 1994). There is evidence that such macromolecules can bind to intra-cellular lactate causing a dramatic reduction in its T_2^* and a corresponding reduction in the spin-echo spectral signal intensity of lactate (Saranthan et al 1997, Chatham and Forder 1995). Graham et al 1994, found a spatial correlation between lactate and lipid/macro-molecules in ischaemic brain. Studies reporting the abundance of lactate in acute stroke (Prichard 1993) should therefore be viewed with some scepticism as the signals may actually originate from lipids/macro-molecules as the two distinct chemical species could be present simultaneously.

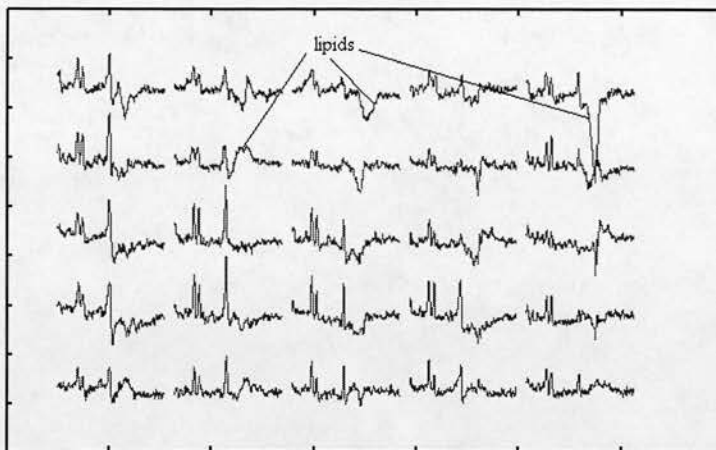


Figure 6.1. Lipid contamination of the uppermost row of an array of in-vivo spectra, localised with a 75 mm square volume of interest and divided into 15 mm square voxels.

Fourier leakage of the lipid signal from the inadvertent excitation of the skull and scalp is also a possible source of lipid signal. Outer volume suppression methods (Spielman et al 1991, Duyn et al 1992, Soher et al 1996) can minimise the chance of sub-cutaneous lipid contamination. These rely on the use of graphically positioned multiple saturation pulses, a feature not found on all scanners. The lipid contribution can be reduced further by tailoring the echo time and repetition time of the sequence so as to exploit the difference in T_1 and T_2 of lipids and lactate (Frahm et al 1990, Spielman et al 1991, Duyn and Moonen 1995). The strength of a residual lipid signal could still be sufficient to obscure the visibility of any lactate and therefore a method of editing out the lactate from lipid is desirable.

A lactate editing sequence would need to be compatible with the scanner used, a Siemens Magnetom SP 63 (Erlangen, Germany) 1.5 T system. As such, it would not have to rely on rapidly switched gradients (10mT/m/s max. ramp time) or spatial-spectral excitation pulses. The latter were not made available for research purposes on this scanner and therefore J -resolved editing by selective decoupling of the lactate spins (Adalsteinsson et al 1993, Williams et al 1986) and longitudinal spin order techniques (Brereton et al 1990) are not feasible. Reviewing the literature for editing techniques suitable for implementation on such a system, there are two properties of the lactate coupled spin system that enable editing; zero quantum (Sotak et al 1988, Bachert et al 1995) and multiple quantum (de Graaf et al 1993, Müller et al 1995) coherence evolution, and homonuclear polarisation transfer (Knüttel et al 1988, Bunse et al 1995). In this chapter both of these methods of lactate editing are investigated theoretically and experimentally by making significant modifications to the stimulated echo (STEAM) and double spin echo (PRESS) sequences

available on the scanner. Before dealing with these two lactate editing methods, it is instructive to consider the NMR spectra and structure of the lactate and lipid molecules in order to gain some insight in to how the editing techniques actually work.

6.1.2 Lactate

The lactate molecule (fig. 6.2.) has two distinct sets of protons attached to carbon atoms, the methine protons (CH) and methyl protons (CH₃). These have a different chemical electron environment due to their position within the molecule with respect to adjacent bonds. As such these protons are subject to different degrees of electron shielding which alters the effective B₀ field felt by the individual proton. This causes the proton spins to resonate at slightly different frequencies, the displacement of an individual resonance from the transmitter frequency is quantified by its chemical shift (Section 2.3).

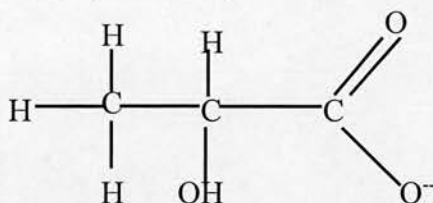


Fig. 6.2. The lactate ion

The resonance of certain spins at one frequency and other spins at another, sets up a spin-spin coupling interaction which introduces some degeneracy in to the available spin up and spin down energy levels of the respective spins. The mechanism by which spin-spin (J) coupling instigates this degeneracy is treated in quantum mechanics as a perturbation to the Hamiltonian (Appendix 1). The J term represents the frequency splitting in Hz of the energy levels in the visible spectrum. For systems in which $J \ll \delta$ the system is said to be weakly coupled (δ is the frequency separation of the methyl and methine peaks). In such cases the perturbation to the Hamiltonian can be approximated to the first order. The number of individual lines (x) in the multiplet peak due to J coupling is given below;

$$x = 2nI + 1 \quad (6.1)$$

where I is the nuclear spin ($1/2$ for a proton), and n is the number of coupled spins resonating at the other frequency. Now the CH and CH₃ proton spins in the lactate molecule constitute a weakly coupled (AX_3) system with $J \approx 7$ Hz and $\delta \approx 180$ Hz. The multiplicity introduced to the methyl (X_3) resonance by the single ($n=1$) methine (A) spin is therefore from eq.(6.1), $x=2$. This explains the doublet appearance of the methyl resonance (fig.6.3).

Similarly the multiplicity of the methine spin due to its coupling with the methyl spins ($n=3$), is $x=4$. The relative intensities of the individual lines constituting the multiplet are predicted by Pascal's triangle (table. 6.1).

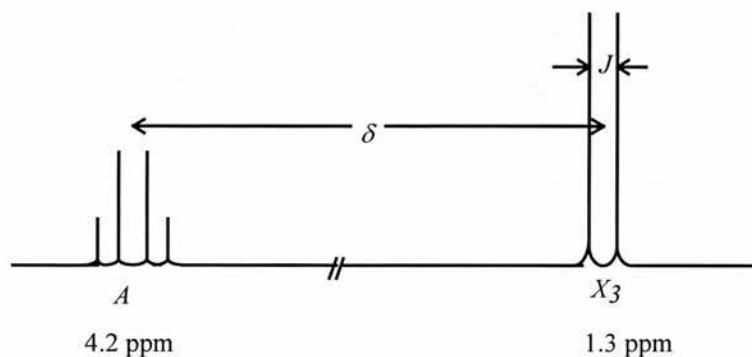


Fig.6.3 Systematic diagram of the lactate spectrum with the methine quartet and the methyl doublet

Number of equivalent coupled nuclei (n)	Multiplicity and relative intensity of lines
0	1
1	1 1
2	1 2 1
3	1 3 3 1
4	1 4 6 4 1

Table 6.1. The multiplicity and relative intensity of spectral lines of n equivalent coupled nuclei determined by Pascal's triangle.

6.1.3 Lipids and their characteristic NMR spectra

Proton spectra collected from a VOI within the brain are prone to lipid contamination through inadvertent excitation of fats in the adipose subcutaneous layer of the scalp and marrow of the skull. This can lead to problems when the resonant frequencies of the metabolites of interest (lactate in particular) overlap with the lipid resonances, largely because these lipids are found in very high molar concentrations within the skull and scalp. Lipids mainly consist of saturated, monounsaturated and polyunsaturated triglycerides. These molecules are in general larger and more complex than those of the metabolites of interest. As such, they contain multiple resonances at different frequencies

corresponding to the chemical environment of the given proton. The primary resonances in the frequency range of interest (5.5-0.0 ppm) are given in table 6.2. below (Thomsen et al 1994, Mulkern et al 1997). With so many different resonances the scope for strong and weak coupling interactions and coherence transfer between spins of protons found on the same molecule, is potentially large. Consequently it is highly likely that a lipid spectrum will be quite complex.

Chemical group of the proton	Positioning of protons	Resonant frequency (ppm)
Olefinic protons	$-\text{CH}_2-\underline{\text{HC}}=\underline{\text{CH}}-\text{CH}_2-$	5.4
Glycerol ester protons	$\text{CH}_2\text{OHCHOHCH}_2\text{OH}$	5.3, 4.3, 4.1
Methyl protons : between 2 double bonds	$-\text{CH}=\text{CH}-\underline{\text{CH}_2}-\text{CH}=\text{CH}-$	2.9
either side of one double bond	$-\text{CH}_2-\underline{\text{CH}_2}-\text{CH}=\text{CH}-\underline{\text{CH}_2}-\text{CH}_2$	2.0
two bonds away from a carboxyl group	$\text{O}=\text{C}-\text{CH}_2-\underline{\text{CH}_2}$	1.6
in a saturated part of the chain	$-\text{CH}_2-\underline{\text{CH}_2}-\text{CH}_2-$	1.3
at the end of a saturated section of a chain	$-\text{CH}_2-\underline{\text{CH}_3}$	0.9

Table 6.2. Protons contributing to the lipid spectrum in the range 6 ppm - 0 ppm

6.1.4 In-vitro lipid spectra at a high B₀ field strength

To investigate the constituent resonances present in adipose tissue, high field NMR spectra of bovine fat (lard) were acquired. This work was performed with the kind assistance of Dr Ian Sadler using a 5.6T (360 Mhz) Bruker 360, small bore spectrometer, housed at the Department of Chemistry, Kings Buildings, West Mains Road, Edinburgh. A simple Hahn spin echo sequence was used (Chapter 2), at an echo time of 298 ms. The samples were first automatically shimmed, (Chapter 3.3) and then a series of 8 acquisitions was made, which were subsequently averaged. Initially a sample of the lipid was dissolved in deuterated methane trichloride DCCl₃, which having a deuterium atom instead of a hydrogen atom acts as a spin inert solvent. This allows the lipid to become completely dissolved in solution permitting the collection of narrow well defined spectra without the relaxation time limitations posed by a more solid matrix of the fatty polymers. The spectrum from this acquisition is illustrated in figure 6.4. The key lipid

resonances as tabulated above are evident at the respective frequencies. A spectrum was then collected from a sample tube containing lipids alone. The spectrum from the sample at room temperature in its solid state is given in figure 6.5. It can be seen that the key resonances are still evident, they do however have broader linewidths as a result of the reduced T_2^* of the solid matrix. This line broadening has obscured some of the fine structure (e.g. the multiplicity of the resonances at 0.9, 1.3, 2.0, 2.3, 4.1 and 4.3 ppm). Of additional interest is the offset in frequency (0.3 ppm) found between the two spectra. This may be due to lack of frequency re-adjustment following shimming in the second spectrum.

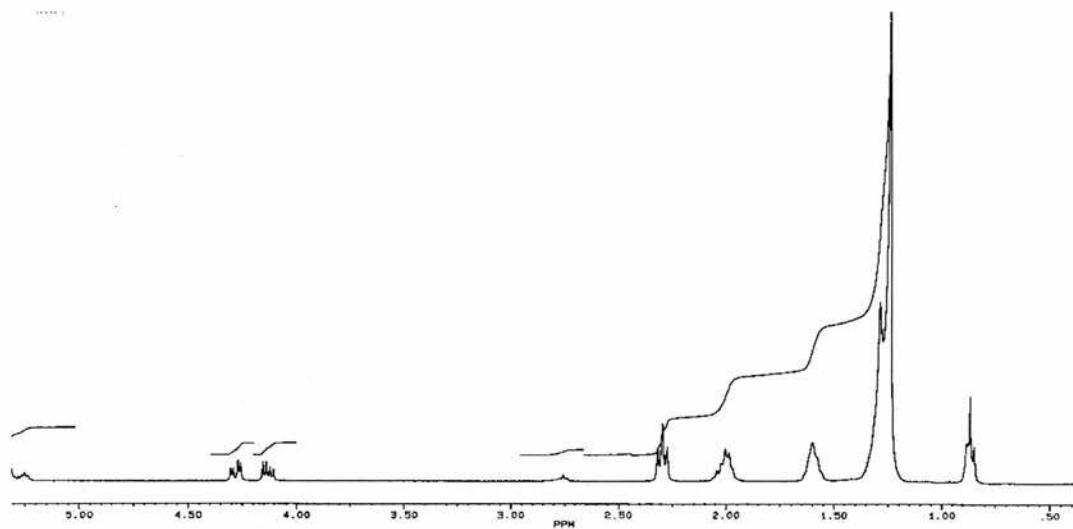


Figure 6.4. 5.6T small bore spectrum of lard dissolved in DCCl_3

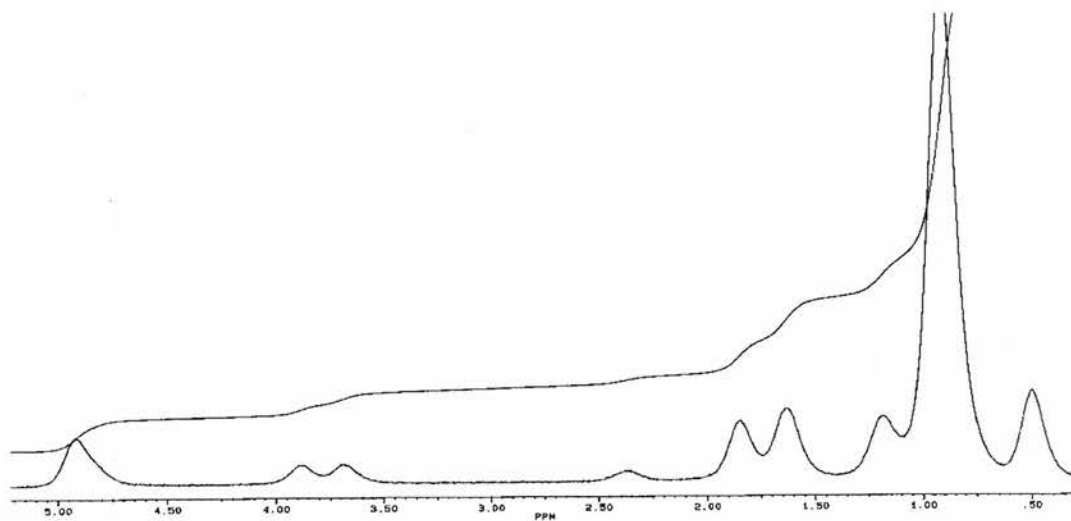


Fig. 6.5. 5.6T small bore spectrum of solid lard

6.2 Homonuclear polarisation transfer in double spin echo spectroscopy

6.2.1 Background

In double spin-echo experiments (such as PRESS) polarisation transfer effects can occur, whereby the product operator states $I_X^A I_Z^X$ and $I_Z^A I_X^X$ present in the X_3 doublet are interchanged by the transfer of polarisation from the other part of the coupled system (A quartet). For a more detailed account of product operator states the reader is referred to Appendix 1. In an AX_3 system (such as lactate) these effects lead to an echo time dependent modulation of the lactate CH_3 doublet. As such, use of multiple echo times is a possible mode of extracting the lactate signal from overlapping lipid signals. It should be noted that the limitations on the lactate S:N imposed by T_2 decay at long echo times still apply. The mechanisms pertaining to these phase modulations will be discussed in the next paragraph.

6.2.2 AX_3 doublet signal modulation in a double spin echo system - experimental evidence

The pulse sequence used in double spin echo inner volume excitation (PRESS localised) spectroscopy is represented by $\alpha-t_1-\beta-t_1-t_2-\gamma-t_2$ -Acq. Where the pulse angles α, β and γ are ideally 90° , 180° and 180° . The pulse sequence timing adds up to the total echo time $2t_1 = TE_1$, $2t_2 = TE_2$, $TE = TE_1 + TE_2$. In practice there is a deviation from these flip angles due to the non-ideal slice profile of the r.f. localisation pulses (Chapter 5). The effects of non-ideal pulse angle distributions and variable echo-times, on the PRESS localised lactate doublet signal intensity were investigated experimentally by Schick et al, 1995. Using PRESS localisation with total echo times of around $1/J$ and $2/J$, they explored the asymmetry of the lactate signal by varying the asymmetric single echo time intervals (TE_1 and TE_2). They found that the timing of the sequence did have a significant bearing upon the phase of the individual peaks within the lactate doublet. Symmetric sequences produced a relatively high intensity signal at $1/J$ but asymmetric timings were more effective at $2/J$. Extending the overall echo time revealed a periodicity in the phase of the lactate resonance at echo times around $2/J$, which is attributed to the polarisation transfer of magnetisation between the spins of the two coupled nuclei (CH_3 and CH). This transfer of polarisation is set up by the application of the 2nd and 3rd (β and γ) pulses and as such its extent was also found to be dependent upon the size of the flip angles used for the refocusing pulses. The

group found that a PRESS sequence with the two 180° pulses replaced by 90° pulses, and a symmetrical timing sequence, was most effective for observing the lactate modulation. This combination is the basis of the HOPE (Bunse et al 1995) editing sequence to be discussed later.

6.2.3 Theoretical predictions of the signal

First it is instructive to study the evolution of the lactate doublet signal intensity as a response to the sequence parameters. Jung and Lutz (1992) did this for a weakly coupled AX system by applying the quantum mechanical product operator formalism (Sørensen et al 1983). This analysis expresses the signal in terms of a basis of the individual x, y and z spin matrices of the A and the X spins plus product combinations of these states. It is able to account for the effects of the r.f. pulses, time evolution during periods of free precession and the effect of spoiler gradients during the sequence. Bunse et al (1995) extended this approach to the AX_3 spin system of lactate for the unique case of $\alpha=\beta=\gamma=90^\circ$ and $T_{E1}=T_{E2}=1/J=290$ ms.

In this work conducted in Edinburgh, the same approach was used, that of product operators to derive an expression for the double spin-echo lactate doublet signal for an arbitrary pulse sequence $\alpha_x-t_1-\beta_x-t_1-t_2-\gamma_x-t_2$ -Acq.

6.2.4 Calculation of the lactate signal in a double spin echo

To simplify the application of the product operator formalism to the pulse sequence above, the spoiler gradients used to dephase unwanted resonances were idealised. As such, terms are retained only if they have been in a single quantum state throughout the whole of the sequence. This corresponds to a $[-1, 1, -1]$ coherence pathway (Barker and Mareci 1989). Using the notation A to represent the A methine spin and X_s ($s=1, 2, 3$) for the X_3 methyl spins, the product operator approach predicts a doublet signal at acquisition;

$$S(t_{acq.}) = (k_1 I_y^{X_s} + k_2 I_x^{X_s} + k_3 2I_y^{X_s} I_z^A + k_4 2I_x^{X_s} I_z^A) \sin \alpha^{X_s} \quad (6.2)$$

The symbols $I_y^{X_s}, I_x^{X_s}$ are states of the product operator basis where the individual peaks of the doublet are aligned, similarly the product states $I_y^{X_s} I_z^A, I_x^{X_s} I_z^A$ represent the states where the peaks are in anti-phase. The basis functions are described in more depth (for the less complicated example of two weakly coupled spins - AX system) in the section on product

operators in Appendix 1. The basis lineshapes of the doublet signal (based on the functions in eq. (6.2)) are plotted in fig. 6.6. The coefficients k are tabulated in the paper by Marshall and Wild (1997) in Appendix 3 of this thesis. They are trigonometric functions which depend upon the parameters t_1 , t_2 , J , δ , α^A , β^A , γ^A , α^X , β^X , and γ^X . This paper explores the influence of these parameters on the appearance of the signal in eq.(6.2) by using Matlab simulated data. Further work using three dimensional surface plots of the simulated PRESS signal with experimental verification using variable echo time PRESS sequences is documented in the other paper (Marshall and Wild 1997(ii)).

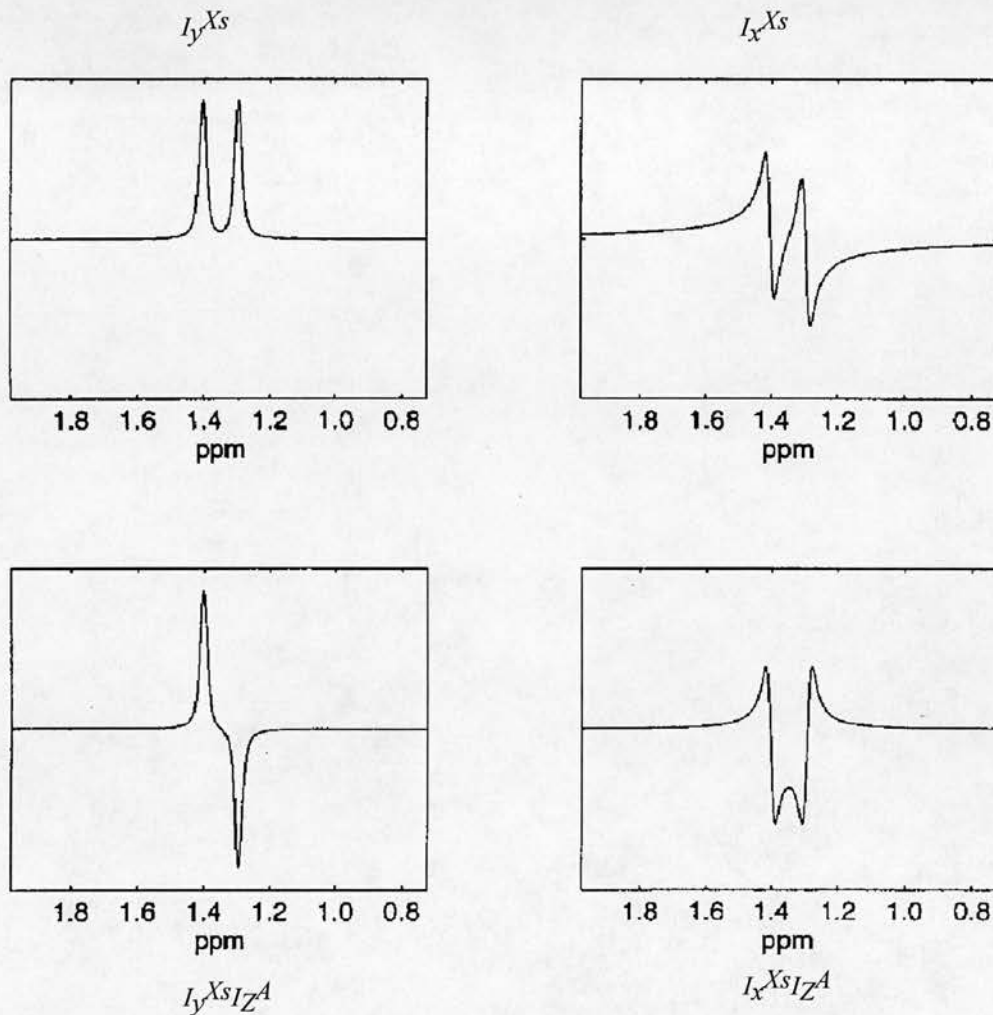


Fig. 6.6 The basis line shapes of the lactate doublet expressed in terms of the product operator basis states.

The pulse angles are A and X_s spin specific since the two sets of spins experience a different pulse flip angle distribution. This is because they have different resonant frequencies (separation $\delta \text{ rad s}^{-1}$) causing the localisation gradients to spatially shift the

VOI localised by these pulses (Chapter 5). Analysis of these coefficients reveals that the only contribution to the final methyl signal from polarisation transfer is a double transferred component (methyl- β -methine- γ -methyl). Setting $\alpha^A = \beta^A = \gamma^A, =\alpha^X = \beta^X = \gamma^X = 90^\circ$ and $t_1 = t_2 = T_E/2$ then the amplitude of polarisation transfer modulation is maximal as terms containing k_3 and k_4 in eq.(6.2) become equal to zero. Using the trigonometric expressions for k_1 and k_2 given in the paper Marshall and Wild (1997) (reprint included in Appendix 3), 3D surface plots of the parameters were made. Fig. 6.7 shows the behaviour of k_1 for $\alpha^A = \beta^A = \gamma^A, =\alpha^X = \beta^X = \gamma^X = 90^\circ$. The polarisation transfer modulation of the signal is obvious, with a well defined time period of around 10 ms. In this case eq.(6.2) becomes identical to that derived by Bunse (1995);

$$S(t_{acq}) = I_y^{X_s} \frac{1}{4} \cos\left(\frac{\delta}{2} T_E\right) - I_x^{X_s} \frac{1}{4} \sin\left(\frac{\delta}{2} T_E\right) \quad (6.3)$$

The angular frequency of modulation imposed on the doublet signal, is equal to half of the difference in chemical shifts of the two coupled resonances ($\delta/2$), giving the signal a time period of around 11 ms. At this stage it is interesting to note that this modulation frequency is half that found when the lactate doublet is observed with variation of the mixing time in a stimulated echo (STEAM) acquisition (See section 6.3).

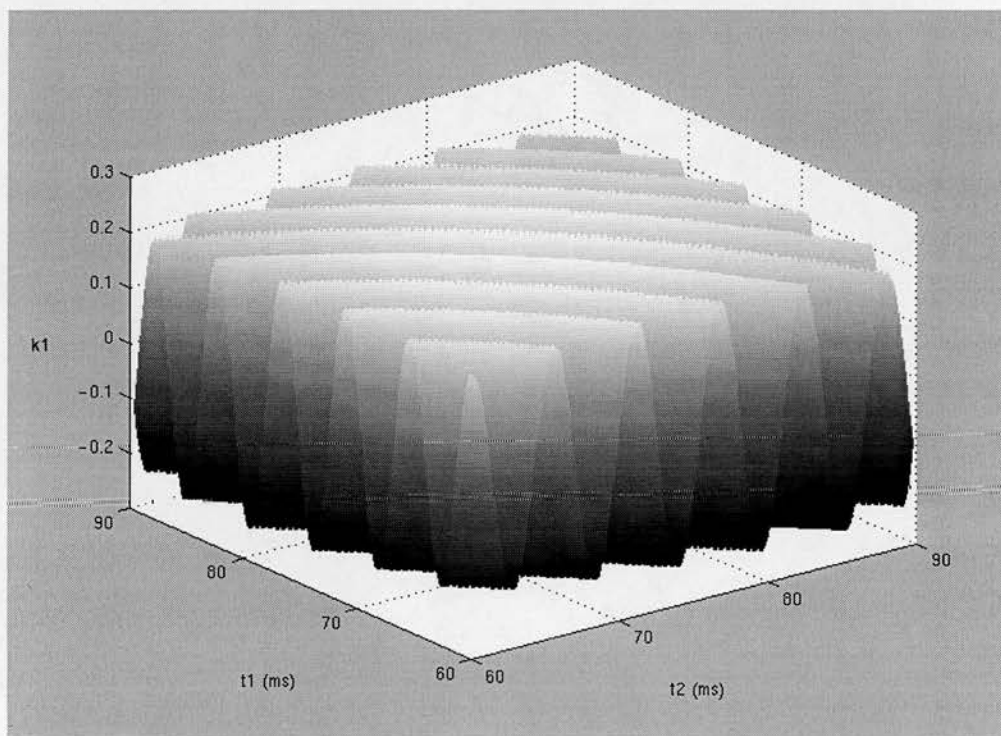


Fig. 6.7 polarisation transfer modulation of the k_1 coefficient used to express the lactate doublet signal in terms of its product operator basis with a sequence $90^\circ - T_E/2 - 90^\circ - T_E/2 - 90^\circ - T_E/2 - Acq.$ (see eq.(6.2)). With increasing $t_1 = t_2 = T_E/4$, the periodicity in t_1/t_2 is more marked.

6.2.5 Experimental verification of the T_E modulation of the HOPE signal

-determination of δ

The PRESS localised single voxel and SI sequences supplied by Siemens (PRESS.UDB and CH16I.UDB) were converted to HOPE sequences (HOPE.UDB and HOPE_CSI.UDB). This involved replacing the two 180° sinc pulses with 90° sinc pulses and making the sequences symmetric with respect to timing i.e. $TE_1=TE_2 = 1/J = TE/2$ with $TE \approx 2/J$ (290 ms). For the purpose of evaluating δ single voxel spectroscopy was used as the spectra are generally of a higher quality than SI versions, largely because the shimming is better over a smaller VOI. A phantom constructed from perspex according to the specifications described by Leach et al 1994, was used. In the initial experiments a solution of 100mM lactic acid and 100mM sodium acetate, doped with 0.1 mM Gd-DTPA (pH 5.9, temperature 21°C) was used to fill the phantom. A cubic voxel of edge 24mm was then positioned at the centre of the phantom with the aid of turbo spin echo localiser images. Shimming and optimisation of the CHES water suppression voltages was then performed using the standard Siemens single voxel PRESS sequence. Having recorded the shim currents and optimum water suppression voltage, the sequence was replaced with the HOPE sequence. This sequence was then executed with T_R increased from 1600 ms to 1800 ms, to allow for an increased echo time. The remaining acquisition parameters were as for the PRESS sequence namely; eight consecutive measurements averaged to gain a water suppressed FID and a water reference FID from the average of two measurements made with the CHES voltages set at zero. The number of data points used was 4096 with a sampling interval of $250\mu\text{s}$. Measurements were made at echo times ($T_E=4t_1=4t_2$) ranging from 270-300 ms with an increment in T_E of $250\mu\text{s}$.

Data processing was then done using the program `eccp_new.c` and `batch_csi_sv` as described in Chapter 4. A waterfall plot of the acetate-lactate spectrum over a range of echo times at 1 ms intervals is given in fig. 6.8. The area under the lactate doublet was then automatically integrated over the range 1.1-1.7 ppm using the program `integrate.c` and was plotted against echo time (see fig 6.9).

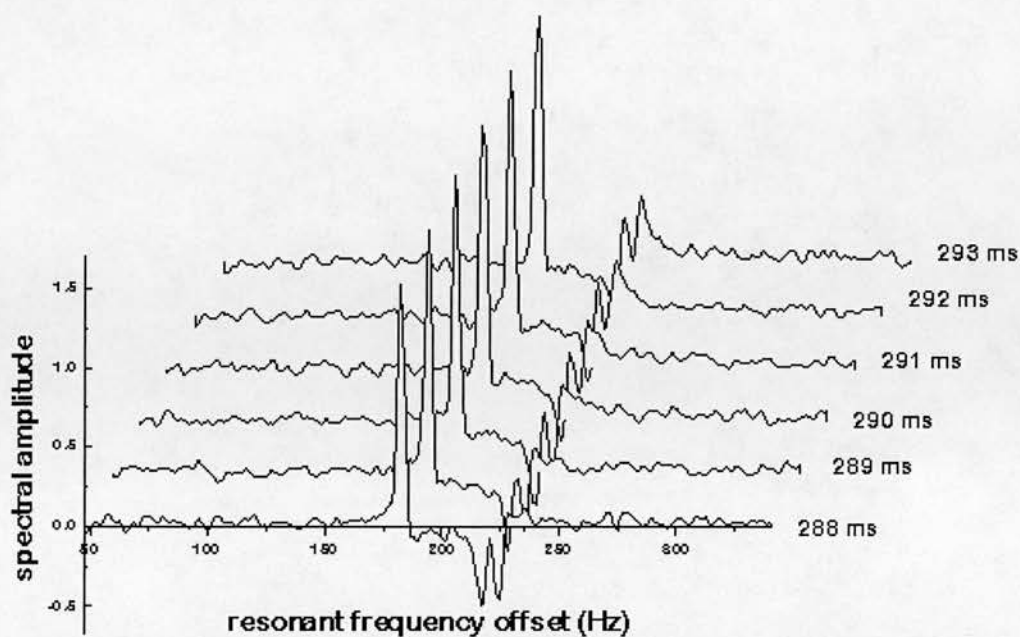


Fig.6.8. The lactate doublet for echo times ranging from 288 ms (front) to 293 ms (rear).

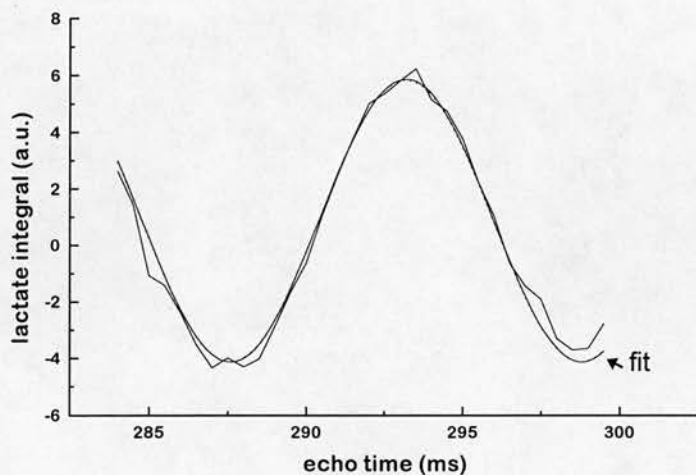


Fig. 6.9. Modulation of the lactate doublet integral with echo time.

The curve in fig.6.9 was then fitted to the function $y = a \cos(\omega t + \phi) + b$, using the program Microcal™ Origin (Northampton, MA, USA). This fit ignores the additional T_2 decay incurred with increasing echo time. Taking a typical value of 300 ms for an in vivo metabolite T_2 (Wilkinson et al 1994) then the difference in signal intensity due to T_2 decay at echo times of 290 ms and 295 ms is 2%. This 2% change is comparable with the

accuracy of the lactate peak integration for in vitro single voxel spectra (Marshall et al 1996). As such it seems safe to omit T_2 relaxation from the fit.

The results of the curve fit gave $\omega=561 \text{ rad s}^{-1}$, the periodicity of the integral as predicted by eq.(6.3) is $\omega= \delta/2$, equating these gives; $\delta/2\pi=178.5 \text{ Hz} \pm 2\text{Hz}$. This value is in reasonable agreement with that found by Bunse et al (1995) of 183 Hz. Differences in δ could be due to differences in pH and temperature of the in vitro solutions used (Bunse et al 1997). The time period of the function plotted in Fig. 6.9 is $2/\delta=11 \text{ ms}$. Thus pairs of measurements made whose echo times differ by 5.5 ms should have lactate doublets in antiphase to one another whilst signals not subject to polarisation transfer (choline, creatine, NAA and lipids) will remain in phase. The choice of echo times (around $2/J$) is arbitrary provided that they differ by 5.5 ms. Any dispersive component in the subtracted spectrum can be removed by phasing. Subtraction of such a pair of measurements from one another should therefore yield a lactate doublet and is the basis of a lipid lactate editing procedure.

6.2.6 Polarisation transfer editing

Polarisation transfer effects are well documented in traditional NMR texts (e.g. Canet 1996). The effect has been used for spectral editing with double spin echo sequences on clinical scanners. No evidence of a SI application of the method in-vivo has to date been published. The first such examples (Dumoulin and Williams 1986, Knüttel et al 1988, 1989) incorporate an additional 90° refocusing pulse in the interval between the two 180° pulses (β and γ) which initiates polarisation transfer between A and X spins and interchanges the direction of precession of the A_1 and A_2 components of the doublet. The result is that the coupled A_1 and A_2 pair are refocused in the same direction as non-coupled resonances. Repetition of the procedure without the polarisation transfer pulse results in an anti-phase alignment of coupled and non-coupled resonances. Subtraction of the two acquisitions from one another will give a spectrum of coupled resonances alone. This editing procedure, like the HOPE method, is a dual acquisition technique. Von Kienlin et al (1987) applied pre-sequence saturation of signals in the lactate frequency range (1.3 ppm). This spoils signals from the CH_3 group but not the CH group. During the following sequence, polarisation is transferred from CH to CH_3 giving a signal in the 1.3 ppm range that consists of the lactate doublet alone. As a result a lactate doublet spectrum can be gained in a single acquisition. The replacement of the PRESS double spin echo sequence with the pulse angles and timing parameters of HOPE enhances the polarisation transfer phase modulation imposed on the

lactate doublet (eq.(6.3)). Using this sequence, Bunse et al 1995, successfully edited lactate from lipid in-vitro but had less success in testing the technique in-vivo.

In the following sections the in-vitro and in-vivo performance of the HOPE editing technique is discussed for single voxel and spectroscopic imaging sequences.

6.2.7 Single voxel edited spectra

Methods

For editing purposes dual acquisitions were made at two overall echo times of TE and $TE + 2\pi/\delta$ with $TE \approx 2/J$. These dual acquisitions were interleaved between successive acquisitions in the single voxel case and between successive phase encodings in the SI case. Interleaving minimises the potential for motion artefact and field drifting errors which are accentuated by the process of subtraction. With 90° refocusing pulses replacing the two 180° pulses of PRESS, half of the magnetisation is rotated out of the xy plane and spoiled each time a pulse is applied. This means that the overall S:N ratio is reduced by a factor of 4, some of this (a factor of $\sqrt{2}$) is retrieved by the editing process. Editing consists of subtraction of the two signals to give a coupled (lactate) signal, or addition to give non-coupled signals (lipids and singlets). Acquisitions were then made at echo times of 287 ms and 292.5 ms both with and without water suppression using the lipid-lactate phantom illustrated in fig.6.10. This is based on the phantom described in section 6.2.5 with a sub container (200 cm^3 plastic bottle) filled with soured cream (animal lipids in suspension) and 10mM sodium lactate (pH 6.2, temperature 21°C).

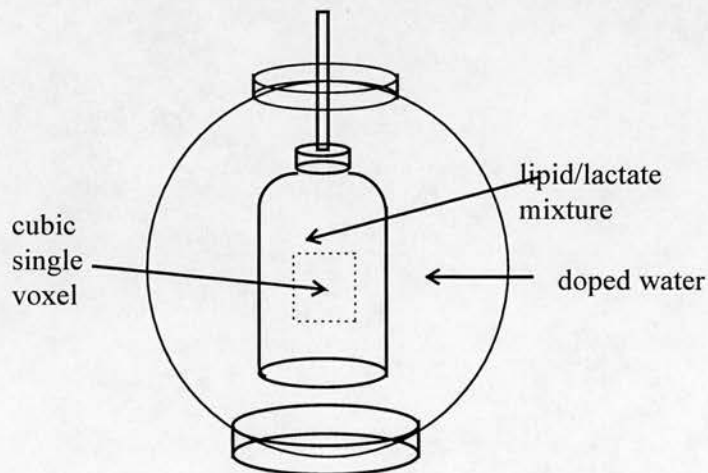


Fig. 6.10 The lipid-lactate phantom with the PRESS localised single voxel positioning.

The lactate edited subtraction spectrum from this lipid-lactate phantom acquisition is shown below in fig.6.11.

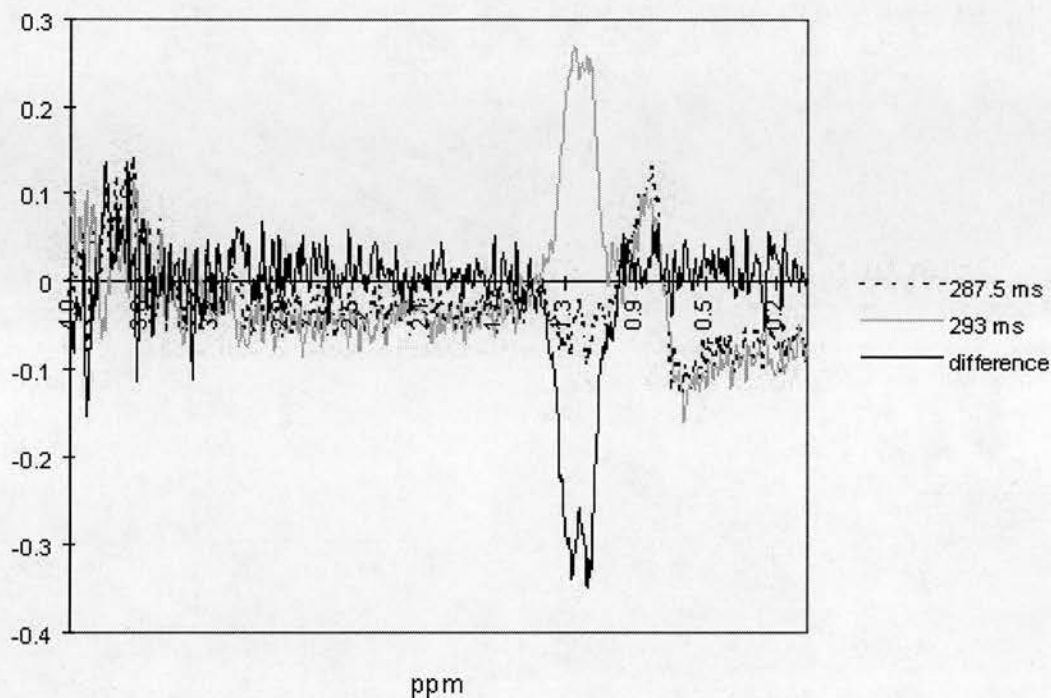


Fig. 6.11.3 The edited spectrum from the VOI shown in fig. 6.10. The cancellation of lipid signals in the range 0.9 ppm -1.5 ppm is complete leaving a well defined lactate doublet of twice the signal strength.

6.2.8 In vivo tests

The technique was then tested for viability in vivo as there was concern over the signal:noise ratio of the sequence and that the subtraction procedure would be prone to motion artefact and drift of metabolite resonant frequencies between successive acquisitions. Having successfully acquired edited spectra from a volunteer the sequence was then tested on a stroke patient. The difference spectrum from a 2 cm cubic voxel placed in the centre of an infarct in the region of the body of the lateral ventricles (fig. 6.12), is shown in fig. 6.13. The lactate signal is well resolved and the signals from all other metabolites have been cancelled.

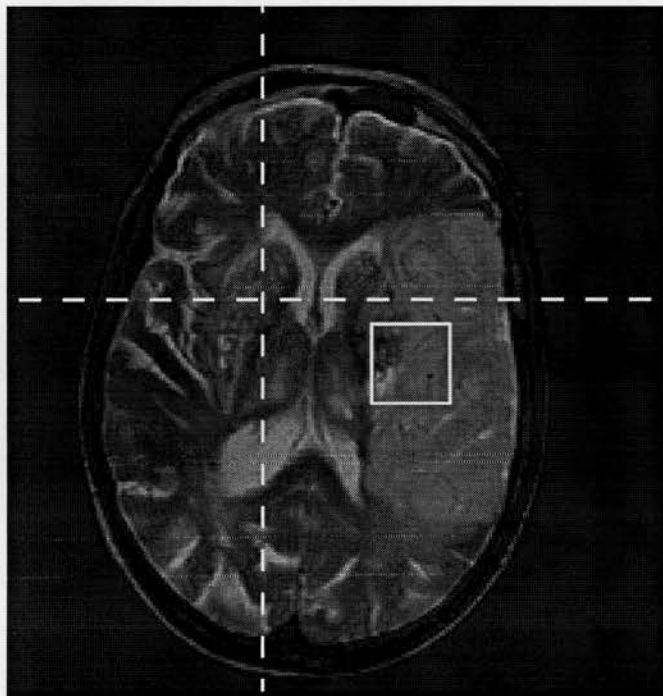


Fig. 6.12. Positioning of the VOI of the HOPE single voxel within the centre of an infarct in the MCA territory of the left cerebral hemisphere of a stroke patient.

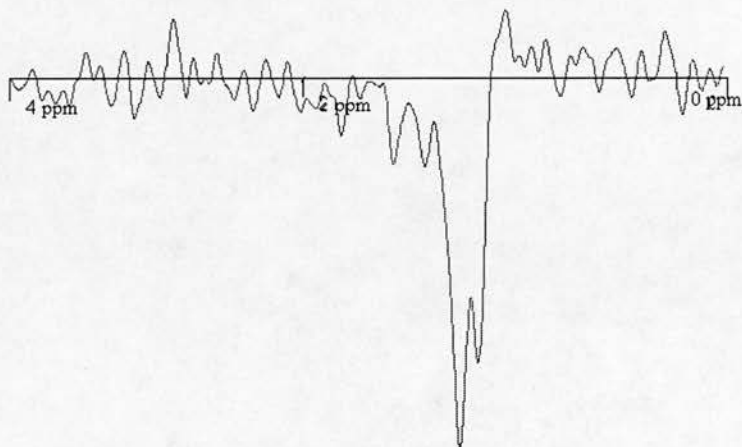


Fig. 6.13. The lactate edited spectrum in the frequency range 4 ppm - 0 ppm, a prominent lactate doublet is evident with cancellation of choline (3.2 ppm), creatine (3.0 ppm) and NAA (2.0 ppm).

66.2.9 HOPE SI editing

Having developed spectroscopic imaging (SI) the next step was to create a HOPE SI sequence for lactate editing. As SI VOIs are larger than the single voxel counterparts, there is a greater likelihood of lipid contamination from the skull and hence a greater need for editing capabilities. This HOPE SI sequence was again interleaved between acquisitions at echo times of 290 ms and 295.5 ms to minimise motion and frequency drift artefacts. As the two 180° pulses of the standard PRESS SI sequence have been replaced by 90° pulses the definition of the HOPE VOI should be sharper at the edges (Chapter 5). To test this a HOPE SI acquisition was made with 32×32 phase encodings, $T_R=1800$ ms. The excitation profile image was then constructed by integrating the area under the water resonance (Chapter 5). This excitation profile is illustrated in fig.6.14. below. If this profile is compared to the PRESS counterpart (fig. 5.3) there is a noticeable increase in delineation of the profile in the sagittal direction, a direct result of the replacement of the 180° pulse with a 90° pulse. However the HOPE SI profile is not perfectly rectangular and as such the position of the voxel will need to be considered before any quantitative conclusions are drawn from HOPE SI measurements.

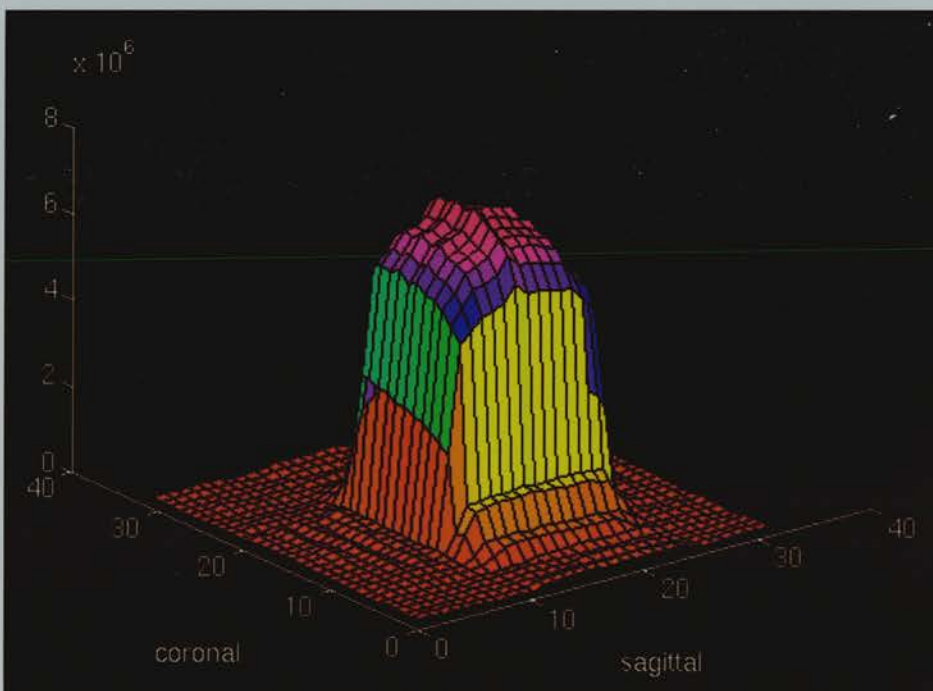


Fig. 6.14. The HOPE SI excitation profile.

A further consequence of the action of the spoiler gradients when the two 180° pulses are replaced with 90° pulses, is the four fold loss in signal (due to spoiling) in a single

acquisition spectrum. This signal loss is compounded by increased T_2 decay with an increase in the overall echo time by a factor of two. As a result the voxel size in a SI experiment needs to be increased. The sequence HOPE_CSI.UDB was tested, initially with 8×8 phase encodings, over a 240 mm field of view to give 3 cm square voxels with a slice thickness of 1.5 cm (nominal voxel volume 13.5 cm^3). This sequence was tested on a phantom containing a solution of 20mM lithium lactate and 5mM sodium acetate doped with 0.1 mM Gd-DTPA, on top of which a layer of sunflower oil was floated (see Fig. 6.15). The VOI was then positioned such that the uppermost voxels contained approximately 50% of magnetised oil so as to emulate the effect of inadvertent lipid excitation from the skull.

The spectral array from one of the echo times (295.5 ms) is shown in fig. 6.16.1, the uppermost row of voxels have a strong lipid signal which obscures any lactate signal. The remaining voxels are also contaminated by Fourier leakage from the strong lipid signals. Fig 6.16.2 shows the edited spectra obtained by subtraction of the two time domain signals. All of the lipid and acetate has been cancelled out leaving well resolved lactate doublets. The strength of the signals from the edge voxels is lessened by the non rectangular excitation profile that results from the imperfect 90° pulses used in VOI localisation (see fig. 6.14).

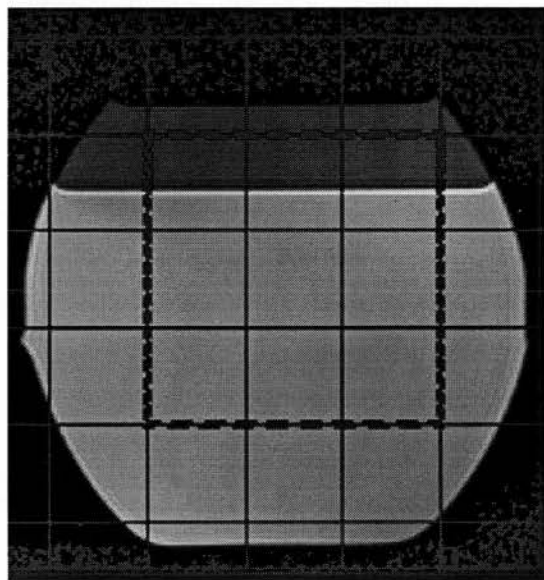


Fig. 6.15. The 3 litre lactate-lipid phantom.

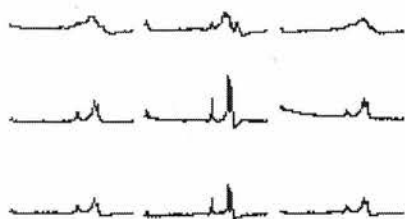


Fig. 6.16.1 Spectra from $T_E=295.5$ ms. Note the contamination of the uppermost row with lipid signals

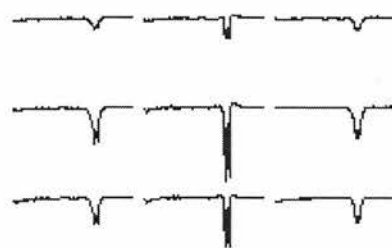


Fig. 6.16.2 The lactate edited spectra obtained by subtraction of the $T_E=295.5$ ms signal from the $T_E=290$ ms signal.

6.2.10 In-vivo tests

Finally the sequence was tested in-vivo on a volunteer to check for complete cancellation of uncoupled resonances. The $T_E=295.5$ ms array of spectra from a 90 mm square by 15mm thick VOI, split in to 9 voxels is shown in fig. 6.17.1. Well resolved choline, creatine and NAA peaks are visible. In the edited spectrum (fig. 6.17.2) these have been cancelled to the level of noise.

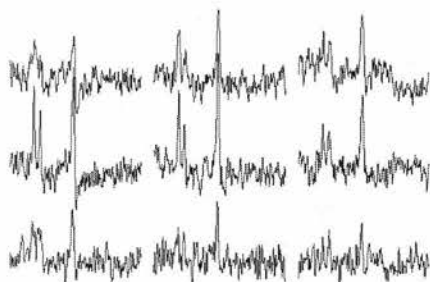


Fig. 6.17.1 In-vivo HOPE SI array for $T_E=295.5$ ms

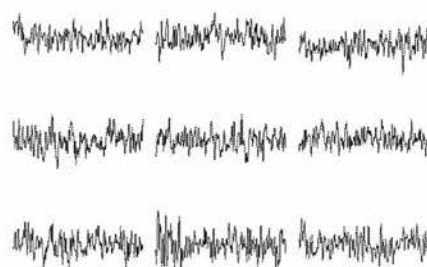


Fig. 6.17.2. Edited spectral array

The sequence was then tested with a smaller voxel size consistent with 16×16 phase encodings (cube of 1.5 cm edge - nominal voxel volume 3.4 cm^3) used routinely in PRESS SI. The single spectral array from a $75 \text{ mm} \times 75 \text{ mm}$ VOI (placed at the centre of the region of the body of the lateral ventricles) in a healthy volunteer's brain is shown in fig. 6.18. This data was acquired at $T_E=290/295.5$ ms and $T_R=1800$ ms, the spectrum was obtained by adding the two echo time signals together. Note that the NAA peak is well defined but the choline and creatine peaks are less obvious. This volunteer was able to maintain a stationary position for a longer period of time than a typical patient would have done. As such it is doubtful that the signals from a 16×16 acquisition from a patient will be of sufficient

strength. If the FOV of the SI was reduced from 240 mm to 180 mm say, then providing there was no wrap around in the T_2 images, 8×8 phase encodings would give an intermediate voxel size of 2.25 cm square edge (nominal voxel volume 7.6 cm^3). Alternatively with a FOV=240 mm and 16×16 phase encodings a slice thickness of 3 cm would give a two fold increase in signal:noise (nominal voxel volume 6.75 cm^3) with a loss in transverse spatial resolution.

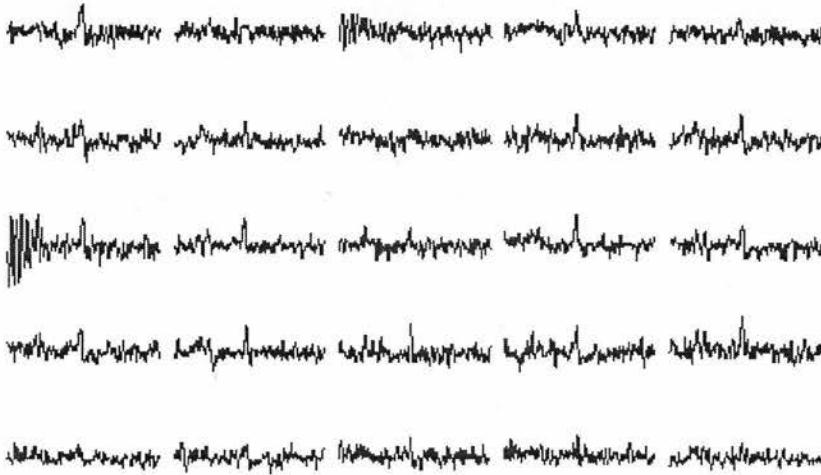


Fig. 6.18 HOPE SI spectra from a $75 \text{ mm} \times 75 \text{ mm}$ array of 15 mm cubic voxels from a healthy volunteer. Note how the NAA resonance is the only obvious peak throughout the array.

6.2.11 Discussion

Using the HOPE sequence, lactate editing has been performed successfully using a single-voxel technique both in-vitro and in-vivo. The SI version of the editing sequence has been tested in-vitro, and volunteer studies show that the signal:noise ratio of the sequence is sufficient to give well defined spectra from a voxel of dimensions $3 \times 3 \times 1.5 \text{ cm}$. The next stage is to test the HOPE CSI sequence in-vivo on stroke patients. The HOPE sequence can be implemented with relative ease on scanners supplied with a PRESS spectroscopy sequence, providing the programmer can alter the timing of the sequence and the size of the flip angles used.

Signal to noise considerations

The action of the spoiler gradients causes a four fold loss in S:N when 90^0 refocusing pulses are used instead of 180^0 pulses. The fact that two data sets are acquired, means that a factor of $\sqrt{2}$ of this loss can be retrieved. This is done by the process of subtraction in the case of the lactate signal and by addition for the uncoupled resonances. This gives the sequence a S:N/unit time of $4\sqrt{2}$ times less than the equivalent PRESS sequence at 290 ms echo time. A further source of signal loss comes from the extension of T_E from 135 ms for the standard PRESS sequence, to 290 ms for the HOPE sequence. T_2 relaxation effects account for a reduction in intensity of approximately 40% for the metabolites choline, creatine and NAA at the longer echo time.

Conclusions

In summary, for spectroscopic studies where the detection of lactate is a priority (e.g. in acute stroke) and there is a possibility of any lactate being obscured by lipids, then the HOPE sequence is recommended. If signal to noise ratio is a priority (e.g. in quantitative studies) or where a smaller voxel size is sought and lipid contamination is not anticipated, then a standard PRESS sequence with a $2\sqrt{2}$ greater signal : noise ratio and a faster collection time (one water suppressed data set compared to two in HOPE) is a better option.

6.3 Zero quantum coherence editing with a STEAM sequence

6.3.1 Introduction

Stimulated echo spectroscopy (STEAM - Frahm et al 1987) is used routinely in both single voxel and SI sequences. The response of uncoupled resonances to the three 90° localisation pulses of STEAM (fig. 6.19), is quite easy to follow, despite the spoiler gradients positioned in the T_m and T_E periods to dephase spin and stimulated echoes originating from outside the VOI. Coupled resonances such as the weakly coupled AX_3 spin system of lactate display a more complex response to STEAM whereby the doublet signal shows some modulation with both echo time T_E and mixing time, T_m . Calculating the theoretical lineshape of the lactate doublet as a function of these parameters, is more awkward than for the PRESS sequence (Marshall and Wild 1997 i). This is largely because of the transfer of zero quantum and multiple quantum coherences between the doublet and quartet spins (Appendix 1).

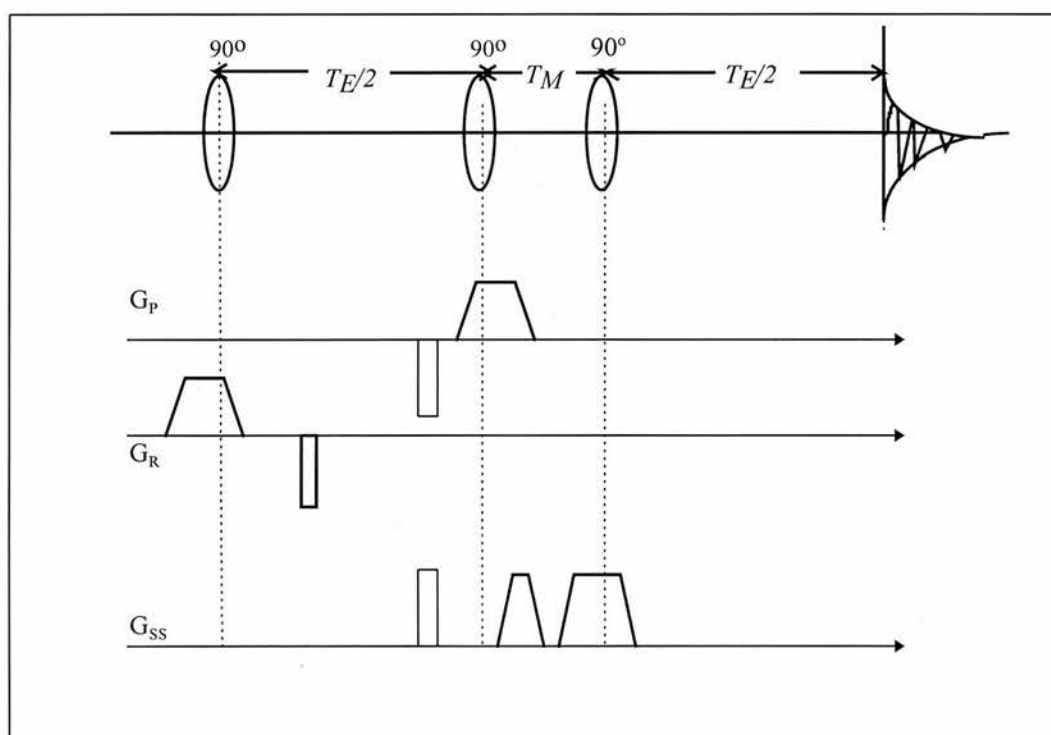


Figure 6.19. The STEAM sequence as used on the Magnetom SP63.

6.3.2 Coherence transfer

Uncoupled spins have two possible energy levels made available to them (-parallel and +anti parallel to the external field). Transitions between two such levels involve a change in quantum number of unity i.e. single quantum (SQ) transitions. A coupled pair of spins have degenerate energy levels and as such can make quantum transitions corresponding to zero change in quantum number or a change of 2 or more (Figure 6.20 illustrates the degeneracy in energy levels of an AX system). Such zero quantum (ZQ) and double quantum (DQ) transitions do not correspond to directly measurable quantities, being represented by off-diagonal phase terms in the density operator (see Appendix 1). These phase coherence evolve with the single quantum transitions magnetisation, and can be observed indirectly as a modulation of the single quantum spin magnetisation.

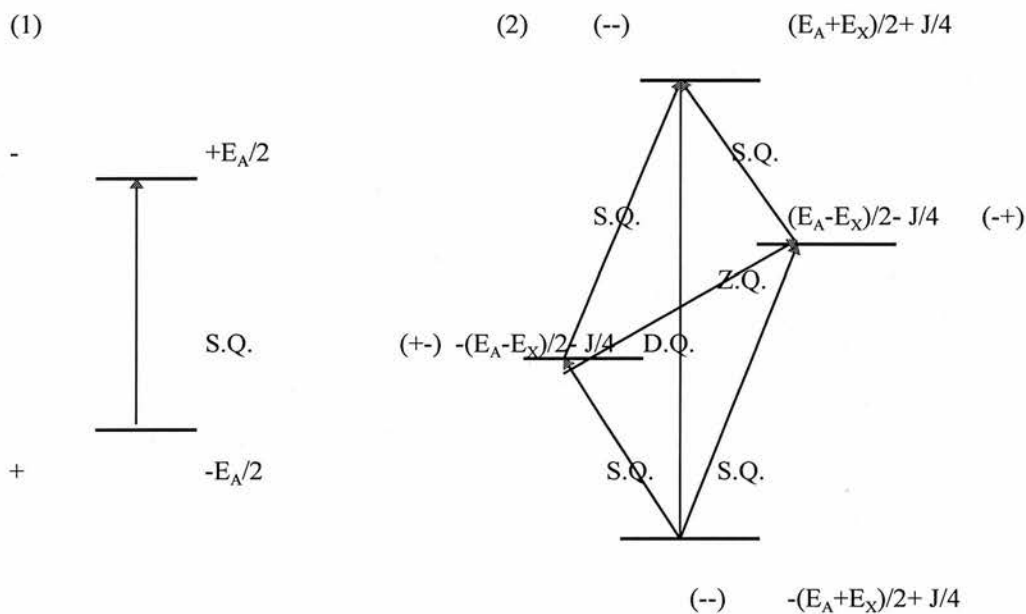


Figure 6.20 Diagram illustrating the splitting of energy levels in (fig 6.20.1) a single spin system and (fig 6.20.2) an AX system, with the various quantum transitions that can take place.

6.3.3 Calculation of the lactate signal for STEAM

The pulse sequences used to implement STEAM localisation on clinical scanners involve quite complicated arrangements of spoiling gradients, needed to dephase echoes from outside the VOI. Prediction of the time evolution of the coupled lactate doublet and its response to gradients and r.f. pulses using product operator formalism (Appendix 1) would be quite a task. To simplify matters the spoiler gradients and r.f. pulses can be approximated to rectangular pulses which maintain the same coherence phase pathways as the real sequences. The approximated STEAM sequence used by Wilman and Allen (1993) is depicted below.

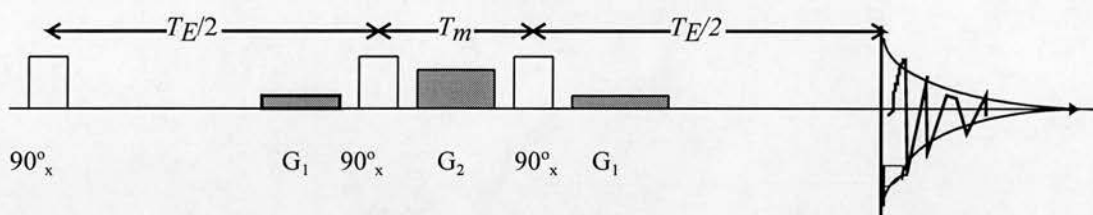


Fig. 6.21. The simplified STEAM sequence which assumes rectangular r.f. pulses and dephasing gradients (shaded) positioned symmetrically with respect to T_E and T_m .

The signal upon acquisition is found by first formulating the density operator at $t=0$ in terms of doublet X_s and quartet A terms ($s=1,2$, and 3 spins of the three X_3 protons). Time evolution operators and r.f. pulse rotation operators are then applied to give a final signal, $S(T_E, T_M)$ -see eq.(6.4). This contains contributions from the longitudinal evolution (during the mixing time) of the doublet term in the density operator and from the transfer of magnetisation between the quartet and doublet spins. T_1 and T_2 relaxation effects are omitted from this calculation.

$$S(T_E, T_M) = \frac{1}{2} \left[\cos^2(\pi J T_E / 2) - \frac{1}{2} \sin^2(\pi J T_E / 2) (1 - \cos^2(\pi J T_E / 2)) \cos(\delta T_E / 2) \cos^2(\pi J T_M) \right] \cos(\pi J T_M) \quad (6.4)$$

Where T_E is the echo time, T_M the mixing time, δ the difference in angular frequency of the centre of the quartet and doublet resonances and J the spin-spin coupling constant for the AX_3 spins of lactate. Inspection of eq.(6.4) reveals two T_M modulations of $S(T_E, T_M)$ with

frequencies $2/J$ and $2\pi/\delta$. There are a further two modulations in T_E with frequencies of $4/J$ and $4\pi/\delta$. Computer simulations were then done using eq.(6.4) to highlight these modulations.

6.3.4. Simulations

The result given in eq.(6.4) was used to perform Matlab simulations to predict the behaviour of the STEAM localised lactate doublet signal with varying T_M and T_E . In these simulations a value of $J=6.9$ Hz was used with a value of $\delta=2\pi \times 183$ Hz as calculated using the HOPE sequence (section 6.2). A T_2 weighting was added by damping the terms in T_E with a T_2 of 300 ms. This is a rough estimate, as definitive T_2 values are very difficult to obtain in vitro and in vivo since the lactate signal undergoes echo time modulations caused by the J coupling (Section 6.3.5). The signal is plotted as a 3D surface in fig.6.22 and as functions of T_E (fig. 6.23) and T_M (fig 6.24). The T_E modulation of this ZQC component arises as a result of transfer of magnetisation from the quartet spins. This T_E ZQC modulation becomes nullified for $T_E \approx 145$ ms ($1/J$), as such there is good reason to use this popular echo time if T_E dependent variations are to be excluded. The periodicity in mixing time is nullified for $T_M \approx 70$ ms ($1/2J$), so use of a $T_M \approx 70$ ms with $T_E \approx 145$ ms will result in a zero intensity lactate doublet. It is the T_M modulation that has been utilised as a mechanism for ZQC based editing and is focused on in the next section.

Tm and Te modulation of the lactate doublet STEAM signal

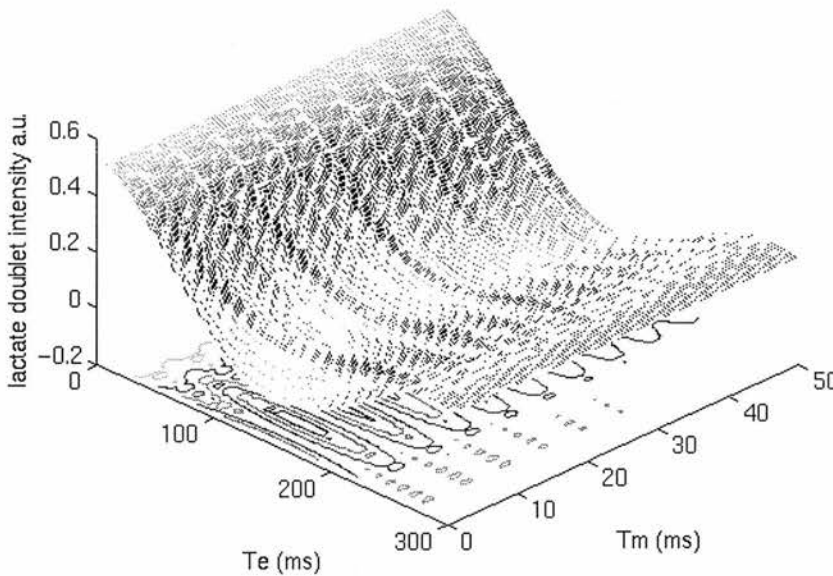


Fig. 6.22. 3D surface plot of the lactate doublet intensity as a function of T_M and T_E . Underneath is plotted a contour map to emphasise the periodicities present.

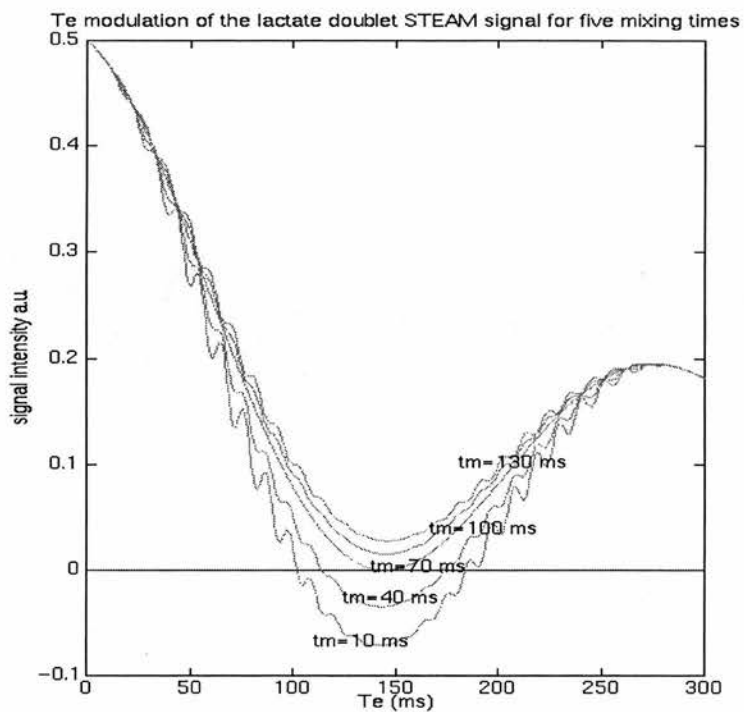


Fig. 6.23 The T_E modulation for a range of T_M

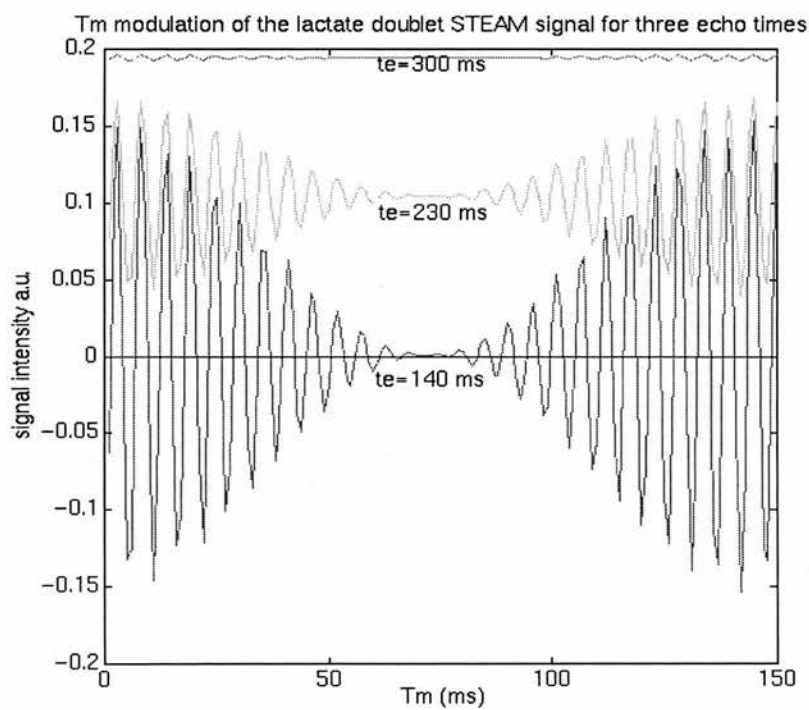


Fig. 6.24. The T_M modulation for a range of T_E

6.3.5 Experimental verification of the T_m modulation of the signal

The variation of the theoretical signal of the real part of the STEAM localised lactate doublet with T_m and T_E was then investigated experimentally. The standard Siemens single voxel STEAM spectroscopy sequence (STEAM_135.UDB) has a fixed echo time of 135 ms (based on $J=7.4$ Hz, $1/J=135$ ms) and a fixed mixing time of 30 ms. This was modified by the author (STEAM_TM_TE.UDB) to give a fixed echo time of 140 ms and a variable mixing time from 30 ms up to 200 ms with 250 μ s minimum increments. A T_E of 140 ms is more consistent with the value of $J=6.9$ Hz, and is the echo time at which the signal in fig.6.24 shows the most dramatic swing about the zero baseline with variation in T_M . A spherical phantom containing an undoped mixture of 100 mM lithium lactate and 50 mM sodium acetate was placed in the head coil of the scanner. A VOI was localised, shimmed and the water suppression voltage optimised as described in Chapter 3. A series of acquisitions was then made with escalating T_m from 30 ms through to 50 ms. Each acquisition consisted of an average of 16 separate acquisitions plus 2 pre-scans for a water suppressed data set and 4 averages plus 2 pre-scans for a water reference data set. The repetition time between acquisitions was set at 2000 ms. The water reference set was collected following the preliminary excitation and dephasing of the water resonance using a broad band frequency selective CHESS pulse as described in section 3.3.

These individual stimulated echo signals were then processed in accordance with Chapter 4 using the programme `eccp_new.c` (listed in Appendix 2). To get as accurate an estimate as possible of the intensity of the lactate doublet, its signal was integrated with respect to frequency. This removes any uncertainties introduced by the phase asymmetry in the signal amplitude of the doublet. The area integration was implemented automatically (using the program `integrate.c`) over the range 0.94 - 1.44 ppm. The plot of the lactate integral versus mixing time for a T_E of 140 ms is shown in fig. 6.25.

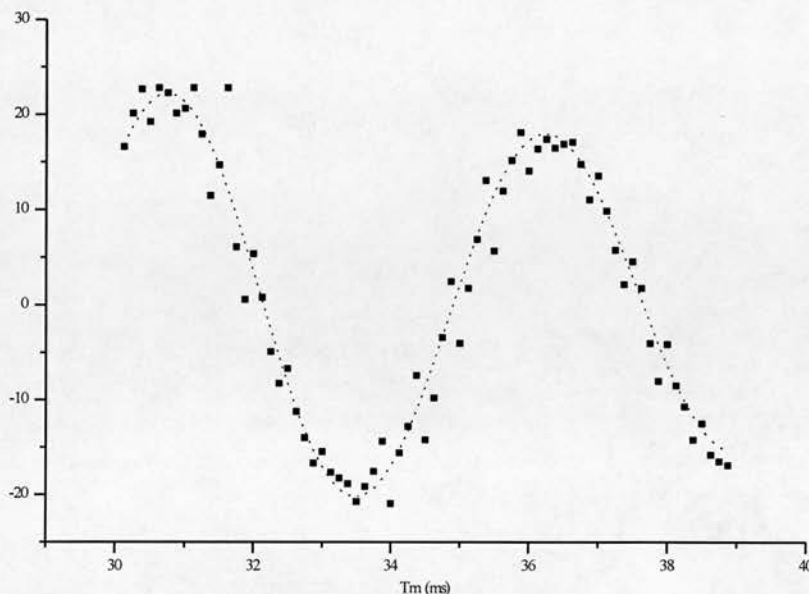


Fig. 6.25. Periodicity in the intensity of the lactate doublet integral with mixing time.

Fig.6.25 shows a marked T_m periodicity in the amplitude of the lactate doublet. The curve was then fitted to the function $y = a \cos^2(\pi Jt) \cdot (1 - e^{-\frac{t}{T}}) \cos(\omega t + c)$, using the program Microcal™ Origin (Northampton, MA, USA). This fitting procedure yielded a time period of $\tau = 2\pi/\omega = 5.46 \pm 0.07$ ms. This value of the periodicity of the zero quantum coherence modulation is consistent with the periodicity of the last term in eq.(6.4) of $2\pi/\delta$ ($=1/183 = 5.5$ ms). The plot also shows a diminishing signal with increasing mixing time, this decay will include the effect of T_1 decay but will also have a zero quantum coherence component ($\cos^2(\pi Jt)$) instigated by the J coupling of the A and X_3 spins. As such, longitudinal relaxation in the mixing time will be much more complicated than the mono-exponential of an uncoupled resonance. Prediction of the longitudinal cross relaxation time of a coupled resonance requires the introduction of a cross relaxation rate to the longitudinal Bloch equation (Chapter 2, eq. (2.26b)). This leads to the Solomon equations, the solution of these is very involved (Canet 1996) and will not be covered here. An alternative method is to attempt to fit a decay curve to the signal intensity obtained over a wide range of mixing times, Straubinger 1995, did this with STEAM spectra of the strongly coupled AB system of citrate. From this limited lactate data set the fitting yielded a damping constant of $T = 83 \pm$

9 ms, this result should be regarded as a very rough approximation as a much wider range of mixing times need to be acquired at intervals of τ . This uniform increment (τ) in T_m will remove uncertainties in signal amplitude induced by the ZQC T_m oscillation of the signal.

6.3.6. Quantum Coherence Editing

The T_m modulation of the lactate doublet forms the basis of a spectral editing technique. In this section a brief review of literature documenting quantum coherence editing performed using clinical MRI spectrometers will be given. This will be followed by the methods used to perform T_m STEAM lactate editing on this scanner.

Quantum Coherence Editing using STEAM - a review

Sotak et al 1988, used a STEAM sequence. The first two 90° pulses set up a ZQ coherence, which then evolves during the mixing period and modulates the longitudinal stimulated echo magnetisation and is finally detected as a modulation of the SQ signal following the 90° flip of the final pulse. With mixing times incremented by an integral number of half cycles of the ZQ modulation frequency of N-Acetyl Alanine (AX_3 , system), the coupled resonance showed an inversion at every step. Subtraction of successive spectra edits out the non coupled methyl resonance. Bachert et al 1995, performed ZQ and DQ editing on brain spectra using the same STEAM sequence on a Magnetom SP 63, and resolved the lactate resonance from lipids. Using STEAM the same group observed the DQC evolution over a range of mixing times and were able to produce a 2D DQC spectrum of a lactate/lipid mixture in-vitro (Müller et al 1995). They point out, however that the DQC sensitivity is lower than ZQC sensitivity and this DQC editing technique may not be sensitive enough for in-vivo work. de Graaf et al 1993, found DQC filtered pulse sequences sufficiently sensitive to resolve a lactate edited signal from a 32×32 phase encoded SI at 1.5 T.

Jung et al 1991, applied DQC editing on a 1.5 T Magnetom with a three pulse sequence (two 90° , one 180°) to create DQCs. They then used the sequence to study in-vitro lactate signals and in-vivo lipid signals. Of particular interest is the passage by the DQC "filter" of signals originating from lipids; CH_2 groups coupled to $-CH=CH-$ groups and CH_3 groups coupled to neighbouring CH_2 groups. This is despite the fact that these couplings do not amount to weakly coupled systems. So if QC filtering sequences are to be used to discern lipid from lactate, particular attention needs to be paid to the ZQCs and DQCs of the lipid spectrum. Apart from the CH_3 signal loss, ZQ (and multiple QC - which use selective excitation pulses) filtering sequences have the drawback of removing SQ coherences such as NAA, choline and creatine. Separate acquisitions are needed to observe these resonances and

direct comparisons of the concentrations of lactate and SQ resonances between edited / non-edited spectra may be awkward as a result of undetermined signal attenuation of the filtering sequence used.

6.3.7. Editing methods

The frequency of the T_m modulation is equal to the difference δ , in the single quantum resonant frequencies (chemical shifts) of the A and X_3 spins. As such the mixing time can be incremented by an amount equal to half the time period (π/δ) with the effect of inverting any resonances subject to ZQC modulation, i.e. coupled resonances.

So successive stimulated echoes can be collected with mixing times differing by $(1/2\delta)=2.75$ ms, which when differenced will leave the signals from coupled species alone. It is interesting to note that this SQC modulation is twice the rate of the HOPE modulation of the lactate doublet (Section 6.2.4/6.2.5). Signals collected to calculate the integral behaviour of the real part of the doublet were used in this part of the study. In the example shown below the signal from $T_m=33.75$ ms (fig.6.26.1) was subtracted from the $T_m=31.00$ ms signal (fig. 6.26.2). Inspection of the difference spectrum (fig. 6.26.3) reveals an enhanced lactate doublet with some residual out of phase acetate signal. From past experiences using subtraction techniques in HOPE editing, this effect could be due to frequency drift of the acetate signal in the time between successive acquisitions (2 minutes). An interleaved sequence might circumvent this problem and warranted further investigation. Alternatively the longitudinal decay of the uncoupled acetate resonance (T_1 relaxation) might explain this effect. If a T_1 of 3000 ms is used (Wild and Marshall 1997) the difference in intensity of these two signals due to T_1 decay alone amounts to less than 0.1%. This suggests that the first explanation is the most plausible. This effect was checked by integrating the area under the acetate peak over the range (1.92-1.7 ppm), over a range of mixing times from 30 to 38 ms. Over this range there was no noticeable change in the acetate signal which confirms that T_1 decay of acetate was negligible.

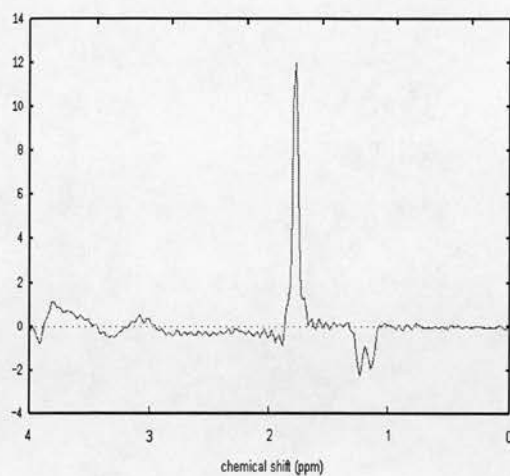
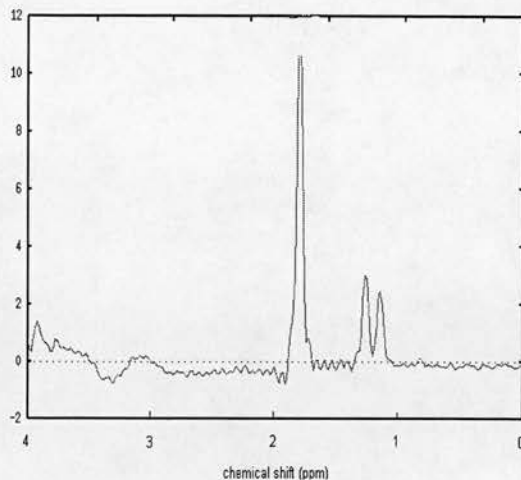
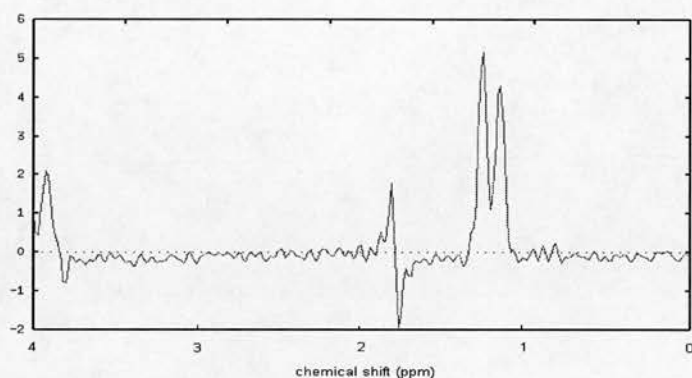
Fig. 6.26.1 $T_m=31$ msFig. 6.26.2 $T_m=33.75$ ms

Fig. 6.26.3 Difference spectrum (Note the different vertical scales used)

6.3.8. Editing with an interleaved sequence

In an attempt to overcome the problem of residual acetate signal brought about by frequency drift between acquisitions, an interleaved acquisition sequence (STEAM_140_INTER.UDB) was written by the author. This sequence uses an echo time of 140 ms with two successive acquisitions at mixing times of 30 ms and 32.75 ms respectively. The sequence is then repeated in this interleaved manner so that any time varying effect due to motion or field drift is distributed more evenly between the two different mixing time signals when they are averaged. The FIDs are then subtracted from one another prior to signal processing to yield a lactate edited FID. An example of such a signal acquired using this sequence under identical experimental conditions as were used in the previous section, is given in fig. 6.27. When compared with fig. 6.26.3, there is less residual acetate at 1.8 ppm, furthermore the sequence is more effective in editing the weaker lactate quartet signal at around 4 ppm, revealing some of the fine structure in the signal.

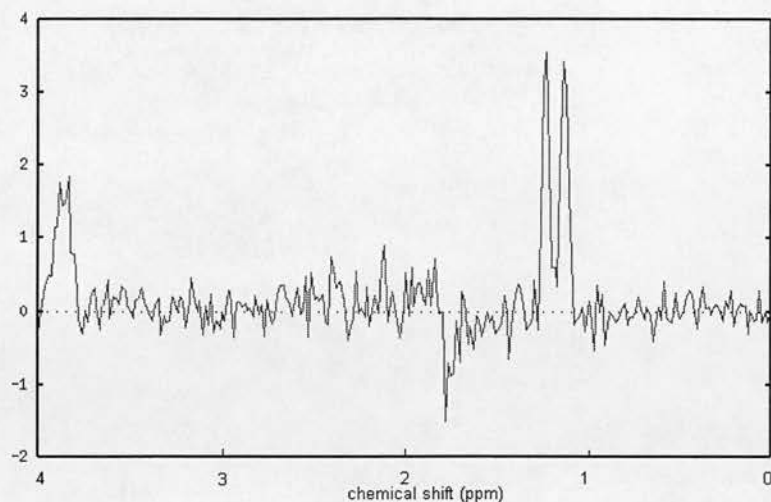


Fig. 6.27. Interleaved lactate edited signal

6.3.9. Editing lactate from lipids

Having tested the interleaved sequence with an acetate-lactate phantom the suitability of the sequence for lipid-lactate discrimination was tested. A solution of doped 60mM lactic acid was made up with tap water and used to fill two thirds of a 200 cm³ plastic bottle. The remaining third of the bottle was filled with sunflower oil which floated above the aqueous solution as an immiscible layer. This container was then immersed in a larger 3000 cm³ phantom full of undoped tap water. An 8cm³ STEAM VOI was then positioned as shown in fig.6.28, and interleaved acquisitions were made (STEAM_140_INTER.UDB) both with and without water suppression. The individual spectra from the two mixing times are displayed in figures 6.29.1 and 6.29.2 whilst their difference is shown in fig.6.29.3.

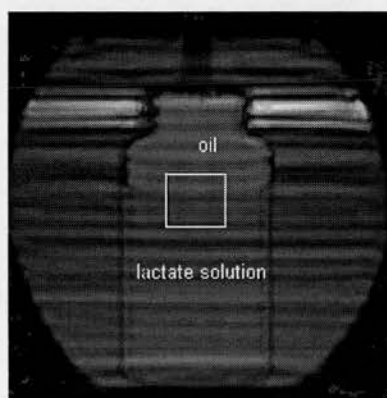


Fig.6.28 Turbo spin-echo single acquisition localiser image of the lactate-lipid phantom used for testing the STEAM editing sequence.

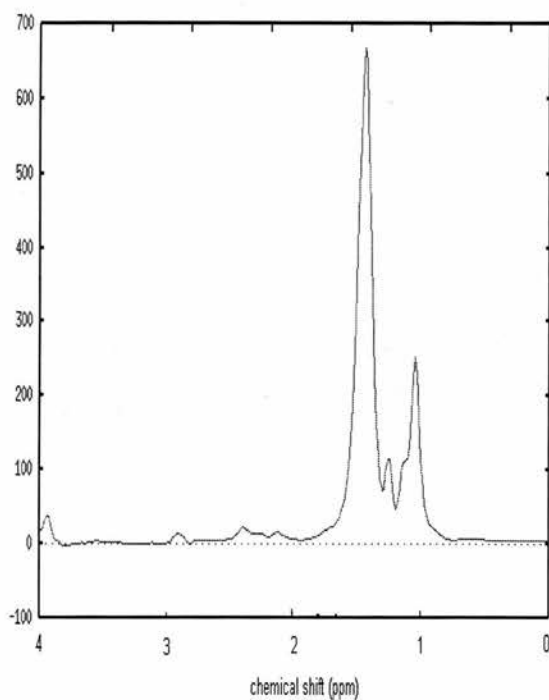
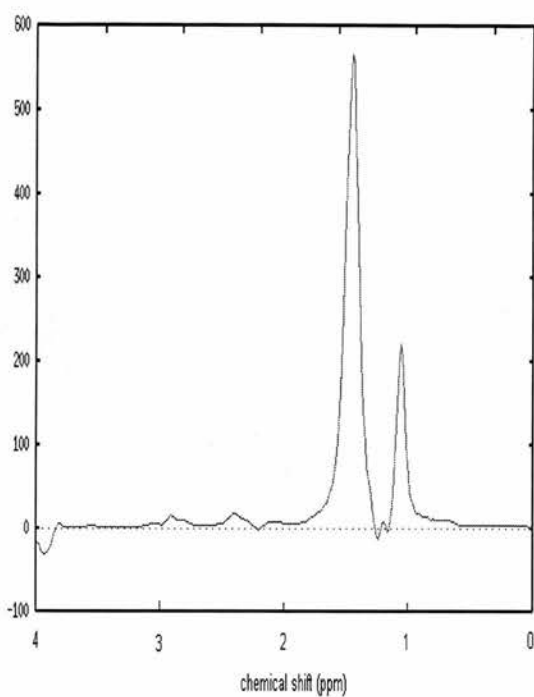
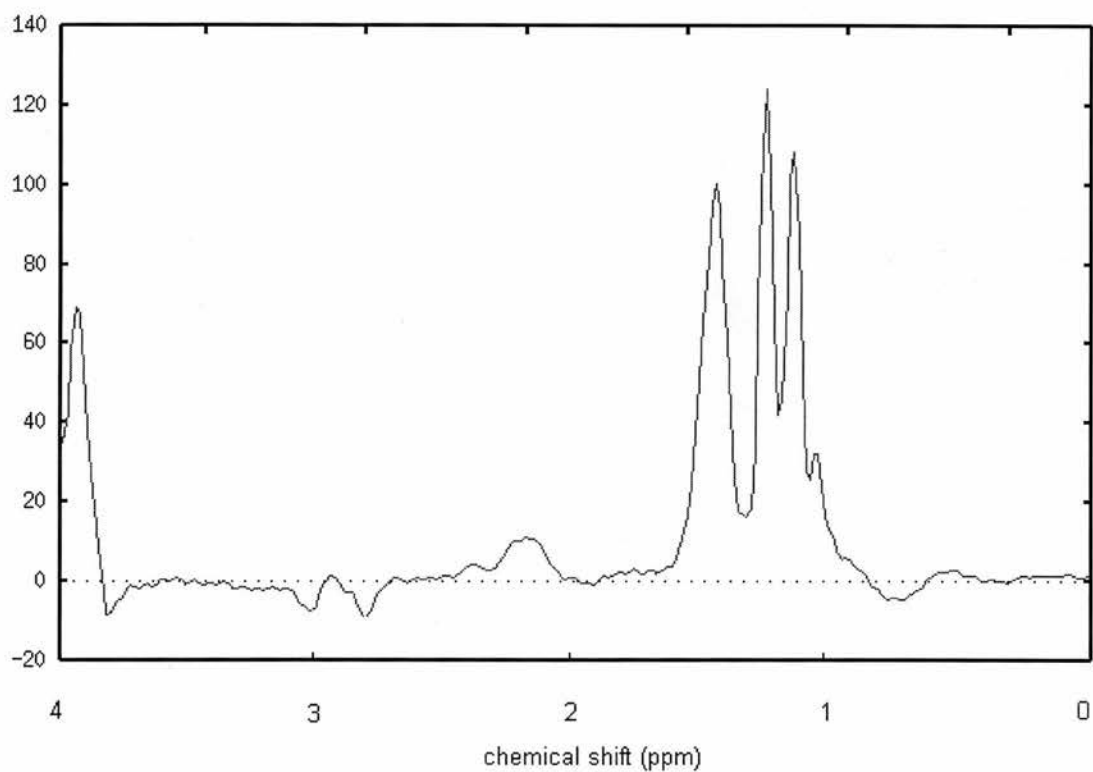
Fig. 6.29.1, $T_m=31$ msFig. 6.29.2, $T_m=33.75$ ms

Fig. 6.29.3 Difference spectrum

The difference spectrum of fig. 6.29.3 shows some residual lipids, if the individual spectra of fig.27.1 and fig.27.2 are inspected closely it can be seen that the signal intensity of the

main lipid peaks (0.9 ppm and 1.3 ppm) differ by about 15% between acquisitions. T_1 decay during the additional 2.75 ms of the mixing time is responsible for this attenuation. The rapid decay in the lipid resonance suggests a very short T_1 . In a study of the T_1 of corn oil, Mulkern et al 1997 quote typical T_1 values of around 100 ms. At these two different mixing times the difference in lipid signal intensity due to this T_1 would be 7%.

As T_1 was not calculated for this oil sample the difference spectrum was corrected by dividing the signal by the ratio of the amplitudes of the main lipid peak at 1.3 ppm from the two acquisitions. This was done for the example shown above, and the amplitudes of the minor lipid peaks at 0.9 ppm were in the same ratio as the 1.3 ppm peak which is reassuring. Having normalised the lipid peaks to the same amplitude, their subtraction leaves a well defined lactate doublet (fig. 6.30). The amplitude of this doublet will be T_1 biased as the lactate signal from the second acquisition is scaled by a factor determined by the lipid relaxation rate. Lactate most probably has a much longer relaxation time than lipids (despite the small value estimated in section 6.3.5) as a result of its mobility. It is therefore likely that T_1 relaxation of lactate in this period is negligible. Consequently this correction factor will lead to an increase in the size of the lactate doublet upon subtraction of the two signals of approximately 7%.

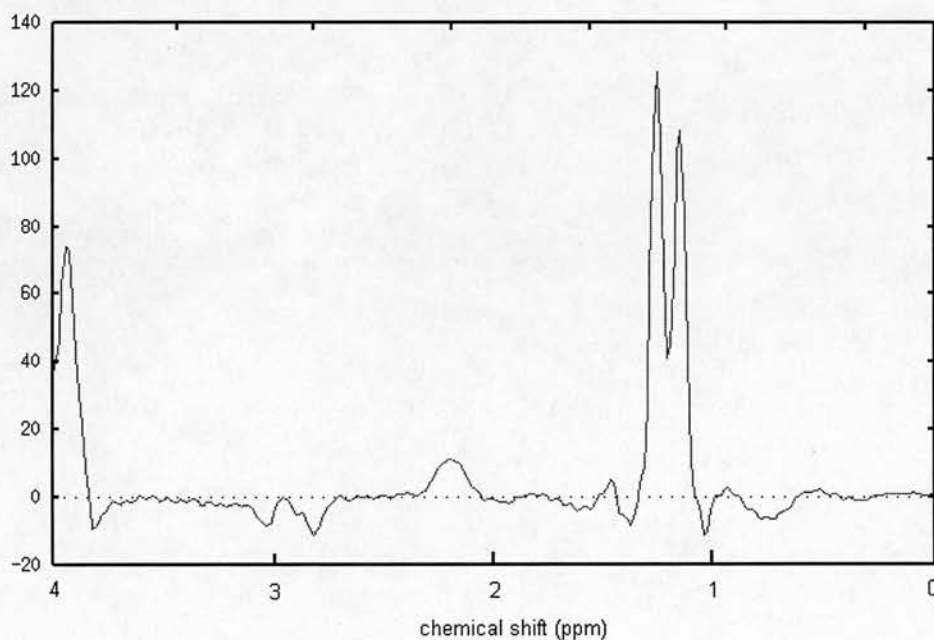


Fig. 6.30. Difference spectrum following correction for lipid T_1 decay.

6.4 Discussion - comparison of HOPE and STEAM techniques

Both techniques have proved effective in editing lactate from lipids in-vitro. The single voxel version of the HOPE sequence has been tested in-vivo and shown to work, this is the first successful implementation of this editing sequence in-vivo. In further work it would be worthwhile evaluating the performance of the STEAM technique in-vivo. A SI version of the HOPE sequence has also been written and tested in-vivo on volunteers, a logical extension of this work would be to write a variable mixing time STEAM SI and evaluate its performance alongside the HOPE SI sequence. When comparing the performance of the two techniques it should be noted that incomplete cancellation of uncoupled lipids arises in STEAM, which will require post acquisition corrections for T_1 to give complete lipid cancellation.

A further consideration are the signal:noise ratios of the two sequences. A double spin echo PRESS sequence has twice the S:N of a stimulated echo STEAM sequence. This is due to the fact that all of the transverse magnetisation is retained whereas in STEAM only half of the transverse magnetisation is rotated out of the xy plane by the 90°_x pulse, the remainder is spoiled by transverse spoiling gradients (Payne et al 1994). Changing the PRESS sequence to HOPE by replacing the two 180° r.f. pulses with 90° pulses, will subject the magnetisation to a second such rotation/spoiling and hence reduce the S:N of the sequence by a factor of 4. This should therefore make the HOPE sequence half as sensitive as the STEAM sequence (neglecting different T_2 weightings due to different T_E for the time being). The different spoiler gradient configurations used in HOPE and STEAM explain (T_2 weighting aside) why the theoretical S:N of STEAM is twice that of HOPE despite the sequences having the same r.f. energy input. These spoiler gradients were idealised in both treatments, i.e. all longitudinal magnetisations were discarded in HOPE and all transverse magnetisation present during T_m in STEAM is discarded. In reality spoiling gradients are not ideal, and there are residual unspoilt contributions plus contributions from outside the slice selected plane. To account for these terms would require the retention of hundreds of different terms throughout the product operator calculations which is impractical when calculations are done by hand. A computer algebra systems for calculating the product operator coefficients (Kanters et al 1993, Guntert et al 1993) residual from non ideal spoiling may make these calculations more feasible.

A further source of signal:noise difference is from T_2 and T_1 decay. In STEAM, T_1 decay takes place during T_m . As short T_m s were used the extent of metabolite T_1 decay is negligible (Section 6.3.7) as metabolites in-vivo have a typically long T_1 (e.g. 1500 ms Spielman et al 1992). More significant is the extent of T_2 decay found in the two sequences, the STEAM sequence has a total T_E of 145 ms whilst the HOPE sequence has $T_E = 290$ ms. Assuming a typical in-vivo metabolite T_2 of 300 ms (Wilkinson et al 1994) then the longer echo time of the HOPE sequence means that more T_2 decay takes place and the acquired signal is 62% of the size of the STEAM equivalent. This may also explain the fact that a residual lipid signal is observed in the STEAM edited spectrum of fig. 6.29.3. Non-ideal spoiling of the residual transverse magnetisation may leave a transverse lipid signal at the end of the mixing time which decays with the lipid T_2 of around 100 ms (Mulkern et al 1997). In HOPE, non ideal spoiling may leave residual lipids, but the extended T_E means that lipid decay is much more drastic with a theoretical acquired lipid signal of only 23% of that found with STEAM (calculated with $T_2 = 100$ ms). In summary the STEAM sequence will give a stronger metabolite signal (and hence a larger lactate edited signal) whilst the HOPE technique gives more complete lipid cancellation.

Chapter 7.

In-vivo SI studies

7.1 Introduction

In the previous chapters the methodology developed to produce spectroscopic images was discussed in detail. As a physics based piece of work it is natural that the emphasis of the thesis should be so directed. At the same time it is worth noting that the aim of the project was to advance the SI method to gain accurate metabolic information from the brain for clinical use. In this chapter the results of the clinical studies carried out using SI on the Magnetom SP 63 scanner are presented. This scanner is a clinical machine which is used at the Department of Clinical Neurosciences for routine neuro radiology on a day to day basis. However, a small portion of the scanner time (2-3 hours per week) was specifically devoted to the study of research patients. These patients have largely been drawn from the Lothian Stroke Register, which is co-ordinated at the Western General Hospital (WGH) in parallel with the MRC funded Clinical Research Initiative (CRI) into stroke and head injury. It is through the CRI that this work, was funded. Over the past three years 23 individual acute stroke patients have been scanned successfully making it one of the largest spectroscopic imaging studies of stroke to date. A further 5 stroke patients were scanned but the spectra that resulted were thought to be too ridden by motion artefacts to enable reliable SI construction. Furthermore another 7 patients could not tolerate the MR scanner environment, giving an overall successful scan rate of about 60%. In the latter stages of the project, patients with acute head injury were recruited from the intensive care unit of the WGH. The complications associated with the intensive care physiological monitoring of these patients has meant that the study of such patients has to date been rather limited. Indeed, this study using SI appears to be the first of its kind. In addition, occasional patients with rare metabolic brain disorders have been scanned from the Royal Hospital for Sick Children. In the latter sections of this chapter (7.3) the results of these patient studies are presented. In the following section (7.2), the accuracy and potential sources of error of the SI technique when used as a routine in vivo imaging modality are examined.

7.2 Accuracy of in-vivo SI

Unlike conventional MRIs which are in effect relaxation time weighted maps of water distribution within tissue, spectroscopic image data is used to map the concentration of proton metabolites in tissue. These metabolites are found in typical concentrations of 10 mM in healthy tissue (Soher et al 1996) whilst water is present at a concentration of around 40 M. Consequently the signal to noise ratio of a spectroscopic acquisition is much lower than in MRI, and a much longer acquisition time is required than for a conventional MRI sequence. In spin echo MRI the whole of the echo is needed for localisation but only the top of the echo is acquired. In spectroscopy as much of the echo as is possible is collected so as to maximise both the signal to noise ratio (S:N) of the spectrum and to maximise the spectral resolution. As a result of the low S:N, the potential for error in the quantitative analysis of spectral data is high. Poor shimming (Chapter 3.3), inadequate water suppression (Chapter 3.4) and artefacts introduced by the data processing techniques (Chapter 4) can further reduce the S:N from the maximum possible using the limited acquisition times of the SI sequences and the B_0 field strength of 1.5 T. In section 7.2.1 the reproducibility of quantitative in vivo SI studies is determined, enabling a prediction of the error incurred. In section 7.2.2 the errors introduced by constructing the images from an array of spectra are discussed and ways of minimising this source of inaccuracy are suggested.

7.2.1 Reproducibility

7.2.1.1 Background

If SI is to be used quantitatively to diagnose abnormalities of metabolite distribution in patients, then some indication of the precision of the technique is needed. Comparisons of repeated phantom acquisitions under identical conditions are useful in predicting the best case scenario where motion artefacts and positioning inaccuracies can be eliminated. To gain an estimate of the error of in-vivo measurements, an in-vivo repeatability study was called for. Marshall et al 1996, performed such a study on 12 volunteers using PRESS localised *single voxel* spectroscopy on the same Magnetom SP 63 scanner. They found a variation in metabolite peak areas calculated from spectra from the same volunteers, from the same part of the brain on different days of between 5% to 7.5%. In PRESS localised SI it is wise to expect a greater variability as the shimming of a SI VOI is less precise than in single voxel work, giving marginally less well defined spectra. The errors due to motion

artefact are likely to be comparable between SI and single voxel techniques. This is because both acquisitions have a similar time duration (8 minutes for 256 single voxel averages and 16×16 SI phase encodings) in which subject motion can manifest itself. In the single voxel repeatability study a voxel volume of 8 cm^3 was used whilst a voxel volume of 3.4 cm^3 is used in SI. As such, a twofold decrease in S:N is anticipated for SI, this alone will increase the random-noise based reproducibility error by a factor of two. The additional factors of poorer spectral resolution due to poorer shimming and Fourier leakage will compound the errors incurred in SI when compared to single voxel spectroscopy. In the only known SI reproducibility study published, Tedeschi et al 1996, looked at the intra-individual (visit), inter-individual (subject), inter-regional and intra-regional (between voxel) reproducibility on a set of 6 volunteers. They use ratios to quantify the metabolite differences. This introduces two variables into the coefficient of variation (CV -the fractional error) and consequently increases the error incurred as opposed to using individual metabolite measurements. A simple error analysis of a compound measurement (ratio of two separate measurements) illustrates this point. The CV of the ratios published by Tedeschi et al, are $\text{NAA/Cr} < 15\%$, $\text{NAA/Cho} < 20\%$ and $\text{Cho/Cr} < 20\%$. Decomposing these in to the individual metabolite CV's gives $\text{NAA} < 11\%$, $\text{Cho} < 17\%$ and $\text{Cr} < 10\%$ i.e. a smaller error is associated with the measurement of a single metabolite than with metabolite ratios. Having said this, much of the systematic spatial dependent corrections (e.g. B_1 inhomogeneity) are removed by the ratio process. What is particularly interesting from Tedeschi's findings is the intra-regional dependence of the CV on the anatomical location of the ROI.

7.2.1.2 Methods

Using the standard PRESS localised SI sequence (16×16 phase encodings, $T_R = 1600 \text{ ms}$, $T_E = 135 \text{ ms}$, $\text{FOV} = 240 \text{ mm}$ - see Chapter 3) a volunteer was studied on three occasions on different days within a ten day period. A transverse spectroscopic imaging plane was selected at the level of the body of the lateral ventricles and within this plane a $75 \text{ mm} \times 75 \text{ mm}$, 15 mm VOI was placed, centred at the origin of the coronal and sagittal axes. Anatomical landmarks evident on the T_2 weighted images and a fiducial marking on the forehead were used to relocate the VOI on subsequent acquisitions. The acquisition, post processing and quantification protocols followed those described in chapters 3, 4 and 5. From this data, metabolite images of choline, creatine and NAA were constructed from each

volunteer scanning session. This data is stored as a 16×16 array of voxels. The statistical analysis of the intra-subject variability then proceeded as follows.

7.2.1.3 Analysis (i).

The mean intensity of the signal arising in a given voxel, r_{ij} ($i = 1, 2, \dots, I$ is row index and $j = 1, 2, \dots, J$ is column index) was calculated from the metabolite map arrays from acquisitions on the three separate days ($N=3$). The residual from subtraction of the mean ($N=3$) image array, \bar{r}_{ij} from the individual arrays r_{ijn} was then calculated for the three ($n=1, \dots, N, N=3$) data sets from different days. The standard deviation of all 75 voxels ($75 = N \times I \times J$) analysed was then calculated for the three separate metabolites:

$$\sigma = \sqrt{\frac{\sum_{i,j=1}^{I,J} \sum_{n=1}^N (r_{ijn} - \bar{r}_{ij})^2}{(N \times I \times J) - 1}} \quad (7.1)$$

As an index of measuring the repeatability of the technique, this standard deviation works on the assumption that the *error in the measurement is not a function of the voxel position and voxel signal intensity* (this assumption is contrary to the findings of Tedeschi et al 1996, who used metabolite ratios). As such the standard deviation calculated is one which applies to all voxels. An estimate of the fractional error of the technique can then be obtained by taking the ratio of the s.d. with the mean voxel intensity from all 75 voxels studied. These figures are tabulated below in table 7.1.

	Choline	Creatine	NAA
Fractional error $\frac{\sigma}{r_{ijN}}$	13%	27%	11%

Table 7.1. Fractional error of the technique for measuring metabolite intensities using statistical analysis (i).

7.2.1.4 Analysis (ii).

An alternative analysis works on the assumption that the standard deviation differs for each voxel i.e. *the standard deviation is related to the voxel intensity*, whilst the *coefficient of variation* is in turn *not related to the voxel intensity*. Using this approach the standard deviation for each voxel is calculated over the run of three sets of data:

$$\sigma_{ij} = \sqrt{\frac{\sum_{n=1}^N (r_{ijn} - \bar{r}_{ij})^2}{N-1}} \quad (7.2)$$

From this standard deviation, a voxel dependent coefficient of variation (fractional error) can be calculated by taking the ratio of the s.d. with the voxel mean intensity over the three days:

$$cv_{ij} = \frac{\sigma_{ij}}{x_{ij}} \quad (7.3)$$

A mean CV (\overline{cv}) can then be calculated over all i and j to give a prediction of the fractional error in measurement of each metabolite.

	Choline	Creatine	NAA
Fractional error \overline{cv}	15%	28%	11%

Table 7.2 Fractional error in reproducibility of measurement of metabolite peak areas using analysis (ii).

7.2.1.5 Discussion

Although the statistical analyses are only based on data from one volunteer they are still viable in that they utilise all the voxels in the array to maximise the numbers of degrees of freedom. In the single voxel reproducibility study of Marshall et al 1996, the only way to get a viable number of degrees of freedom on which to base the statistical analysis was to study volunteers six times on each of four days.

The fractional errors associated with either analysis are very similar, which one gives a better prediction of the error in measurement is very much down to which model hypotheses the reader chooses to believe. Both analyses have their flaws, in (i) there is an inaccuracy introduced by using the mean signal intensity from all voxels and all acquisitions when calculating the CV. This analysis works on the assumption that noise present in a signal will be in direct proportion to the signal strength, which is not the case for random (Gaussian) noise. This effect could be investigated further both in-vitro and in-vivo using SI data from different positions within the magnet. With single slice SI, this would require multiple slice studies on the same volunteer and as such serial studies would involve many separate scanning sessions. Multi-slice SI is better suited to performing such a repeatability study.

On the other hand when using analysis (ii), there is a large spread in the range of the individual CVs that are used in calculating the mean CV. If there was an option of scanning the same patient on at least 5 or 6 separate occasions then the analysis of (ii) would become more accurate as the standard deviation would become more stable with increasing N , ($N=6$ is a suitable minimum number). Ideally in a more complete study this analysis would be adopted with the addition of inter-individual and intra-regional comparisons. Such a study would require six volunteers and SI acquisitions in multiple transverse planes and as such is only practicable with multi-slice SI (Chapter 2.8.4.2) Without doing this a more accurate estimate can be gained by using method (i), with its inherent assumption that the CV in the voxel intensity is not a function of the signal intensity itself.

Finally, comparing these reproducibility figures with those published for the same metabolites in-vivo using single voxel spectroscopy (Marshall et al 1996), the CV's of NAA and choline measurement are in fact twice as large with SI, as predicted in the introduction. The CV of creatine of 27% is much larger than that of 7.4 % reported for the single voxel work. When calculating the peak areas using a fitting program as opposed to a manual integration, Marshall et al 1996, found a much worse reproducibility in the creatine peak area of 21%. As the signals from choline and creatine overlap there is bound to be some error introduced by the peak integration. Whether this is due to operator misjudgement of peak frequency limits of integration in the manual case or unreliability in fitting of overlapping peaks in the automated approach, it is difficult to say. Comparisons of the two methods of peak integration have been done (Kreis et al 1993), but the problem is that when constructing the in-vivo metabolite images, quite often a combination of the two methods is

used. The choice of method used depends upon the clarity of the spectrum found in the specific voxel. If the size of choline and creatine peaks were the same then a similar CV in their integration would be expected provided that the software (or user) is not biased towards either peak. In vivo the creatine peak is typically two thirds of the height of the choline peak and. It is therefore probable that the smaller subsidiary peak of the overlapping ensemble is more prone to measurement error. The spatial Fourier transform used in SI adds to the problem of accurately integrating choline and creatine. Fourier leakage of signals between voxels introduced by the spatial Fourier transform, means that the signal in each voxel is not entirely independent of the signals in surrounding voxels (section 4.8.5). With a spatial variation in B_0 homogeneity across a SI VOI, it is plausible that the signal from choline in a given voxel contains contributions from the creatine signals from adjacent voxels (and vice versa) which are resonating at slightly different frequencies due to B_0 inhomogeneity. A similar explanation accounts for the poorer resolution of the lactate doublet in SI when compared with single voxel spectra.

7.2.2 Errors introduced by image construction

With a VOI containing typically 25-36 separate voxels, the spatial resolution of a SI is coarse. In chapter 3, the artefacts introduced into the spectra from non-optimum acquisition conditions (poor shimming, patient movement and incomplete water suppression) were mentioned as a source of error. In chapter 4, the errors due to post acquisition processing, chiefly by bad phasing and FFT artefacts were described and methods of minimising these sources were proposed. These errors are beyond the control of the user, however some user dependent bias is introduced when the images are constructed from spectra using the program `display_SI_phase`. Without a fully robust automatic spectral fitting routine for in-vivo data, some user involvement in peak quantification is inevitable. Selection of area integration limits for a given peak may vary depending upon the uniformity of the baseline and line width of the peak in question. To rule out inter user variability in the present study, all spectroscopic images were constructed by the author.

Having constructed the coarse metabolite image from say 25 voxels, a bilinear interpolation can be applied to give a smoother image (Chapter 4.12). This smoothed image can then be used to make quantitative measurements using the interactive ROI tool. Although more visually appealing, the smoothed images need to be treated with a certain amount of caution as the smoothing procedure may introduce a false representation of the actual spatial

distribution of metabolites. Strictly speaking the most reliable measurements are those made from individual voxels, these are still subject to the spatial inaccuracy introduced by Fourier leakage due to the shape of the point spread function (4.8.3).

To highlight this source of error it is instructive to consider the interpolated version of an image which has a uniform intensity with the exception of an abnormally high/low intensity solitary voxel. Such an image could foreseeably arise in vivo with a single infarct small enough to be contained within one voxel, surrounded by otherwise healthy tissue. It is reasonable to guess that in such an image, an abnormally high level of lactate and a corresponding low level of NAA might be expected (section 7.3.2). Following normalisation (Chapter 5) such a lactate image (Fig. 7.1) would upon application of bilinear interpolation appear smoothed (Fig. 7.2). From fig. 7.2, it is clear that regions inside the voxel but near to its edge have a higher image intensity than the raw image, whilst the edges of adjacent voxels have lower intensities than are found in the raw image. In reality this is probably a more realistic representation of metabolite distribution than the sharp edged picture gained from the raw image. The fact remains however, that any abrupt spatial changes in metabolite distribution will be smoothed out by the interpolation. Such abrupt changes in metabolite concentration do arise, at the edge of the ventricles (which in healthy brain contain negligible traces of choline, creatine and NAA) and at the edge of the VOI. The smoothing process can therefore infer concentrations of metabolites that are not physically realistic.

Methods exist that allow correction for these effects, a reflective kernel filter (Wand and Jones 1995, Gonzalez et al 1987) could be applied to the data at the edge of the VOI to prevent the smoothed image leaking outside the VOI. Similarly a zero intensity mask of the same shape as the ventricles could be used to ensure zero signal intensity inside the ventricles. These techniques are more suitable when processing a larger number of voxels, with the coarse raw image matrices used in SI their use will be limited. The only definitive way of circumventing the image smoothing problem is to acquire a larger image matrix which really requires a fast SI sequence (see sections 2.4.8.1 and 2.8.4.2).

Finally it is worth emphasising the fact that the SI transverse plane is 15 mm thick and so encompasses three of the contiguous T_2 weighted MR images. A T_2 visible feature such as a lesion may be evident in all three of these slices but in different proportions. As such the contribution to the voxel from such a feature may change with transverse position. This concept is called the “partial volume effect” (Blamire et al 1994) and is best illustrated diagrammatically in fig. 7.3. Methods have been proposed to correct for the contribution of

the partial volume effect to spectra (Metzger et al 1997). These are based on a spectral fitting of the signal from each tissue present in the sample and are consequently quite involved. To avoid an anatomical biasing of the background image towards the central slice, a mean representation of the three contiguous MRIs should really be used as a background image. An example of such a mean image is shown in fig. 7.5 having been formed from the three images in fig. 7.4. It is obvious that this image is much more blurred than any of the component images, it does however give a fairer representation of the axial extent of any anatomical features in the z direction.

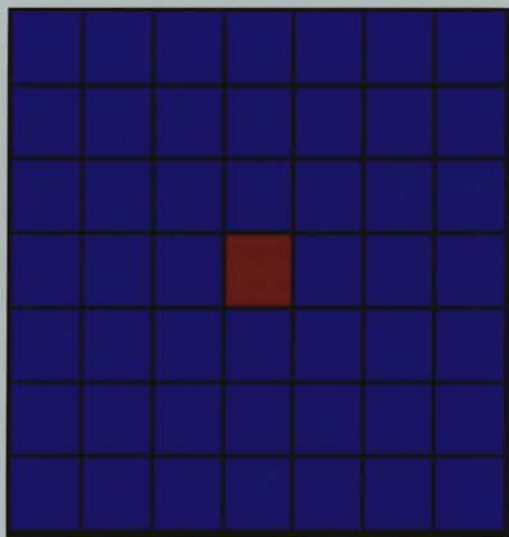


Fig. 7.1 Image with one abnormally high intensity voxel

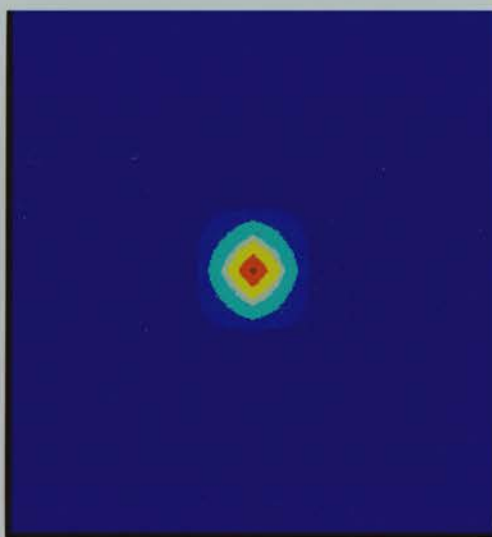


Fig. 7.2 The same image with smoothing

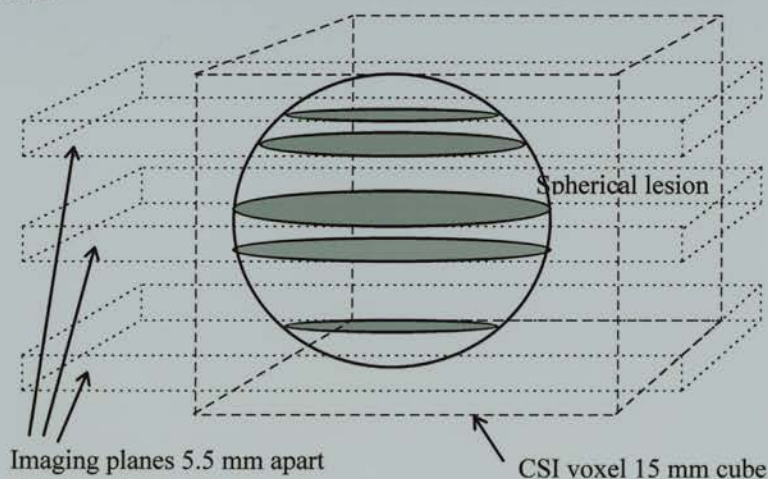


Fig. 7.3 This diagram illustrates how the proportion of a hypothetical spherical lesion visible in the contiguous T_2 images (shaded region) varies with transverse position. This lesion fills the bulk of the voxel in the central slice, as such the user may think that the majority of the volume (and hence signal in the spectrum) of the voxel represents the lesion tissue. Observing the visibility of the lesion in the adjacent T_2 images it can be seen that this is clearly not the case.

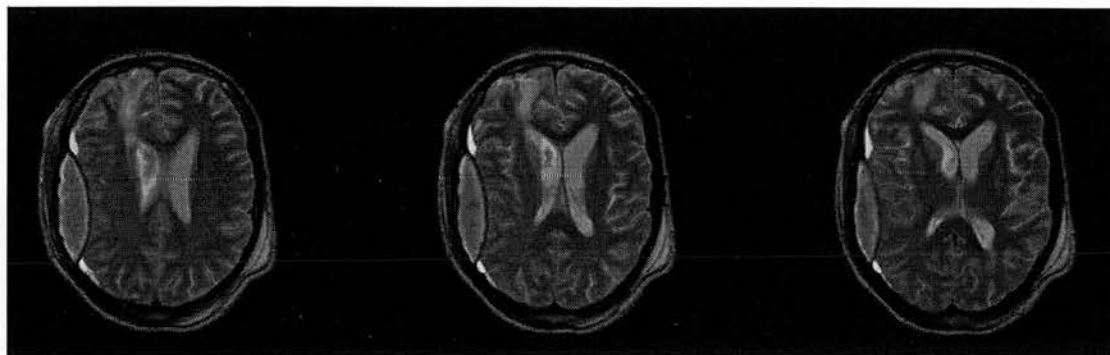


Fig. 7.4 The three contiguous images contained within the SI plane of a head injury patient

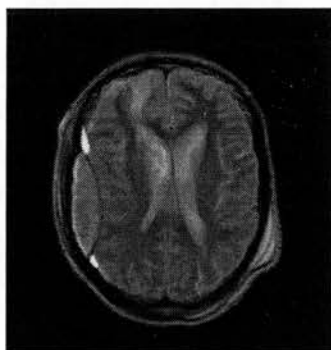


Fig. 7.5 the average image of the three contiguous MRIs in fig. 7.4. Note how the image is more blurred, particularly around the anatomical features of the ventricles and the lesion present in the anterior right hemisphere.

7.3 Patient studies

Having alerted the reader to some of the possible pitfalls and limitations of quantitative metabolite measurements made using SI, the results of the in-vivo studies conducted during the last three years are now presented. As the work described in earlier chapters dealing with refinements of data processing techniques, was progressing simultaneously, all the work presented in this chapter was quantitatively analysed in the final stages of the project. It is worth stressing that the acquisition protocols did not change throughout the ongoing stroke patient study and the following parameters were kept constant: T_E 135 ms, T_R 1600 ms.

Before presenting the results of patient studies, an indication of the levels of the metabolites choline, creatine and NAA found in healthy subjects is given in the results from a volunteer study (section 7.3.1). In section 7.3.2 the results from all of the stroke patients scanned with SI over the three years are presented. A smaller sub group of these patients presenting with visibly extensive infarcts was used to investigate the existence of an ischaemic “penumbra” region from SI data alone (section 7.3.3). In the final section (7.3.4) the findings from a study of acute head injury patients are presented with the aim of identifying any brain injury (e.g. diffuse axonal injury) that is not evident on conventional T_2 weighted MRI.

7.3.1 Healthy volunteer study

If quantitative comparisons in spectroscopic studies of patients with brain disorders are to be made then an indication of the levels of the metabolites found in healthy brain using the SI technique need to be made. Numerous single voxel volunteer studies report quantification of the levels of the metabolites choline, creatine and NAA (Marshall et al 1996, Kreis et al 1993). Many of these use ratios of NAA:choline and NAA: creatine etc. to avoid the complications of absolute quantification (relaxation time correction and r.f. coil calibration) (Soher et al 1996, Kreis et al 1993, Christiansen et al 1993, Danielsen et al 1995). In these studies the use of ratios has been avoided as significant changes in all three metabolite levels have been observed in ischaemia (section 7.3.2). Absolute quantification of SI spectra is envisaged in future work. As all work was carried out on the same scanner and the system dependent sources of discrepancy have been removed (coil loading corrections, normalisation for B_1 profile and transverse slice position -see chapter 5) then it is reasonable to quantify metabolite images in arbitrary system dependent units. Errors introduced by regional T_1 and T_2 were minimised by using as short a T_E and a relatively long T_R . To compare diseased brain metabolite image intensities with the corresponding regions in healthy brain it was necessary to conduct a study on a series of healthy volunteers:

7.3.1.1 Methods

Six healthy male volunteers in the age range 21-37 were studied using standard PRESS localised SI as described in the early chapters of the thesis. A $75 \times 75 \times 15 \text{ mm}^3$ VOI was placed at the isocentre of the magnet in the transverse plane of the brain corresponding to the level of the bodies of the lateral ventricles and adjacent parenchyma. Interactive ROI calculations (Chapter 4.12) were then done using the choline, creatine and NAA images from all six subjects taking care to position the ROI at the same site in the right hemisphere (fig. 7.6).

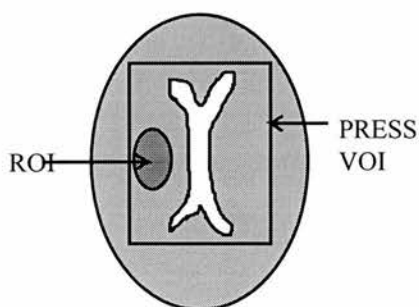


Fig. 7.6 Positioning of the interactive ROI in the right cerebral hemisphere at the level of the body of the lateral ventricles.

7.3.1.2 Results

Metabolite	NAA	Choline	Creatine
mean intensity \pm s.d	1169 \pm 140	747 \pm 36	579 \pm 70
(system dependent units)			

Table 7.3 Metabolite distributions from a group ($n=6$) of healthy volunteers.

7.3.1.3 Discussion

The small variation in the means of these metabolite measurements is encouraging as they give quite definite control levels against which patient data can be compared. The reason for the small variation is probably due to the sex and age matching of the subjects and the careful systematic placement of the ROI between subjects. The fact that all subjects were of the same sex could bias the validity of the group as a control, as metabolite levels have been reported as being sex dependent (Wilkinson et al 1997). Ideally a mixed sex group of volunteers in the age range 50-80 would be used as a control for the stroke study, but examining such a group within the scanner time constraints was not practicable. The volunteer group is however more valid as a control for the head injury study which largely consisted of young males with closed head injuries.

7.3.2 Stroke patient study

7.3.2.1 Review of metabolite changes in stroke

Before going on to list the brain metabolites which are affected in stroke it is worth remembering that the raised water concentration of oedema will have a diluting effect upon the concentration of the metabolites within tissue. This is before considering any changes that arise from the accompanying chemical changes in ischaemia. Bruhn et al 1989, predict a threefold dilution of concentration of lactate and NAA with oedema. Saunders et al 1995, quote a maximum increase in water concentration of 30% with oedema, whilst observing larger changes in metabolite concentration.

Lipids

Signals with a resonant frequency around that of lactate may be observed in human/animal brain spectra. Sometimes present in an ill defined broad resonance these signals were first thought to originate from fatty deposits bound within membranes such as the scalp and the

marrow of the skull. The immobility of membrane bound lipid molecules leads to a very short T_1 , which significantly reduces the contribution of bound lipids to the lipid signal. Therefore the observation of lipid resonances in ischaemia suggests an increase in molecular mobility, attributed to membrane degradation by Williams 1989. Recent work by Behar et al 1993 and 1994, suggests that the resonances found in this chemical shift range are not only due to lipids but macro-molecular proteins (found in cells such as macrophages and leukocytes) as well. Leukocytes infiltrate damaged areas of the brain as part of the inflammatory response during ischaemia. A by product of the action of these cells in the anaerobic conditions of ischaemia is lactate (Graham et al 1995, Petroff et al 1992). Graham et al, suggest that the elevation of lactate in acute ischaemia is due to the presence of leukocytes. As such an elevated lactate signal could be expected alongside a signal from mobile lipids. A further source of complication arises from the findings of Saranathan et al 1997, who observed a binding interaction between lipid and lactate molecules. Mobile lipids have a much shorter T_2^* than free lactate. As such any binding interaction will significantly reduce the T_2^* of the lactate signal and hence reduce its visibility in spin/stimulated echo spectroscopy. A similar binding effect was noticed when lactate was studied in the presence of protein macro-molecules. Chatham and Forder 1995 noticed a 60% reduction in the visibility of the peak when albumin was added to the lactate solution. Howe et al 1995 report an elevation in the concentration of lipid/macrophage peaks 16 hours after the onset of stroke. Using inversion recovery suppression techniques after Graham et al 1994, they went on to remove their contribution to the spectrum in an attempt to elucidate lactate peaks. Methods of discerning lipids from lactate were covered in much greater depth in chapter 6.

Lactate (1.3-1.5)ppm;

Lactate is present in very low concentrations in healthy brain tissue (less than 0.5mM Duyn et al 1992) and is not normally detectable. The lactate resonance shows J modulation from spin-spin coupling of the methyl and methine protons. Lactate editing techniques which exploit this property were discussed in chapter 6. As a by-product of anaerobic glycolysis that is induced by impaired cerebral blood perfusion (hypo-perfusion), lactate elevation might be expected in regions where there is an imbalance between lactate production and blood flow clearance. Felber et al 1992, found the highest levels of lactate occurred in infarcts corresponding to a maximum state of hypo-perfusion i.e. occlusion of the carotid artery. Graham et al 1994 in a tandem 1D SI/SPECT study of 32 acute stroke patients found

elevated lactate correlated significantly with reduced perfusion. Soher et al 1995, in a multi slice 3D SI study with perfusion MRI found that lactate levels and perfusion deficits were significantly spatially correlated and both extended beyond the T_2^* visible extent of infarction. This supports the notion of an "ischaemic penumbra" region of semi-viable tissue proposed in the early eighties and described by Prichard 1993.

The elevation of lactate in the early hours of stroke onset (Houkin et al 1993, Graham et al 1993, Gideon et al 1992 (ii) and 1994, Prichard 1993) suggests anaerobic glycolysis in tissue that is still viable. In-vitro reperfusion experiments performed on primates (Monsein et al 1993) show a steady rise in lactate following occlusion of the middle cerebral artery. The fact that lactate levels continued to rise might suggest surviving brain cells still respiring under anaerobic conditions. Upon reperfusion lactate levels fell, as they did with Gideon et al 1992, implying that the imbalance is cleared by restoration of blood flow. Continued exposure of such tissue to a state of hypo-perfusion would presumably lead to cell death and as such a tailing off of lactate concentration in acute infarcts might be expected. In a long term serial spectroscopic study of six patients (Prichard 1993 up to 200 days post ictus) lactate levels were reported to tail off very slowly, persisting as a detectable signal up to 100 days after onset. Long term studies by Duyn et al 1992, Houkin et al 1993 and Sappey-Mariniere et al 1992, show elevated lactate levels months after the onset, which may be due to the anaerobic metabolism of macrophages that invade the infarcted region to destroy dead tissue, (Berkelbach van der Sprenkel et al 1988, Graham et al 1995). In a spectroscopy study of a patient who subsequently underwent post-mortem, Petroff et al 1992 report a spatial correlation between lactate concentration and the density of macrophage cells. Rothman et al 1991, tested whether persistent lactate was due to ongoing glycolysis or an inability to clear the lactate produced earlier by tissue that has since died. By infusing the blood supply of a 1 month post-ictus stroke patient with ^{13}C labelled glucose, they found that virtually all the lactate was ^{13}C radio-active. This favours the former explanation for ongoing lactate detectability as glycolysis continues under anaerobic conditions. Further evidence supporting the existence of an ischaemic penumbra - a region of semi-viable tissue surrounding the infarcted core, comes from a higher concentration of lactate in the region separating visible infarcts, Berkelbach van der Sprenkel et al 1988. Kugel et al 1994, found elevated levels in the hemisphere contra-lateral to the infarct, the explanation of which is not obvious.

Summarising the literature to date it seems as though lactate detection in both the acute and late stages of ischaemia is to be expected. Examination of the spectra published by many of

these studies reveal a broad signal in the 1.3 ppm region, quite often without a resolved doublet. As published spectra are likely to be the best examples found in the study then there is some suspicion as to whether these signals originated from lactate or from lipids. As both of these signals could be found in ischaemic brain, the only truly reliable data are those collected with lactate editing sequences or those exhibiting a well defined methyl doublet.

N Acetyl-Aspartate (NAA) (2ppm);

Found in concentrations of 5-10mM in normal adult brain tissue and evident as a well defined spectral resonance, NAA is an amino acid found only in neurones, being absent in oligodendrocytes and astrocytes in adult tissue extracts, Williams 1995. In the infant brain, NAA concentration increases with age and is found in neurones and oligodendrocytes, Bachelard et al 1993. In studies which related clinical outcome to NAA, Saunders et al 1995 (26 patients scanned within the first 72 hours) found a significant correlation between good outcome and relatively high NAA in the infarct whilst Federico et al 1996 (14 patients scanned within 1 week) report a correlation between low NAA and the severity of subsequent neurological deficit. In NMR spectroscopy studies of other degenerative neurological disorders, (e.g. Alzheimer's disease, brain tumours, MS, AIDS and epilepsy), reductions in NAA concentration were found, (Christiansen et al 1995, Luyten et al 1990, Meyerhoff et al 1994, Hugg et al 1993). The findings from the above reports confirm the role of the NAA resonance as a marker of intact neurones.

With specific reference to ischaemia, a decreased NAA concentration within infarcted regions has been observed by; Duyn et al 1992, Petroff et al 1992, Christiansen et al 1993, Gideon et al 1992 and 1994. The dramatic decrease in NAA when compared to the other metabolites Cr and Cho, (as observed by Sappey-Marinier et al 1992 and Duyn et al 1992), suggests a higher proportional loss of neurones than of glial cells. Having said this, the function of NAA within neurones is still unknown, however it is known that the amino acid is produced by the mitochondria of neurones, Baker et al 1991. Bruhn et al 1989, suggest that NAA is broken down by enzymes under ischaemic conditions but do not define the physiological conditions needed for such a mechanism to take place. In a spectroscopy study of a patient who subsequently died and underwent post-mortem, Petroff et al 1992, found a correlation between NAA reduction and high concentration of macrophages, which suggests that macrophages are responsible for the decomposition of neurones. The higher concentration of NAA found at the edges as opposed to in the core of the infarct (Gideon et al 1992), supports the existence of a penumbra region of less impaired neuronal function

and probably better blood perfusion. This is supported by Kugel et al 1995, in a study of six stroke patients with single voxel spectroscopy and PET, which shows a correlation between decreased perfusion and NAA reduction. Further evidence comes from Fazekas et al 1995, with a correlation between reduced NAA, elevated lactate and impaired perfusion as measured with SPECT. In a follow up study of the NAA resonance, Graham et al 1993 show a delayed NAA loss at periods up to 2 weeks post-ictus implying a late death of viable cells after infarction.

Creatine (Cr) (3ppm)

The creatine resonance encompasses two species; creatine and phospho-creatine, which together are found in fairly constant concentrations of around 10mM in human brain. Creatine is found both in neurones and glial cells and has been proposed as a mechanism for phosphate transfer in the ATP cycle, acting as an energy buffer. The majority of studies to date have found very little alteration in Cr concentration and as such it has been used in determining the relative amounts of other metabolites. Duyn et al 1992 and Howe et al 1995 report significant decreases in Cr. The fact that the decline in NAA concentration is much more marked confirms the experimental model evidence that neurones are more susceptible to ischaemic injury than glial cells.

Choline (Cho) (3.2ppm)

The choline resonance arises from choline containing intermediate compounds formed in phospholipid metabolism. Therefore raised levels of choline might be interpreted as an indication of increased phospholipid turnover, Luyten et al 1990. One possible source of release of phospholipids is the breakdown of cell membranes in decaying tissue. As such elevated choline levels might be expected in ischaemia. Sappey-Marini et al 1992 do report increased levels, especially within areas of white matter hyper-intensity. Conversely Duyn et al 1992 and Felber et al 1992, found decreased levels within infarcted tissue. These results seem to suggest that choline concentration is not as reliable an indicator of ischaemia as lactate/NAA concentrations.

Short echo time metabolites ; glutamate, glutamine, GABA.(2.1-2.5ppm)

An additional set of resonances is evident all at low levels on the ^1H spectrum of brain tissue when short T_E (<50 ms) acquisitions are made. These species, all amino acids, have strongly coupled spins and as such are J modulated making their detection at longer echo times more difficult. Blamire et al 1994, made spin echo acquisitions at $T_E=30$ ms & 270 ms and subtracted the first set of spectra from the second so as to remove the contribution from these spin-coupled resonances from the NAA peak. Similarly, Frahm et al 1989 attribute the apparent overestimate of the concentration of NAA, (when compared to in vitro NMR), to these resonances. Glutamate is an excitatory amino acid and can be toxic in physiological concentrations. It is thought to be released in a chain reaction of cell death, and as such might be expected at elevated levels in and around infarcts. In animal studies (Choi 1988) the administration of glutamate blockers has shown a marked decrease in infarct size. Studies of alterations in concentration of these metabolites in healthy volunteers (Seeger et al 1997) and hepatic encephalopathy (Kreis et al 1994) have been made. Little information as to their involvement in stroke seems to have been published.

7.3.2.2 Stroke study

Patients admitted to hospital within three days off an acute stroke were the basis of this study. On the basis of the history and clinical examination (conducted by the stroke physicians), the patients were classified according to the possible size and position of the infarct. Patients with symptoms indicative of ischaemia in a large part of one carotid territory (a large total anterior circulation infarct -TACI) or (large partial anterior circulation infarct -PACI) were chosen for MRI/SI examination. In all 23 separate patients were studied within the acute phase of stroke (<72 hours after stroke onset). From this group of 23, a further 5 were scanned on a second occasion and, 4 more scanned on 3 occasions and within 12 days of onset. The size of the infarct and its position within the brain were classified according to the T_2 weighted MRI visibility of the lesion using the template shown in fig. 7.7. This template had been devised in a previous study which used CT in over 100 stroke patients. It is based on the observation that most TACI and PACI infarcts fell into one of these patterns. The method was tested for observer variability and thoroughly validated (Wardlaw and Sellar 1994). The patients were followed up clinically after the stroke and their clinical outcomes registered on the Rankin scale (which tests the patients ability to do routine activities of daily living) from 1-6 (see table 7.4):

Independent		Dependent/Dead	
0	normal	3	need help with daily activities
1	mild symptoms	4	disabled
2	not normal but manage without help	5	vegetative
		6	dead

Table 7.4 Numerical Rankin indices of clinical outcome after stroke

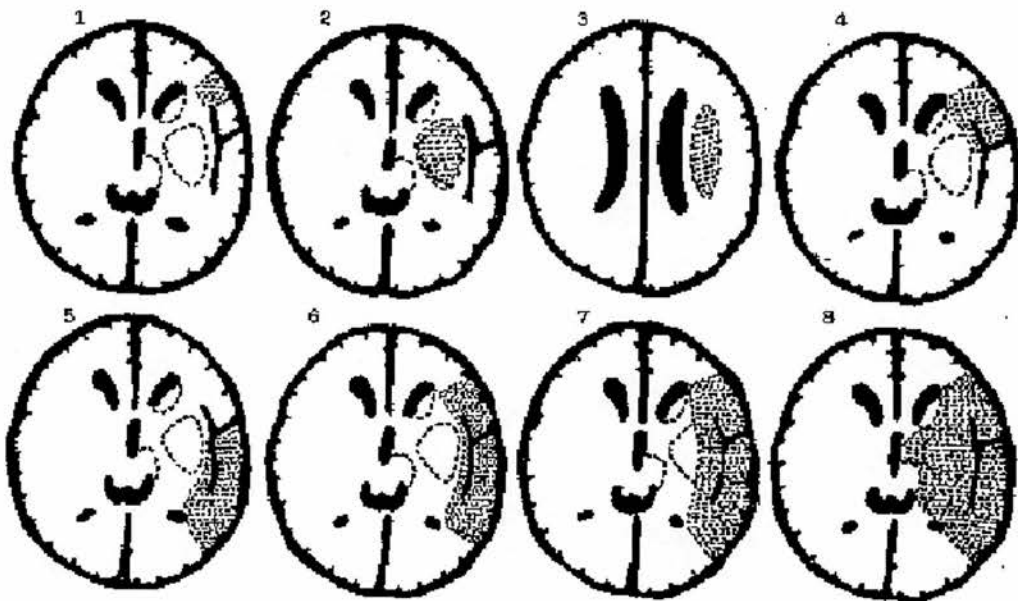


Fig. 7.7 Template for indexing infarct size in accordance with the MRI visibility of the lesion.

7.3.2.3 Methods

Localiser images, T_2 weighted and proton density images and a 16×16 SI acquisition (see chapter 3) were collected whilst the patient was positioned inside the scanner. SI processing then proceeded as described in chapters 4 and 5. Having constructed the normalised metabolite images, ROI calculations proceeded by drawing an interactive ROI around the edge of the T_2 visible infarct as defined by the consultant neuro-radiologist (Dr Joanna Wardlaw). When no such lesion was visible, an infarcted ROI was positioned on the basis of clinical symptoms with the advice of the neuro-radiologist. As the volunteer SI data set is neither age or sex matched its use as a control is limited. Instead measurements were made from a mirror image position, with the same sized ROI, in the contra-lateral hemisphere

where the brain appeared normal. Providing the contra-lateral hemisphere contains no old or recent ischaemic lesions then the tissue should serve as an ideal age and sex matched control. As the metabolites lactate/lipids were only found in 50% of the patients (usually found in a small number of voxels (1 or 2)) it is impossible to construct accurate lactate images from the group data. Instead lactate visibility in the infarcted region was indexed on a yes/no basis, with visible lipids (thought not to originate from Fourier leakage from the scalp) included.

7.3.2.4 Results

(i) *Metabolite distribution in the infarcted and contra-lateral ROIs*

	NAA	Cho	Cr
Infarct	442±295	531±196	462±192
Contra-lateral	1026±339	697±218	616±173
ratio (infarct:contra)	0.42	0.78	0.74
paired t-test significance	p<0.01	p<0.01	p<0.01

Table 7.5 Comparisons of metabolite levels in the visibly infarcted and contra-lateral regions of interest.

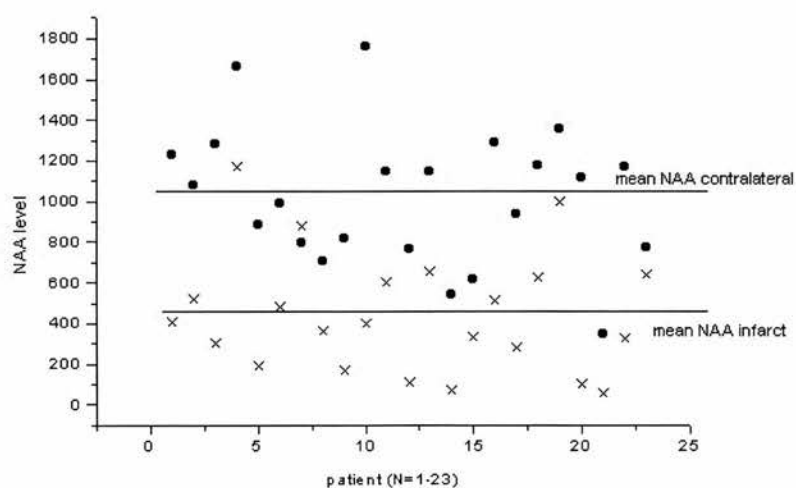


Fig.7.8 The scatter of NAA levels in the 23 patients studied in both the contra-lateral ROI (●) and the infarct (×).

(ii) Are reduced NAA levels associated with the visibility of lactate/lipids

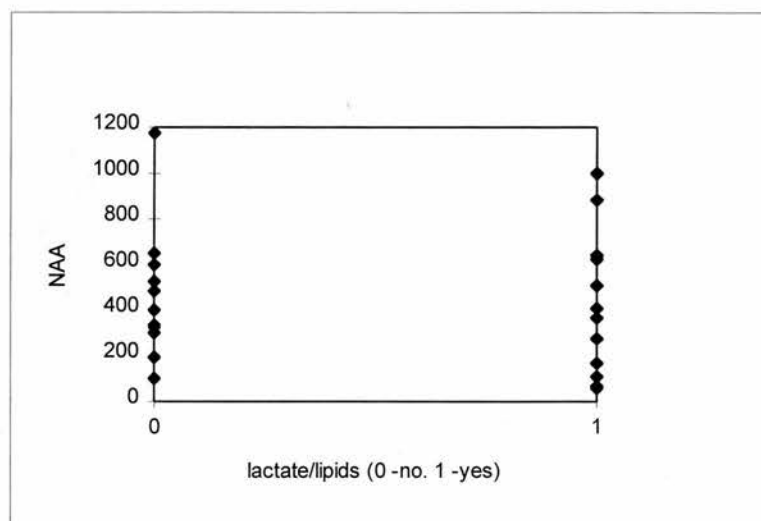


Fig. 7.9 Scatter plot indicating the NAA levels in infarcts associated with the presence of lactate/lipids (1) and those showing no lactate/lipids (0). From the plot there is no obvious difference in the distributions between the two groups. The mean NAA values for the lactate and no-lactate subgroups are tabulated in Table 7.6. The subgroups were tested for significant differences in NAA levels using a non-paired equal variance *t*-test for groups of unequal sample size. No significant difference in NAA levels between the two groups was noted using this test. When the ratio of NAA in infarcted :contra-lateral tissue was tested again no significant difference between the two subgroups was found.

	lactate/lipids evident (n=12)	no lactate/lipids evident (n=11)
subgroup mean NAA level	424±314	461±288
mean NAA ratio infarct:contra	0.45	0.41

Table 7.6 The mean NAA values for the lactate and no-lactate subgroups.

(iii) Are NAA levels correlated to subsequent clinical outcome

clinical outcome (Rankin scale)	independent (n=10)	dead/dependent (n=13)
subgroup mean NAA level	539± 323	400±282
mean NAA ratio infarct:contra	0.44	0.41

Table 7.7 The mean NAA values for the dependent and independent subgroups.

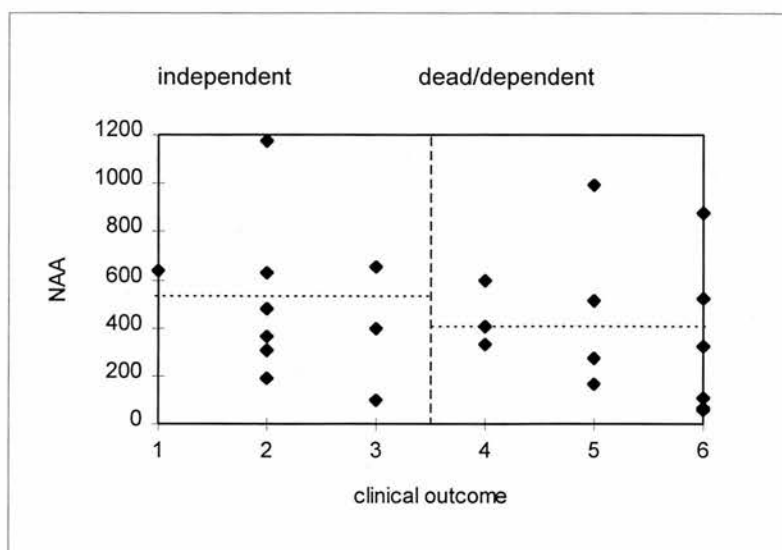


Fig. 7.10 Scatter plot indicating the NAA levels in infarcts versus the subsequent clinical outcome determined from the Rankin scale. The patients were then divided into a dead/dependent subgroup and an independent subgroup according to the Rankin criteria of table 7.4. The subgroups were tested for significant differences in NAA levels using a non-paired equal variance t -test for groups of unequal sample size. No significant difference in NAA levels between the two groups was noted using this test. The mean NAA levels for the two categories are denoted by the fine dotted lines. The ratio of NAA in infarct: contra-lateral tissue was tested using the same method and no significant difference in the ratio was found between the two groups.

(iv) *Is infarct size correlated to NAA depression*

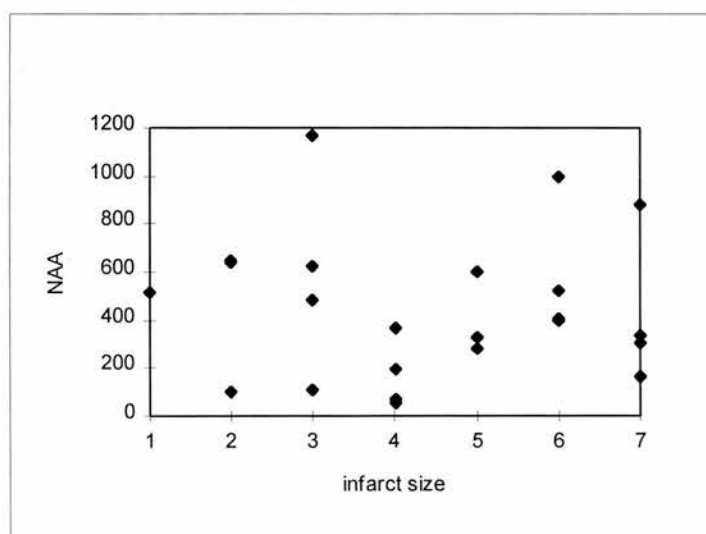


Fig. 7.11 Relationship between T_2 visible infarct size and NAA levels. The data were tested for correlation using the Pearson correlation coefficient. With a 2 tailed test, and $n=23$ the coefficient fell outside the 10% confidence interval, indicating no significant correlation.

(v) Is NAA depression related to the age of the insult when scanned

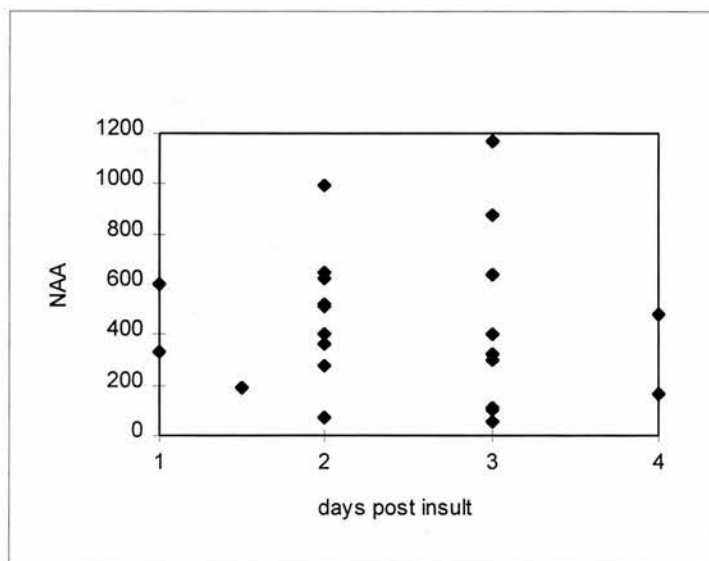


Fig. 7.12 Relationship between time after the stroke onset and NAA levels. The data was tested for correlation using the Pearson correlation coefficient. With a 2 tailed test, and $n=23$ the coefficient fell well outside the 10% confidence interval indicating no correlation.

(vi) Do NAA levels continue to fall in patients scanned serially with SI.

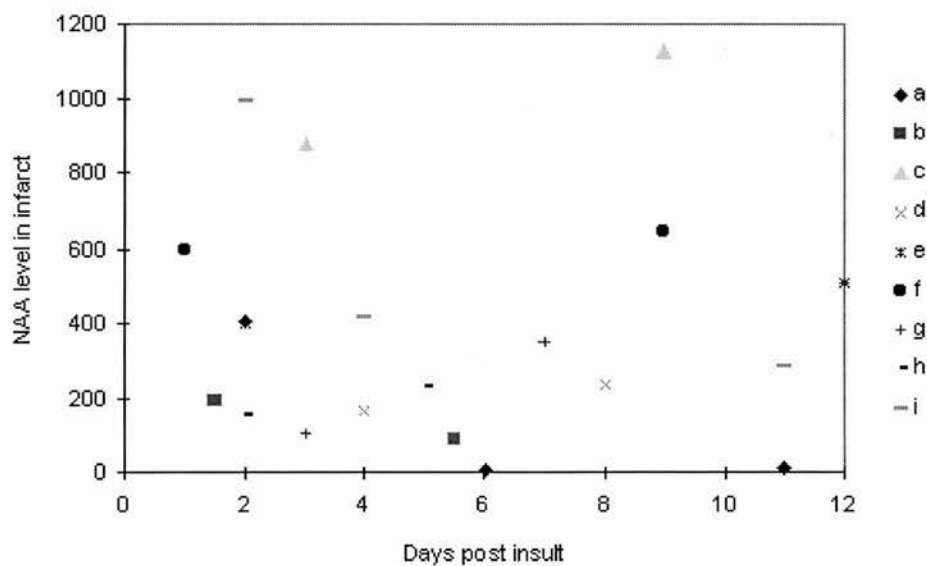


Fig. 7.13 The scatter plot of NAA data from patients scanned on more than one occasion. The plot is quite confusing and no obvious linear relationships are evident. 50% of the patients showed a decline in NAA levels with time, whilst the other 50% showed a rise.

7.3.2.5 Conclusions

The most significant finding of this study was the significant depression in levels of choline and creatine as well as NAA in infarcted regions when compared with contra-lateral control regions. The reduction of NAA levels in ischaemia is well documented (Duyn et al 1992, Petroff et al 1992, Christiansen et al 1993, Gideon et al 1992 and 1994) and is attributed to neuronal degradation and necrosis (Baker et al 1991, Bruhn et al 1989). Significant changes in choline and creatine in stroke are less well documented. Sappey-Marini et al 1992 reported increased levels of choline, especially within areas of white matter hyper-intensity. Conversely Duyn et al 1992 and Felber et al 1992 found decreased levels within infarcted tissue. These results support the findings of the latter two studies. Luyten et al 1990, predicted elevated choline levels with cell wall breakdown, presumably once the debris from this breakdown has been cleared (after re-perfusion) choline levels will be reduced accordingly.

A significant creatine reduction was also noticed by Duyn et al 1992 and Howe et al 1995, a reduction in the number of viable metabolic cells (still able to maintain the ATP cycle) is a possible mechanism for this decrease.

The hypothesis that higher NAA levels in the first three days of stroke were correlated with a good subsequent clinical outcome (iii) was not proved.

The lack of any significant correlation between decreased NAA and the presence of lactate/lipids (hypothesis ii) is interesting. Most studies report elevated lactate levels in the acute stage of stroke presumably due to states of compromised blood oxygenation. For reasons described in much greater depth in chapter 6 and section 7.3.2.1, the detection/distinction of lactate/lipids was a major challenge throughout the course of the study. Ideally a quantified lactate signal would be used in the statistical analysis. This would require a definitive method of distinguishing lactate from lipids. NAA reduction involves neuronal death (Graham et al 1993). As such severe reductions in NAA might be expected in the core of the infarct hours after the insult. The results of hypotheses (v) and (vi) do not confirm this prediction, with no significant relationship between NAA levels and the time at which the patient was scanned post insult. There is the distinct possibility that the majority of neuronal death has taken place i.e. NAA levels have reached their minimum.

No indication of correlation between visible infarct extent and levels of NAA (hypothesis iv) was found using this technique. This is probably due to the fact that the NAA levels throughout the infarct were averaged out by the ROI calculation. Consequently a large infarct might be expected to contain an inner core of particularly low NAA, but will also contain a larger area of “penumbra” region than a smaller infarct. As such the severe depression of NAA may be moderated by the relatively extensive “penumbra”. A better indication of NAA distribution within an infarct is gained from the following “penumbra” study.

7.3.3 Ischaemic penumbra study

7.3.3.1 Introduction

In this study, acute stroke patients with large MR visible infarcted regions were used ($n=18$) as these infarcts covered several whole voxels in the plane of the metabolite image (Fig. 7.14). These large infarcts can be used to analyse the distribution of metabolites within and around the MRI visible extent of the infarct. Furthermore, these infarcts were evident in approximately the same place on the three contiguous transverse T_2 images covered by the spectroscopic imaging plane. The condition for inclusion was that the infarct should show an area of overlap of >75% between adjacent images. This condition was determined with an interactive ROI area measurement using the software ANALYZE. This means that inaccuracies introduced by the partial volume effect, explained in section 7.2.2 (fig. 7.3) were minimised in this study.

7.3.3.2 Methods

Acquisition of the SI data and its processing into images proceeded as described in chapters 3-5. The levels of NAA in voxels located at the core, inner edge and outside edge of the T_2 visible infarcts were read directly from the raw NAA image. This ensures that any differences in the NAA signal are unbiased by the errors introduced by the smoothing of a coarse image matrix (section 7.2.2). The voxels were classified in terms of these three categories on the basis of the T_2 visibility of the infarct by a neuro-radiologist. An inner “core” voxel would contain 100% of visibly infarcted tissue, an inner edge voxel would contain between 50% and 100% visibly infarcted tissue whilst an outer edge voxel would contain less than 50% visibly infarcted tissue. This classification scheme is illustrated in fig. The mean distribution of NAA throughout the whole of the infarct was also compared to

that found in a contra-lateral region of equal size and position. To calculate these two mean measurements the smoothed image was used with an interactive ROI (Chapter 4.12). NAA levels measured from individual voxels and the infarct as a whole were then tested for significant differences with the contra-lateral readings using a 2-tailed paired Student's t-test.

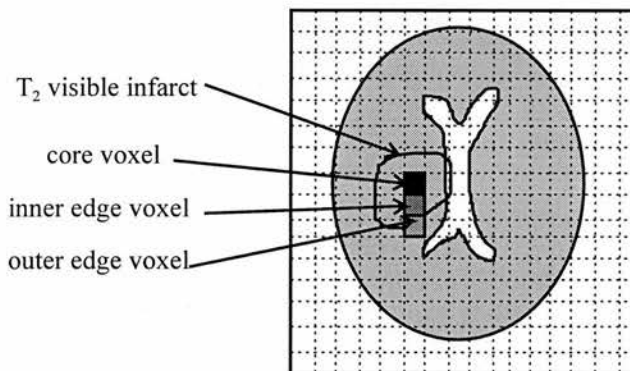


Fig. 7.14 Diagram indicating how the large visible infarcts were partitioned in to core, inner edge and outer edge voxel categories.

7.3.3.3 Results

Region	Infarct core (voxel)	Inner edge (voxel)	Outer edge (voxel)	Whole infarct (ROI)	Contra- lateral(ROI)
mean NAA (a.u.)	171	371	875	430	987
t test significance	p<0.001	p<0.001	p=0.1	p<0.001	

Table 7.8 Distribution of NAA levels within and around an infarct.

7.3.3.4 Discussion

The study of NAA distribution in voxels within the infarct itself shows significantly higher levels at the edge of the visible infarct than at the centre. This supports the notion of a “penumbra” region of potentially viable tissue at the edges of the MRI visible infarct, that has incurred less neuronal damage. Such tissue may well be receptive to neuro-protective treatment (Peruche and Krigstein 1993). The lack of any significant difference between NAA levels on the outer edge of the visible infarct and those in the contra-lateral region

suggests minimal neuronal impairment beyond the extent of the infarct visible on the T_2 image. This finding would appear to be consistent with those of Gideon et al 1992 and Barker et al 1994. Barker's group reported an elevated lactate signal in this region whilst NAA levels remained 'significant' which presumably means normal. One possible source of error is the partial volume effect of inclusion of tissue of a different composition to that suggested by the in-plane T_2 image (see section 7.2.2). This was minimised by studying large infarcts, whose position and size were found to be consistent (to within a 75% overlap) in the images inferior and superior to the plane of the spectroscopic image. Care must be taken when quantitatively interpreting smoothed metabolite images, as a voxel of abnormally high/low intensity surrounded by voxels of uniform intensity will upon smoothing give the impression of a core region surrounded by a penumbra region of intermediate intensity.

7.3.4 Acute head injury study

In closed head injuries, focal lesions such as contusions resulting from mechanical distortion of tissue and haematoma (blood in the brain parenchyma) may be detected on conventional MR and CT images. Less identifiable using such modalities are diffuse axonal injuries (DAI), such as axonal shear, and hypoxic brain damage. With the capability of highlighting the chemical changes that accompany such diffuse head injuries, NMR spectroscopy has the potential to demonstrate such disorders.

Current accident and emergency management means all unconscious (Glasgow Coma Scale ≤ 8) or deteriorating head injured patients are paralysed, intubated, ventilated and sedated at the scene of the incident or upon arrival at hospital. This means that clinical examination of the CNS is limited to pupillary light response tests. If a CT scan shows no visible lesion the patient has a trial wakening up period without further intervention. If during this period the patient awakens then all is well. Patients who do not wake up can suffer secondary insults such as rises in intra-cranial pressure (ICP) which will add to the brain injury. If patients could be scanned with MRI and SI as a first line scan then patients showing no focal abnormalities on MRI but evidence of DAI (from the spectroscopic data) could be kept in ITU in the knowledge that they have sustained a serious injury. The anaesthetic complexity of scanning an unconscious patient with acute head injuries, such as ventilation and monitoring of intra-cranial pressure, probably explains the scarcity of published results. If

however these problems can be circumvented there is no reason why SI should not be used in an attempt to identify DAI.

In this section the findings from previous proton spectroscopy studies of acute closed head injury will be reviewed. The results of the SI study carried out on nine acute closed head injury patients will then be presented. This study is believed to be the first one that uses SI to study closed head injury.

7.3.4.1 Review of proton spectroscopy in head injury

Proton spectroscopic studies of acute head injury in vivo in humans have to date been relatively scarce. Further work has been done using brain injury models in animals, whilst not being directly indicative of the corresponding changes in humans, these studies are still relevant. In this section a review of metabolite changes reported in the literature of spectroscopic head injury studies is given.

NAA

In a study of six acute head injured patients (Davie et al 1995), a significant reduction in NAA was observed in the left frontal lobe. This corresponded to MRI visible signs of ventricular dilatation and slight cerebral atrophy (when compared with a control group of volunteers). In a larger study of 25 closed head injury patients (Danielsen et al 1996), a similar finding of reduced NAA levels (in 92% of subjects) in both white and grey matter was reported. They found that patients with a less severe NAA depression were more likely to have a subsequent improved clinical outcome. Choe et al 1995, measured the ratio of NAA:creatine peaks in 10 closed head injury patients and found a significant reduction when compared to healthy subjects. Patients with the worst outcomes had the lowest ratios of NAA:creatine. The use of ratios to quantify metabolite changes needs to be viewed with some care as creatine levels have been observed to vary (Danielsen et al 1996). In a single voxel serial study of 4 patients (scanned at times from 3 days to 10 weeks post injury), Fenstermacher et al (1990), found decreases in NAA to be indicative of serious ischaemic injury. Prescutti et al (1997), used single voxel spectroscopy to monitor the recovery of acute head injury patients and noted an increase in NAA levels as the patient recovered. Haseler et al 1995, studied 10 children with closed head injury (follow up studies in 50%) using single voxels placed away from MRI visible regions of haemorrhage and noticed decreased NAA in these sites. They also found that NAA levels correlated with clinical

outcome using the Glasgow outcome scale. In a primate study, Handa et al 1997, used sub-arachnoid haemorrhage (SAH) to induce vasospasm and monitored metabolite levels before SAH and at 7 and 14 days afterwards noticing a significant reduction in the NAA:Cr ratio on days 7 and 14.

Choline

Danielsen et al 1996, observed an increase in choline levels from their 25 patient study and suggest that choline is released from the breakdown of myelin as a result of diffuse axonal shear. It is interesting to note that Prescutti et al (1997), noted a falling in choline levels (towards normal levels) with recovery which could be due to the repair of the blood brain barrier after axonal shear.

Creatine

Both Danielsen's (1996) and Fenstermacher's (1990) studies report a reduction in creatine levels in the majority of patients.

Lactate/lipids

Danielsen noted the visibility of lactate/lipids in 12% of patients. Those with subsequent bad clinical outcomes generally showed a reduction in NAA below 70% of normal levels together with lower than normal creatine levels *and* the evidence of lactate/lipids. In a paediatric HI study of 17 patients, Sutton et al 1995, noticed no increased lactate in areas of suspected DAI, but significant levels in regions of MRI visible contusion and infarction. In Haseler's study of 10 paediatric head injuries (1997), lactate/lipids were present in 100% of the patients who stayed in a persistent vegetative state but in only 43% of the patients who had a moderate to good outcome. Using 1D SI with surface coil localisation, Cohen et al 1991, were able to monitor the evolution of metabolite levels along an axial row of voxels in the brains of rats subjected to fluid percussion injury. In the study of six animals they found an immediate elevation in the lactate:NAA ratio post trauma at the injury site. This ratio also increases slowly in remote regions following the incident and persists after four hours in these areas. They suggest that NAA levels remain constant during the first four hours and hence the changes are due to elevated lactate alone. In a similar study using fluid percussion injury on 43 rats, McIntosh et al 1987, monitored metabolite levels for 8 hours post incident in single voxel sites. They found that elevated lactate levels correlated with decreased pH (measured from the chemical shift of phosphorous NMR spectra). At 40 minutes the levels

reached a peak and tailed off to normal levels after 80 minutes. The tailing off of lactate at the injury site may have something to do with the persistent elevated levels found in remote areas by Cohen et al. A further finding of this study was that the level of lactate elevation (and pH reduction) was not related to the severity of the insult. This implies that the severity of acidosis (which may be initiated by lactate accumulation) is not directly related to the likelihood of severe neurological damage. In a fluid percussion study of cats, Inao et al 1988, observed lactate levels to rise in the first hour post injury, falling to normal levels 8 hours post trauma. They propose CSF clearance as a mechanism for lactate removal.

The encouraging finding from this review of published work with respect to the work presented here is the lack of SI data in humans with acute head injury. As diffuse head injury is not obvious on MRIs then the placement of a single spectroscopic voxel is rather haphazard. A 2D SI examination will potentially give a much more complete picture from an axial slice within the brain and hence has the potential of identifying such sites of diffuse injury that are not highlighted by CT or MRI. In the next section the results of the study are presented.

7.3.4.2 SI acute head injury study-methods

The patients in this study were recruited from the ITU ward by the research anaesthetist Dr Carol McMillan, who was responsible for the continuing intensive care of the patient during the scan. The ITU monitoring of these patients within an MRI scanner presents many logistical problems, the fact that a dedicated anaesthetist was able to look after the patients for the duration of the scan made this work possible. The paralysed state of the patients has positive implications for MRI and SI as motion artefacts are limited to the respiratory motion of ventilation. One source of artefact not found normally is from the ICP monitoring transducers and leads. An MRI compatible ICP transducer and monitoring box (Codman, Johnson & Johnson Professional, Inc. Raynham, MA) was tested for artefacts and signal to noise degradation in both T_2 weighted and spectroscopy sequences. The device was found to cause a 10% degradation in the signal:noise ratio of the acetate spectral peak, which was felt to be acceptable. The artefacts introduced into the T_2 weighted images were more considerable with a decrease by a factor of 2.5 in signal:noise ratio when the Codman monitoring device was in place and operational. The differences in S:N degradation for spectroscopy and imaging are probably a direct result of the greater r.f. energy and r.f.

bandwidth of a fast spin-echo imaging sequence when compared to a low energy spectroscopy sequence. Large amounts of r.f. will increase the likelihood of induced currents in the monitoring leads and hence increase artefacts.

Having placed the patient in the scanner with all the physiological monitoring equipment in place (including a finger pulse transducer for cardiac gating of diffusion weighted images) the patient was scanned according to the protocols outlined in Chapter 3. In addition, certain patients ($n=3$) were scanned with diffusion weighted imaging (DWI) with diffusion gradients applied in one direction (the y -phase encode direction) following completion of the SI acquisition. With practice scan times were kept under one hour which is not excessive when one considers the duration of the SI sequence (Chapter 2).

Nine AHI patients (8 trauma and 1 SAH) were scanned as part of the study. The VOI was placed in the basal ganglia and medial temporal regions as these are common sites of injury. Damage in these regions is responsible for much of the impairment after head injury e.g. memory loss. The metabolite SIs were constructed in accordance with chapter 4 and 5. Interactive ROI measurements were then made using neuro-radiological advice (Dr Wardlaw) as to their placement. In patients showing visible lesions a ROI was drawn around the lesion and a second measurement was made in a contra-lateral mirror image position. When no lesions were evident two separate measurements were made in the left and right cerebral hemispheres and the mean from these two ROIs was calculated.

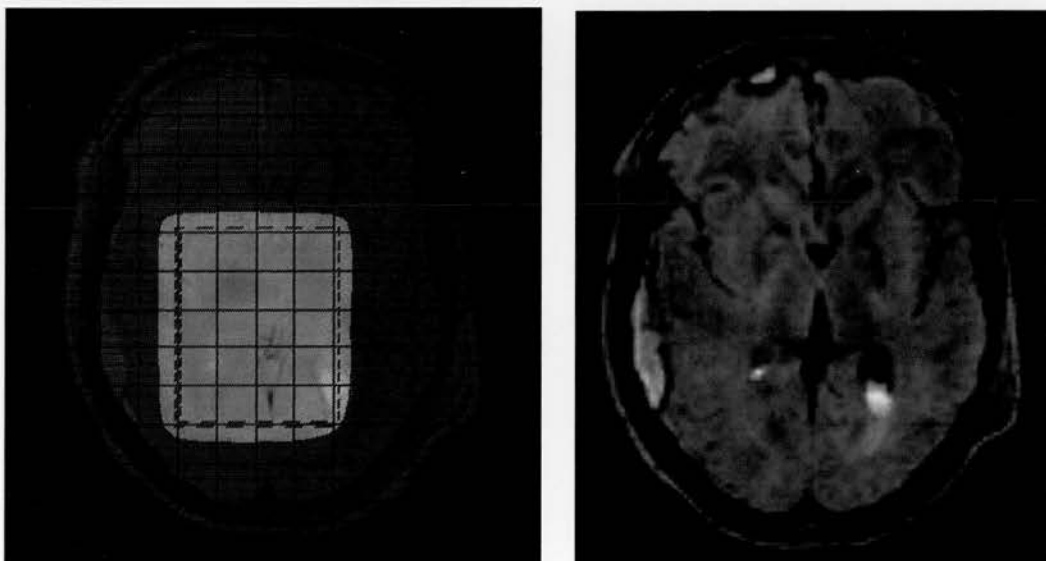


Fig. 7.15 The correlation between NAA metabolite distribution (left) and diffusion weighted image hyper-intensity (right). Of particular interest is the depressed levels of NAA corresponding to the diffusion image hyper-intensity (blood in the lateral ventricle) in the posterior left cerebral hemisphere.

7.3.4.3 Statistical analysis and results

The group data was combined by taking an average of the two measurements made in either hemisphere for each patient. The group mean and s.d. of this mean was then compared with the group mean and s.d. from the control group. This test was conducted using a non-paired equal variance *t*-test for groups of unequal sample size. The mean metabolite readings and the *p* levels for significances in differences are tabulated in Table 7.9.

Group	NAA	Cho	Cr
HI group	646±191	614±188	511±77
controls	1169±140	747±36	579±70
<i>t</i> -test group means.	<0.01	0.3	0.2
<i>c.f.</i> controls (<i>p</i>)			

Table 7.9 The whole group combined by taking the average metabolite levels from the ROIs in the right and left hemispheres

7.3.4.4 Discussion

The pooled data from all nine patients shows a significant decrease in mean NAA when compared to healthy controls. This finding appears to be consistent with the single voxel spectroscopy studies discussed in section 7.3.4.1

This study is ongoing and as such an increase in patient numbers may well confirm the patterns observed early on in this study. The advantage of SI as opposed to single voxel spectroscopy in diffuse head injury has been confirmed. SI has enabled quantitative measurements to be made from the whole of the imaging plane and in patients with diffuse injuries has highlighted significant NAA deficits.

Chapter 8.

Conclusions

8.1 Introduction

In this the final chapter, the conclusions drawn from the three years of work that culminated in the writing of this thesis are discussed. The novel aspects of pulse sequence design (section 8.2.2) and SI data processing methods (8.3), discussed in earlier chapters will be emphasised. A critical appraisal of the viability of the SI technique as a routine MR metabolic imaging modality will then be given (section 8.4). Particular reference to its usefulness in stroke and head injury is made. In each of these categories, scope for improvements in further work will be mentioned.

8.2 Pulse sequences and acquisition protocols

8.2.1 Hardware limitations

The MRI scanner used throughout this work was a standard medium field strength (1.5 T) clinical machine. When the machine was installed in 1992, the manufacturer's (Siemens) released the PRESS localised SI package as a research based sideline, with the clause that they were not prepared to support the sequence in the event of problems. At the same time Siemens were focusing most of their attention on the next generation of Vision MRI machines which came equipped with quicker, actively shielded gradients. Consequently all work described here has been done under the constraints imposed by the machine's hardware capabilities. These are outlined below:

In NMR spectroscopy the strength of the signal is directly proportional to the B_0 field strength. A field strength of 1.5 T is ideal for high quality MRI, as the susceptibility artefacts encountered in state of the art imaging sequences such as EPI are less severe than at high field strengths. For spectroscopic imaging purposes, 1.5 T will give acceptable signal to noise levels for voxel volumes of around 3 cm^3 with a lower limit of 1 cm^3 .

Higher field strengths (e.g. 4.1 T - Hetherington et al 1995) will enable a smaller voxel size and give finer spatial resolution of the SI.

The relatively slow gradient speed of the Magnetom SP63, means that fast spectroscopic imaging pulse sequences based on echoplanar methods were not possible. The gradient speeds have also limited the minimum echo time of pulse sequences used. This, in conjunction with the fact that the gradients are not actively shielded (i.e. eddy currents are significant) has meant that the study of strongly coupled spin species such as glutamate has not been possible.

Finally the range of r.f. pulses available to the programmer for spectroscopic pulse sequence programming has been limited. In particular the unavailability of spatially localised, frequency selective (spatial-spectral) r.f. pulses has limited the scope of advanced SI pulse sequence design. With such pulses outer volume suppression of lipids in the skull could be performed (Spielman et al 1991), allowing spectra from a larger proportion of the brain to be collected. Such pulses would have been particularly useful in designing lactate editing sequences based on the selective inversion of the methyl doublet through J coupling. Instead more subtle pulse sequence designs were used which exploit the same physical property of the lactate spins but in a more roundabout way.

Having discussed the drawbacks of performing SI on this machine, the remainder of this section continues on a more optimistic note. Improvements made to the basic PRESS SI method will be described and further optimisations that could be made will be proposed.

8.2.2 The SI pulse sequence and how it can be optimised

Of the two inner volume spectroscopic localisation techniques, (PRESS and STEAM), PRESS theoretically has twice the signal strength. This was presumably the reason why the manufacturers chose to use PRESS for their SI program. The use of 180° r.f. pulses for spatial selection has the drawback that they are less uniform. In chapter 5, a post processing technique for removing this non-uniformity was described and the merits of this procedure are discussed in section 8.3.

Acquisition of a 16×16 phase encoded SI data set at $T_E=145$ ms, $T_R=1600$ ms take 7 minutes. In order to remove zero order phase inhomogeneities, a second water reference

data set was required. If this reference acquisition is also 16×16 phase encoded, then acquisition of the data alone will take 14-15 minutes. In Chapter 4, the viability of using a reduced number of phase encodings for the water reference (8×8) was investigated. This technique was found not to compromise the accuracy of the metabolite spectrum and as such is an effective means of reducing the overall acquisition time from 14 minutes to closer to 9 minutes.

Further reductions in the overall scan time could be made by automating the processes of shimming and water suppression optimisation. In Chapter 3 an automated shimming routine, based on the calculation of phase difference images was tested and found to work effectively. If the shim currents of the machine were capable of being adjusted remotely following computation of their optimum configuration then routine use of the method would be of benefit. In practice the automated shimming routine was found to be too cumbersome. A more flexible computer operating system based on UNIX rather than VAX should help overcome this problem and as such the method holds promise for use on newer scanners.

In Chapter 6, two lactate editing sequences compatible with the Magnetom's r.f. pulses were investigated. The HOPE sequence (Bunse et al 1995) was tested in-vivo for the first time and shows promising results in separating the lactate doublet from lipids. The technique was first developed in a single voxel format, having obtained positive results a SI sequence was written by the author. This is the first example of lactate editing in SI based on the principle of homonuclear polarisation transfer. The drawbacks of the HOPE sequence are firstly the low signal strength (four times less than the equivalent PRESS signal) which means that the voxel size in SI needs to be increased. Secondly the sequence is a dual acquisition technique involving subtraction of two sets of data (acquired at slightly different echo times) from one another. By interleaving these two acquisitions, motion artefact and field drift errors were minimised.

The second lactate editing sequence was based on the zero quantum coherence modulation of the lactate signal during the mixing time of a single voxel STEAM sequence and has been used in vivo before (Sotak et al 1988, de Graaf et al 1993). The advantages of this sequence are a potential twofold increase in lactate signal strength when compared to HOPE. In-vitro examples of edited spectra do reveal a twofold signal to noise increase in the spectral intensity of the lactate doublet. The STEAM editing technique was found to be less effective

in totally cancelling the lipid signal. T_1 based corrections are proposed as a way of removing residual lipids. A preliminary 180° inversion pulse prior to the STEAM r.f. pulses could reduce the initial lipid signal intensity. In further work using this scanner to perform lactate editing it would be worthwhile adding such a pulse to the STEAM sequence.

8.3 Data processing aspects

The processing of raw FIDs (more accurately spin echoes) into metabolite images involves a considerable amount of data processing. The program `centrefill2.c` was used to carry out the bulk of this processing. This program was based on the initial software `csi.c` written by Ian Marshall. Modifications to perform a spatial shifting of the voxels, zero-filling of the water reference data set and spatial filtering of the data prior to the 2D-FFT were made by the author.

The voxel shifting facility (section 4.9) is useful in that it allows post acquisition corrections to be made for a misalignment of the VOI of excitation and the spatial delineation of the voxel grid. Using this technique, the maximum number of useful voxels can be extracted from the VOI. The technique is particularly useful when anatomical features (such as lipids in the skull) necessitate a VOI placement that does not coincide with the boundaries of the voxel grid.

The zero-filling of a k-space encoded signal (section 4.6) allowed a water reference data set to be acquired in a shorter acquisition time thus reducing the overall scan time. The technique can also be used as a method of increasing the visual smoothness of the water suppressed (metabolite) spectroscopic image matrix.

Spatial filtering of the k-space encoded data prior to the 2D-FFT was shown to reduce the Fourier leakage of lipid artefacts throughout the spectral array (section 4.8). The Hann window function was found to be the most effective of the three filters tested. The drawback of this method is the 70% increase in the effective voxel volume. When Fourier leakage of lipids is not evident, the use of a spatial filter is not recommended as a greater degree of spatial uncertainty is introduced in to the image. In further work, alternative methods to the 2D-FFT for spatially decoding the k-space encoded data could be investigated (Wear et al 1995).

In Chapter 5, a detailed account of a post acquisition technique for removing the B_1 inhomogeneity of the VOI profile was given. This technique should be used routinely when there is a marked non-uniformity in the excitation profile of a spectroscopic VOI. Many new scanners, will be capable of using optimised r.f. pulses (Matson 1995) which have a more uniform slice profile. In such cases this technique may be of limited use.

With the possibility of 3D echo planar multi-slice SI on many new machines, there is scope for acquiring spectra from a lot more voxels. To cope with the increase in data, processing techniques will require more automation. The need for user involvement in constructing the metabolite image (section 4.12) is particularly labour intensive. Automatic first order phasing and metabolite peak fitting algorithms will significantly reduce the need for user involvement at this stage. A basic first order phase correction algorithm was described in section 4.7.4, this routine is less effective when phasing overlapping peaks and multiplets. A more robust algorithm could be investigated (Siegel 1981).

In section 4.11.6, preliminary investigations using a Maximum Entropy Model to fit the spectrum showed promising results. This approach is being extended, to incorporate both the real and imaginary time domain data. In the same vein, parametric modelling of the spectra using a combination of Lorentzian and Gaussian lineshapes carried out by Ian Marshall and Stephen Bruce, has given accurate estimates of peak areas. Incorporation of such techniques in a batch routine for fitting of data from a whole SI array should be pursued as a move towards total automation. Combining these fitting techniques with T_1 and T_2 relaxation time corrections and use of an external reference signal (Danielsen et al 1995) will enable absolute molar quantification of metabolites from the SI.

8.4 In-vivo findings with SI

In the course of the last three years, 23 individual acute (<3 days post insult) stroke patients have been scanned at least once with SI. This appears to be the largest such study using SI to date as well as being one of the largest proton spectroscopic studies of stroke. Using the smoothed metabolite images to measure choline, creatine and NAA in infarcts and contra-lateral regions, significant decreases in all three metabolites were found in infarcted regions when compared to the contra-lateral region.

No significant correlation was found between NAA levels in the infarct and with; (i) the visibility of lactate/lipids, (ii) subsequent clinical outcome, (iii) the size of the infarct and (iv) the time following insult at which SI was performed. This data has since been amalgamated with the data from the 20 + patients scanned with single voxel spectroscopy in the period (October 1992-December 1994). This combined single voxel/SI is the largest spectroscopic study of acute stroke to date ($n=43$). Within this larger group, significant correlations were found (using multivariate analysis) between NAA reduction and; infarct size, impaired cerebral perfusion (as measured using TCD), lactate visibility in the infarct and clinical outcome. This combined data is presented in the forthcoming paper (Wardlaw et al 1997).

Evidence for a more severe reduction in NAA in the core of an infarct when compared to the visible boundary regions (the "penumbra") was found from the analysis carried out on patients showing visibly extensive infarcts (section 7.3.3). This could have important implications in future work using SI to pinpoint regions of ischaemic tissue that may benefit from the administration of reperfusion pharmaceuticals.

In future SI studies of stroke, it would be very interesting to examine patients at the very early stage (<1 day). Using short echo times, the role of glutamate in the early stages of infarction could be more thoroughly explored. Such a strategy would probably require an accelerated referral process and is better suited to a hospital with a constant throughput of stroke patients in accident and emergency.

In the study of nine acute head injury patients (the first to use SI), a significant reduction in NAA levels when compared to healthy age matched controls was noted. This work is ongoing, and the aim is to integrate the spectroscopic examinations with diffusion weighted sequences (Armitage et al 1997), in an attempt to identify regions of diffuse axonal injury.

8.5 Summary

In this chapter, novel aspects of this piece of work have been stressed and their significance in terms of relevance to spectroscopic imaging techniques and clinical applications has been

critically assessed. The question remains whether proton spectroscopic imaging (and spectroscopy in general) is of clinical use.

With the sequence used throughout this study, a single transverse slice of the brain was imaged yielding a grid of 25-36 voxels of volume 3.75 cm^3 , in a total acquisition time of around 45 minutes. Using this sequence, significant spatially dependent alterations of metabolites have been detected in stroke and head injury. With advances in MRI scanner technology, the use of fast imaging sequences (Posse 1994, Adalsteinsson 1995) will enable 3D-SI data to be collected in an equivalent period of time. As stronger magnetic fields become more common place, the spatial resolution of these images will improve such that a grid of 32×32 voxels of spatial resolution under 1 cm is a realistic prospect. If these sequences can in turn be made lactate sensitive then a 3D SI data set showing the distribution of lactate throughout the whole brain is possible. Such a facility will have a definite role to play (alongside diffusion weighted and perfusion MRI) in detecting regions of the brain at risk from the onset of infarction in acute stroke.

At the present time a 2T state of the art research dedicated MRI scanner is being installed at the Department of Clinical Neurosciences. This machine has the hardware capabilities to support such a fast 3D-SI sequence. The fact that the scanner will be on standby to scan research stroke and head injury patients means that early diagnosis of metabolic changes will be possible. It is hoped that the work described here will contribute towards the successful implementation of the next generation of spectroscopic imaging sequences on this machine.

Appendix 1

Quantum mechanical description using density operators and product operators

A 1.1 Introduction

In the previous section the response of a sample of single spin half nuclei to the application of basic NMR pulse sequences was predicted using a classical vector approach using the Bloch equations. When dealing with more complicated spin systems such as a weakly coupled pair (AX), a weakly coupled multiple set (AX_3 e.g. lactate) or with more complex pulse sequences, this approach becomes impractical. Here a more fundamental quantum mechanical description is required.

An example of such a case is the antiphase doublet of an AX system.

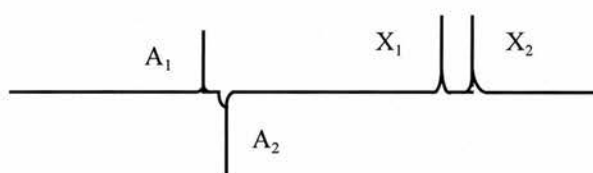


Fig. A1.1 Schematic diagram of an antiphase A_1 - A_2 doublet in a weakly coupled AX system

The density operator formalism which stems from the Schrödinger equation, is well designed to follow the time evolving response of a spin system to applied r.f. pulse sequences. This formalism leads to the product operator approach, which extends the density approach to express the spin magnetisation evolution in terms of more classically meaningful spin vectors. In this section a brief outline of the density operator approach applied to a single spin will be given. This then leads to the product operator approach which is well suited to routine calculations of magnetisation evolution for an arbitrary pulse sequence.

A 1.2 The density operator

In this description the approach adopted by Canet 1996, is followed, whereby the density matrix is defined from the expansion coefficients of an arbitrary spin wave vector $\psi(t)$, whose basis states are the spin-up/down eigenstates $|\uparrow\rangle, |\downarrow\rangle$ of the static Hamiltonian, \hat{H}_0 . In

Chapter 2 eq.(4), the static Hamiltonian was defined for a single spin ($n=1$) and was found to have 2^n eigenvalues corresponding to the split energy levels of the system and orthogonal eigenvectors (ψ_k) corresponding to the spin up and spin down states. As these eigenvectors are time independent, the time dependence of the arbitrary spin wave vector $\psi(t)$, is incorporated in the expansion coefficients, $c_k(t)$;

$$\psi(t) = \sum_{k=1}^{2^n} c_k(t) \psi_k \quad (1)$$

The density matrix is now defined as having a (k,l) th element equal to;

$$\rho_{kl} = \overline{c_k c_l^*} \quad (2)$$

This represents the ensemble average of all spin states in the system. The density matrix as defined above is hermitian which implies that the corresponding density operator must also be hermitian. Furthermore the k th diagonal element represents the population of the k th energy level as it is in effect the probabilistic weighting, p_k of the k th eigenvector in the overall wave function.

$$\rho_{kk} = \overline{|c_k|^2} = p_k \quad (3)$$

The sum of the probabilities of finding the wave function in a given state, when normalised must add up to unity as these are the only available quantum states. Therefore the trace of the density matrix (the sum of the diagonal elements) is equal to unity.

$$\sum_k \rho_{kk} = 1 \quad (4)$$

The off diagonal elements of the matrix ρ_{kl} represent phase coherences between the k and l eigenstates. Such a coherence does not apply in thermal equilibrium as the relative phases of the k and l eigenstates are randomly distributed. The corresponding phase factors $e^{i\varphi}$ are averaged out when the probability of the system being found in the k th state is calculated by taking the modulus $|\psi_k|^2$. External perturbations to the Hamiltonian such as r.f. pulses can produce a phase relationship and induce a coherence in phase. These coherences are classified in terms of the difference in eigenvalues of the operator; $\hat{F}_z = \sum_{i=1}^n \hat{I}_z^i$ where i is the number of spins in the system.

As such the following differences in eigenvalues; $|(F_z)_{kk} - (F_z)_{ll}| = 0, 1, 2, \dots$, represent zero quantum (ZQ), single quantum (SQ), double quantum (DQ),... coherences. The SQ coherence is the only one which is directly observable. The other coherences may manifest themselves as a phase modulation super imposed on the SQ coherence (see section on STEAM editing).

A 1.2.1 Time evolution of the density operator

In the introduction to this section it was mentioned that the time evolution of the density operator follows from the application of Schrödinger's equation to the quantum wave function;

$$\hat{H}(t)\psi = -\frac{1}{2\pi i} \frac{\partial \psi}{\partial t} \quad (5)$$

If the expansion of ψ in eq.(1) is substituted in to eq.(5) and the condition of orthogonality of eigenvectors is used then the Liouville-von Neumann equation can be derived;

$$\frac{d\hat{\rho}}{dt} = 2\pi i [\hat{\rho}, \hat{H}(t)] \quad (6)$$

A 1.2.3 Expectation value of a measurable quantity

Now using the expansion of eq.(1) the ensemble average expectation value of any measurable quantity G with an associated operator \hat{G} , can be determined;

$$\begin{aligned} \overline{\langle \hat{G}(t) \rangle} &= \overline{\langle \psi | \hat{G} | \psi \rangle} = \overline{\left(\sum_l c_l \psi_l \left| \hat{G} \right| \sum_k c_k \psi_k \right)} \\ &= \sum_{l,k} \overline{c_l^* c_k} \langle \psi_l | \hat{G} | \psi_k \rangle = \sum_{l,k} \rho_{l,k} G_{lk} \\ &= \sum_k (\rho G)_{kk} = \text{Tr}(\rho G) \end{aligned} \quad (7)$$

The definition of the density matrix and its hermitian properties as given above assume properties of the matrix which allow its subsequent definition. A more rigorous treatment can be found in the book by Farrar and Harriman (1992). With the density operator the time evolution of a quantum spin system can now be predicted.

A 1.2.4 Density operator of a single spin 1/2

The density operator of a system of single spin half nuclei is now considered. In section (NMR.DOC) it was shown that the number of states available to a single ($n=1$) spin of $I=1/2$ is given by 2^n . The density operator of this system is therefore an $n \times n$ matrix.

$$\hat{\rho} = \begin{pmatrix} \rho_{11} & \rho_{12} \\ \rho_{21} & \rho_{22} \end{pmatrix} \quad (8)$$

First of all the condition of the density operator of such a spin system in thermal equilibrium needs to be calculated. The k th element of the density operator at equilibrium is defined by the probability p_k of finding the system in the k th eigenstate. For a single spin, this probability is defined by the Boltzmann expression;

$$\rho_{kk} = p_{kk} = e^{\frac{-E_k}{k_b T}} / \sum_K e^{-(E_k/k_b T)} \approx (1 - E_k / k_b T) / N \quad (9)$$

Where N denotes the number of energy levels available to the spin system, for n spin half nuclei which constitute the microscopic quantum system, $N=2^n$. Coupling terms cause a microscopic splitting in E_k and a negligible population difference. For the purposes of determining relative populations it is valid to approximate the Hamiltonian to the Zeeman term (Chapter 2, eq. 2.4). As such E_k can be calculated from the expectation value;

$$E_k = \frac{\langle \psi_k | \hat{H} | \psi_k \rangle}{\langle \psi_k | \psi_k \rangle} \quad (10)$$

Which gives;

$$E_1 = -\frac{\hbar\gamma B_0}{2} \quad \text{and} \quad E_2 = +\frac{\hbar\gamma B_0}{2}$$

Therefore

$$\rho_{11} = \frac{I}{2}[I+q] \quad \text{and} \quad \rho_{22} = \frac{I}{2}[I-q] \quad (11)$$

Where $q = \frac{\gamma \hbar B_0}{kT}$. These elements obey the trace condition stipulated by eq.(4), i.e.

$\sigma_{11} + \sigma_{22} = 1$. The density matrix at equilibrium can now be expressed as;

$$\hat{\rho} = \frac{1}{2} \begin{pmatrix} 1+q & 0 \\ 0 & 1-q \end{pmatrix} = \frac{1}{2} \begin{pmatrix} 1 & 0 \\ 0 & 1 \end{pmatrix} + \frac{1}{2} \begin{pmatrix} q & 0 \\ 0 & -q \end{pmatrix} = \frac{1}{2} (\hat{\sigma}_0 + q \hat{\sigma}_z) \quad (12)$$

The terms σ_0 and σ_z represent the identity matrix and the z spin matrix of the Pauli basis set of spin matrices for a single spin $1/2$. For $r = x, y$ and z these matrices are given by;

$$\sigma_{r_j} = \langle \phi_i | \hat{I}_r | \phi_j \rangle \quad \hat{\sigma}_r^2 = \begin{pmatrix} 1 & 0 \\ 0 & 1 \end{pmatrix} = \hat{\sigma}_0 \quad (13)$$

$$\hat{\sigma}_x = \begin{pmatrix} 0 & 1 \\ 1 & 0 \end{pmatrix} \quad \hat{\sigma}_y = \begin{pmatrix} 0 & -i \\ i & 0 \end{pmatrix} \quad \hat{\sigma}_z = \begin{pmatrix} 1 & 0 \\ 0 & -1 \end{pmatrix}$$

For the single spin the Pauli operator of the spin in the r^{th} direction is then given by

$$\hat{I}_r = \frac{1}{2} \hat{\sigma}_r \quad (14)$$

The second term in σ_z in eq.(12) is the only one that represents a directly measurable property and hence an observable signal. Consequently in an NMR experiment this partial density matrix is used $\hat{\rho} = \frac{1}{2} (q \hat{\sigma}_z)$, is all that is needed as a starting point for following magnetisation evolution.

A 1.2.4.1 Time evolution

The evolution of the density operator follows from eq. (6), in periods of free precession the Hamiltonian is not perturbed ($\hat{H} = -\frac{\omega}{2\pi} \hat{I}_z$). Eq.(6) thus yields the expression for the partial density matrix at time t ;

$$\hat{\rho}(t) = e^{(-2\pi i \hat{H}_0 t)} \hat{\rho}(0) e^{(2\pi i \hat{H}_0 t)} = e^{(i\omega \hat{I}_z t)} \hat{\rho}(0) e^{(-i\omega \hat{I}_z t)} \quad (15)$$

A 1.2.4.2 Evolution under r.f. pulses

To account for the rotation effect of an external r.f. pulse, the perturbation effect of the B_1 field on the Hamiltonian needs to be considered. This is best done in the rotating frame(?) in which eq. (6) becomes;

$$\frac{d\hat{\rho}'}{dt} = 2\pi i [\hat{\rho}', \hat{H}_0(t) + \hat{H}_1'] \quad (16)$$

Now as the Zeeman term of the Hamiltonian involves only the \hat{I}_z operator, it is rotationally invariant and hence $\hat{H}_0 = \hat{H}_0'$. The perturbation to the Hamiltonian due to a B_1 r.f. pulse is given in section (NMR.doc) for the laboratory frame as;

$$\hat{H}_1 = -\frac{\gamma B_1}{2\pi} (\hat{I}_x \cos \omega_0 t - \hat{I}_y \sin \omega_0 t) \quad (17)$$

Where $\omega_1 = \gamma B_1$, the precessional frequency due to the component of the r.f. pulse that rotates in the same sense as the nuclear precession due to B_0 . This Hamiltonian is transformed in to the rotating frame (rotational frequency ω_0) as follows;

$$\hat{H}_1' = e^{-i\hat{I}_z \omega_0 t} \hat{H}_1 e^{i\hat{I}_z \omega_0 t} \quad (18)$$

Substituting (17) in (18) and utilising the relations;

$$\begin{aligned} e^{i\theta \hat{I}_z} \hat{I}_z e^{i\theta \hat{I}_z} &= \hat{I}_z \\ e^{i\theta \hat{I}_z} \hat{I}_x e^{i\theta \hat{I}_z} &= \hat{I}_x \cos \theta - \hat{I}_y \sin \theta \\ e^{i\theta \hat{I}_z} \hat{I}_y e^{i\theta \hat{I}_z} &= \hat{I}_y \cos \theta + \hat{I}_x \sin \theta \end{aligned} \quad (19)$$

which stem from the commutative properties of the spin operators, then (18) becomes;

$$\hat{H}_1' = -\frac{\gamma B_1}{2\pi} \hat{I}_x \quad (20)$$

and (16) becomes;

$$\frac{d\hat{\rho}'}{dt} = 2\pi i \left[\hat{\rho}', \hat{H}_0 - \frac{\omega_1}{2\pi} \hat{I}_x \right] \quad (21)$$

For strong r.f. pulses where the r.f. frequency is much greater than the chemical shift (difference between the transmitter frequency and the specific resonance frequency) then the \hat{H}_0 term in (21) can be neglected leaving

$$\frac{d\hat{\rho}'}{dt} = 2\pi i \left[\hat{\rho}', -\frac{\omega_I}{2\pi} \hat{I}_x \right] \quad (22)$$

If the r.f. pulse has a duration of time τ such that the flip angle due to the pulse is $\alpha = \omega_I \tau$ then the differential equation (22) has a solution in the rotating frame. This is expressed in terms of the density operator immediately before and after the pulse application.

$\hat{\rho}'_+ = e^{i\alpha \hat{I}_x} \hat{\rho}'_- e^{-i\alpha \hat{I}_x}$ this transforms back in to the laboratory frame as;

$$\hat{\rho}_+ = e^{i\alpha \hat{I}_x} \hat{\rho}_- e^{-i\alpha \hat{I}_x} \quad (23)$$

A 1.3 Product operator expansion of the density operator

In Chapter 2 it was shown that the number of eigenstates available to an n spin system was 2^n which gives a density matrix of 2^{2n} elements. The product operator expands these elements of the density operator in terms of products of the spin operators

$$\hat{I}_r^j \quad (j = 1, \dots, n \text{ and } r = x, y, z, 0) .$$

$$\hat{\rho}_r = \sum_{r=1}^{2^{2n}} c_r \hat{U}_r \quad (24)$$

Where the product operators are given as products of the individual j^{th} spin operators;

$$\hat{U}_r = \frac{1}{2^{e_r - n/2}} \prod_{j=1}^n \hat{I}_r^j \quad (25)$$

Now each of the \hat{U}_r product operators are independent from one another meaning that they must differ from one another by at least one \hat{I}_r^j . The normalisation factor $N_r = \frac{1}{2^{e_r - n/2}}$, is derived from the trace properties of the product operators eq.(26), which arise from them being orthogonal and normalised. The coefficient e_r is the number of identity operators \hat{I}_r^j used to construct \hat{U}_r . The orthogonality of eq. (26) is a direct result of the product operators differing from each other by at least one \hat{I}_r^j .

$$\text{Tr}(\hat{U}_r \hat{U}_s) = N_r N_s \prod_{j=1}^n \text{Tr}(\hat{I}_r^j \hat{I}_s^j) = \delta_{rs} \quad (26)$$

Having defined the density operator in terms of product operators, eq. (24), this expression can be substituted in to eq. (7) to predict the expectation value $\langle G \rangle$ of a quantity on a system represented by density operators.

$$\langle G \rangle = \text{Tr}(\hat{\rho}\hat{G}) = \sum_{r=1}^{2^{2n}} c_r \text{Tr}(\hat{U}_r \hat{G}) \quad (27)$$

A 1.3.1 Application to a weakly coupled system of two spin 1/2 protons (AX) system.

In the previous sections the density operator and product operator were defined for a single spin 1/2 system. Their use in describing the evolution of the spins under an r.f. pulse sequence was also highlighted. Where the product operator approach really come into its own is in predicting response of more complex spin systems, such as two strongly coupled protons (AB) or two weakly coupled protons (AX). In the remaining discussion a weakly coupled system of two protons will be described since it is a logical precursor to the treatment of an AX₃ weakly coupled system such as lactate.

The basis set of a two spin 1/2 system are chosen as products of the one spin system eigenfunctions (Chapter 2 eq.(2.2)):

$$|\phi_i\rangle = |m_i^A, m_i^X\rangle, |\phi_1\rangle = |\uparrow\uparrow\rangle, |\phi_2\rangle = |\uparrow\downarrow\rangle, |\phi_3\rangle = |\downarrow\uparrow\rangle, |\phi_4\rangle = |\downarrow\downarrow\rangle \quad (28)$$

From eq. (25) the two-spin system operators can be defined as products of the one spin operators; $\hat{I}_0^A, \hat{I}_x^A, \hat{I}_y^A, \hat{I}_z^A$ and $\hat{I}_0^X, \hat{I}_x^X, \hat{I}_y^X, \hat{I}_z^X$. For an $n=2$ system there are $2^{2n} = 16$ spin operators. These have associated vector representations corresponding to the alignment of the lines in the frequency spectrum. (see figure A1.2.)

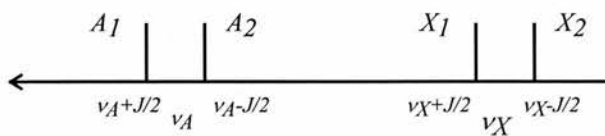


Fig. A1.2 Frequency splitting into doublets of the A and X lines. Each of these operators can then be subdivided in to one of four categories corresponding to the symmetry of the operator matrix and its associated spin evolution properties.

A 1.3.2 Classes of the AX product operator

1. Populations

These have a diagonalised density matrix, the first is the identity operator, the second and third represent a single coupled spin and as such can be represented by the vectors of transitions involving that spin alone. The fourth is a product operator and the global vector notation is less obvious, the direction of the individual transitions can be worked out from density matrix calculations.

2 & 3. Transverse A and X single quantum coherences

The density matrix here is purely off-diagonal with elements ρ_{kl} such that $|(F_z)_k - (F_z)_l| = 1$ (see section A1.2). The single spin operators can be represented by vectors corresponding to individual transitions, the product operators for SQC can also be represented meaningfully in single vector form (aligned in anti parallel) for both A and X spins. This is because SQC's are detectable.

4. Zero and double quantum coherences

The density matrices are again purely off-diagonal with elements ρ_{kl} such that $|(F_z)_k - (F_z)_l| = 0$ and 2 respectively. These transitions are not directly detectable and as such their representations as combinations of antiphase vectors is not physically meaningful. The actual operators that describe pure zero and double QC's are linear combinations of those given in fig. A 1.3 The ZQC can be expressed as a sum of products of raising operators with lowering operators (hence no change in overall quantum number). Similarly a DQC can be expressed as a sum of the products of raising operators with raising operators and lowering operators with lowering operators (hence the net change in quantum number of 2).

A 1.3.3 Time evolution and r.f. pulses

The evolution of these operators under the effect of r.f pulses by extending the Hamiltonian of eq. (20) to the two spin case :

$$\hat{H}_1 = -\frac{\gamma B_1}{2\pi} (\hat{I}_x^A + \hat{I}_x^X) \quad (29)$$

The associated rotation is then an application of the operator in eq. (23) to both A and X states. With the weak J coupling interaction the free precession Hamiltonian incorporates the perturbation due to the coupling term and becomes;

$$\hat{H}_0 = -\frac{\omega_A}{2\pi} \hat{I}_z^A - \frac{\omega_X}{2\pi} \hat{I}_z^X + J \hat{I}_z^A \hat{I}_z^X \quad (30)$$

Populations -diagonal forms

Transverse X-single QC

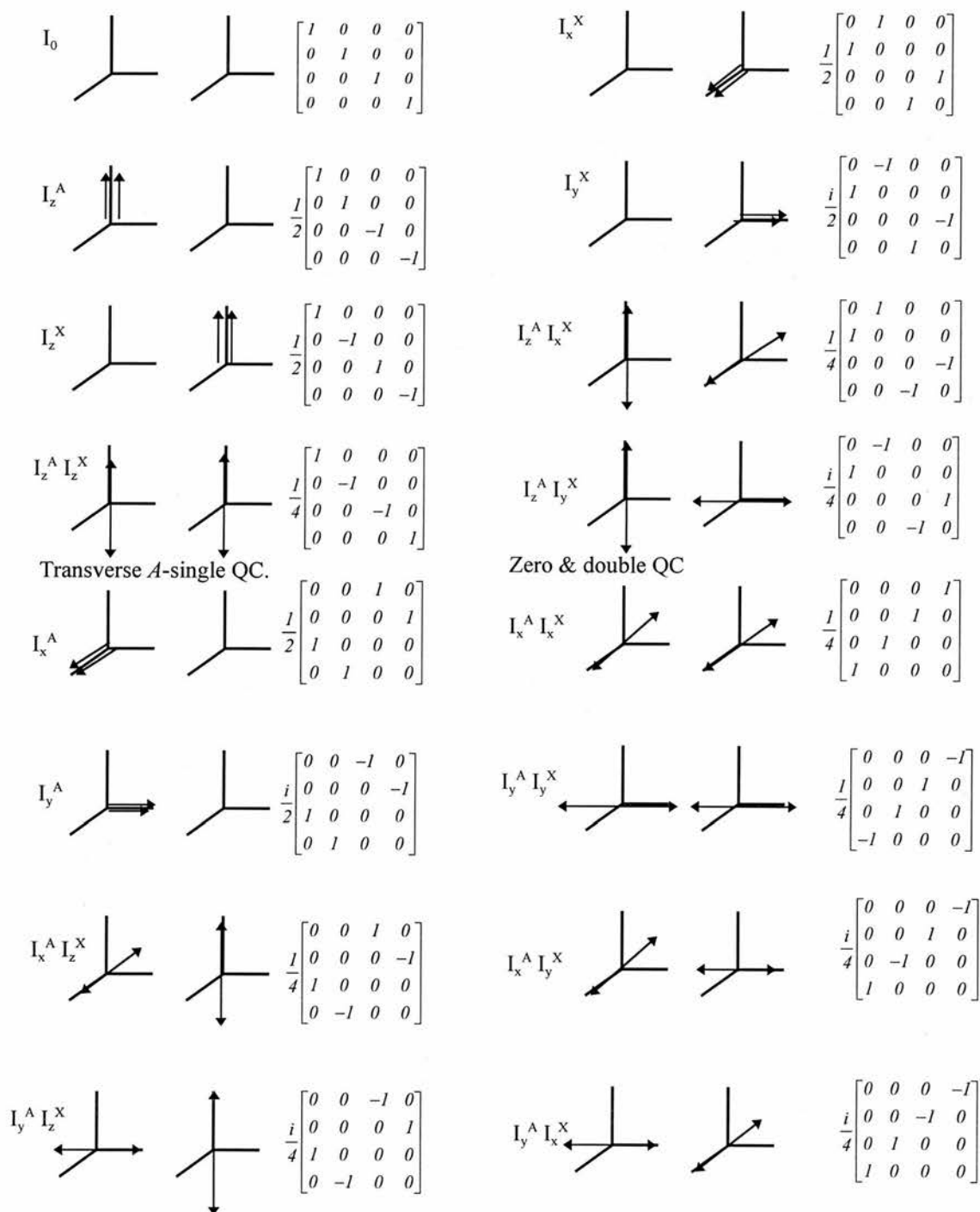


Fig. A1.3 Product operator representations as vector models and in matrix form.

The time evolution operator of eq.(15) is altered accordingly to account for the two spins coupled by a constant J . These two operations can then be applied to any of the 16 basis operators to predict the development of the magnetisation polarisation during a pulse sequence. In the manipulations involving these time evolution and rotation operators it is useful to bear in mind that the Pauli matrices are commutative and as such the spin operators of eq. (14) obey the relations:

$$\begin{aligned}\hat{I}_x^2 = \hat{I}_y^2 = \hat{I}_z^2 &= \frac{I}{4} \hat{I}_0 \\ \hat{I}_x \hat{I}_y &= -\hat{I}_y \hat{I}_x = \frac{i}{2} \hat{I}_z\end{aligned}\quad (31)$$

Where x, y, z can be cyclically replaced by y, z, x and z, x, y . The following relations are also useful:

$$\begin{aligned}\cos(2u\hat{I}_z) &= \hat{I}_0 \cos(u) \\ \sin(2u\hat{I}_z) &= 2\hat{I}_z \sin(u)\end{aligned}\quad (32)$$

A breakdown of the effects of free precession and r.f rotation on all 16 operators would be lengthy. Instead a set of rules for implementing the operations are outlined.

A1.3.4 Free precession

SQ coherence states correspond to detectable states and as such can be represented by vector orientations A_1 and A_2 of the A doublet and X_1 and X_2 of the X doublet. Such states in periods of free precession can be described by a precession where A_1 precesses at a frequency $\nu_A + J/2$ and A_2 precesses at a frequency $\nu_A - J/2$. Similarly X_1 and X_2 precess at frequencies $\nu_X + J/2$ and $\nu_X - J/2$ respectively. This vector representation is illustrated for the evolution of \hat{I}_x^A in fig. A1.4.

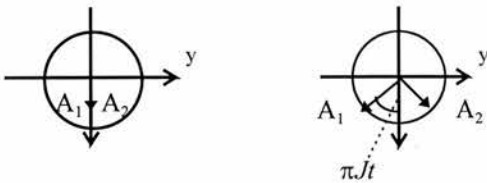


Fig. A1.4. Vector representation of free precession of SQC product operator states

Population vectors of the first category being functions of the direction z , are rotationally invariant in the transverse plane and remain unchanged by free precession.

Zero and double quantum coherences are expressed in terms of the antiphase ‘global’ vectors. These precess at frequencies ν_A and ν_X regardless of the J coupling constant. Their independence from J comes from the fact that the product operators of these coherences commute with the $\hat{J}_z^A \hat{I}_z^X$ term when the Hamiltonian of eq. (30) is inserted in to the time evolution operator of eq. (15). As an example the evolution of $\hat{I}_x^A \hat{I}_x^X$ after a time t is:

$$e^{-2\pi i \hat{H}_0 t} (\hat{I}_x^A \hat{I}_x^X) e^{2\pi i \hat{H}_0 t} = \hat{I}_x^A \hat{I}_x^X \cos(2\pi \nu_A t) \cos(2\pi \nu_X t) + \hat{I}_y^A \hat{I}_y^X \sin(2\pi \nu_A t) \sin(2\pi \nu_X t) \\ - \hat{I}_x^A \hat{I}_y^X \cos(2\pi \nu_A t) \sin(2\pi \nu_X t) - \hat{I}_y^A \hat{I}_x^X \sin(2\pi \nu_A t) \cos(2\pi \nu_X t) \quad (33)$$

This evolution is represented graphically in fig. A1.5 below.

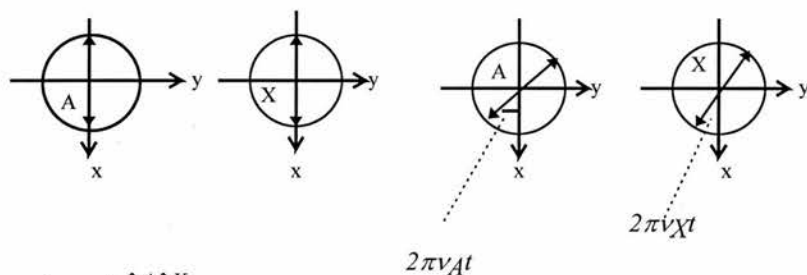


Fig.A1.5. Precession of $\hat{I}_x^A \hat{I}_x^X$

Following periods of free precession it is wise to “book-keep” all like terms and ensure all terms are expressed in the basis 16. The main points to remember are summarised below.

- ZQ and DQ coherences remain in states that are themselves ZQ and DQ coherences.
- An in phase doublet is represented by the form \hat{I}_x^A
- An antiphase doublet (fig. 1) is represented by the form $\hat{I}_x^A \hat{I}_z^X$. The orientation of the A_1 and A_2 tails of the global vector is determined by the eigenvalue of the component with respect to the \hat{I}_z^X operator. For example the A_1 (high energy) state corresponds to an anti-parallel alignment with the z direction and a negative eigenvalue of \hat{I}_z^X . As such the A_1 tail of the global vector is aligned with the -ve x axis.

These last two conditions are equally valid when the axes and nuclei are interchanged e.g. an in phase X doublet aligned along the y axis is given by \hat{I}_y^X .

A1.3.5 R.F. pulses

Using the vector notation of the operators the effect of r.f. pulse rotations can be incorporated. For the in phase doublet operators e.g. \hat{I}_x^A , this rotation is analogous to the rotation of M_x component of the magnetisation in the classical vector treatment. The effect of a flip angle α_y (rotating anti-clockwise about the y axis) is shown below in fig. A1.6.

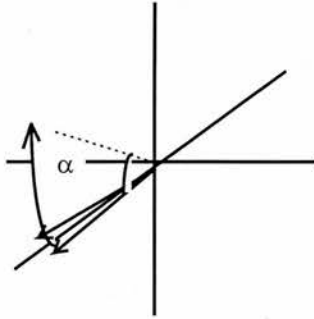


Fig. A1.6. $\hat{I}_x^A - 90^0_x \rightarrow \hat{I}_x^A \cos \alpha + \hat{I}_z^A \sin \alpha$

The vector model would not be able to account for rotations of antiphase configurations as these cannot be expressed as classical vectors. By applying the rotation to the individual A and X global vectors of the product operator the net rotation can be calculated. As an example the effect of a 90^0_x pulse on the anti-phase doublet $\hat{I}_x^A \hat{I}_z^X$ is illustrated in Fig. 6.

Fig.A1.6. The rotational effect of a 90^0_x pulse on the anti-phase doublet $\hat{I}_x^A \hat{I}_z^X$.

Figure 6. illustrates how a detectable coherence A antiphase doublet ($\hat{I}_x^A \hat{I}_z^X$) is converted to a non-detectable DQ coherence $\hat{I}_x^A \hat{I}_y^X$. If a 90^0_y pulse is applied instead, the antiphase A doublet is converted to an antiphase X doublet, (Fig. 7.) this is the principle of coherence transfer and is exploited in stimulated echo editing (STEAM).

Fig.7. Transfer of coherence between SQC from an A antiphase doublet to an X antiphase doublet.

The above examples using an AX system have been chosen to illustrate the use of product operators in determining the outcome of a pulse sequence on a given line in the frequency spectrum. The effect of spoiler gradients can also be taken into account to give a complete prediction of a pulse sequence outcome. By collating all terms representing the operator

notation of the chosen line in the spectrum after the sequence the final signal can be predicted. The AX analogy is extended to the AX_3 system with the exception that for 4 spins there are 16 eigenstates and 256 product operators. A description of all these is impractical. As such when using the approach on the AX_3 system meticulous bookkeeping is required in order to avoid mistakes.

Appendix 2.

Computer source code and pulse sequence listings

Contains listings of the main programs and sequences developed and used by the author.

centrefill2.c	SI data processing program
normalise.c	B₁ normalisation program
armatd.c	Maximum Entropy modelling program
hope.udb	Single voxel HOPE sequence
hope_csi.udb	HOPE SI sequence
steam_tm_te_140.udb	variable T_m & T_E STEAM sequence

```

/*****centrefill2.c*****/
Calculates SI array of FID's and spectra from raw data files from
Siemens SI sequences.
Based on the program csi.c written by Ian Marshall 1994. Major
modifications include;
Zero filling of water reference data from 16*16 to 32*32 matrix.
Voxel shifting of the VOI relative to the image grid of voxels.
Integration of the individual spectra across the grid of voxels to
compute B1 excitation profiles.
Application of optional k-real space filtering prior to the 2D-FFT.
User interactive commands at run time to assist in operation.

Jim Wild January 1998
*****/

#include <stdio.h>
#include <stdlib.h>
#include <string.h>
#include <math.h>

#define n_rows 32
#define n_cols 32
#define n_samples 1024
#define n_F_pts 1024

#define delta_t 1000 /* sample interval in us */
#define B 4.0 /* Gaussian line-broadening in Hz */

/* define parameters for saving of spectral data */
#define first_point 1
#define last_point 2048
#define first_ppm 5.4
#define last_ppm 4.0
#define first_limit 5.1 /* for peak integration */
#define last_limit 4.4

#define SQR(x) (x)*(x)
#define pi 3.14159

#define SWAP(a,b) tempr=(a);(a)=(b);(b)=tempr

char in_path[50] = "/image3/mri/csi/";
char out_path[50] = "/image3/mri/csi/";

char full_file_name[80];
double ***FID,***phase;
FILE *data_file, *save_file;
char pat_dir[20];
char file_name[15], file_num[6], pat_name[29],
phase_file_name[80];
char ref_file_string[10], ws_file_string[10];
char study_date[10], order_number[9];
double f_sample, scale_factor;
int num_ACQs;
double *col_FT_temp, *row_FT_temp, *spec_FT_temp;
double header[64];

int delx;
int dely;
int read_data_file(void);
int read_int(void);
int first_row;
int last_row;
int first_col;
int last_col;
int row_spacing;
int row_num;
int col_num;
char ans;
long read_long(void);
double read_VMS float(void);
void save_raw_files(void);
void save_multi_fids(void);
void column_transforms(void);
void save_col_fids(void);
void calc_phase_corrections(void);
void save_phase_corrections(void);
void apply_phase_corrections(void);

void save_uncorrected_fids(void);
void save_corrected_fids(void);
void save_phase_fids(void);
void save_row_fids(void);
void row_transforms(void);
void save_rearranged_fids(void);
void spectral_transforms(void);
void save_raw_data(void);
void save_col_transforms(void);
void display_data(void);
void rearrange_FIDs(void);
void line_broadening(void);
void save_FIDs(void);
void save_FIDs_for_Delft(void);
void save_individual_spectra(void);
void save_ind_met(void);
void save_spectra_for_gnu(void);
void save_met_data(void);
void save_spectra_for_display_csi(void);
void save_ind_time_domain(void);
void area_integration(void);
void voxel_shiftx(void);
void voxel_shifty(void);

/* functions taken from Numerical Recipes */
void fourl(double data[], int nn, int isign);
void nerror(char error_text[]);
double *dvector(int nl,int nh);
void free_dvector(double *v,int nl,int nh);
double **dmatrix(int nrl,int nrh,int ncl,int nch);
void free_dmatrix(double **m,int nrl,int nrh,int ncl,int nch);
double ***CSI_matrix(long nrl,long nrh,long ncl,long nch,long
ndl,long ndh);
void free_CSI_matrix(double ***t,long nrl,long nrh,long ncl,long
nch,
long ndl,long ndh);

*****/

main()
{
    int i,j,k;

    /* declare arrays */
    FID=CSI_matrix(1,n_rows,1,n_cols,1,2*n_samples);

    col_FT_temp=dvector(1,2*n_rows);
    row_FT_temp=dvector(1,2*n_cols);
    spec_FT_temp=dvector(1,2*n_samples);
    phase=CSI_matrix(1,n_rows,1,n_cols,1,n_samples);

    printf("\n\nPatient name :");
    scanf("%s",pat_dir);

    /*-----*/
    Read Water Reference data,
    calculate FIDs and phase corrections
    -----*/

    printf("\n");

    printf("\nFile number of water reference data (5
digits):");
    scanf("%s",file_num);
    strcpy(ref_file_string,file_num);
    printf("Water reference file: ");
    if (read_data_file()!=0)
    {
        printf("Error reading data file\n");
        return(1);
    }

    /*-----*/
    Defining the row spacing of spectra in the gnuplot
display of spectra
    -----*/

    printf("\nSpecify the spacing of spectra plots in
'gnuplot.'");

```

```

printf("\n");
printf("\nfor phantom spectra row spacing~1500,");
printf("\nfor patient spectra row spacing~200.");
printf("\n");
printf("\nEnter row spacing:");
scanf("%d",&row_spacing);
printf("row spacing is %d",row_spacing);

/*-----*/
/*
Row and column specification of the grid
-----*/
printf("\nSpecify the grid by the range of rows and
columns covered:");
printf("\n");
printf("\nFirst row number:");
scanf("%d",&first_row);
printf("\nLast row number:");
scanf("%d",&last_row);
printf("\nFirst column number:");
scanf("%d",&first_col);
printf("\nLast column number:");
scanf("%d",&last_col);

/*-----*/
/*
Specification of voxel shift
-----*/
printf("\nSpecification of voxel shift required to bring
the grid into alignment with the ROI:");
printf("\n");
printf("\nx shift:");
scanf("%d",&deltx);
printf("\ny shift:");
scanf("%d",&dely);

/*-----*/
/*-----*/

printf("Print individual spectrum & fid from a
given row and column:\n");
/*
scanf("%c",&ans);
if (ans=='y')
{
printf("Enter row number:\n");
scanf("%d",&row_num);
printf("Enter column number:\n");
scanf("%d",&col_num);
}
else
{
printf("Continuing compilation\n");
}
*/

/*-----*/
/*
save_multi_fids();*/
/*
save_raw_files();*/
voxel_shifty();
column_transforms();
/*
save_col_fids(); */
voxel_shiftx();
row_transforms();
/*
save_row_fids(); */
rearrange_FIDs();
save_rearranged_fids(); */

calc_phase_corrections();
save_phase_corrections();*/

/*-----*/
/*
Read Water-suppressed data, calculate the FIDs,and
use the pre-calculated phase angles to correct them
-----*/

printf("\nFile number of water-suppressed data (5
digits):");
scanf("%s",file_num);
strcpy(ws_file_string,file_num);
printf("Water suppressed file: ");

if (read_data_file()!=0)
{
printf("Error reading data file\n");
return(1);
}

/*-----*/
/*
save_multi_fids(); */
/*
save_raw_files(); */
voxel_shifty();
column_transforms();
/*
save_col_fids(); */
voxel_shiftx();
row_transforms();
/*
save_row_fids(); */
rearrange_FIDs();
/*
save_rearranged_fids(); */
save_uncorrected_fids();*/
apply_phase_corrections();
save_phase_fids(); */
save_corrected_fids(); */
line_broadening();
save_FIDs_for_Delft();
/*
save_ind_time_domain();*/
spectral_transforms();
save_spectra_for_gnu();
area_integration();
save_individual_spectra();
save_ind_met(); */
save_met_data(); */
save_spectra_for_display_csi();

/* free memory */
free_CSI_matrix(phase,1,n_rows,1,n_cols,1,n_sample
s);
free_dvector(spec_FT_temp,1,2*n_samples);
free_dvector(row_FT_temp,1,2*n_cols);
free_dvector(col_FT_temp,1,2*n_rows);
free_CSI_matrix(FID,1,n_rows,1,n_cols,1,2*n_sampl
es);
free_CSI_matrix(FID,1,n_rows/2,1,n_cols/2,1,2*n_sa
mples);

return(0);
} /* main */

/*-----*/
*****
*****/
int read_data_file(void)
{
int row, col, i, j, k, fn, response;
double mul;
long a,b;

strcpy(full_file_name,in_path);
strcat(full_file_name,pat_dir);
strcat(full_file_name,"");
strcat(full_file_name,file_num);
strcat(full_file_name,".raw");
printf("%s\n",full_file_name);

if ((data_file=fopen(full_file_name,"rb"))==NULL)
return(1);

/* read header */
fseek(data_file,0x1094,SEEK_SET);
scale_factor=read_VMS_float();
fseek(data_file,0x1C1A,SEEK_SET);
fgets(file_num,6,data_file);
fseek(data_file,0x1C23,SEEK_SET);
fgets(pat_name,29,data_file);
fseek(data_file,0x1C75,SEEK_SET);

```

```

fgets(study_date,10,data_file);
fseek(data_file,0x1D1C,SEEK_SET);
fscanf(data_file,"%d",&num_ACQs);

printf("\n\n");
printf("Name      : %s\n",pat_name);
printf("Study date  : %s\n",study_date);
printf("File number : %s\n",file_num);
printf("%d acquisition(s), scale
%f\n",num_ACQs,scale_factor);

/* extract data */
fn = atoi(file_num);
if (fn>1)
{
fseek(data_file,0x2000,SEEK_SET);
printf("\n reading file: %d",fn);
printf("\nReading data for row...\n");
for (row=1; row<=n_rows; row++)
{
printf("%d : ",row);
for (col=1; col<=n_cols; col++)
{
printf("%d ",col);
for (i=1; i<2*n_samples; i+=2)
{
a=read_long();
FID[row][col][i] =
(float)a;
FID[row][col][i+1]=
(float)b;
}
printf("\n");
}
}

else if (fn==1)
{
fseek(data_file,0x2000,SEEK_SET);
printf("\n reading file: %d", fn);

for (row=1+(n_rows/4); row<=3*n_rows/4; row++)
{
printf("\nfilling centre of array with 16*16 data set for
row and columns :\n");
for (col=1+(n_cols/4); col<=3*n_cols/4;
col++)
{
printf("%d %d ",row,col);
printf("\n");
for (i=1; i<2*n_samples; i+=2)
{
a=read_long();
FID[row][col][i] =
(float)a;
FID[row][col][i+1]=
(float)b;
}
printf("\n");
}
}

for (row=1; row<=n_rows; row++)
{
printf("\nzero padding data for row &
col...\n");
for (col=1+3*(n_cols/4); col<=n_cols;
col++)
{
printf("%d %d ",row,col);
printf("\n");
for (i=1; i<2*n_samples; i+=2)
{
FID[row][col][i] = 0.0;
FID[row][col][i+1]= 0.0;
}
printf("\n");
}
}

for (row=1+(3*n_rows/4); row<=n_rows; row++)
{
printf("\nzero padding data for row &
col...\n");
for (col=1+(n_cols/4); col<=3*n_cols/4;
col++)
{
printf("%d %d",row,col);
printf("\n");
for (i=1; i<2*n_samples; i+=2)
{
FID[row][col][i] = 0.0;
FID[row][col][i+1]= 0.0;
}
printf("\n");
}
}

for (row=1; row<=(n_rows/4); row++)
{
printf("\nzero padding data for row &
col...\n");
for (col=1+(n_cols/4); col<=3*n_cols/4;
col++)
{
printf("%d %d ",row,col);
printf("\n");
for (i=1; i<2*n_samples; i+=2)
{
FID[row][col][i] = 0.0;
FID[row][col][i+1]= 0.0;
}
printf("\n");
}
}

for (row=1; row<=n_rows; row++)
{
printf("\nzero padding data for row &
col...\n");
for (col=1; col<=n_cols/4; col++)
{
printf("%d %d ",row, col);
printf("\n");
for (i=1; i<2*n_samples; i+=2)
{
FID[row][col][i] = 0.0;
FID[row][col][i+1]= 0.0;
}
printf("\n");
}
}

```

```

    }

    fclose(data_file);

    return(0);
} /* read_data_file */
/*****
*****/

void save_multi_fids(void)
/* save the raw data prior to row & column transformation in a file
of form col,row,fid */
{
    int row, col, i;

    strcpy(full_file_name,in_path);
    strcat(full_file_name,pat_dir);
    strcat(full_file_name,"/");
    strcat(full_file_name,file_num);
    strcat(full_file_name,".");
    strcat(full_file_name,"raw_fids");

    printf("%s\n",full_file_name);
    save_file=fopen(full_file_name,"wb");

    printf("\n row spacing is %d",row_spacing);
    printf("\n saving raw fids in multiple gnuplot
format");
    printf("\n");
    for(row=1; row<=n_rows; row++)
    {
        for(col=1;col<=n_cols;col++)
        {
            for (i=1; i<2*n_samples; i+=2)
            {
                fprintf(save_file,"%f %f\n",
-(float)(col)*1.1*2*n_samples+i,(float)(row-
1)*n_rows*n_cols*row_spacing+FID[row][col][i]);
            }
            fprintf(save_file,"\n");
        }
        fprintf(save_file,"\n");
    }
    fclose(save_file);
} /* save_multi_fids */

/*****
*****/

/*void save_raw_files(void)*/
/* save the raw data prior to row & column transformation in a file
of form col,row,fid */
/* {
    int row, col, i;
    double time;
    char fid_number[10];

    printf("\n saving row raw data");
    for(row=1; row<=n_rows; row++)
    {
        printf("%d", row);
        for(col=1;col<=n_cols;col++)
        {
            printf("%d ",col);

```

```

        strcpy(full_file_name,in_path);
        strcat(full_file_name,pat_dir);
        strcat(full_file_name,"/");
        strcat(full_file_name,file_num);
        strcat(full_file_name,".");
        sprintf(fid_number,"_%d_%d",row,col);
        strcat(full_file_name,fid_number);
        strcat(full_file_name,".");
        strcat(full_file_name,"raw_file");

        printf("%s\n",full_file_name);
        save_file=fopen(full_file_name,"wb");

        for (i=1; i<=2*n_samples; i+=2)
        {
            time=(i*delta_t*1e-6)/2;
            fprintf(save_file,"%d
%f\n",i,FID[row][col][i]);
        }
        fclose(save_file);
    }
    printf("\n\n");
} /* save_raw_files */

/*****
*****/

int read_int(void)
{
    long value, temp;
    int j;
    char b[2];

    for (j=0; j<2; j++) b[j]=fgetc(data_file);

    temp=b[1] & 0xFF;
    temp=temp << 8;
    value=temp | (b[0] & 0xFF);
    if (value > ((32*1024)-1)) value=value-(64*1024);
    return(value);
} /* read_int */

/*****
*****/

long read_long(void)
{
    long value, temp;
    int j;
    char b[4];

    for (j=0; j<4; j++) b[j]=fgetc(data_file);

    value=b[3] & 0xFF;
    value=value << 24;
    temp=b[2] & 0xFF;
    temp=temp << 16;
    value=value | temp;
    temp=b[1] & 0xFF;
    temp=temp << 8;
    value=value | temp;
    value=value | (b[0] & 0xFF);
    return(value);
} /* read_long */

```

```

/*****
*****/

double read_VMS_float(void)

/* read a VMS-style floating-point number */

{
    char byte1, byte2, byte3, byte4;
    char temp1, temp2, sign_byte;
    int sign, j;
    double sig, multiplier;
    double exponent, bit_value;

    byte1=fgetc(data_file);
    byte2=fgetc(data_file);
    byte3=fgetc(data_file);
    byte4=fgetc(data_file);

    /* get sign */
    sign_byte=(byte2 & 0x80);
    if (sign_byte == 0x00) sign=1; else sign=-1;

    /* get exponent */
    temp1=byte2 & 0x7F;
    temp2=byte1 & 0x80;
    if (temp2 == 0x00) exponent=(temp1 * 2) - 128;
    else exponent=(temp1 * 2) - 128 +1;

    multiplier=exp((exponent)*log(2));

    /* get significand */
    sig=0.5; /* due to "hidden" bit */
    bit_value=0.25; /* value of MSB actually stored */

    temp1=byte1 & 0x7F;
    temp1=temp1 << 1;
    for (j=22; j>=16; j--)
    {
        if ((temp1 & 0x80) == 0x80) sig=sig+bit_value;
        bit_value=bit_value/2;
        temp1=(temp1 & 0x7F) << 1;
    }
    temp2=byte4;
    for (j=15; j>=8; j--)
    {
        if ((temp2 & 0x80) == 0x80) sig=sig+bit_value;
        bit_value=bit_value/2;
        temp2=(temp2 & 0x7F) << 1;
    }
    temp1=byte3;
    for (j=7; j>=0; j--)
    {
        if ((temp1 & 0x80) == 0x80) sig=sig+bit_value;
        bit_value=bit_value/2;
        temp1=(temp1 & 0x7F) << 1;
    }

    /* now assemble the result */
    if (exponent == -128) return(0);
    else return(sign * multiplier * sig);
}

/* read_VMS_float */

/*****
*****/

void column_transforms(void)

/* perform (n_cols*n_samples) transforms, each of length n_rows */

{
    int i, row, col;
    double mul, weight, tempr;

    mul=1.0;

    printf("Transforming column ");

    for (col=1; col<=n_cols; col++)
    {
        /* weight=(1.01-SQR((col-
n_cols/2)/(n_cols/2))); */
        /* weight=0.54-0.46*cos(2*pi*col/n_cols); */
        printf("%d ",col);

        for (i=1; i<=2*n_samples; i+=2)
        {
            weight =1;
            for (row=1; row <= n_rows;
row++)
            {
                col_FT_temp[2*row-1] =
weight*FID[row][col][i];
                col_FT_temp[2*row] =
weight*FID[row][col][i+1];
            }

            four1(col_FT_temp,n_rows,1);

            for (row=1; row <= n_rows;
row++)
            {
                FID[row][col][i] =
col_FT_temp[2*row-1] * mul;
                FID[row][col][i+1] =
col_FT_temp[2*row] * mul;
            }

            }
            mul=mul*-1; /*
        }

        printf("\n");

        /* now rearrange row order to keep zero k-space at
the centre */
        for (col=1; col <= n_cols; col++)
        {
            for (i=1; i<=2*n_samples; i++)
            {
                for (row=1; row <=
n_rows/2; row++)
                {
                    SWAP(FID[row][col][i],FID[row+n_rows/2][col][i]);
                }
            }
        }

    } /* column_transforms */

/*****
*****/

void save_col_fids(void)

/* save the column transformed data prior t row transformation and
phase correction in a file of form col_row_fid */

{
    int row, col, i;

    strcpy(full_file_name,in_path);
    strcat(full_file_name,pat_dir);
    strcat(full_file_name,"");
    strcat(full_file_name,file_num);
    strcat(full_file_name,"");
    strcat(full_file_name,"col_fids_no_win");
}

```



```

    }

    printf("%s\n",full_file_name);
    save_file=fopen(full_file_name,"wb");

    printf("\n saving column transformed fids in multiple
gnuplot format");
    printf("\n");
    for(row=1; row<=n_rows; row++)
    {
        for(col=1;col<=n_cols;col++)
        {
            for (i=1; i<2*n_samples; i+=2)
            {
                fprintf(save_file,"%f %f\n",
-(float)(col)*1.1*2*n_samples+i,(float)(row-
1)*n_cols*n_rows*row_spacing+FID[row][col][i]);
            }
            fprintf(save_file,"\n");
        }
        fprintf(save_file,"\n");
    }
    fclose(save_file);
} /* save_col_fids */

/*****
*****

void row_transforms(void)
/* perform (n_rows*n_samples) transforms, each of length n_cols
*/
{
    int i, row, col;
    double mul, weight, tempr;

    mul=1.0;
    printf("Transforming row ");

    for (row=1; row<=n_rows; row++)
    {
        /* weight=(1.01-SQR((row-
n_rows/2)/(n_rows/2)));*/
        /* weight=0.54-
0.46*cos(2*pi*row/n_rows); */
        printf("%d ",row);
        for (i=1; i<2*n_samples; i+=2)
        {
            weight=1;
            for (col=1; col <= n_cols;
col++)
            {
                row_FT_temp[2*col-1] =
weight*FID[row][col][i];
                row_FT_temp[2*col] =
weight*FID[row][col][i+1];
            }

            four1(row_FT_temp,n_cols,1);

            for (col=1; col <= n_cols;
col++)
            {
                FID[row][col][i] =
row_FT_temp[2*col-1] * mul;
                FID[row][col][i+1] =
row_FT_temp[2*col] * mul;
                mul=mul*-1;

```

```

        }
        mul=mul*-1;
    }

    printf("\n\n");

    /* now rearrange column order to keep zero k-space
at the centre */
    for (row=1; row <= n_rows; row++)
    {
        for (i=1; i<=2*n_samples; i++)
        {
            for (col=1; col <= n_cols/2;
col++)
            {
                SWAP(FID[row][col][i],FID[row][col+n_cols/2][i]);
            }
        }
    }

} /* row_transforms */

/*****
*****
void save_row_fids(void)
/* save the column and row transformed data prior to phase
correction
and rearranging in a file of form col,row,fid */
{
    int row, col, i;

    strcpy(full_file_name,in_path);
    strcat(full_file_name,pat_dir);
    strcat(full_file_name,"");
    strcat(full_file_name,file_num);
    strcat(full_file_name,".");
    strcat(full_file_name,"row_fids_no_win");

    printf("%s\n",full_file_name);
    save_file=fopen(full_file_name,"wb");

    printf("\n saving column and row transformed fids in
multiple gnuplot format");
    printf("\n");
    for(row=1; row<=n_rows; row++)
    {
        for(col=1;col<=n_cols;col++)
        {
            for (i=1; i<2*n_samples; i+=2)
            {
                fprintf(save_file,"%f %f\n",
-(float)(col)*1.1*2*n_samples+i,(float)(row-
1)*n_rows*n_cols*row_spacing+FID[row][col][i]);
            }
            fprintf(save_file,"\n");
        }
        fprintf(save_file,"\n");
    }
    fclose(save_file);
} /* save_row_fids */

/*****
*****

```

```

void spectral_transforms(void)
/* perform (n_rows*n_cols) transforms, each of length n_samples
*/
{
    int i, row, col;
    double mul, weight, tempr;

    mul=1.0;
    printf("Spectral transform of row ");

    for (row=1; row<=n_rows; row++)
    {
        printf("%d ",row);
        for (col=1; col<=n_cols; col++)
        {
            weight=1;
            for (i=1; i <= n_samples;
i++)
            {
                spec_FT_temp[2*i-1] =
weight*FID[row][col][2*i-1];
                spec_FT_temp[2*i] =
weight*FID[row][col][2*i];
            }

            four1(spec_FT_temp,n_samples,1);

            for (i=1; i <= n_samples;
i++)
            {
                FID[row][col][2*i-1] =
spec_FT_temp[2*i-1] * mul;
                FID[row][col][2*i] =
spec_FT_temp[2*i] * mul;
                /*
                mul=mul*-1; */
            }
            /*
            mul=mul*-1; */

            printf("\n\n");

            /* now rearrange the frequency order to keep zero at
the centre */
            for (row=1; row <= n_rows; row++)
            {
                for (col=1; col <= n_cols; col++)
                {
                    for (i=1; i<=n_samples;
i++)
                    {
                        SWAP(FID[row][col][i],FID[row][col][i+n_samples]);
                    }
                    for (i=1; i<n_samples;
i+=2)
                    {
                        SWAP(FID[row][col][i],FID[row][col][2*n_samples-i]);
                        SWAP(FID[row][col][i+1],FID[row][col][2*n_samples-i+1]);
                    }
                }
            }

        } /* spectral_transforms */
}
/******

```

```

void rearrange_FIDs(void)
{
    int row, col, i;
    double tempr;

    /* rearrange rows */
    for (row=2; row <= n_rows/2; row++)
    {
        for (i=1; i<=2*n_samples; i++)
        {
            for (col=1; col <= n_cols;
col++)
            {
                SWAP(FID[row][col][i],FID[n_rows-row+2][col][i]);
            }
        }

        /* rearrange columns */
        for (col=2; col <= n_cols/2; col++)
        {
            for (i=1; i<=2*n_samples; i++)
            {
                for (row=1; row <= n_rows;
row++)
                {
                    SWAP(FID[row][col][i],FID[row][n_cols-col+2][i]);
                }
            }
        }
    } /* rearrange_FIDs */

    /******
    void save_rearranged_fids(void)
    /* save the column and row transformed data after rearranging, in
a file of form col,row,fid */

    {
        int row, col, i;
        char fid_number[10];

        for(row=first_row; row<=last_row; row++)
        {
            for(col=first_col; col<=last_col; col++)
            {
                strcpy(full_file_name,in_path);
                strcat(full_file_name,pat_dir);
                strcat(full_file_name,"");
                strcat(full_file_name,file_num);
                strcat(full_file_name,"");
                sprintf(fid_number,"%d_%d",row,col);
                strcat(full_file_name,fid_number);
                strcat(full_file_name,".");

                strcat(full_file_name,"rearranged_fids");

                printf("%s\n",full_file_name);
                save_file=fopen(full_file_name,"wb");

                printf("\n saving column and row transformed fids
after rearranging, in multiple gnuplot format");
                printf("\n");

                for (i=1; i<2*n_samples;
i+=2)
                {

```

```

                                fprintf(save_file,"%d
%f\n", (int)i,FID[row][col][i]);
                                }
                                fclose(save_file);
                                }
                                fclose(save_file);

} /* save_rearranged_fids */

/*****
*****/

void display_data(void)

{
    int row, col, i;

    printf("\nCol 1\t2\t3\t4\t5\t6\t7\t8\n");
    for (row=1; row<=n_rows; row++)
    {
        printf("Row %d ",row);
        for (col=1; col<=n_cols; col++)
        {
            printf("%f\t",FID[row][col][1]);
        }
        printf("\n");
    }
    printf("\n");
} /* display_data */

/*****
*****/

void save_uncorrected_fids(void)

/*saves real and imaginary parts of phase fids for comparison with
the phase angle file*/

{
    int row, col, i;

    strcpy(full_file_name,in_path);
    strcat(full_file_name,pat_dir);
    strcat(full_file_name,"/");
    strcat(full_file_name,file_num);
    strcat(full_file_name,".");
    strcat(full_file_name,"uncorrected_fids");

    printf("%s\n",full_file_name);
    save_file=fopen(full_file_name,"wb");

    printf("\n saving phase uncorrected fids ");
    printf("\n");
    /*for(row=first_row; row<=last_row;
row++)*/row=row_num;
    /*{*/

        /*for(col=first_col; col<=last_col;
col++)*/col=col_num;
        /*{*/

            for (i=1; i<=n_samples; i++)
            {
                fprintf(save_file,"%d %f
%f\n", (int)i,FID[row][col][2*i],FID[row][col][2*i-1]);
            }

```

```

                                /* fprintf(save_file,"\n");
                                }
                                fprintf(save_file,"\n");*/
                                /*}*/
                                fclose(save_file);
                                } /* save_uncorrected_fids */
/*****
*****/
void calc_phase_corrections(void)

/* calculate phase angles as a function of time for the Water
Reference
FIDs, as per Ordidge & Cresshull */

{
    int row, col, i;
    double theta;

    printf("\n calculating phase correction angles
(theta)");
    for (row=1; row<=n_rows; row++)
    {
        for (col=1; col<=n_cols; col++)
        {
            printf("\n calculating for %d %d",
row,col);
            for (i=1;
i<=n_samples; i++)
            {
                theta=atan2(FID[row][col][2*i],FID[row][col][2*i-1]);
                phase[row][col][i]=theta;
            }
        }
    }
} /* calc_phase_corrections */

/*****
*****/

void save_phase_corrections(void)

/* save the theta values*/

{
    int row, col, i;
    char fid_number[10];

    for(row=first_row; row<=last_row; row++)
    {
        for(col=first_col; col<=last_col; col++)
        {
            strcpy(full_file_name,in_path);
            strcat(full_file_name,pat_dir);
            strcat(full_file_name,"/");
            strcat(full_file_name,file_num);
            strcat(full_file_name,".");
            sprintf(fid_number,"%d_%d",row,col);
            strcat(full_file_name,fid_number);
            strcat(full_file_name,".");
            strcat(full_file_name,"phase_angles");
            printf("%s\n",full_file_name);
            save_file=fopen(full_file_name,"wb");

            printf("\n saving phase correction angles (theta)");
            printf("\n");

            for (i=1; i<=n_samples; i++)
            {

```

```

                                fprintf(save_file,"%d %f
%f %f %f\n", (int)i,
(float)phase[row][col][i], FID[row][col][2*i], FID[row][col][2*i-
1], sqrt((FID[row][col][2*i]*FID[row][col][2*i])+(FID[row][col][2
*i-1]*FID[row][col][2*i-1])));
                                }
                                fclose(save_file);
                                }
                                }
                                /* save phase angles */
/*****
*****/

void apply_phase_corrections(void)
/* phase correction of FIDs so that 'Real' part really is in phase,
and Imag part is 90 degrees out of phase.

At each data point, apply the pre-determined phase angle */
{

    int row, col, i;
    double temp_Re, temp_Im;
    double cos_theta, sin_theta;

    for (row=1; row<=n_rows; row++)
    {
        for (col=1; col<=n_cols; col++)
        {
            for (i=1; i<=n_samples; i++)
            {
                cos_theta=cos(phase[row][col][i]);
                sin_theta=sin(phase[row][col][i]);
                temp_Re=(FID[row][col][2*i-
1]*cos_theta + FID[row][col][2*i] *sin_theta);
                temp_Im=(FID[row][col][2*i]*cos_theta
-FID[row][col][2*i-1]*sin_theta);
                FID[row][col][2*i-1] = temp_Re;
                FID[row][col][2*i] = temp_Im;
            }
        }
    }

} /* apply_phase_corrections */
/*****
*****/

void save_phase_fids(void)
/* save the column and row transformed data after rearranging and
PHASE CORRECTION in a file of form col,row,fid */
{

    int row, col, i;

    strcpy(full_file_name, in_path);
    strcat(full_file_name, pat_dir);
    strcat(full_file_name, ".");
    strcat(full_file_name, file_num);
    strcat(full_file_name, ".");
    strcat(full_file_name, "phase_fids");

    printf("%s\n", full_file_name);
    save_file=fopen(full_file_name, "wb");

```

```

                                printf("\n saving phase corrected fids in multiple
gnuplot format");
                                printf("\n");
                                for (row=first_row; row<=last_row; row++)
                                {
                                    for (col=first_col; col<=last_col; col++)
                                    {
                                        for (i=1; i<=2*n_samples; i+=2)
                                        {
                                            fprintf(save_file, "%f %f\n",
-(float)(col)*1.1*2*n_samples+i, (float)(row-
1)*n_rows*n_cols*row_spacing+FID[row][col][i]);
                                            }
                                        fprintf(save_file, "\n");
                                    }
                                    fprintf(save_file, "\n");
                                }
                                fclose(save_file);

} /* save_phase_fids */

/*****
*****/

void save_corrected_fids(void)
/* saves real and imaginary parts of phase corrected fids for
comparison with the phase angle file*/
{

    int row, col, i;

    strcpy(full_file_name, in_path);
    strcat(full_file_name, pat_dir);
    strcat(full_file_name, ".");
    strcat(full_file_name, file_num);
    strcat(full_file_name, ".");
    strcat(full_file_name, "corrected_fids");

    printf("%s\n", full_file_name);
    save_file=fopen(full_file_name, "wb");

    printf("\n saving phase corrected fids ");
    printf("\n");
    /*for (row=first_row; row<=last_row;
row++)*/row=row_num;
    /*{

        for (col=first_col; col<=last_col; col++)
        {/col=col_num;

            for (i=1; i<=2*n_samples; i+=2)
            {

                fprintf(save_file, "%d %f
%f\n", (int)i, FID[row][col][i], FID[row][col][i+1]);
            }
            /*
                fprintf(save_file, "\n");
            */
            fprintf(save_file, "\n");
        }/
        fclose(save_file);
    } /* save corrected fids */

/*****
*****/

void line_broadening(void)
/* Apply a Gaussian window in the time domain, equivalent to

```

line-broadening by B Hz in the frequency domain. The sampling interval is delta_t microseconds */

```
{
    int row, col, i;
    double atten, factor;

    for (row=1; row<=n_rows; row++)
    {
        for (col=1; col<=last_col; col++)
        {
            for (i=1; i<=n_samples; i++)
            {
                factor= 1e-6 * B * i * delta_t;
                if (factor > 10) atten=0;
            else atten = exp(-log(2)*factor*factor);
                FID[row][col][2*i-1]=FID[row][col][2*i-1] * atten;
                FID[row][col][2*i] =FID[row][col][2*i] * atten;
            }
        }
    }
}
```

*/ line-broadening */

```
/******
******/
```

void save_ind_time_domain(void)

/*save individual time domain fid's in a format readable by gnuplot*/

```
{
    int row, col, i;
    double time;
    char fid_number[10];

    row=row_num;
    col=col_num;

    strcpy(full_file_name,out_path);
    strcat(full_file_name,pat_dir);
    strcat(full_file_name,"/");
    strcat(full_file_name,"time_domain");
    sprintf(fid_number,"%d_%d",row,col);
    strcat(full_file_name,fid_number);

    save_file=fopen(full_file_name,"wb");

    for(i=1; i<2*n_samples; i+=2)
    {
        time=(i*delta_t*1e-6)/2;
        fprintf(save_file,"%f %f\n",time,FID[row][col][i]);
    }

    fclose(save_file);
} /* save_ind_time_domain */
/******
******/
```

void save_raw_data(void)

/* save raw data in a form suitable for gnuplot to read */

```
{
    int row, col, i;

    strcpy(full_file_name,out_path);
    strcat(full_file_name,"test.tim");

    save_file=fopen(full_file_name,"wb");

    for (row=1; row<=n_rows; row++)
    {
```

```
        for (col=1; col<=n_cols; col++)
        {
            for (i=1; i< 2*n_samples; i+=2)
            {
                fprintf(save_file,
                    "%f %f %f\n",-(float)(col-
                    1)*2*n_samples+i,
                    FID[row][col][i]+(float)(row-
                    1)*row_spacing,
                    FID[row][col][i+1]+(float)(row-
                    1)*row_spacing);
            }
            fprintf(save_file,"\n");
        }
        fprintf(save_file,"\n");
    }
}
```

fclose(save_file);

*/ save_raw_data */

```
/******
******/
```

void save_col_transforms(void)

/* save column-transformed data in a form suitable for gnuplot to read */

```
{
    int row, col, i;

    strcpy(full_file_name,out_path);
    strcat(full_file_name,"test.col");

    save_file=fopen(full_file_name,"wb");

    for (row=1; row<=n_rows; row++)
    {
        for (col=1; col<=n_cols; col++)
        {
            for (i=1; i< 2*n_samples; i+=2)
            {
                fprintf(save_file,
                    "%f %f %f\n",-(float)(col-
                    1)*2*n_samples+i,
                    FID[row][col][i]+(float)(row-
                    1)*n_rows*row_spacing,
                    FID[row][col][i+1]+(float)(row-
                    1)*n_rows*row_spacing);
            }
            fprintf(save_file,"\n");
        }
        fprintf(save_file,"\n");
    }
}
```

fclose(save_file);

*/ save_col_transforms */

```
/******
******/
```

void save_FIDs(void)

/* save transformed data in a form suitable for gnuplot to read */

```
{
    int row, col, i;

    strcpy(full_file_name,out_path);
```

```

strcat(full_file_name,file_num);
strcat(full_file_name,".fid");

save_file=fopen(full_file_name,"wb");

for (row=1; row<=n_rows; row++)
{
  for (col=1; col<=n_cols; col++)
  {
    for (i=1; i< 2*n_samples; i+=2)
    {
      fprintf(save_file,
"%f %f %f\n",-(float)(col-
1)*2*n_samples+i,
FID[row][col][i]+(float)(row-
1)*n_cols*n_rows*row_spacing,
FID[row][col][i+1]+(float)(row-
1)*n_cols*n_rows*row_spacing);
    }
    fprintf(save_file,"\n");
  }
  fprintf(save_file,"\n");
}

fclose(save_file);

} /* save_FIDs */

/*****
*****/

void save_FIDs_for_Delft(void)

/* save transformed data in a form suitable for Delft fitting
software */

{
  int row, col, i;
  char fid_number[10];

  header[0]=2048.0;
  header[1] = delta_t*0.001;

  for (row=first_row; row<=last_row; row++)
  {
    for (col=first_col; col<=last_col; col++)
    {
      strcpy(full_file_name,out_path);
      strcat(full_file_name,pat_dir);
      strcat(full_file_name,"/");
      strcat(full_file_name,"csi_");
      sprintf(fid_number,"%d_%d",row,col);
      strcat(full_file_name,fid_number);
      strcat(full_file_name,".asc");
      save_file=fopen(full_file_name,"wb");

      /* header */
      for(i=0;i<64;i++)
      {
        fprintf(save_file,"%15.5E",header[i]);
        if(((i+1)%4)==0) fputc(0x0A,save_file);
      }

      /* real data */
      for (i=1; i<= 2*n_samples; i+=2)
      {
        fprintf(save_file,"%17.10e
",FID[row][col][i]);
        if (((i+1)%8)==0)
        fputc(0x0A,save_file);
      }

      /* imag data */
      for (i=1; i<= 2*n_samples; i+=2)
      {
        fprintf(save_file,"%17.10e
",FID[row][col][i+1]);
        if (((i+1)%8)==0)
        fputc(0x0A,save_file);
      }
    }
  }
  fclose(save_file);
}

/*****
*****/

void save_individual_spectra(void)

/* save individual transformed spectra from a user defined row /
column position
in a form suitable for gnuplot to read */

{
  int row, col, i;
  int first_pt, last_pt, n_pts;
  double freq;
  char fid_number[10];

  freq=63.63*(4.7-first_ppm);
  first_pt=n_samples + freq*n_samples*2*delta_t*1e-
6;
  first_pt=2*(first_pt/2)+1;

  freq=63.63*(4.7-last_ppm);
  last_pt=n_samples + freq*n_samples*2*delta_t*1e-6;
  last_pt=2*(last_pt/2)+1;

  n_pts=last_pt-first_pt;

  row=row_num;
  col=col_num;
  strcpy(full_file_name,out_path);
  strcat(full_file_name,pat_dir);
  strcat(full_file_name,"/");
  strcat(full_file_name,"spectrum_");
  sprintf(fid_number,"%d_%d",row,col);
  strcat(full_file_name,fid_number);
  save_file=fopen(full_file_name,"wb");

  for (i=first_pt; i< last_pt; i+=2)
  {
    fprintf(save_file,
"%f %f\n",-(float)1.1*n_pts+i,
FID[row][col][i]+(float)(row-
1)*n_cols*n_rows*row_spacing);
  }

  fclose(save_file);
}

} /* save_individual_spectra_for_gnu */

/*****
*****/

void save_ind_met(void)

/* save metabolite region of Real part of individual transformed
spectra
in a form suitable for gnuplot to read */

{
  int row, col, i;
  char fid_number[10];

```

```

double freq, ppm;

row=row_num;
col=col_num;

strcpy(full_file_name,out_path);
strcat(full_file_name,pat_dir);
strcat(full_file_name,"/");
strcat(full_file_name,"ind_met_");
sprintf(fid_number,"%d_%d",row,col);
strcat(full_file_name,fid_number);
save_file=fopen(full_file_name,"wb");

        for (i=first_point; i<=last_point; i+=2)
        {
            freq=1/(2*delta_t*1e-6) + ((i-
1)/2)*1/(n_samples*delta_t*1e-6);
            ppm= 4.7-(freq/63.63);
            fprintf(save_file,"%f
%f\n",ppm,FID[row][col][i]);
        }
        fclose(save_file);
        printf("\n\n");
} /* save_ind_met */

/*-----*/
void save_spectra_for_gnu(void)

/* save transformed spectra in a form suitable for gnuplot to read
*/

{
    int row, col, i;
    int first_pt, last_pt, n_pts;
    double freq;

    freq=63.63*(4.7-first_ppm);
    first_pt=n_samples + freq*n_samples*2*delta_t*1e-
6;
    first_pt=2*(first_pt/2)+1;

    freq=63.63*(4.7-last_ppm);
    last_pt=n_samples + freq*n_samples*2*delta_t*1e-6;
    last_pt=2*(last_pt/2)+1;

    n_pts=last_pt-first_pt;

    strcpy(full_file_name,out_path);
    strcat(full_file_name,pat_dir);
    strcat(full_file_name,"/");
    strcat(full_file_name,"gnu.spectra");

    save_file=fopen(full_file_name,"wb");

    for (row=first_row; row<=last_row; row++)
    {
        for (col=first_col; col<=last_col; col++)
        {
            for (i=first_pt; i< last_pt; i+=2)
            {
                fprintf(save_file,
"%f %f\n",-(float)(col-1)*1.1*n_pts+i,
sqrt(FID[row][col][i]*FID[row][col][i]+FID[row][col][i+1]*FID[r
ow][col][i+1])+(float)(row-1)*n_cols*n_rows*row_spacing);
            }
            fprintf(save_file,"\n");
        }
        fprintf(save_file,"\n");
    }

    fclose(save_file);

```

```

} /* save_spectra_for_gnu */

/*-----*/

void area_integration(void)

/* Save the integrated peak area in a Matlab-readable file.
The ppm range from 'first_limit' to 'last_limit' is integrated */

{
    int row, col, i;
    int first_pt, last_pt, n_pts;
    double peak_area, freq;

    freq=63.63*(4.7-first_limit);
    first_pt=n_samples + freq*n_F_pts*2*delta_t*1e-6;
    first_pt=2*(first_pt/2)+1;

    freq=63.63*(4.7-last_limit);
    last_pt=n_samples + freq*n_F_pts*2*delta_t*1e-6;
    last_pt=2*(last_pt/2)+1;

    n_pts=last_pt-first_pt;

    strcpy(full_file_name,out_path);
    strcat(full_file_name,pat_dir);
    strcat(full_file_name,"/");
    strcat(full_file_name,"peak_area");
    save_file=fopen(full_file_name,"wb");

    for (row=first_row; row<=last_row; row++)
    {
        for (col=first_col; col<=last_col; col++)
        {
            peak_area=0;
            for (i=first_pt; i< last_pt; i+=2)
            {
                peak_area+=FID[row][col][i];
            }
            fprintf(save_file,"%f ",fabs(peak_area));
        }
        fprintf(save_file,"\n");
    }

    fclose(save_file);
} /* area_integration */

/*-----*/

void voxel_shifty(void)

/* shift the voxels in the y (vertical) directions by prespecified
angle yang such that the grid and ROI are aligned*/

{
    int i, row, col;
    double temp_Re, temp_Im, yang;
    double cos_theta, sin_theta;

    for (row=1;row<=n_rows;row++)
    {
        for (col=1;col<=n_cols;col++)
        {
            for (i=1;i<=n_samples;i++)
            {
                yang=0.01*2*pi*dely*row/n_rows;
                cos_theta=cos(yang);
                sin_theta=sin(yang);
                temp_Re =FID[row][col][2*i-
1]*cos_theta+FID[row][col][2*i]*sin_theta;
                temp_Im =FID[row][col][2*i]*cos_theta-
FID[row][col][2*i-1]*sin_theta;

```

```

        FID[row][col][2*i-1]=temp_Re;
        FID[row][col][2*i]=temp_Im ;
    }
}
} /* voxel_shifty */

/*****
*****

void voxel_shiftx(void)

/* shift the voxels in the x (horizontal)directions by prespecified
increment dx such that the grid and ROI are aligned*/

{
    int i, row, col;
    double xang;
    double temp_Re, temp_Im;
    double cos_theta, sin_theta;

    for (row=1;row<=n_rows;row++)
    {
        for (col=1;col<=n_cols;col++)
        {
            for (i=1;i<=n_samples;i++)
            {
                xang=0.01*2*pi*delx*col/n_cols;
                cos_theta=cos(xang);
                sin_theta=sin(xang);
                temp_Re =FID[row][col][2*i-
1]*cos_theta+FID[row][col][2*i]*sin_theta;
                temp_Im =FID[row][col][2*i]*cos_theta-
FID[row][col][2*i-1]*sin_theta;
                FID[row][col][2*i-1]=temp_Re;
                FID[row][col][2*i]=temp_Im ;
            }
        }
    }
} /* voxel_shiftx */

/*****
*****

void save_spectra_for_display_csi(void)

/* save spectra in a format suitable for Martin's display_csi
program */

{
    int row, col, i;
    float Re_data;

    strcpy(full_file_name,out_path);
    strcat(full_file_name,pat_dir);
    strcat(full_file_name,"/");
    strcat(full_file_name,"00099.spectra");

    save_file=fopen(full_file_name,"wb");

    for (row=1; row<=n_rows; row++)
    {
        for (col=1; col<=n_cols; col++)
        {
            for (i=1; i< 2*n_samples; i+=2)
            {
                Re_data=FID[row][col][i];

                fwrite(&Re_data,sizeof(Re_data),1,save_file);
            }
        }
    }

    fclose(save_file);
} /* save_spectra_for_display_csi */

/*****
*****

```

```

void save_met_data(void)

/* save metabolite region of Real part of transformed spectra
in a form suitable for gnuplot to read */

{
    int row, col, i;
    char fid_number[10];
    double freq, ppm;

    printf("Saving metabolite data for row ");

    for (row=first_row; row<=last_row; row++)
    {
        printf("%d ",row);
        for (col=first_col; col<=last_col; col++)
        {
            strcpy(full_file_name,out_path);
            strcat(full_file_name,pat_dir);
            strcat(full_file_name,"/");
            strcat(full_file_name,"spec ");
            sprintf(fid_number,"%d %d",row,col);
            strcat(full_file_name,fid_number);
            strcat(full_file_name,".Real");
            save_file=fopen(full_file_name,"wb");

            for (i=first_point; i<=last_point; i+=2)
            {
                freq=-1/(2*delta_t*1e-6) + ((i-
1)/2)*1/(n_samples*delta_t*1e-6);
                ppm= 4.7-(freq/63.63);
                fprintf(save_file,"%f
%f\n",ppm,FID[row][col][i]);
            }
            fclose(save_file);
        }

        printf("\n\n");
    }

} /* save_met_data */

/*****
*****

void fourl(double data[], int nn, int isign)

/* complex Fourier transform routine from 'Numerical Recipes'.
Replaces 'data' by its discrete Fourier transform if 'isign'=1,
or by 'nn' times its inverse Fourier transform if 'isign'=-1.
'data' is an array of length 2*nn, holding interleaved real
and imaginary values.
*/

{
    int n,mmax,m,j,istep,i;
    double wtemp,wr,wpr,wpi,wi,theta;
    float tempr,tempi;

    n=nn << 1;
    j=1;
    for (i=1;i<n;i+=2) {
        if (j > i) {
            SWAP(data[j],data[i]);
            SWAP(data[j+1],data[i+1]);
        }
        m=n >> 1;
        while (m >= 2 && j > m) {
            j -= m;
            m >>= 1;
        }
        j += m;
    }
    mmax=2;
    while (n > mmax) {
        istep=2*mmax;

```



```

theta=6.28318530717959/(isign*mmax);
wtemp=sin(0.5*theta);
wpr = -2.0*wtemp*wtemp;
wpi=sin(theta);
wr=1.0;
wi=0.0;
for (m=1;m<mmax;m+=2) {
    for (i=m;i<=n;i+=istep) {
        j=i+mmax;

temp=wr*data[j]-wi*data[j+1];

temp=wr*data[j+1]+wi*data[j];

temp;

data[j]=data[i]-
data[j+1]=data[i+1]-temp;

temp;

data[i] +=
data[i+1] +=
temp;
}
wr=(wtemp*wr)*wpr-
wi*wpi+wr;

wi=wi*wpr+wtemp*wpi+wi;
}
mmax=istep;
} /* four1 */

/*****
*****/

void nerror(char error_text[])
/* Print an error message and exit the program */
{
    fprintf(stderr,"Numerical Recipes run-time
error...\n");
    fprintf(stderr,"%s\n",error_text);
    fprintf(stderr,"...now exiting to system...\n");
    exit(1);
} /* nerror */

/*****
*****/

double *dvector(int nl,int nh)
/* Declare a dynamic, double precision vector with elements
[nl..nh] */
{
    double *v;

    v=(double *)malloc((unsigned) (nh-
nl+1)*sizeof(double));
    if (!v) nerror("allocation failure in dvector()");
    return v-nl;
} /* dvector */

/*****
*****/

void free_dvector(double *v,int nl,int nh)
/* Free memory previously allocated by dvector() */
{
    free((char*) (v+nl));
} /* free_dvector */

/*****
*****/

double **dmatrix(int nrl,int nrh,int ncl,int nch)
/* Declare a dynamic, two dimensional double precision matrix
with
elements [nrl..nrh][ncl..nch] */
{
    int i;
    double **m;

    m=(double **) malloc((unsigned) (nrh-
nrl+1)*sizeof(double*));
    if (!m) nerror("allocation failure 1 in dmatrix()");
    m -= nrl;

    for(i=nrl;i<=nrh;i++) {
        m[i]=(double *) malloc((unsigned) (nch-
ncl+1)*sizeof(double));
        if (!m[i]) nerror("allocation failure 2 in
dmatrix()");
        m[i] -= ncl;
    }
    return m;
} /* dmatrix */

/*****
*****/

void free_dmatrix(double **m,int nrl,int nrh,int ncl,int nch)
/* Free memory previously allocated by dmatrix() */
{
    int i;

    for(i=nrh;i>=nrl;i--) free((char*) (m[i]+ncl));
    free((char*) (m+nrl));
} /* free_dmatrix */

/*****
*****/

double ***CSI_matrix(long nrl,long nrh,long ncl,long nch,long
ndl,long ndh)
/* allocate a 3-dimensional, double precision matrix */
{
    long i,j,nrow=nrh-nrl+1,ncol=nch-ncl+1,ndep=ndh-
ndl+1;
    double ***t;

    /* allocate pointers to pointers to rows */
    t=(double ***) malloc((unsigned)
(nrow+1)*sizeof(double**));
    if (!t) nerror("allocation failure 1 in CSI_matrix()");
    t+=1;
    t-=nrl;

    /* allocate pointers to rows and set pointers to them */
    t[nrl]=(double **) malloc((unsigned)
(nrow*ncol+1)*sizeof(double*));
    if (!t[nrl]) nerror("allocation failure 2 in
CSI_matrix()");
    t[nrl] += 1;
    t[nrl] -= ncl;

    /* allocate rows and set pointers to them */
    t[nrl][ncl]=(double *) malloc((unsigned)
(nrow*ncol*ndep+1)*sizeof(double));
    if (!t[nrl][ncl]) nerror("allocation failure 3 in
CSI_matrix()");
    t[nrl][ncl] += 1;
    t[nrl][ncl] -= ndl;

    for (j=ncl+1;j<=nch;j++) t[nrl][j]=t[nrl][j-1]+ndep;
    for (i=nrl+1;i<=nrh;i++)
    {
        t[i]=t[i-1]+ncol;
        t[i][ncl]=t[i-1][ncl]+ncol*ndep;
        for (j=ncl+1;j<=nch;j++) t[i][j]=t[i][j-1]+ndep;
    }
}

```

```

    }
    return(t);
} /* CSI_matrix */

/*****
*****/

void free_CSI_matrix(double ***t,long nrl,long nrh,long ncl,long
                    long ndl,long ndh)

/* free a matrix previously declared by CSI_matrix */

{
    free((char *) (t[nrl][ncl]+ndl-1));
    free((char *) (t[nrl]+ncl-1));
    free((char *) (t+nrh-1));
} /* free_CSI_matrix */

/*****
*****/

/* *****eccp_new.c***** *****
single voxel spectroscopy data processing software Generates
eddy current corrected FID files for Delft water removal
*****/

#include <stdio.h>
#include <stdlib.h>
#include <string.h>
#include <math.h>

#define phi 0 /*manual phase correction*/
#define pi 3.1415926534
#define n_samples 4096
#define B 0.0 /* Gaussian line-broadening in Hz */
#define template_width 40 /* number of data points included in
template */
#define delta_t 250

#define SWAP(a,b) temp=(a);a=(b);b=temp
static double at,bt,ct;
#define PYTHAG(a,b) ((at=fabs(a)) > (bt=fabs(b)) ? \
(ct=bt/at,at*sqrt(1.0+ct*ct)) : (bt ? (ct=at/bt,bt*sqrt(1.0+ct*ct)) :
0.0))
static float maxarg1,maxarg2;
#define MAX(a,b) (maxarg1=(a),maxarg2=(b),(maxarg1) >
(maxarg2) ? \
(maxarg1) : (maxarg2))
#define SIGN(a,b) ((b) >= 0.0 ? fabs(a) : -fabs(a))

enum Boolean{false,true} choline, NAA, acetate, lactate,
phantom=false, human=true;

FILE *ref_file, *ws_file, *data_file, *save_file;

/*char in_path[50]="/images/mri/fids/"; */
char in_path[50]="/image3/mri/csi/h_i/";

char order_number[5], file_name[12], file_num[6];
char study_date[10], pat_name[28], NACQ_string[4];
char ref_file_name[8], ws_file_name[8];
int num_ACQs, ref_ACQs, ref_scale, ws_ACQs, ws_scale;
int *FID;

```

```

double *reference, *spectrum, *correction;
double header[64];
double temp_scale_factor;

/* derivation of line template */
int FWHM; /* in data points */
double water_max;
double template[template_width+1];
double template_area;

/* water fitting using singular value decomposition */
#define max_pts 1000 /* max number of data points to be used in
fit */
#define max_funcs 10 /* max number of basis functions to be
used in fit */
int ma; /* number of basis functions and coefficients */
int ndata=0; /* number of data points included in fit */
double x[max_pts], y[max_pts], *fit; /* data points */
double a[max_funcs]; /* coefficients of the functions */
double *afunc;
double chisq;
double **u, **v, *w;

/* spectral modelling of metabolites */
double search_pos[10], est_amp[10], est_pos[10];
double fitted_pos[10], fitted_amp[10], fitted_error[10];
double fitted_uncertainty[10], goodness_of_fit[10];
int temp_int[10];
double std_dev, spec_shift;
int n_peaks;

int read_data_file(void);
int read_int(void);
long read_long(void);
double read_VMS_float(void);
void calc_phase_correction(void);
void phase_correct(double data[]);
void filter(double data[]);
void transform(double data[]);
void twiddle_spectrum(double data[]);
void store_template(void);
void include_range(double hi, double lo);
void func(double xdata, int n_terms);
void subtract_water(void);
void fit_singlet(double cs);
void fit_doublet(double cs, double J_coupling);
void fit_overlapping_peaks(double cs1, double cs2);
void spectral_fitting(void);
void report_results(void);
void save_data(double data[], char ext[]);

/* functions taken from Numerical Recipes */
void nerror(char error_text[]);
int *ivector(int nl, int nh);
void free_ivector(int *v, int nl, int nh);
int **imatrix(int nrl,int nrh,int ncl,int nch);
void free_imatrix(int **m,int nrl,int nrh,int ncl,int nch);
double *dvector(int nl,int nh);
void free_dvector(double *v,int nl,int nh);
double **dmatrix(int nrl,int nrh,int ncl,int nch);
void free_dmatrix(double **m,int nrl,int nrh,int ncl,int nch);
void fourl(double data[], int nn, int isign);
void svdvar(double **v,int ma,double w[],double **cvm);
void svdcmp(double **a,int m,int n,double *w,double **v);
void svbksb(double **u,double w[],double **v,int m,int n,double
b[],double x[]);

/*****
*****/

main()
{
    int i, j, data_pt, product;

    /* declare arrays */
    FID=ivector(1,2*n_samples);

```

```

reference=dvector(1,2*n_samples);
correction=dvector(1,2*n_samples);
spectrum=dvector(1,2*n_samples);
u=dmatrix(1,max_pts,1,max_funcs);
v=dmatrix(1,max_funcs,1,max_funcs);
w=dvector(1,max_funcs);
afunc=dvector(1,max_funcs);
fit=dvector(1,n_samples);

printf("\nPatient Identifier :");
scanf("%s",order_number);

/* read water reference file */
printf("\nNumber of water reference file (3 digits) :");
scanf("%s",file_name);
strcpy(ref_file_name,file_name);
if (read_data_file()!=0)
{
    printf("Error reading data file %s\n",ref_file_name);
    return(1);
}
for (data_pt=1; data_pt<=2*n_samples; data_pt++)
{
    reference[data_pt]=(float)FID[data_pt]/(32*1024);
}
ref_scale=scale_factor;
ref_ACQs=num_ACQs;

/* read water-suppressed file */
printf("\nNumber of water suppressed file (3 digits)");
scanf("%s",file_name);
strcpy(ws_file_name,file_name);
if (read_data_file()!=0)
{
    printf("Error reading data file %s\n",ws_file_name);
    return(1);
}
for (data_pt=1; data_pt<=2*n_samples; data_pt++)
{
    spectrum[data_pt]=(float)scale_factor*FID[data_pt]/(32*1024);
}
ws_scale=scale_factor;
ws_ACQs=num_ACQs;

calc_phase_correction();

strcpy(file_name,ws_file_name);
phase_correct(spectrum);

save_data(spectrum,"asc");

/* dispose of arrays */
free_dvector(fit,1,n_samples);
free_dvector(afunc,1,ma);
free_dvector(w,1,max_funcs);
free_dmatrix(v,1,max_funcs,1,max_funcs);
free_dmatrix(u,1,max_pts,1,max_funcs);
free_dvector(spectrum,1,2*n_samples);
free_dvector(correction,1,2*n_samples);
free_dvector(reference,1,2*n_samples);
free_ivector(FID,1,2*n_samples);

return(0);
} /* main */

/*****
*****/

void prntft(double data[],int nn)
{
    int n;

    printf("%4s %13s %13s %12s %13s\n",

```

```

        "n", "real(n)", "imag(n)", "real(N-
n)", "imag(N-n)");
    printf(" 0 %14.6f %12.6f %12.6f %12.6f\n",
        data[1],data[2],data[1],data[2]);
    for (n=3;n<=nn+1;n += 2) {
        printf("%4d %14.6f %12.6f %12.6f
%12.6f\n",
            ((n-1)/2),data[n],data[n+1],
            data[2*nn+3-n]);
    }
    printf(" press return to continue ... \n");
    getchar();
    return;
}

/*****
*****/

int read_data_file(void)
{
    char full_file_name[80];
    int i;

    strcpy(full_file_name,in_path);
    strcat(full_file_name,"p0000"); /*
    strcat(full_file_name,order_number);
    strcat(full_file_name,"00");
    strcat(full_file_name,file_name);
    strcat(full_file_name,".ima");

    printf("%s\n",full_file_name);

    if ((data_file=fopen(full_file_name,"rb"))==NULL)
return(1);

    /* read header */
    fseek(data_file,0x1094,SEEK_SET);
    scale_factor=read_VMS_float();
    fseek(data_file,0x1C1A,SEEK_SET);
    fgets(file_num,6,data_file);
    fseek(data_file,0x1C23,SEEK_SET);
    fgets(pat_name,29,data_file);
    fseek(data_file,0x1C75,SEEK_SET);
    fgets(study_date,10,data_file);
    fseek(data_file,0x1D1C,SEEK_SET);
    fscanf(data_file,"%d",&num_ACQs);

    printf("\n\n");
    printf("Name : %s\n",pat_name);
    printf("Study date : %s\n",study_date);
    printf("File number : %s\n",file_num);
    printf("%d acquisition(s), scale
%f\n",num_ACQs,scale_factor);

    /* extract data */
    fseek(data_file,0x2000,SEEK_SET);
    for (i=1; i <= n_samples; i++)
    {
        FID[2*i-1] = read_int();
        FID[2*i] = read_int();
    }

    fclose(data_file);
    printf("\n");

    return(0);
} /* read_data_file */

/*****
*****/

int read_int(void)
{
    long value, temp;

```

```

int j;
char b[2];

for (j=0; j<2; j++) b[j]=fgetc(data_file);

temp=b[1] & 0xFF;
temp=temp << 8;
value=temp | (b[0] & 0xFF);
if (value > ((32*1024)-1)) value=value-(64*1024);
return(value);
} /* read_int */

/*****
*****

long read_long(void)
{
    long value, temp;
    int j;
    char b[4];

    for (j=0; j<4; j++) b[j]=fgetc(data_file);

    value=b[3] & 0xFF;
    value=value << 24;
    temp=b[2] & 0xFF;
    temp=temp << 16;
    value=value | temp;
    temp=b[1] & 0xFF;
    temp=temp << 8;
    value=value | temp;
    value=value | (b[0] & 0xFF);
    return(value);
} /* read_long */

/*****
*****

double read_VMS_float(void)
/* read a VMS-style floating-point number */
{
    char byte1, byte2, byte3, byte4;
    char temp1, temp2, sign_byte;
    int sign, j;
    double sig, multiplier;
    double exponent, bit_value;

    byte1=fgetc(data_file);
    byte2=fgetc(data_file);
    byte3=fgetc(data_file);
    byte4=fgetc(data_file);

    /* get sign */
    sign_byte=(byte2 & 0x80);
    if (sign_byte == 0x00) sign=1; else sign=-1;

    /* get exponent */
    temp1=byte2 & 0x7F;
    temp2=byte1 & 0x80;
    if (temp2 == 0x00) exponent=(temp1 * 2) - 128;
    else exponent=(temp1 * 2) - 128 + 1;

    multiplier=exp((exponent)*log(2));

    /* get significand */
    sig=0.5; /* due to "hidden" bit */
    bit_value=0.25; /* value of MSB actually stored */

    temp1=byte1 & 0x7F;
    temp1=temp1 << 1;
    for (j=22; j>=16; j--

```

```

    {
        if ((temp1 & 0x80) == 0x80) sig=sig+bit_value;
        bit_value=bit_value/2;
        temp1=(temp1 & 0x7F) << 1;
    }
    temp2=byte4;
    for (j=15; j>=8; j--)
    {
        if ((temp2 & 0x80) == 0x80) sig=sig+bit_value;
        bit_value=bit_value/2;
        temp2=(temp2 & 0x7F) << 1;
    }
    temp1=byte3;
    for (j=7; j>=0; j--)
    {
        if ((temp1 & 0x80) == 0x80) sig=sig+bit_value;
        bit_value=bit_value/2;
        temp1=(temp1 & 0x7F) << 1;
    }

    /* now assemble the result */
    if (exponent == -128) return(0);
    else return(sign * multiplier * sig);
}

```

```

} /* read_VMS_float */

```

```

/*****
*****

```

```

void calc_phase_correction(void)

```

```

/* Use the water reference data to calculate the eddy current
phase correction as per Ordidge and Cresshull */

```

```

{
    int i;
    double theta;

    for (i=1; i<=n_samples; i++)
    {
        theta=atan2(reference[2*i],reference[2*i-1])-
12*pi/180+phi;
        correction[2*i-1]=cos(theta);
        correction[2*i] =sin(theta);
    }
}

```

```

} /* calc_phase_correction */

```

```

/*****
*****

```

```

void phase_correct(double data[])

```

```

/* apply the phase correction already calculated */

```

```

{
    int i;
    double temp_Re, temp_Im;

    for (i=1; i<=n_samples; i++)
    {
        temp_Re=data[2*i-1]*correction[2*i-
1]+data[2*i]*correction[2*i];
        temp_Im=data[2*i]*correction[2*i-1]-data[2*i-
1]*correction[2*i];
        data[2*i-1]=temp_Re;
        data[2*i] =temp_Im;
    }
}

```

```

} /* phase_correct */

```

```

/*****
*****

```

```

void filter(double data[])

```

```

/* Apply a Gaussian window in the time domain, equivalent to

```

```

line-broadening by B Hz in the frequency domain. */

{
    int i;
    double atten, factor;

    for (i=1; i<=n_samples; i++)
    {
        factor=1e-6*B*(i-1)*delta_t*pi;
        if (factor > 10) atten=0;
        else atten = exp(-factor*factor/(4*log(2)));
        data[2*i-1]=data[2*i-1] * atten;
        data[2*i] =data[2*i] * atten;
    }
} /* filter */

/*****
*****/

void transform(double data[])
{
    int i, isign;

    isign=1;
    fourl(data,n_samples,isign);

} /* transform */

/*****
*****/

void twiddle_spectrum(double data[])

/* re-arrange the spectrum so that zero frequency is in the middle,
and the metabolites are in the conventional order.
*/

{
    int i;

    for (i=1; i<n_samples; i++)
    {
        SWAP(data[i],data[i+n_samples]);
    }

    for (i=1; i<n_samples; i=i+2)
    {
        SWAP(data[i],data[2*n_samples-i]);
        SWAP(data[i+1],data[2*n_samples-i+1]);
    }

} /* twiddle_spectrum */

/*****
*****/

void store_template(void)

/* locate the corrected water peak in the reference data,
and extract a normalised template. Also estimate FWHM (in data
points). */

{

    int i, peak_pos, low_pt, high_pt;
    double factor;

    peak_pos=n_samples/2;
    water_max=0;
    for (i=n_samples/2-50; i<=n_samples/2+50; i++)
    {
        if (reference[2*i-1] > water_max)
            {
                water_max=reference[2*i-1];
                peak_pos=i;
            }

        template_area=0;
        for (i=0; i<=template_width; i++)
            {
                template[i]=
                    reference[2*(peak_pos-(template_width/2)+i)-
1]/water_max;
                template_area=template_area + template[i];
            }

        template_area=template_area * 2000.0/(2048*63.63); /* in Arb.
units */

        i=0;
        do
            {
                i=i+1;
            }
        while (reference[2*i-1] <= water_max/2);
        low_pt=i;

        i=peak_pos;
        do
            {
                i=i+1;
            }
        while (reference[2*i-1] > water_max/2);
        high_pt=i;

        FWHM=(high_pt-low_pt);
    }

} /* store_template */

/*****
*****/

void include_range(double hi, double lo)

/* include data points from 'hi' ppm to 'lo' ppm in the water-fitting
routine */

{
    int i, first_pt, last_pt;

    first_pt = 2048+(floor)((4.7-hi)*63.63*2048/2000);
    last_pt = 2048+(floor)((4.7-lo)*63.63*2048/2000);

    for (i=first_pt; i<=last_pt; i++)
    {
        ndata=ndata+1;
        x[ndata]=i;
        y[ndata]=spectrum[2*i-1];
    }

} /* include_range */

/*****
*****/

void func(double xdata, int n_terms)

/* evaluate 'nterms' of 'afunc' at x=xdata */

{
    int j;

    afunc[1]=1.0; /* constant term */

    temp=2*(xdata-2048)/FWHM;
    afunc[2]=1/(1+temp*temp); /* Real part of
Lorentzian */

```

```

    afunc[3]=(xdata-2048)/(1+temp*temp); /* Imag part
of Lorentzian */
} /* func */
/*****
*****/

void subtract_water(void)

/* Remove the residual water from the water-suppressed spectrum.
Adapted from Numerical Recipes 'svdfit' .
Also, calculate 'std dev' of the spectrum */

{
    #define TOL 1.0e-5

    int j,i;
    double wmax, thresh, sum, temp, sq_error;
    int point, start_pt, end_pt, num_pts;

    /* base the fit on metabolite-free sections of the
spectrum */
    include_range(4.15,4.05); include_range(3.85,3.5);
    include_range(2.8,2.5); include_range(0.7,-1.0);

    /* evaluate basis functions at the data points, and
hence prepare the
fitting matrix. */
    ma=3; /* number of terms in fit */
    for (i=1;i<=ndata;i++)
    {
        func(x[i],ma);
        for (j=1;j<=ma;j++) u[i][j]=afunc[j];
    }

    /* singular value decomposition */
    svdemp(u,ndata,ma,w,v);

    /* edit singular values */
    wmax=0.0;
    for (j=1;j<=ma;j++)
        if (w[j] > wmax) wmax=w[j];
    thresh=TOL*wmax;
    for (j=1;j<=ma;j++)
        if (w[j] < thresh) w[j]=0.0;

    /* back-substitute to find coefficients */
    svbksb(u,w,v,ndata,ma,y,a);

    /* evaluate chi-square over the fitting region */
    chisq=0.0;
    for (i=1;i<=ndata;i++)
    {
        func(x[i],ma);
        for (sum=0.0,j=1;j<=ma;j++) sum += a[j]*afunc[j];
        chisq += (temp=(y[i]-sum)/std_dev,temp*temp);
    }

    /* evaluate the fit over the whole spectrum */
    for (i=1;i<=n_samples;i++)
    {
        func((float)i,ma);
        for (fit[i]=0.0,j=1;j<=ma;j++) fit[i] += a[j]*afunc[j];
    }

    /* now subtract the water baseline from the data */
    for (i=1; i<=n_samples; i++)
    {
        spectrum[2*i]=spectrum[2*i-1]-fit[i];
        spectrum[2*i-1]=0;
    }

    /* estimate the standard deviation of the experimental data,
from a metabolite-free region of the spectrum */

    start_pt= 2048+((4.7-0.7)*63.63*2048.0/2000);
    end_pt= 2048+((4.7-(-1.0))*63.63*2048.0/2000);

```

```

    num_pts=0; sq_error=0;
    for (point=start_pt; point <=end_pt; point++)
    {
        sq_error=sq_error + spectrum[2*point] *
spectrum[2*point];
        num_pts=num_pts+1;
    }
    std_dev=sqrt(sq_error/num_pts);

    #undef TOL
} /* subtract_water */

/*****
*****/

void fit_singlet(double cs)

/* Chi-squared fitting of the reference template to a single peak
around chemical shift 'cs'. */

{
    int limit_step;
    int i, search_pt, est_pt, best_pt, centre_pt;
    int best_amp, amp_step;
    double max_value, min_error, sq_error, amp;
    double error_limit, temp;

    n_peaks=n_peaks+1;

    /* first locate the maximum amplitude around the search
position */
    search_pos[n_peaks]=cs;
    search_pt= 2048+((4.7-cs)*63.63*2048.0/2000);
    max_value=0; est_pt=search_pt; est_amp[n_peaks]=0;

    for (i=search_pt-4; i<=search_pt+4; i++)
    {
        if (spectrum[2*i] > max_value)
        {
            max_value=spectrum[2*i];
            est_pt=i;
            est_amp[n_peaks]=max_value;
        }
    }
    est_pos[n_peaks]=4.7-((est_pt-2048)*(2000.0/2048)/63.63);

    /* now optimize the template fit around the estimated
position */
    best_pt=est_pt; best_amp=100; min_error=1E8;
    /* shift the template */
    for (centre_pt= est_pt-2; centre_pt<=est_pt+2; centre_pt++)
    {
        for (amp_step=70; amp_step<=130; amp_step++) /* vary its
amplitude */
        {
            amp=(amp_step/100.0) * est_amp[n_peaks];
            sq_error=0;
            /* calculate squared error */
            for (i=0; i<=template_width; i++)
            {
                temp=amp*template[i]
-spectrum[2*(centre_pt+i-(template_width/2))];
                sq_error += temp*temp;
            }
            if (sq_error < min_error)
            {
                min_error=sq_error;
                best_pt=centre_pt;
                best_amp=amp_step;
            } /* sq_error < min_error */
        } /* amp_step */
    } /* centre_pt */

    fitted_pos[n_peaks]=4.7-(best_pt-2048)*(2000.0/2048)/63.63;
    fitted_amp[n_peaks]=(best_amp/100.0) * est_amp[n_peaks];

```

```

    fitted_error[n_peaks]=min_error;
goodness_of_fit[n_peaks]=min_error/(template_width*std_dev*std_dev);

    /* update model spectrum */
    i=best_pt-template_width/2;
    do
    {
        spectrum[2*i-1]=spectrum[2*i-1]
            + fitted_amp[n_peaks] *
template[template_width/2+i-best_pt];
        i=i+1;
    }
    while (i <= best_pt+template_width/2);
} /* fit_singlet */

/*****
*****

void fit_overlapping_peaks(double cs1, double cs2)

/* Chi-squared fitting of the reference template to two peaks
around chemical shifts 'cs1' and 'cs2'. */

{
    int pk, i, delta_E;
    double max_value, min_error, sq_error;
    double error_limit;
    int first_pt, last_pt, x, y;
    double chem_shift[3], amp[3];
    int search_pt[3], est_pt[3], best_pt[3], best_amp[3];
    int amp_step[3], centre_pt[3], limit_step[3];

    n_peaks=n_peaks+2;
    chem_shift[1]=cs1; chem_shift[2]=cs2;
    /* first locate the maximum amplitudes around the search
positions */
    for (pk=1; pk<=2; pk++)
    {
        search_pos[n_peaks-2+pk]=chem_shift[pk];
        search_pt[pk]= 2048+(4.7-
chem_shift[pk])*63.63*2048/2000;
        max_value=0; est_pt[pk]=search_pt[pk]; est_amp[n_peaks-
2+pk]=0;

        for (i=search_pt[pk]-4; i<=search_pt[pk]+4; i++)
        {
            if (spectrum[2*i] > max_value)
            {
                max_value=spectrum[2*i];
                est_pt[pk]=i;
                est_amp[n_peaks-2+pk]=max_value;
            }
        }
        est_pos[n_peaks-2+pk]=4.7-(est_pt[pk]-
2048)*(2000.0/2048)/63.63;
    } /* pk */

    for (pk=1; pk<=2; pk++)
    {
        best_pt[pk]=est_pt[pk]; best_amp[pk]=100;
    }

    /* now optimize the template fit around the estimated positions
*/
    min_error=1E8;

    for (centre_pt[1]=est_pt[1]-1; centre_pt[1]<=est_pt[1]+1;
centre_pt[1]++)
    {
        for (centre_pt[2]=est_pt[2]-1; centre_pt[2]<=est_pt[2]+1;
centre_pt[2]++)
        {
            delta_E=centre_pt[2]-centre_pt[1];
            for (amp_step[1]=70; amp_step[1]<=110; amp_step[1]++)
            {

```

```

amp[1]=(amp_step[1]/100.0) * est_amp[n_peaks-1];
/* vary amplitude of right peak */
for (amp_step[2]=70; amp_step[2]<=110; amp_step[2]++)
    {
        amp[2]=(amp_step[2]/100.0) * est_amp[n_peaks];

        sq_error=0; /* calculate squared error */
        for (i=0; i<=delta_E; i++) /* 1st region : left pk */
        {
            temp=amp[1]*template[i]
                -spectrum[2*(centre_pt[1]+i-(template_width/2))];
            sq_error += temp*temp;
        }
        for (i=delta_E+1; i<=template_width; i++)
            /* 2nd region : both peaks */
            {
                temp=amp[1]*template[i] +
amp[2]*template[i-delta_E]
                -spectrum[2*(centre_pt[1]+i-(template_width/2))];
                sq_error += temp*temp;
            }
        for (i=template_width+1; i<=template_width+delta_E;
i++)
            /*
3rd region : right peak */
            {
                temp=amp[2]*template[i-delta_E]
                -spectrum[2*(centre_pt[1]+i-(template_width/2))];
                sq_error += temp*temp;
            }

        if (sq_error < min_error)
        {
            min_error=sq_error;
            best_amp[1]=amp_step[1];
            best_amp[2]=amp_step[2];
            best_pt[1]=centre_pt[1];
            best_pt[2]=centre_pt[2];
        } /* sq_error < min_error */
    } /* amp_step[2] */
} /* amp_step[1] */
} /* centre_pt[2] */
} /* centre_pt[1] */

for (pk=1; pk<=2; pk++)
    {
        fitted_pos[n_peaks-2+pk]=4.7-(best_pt[pk]-
2048)*(2000.0/2048)/63.63;
        fitted_amp[n_peaks-
2+pk]=(best_amp[pk]/100.0)*est_amp[n_peaks-2+pk];
        fitted_error[n_peaks-2+pk]=min_error;
        goodness_of_fit[n_peaks-2+pk]=
min_error/((template_width+delta_E)*std_dev*std_dev);
    }

    /* update model spectrum */
    for (pk=1; pk<=2; pk++)
    {
        i=best_pt[pk]-template_width/2+1;
        do
        {
            spectrum[2*i-1]=spectrum[2*i-1]
                + fitted_amp[n_peaks-2+pk] *
template[template_width/2+i-best_pt[pk]];
            i=i+1;
        }
        while (i <= best_pt[pk]+template_width/2);
    }
} /* fit_overlapping_peaks */

/*****
*****

void fit_doublet(double cs, double J_coupling)

```

```

/* Chi-squared fitting of the reference template to an inverted
doublet
centred on chemical shift 'cs' with given J-coupling (in Hz) */
{
    int  pk, i, delta_E, amp_step, limit_step;
    double min_value, min_error, sq_error;
    double error_limit, sum;
    int  first_pt, last_pt, x, y, best_shift;
    double chem_shift[3], amp[3], temp;
    int  search_pt[3], est_pt[3], best_pt[3], best_amp[3];
    int  centre_pt[3];

    n_peaks=n_peaks+2;
    chem_shift[1]=cs+J_coupling/(2.0*63.63); /* convert to ppm
*/
    chem_shift[2]=cs-J_coupling/(2.0*63.63);
    /* first locate the minimum combined amplitude
    around the search position */
    for (pk=1; pk<=2; pk++)
    {
        search_pos[n_peaks-2+pk]=chem_shift[pk];
        search_pt[pk]= 2048+(4.7-
chem_shift[pk])*63.63*2048.0/2000;
        min_value=100;
        est_pt[pk]=search_pt[pk]; est_amp[n_peaks-2+pk]=0;
    }
    best_shift=0;
    for (i=-3; i<=3; i++)
    {
        sum=spectrum[2*(search_pt[1]+i)] +
spectrum[2*(search_pt[2]+i)];
        if (sum < min_value)
        {
            min_value=sum;
            best_shift=i;
        }
    }
    for (pk=1; pk<=2; pk++)
    {
        est_pt[pk]=search_pt[pk]+best_shift;
        est_pos[n_peaks-2+pk]=4.7-(est_pt[pk]-
2048)*(2000.0/2048)/63.63;
    }

    for (pk=1; pk<=2; pk++)
    {
        est_amp[n_peaks-2+pk]=
(spectrum[2*est_pt[pk]] + spectrum[2*(3-pk)])/2;
        best_pt[pk]=est_pt[pk]; best_amp[pk]=100;
    }

    /* now optimize the template fit around the estimated positions
*/
    min_error=1E8;

    for (centre_pt[1]=est_pt[1]-1; centre_pt[1]<=est_pt[1]+1;
centre_pt[1]++)
    {
        for (centre_pt[2]=est_pt[2]-1; centre_pt[2]<=est_pt[2]+1;
centre_pt[2]++)
        {
            delta_E=centre_pt[2]-centre_pt[1];
            /* vary amplitude of both peaks together */
            for (amp_step=70; amp_step<=110; amp_step++)
            {
                amp[1]=(amp_step/100) * est_amp[n_peaks-1];
                amp[2]=(amp_step/100) * est_amp[n_peaks];

                sq_error=0; /* calculate squared error */
                for (i=0; i<=delta_E; i++) /* 1st region : left pk */
                {
                    temp=amp[1]*template[i]
-spectrum[2*(centre_pt[1]+i-template_width/2)];
                    sq_error=sq_error + temp*temp;

```

```

}
for (i=delta_E+1; i<=template_width ; i++)
    /* 2nd region : both peaks */
    {
        temp=amp[1]*template[i] +
amp[2]*template[i-delta_E]
-spectrum[2*(centre_pt[1]+i-template_width/2)];
        sq_error=sq_error + temp*temp;
    }
for (i=template_width+1; i<=template_width+delta_E ;
i++)
    /* 3rd region : right peak */
    {
        temp=amp[2]*template[i-delta_E]
-spectrum[2*(centre_pt[1]+i-template_width/2)];
        sq_error=sq_error + temp*temp;
    }

    if (sq_error < min_error)
    {
        min_error=sq_error;
        best_amp[1]=amp_step;
        best_amp[2]=amp_step;
        best_pt[1]=centre_pt[1];
        best_pt[2]=centre_pt[2];
    } /* (sq_error < min_error) */
    } /* amp_step */
    } /* centre_pt[2] */
    } /* centre_pt[1] */

    for (pk=1; pk<=2; pk++)
    {
        fitted_pos[n_peaks-2+pk]=4.7-(best_pt[pk]-
2048)*(2000.0/2048)/63.63;
        fitted_amp[n_peaks-
2+pk]=(best_amp[pk]/100.0)*est_amp[n_peaks-2+pk];
        fitted_error[n_peaks-2+pk]=min_error;
        goodness_of_fit[n_peaks-2+pk]=
min_error/((template_width+delta_E)*std_dev*std_dev);
    }

    /* update model spectrum */
    for (pk=1; pk<=2; pk++)
    {
        i=best_pt[pk]-template_width/2+1;
        do
        {
            spectrum[2*i-1]=spectrum[2*i-1]
+ fitted_amp[n_peaks-2+pk] *
template[template_width/2+i-best_pt[pk]];
            i=i+1;
        }
        while (i <= best_pt[pk]+template_width/2);
    }

}

/* fit_doublet */

/*****
*****
void spectral_fitting(void)
/* Use a priori knowledge to model the spectrum */
{
    n_peaks=0;
    spec_shift=0.00;
    if (phantom)
    {
        fit_singlet(1.8+spec_shift);
        fit_doublet(1.2+spec_shift,7);

```



```

    }
    else
    {
fit_overlapping_peaks(3.22+spec_shift,3.03+spec_shift);
        fit_singlet(2.01+spec_shift);
    }

} /* spectral_fitting */

/*****
*****/

void save_data(double data[], char ext[])

/* save complex array 'data' with file extension 'ext' in a format
suitable for Delft software. First data point is save with half-
amplitude
so that subsequent FFTs work properly. */

{
    char label[30], full_file_name[80];
    int i;

    strcpy(full_file_name,in_path);
    strcat(full_file_name,order_number);
    strcat(full_file_name,"/");
    strcat(full_file_name,file_name);
    strcat(full_file_name,".");
    strcat(full_file_name,ext);

    save_file=fopen(full_file_name,"wb");

    /* header */
    header[0]=2*n_samples;
    header[1] = (float)delta_t/1000;
    for(i=0;i<64;i++)
    {
        fprintf(save_file,"%15.5E",header[i]);
        if(((i+1)%4)==0) fputc(0x0A,save_file);
    }

    /* real data */
    fprintf(save_file,"%17.10e ",data[1]/2);
    for (i=3; i <= 2*n_samples; i+=2)
    {
        fprintf(save_file,"%17.10e ",data[i]);
        if (((i+1)%8)==0) fputc(0x0A,save_file);
    }

    /* imag data */
    fprintf(save_file,"%17.10e ",data[2]/2);
    for (i=3; i <= 2*n_samples; i+=2)
    {
        fprintf(save_file,"%17.10e ",data[i+1]);
        if (((i+1)%8)==0) fputc(0x0A,save_file);
    }

    fclose(save_file);
} /* save_data */

/*****
*****/

void report_results(void)

{
    int peak;
    double area, pos;

    printf("\n\n%s Study date %s\n",pat_name,study_date);

```

```

    printf("Ref file %s, WS file
%s\n",ref_file_name,ws_file_name);
    printf("FWHM is %4.2fppm",2000.0*FWHM/(2048*63.63));
    printf(" (%3.1fHz line-broadening)\n",B);
    printf("Area of water ref is %5.0f sq units\n",
1000.0*(water_max*template_area*ref_scale/ref_ACQs));
    printf("Estimated data std dev is %5.3f\n",std_dev);
    printf("-----");
    printf("-----\n");

    for (peak=1; peak<=n_peaks; peak++)
    {
        area=1000.0*fitted_amp[peak]*template_area*ws_sc
ale/ws_ACQs;
        pos=fitted_pos[peak]-spec_shift;
        printf("Peak %d: area=%4.2f at %4.2fppm.
(Amplitude=%5.2f units, G=%5.1f)\n",
            peak,area,pos,fitted_amp[peak],goodness_of_fit[peak
]);
        } /* peak */
        printf("\n\n");
    }

/* report_results */

/*****
*****/

void fourl(double data[], int nn, int isign)

/* complex Fourier transform routine from 'Numerical Recipes'.
Replaces 'data' by its discrete Fourier transform if 'isign'=1,
or by 'nn' times its inverse Fourier transform if 'isign'=-1.
'data' is an array of length 2*'nn', holding interleaved real
and imaginary values.
*/

{
    int n,mmax,m,j,istep,i;
    double wtemp,wr,wpr,wpi,wi,theta;
    double tempr,tempi;

    n=nn << 1;
    j=1;
    for (i=1;i<n;i+=2) {
        if (j > i) {
            SWAP(data[j],data[i]);
            SWAP(data[j+1],data[i+1]);
        }
        m=n >> 1;
        while (m >= 2 && j > m) {
            j -= m;
            m >>= 1;
        }
        j += m;
    }
    mmax=2;
    while (n > mmax) {
        istep=2*mmax;
        theta=6.28318530717959/(isign*mmax);
        wtemp=sin(0.5*theta);
        wpr = -2.0*wtemp*wtemp;
        wpi=sin(theta);
        wr=1.0;
        wi=0.0;
        for (m=1;m<mmax;m+=2) {
            for (i=m;i<=n;i+=istep) {
                j=i+mmax;
                tempr=wr*data[j]-wi*data[j+1];
                tempi=wr*data[j+1]+wi*data[j];
                data[j]=data[i]-
                tempr;
                data[j+1]=data[i+1]-tempi;
            }
        }
    }

```

```

                                data[i] +=
temp;                                int i;
                                data[i+1] +=
temp;                                for(i=nrh;i>=nrl;i--) free((char*) (m[i]+ncl));
                                }                                free((char*) (m+nrl));
                                } /* free_imatrix */
                                wr=(wtemp=wr)*wpr-
wi*wpi+wr;                                /******
                                wi=wi*wpr+wtemp*wpi+wi;                                *****/
                                }                                double *dvector(int nl,int nh)
                                mmax=istep;                                /* Declare a dynamic, double precision vector with elements
                                }                                [nl..nh] */
                                } /* four1 */                                {
                                /******                                double *v;
                                *****/                                v=(double *)malloc((unsigned) (nh-
void nerror(char error_text[])                                nl+1)*sizeof(double));
/* Print an error message and exit the program */                                if (!v) nerror("allocation failure in dvector()");
{                                return v-nl;
    fprintf(stderr,"Numerical Recipes run-time                                } /* dvector */
    error...\n");                                /******
    fprintf(stderr,"%s\n",error_text);                                *****/
    fprintf(stderr,"...now exiting to system...\n");                                void free_dvector(double *v,int nl,int nh)
    exit(1);                                /* Free memory previously allocated by dvector() */
} /* nerror */                                {
                                free((char*) (v+nl));
/******                                } /* free_dvector */
*****/                                /******
int *ivector(int nl, int nh)                                *****/
{                                double **dmatrix(int nrl,int nrh,int ncl,int nch)
    int *v;                                /* Declare a dynamic, two dimensional double precision matrix
                                v=(int *)malloc((unsigned) (nh-nl+1)*sizeof(int));                                with
                                if (!v) nerror("allocation failure in ivector()");                                elements [nrl..nrh][ncl..nch] */
                                return v-nl;                                {
} /* ivector */                                int i;
                                double **m;
/******                                m=(double **) malloc((unsigned) (nrh-
*****/                                nrl+1)*sizeof(double*));
                                if (!m) nerror("allocation failure 1 in dmatrix()");
                                m -= nrl;
                                for(i=nrl;i<=nrh;i++) {
void free_ivector(int *v, int nl, int nh)                                m[i]=(double *) malloc((unsigned) (nch-
{                                ncl+1)*sizeof(double));
    free((char*) (v+nl));                                if (!m[i]) nerror("allocation failure 2 in
} /* free_ivector */                                dmatrix()");
                                m[i] -= ncl;
/******                                }
*****/                                return m;
                                } /* dmatrix */
                                /******
                                *****/
                                void free_dmatrix(double **m,int nrl,int nrh,int ncl,int nch)
                                /* Free memory previously allocated by dmatrix() */
                                {
                                int i;
                                for(i=nrh;i>=nrl;i--) free((char*) (m[i]+ncl));
                                free((char*) (m+nrl));
                                } /* free_dmatrix */
                                /******
                                *****/
                                void free_imatrix(int **m,int nrl,int nrh,int ncl,int nch)
                                {

```

```
void svbksb(double **u,double w[],double **v,int m,int n,double
b[],double x[])
```

```
/* Solves the matrix equation A.X=B for X. A is specified by
U.W.V'
with the arrays u[1..m][1..n] and v[1..n][1..n] as returned by
function svdcmp. The input data is b[1..m] and the solution vector
is x[1..n].
*/
```

```
{
    int jj,j,i;
    double s,*tmp;

    tmp=dvector(1,n);
    for (j=1;j<=n;j++) {
        s=0.0;
        if (w[j]) {
            for (i=1;i<=m;i++) s +=
u[i][j]*b[i];
        }
        tmp[j]=s;
    }
    for (j=1;j<=n;j++) {
        s=0.0;
        for (ij=1;jj<=n;jj++) s += v[ij][j]*tmp[jj];
        x[j]=s;
    }
    free_dvector(tmp,1,n);
} /* svbksb */
```

```
*****
*****
```

```
void svdcmp(double **a,int m,int n,double *w,double **v)
```

```
/* Singular value decomposition of matrix a[1..m][1..n] into
U.W.V'.
Matrix U replaces a on output. The singular values are in vector
w[1..n].
V (not its transpose V') is output as v[1..n][1..n].
```

```
NB m >= n. */
```

```
{
    int flag,i,its,j,jj,k,l,nm;
    double c,f,h,s,x,y,z;
    double anorm=0.0,g=0.0,scale=0.0;
    double *rv1;

    if (m < n) nrerror("SVDcmp: You must augment A
with extra zero rows");
    rv1=dvector(1,n);
    for (i=1;i<=n;i++) {
        l=i+1;
        rv1[i]=scale*g;
        g=s=scale=0.0;
        if (i <= m) {
            for (k=i;k<=m;k++) scale
+= fabs(a[k][i]);
            if (scale) {
                for (k=i;k<=m;k++) {
                    a[k][i] /= scale;
                    s
+= a[k][i]*a[k][i];
                }
                f=a[i][i];
                g = -
SIGN(sqrt(s),f);
                h=f*g-s;
                a[i][i]=f-g;
                if (i != n) {
                    for (j=l;j<=n;j++) {

```

```
for (s=0.0,k=i;k<=m;k++) s += a[k][i]*a[k][i];
```

```
f=s/h;
```

```
for (k=i;k<=m;k++) a[k][j] += f*a[k][i];
```

```
(k=i;k<=m;k++) a[k][i] *= scale;
```

```
w[i]=scale*g;
```

```
g=s=scale=0.0;
```

```
if (i <= m && i != n) {
    for (k=i;k<=n;k++) scale +=
fabs(a[i][k]);
    if (scale) {
```

```
(k=i;k<=n;k++) {
```

```
a[i][k] /= scale;
```

```
+= a[i][k]*a[i][k];
```

```
SIGN(sqrt(s),f);
```

```
(k=i;k<=n;k++) rv1[k]=a[i][k]/h;
```

```
for (j=l;j<=m;j++) {
```

```
for (s=0.0,k=l;k<=n;k++) s += a[j][k]*a[i][k];
```

```
for (k=l;k<=n;k++) a[j][k] += s*rv1[k];
```

```
(k=l;k<=n;k++) a[i][k] *= scale;
```

```
anorm=MAX(anorm,(fabs(w[i])+fabs(rv1[i])));
```

```
for (i=n;i>=1;i--) {
```

```
if (i < n) {
```

```
(j=l;j<=n;j++)
```

```
v[j][i]=(a[i][j]/a[i][i])/g;
```

```
(j=l;j<=n;j++) {
```

```
for (s=0.0,k=l;k<=n;k++) s += a[i][k]*v[k][j];
```

```
for (k=l;k<=n;k++) v[k][j] += s*v[k][i];
```

```
v[i][j]=v[j][i]=0.0;
```

```
v[i][i]=1.0;
```

```
g=rv1[i];
```

```
l=i;
```

```
for (i=n;i>=1;i--) {
```

```
l=i+1;
```

```
g=w[i];
```

```
if (i < n)
```

```
a[i][j]=0.0;
```

```
if (g) {
```

```
g=1.0/g;
```

```
if (i != n) {
```

```

                                for
(j=1;j<=n;j++) {
    for (s=0.0,k=1;k<=m;k++) s += a[k][i]*a[k][j];
    f=(s/a[i][i])*g;
    for (k=i;k<=m;k++) a[k][j] += f*a[k][i];
}
g;
                                } else {
a[j][i]=0.0;
                                for (j=i;j<=m;j++) a[j][i] *=
}
                                ++a[i][i];
}
for (k=n;k>=1;k--) {
    for (its=1;its<=30;its++) {
        flag=1;
        for (l=k;l>=1;l--) {
            nm=l-1;
            if
(fabs(rv1[l])+anorm == anorm) {
                flag=0;
                break;
            }
            if
(fabs(w[nm])+anorm == anorm) break;
        }
        if (flag) {
            c=0.0;
            s=1.0;
            for
(i=1;i<=k;i++) {
                f=s*rv1[i];
                if
(fabs(f)+anorm != anorm) {
                    g=w[i];
                    h=PYTHAG(f,g);
                    w[i]=h;
                    h=1.0/h;
                    c=g*h;
                    s=(-f*h);
                    for (j=1;j<=m;j++) {
                        y=a[j][nm];
                        z=a[j][i];
                        a[j][nm]=y*c+z*s;
                        a[j][i]=z*c-y*s;
                    }
                }
            }
            z=w[k];
            if (l == k) {
                if (z < 0.0) {
                    w[k] = -z;
                    for (j=1;j<=n;j++) v[j][k]=(-v[j][k]);
                }
                break;
            }
        }
    }
}
                                if (its == 30) nerror("No
convergence in 30 SVDcmp iterations");
                                x=w[l];
                                nm=k-1;
                                y=w[nm];
                                g=rv1[nm];
                                h=rv1[k];
                                f=((y-z)*(y+z)+(g-
h)*(g+h))/(2.0*h*y);
                                g=PYTHAG(f,1.0);
                                f=((x-
z)*(x+z)+h*((y/(f+SIGN(g,f))-h))/x;
                                c=s=1.0;
                                for (j=l;j<=m;j++) {
                                    i=j+1;
                                    g=rv1[i];
                                    y=w[i];
                                    h=s*g;
                                    g=c*g;
                                }
                                z=PYTHAG(f,h);
                                rv1[j]=z;
                                c=f/z;
                                s=h/z;
                                f=x*c+g*s;
                                g=g*c-x*s;
                                h=y*s;
                                y=y*c;
                                for
(ij=1;jj<=n;jj++) {
                                    x=v[ij][j];
                                    z=v[ij][i];
                                    v[ij][j]=x*c+z*s;
                                    v[ij][i]=z*c-x*s;
                                }
                                z=PYTHAG(f,h);
                                w[j]=z;
                                if (z) {
                                    }
                                f=(c*g)+(s*y);
                                x=(c*y)-(s*g);
                                for
(ij=1;jj<=m;jj++) {
                                    y=a[ij][i];
                                    z=a[ij][j];
                                    a[ij][j]=y*c+z*s;
                                    a[ij][i]=z*c-y*s;
                                }
                                }
                                rv1[l]=0.0;
                                rv1[k]=f;
                                w[k]=x;
                                }
                                }
                                free_dvector(rv1,1,n);
} /* svdcmp */
#undef SIGN
#undef MAX
#undef PYTHAG
/*****
*****/

```

```

void svdvar(double **v,int ma,double w[],double **cvm)

/* Calculates the covariance matrix cvm[1..ma][1..ma] of the fit
for the ma parameters obtained by svd fitting. Call this routine
with
the matrices v[1..ma][1..ma] and w[1..ma] as returned by svdfit. */

{
    int k,j,i;
    double sum,*wti;

    wti=dvector(1,ma);
    for (i=1;i<=ma;i++) {
        wti[i]=0.0;
        if (w[i]) wti[i]=1.0/(w[i]*w[i]);
    }
    for (i=1;i<=ma;i++) {
        for (j=1;j<=i;j++) {
            for
(sum=0.0,k=1;k<=ma;k++) sum += v[i][k]*v[j][k]*wti[k];
            cvm[j][i]=cvm[i][j]=sum;
        }
    }
    free_dvector(wti,1,ma);
} /* svdvar */

/*****
*****

/*****normalise.c*****/
*****
Program that performs the B1 normalisation profile operation on a
metabolite image. The program calls upon a water phantom
spectroscopic image of the water resonance (calculated by the
area_integration function in centrefill2.c). The metabolite image
matrix is then divided by the water uniform phantom image on a
voxel by voxel basis(after shifting the VOI of the two images to
account for chemical shift). The normalised images are stored in
files of the form *.naa_new etc.

Jim Wild January 1997
*****
*****
#include <stdio.h>
#include <stdlib.h>
#include <string.h>
#include <math.h>
/*#include "/images/numrecipes/recipes/nrutil.h"*/

char in_path[50] = "/image1/jim_csi_temp";
char out_path[50] = "/image1/jim_csi_temp";

char full_file_name1[80],
      full_file_name2[80],in_file_number[20],full_file_name3[80],full_file_name4[80];
char pat_dir[20];
double **profile;
double **pro_matlab;

void save_profile(void);
double **dmatrix(int nrl,int nrh,int ncl,int nch);
void free_dmatrix(double**m,int nrl,int nrh,int ncl,int nch);
void nrerror(char error_text[]);
FILE *in_file1,*in_file2,*save_file1,*save_file2,*save_file4;
#define n_rows 16
#define n_cols 16
#define first_row 1
#define last_row 16
#define first_col 1
#define last_col 16
#define eps 10 /*prevents division by zero water area*/

```

```

main()
{
    int i, row, col;

    printf("\n\nPatient name :");
    scanf("%s",pat_dir);

    strcpy(full_file_name,out_path);
    strcat(full_file_name,pat_dir);
    strcat(full_file_name,"/");
    strcat(full_file_name,"prof_cr_new");
    save_file1=fopen(full_file_name,"wb");
    printf("Saving data in %s\n",full_file_name);

    strcpy(full_file_name3,out_path);
    strcat(full_file_name3,pat_dir);
    strcat(full_file_name3,"/");
    strcat(full_file_name3,"00045_cr_new");
    save_file2=fopen(full_file_name3,"wb");
    printf("Saving data in %s\n",full_file_name3);

    strcpy(full_file_name4,out_path);
    strcat(full_file_name4,pat_dir);
    strcat(full_file_name4,"/");
    strcat(full_file_name4,"prof_cr_old");
    save_file4=fopen(full_file_name4,"wb");
    printf("Saving data in %s\n",full_file_name4);

    strcpy(full_file_name1,out_path);
    strcat(full_file_name1,pat_dir);
    strcat(full_file_name1,"/");
    strcat(full_file_name1,"00045_cr");
    in_file1=fopen(full_file_name1,"rb");
    printf("Reading data from %s\n",full_file_name1);

    strcpy(full_file_name2,out_path);
    strcat(full_file_name2,"normalise");
    strcat(full_file_name2,"/");
    strcat(full_file_name2,"peak_area");
    strcat(full_file_name2,in_file_number);
    in_file2=fopen(full_file_name2,"rb");
    printf("Reading data from %s\n",full_file_name2);

    save_profile();

    fclose(in_file1);
    fclose(in_file2);

    fclose(save_file1);
    fclose(save_file2);
    fclose(save_file4);

    return(0);
} /* main */
/*****
*****
void save_profile(void)
{
    float data, area;
    int row,col,dumcol,dumrow;
    /* factor 0.416 used for 90*90 set ,0.736 for 105*105
and 90*75 sets and 1 for 75*75 set (ratio of maxima)*/
    profile=dmatrix(1,n_rows,1,n_cols);
    pro_matlab=dmatrix(1,n_rows,1,n_cols);

    for (col=1; col<=n_cols; col++)
    {
        for (row=1; row<=n_rows; row++)
        {
            fscanf(in_file1,"%d %d
%n",&dumcol,&dumrow,&data);

            fscanf(in_file2,"%f",&area);
            /*printf("column,row and
data %d %d %f\n",dumcol,dumrow,data);*/

```

```

profile[row][col]=1.2263e6*1*data/(area+eps);
                    pro_matlab[row][col]=data;
                }
            }

printf("Read data from input to matrix profile \n");

for (col=first_col; col<=last_col; col++)
{
    for (row=first_row; row<=last_row;
row++)
        {
            fprintf(save_file1,"%f\t",profile[row][col]);
            fprintf(save_file4,"%f\t",
pro_matlab[row][col]);
        }
        fprintf(save_file1,"\n");
        fprintf(save_file4,"\n");
    }
    fprintf(save_file1,"\n");
    fprintf(save_file4,"\n");

for (col=first_col; col<=last_col; col++)
{
    for (row=first_row; row<=last_row;
row++)
        {
            fprintf(save_file2,"%d %d %f\n",col,
row, profile[row][col]);
        }
    }

free_dmatrix(profile,1,n_rows,1,n_cols);
free_dmatrix(pro_matlab,1,n_rows,1,n_cols);
}
/*****
*****/

double **dmatrix(int nrl,int nrh,int ncl,int nch)

/* Declare a dynamic, two dimensional double precision matrix
with
elements [nrl..nrh][ncl..nch] */

{
    int i;
    double **m;

    m=(double **) malloc((unsigned) (nrh-
nrl+1)*sizeof(double*));
    if (!m) nerror("allocation failure 1 in dmatrix()");
    m -= nrl;

    for(i=nrl;i<=nrh;i++) {
        m[i]=(double *) malloc((unsigned) (nch-
ncl+1)*sizeof(double));
        if (!m[i]) nerror("allocation failure 2 in
dmatrix()");
        m[i] -= ncl;
    }
    return m;
} /* dmatrix */

/*****
*****/

/*****
*****/

void free_dmatrix(double**m,int nrl,int nrh,int ncl,int nch)

```

```

/* Free memory previously allocated by dmatrix() */
{
    int i;

    for(i=nrh;i>=nrl;i--) free((char*) (m[i]+ncl));
    free((char*) (m+nrl));
} /* free_dmatrix */

/*****
*****/

void nerror(char error_text[])

/* Print an error message and exit the program */
{
    fprintf(stderr,"Numerical Recipes run-time
error...\n");
    fprintf(stderr,"%s\n",error_text);
    fprintf(stderr,"...now exiting to system...\n");
    exit(1);
} /* nerror */

/*****
*****/

diff.c*****
differences two mets files input patient name followed by two
mets file numbers padded with zeros to three figures e.g. 003.mets
T1 weighting in steam -differences accounted for by
multiplying 2nd file by a factor of 1.17
Jim Wild January 1997
*****
*****/

#include <stdio.h>
#include <stdlib.h>
#include <string.h>
#include <math.h>

#define n_samples 4096
#define delta_t 250.0 /* sample interval in us */
#define row_spacing 200 /* 200 for humans, 2000 for Siemens
sphere */
#define n_fpts 4096 /* number of frequency domain points */

/* define parameters for saving of spectral data */
#define first_point 1
#define last_point 4096
#define st_pt 1803
#define np 30
#define SWAP(a,b) tempr=(a);(a)=(b);(b)=tempr

char in_path[50] = "image3/mri/csi/";
char out_path[50]= "image3/mri/csi/";

int first_pt, last_pt, n_pts, file_num1,file_num2;
float diff[4096], data_pt[4096];
char full_file_name[80], in_file_number[20];
FILE *in_file1,*in_file2, *save_file;
char pat_dir[20];

void difference();
void nerror(char error_text[]);

/*****
*****/

```

```

int main(int argc, char *argv[])
{
    int i;
    double freq;

    long f_r;
    char *endptr;

    file_num1 = strtol(argv[2], &endptr, 10);
    file_num2 = strtol(argv[3], &endptr, 10);

    for (i=0; i<argc; i++) printf("%d %s\n", i, argv[i]);

    strcpy(full_file_name, out_path);
    strcat(full_file_name, argv[1]);
    strcat(full_file_name, ".");
    sprintf(in_file_number, "%d", file_num2,
file_num1);
    strcat(full_file_name, in_file_number);
    strcat(full_file_name, "difference");
    save_file = fopen(full_file_name, "wb");
    printf("Saving data in %s\n", full_file_name);

    strcpy(full_file_name, out_path);
    strcat(full_file_name, argv[1]);
    strcat(full_file_name, "/0");
    sprintf(in_file_number, "%d", file_num1);
    strcat(full_file_name, in_file_number);
    strcat(full_file_name, ".mets");
    in_file1 = fopen(full_file_name, "rb");
    printf("Reading data from %s\n", full_file_name);

    strcpy(full_file_name, out_path);
    strcat(full_file_name, argv[1]);
    strcat(full_file_name, "/0");
    sprintf(in_file_number, "%d", file_num2);
    strcat(full_file_name, in_file_number);
    strcat(full_file_name, ".mets");
    in_file2 = fopen(full_file_name, "rb");
    printf("Reading data from %s\n", full_file_name);

    printf("calling differencing routine\n");
    difference();

    fclose(in_file1);
    fclose(in_file2);

    fclose(save_file);

    return(0);
} /* main */

/*****
*****/

void difference()
/* save the selected part of the spectrum corresponding to voxel
(row,col) */
{
    int i;
    float dummy1, dummy2, data1, data2;

    printf("reading two files\n");
    for (i=1; i<=4096; i++)
    {
        fscanf(in_file1, "%f %f\n", &dummy1, &data1);
        fscanf(in_file2, "%f %f\n", &dummy2, &data2);
        diff[i] = data1 - data2;
        data_pt[i] = dummy1;
    }
    printf("two mets files read\n");
    for (i=1; i<=4096; i+=1)
    {
        fprintf(save_file, "%f %f\n ", data_pt[i],
diff[i]);
    }
} /* save_area */

/*****
*****/
double **dmatrix(int nrl, int nrh, int ncl, int nch)
/* Declare a dynamic, two dimensional double precision matrix
with
elements [nrl..nrh][ncl..nch] */
{
    int i;
    double **m;

    m = (double **) malloc((unsigned) (nrh-
nrl+1)*sizeof(double*));
    if (!m) perror("allocation failure 1 in dmatrix()");
    m -= nrl;

    for (i=nrl; i<=nrh; i++) {
        m[i] = (double *) malloc((unsigned) (nch-
ncl+1)*sizeof(double));
        if (!m[i]) perror("allocation failure 2 in
dmatrix()");
        m[i] -= ncl;
    }
    return m;
} /* dmatrix */

/*****
*****/
void free_dmatrix(double **m, int nrl, int nrh, int ncl, int nch)
/* Free memory previously allocated by dmatrix() */
{
    int i;

    for (i=nrh; i>=nrl; i--) free((char*) (m[i]+ncl));
    free((char*) (m+nrl));
} /* free_dmatrix */

/*****
*****/
void perror(char error_text[])
/* Print an error message and exit the program */
{
    fprintf(stderr, "Numerical Recipes run-time
error...\n");
    fprintf(stderr, "%s\n", error_text);
    fprintf(stderr, "...now exiting to system...\n");
    exit(1);
} /* perror */

/*****
*****/
/*Maximum entropy model fitting routine -armatd.c

```

This program needs compiling with the NRC programs, nrutil.c, memcof.c and evlmem.c found in the directory /usr/utlils/numrecipes/recipes/. The number of linear prediction coefficients (M) as calculated by memcof.c is set by the parameter "order". The program evlmem.c then calculates the Power Spectral Density estimate based on these M l.p. coefficients. To get an MEM estimate of the real part of the spectrum the sqrt of the PSD is calculated in the routine save_arma(void)
Jim Wild 14.1.98 */

```
#include <stdio.h>
#include <stdlib.h>
#include <string.h>
#include <math.h>
#include "/usr/utlils/numrecipes/recipes/nrutil.h"

/* define parameters for calculation of arma coefficients */
#define order 400
#define n_samples 1024

#define SWAP(a,b) tempr=(a);(a)=(b);(b)=tempr;
char out_path[50]= "/image3/mri/csi/h_i/";

char full_file_name[80], in_file_number[20];
FILE *in_file, *save_file;
char pat_dir[20];

void save_arma();
float *armain,*armout,*xms;
void memcof(float data[], int n, int m, float *xms, float d[]);
float evlmem(float fdt, float d[], int m, float xms);
float *vector(long nl, long nh);
void free_vector(float *v, long nl, long nh);
void nerror(char error_text[]);

/*****
*****/

int main(int argc, char *argv[])
{
    int i, row, col;
    int row_num, col_num;

    double freq;
    long f_r;
    char *endptr, fid_number[10];

    for (i=0; i<argc; i++) printf("%d %s\n", i, argv[i]);

    row_num = strtol(argv[2], &endptr, 10);
    col_num = strtol(argv[3], &endptr, 10);

    strcpy(full_file_name, out_path);
    strcat(full_file_name, argv[1]);
    strcat(full_file_name, "/");
    strcat(full_file_name, "arma_coef");
    sprintf(fid_number, "%d_%d", row_num, col_num);
    strcat(full_file_name, fid_number);
    save_file = fopen(full_file_name, "wb");
    printf("Saving data in %s\n", full_file_name);

    row = row_num;
    col = col_num;

    strcpy(full_file_name, out_path);
    strcat(full_file_name, argv[1]);
    strcat(full_file_name, "/");
    strcat(full_file_name, "real_td");
    sprintf(fid_number, "%d_%d", row, col);
    strcat(full_file_name, fid_number);
    in_file = fopen(full_file_name, "rb");
    printf("Reading data from
%s\n", full_file_name);

    save_arma();
    printf("save arma called\n");

```

```
fclose(in_file);

fclose(save_file);

return(0);

} /* main */

/*****
*****/

void save_arma(void)

/* breakdown the fid in to m (order) LP coefficients with a super
imposed variance (noise) of xms*, the range of the paramter fdt is
set at 0.05-0.3 to represent the frequency range of 4-0 ppm*/

{
    int i, j;
    float data, fdt;
    armain = vector(1, n_samples);
    armout = vector(1, order*0.5);
    xms = vector(1, order*0.5);

    for (i=1; i<= n_samples; i++)
    {
        /* printf("Reading data from input file
data point %d\n", i); */
        fscanf(in_file, "%f\n", &data);
        /* printf("Read data from data
point %d\n", i); */
        armain[i] = data;

        memcof(armain, i, order, xms, armout);
    }
    fprintf(save_file, "\n");

    for (fdt=0.05; fdt<= 0.3; fdt+=0.0001)
    {
        evlmem(fdt, armout, order, *xms);
        fprintf(save_file, "%f %f\n", fdt, sqrt(-
1*evlmem(fdt, armout, order, *xms)));
    }
    printf("P.S.D calculated from ARMA coefficients by
subroutine evlmem.c\n");
    /* printf("saving arma coefficients\n");
    for (j=1; j<= order; j++)
    {
        fprintf(save_file, "%d %f %f\n", j, *xms,
armout[j]);
    } */
} /* save_arma */

/*****
*****/

```


Appendix 2 ii.

Pargen pulse sequence listings

```

=====
!          loaded from file  __DUA0:[SPEC]HOPE.UDB;1      !
! sequence compatible version VD2/GBS2                !
! saving date      12-AUG-1996 13:10:39.64          !
! owner           USER                               !
=====
!
! .comment= ---- SPECTROSCOPY HOPE SPIN ECHO SEQUENCE -----
! .comment= ---- FOR FUNCTION VOI -----
! .comment= ---- ECHO TIME 290 MSEC -----
!
!===== global parameters =====!
!
! .available directives are controlling the possible features
! that are available with this sequence file
!
! .available/SEQUENCE_TYPE = SPECTROSCOPY
! .available/FILE_ACCESS_OPTIMIZATION = no
! .available/PHASE_IMAGE = no
! .available/SLICE_SHIFT = YES
! .available/RECTANGULAR_FOV = no
! .available/FILTER/GAUSS= no /HANNING= no /FERMI= no /default=none
! .available/INTERPOLATIONS/SINC= no /default=none
! .available/MATRIX/SQUARE= no /RECTANGULAR= no /HALF_FOURIER = no
! .available/MATRIX/OVERSAMPLING= no
!
! .dialog parameters for the dialog choices in NUMARIS
!
! .dialog/SEQUENCE_STRING = SE
! .dialog/MATRIX_SIZE /min= 64/max= 4096/inc= BASE2 /def= 2048
! .dialog/LINES /min= 1/max= 1/inc= BASE2 /def= 1
! .dialog/COLUMNS /min= 64/max= 4096/inc= BASE2 /def= 2048
! .dialog/ACQUISITIONS /min= 1/max= 16384/inc= BASE2 /def= 1
! .dialog/FLIP_ANGLE_ALPHA /none
! .dialog/3D_PART_THICKNESS/min= 0.000
! .dialog/3D_PARTITIONS /min= 0
! .dialog/TR /num= 1/min= 1500000/max=20000000/inc= 1000
! .dialog/TI /none
! .dialog/TE /num= 1/min= 67500/max= 200000/inc= 500
! .dialog/TE /num= 2/min= 135000/max= 400000/inc= 500
! .dialog/TD /none
! .dialog/MSMA = no /OFFCENTER = no
! .dialog/RETRO_GATING = NO
! .dialog/SAT_REGIONS /min= 3/max= 3/inc= 1
! .dialog/SAT_DELAY /none
! .dialog/SAT_THICK /min= 10.000/max= 40.000/inc= 0.100
! .dialog/SLICES /min= 1/max= 1/inc= 1
! .dialog/SLICE_THICK /min= 10.000/max= 10.000/inc= 1.000
! .dialog/SLICE_DIST /min= 0.000/max= 0.000/inc= 0.100
! .dialog/VOI /min= 1/max= 1/inc= 1
! .dialog/FOV /min= 500.000/max= 500.000/inc= 1.000
! .dialog/OBLIQUE_SLICES /single = NO/double = NO
! .dialog/DWELL_TIME /min= 10/max= 4000/inc= 1
! .dialog/PREPARING_SCANS/min= 0/max= 100/inc= 2/def= 0
! .dialog/RF_BAND_WIDTH /none
! .dialog/GATING_RATIO /none
! .dialog/PHASES /none
!
! .dps (Data Processing System) directives for the
! preprocessing and FFT software in the BSP & VAX
!
! .dps/CALC_ALGO = FID
! .dps/LOOP_STRUCTURE = SE
! .dps/LINE_FFT = no
! .dps/OFFSET_IGNORE = no
! .dps/ANGIO_SUBTRACTION = no
! .dps/INTERNAL_FILTER = YES
! .dps/NO_ME_COMBINATION = no
! .dps/ECHO_ALTERNATING = YES

```

```

.dps/DIRAC_ELIMINATION = no
.dps/3D_RESOLUTION_FFT = no
.dps/TIMEOUT_FACTOR = 1.000
.dps/CSI_SEQUENCE = no
.dps/TURBO_PHASE_CORRECTION = no
.dps/TURBO_FILTER /none
.dps/ADC_ALTERNATE = NO
!
!
!
!
! .gradampl the logical reference gradient amplitudes in [mT/m] for
!       matrix size 256, FOV 500mm , slice thickness 10 mm
!
.gradampl/GP= 1.000000/GR= 1.000000/GS= none
.gradampl/GS_MIN= none /GS_MAX= none
!
! .msc parameters for the Measurement and Sequence Controller
!
.msc/GRADIENT_DELAY_CORRECTION = YES
.msc/LOGICAL_GRADIENTS = no
.msc/LINES_PER_SEGMENT/value= 0
.msc/TR_TRUNCATION/max= 0
!
!
.external/ SRF_FILENAME = none
.external/ R_P_FILENAME = none
.external/GRAD_TAB_FILENAME = none
.external/GRAD_SHAPES_FILENAME = none
!
.adj/READOUT_TIME = 1024000
.adj/TRANSMITTER_LPF_FREQUENCY = 0
.adj/REC_LINES = 1
!
!
===== sequence timing =====
!TIMINGTABLE
!Time| RF-Cabinet| ADC | Gradient references |Sync-|Relative
! usec| 01 | 02 | |phasecode| readout |selection| Bits| Time
.grad_rastertime = 50
.do /OFFSET /REP= 1 ! offset correction measurement +
2560 OSC0 2560
1024000 ON 1026560
SAFIL01 !
3440 1030000
.enddo ! offset correction measurement +
.do /ACQUISITIONS ! acquisitions loop - - - - +
.do /PREPARE ! prepare the inner loops * - - +
.do /SLICES ! slice loop, I=SLICE/SERIES - - +
.t_marker /begin_tr
.slice_def /slice
.slice_def /sat = 1
1000 1000
2560 OSC0 3560
25600 SRF01 29160
1600 30760
51200 PULS02 81960
2000 PULS02 83960
2560 SAT02 PULS02 86520
660 87180
125 87305
TEFIL01 !
4750 92055
.slice_def /sat = 2
1000 PULS03 93055
1000 PULS03 94055
22000 PULS03 116055
1780 PULS03 117835
2560 SAT03 PULS03 120395

```

```

1780      PULS03 PULS04      122175
22000    PULS03      144175
1000     PULS03      145175
1000      146175
TEFIL01      !
125      146300
125      146425
TEFIL02      !
1000      147425
.slice_def/sat = 3
9440      156865
1000      157865
1000      PULS05 158865
1000      PULS05 159865
23000    PULS05 182865
2720    PULS05 185585
2560 SAT04      PULS05 188145
2720    PULS05 190865
23000    PULS05 213865
1000     PULS05 214865
1000      215865
TEFIL02      !
125      215990
4750     220740
1024000  ON      1244740
SAFIL01      !
3000      1247740
57000    PULS06 1304740
11150    1315890
560      1316450
184050   1500500
TRFIL01      !
.t_marker/end_tr
.RF / ALTERNATE
.ADC / ALTERNATE
.enddo      ! slice loop -----+
.enddo      ! prepare loop -+*+-+*+-+
.enddo      ! acquisitions loop -----+
.END / TIMINGTABLE
!
!===== rf types definitions =====!
.RFTABLE
!Name| Slice |Flip |Phase|Altern.|Scale|Supp-| Family name |
!(type)|(position)|angle|angle| code | pt | pts.| (Calc. Algo.) |
SRF01  I    90  0  ++  1  512 GAUSSIAN #60.000000
SAT02   90  0  +-  2  512 NORMAL #1.000000
SAT03   90  90 ++  3  512 NORMAL #1.000000
SAT04   90  270 ++  4  512 NORMAL #1.000000
.END / RFTABLE
!
!
!===== gradient pulse definitions =====!
.PULSETABLE
!Pulse| pulse | Ramp Up | Ramp Down |
!Name |amplitude|algo| time |algo| time |
PULS01 #0.000001 NORM 1000 NORM 1000
PULS02 #2.000000 NORM 1000 NORM 1000
PULS03 #2.000000 NORM 1000 NORM 1000
PULS04 #2.000000 NORM 1000 NORM 1000
PULS05 #2.000000 NORM 1000 NORM 1000
PULS06 #-2.000000 NORM 1000 NORM 1000
.END / PULSETABLE
!
.END

!=====
! loaded from file __DUA0:[SEQUENCE]HOPE_CSI.UDB !

```

```

! sequence compatible version VD2/GBS2          !
!   saving date      3-JUL-1997 16:46:07.22    !
!   owner           USER                      !
!=====!
!
.comment= * INTERLEAVED HOPE SI SEQUENCE *****
.comment= * (DUAL ACQ'S AT TE=292 ms & TE=297.5 ms *
.comment= * 2D HCSI SEQUENCE (3D IMAGING MODE) **
.comment= * FLEXIBLE FOV, echo time 292-297.5 ***
.comment= *----- Jim Wild 1997 -
!
!===== global parameters =====!
!
! .available directives are controlling the possible features
!   that are available with this sequence file
!
.available/SEQUENCE_TYPE = IMAGING
.available/FILE_ACCESS_OPTIMIZATION = no
.available/PHASE_IMAGE = no
.available/SLICE_SHIFT = no
.available/RECTANGULAR_FOV = no
.available/FILTER/GAUSS= no /HANNING= no /FERMI= no /default=none
.available/INTERPOLATIONS/SINC= no /default=none
.available/MATRIX/SQUARE= YES /RECTANGULAR= YES /HALF_FOURIER = no
.available/MATRIX/OVERSAMPLING= YES
!
! .dialog parameters for the dialog choices in NUMARIS
!
.dialog/SEQUENCE_STRING = SE
.dialog/MATRIX_SIZE /min= 1024/max= 1024/inc= BASE2 /def= 1024
.dialog/LINES /min= 8/max= 8/inc= BASE2 /def= 8
.dialog/COLUMNS /min= 1024/max= 1024/inc= BASE2 /def= 1024
.dialog/ACQUISITIONS /min= 1/max= 512/inc= 1/def= 1
.dialog/FLIP_ANGLE_ALPHA /none
.dialog/3D_PART_THICKNESS/min= 0.031
.dialog/3D_PARTITIONS /min= 8
.dialog/TR /num= 1/min= 3119500/max= 3119500/inc= 500
.dialog/TI /none
.dialog/TE /num= 1/min= 292000/max= 292000/inc= 1000
.dialog/TE /num= 2/min= 1697500/max= 1697500/inc= 1000
.dialog/TD /none
.dialog/MSMA = no /OFFCENTER = no
.dialog/RETRO_GATING = NO
.dialog/SAT_REGIONS /none
.dialog/SAT_DELAY /none
.dialog/SAT_THICK /none
.dialog/SLICES /min= 1/max= 1/inc= 1
.dialog/SLICE_THICK /min= 10.000/max= 10.000/inc= 1.000
.dialog/SLICE_DIST /min= 0.000/max= 0.000/inc= 0.100
.dialog/VOI /none
.dialog/FOV /min= 40.000/max= 400.000/inc= 1.000
.dialog/OBLIQUE_SLICES /single = YES/double = NO
.dialog/DWELL_TIME /min= 15/max= 4000/inc= 1
.dialog/PREPARING_SCANS/min= 0/max= 100/inc= 1/def= 4
.dialog/RF_BAND_WIDTH /none
.dialog/GATING_RATIO /none
.dialog/PHASES /none
!
! .dps (Data Processing System) directives for the
! preprocessing and FFT software in the BSP & VAX
!
.dps/CALC_ALGO = none
.dps/LOOP_STRUCTURE = SE
.dps/LINE_FFT = no
.dps/OFFSET_IGNORE = no
.dps/ANGIO_SUBTRACTION = no
.dps/INTERNAL_FILTER = no
.dps/NO_ME_COMBINATION = no
.dps/ECHO_ALTERNATING = YES

```

```

.dps/DIRAC_ELIMINATION = no
.dps/3D_RESOLUTION_FFT = no
.dps/TIMEOUT_FACTOR = 2.000
.dps/CSI_SEQUENCE = YES
.dps/TURBO_PHASE_CORRECTION = no
.dps/TURBO_FILTER /none
.dps/ADC_ALTERNATE = NO
!
!
!
!
! gradampl the logical reference gradient amplitudes in [mT/m] for
!       matrix size 256, FOV 500mm , slice thickness 10 mm
!
gradampl/GP= 1.000000/GR= 1.000000/GS= none
gradampl/GS_MIN= none /GS_MAX= none
!
! .msc parameters for the Measurement and Sequence Controller
!
.msc/GRADIENT_DELAY_CORRECTION = YES
.msc/LOGICAL_GRADIENTS = YES
.msc/LINES_PER_SEGMENT/value= 0
.msc/TR_TRUNCATION/max= 0
!
!
.external/ SRF_FILENAME = MR_SYSDEV:[MR]SRF_1HCSI.DAT
.external/ R_P_FILENAME = none
.external/GRAD_TAB_FILENAME = none
.external/GRAD_SHAPES_FILENAME = none
!
.adj/READOUT_TIME = 1024000
.adj/TRANSMITTER_LPF_FREQUENCY = 0
.adj/REC_LINES = 1
!
!
===== sequence timing =====
.TIMINGTABLE
!Time/ | RF-Cabinet| ADC | Gradient references |Sync-|Relative
! usec| 01| 02| |phasecode| readout |selection| Bits| Time
.grad_rastertime = 20
.do /OFFSET /REP= 1 ! offset correction measurement +
1000 OSC0 1000
1024000 ON 1025000
.enddo ! offset correction measurement +
.do /LINES ! fourier lines loop -----+
.do /ACQUISITIONS ! acquisitions loop -----+
.do /3DPARTITIONS ! 3D partition loop -----+
.do /PREPARE ! prepare the inner loops * - - +
.do /FIXED /REP= 1 ! fixed repetition loop - - - - +
.t_marker /begin_tr
1000 1000
1000 OSC0 2000
45840 47840
25600 SRF01 73440
1000 74440
51200 PULS02 125640
1000 PULS02 126640
1000 PULS02 127640
5120 SRF02 PULS02 132760
4890 137650
39250 176900
1000 TAB01 TAB02 177900
15500 193400
1000 PULS04 194400
5240 PULS06 PULS04 199640
1000 PULS06 200640
5120 SRF03 PULS06 205760
5240 PULS07 PULS05 211000
1000 PULS05 212000

```

```

3060          PULS03          215060
2640          217700
28740        246440
78500        324940
TEFIL01      !
4300          PULS08          329240
16400        PULS08          345640
1000         PULS08          346640
5120 SRF04   PULS08          351760
16400        PULS09          368160
4300         PULS09          372460
700          373160
39250        412410
TEFIL01      !
9790         422200
1024000     ON              1446200
60000        PULS10          1506200
50800        1557000
1000         1558000
1000         OSC0 1559000
45840        1604840
25600 SRF01  1630440
1000         1631440
51200        PULS02          1682640
1000         PULS02          1683640
1000         PULS02          1684640
5120 SRF02   PULS02          1689760
4890         1694650
375          1695025
40250        1735275
1000         TAB01 TAB02    1736275
15500        1751775
1000         PULS04          1752775
5240         PULS06 PULS04    1758015
1000         PULS06          1759015
5120 SRF03   PULS06          1764135
5240         PULS07 PULS05    1769375
1000         PULS05          1770375
3060         PULS03          1773435
2640         1776075
28740        1804815
375          1805190
80500        1885690
375          1886065
TEFIL02      !
4300          PULS08          1890365
16400        PULS08          1906765
1000         PULS08          1907765
5120 SRF04   PULS08          1912885
16400        PULS09          1929285
4300         PULS09          1933585
700          1934285
TEFIL02      !
40250        1974535
375          1974910
9790         1984700
1024000     ON              3008700
60000        PULS10          3068700
50800        3119500
TRFIL01      !
.t_marker /end_tr
.RF / ALTERNATE
.ADC / ALTERNATE
.enddo      ! fixed repetition loop ----+
.enddo      ! prepare loop - + * + - + * + - +
.enddo      ! 3D partition loop -----+
.enddo      ! acquisitions loop -----+
.enddo      ! fourier lines loop -----+
.END / TIMINGTABLE

```

```

!
===== rf types definitions =====
!
.RFTABLE
! Name | Slice | Flip | Phase | Altern. | Scale | Supp- | Family name |
!(type)|(position)|angle|angle| code | pt | pts. | (Calc. Algo.) |
SRF01 I 100 0 ++ 1 512 GAUSSIAN #60.000000
SRF02 I 90 0 +- 2 512 SRF.SINCP
SRF03 I 180 0 ++ 3 512 SRF.SINCR
SRF04 I 180 0 ++ 4 512 SRF.SINCS
.END / RFTABLE
!
!
===== gradient table definitions =====
!
.GRADTABLE
!TAB-| Steps | Amplitudes | Calc| Ramp Up | Ramp Down |
!Name|through| First | Last | Offset | algo|algo| time | algo| time |
TAB01 3D 0.046970 -0.04697 0.000000 3D NORM 1000 NORM 1000
TAB02 LINES 6.012640 -6.01264 0.000000 NORM NORM 1000 NORM 1000
.END / GRADTABLE
!
!
===== gradient pulse definitions =====
!
.PULSETABLE
!Pulse| pulse | Ramp Up | Ramp Down |
!Name |amplitude|algo| time | algo| time |
PULS01 #2.000000 NORM 1000 NORM 1000
PULS02 #0.800000 NORM 1000 NORM 1000
PULS03 #0.800000 NORM 1000 NORM 1000
PULS04 #3.000000 NORM 1000 NORM 1000
PULS05 #3.000000 NORM 1000 NORM 1000
PULS06 #0.800000 NORM 1000 NORM 1000
PULS07 #0.800000 NORM 1000 NORM 1000
PULS08 #3.000000 NORM 1000 NORM 1000
PULS09 #3.000000 NORM 1000 NORM 1000
PULS10 #-3.000000 NORM 1000 NORM 1000
.END / PULSETABLE
!
.END

=====
!
! loaded from file __DUA0:[SPEC]STEAM_TM_TE_140.UDB !
! sequence compatible version VD2/GBS2 !
! saving date 13-OCT-1997 17:34:12.23 !
! owner USER !
=====
!
!
.comment= ----- SPECTROSCOPY STEAM SEQUENCE -----
.comment= ----- FOR FUNCTION VOI -----
.comment= ----- ECHO TIME 145 MSEC -----
.comment= ----- VARIABLE MIXING TIME -----
.comment= ----- JIM WILD 1997 -----
!
!
===== global parameters =====
!
!
! .available directives are controlling the possible features
! that are available with this sequence file
!
.available/SEQUENCE_TYPE = SPECTROSCOPY
.available/FILE_ACCESS_OPTIMIZATION = no
.available/PHASE_IMAGE = no
.available/SLICE_SHIFT = YES
.available/RECTANGULAR_FOV = no
.available/FILTER/GAUSS= no /HANNING= no /FERMI= no /default=none
.available/INTERPOLATIONS/SINC= no /default=none
.available/MATRIX/SQUARE= no /RECTANGULAR= no /HALF_FOURIER = no
.available/MATRIX/OVERSAMPLING= no
!

```



```

! .dialog    parameters for the dialog choices in NUMARIS
!
.dialog/SEQUENCE_STRING = STE
.dialog/MATRIX_SIZE /min= 64/max= 4096/inc= BASE2 /def= 2048
.dialog/LINES      /min= 1/max= 1/inc= BASE2 /def= 1
.dialog/COLUMNS   /min= 64/max= 4096/inc= BASE2 /def= 2048
.dialog/ACQUISITIONS /min= 1/max= 16384/inc= BASE2 /def= 1
.dialog/FLIP_ANGLE_ALPHA /none
.dialog/3D_PART_THICKNESS/min= 0.000
.dialog/3D_PARTITIONS /min= 0
.dialog/TR         /num= 1/min= 1500000/max=20000000/inc= 1000
.dialog/TI         /none
.dialog/TE         /num= 1/min= 140000/max= 300000/inc= 250
.dialog/TD         /none
.dialog/MSMA = no /OFFCENTER = no
.dialog/RETRO_GATING = NO
.dialog/SAT_REGIONS /min= 3/max= 3/inc= 1
.dialog/SAT_DELAY /none
.dialog/SAT_THICK /min= 20.000/max= 40.000/inc= 0.100
.dialog/SLICES /min= 1/max= 1/inc= 1
.dialog/SLICE_THICK /min= 10.000/max= 10.000/inc= 1.000
.dialog/SLICE_DIST /min= 0.000/max= 0.000/inc= 0.100
.dialog/VOI /min= 1/max= 1/inc= 1
.dialog/FOV /min= 500.000/max= 500.000/inc= 1.000
.dialog/OBLIQUE_SLICES /single = NO/double = NO
.dialog/DWELL_TIME /min= 10/max= 4000/inc= 1
.dialog/PREPARING_SCANS/min= 0/max= 100/inc= 2/def= 0
.dialog/RF_BAND_WIDTH /none
.dialog/GATING_RATIO /none
.dialog/PHASES /none
!
! .dps (Data Processing System) directives for the
! preprocessing and FFT software in the BSP & VAX
!
.dps/CALC_ALGO = FID
.dps/LOOP_STRUCTURE = SE
.dps/LINE_FFT = no
.dps/OFFSET_IGNORE = no
.dps/ANGIO_SUBTRACTION = no
.dps/INTERNAL_FILTER = YES
.dps/NO_ME_COMBINATION = no
.dps/ECHO_ALTERNATING = no
.dps/DIRAC_ELIMINATION = no
.dps/3D_RESOLUTION_FFT = no
.dps/TIMEOUT_FACTOR = 1.000
.dps/CSI_SEQUENCE = no
.dps/TURBO_PHASE_CORRECTION = no
.dps/TURBO_FILTER /none
.dps/ADC_ALTERNATE = NO
!
!
!
!
! .gradampl the logical reference gradient amplitudes in [mT/m] for
! matrix size 256, FOV 500mm , slice thickness 10 mm
!
.gradampl/GP= 1.000000/GR= 1.000000/GS= none
.gradampl/GS_MIN= none /GS_MAX= none
!
! .msc parameters for the Measurement and Sequence Controller
!
.msc/GRADIENT_DELAY_CORRECTION = YES
.msc/LOGICAL_GRADIENTS = no
.msc/LINES_PER_SEGMENT/value= 0
.msc/TR_TRUNCATION/max= 0
!
!
.external/ SRF_FILENAME = none
.external/ R_P_FILENAME = none

```

```

.external/GRAD_TAB_FILENAME = none
.external/GRAD_SHAPES_FILENAME = none
!
.adj/READOUT_TIME = 1024000
.adj/TRANSMITTER_LPF_FREQUENCY = 0
.adj/REC_LINES = 1
!
!
===== sequence timing =====
.TIMINGTABLE
!Time/| RF-Cabinet| ADC | Gradient references |Sync|Relative
! usec | 01 | 02 | |phasecode| readout |selection| Bits| Time
.grad_rastertime = 50
.do /OFFSET /REP= 1 ! offset correction measurement +
2560 OSC0 2560
1024000 ON 1026560
SAFIL01 !
3440 1030000
.enddo ! offset correction measurement +
.do /ACQUISITIONS ! acquisitions loop -----+
.do /PREPARE ! prepare the inner loops *--+
.do /SLICES ! slice loop, I=SLICE/SERIES --+
.do /FIXED /REP= 1 ! fixed repetition loop ----+
.t_marker /begin_tr
.slice_def /slice
.slice_def /sat = 1
1000 1000
2560 OSC0 3560
25600 SRF01 29160
1600 30760
51200 PULS03 81960
2000 PULS03 83960
2560 SAT02 PULS03 86520
1600 88120
2780 PULS04 90900
45680 136580
.slice_def /sat = 2
1000 137580
8000 PULS05 145580
2780 PULS06 PULS05 148360
2500 150860
1600 152460
1500 PULS02 153960
2560 SAT03 PULS02 156520
23940 PULS02 PULS07 180460
TEFIL01 !
1000 181460
.slice_def /sat = 3
1000 182460
1500 PULS07 183960
2560 SAT04 PULS07 186520
15220 PULS07 201740
2500 204240
51000 255240
1024000 ON 1279240
SAFIL01 !
3920 1283160
35000 PULS08 1318160
3000 1321160
183840 1505000
TRFIL01 !
.t_marker /end_tr
.enddo ! fixed repetition loop ----+
.RF / ALTERNATE
.enddo ! slice loop -----+
.enddo ! prepare loop -+*+-+*+-+
.enddo ! acquisitions loop -----+
.END / TIMINGTABLE
!

```

```
===== rf types definitions =====!
```

```
.RFTABLE
```

```
! Name | Slice | Flip | Phase | Altern. | Scale | Supp- | Family name |
!(type)|(position)|angle|angle| code | pt | pts.| (Calc. Algo.) |
SRF01 I 90 0 ++ 1 512 GAUSSIAN #60.000000
SAT02 90 0 +- 2 512 NORMAL #1.000000
SAT03 90 0 ++ 3 512 NORMAL #1.000000
SAT04 90 0 +- 4 512 NORMAL #1.000000
```

```
.END / RFTABLE
```

```
!
```

```
!
```

```
!
```

```
===== gradient pulse definitions =====!
```

```
.PULSETABLE
```

```
!Pulse| pulse | Ramp Up | Ramp Down |
!Name |amplitude|algo| time |algo| time |
PULS01 #0.000001 NORM 1000 NORM 1000
PULS02 #2.000000 NORM 1000 NORM 1000
PULS03 #2.000000 NORM 1000 NORM 1000
PULS04 #-1.280000 NORM 1000 NORM 1000
PULS05 #3.154000 NORM 1000 NORM 1000
PULS06 #-1.640000 NORM 1000 NORM 1000
PULS07 #2.000000 NORM 1000 NORM 1000
PULS08 #-3.441000 NORM 1000 NORM 1000
```

```
.END / PULSETABLE
```

```
!
```

```
.END
```

Appendix 3.

Publications and presentations

Publications

Wild JM, Marshall I, Normalisation of metabolite images in ^1H NMR spectroscopic imaging, *Magn. Reson. Imag.* 15, 9, 1057-1069, 1997.

Marshall I, **Wild JM**. Calculations and experimental studies of the lineshape of the lactate doublet in PRESS localised ^1H MRS, *Magn. Reson. Med.* 38, 415-419, 1997.

Wild JM, Marshall I, In vivo lactate editing in single voxel proton spectroscopy and proton spectroscopic imaging by homonuclear polarisation transfer. *Magn. Reson. Imag.* (in press)

Marshall I, **Wild JM**. A systematic study of the lactate lineshape in PRESS-localised ^1H MRS. *Magn. Reson. Med.* (in press)

Wardlaw JM, Marshall I, **Wild JM**, Dennis MS, Cannon J, Lewis SC. Studies of acute ischaemic stroke with proton magnetic resonance spectroscopy-the relationship between time from onset, neurological deficit, metabolite abnormalities in the infarct, blood flow and clinical outcome. *submitted Stroke*

Posters and presentations

Marshall I, **Wild JM**, Wardlaw JM, Cannon J. Proton Spectroscopic Imaging in Stroke, British Chapter ISMRM, 1995.

Marshall I, **Wild JM**, Wardlaw JM. Spectral distortion caused by PRESS excitation, BIR meeting on spectral localisation, June 1996.

Wardlaw JM, Marshall I, **Wild JM**, Cannon J, Dennis M. The relationship between lactate, infarct swelling and blood flow to the infarct in patients with a recent ischaemic stroke. 3rd World Stroke Congress, September 1996.

Wild JM, Marshall I, Wardlaw JM, Cannon J. Normalised ^1H spectroscopic images of stroke patients', 2nd meeting of British Chapter ISMRM 1996.

Wild JM, Marshall I. Lactate editing in selective excitation spectroscopy. Seventh annual NMR symposium, London, 1997

Wild JM, Marshall I, Wardlaw JM, Cannon J. A quantitative study of brain metabolites in stroke using PRESS localised ^1H NMR spectroscopic imaging. In abs. 3rd conf. IPEM, 51, 1997.

Wild JM, Marshall I. Normalisation of metabolite images in ^1H NMR spectroscopic imaging, p1457 ISMRM 1997.

Marshall I, **Wild JM**. Calculations and experimental studies of the lineshape of the lactate doublet in PRESS ^1H NMR spectra, p1416 ISMRM 1997.

Wild JM, Marshall I. In vivo lactate editing in single voxel proton spectroscopy and proton spectroscopic imaging by homonuclear polarisation transfer. Accepted for oral presentation ISMRM 1998.

Macmillan CSA, **Wild JM**, Armiatge PA, Wardlaw JM, Marshall I, Bastin ME, Cannon J, Andrews PJ. Value of combined proton MRS and diffusion weighted imaging following traumatic brain injury. Neuro-anaesthesia and neuro-ITU, Genk, Belgium, 1998.

Wild JM, Marshall I 'Artefacts introduced by zero order phase correction in proton NMR spectroscopy'. Submitted ESMRMB 1998.

Wild JM, Wardlaw JM, Marshall I, Signorini DF, Cannon J. 'NAA distribution in ^1H spectroscopic images of stroke patients- metabolite evidence of a "penumbra"' Submitted ESMRMB 1998.

Wild JM, Macmillan CSA, Wardlaw JM, Marshall I, Easton VJ, Cannon J, Andrews PJD. ' ^1H spectroscopic imaging of acute head injury - evidence of diffuse axonal injury'. Submitted ESMRMB 1998.

References

1. Aaslid R., Markwalder T.H., Nomes H. Non invasive trans-cranial doppler ultrasound recording flow velocity in basal cerebral arteries. *J Neurosurg.*, 57, 769-774, 1982.
2. Adalsteinsson E., Irrazabal P., Spielman D.M., Macovski A. Three-dimensional spectroscopic imaging with time-varying gradients. *Magn.Reson.Med*, 33, 461-466, 1995.
3. Adalsteinsson E., Spielman D., Wright G.A., Pauly J.M., Meyer C.H., Macovski A. Incorporating lactate/lipid discrimination into a spectroscopic imaging sequence. *Magn. Reson. Med.* 30, 124-30, 1993.
4. Armitage P.A., Marshall I., Wardlaw J.M., Cannon J. Diffusion anisotropy in stroke. *In Abs. 14th meeting ESMRMB*, 491, 1997.
5. Axel L., Morton D. Correction of phase wrapping in MRI. *Med Phys.* 1,2, 284-287, 1989.
6. Barker P.B., Gillard J.H., van Zijl P.C.M., Oppenheimer S.M., Bryan R.N. Proton magnetic resonance spectroscopic imaging in acute stroke: identification of the ischaemic penumbra. *In Abs. 2nd Scientific Meeting of SMR*, Berkeley CA, 186, 1994
7. Bachelard H., Badar-Goffer R. NMR Spectroscopy in Neurochemistry. *J of Neuro-Chemistry*, 61, 2, 1993.
8. Bachert P., Müller C., Hess T., Essig M., Lorenz W.J. Detection of lactate in a human brain tumour in vivo by means of localised two dimensional ¹H zero quantum coherence NMR spectroscopy. *In Abs. 3rd Scientific Meeting of SMR*, Berkeley CA, p1670, 1995.
9. Bailes D.R., Bryant D.J., Case H.A., Collins A.G., Cox I.J., Hall A.S., Harman R.R., Khenia S., McArthur P., Ross B.D., Young I.R. In vivo implementation of three-dimensional phase encoded spectroscopy with a correction for field inhomogeneity. *J.Magn.Reson*, 77, 460-470, 1988.
10. Baker L.L., Kucharczyk J., Sevick R.J., Mitorovitch J., Moseley M.E. Recent advances in MR imaging/spectroscopy of cerebral ischaemia. *AJR*, 156, 113-143, 1991.
11. Bárány M. In vivo ¹H spectroscopy in humans at 1.5 T. *Radiology*, 167, pp 839-44, 1988.
12. Barker G.J., Mareci T.H. Suppression of artefacts in multiple-echo magnetic resonance. *J. Magn. Reson.*, 83, 11-28, 1989.
13. Barkhuijsen H., de Beer R, van Ormondt D. Error Theory for Time Domain Analysis with Linear Prediction and SVD. *J.Magn.Reson*, 67,371-75, 1986.
14. Barkhuijsen H., de Beer R, Boveé W.M.M.J., van Ormondt D. Retrieval of Frequencies, Amplitudes, Damping Factors and Phases from T-Domain Signals Using a Linear Least Squares Procedure. *J.Magn.Reson*, 61, 465, 1985.
15. Behar K., Ogoh T. Characterisation of Macro-molecule Resonances in the ¹H NMR Spectrum of Rat Brain. *Magn.Reson.Med*, 30, 38-44, 1993.
16. Behar K., Rothman D.L., Spencer D.D., Petroff O.A.C. Analysis of Macro-molecule Resonances in ¹H NMR Spectra in Human Brain. *Magn.Reson.Med*, 32, 294-302, 1994.
17. Berkelbach Van Der Sprenkel J.W. Cerebral Lactate Detected by Regional Proton MRS in a Patient with a Cerebral Infarction. *Stroke*, 19,12, 1988.
18. Bizzi A., Righini A., Turner R., le Bihan D. Bockworst K.H., Alger J.R. Imaging local reperfusion injury following global ischaemia with diffusion weighted magnetic resonance imaging and ¹H magnetic resonance spectroscopy. *Magn. Reson. Imag.* 14, 581-592, 1996.
19. Blamire A.M., Graham G.D., Rothman D.L., Prichard J.W. Proton Spectroscopy of Human Stroke: Assessment of Transverse Relaxation Times and Partial Volume Effects in Single Voxel Steam MRS. *Magn. Reson.Imag*, 12, 8, 1227-35, 1994.
20. Bland J.M., Altman D.G. Statistical methods for assessing agreement between two methods of clinical measurement. *Lancet* 8 Feb, 307-310, 1986.
21. Bloch F. *Phys. Rev*, 70, 460, 1946.
22. Bottomley P.A., Hart H.R., Edelstein W.A., Schenk J.F., Smith L.S., Leue W.M., Mueller O.M., Redington R.W. *Lancet*, 8344, 273.
23. Bottomley P.A., Foster T.H., Darrow R.D. Depth Resolved Surface Coil Spectroscopy (DRESS) for In-Vivo H-1, P-31 and C-13 NMR. *J.Magn.Reson.*, 59, 338, 1984.
24. Bottomley P.A. Spatial localisation in NMR spectroscopy in vivo. *Ann. N.Y. Acad. Sci.* 508, 333-348, 1987.

25. Breerton I.M., Rose S.E., Galloway G.J., Moxon L.N., Doddrell D.M. In vivo volume selective metabolite editing via correlated z-order. *Magn.Reson.Med.*, 16, 460-469, 1990.
26. Broich K., Alavi A., Kushner M. Positron emission tomography in cerebrovascular disorders. *Seminars in Nuclear Medicine.*, 4, 224-232, 1992.
27. Brown M.A., Semelka R.C. MRI Basic Principles and Applications. *Wiley-Liss*, 1995.
28. Brown T.R., Kincaid B.M., Ugurbil D. NMR chemical shift imaging in three dimensions. *Proc. Natl. Acad. Sci., USA*, 79, 3523-3526, 1982.
29. Bruhn H., Frahm J., Gyngell M.L., Merboldt K.D., Hänicke W., Sauter R. Cerebral Metabolism in Man After Acute Stroke: New Observations Using Localised Proton NMR Spectroscopy. *Magn.Reson.Med*, 9, 126-131, 1989.
30. Bryan R.N., Levy L.M., Whitlow W.D., Killian J.M., Prezios T.J., Rosario J.A. Diagnosis of acute cerebral infarction: comparison of CT and MRI. *AJNR*, 12, 611-620, 1991.
31. Bunse M., Jung W.I., Zutt A., Schick F., Dietze G., Lutz O. Determination of the pH dependent optimised echo time for quantitative spectroscopy of lactate with PRESS and HOPE *In Abs 5th scientific meeting ISMRM*, 487, 1995.
32. Bunse M., Jung W.I., Zutt A., Schick F., Dietze G., Lutz O. HOPE a new lactate editing method. *J.Magn. Reson.*, 109, 270-274, 1995.
33. Callaghan P.T. Principles of Nuclear Magnetic Resonance Microscopy. *Oxford University Press*. 1995.
34. Canet D. Nuclear Magnetic Resonance- Concepts and Methods. *Wiley*. 1996.
35. Chatam J.C., Forder J.R. An investigation into the interaction between lactate and protein using ¹H-NMR spectroscopy: implications for the NMR visibility of lactate in biological systems. *In Abs 3rd scientific meeting SMR*, 261, 1995.
36. Chew Y.I. Error Analysis of ¹H-MRS Measurement of Cerebral Metabolite Concentrations. *In Abs. 2nd scientific meeting , SMR*, 43, 1994.
37. Choe B.Y., Suh T.S., Choi K.H., Shinn K.S., Park C.K., Kang J.K. Neuronal dysfunction in patients with closed head injury evaluated by in-vivo ¹H magnetic resonance spectroscopy. *Investigative Radiology*, 30, 502-506, 1995.
38. Choi D.W. Glutamate neurotoxicity and diseases of the nervous system. *Neuron*, 623-634, 1988.
39. Christiansen P. Reduced N-AA Content in the Frontal Part of the Brain in Patients with Probable Alzheimer Disease. *Magn.Reson.Imag*, 13, 3, 457-62, 1995.
40. Christiansen P. In Vivo Quantification of Brain Metabolites by ¹H-MRS Using Water as an Internal Standard; *Magn.Reson.Imag*, 11, 1, 107, 1993.
41. Christiansen P., Toft P., Larsson H.B.W., Stubgaard M., Henriksen O. Concentration of N-AA, Cr + Pcr, and Cho in Different Parts of the Brain in Adulthood and Senium. *Magn.Reson.Imag*, 11, 799-806, 1993.
42. Christiansen P., Toft P.B., Gideon P., Danielsen E.R., Ring P. M-R Visible Water Content in Human Brain: A proton MRS Study. *Magn.Reson.Imag*, 12, 8, 1994.
43. Cohen Y., Sanada T., Pitts L.H., Chang L.H., Nishimura M.C., Weinstein P.R., Litt L. James T.L. Surface coil imaging: time and spatial evolution of lactate production following fluid percussion brain injury. *Magn. Reson. Med*, 17, 225-236, 1991.
44. Daniell G.J., Hore P.J. Maximum entropy and NMR - a new approach. *J.Magn.Reson* 84, 515-536, 1989.
45. Danielsen E.R. *In Abs. 1st meeting SMR*, 976, 1993.
46. Danielsen E.R., Michaelis T., Ross B.D. Three Methods of Calibration in Quantitative Proton MR Spectroscopy. *J.Magn.Reson*, 106, 287-291, 1995.
47. Davie C.A., Greenwood R., Moseley I.F., McDonald W.I., Miller D.H. An Investigation of Diffuse Axonal Injury After Closed Head Trauma. *Proc.ABN*, 6, 1995.
48. de Beer R., Michels F., van Ormondt D., van Tongeren B.P.O., Luyten P.R., van Vroonhoven H. Reduced Lipid Contamination in In Vivo ¹H-MRSI Using Time Domain Fitting and Neural Network Classification., *Magn.Reson.Imag*, 11, 1019-1026, 1993.
49. de Beer R., van Ormondt D., Pijnappel W.W.F., van der Veen J.W.C. Quantitative Analysis of MR Signals in the Time Domain., *Isr. J of Chem.* 28, 249-261, 1988.
50. de Graaf A.A., Luyten P.R., den Hollander J.A., Heindel W., Bovee W.M.M.J., Lactate imaging of the human brain at 1.5 T using a double-quantum filter. *Magn. Reson. Med*, 30, 231-235, 1993.

51. Desluc M.A., Ni f., Ling G.C., Improvement of Linear Prediction Processing of NMR Spectra Having Very Low Signal to Noise. *J.Magn.Reson*, 73, 548-552, 1987.
52. Dickinson W.C., *Phys. Rev*, 77, 736, 1950.
53. Diop A., Kölbl W., Michel D., Briquet A., Graveron-Denilly D. Full Automation of Quantification of in Vivo NMR by LPSVD(CR) and EPLPSVD. *J.Magn.Reson*, 103, 217-221, 1994.
54. Doyle T.J., Pathak R., Wolinsky J.S., Narayana P.A. Automated Proton Spectroscopic Image Processing. *J.Magn.Reson* 106, 58-63, 1994.
55. Dumoulin C.L., Williams E.A. Suppression of uncoupled spins by single-quantum homonuclear polarisation transfer. *J. Magn. Reson.*, 66, 86-92, 1986.
56. Duyn J.H., Matson G.B., Maudsley A.A., Hugg J.W., Weiner M.W. Human Brain Infarction-PMRS. *Radiology*, 183, 711-718, 1992.
57. Duyn J.H., Matson G.B., Maudsley A.A., Weiner M.W. 3-D Phase Encoding ¹H Spectroscopic Imaging of Human Brain. *Magn.,Reson., Imag.*, 10, 315-319, 1992.
58. Duyn J.H., van Gelderen P., Barker P., Frank J.A., Mattay V.S., Moonen C.T.W. 3D bolus tracking with frequency shifted BURST MRI., *J, Comp, Assist, Tomog.* 18, 680-687, 1994.
59. Duyn J.H., Frank J.A., Moonen C.T.W. Incorporation of lactate measurement in mult-spin echo proton spectroscopic imaging. *Magn. Reson. Med.*, 33, 101-7, 1995.
60. Duyn J.H., Moonen C.T.W. Fast proton spectroscopic imaging of human brain using multiple spin-echoes. *Magn. Reson. Med.*, 30, 409-14, 1993.
61. Edelman R.R., Siewert B., Darby D.G., Thangaraj V., Nobre A.C., Mesulam M.M, Warach S. Qualitative mapping of cerebral blood flow and functional localisation with echo planar MR imaging and signal targeting with alternating radio frequency. *Radiology*, 192, 513-520, 1994.
62. Edelstein W.A., Hutchinson J.M.S., Johnson G., Redpath T.W. Spin-warp NMR imaging and applications of human whole body imaging. *Physics in Medicine and Biology*, 25, 751-753.
63. Ernst T., Hennig J. Coupling Effects in Volume Selective ¹H Spectroscopy of Major Brain Metabolites. *Magn.Reson.Med*, 21, 82-96, 1991.
64. Farrar T.C., Harriman J.E. *Density matrix theory and its application in NMR spectroscopy.* Farragut Press, Madison, WI, 1992.
65. Fazekas F., Kapeller P., Stollberger R., Offenbacher H., Schmidt R., Valettisch H., Fazekas G., Scheuher R., Flooh E., Lechner H. A follow up study of cerebral ischaemic stroke with ¹H MRS and TC-99- HMPAO SPECT. *Cerebrovasc. Dis*, 255, 1995.
66. Felber S.R., Aichner F.T., Sauter R., Gerstenbrand F. Combined MRI and PMRS of Patients with Acute Stroke. *Stroke*, 23, 8, 1992.
67. Fenstermacher M.J., Narayana P.A. Serial proton magnetic resonance spectroscopy of ischemic brain injury in humans. *Investigative Radiology*, 25, 1034-1039, 1990.
68. Fernandez E.J., Maudsley A.A. ¹H Spectroscopic Imaging of Rat Brain at 7T. *Magn.Reson.Med* 25, 1, 107-19, 1992.
69. Frahm J., Bruhn H., Gyngell M., Merboldt K., Hänicke W., Sauter R. Localised proton NMR spectroscopy in different regions of the human brain using relaxation times and concentrations of cerebral metabolites *Magn.Reson.Med.*, 11, 47-63, 1989.
70. Frahm J., Bruhn H., Gyngell M.L., Merboldt K.D., Hanicke W., Sauter R. Localised PMRS in Different Regions of the Human Brain Using Relaxation Times and Concentrations of Cerebral Metabolites. *Magn.Reson.Med*, 11, 47-63, 1989.
71. Frahm J., Merboldt K.D., Hänicke W. Localised Proton Spectroscopy Using Stimulated Echoes. *J.Magn.Reson*, 72, 502-8, 1987.
72. Frahm J., Michaelis T., Merboldt K.D., Bruhn H., Gyngell M.L., Hänicke W. Improvements in Localised Proton NMR Spectroscopy of Human Brain ; Water Suppression, Short Echo Times and Im Resolution. *J.Magn.Reson*, 90, 464-73, 1990.
73. Freeman R., Robert J.B. *NMR Basic Principles and Progress.* 25, 1-16, 1991.
74. Gabbillard R. *C.R. Acad. Sci Paris*, 232, 1551, 1951.
75. Gartland K.P.R., Sanins S.M., Nicholson J.K., Sweatman B.C., Beddell C.R., Lindon J.C. Pattern Recognition Analysis of High Resolution ¹H NMR Spectra of Urine. A Non-Linear Mapping Approach to the Classification of Toxicological Data. *NMR in Biomed.*, 3, 166,172, 1990.

76. Gesmar H., Hasen P.C. 'Fast' Linear Prediction and its Application for NMR Spectroscopy. *J.Magn.Reson.* 106, 236-240, 1994.
77. Gesmar H., Led J.J., Abildgaard F., Improved methods for quantitative spectral analysis of NMR data. *Prog NMR Spectr.*, 27, 255-288, 1990.
78. Gideon P. Early Time Course of N-AA, Cr + Pcr and Compounds Containing Choline in the Brain After Acute Stroke *Stroke*, 23, 11, 1992.
79. Gideon P. In Vivo Relaxation of N-AA, Cr + Pcr, and Cho Containing Compounds During the Course of Brain Infarction ; a Proton MRS Study. *Magn.Reson.Imag*, 10, 983-88, 1992.
80. Gideon P. Sperling B., Arlien-Søborg P., Olsen T.S., Henriksen O. Long Term Follow Up of Cerebral Infarction Patients with PMRS. *Stroke* 25, 5, May, 1994.
81. Gonen. O., Jiani H., Stoyanova R., Leigh J.S., Goelman G., Brown T.R. Hybrid 3-D Proton Localised Spectroscopy of Phantom and Human Brain *Magn Reson in Med*, 33, 300- 308, 1995.
82. Gonzalez R.C., Wintz P. *Digital Image Processing. Addison-Wesley.* 1997.
83. Götz C. Magnet shimming for in vivo NMR spectroscopy. Project report, University of Edinburgh, 1997.
84. Graham G.D., J.H. Wang, Rothman D.L., Prichard J.W. Spatial correlation of lactate and lipids in subacute cerebral infarction. *In Abs. 2nd meeting SMR*, 136, 1995.
85. Graham G.D., Blamire A.M., Howseman A.M., Rothman D.L., Fayad P.B., Brass L.M., Petroff O.A.C., Shulman R.G., Prichard J.W. Proton MRS of cerebral Lactate and Other Metabolites in Stroke Patients. *Stroke*, 23,3, 1992.
86. Graham G.D., Kalvach P., Blamire A.M., Brass L.M., Fayad P., Prichard J.W. Clinical Correlates of proton MRS After Acute Cerebral Infarction *Stroke*,26, 2, 1995.
87. Gruetter R., Boesch C. Fast, non iterative shimming of spatially localised signals. In vivo analysis of the magnetic field along axes. *J Magn. Reson.* 96, 323-334, 1992.
88. Güntert P., Schaefer N., Otting G., Wüthrich K. POMA a complete Mathematica implementation of the product operator. *J.Magn. Reson.* 101, 103-105, 1993.
89. Haase A., Frahm J., Hänicke W., Matthaei D. 1H NMR Chemical Shift (CHESS) Imaging. *Phy. Med. Biol.*, 30, 431-44, 1985.
90. Haase A. Snapshot FLASH MRI -applications to T₁, T₂ and chemical shift imaging. *Magn. Reson. Med*, 13, 77-89, 1990.
91. Hahn E. *Phys. Rev*, 80, 580, 1950.
92. Handa Y., Kaneko M., Matuda T., Kobayashi H., Kubota T., Thomas D.G.T, Dacey R.G., Mayberg M.R., Solomon R.A. In vivo proton magnetic resonance spectroscopy for metabolic changes in brain during chronic cerebral vasospasm in primates. *Neurosurgery*, 40, 773-781, 1997.
93. Haseler L.J., Ernst T., Caton W., Moats R.A., Shonk T., Ross B.D. Clinical outcome after closed head injury ¹H MRS in children. *In Abs 3rd scientific meeting SMR*, 381, 1995.
94. Hetherington H.P., Avison M.J., Shulman R.G. ¹H homonuclear editing of rat brain using semiselective pulses *Proc. Nat. Acad. Sci. USA*, 82, 3115-8, 1985.
95. Hetherington H.P., Mason G.F., Pan J.W., Twieg D.B., Adams D., Pohost G.M., Quantitative high resolution SI of human brain at 4.1 T. *In Abs. 3rd scientific meeting SMR*, 254, 1995.
96. Hiltunen Y., Ala-Korpela M., Jokisaari J., Eskilinen S., Kivinitty K., Savolainen M., Kesäiemä Y.A. A Lineshape Fitting Model for ¹H NMR Spectra of Human Blood Plasma. *Magn.Reson.Med*, 21, 222-232, 1991.
97. Hoffman R.E., Levy G.C. Spectral Deconvolution by Simulated Annealing. *J.Magn.Reson.* 83, 411-417, 1989.
98. Hore P.J. Solvent Suppression in Fourier Transform NMR. *J.Magn.Reson.* 55, 283-300, 1983.
99. Houkin K., Kamada K., Kamiyama H., Iwasaki Y., Abe H., Takeshi K. Longitudinal Changes in Proton MRS in Cerebral Infarction. *Stroke*, 24, 9, 1993.
100. Hoult D.I., Busby S.J.W., Gadian D.G., Radda G.K., Richards R.G., Seeley P.J. *Nature*, 252, 285, 1974.
101. Hoult D.I., Rotating frame zeugmatography. *J Magn. Reson.* 33, 183-197, 1979.
102. Hounsfield G.N. Computerised transverse axial scanning (tomography) I. Description of system. *Br. J. Radiol.*, 46, 1023-1047, 1973.

103. Howe F.A., Maxwell R.J., Saunders D.E., Brown M.M., Griffiths J.R. Proton Spectroscopy In Vivo *MR Quarterly*, 9, 1, 31-59, 1993.
104. Howe F.A., Saunders D.E., McLean M.A., Brown M.M., Griffiths J.R. Discrimination of Lactate and Lipid/Macromolecules Using Short Echo Time ¹H MRS of Stroke in Humans. *In Proc. BIR*, 1995.
105. Hu J., Javaid T., Arias-Mendoza F., Liu Z., McNamara R. and Brown T.R. A fast, reliable, automatic shimming procedure using ¹H chemical-shift-imaging spectroscopy. *J. Magn. Reson.*, 108, 213-219, 1995.
106. Hugg J.W., Duijn J.H., Matson G.B., Maudsley A.A., Tsuruda J.S., Gelinas D.F., Weiner M.W. Elevated Lactate and Alkalosis Chronic Human Brain Infarction by ¹H and ³¹P MRSI. *Jn. of Cerebral Blood Flow and Metabolism*, 12, 733-744, 1992.
107. Hugg J.W., Laxer K.D., Matson G.B., Maudsley A.A., Weiner M.W. Neuron Loss Localises Human Temporal Lobe Epilepsy by In Vivo PMRS *Annals of Neurology*, 34(6), 788-94, 1993.
108. Husted C.A. Duijn J.H., Matson G.B., Maudsley A.A., Weiner M.W. Molar Quantification of in Vivo Proton Metabolites in Human Brain. *Magn. Reson. Imag*, 12, 4, 661, 1994.
109. Inao S., Marmarou A., Clarke G.D., Andersen B.J., Fatouros P.P., Young H.F. Production and clearance of lactate from brain tissue, cerebro spinal fluid and serum following experimental brain injury. *Journal of Neurosurgery*, 69, 736-744, 1988.
110. Jones J.A., Hore P.J. The Maximum Entropy Method and Fourier Transformation Compared. *J Magn Reson*, 92, 276-292, 1991.
111. Jones J.A., Hore P.J. The Maximum Entropy Method, Appearance and Reality., *J Magn Reson.*, 92, 363-376, 1991.
112. Jung W.I., Lutz O. Localised double-dpin-echo proton spectroscopy of weakly coupled homonuclear spin systems. *J. Magn. Reson.*, 96, 237-251, 1992.
113. Jung W.I., Lutz O. Localised single shot double quantum filter for spectral editing of human in-vivo spectra. *J. Magn. Reson.* 94, 587-595, 1991.
114. Kamada K., Houkin K., Hida K., Matsuzawa H., Iwasaki Y., Abe H., Nakada T. Localised Proton Spectroscopy of Focal Brain Pathology in Humans: Significant Effects of Edema on Spin-Spin Relaxation Times. *Magn. Reson. Med*, 31, 537-540, 1994.
115. Kanters R.P.F., Char B., Addison A.W. A computer algebra application for the description of NMR experiments using the product operator formalism. *J. Magn. Reson.*, 101, 23-29, 1993.
116. Kay S.M., *Modern spectral estimation*, Prentice-Hall, Englewood Cliffs, New Jersey, 1988.
117. Klose U. In Vivo Proton Spectroscopy in Presence of Eddy Currents. *Magn. Reson. Med*, 14, 26-30, 1990.
118. Knüttel A., Kimmich R. Single-scan volume selective spectral editing by homonuclear polarisation transfer. *Magn. Reson. Med*, 9, 254-260, 1989.
119. Koehl C., Ling F.C., leFevre J.F. Statistics and Limits of Linear Prediction Quantification of MR Spectral Parameters. *J. Magn. Reson.*, 109, 32-40, 1994.
120. Kreis R. Inter Individual and Regional Differences of Brain Metabolite Concentrations Determined by ¹H-MRS. *Proc of SMR*, 1, 45, 1994.
121. Kreis R., Ernst T., Ross D.B., Absolute quantitation of water and metabolites in the Human Brain. *J. Magn. Reson. Series B*, 102, 9-19, 1993.
122. Kugel H., Lafeman H., Heindel W., Herholz K., Heiss W.D., Lactner K. Proton MR Spectroscopic Imaging in Patients Suffering from Acute and Sub-acute Infarcts. *In Abs. 2nd scientific meeting . SMR*, 189, 1994.
123. Kuhl D.E., Edwards R.Q. Image separation of radio-isotope scanning. *Radiology*, 80, 653-662, 1963.
124. Kumaresan R., Tufts D.W., Kirstens I. Data Adaptive Estimation by SVD of a Data Matrix. *In Abs. Proc IEEE 70*, 6, 1982.
125. Kwok L., Brown M.A. Castillo M. Extraneous lipid contamination in single-voxel proton MR spectroscopy: phantom and human studies. *AJNR*, 18, 1349-1357, 1997.
126. Lauterbur P. Image formation by induced local interactions: examples employing nuclear magnetic resonance zeugmatography. *Nature*, 242, 190-191.

127. Leach M.O., Collins D.J., Keevil S., Rowland I., Smith M.A., Henriksen O., Bovée W.M.M.J., Podo F. Clinical test objects: design, construction and solutions. *Magn. Reson. Imag.*, 13 131-139, 1995.
128. Luyten P.R., Marien A.J.H., Heindel W., van Gerwen P.H.J., Herholz K., den Hollander J.A., Friedmann G, Heiss W.D. Metabolic Imaging of Patients with Intracranial Tumours: H-1 MR Spectroscopic Imaging and PET. *Radiology* 6, 791-99, 1990.
129. Mansfield P. and Granell P.K., *J. Phys. C.*, 6, 1422, 1973.
130. Mansfield P., Pykett I.L., Morris P.G., Coupland R.E. *Br. J. Radiol.*, 51, 921, 1978.
131. Mansfield P. Multi-planar image formation using NMR spin echoes. *J. Phys.*, L55-L58, 1977.
132. Marion D., Ikura M., Bax A. Improved Solvent Suppression in One and Two Dimensional NMR Spectra by Deconvolution of Time Domain Data. *J. Magn. Reson.*, 84, 1025-1030, 1989.
133. Marple S.L. *Digital spectral analysis with applications*. Prentice-Hall, Englewood Cliffs, New Jersey, 1988.
134. Marshall I., Wardlaw J., Cannon J., Slattery J., Sellar R.J., Reproducibility of metabolite peak areas in ¹H MRS of brain. *Magn. Reson. Imaging*, 14, 281-292, 1996.
135. Marshall I., Wild J.M. A systematic study of the lactate lineshape in PRESS -localised proton spectroscopy. *Magn. Reson. Med.* revised 1998,
136. Marshall I., Wild J.M. Calculations and experimental studies of the lineshape of the lactate doublet in PRESS -localised ¹H MRS. *Magn. Reson. Med.*, 38, 415-419, 1997.
137. Marshall I., Higginbotham J., Bruce S. Freise A. Use of Voigt lineshape for quantification of in-vivo ¹H spectra. *Magn. Reson. Med* 37, 651-657, 1997.
138. Mason G.F., Pohost G.M., Hetherington H.P. Numerically Optimised Experiment Design for Measurement of Grey/White Matter Metabolite T2 in High Resolution Spectroscopic Images of Brain. *J. Magn. Reson.*, 107, 68-73, 1995.
139. Matson G.B. An integrated program for amplitude modulated r.f. pulse generation and re-mapping with shaped gradients. *Magn. Reson. Imag.* 12, 1205-1225, 1994.
140. Maudsley A.A. Automated Processing for Proton Spectroscopic Imaging Using Water Reference Deconvolution. *Magn Reson Med.* 31, 6, 1994.
141. Maudsley A.A. Spectral Lineshape Determination by Self-Deconvolution. *J. Magn. Reson.*, 106, 47-57, 1995.
142. Maudsley A.A., Hilal S.K., Perman W.H., Simon H.E. Spatially Resolved High Resolution Spectroscopy by Four Dimensional NMR. *J. Magn. Reson.*, 51, 147 -52, 1983.
143. Maudsley A.A., Lin E., Weiner M.W. Spectroscopic Imaging Display and Analysis. 1 *Magn. Reson. Imag.* 0, 3, 471-85, 1992.
144. Metzger G., Kadah Y.M., Hu X. A regional approach for partial volume correction in spectroscopic imaging. *In Abs. fourth scientific meeting ISMRM*, 1455, 1997.
145. Meyerhoff D. J., McKay S., Poole N., Dillon W.P., Weiner M.W., Fein G. N-AA Reductions Measured by ¹H-MRSI in Cognitively Impaired HIV-Seropositive Individuals. *Magn. Reson. Imag.*, 12, 4, 653-659, 1994.
146. Michaelis T., Merboldt K.D., Bruhn H., Hänicke W., Frahm J. Absolute Concentration of Metabolites in the Adult Human Brain in Vivo: Quantification of Localised Proton MR Spectra, *Radiology*, 187, 219-227, 1993.
147. Minematsu K., Fisher M. Diffusion and perfusion magnetic resonance imaging studies to evaluate a non-competitive NMDA antagonist and reperfusion in experimental stroke in rats. *Stroke*, 24:2074-2081, 1993.
148. Monsein L.H., Matthews V.P., Barker P.B., Pardo C.A., Blackband S.J.K., Whitlow W.D., Wong D.F., Bryan R.N. Irreversible Regional Cerebral Ischaemia ; Serial MR Imaging and Proton MR Spectroscopy in a Non-Human Primate Model. *AJNR*, 14, 963-970, 1993.
149. Moonen C.T.W. Sobering G., van Zijl P.C.M., Gillen J., von Keinlin M., Bizzi A. Proton Spectroscopic Imaging of the Human Brain. *J. Magn. Reson.*, 98, 556-75, 1992.
150. Moonen C.T.W., Pejar J., de Vleeschouwer M.H.M., van Gelderen P., van Zijl P.C.M., Des Pres D. Restricted and anisotropic displacement of water in healthy cat brain and in stroke studied by NMR diffusion imaging. *Magn. Reson. Med.* 19, 317-332, 1991.
151. Moonen C.T.W., van Zijl P.C.M. Highly Effective Water Suppression for in vivo NMR Spectroscopy (DRYSTEAM). *J. Magn. Reson.*, 88, 28-41, 1990.

152. Morris G.A. Compensation of Instrumental Imperfections by Deconvolution Using an Internal Reference Signal. *J. Magn. Reson*, 80, 547, 1988.
153. Morris P.G. *Nuclear Magnetic Resonance Imaging in Medicine and Biology*. Oxford University Press. 1986.
154. Moseley M., Cohen Y., Mintorovic J., Chileuitt L., Shimizu H., Kucharczyk J., Wendland M.F., Weinstein P.R. Early detection of regional cerebral ischaemia in cats: comparison of diffusion and T2 weighted MRI and spectroscopy. *Magn. Res. Med.* 14:330-346, 1990.
155. Mulkern R.V., Meng J., Bowers J.L., Oshio K., Zuo C., Li H., Kraft R.A., Williamson D.S., Jaramillo D. In vivo bone marrow lipid characterisation with line scan Carr-Purcell-Meiboom-Gill proton spectroscopic imaging. *Magn. Reson. Imag.* 15, 823-837, 1997.
156. Müller C., Bachert P., Lorenz W.J. Two dimensional double quantum coherence ¹H NMR spectroscopy in a whole body MR system. *In Abs. 3rd Scientific Meeting of SMR*, Berkeley CA, p1918, 1995.
157. Narayana P.A., Johnston D., Flamig D.P. In Vivo Proton MRS Studies of Human Brain. *Magn. Reson. Imag.*, 9, 303-308, 1991.
158. Norris D.G., Dreher W. Fat proton spectroscopic imaging using the sliced k-space method. *Magn. Reson. Med.* 641-645, 1993.
159. Odelblad E. Lindstrom G., Some preliminary observations PMR in biological samples. *Acta Radiologica*, 43, 469-476, 1955.
160. Ordidge R.J., Connely A., Lohman J.A. Image Selected In Vivo Spectroscopy (ISIS). A New Technique for Spatially Selective NMR Spectroscopy. *J. Magn. Reson*, 66, 283, 1986.
161. Ordidge R.J., Cresshull I.D. The Correction of Transient B₀ Field Shifts Allowing for the Application of Pulsed Gradient by Phase Correction in the Time Domain. *J. Magn. Reson*, 69, 151-55, 1986.
162. Pan J.W., Hamm J.R., Hetherington H.P., Rothman D.L., Shulman R.G. Correlation of Lactate and pH in Human Skeletal Muscle after Exercise by ¹H NMR. *Magn Reson Med*, 20, 57-65, 1991.
163. Pan J.W., Hamm J.R., Hetherington H.P., Shulman R.G. Quantification of Metabolites by ¹H NMR. *Magn. Reson. Med.* 20, 48-56, 1991.
164. Patt S.L., Sykes B.D. T₁ Water Eliminated Fourier Transform NMR Spectroscopy *Chem. Phys.*, 56, 3182-3184, 1972.
165. Pauly J., le-Roux P., Nishimura D., Macovski A. Paramete relations for the Shinnar-le roux selective excitation pulse design algorithm. *In Abs. of IEEE trans on med imag*, 10, 53-65, 1991.
166. Payne G.S., Leach M.O. On Doubling the Signal in Localised Stimulated Echo Measurements. *In Abs 3rd scientific meeting SMR*, 740, 1994.
167. Peruche B., Krieglstein J. Mechanisms of drug actions against neuronal damage caused by ischaemia - An overview. *Prog. Neuro-Psycopharmacol & Biol Psychiat.* 17(1) 21:70, 1993.
168. Petroff O.A.C., Graham G.D., Blamire A.M., Al-Rayess M., Rothman D.L., Fayad P.B., Brass L.M., Shulman R.G., Prichard J.W. Spectroscopic Imaging of Stroke in Humans: Histopathology Correlates of Spectral Change. *Neurology*, 42, 1349-1354, 1992.
169. Pijnappel W.W.F., van den Boogart A., de Beer R., van Ormondt D. SVD Based Quantification of Magnetic Resonance Signals. *J. Magn. Reson*, 97, 1222-134, 1992.
170. Posse S., DeCarli C., Le Bihan D. Three Dimensional Echo-planar Spectroscopic Imaging at Short Echo Times in the Human Brain. *Radiology*, 192, 733-738, 1994.
171. Prescutti O., Tarduci R., Gobbi G., Pelliccioli G.P., Todeschini E., Franceschini M., Zampolini M. Monitoring recovery after traumatic brain injury with ¹H MR sepectroscopy. *In abs. of the 5th scientific meeting of ISMRM*, 1230, 1997.
172. Press W.H., Teukolsky S.A., Vetterling W.T., Flannery B. *Numerical recipes in C*. Cambridge University Press, Cambridge, England, 1992.
173. Proctor W.G., Yu F.C. *Phys. Rev*, 77, 717, 1950.
174. Prichard J.W. The ischaemic penumbra in stroke: prospects for analysis by m spectroscopy. Molecular and cellular approaches to the treatment of neurological disease. Raven Press, NY, 1993.
175. Prichard J.W. The Ischaemic penumbra in stroke: prospects for analysis by nuclear magnetic resonance spectroscopy. *Molecular and cellular approaches to the treatment of neurological disease*, Raven Press, New York, 1993.

176. Purcell E.M., Torrey H.C., Pound R.V. *Phys. Rev.* 69, 37, 1946.
177. Roebuck J.R., Hearshen D.O., O'Donnell M., Raidy T. Correction of Phase Effects Produced by Eddy Currents in Solvent Suppressed ^1H CSI. *Magn. Reson. in Med.*, 30, 277-282, 1993.
178. Romeo F., Hoult D.I. Magnet field profiling: analysis and correcting coil design, *Magn. Reson. Med.*, 1, 44-65, 1984.
179. Rosen B.R., Belliveau J., Vevea J., Brady T. Perfusion imaging with NMR contrast agents. *Mag. Res. Med.* 14:249-266, 1990.
180. Rothman D.L. Localised Proton NMR Observation of [$3\text{-}^{13}\text{C}$] Lactate in Stroke After [$1\text{-}^{13}\text{C}$] Glucose Infusion. *Magn. Reson. Med.*, 21, 302-7, 1991.
181. Sappey-Marinié D., Calabrese G., Hetherington H.P., Fisher S.N.G., Deiken R., van Dyke C., Fein G., Weiner M.W. Proton MRS of Human Brain : Applications to Normal White Matter , Chronic Infarction and MRI White Matter Signal Hyperintensities., *Magn. Reson. Med.*, 26, 313-327, 1992.
182. Saranathan M., Shankland E.G., Kushmerick M.J. ^1H NMR studies of lactate-macromolecule interactions. *In abs 5th scientific meeting ISMRM* p1165, 1997.
183. Saunders D.E., Howe F.A., van den Boogart A, McLean M.A., Griffiths J.R., Brown M.M. Continuing Ischaemic Damage Following Acute Middle Cerebral Artery Infarction in Man Demonstrated by Short Echo Proton Spectroscopy. *Stroke* 26, 1007-1013, 1995.
184. Schick F., Nägele T., Klose U., Lutz O. Lactate quantification by means of PRESS spectroscopy - influence of refocussing pulses and timing scheme. *Magn. Reson. Imag.* 13, 309-319, 1995.
185. Schick F., Straubinger K., Machann J., Nägele T., Bunse M., Klose U., Lutz O. Sequence parameters of double spin echo sequences affect quantification of citrate. *Magn. Reson. Imag.* 14, 663-672, 1996.
186. Schneider E., Glover G. Rapid in vivo proton shimming. *Magn. Reson. Med.* 18, 335-347, 1991.
187. Seeger U., Klose., Seitz D., Nägele T., Lutz O., Grodd W. Proton spectroscopy of human brain with very short echo time using high gradient amplitudes. *Magn. Reson. Imag.* 16, 55-62, 1998.
188. Sekihara K., Ohya N. Parameter Estimation for In Vivo Magnetic Resonance Spectroscopy (MRS) Using Simulated Annealing. *Magn. Reson. Med.*, 13, 332-339, 1990.
189. Siegel M.M The Use of the Modified Simplex Algorithm for Automatic Phase Correction in Fourier-Transform Nuclear Magnetic Resonance Spectroscopy. *Analytica Chimica Acta*, 133, 103-108, 1981.
190. Soher B.J., van Zijl P.C.M., Duijn J.H., Barker P.B. Quantitative Proton Spectroscopic Imaging of the Human Brain. *Magn. Reson. Med.*, 35, 356-36-, 1996.
191. Soher B.J., van Zijl P.C.M., Duyn J.H., Barker P.B. Quantitative Proton MR Spectroscopic Imaging of the Human Brain. *In Abs third meeting of SMR*, 1961 1995.
192. Sokoloff L., Reinich M., Kumal C. The ^{14}C deoxyglucose method for the measurement of local cerebral glucose utilisation. Theory procedure and normal values in the conscious and anaesthetised albino rat. *Neurochem*, 28, 897-916, 1977.
193. Sørensen O.W., Eich G.W., Levitt M.H., Bodenhausen G., Ernst R.R. Product operator formalism for the description of NMR pulse experiments. *Progress in NMR Spectroscopy*. 16, 163-192, 1983.
194. Sotak C.H., Freeman D.M. A method for volume -localised lactate editing using zero-quantum coherence created in a stimulated -echo pulsed sequence. *J. Magn. Reson.* 77, 382-388, 1988.
195. Siegel M.M. The use of the modified simplex method for automatic phase correction in Fourier-transform nuclear magnetic resonance spectroscopy. *Analytica Chimica Acta*, 133, 103-108, 1981.
196. Spielman D, Webb P., Macovski A. Water Referencing for Spectroscopic Imaging. *Magn. Reson. Med.*, 12, 38-49, 1989.
197. Spielman D., Meyer C., Macovski A., Enzman D. ^1H Spectroscopic Imaging Using a Spectral-Spatial Excitation Pulse. *Magn. Reson. Med.*, 18, 269-279, 1991.
198. Spielman D., Pauly J., Macovski A., Enzman D. Spectroscopic Imaging with Multi-dimensional Pulses for Excitation: SIMPLE. *Magn. Reson. Med.*, 19, 67-84, 1991.

199. Spielman D.M., Pauly J., Macovski A., Glover G., Enzmann D. Lipid suppressed single and multi section proton spectroscopic imaging of the human brain *J. Magn. Reson. Imaging*, 2, 253-62, 1992.
200. Star-Lack J., Nelson S.J., Kurhanewicz J., Huang R., Vigneron D.B. Improved water and lipid suppression for 3D PRESS CSI using rf band selective inversion with gradient dephasing (BASING). *Magn. Reson. Med.* 38, 311-321, 1997.
201. Straubinger K., Schick F., Lutz O. Relaxation in stimulated echo spectroscopy of citrate. *In Abs. 3rd Scientific Meeting of SMR*, p1756, 1995.
202. Sutton L.N., Wang Z., Duhaime A.C., Costarino D., Sauter R., Zimmerman R. Tissue lactate in paediatric head trauma: a clinical study using ^1H NMR spectroscopy. *Paediatric Neurosurgery*, 22, 81-87, 1995.
203. Szafer A., Zhong J., Gore J.C. Theoretical model for water diffusion in tissues. *Magn. Reson. Med*, 33, 697-712, 1995.
204. Tang C. An Analysis of Baseline Distortion and Offset in NMR Spectra. *J. Magn. Reson.*, 109, 232-240, 1994.
205. Tedeschi G., Bertolino A., Campbell G., Barnett A.S., Duyn J.H., Jacob P.K., Moonen C.T.W., Alger J.R., DiChiro G. Reproducibility of proton magnetic resonance spectroscopic imaging. *In Abs 5th scientific meeting ISMRM*, 1226, 1997.
206. Ter-Pegossian M.M., Phelps M.E., Hoffman E.J. A positron emission transaxial tomograph for nuclear medicine imaging (PET). *Radiology*, 114, 89-98, 1975.
207. Thomsen C., Becker U., Winkler K., Christoffersen P., Jensen M., Henriksen O. Quantification of liver fat using magnetic resonance spectroscopy. *Magn. Reson. Imag.*, 12, 487-495, 1994.
208. Thomsen J.U., Meyer B. Pattern Recognition of the ^1H NMR Spectra of Sugar Alditols Using a Neural Network. *J. Magn. Reson.*, 84, 212-217, 1989.
209. Turner R, Le Bihan D., Moonen C.T.W., DesPres D., Frank J. Echo planar time course MRI of cat brainoxygenation changes. *Magn. Reson. Med.* 22, 159-166, 1991.
210. van den Boogart A., Ala-Korpela M., Jokisaari J., Griffiths J.R. Time and Frequency Domain Analysis of NMR Data Compared : An Application to 1D ^1H Spectra of Lipoproteins. *Magn. Reson. Med* , 31, 347-358, 1994.
211. van der Veen J.C.W, de Beer R., Luyten P.R., van Ormondt D. Accurate Quantification of in Vivo ^{31}P Using the Variation Projection Method and Prior Knowledge. *Magn. Reson. Med*, 6, 92-98, 1988.
212. van Gelderen P, de Vleeschouwer M.H.M, DesPres D., Pekar J., van Zijl P.C.M, Moonen C.T.W. Water diffusion and acute stroke. *Magn. Reson. Med.* 31, 154-163, 1994.
213. Von Kienlin M., Albrand J.P., Authier B., Blondet P., Lolito S., Decorps M. Spectral editing in vivo by homonuclear polarisation transfer. *J. Magn. Reson.*, 75, 371-377, 1987.
214. Wand M.P., Jones M.C. *Kernel Smoothing*, Chapman and Hall, London, 1995.
215. Wang J.H., Ghraham G.D., Behar K.L., Alger J.R., Prichard J.W, Rothman D.L., Short echo time proton magnetic spectroscopic imaging of macromolecule and metabolite signal intensities in the human brain. *Magn. Reson. Med*, 35, 633-639, 1996.
216. Wardlaw J.M., Sellar R.J. A simple practical classification of cerebral infarcts on CT and its inter observer reliability. *AJNR*, 15, 11933-1939, 1994.
217. Wear K.A., Myers K.J., Grossman L.W., Rajan S.S. Constrained Reconstruction Applied to 2D Chemical Shift Imaging. *In Abs 5th scientific meeting proc. ISMRM*, 1912, 1995.
218. Wear K.A., Myers K.J., Wagner R.F., Rajan S.S., Grossman L.W. An Autoregressive method for High Resolution One Dimensional Chemical Shift Imaging. *J. Magn. Reson.*, 105, 172-176, 1994.
219. Webb P., Macovski A. Rapid, Fully Automatic, Arbitrary-Volume in Vivo Shimming. *Magn. Reson. Med*, 20, 113-122, 1991.
220. Webb P., Spielman D., Macovski A. Inhomogeneity Correction for In Vivo Spectroscopy by High Resolution Water Referencing. *Magn. Reson. Med*, 23, 1-11, 1992.
221. Webb P., Spielman D., Macovski A. A fast spectroscopic imaging method using a blipped phase encode gradient. *Magn. Reson. Med*, 12, 306-315, 1989.
222. Wen H., Jaffer F.A. An in vivo automated shimming method taking into account shim current constraints. *Magn. Reson. Med* . 34, 898-904, 1995.

223. Wild J.M., Marshall I. Normalisation of metabolite images in ^1H NMR spectroscopic imaging. *Magn. Reson. Imag.*, 15, 1057-1066, 1997.
224. Wilkinson I.D., Paley M., Chong W.K., Sweeney B.J., Shepherd J.K., Kendall B.E., Hall-Craggs M.A., Harrison M.J.G. Proton spectroscopy in HIV infection: relaxation times of cerebral metabolites. *Magn. Reson. Imaging*, 12, 951-957, 1994.
225. Wilkinson I.D., Mizkiel K.A., Chinn R.J.S., Paley M., Maloney M.A., Hall-Craggs M.A., Harrison M.J.G. The influence of gender on cranial H-MRS and volumetry. *In Abs. 5th scientific meeting ISMRM*, 1163, 1997.
226. Williams S.R., Crockard H.A., Gadian D.G., Proctor E., Allen K. Quantitative Estimation of Lactate in the Brain by ^1H NMR. *Magn. Reson. in Med.*, 7, 425-431, 1988.
227. Williams S.R., Gadian D.G., Proctor E. A method for lactate detection in vivo by spectral editing without the need for double irradiation. *J. Magn. Reson.*, 66, 562-67, 1986.
228. Williams S.R. In-vivo proton spectroscopy. *In NMR basic principles and progress.* ed. by Diehl P., Fluck E., Gunther H., Kosfeld R., Seelig J. Vol. 26, 56-71, Springer, Berlin, 1992.
229. Wilman A.H., Allen P.S. An analytical and experimental evaluation of STEAM versus PRESS for the observation of the lactate doublet. *J. Magn. Reson.* 101, 102-105, 1993.

Acknowledgements.

I am grateful to the Medical Research Council for supporting this work.

Firstly I would like to thank my supervisor Dr Ian Marshall (Senior Lecturer in MRI, Medical Physics), for his support throughout the course of the last three years. The groundwork done by Ian in developing spectroscopic imaging in the early stage was vital for the success of this project. More recently, his critical proof reading of this script has been much appreciated.

Secondly I would like to thank Dr Joanna Wardlaw (Consultant Research Neuro-radiologist, DCN) for her enthusiastic encouragement, clinical advice and for providing the clinical drive behind the project.

The following people have also been of great assistance within the University;

Martin Connell (Medical Physics) -for comprehensive computer support and developing the excellent SI display facility.

Professor Norman McDicken- for useful advice throughout the course of the PhD.

Jim Cannon (Senior Research Radiographer, DCN)- for enthusiastically recruiting research patients from the wards, acquiring the in-vivo spectroscopic data on a routine basis and being a reliable canteen regular and general Mr.Fixit.

Dr Robin Sellar (Head of Department, DCN -X ray)- for providing free access to the clinical MRI scanner out of hours and financial assistance in attending conferences.

Professor Charles Warlow (Head of Department, DCN) and Laurette Daly (DCN) -for much needed financial assistance to attend conferences.

Dr Carol McMillan (Research Anaesthetist DCN)- for the clinical enthusiasm needed to get a spectroscopic study of head injury off the ground.

Dave Signorini (Senior Statistician, DCN)- for comprehensive statistical advice.

David Perry (DCN)- for p.c. support.

Dr Ian Sadler (Department of Chemistry)- for providing access to the high field strength spectrometer and useful advice on NMR.

Dr Jim Hannan (Medical Physics)- for guidance on how to go about writing up a PhD thesis.

The radiography, radiology and nursing staff of DCN, Mrs Isobelle McNaughton in particular- for co-operating with research scanning whilst trying to meet the heavy NHS demands on the MRI scanner.

Mrs Caroline Ness and Mrs Irene Craig, Medical Physics secretaries.

George Campbell (Workshop Engineer, Medical Physics) - for phantom construction.

The department of Medical Illustration for producing high quality colour posters.

Last and not least my immediate colleagues, Paul Armitage (PhD student Medical Physics) - for offering to read the thesis, advice on diffusion weighted imaging and useful discussions on the Vauxhall conference and canteen food. Steve Bruce (PhD student Napier University) for supplying me with p.c. software. Dr Mark Bastin (Research Associate in MRI) -a reliable source of bad jokes and useful computer tips. Uwe Köhler for his willing advice.

A big thank you goes to all the patients and volunteers who participated in the in-vivo studies throughout the three years (in particular; Ian Marshall, Paul Armitage, Peter Reid, Brian Porteous, Lionel Morey, Liz Caddick, Dave Sykes, Bezhad Nadeem, Colin Brown, Cameron Ager, David Charlton, David Thompson) .

I would also like to thank the following people from outside the University;

Dr Michael Bunse, University of Tübingen, Germany - for useful discussions on lactate editing and the HOPE sequence.

Carlo Götz, University of Heidelberg, Germany- for his work on automated shimming.

Dr Barrie Condon, Southern General Hospital Glasgow - for the extended loan of a spectroscopy phantom.

Dr Chrit Moonen, University of Bordeaux 2 -for advice on spectroscopic imaging sequences and great help in writing numerous grant proposals.

Finally I would like to thank all my family;

In particular; Mum, Dad, Neil, Tom, Grandma, George, Liam, Daniel, Luke, Dolores, Gid, Dave, Chris, Linda, and Brin.

and friends;

Laura, Pete, Bri, Dave, Mike, Dave, Paul, Nige, Phipps, Pete, Mary-Jane, Roan, Frank, Amber, Paul, Gordon, the Negotiants regulars, Usonia crew, my friends in Woodseats-Sheffield, Cambridge, Newcastle, and London.

Declaration

I hereby declare that this thesis has been written by myself, and the work is my own. Where work is published that has been done by other people associated with the research group, acknowledgement is made.

● *Original Contribution*

NORMALISATION OF METABOLITE IMAGES IN ^1H NMR SPECTROSCOPIC IMAGING

J.M. WILD AND I. MARSHALL

*Department of Medical Physics and Medical Engineering, University of Edinburgh, Western General Hospital, Edinburgh, UK

Single slice proton magnetic resonance spectroscopic images were taken from a volume of interest (VOI), which was localised using the point resolved spectroscopy (PRESS) sequence. Non-uniformities in the excitation profile of the VOI within the image plane were accounted for using a uniformity correction image. Metabolite images were divided on a voxel-by-voxel basis with a water image obtained from a VOI of the same spatial dimensions from a phantom acquisition. Normalisation procedures carried out on phantom metabolite images were needed to account for the spatial shift in the excitation profile of the VOI, which varies linearly with the chemical shift of the metabolite. Patient metabolite images were then normalised using a VOI water image from a phantom acquisition, which was spatially shifted according to the metabolite chemical shift. In a study of 14 stroke patients, metabolite maps of the distribution of choline, creatine and *N*-acetyl aspartate (NAA) were constructed. The spectral signal intensities from these metabolites in the infarcted and in the contralateral region were calculated using the raw maps and secondly with the same maps after the B_1 normalisation process. In the initial analysis only the metabolite NAA showed a significant decrease, whilst all three metabolites showed a significant reduction in the normalised analysis. These results confirm that normalisation of PRESS localised images does have a significant bearing upon any quantitative measurements made using such images. © 1997 Elsevier Science Inc.

Keywords: Spectroscopic imaging; Normalisation; Localisation; Chemical shift artefact.

INTRODUCTION

If spectroscopic imaging (SI) is to be used in the metabolic diagnosis of pathology and disease then the spectra need to be quantified so that inter and intra patient comparisons can be made. In this study two dimensional (2D) spectroscopic images of the transverse (x - y) plane were obtained using point resolved spectroscopy (PRESS) selective excitation,⁵ where the z axis is along the slice select direction (head to foot of the patient). Quantification of an array of such spectra requires

- (i) accurate measurement of spectral peak areas
- (ii) correction for coil loading
- (iii) correction for coil inhomogeneity in the slice select direction
- (iv) spatially dependent signal amplitude correction within the transverse plane

- (v) T_1 and T_2 relaxation time measurements, and reference to some standard for absolute molar quantification.

Steps ii-iii can be omitted if metabolite ratios are being studied voxels within the same plane. Step v is time consuming and is only necessary if absolute concentrations need to be known. Steps i-iv allow serial studies of concentration of individual metabolites (expressed in system-dependent units) and inter-patient comparisons. Steps i-iii have been previously discussed in the context of measuring the reproducibility of single voxel ^1H spectroscopy.¹

In spectroscopic imaging, step iv needs particular attention, as spectra are collected from an array of voxels spatially distributed within a transverse imaging plane. Many implementations of SI use selective excitation of a

RECEIVED 3/18/97; ACCEPTED 5/30/97.

Address correspondence to Jim Wild, Department of Medical Physics and Medical Engineering, University of Edinburgh,

burgh, Western General Hospital, Crewe Road, Edinburgh EH4 2XU, UK. E-mail: jw@skull.dcn.ed.ac.uk

volume of interest (VOI) inside the skull to avoid lipid contamination. The radiofrequency pulse shapes used to define such a VOI often lead to non-uniformities in the excitation profile of this VOI, and as such within plane correction for x and y position is necessary. When performing SI using outer volume suppression, the B_1 homogeneity may be sufficient to omit such an in-plane correction.⁴ Reviewing the literature describing inner volume excitation techniques, Duyn et al.³ recognise a 10% variation in intensity of their PRESS VOI but do not report any corrections performed to remove this source of error. In our studies a variation of 50% in intensity between voxels at the edges and centre of the VOI was found and as such a normalisation procedure to remove this source of error was thought to be essential.

Such corrections were found to be best implemented by using a uniformity correction image from a phantom VOI of the same physical dimensions as that used in vivo SI. Phantom replacement techniques have been reported in outer volume suppression SI⁴ and PRESS localised SI.² These studies use phantom measurements combined with steps ii and v above to get an absolute quantification of the signal from selected voxels in a spectroscopic image. These uniform phantom methods will implicitly remove discrepancies caused by the B_1 inhomogeneity of the volume of interest but no specific mention of this correction is made. Furthermore such voxel-by-voxel corrections do not account for the spatial offsets due to chemical shift. In this paper a technique for normalisation of a complete metabolite image is outlined. This process removes the non-uniformity introduced by a non-rectangular PRESS VOI profile and accounts for the spatial shifting of this VOI according to the chemical shift of the metabolite being imaged.

METHOD

Data Acquisition

Measurements were made on a spherical phantom containing a solution of either 20 mM sodium acetate or 50 mM lithium lactate, both doped with 0.1 mM Gd-DTPA. Additional measurements were made on human subjects drawn from a group of stroke patients. Using a Siemens 63 SP 1.5 T Magnetom (Erlangen, Germany), fitted with a standard circularly polarised head coil, transverse T_2 -weighted images were used to place a rectangular VOI within the field of view FOV that covers the brain or phantom being imaged. The extent of the VOI typically used was either 75 mm square or 90 mm square. For routine patient SI studies a 240-mm square FOV was used; for higher resolution phantom studies a 160-mm FOV was used. The VOI was localised using PRESS⁵ (see Fig. 1) with 0.8 mT/m in plane gradients and an orthogonal 3mT/m gradient, with a transverse

slice selection thickness of 15 mm for humans and 10 mm for phantoms.

Phase encoding was applied in the x and y directions before the acquisition of the double spin echoes (TR = 1600 ms, TE = 135 ms). The number of phase encoding steps applied in human studies was restricted to 16×16 giving an acquisition time of 7 min. When performing SI on phantoms a much smaller voxel can be used as metabolite concentrations are much greater than those found in vivo, and there is no restriction on acquisition time. Consequently 32×32 acquisitions were used with a smaller FOV (160 mm), with the specific aim of achieving a finer spatial resolution (0.5 cm square) across the VOI of excitation. Prior to acquisition, a global shim of the water resonance across the whole of the head coil was performed followed by a local shim of the VOI. Two sets of data were acquired: one with water suppression and the other without so as to enable a first order phase correction for the effects of eddy currents and field inhomogeneities.⁶ Water suppression was implemented prior to the PRESS localisation, by applying a frequency selective excitation pulse (CHESS) of 60 Hz bandwidth,⁷ to excite the water signal which was subsequently dephased by spoiler gradients.

Data Processing

Data processing was performed on a Sun SPARC 20 with in-house software written in C, and consisted of voxel shifting of the VOI position, 2D spatial fast Fourier transform (FFT), phase correction of the water suppressed signals using the water reference signal,⁶ residual water removal^{8,9} and a FFT of the time domain data to give spectra. Areas under the spectrum corresponding to the concentration of the metabolites (Choline 3.2 ppm, Creatine 3.0 ppm, *N*-acetyl aspartate (NAA) 2.0 ppm, Acetate 2.15 ppm and Lactate 1.4 ppm) were then calculated using in-house display software either by fitting a Gaussian line shape to the individual peaks or by integration between user defined ppm limits. This display package also allowed the option of phasing individual spectra manually. A metabolite map of area under a given peak was then made by bilinear interpolation of the areas calculated from the spectrum from each voxel. Corrections to account for head coil sensitivity in the slice selection direction were made using phantom data, and coil loading corrections based upon the size of the reference voltage of 90° radiofrequency pulse were then implemented.¹ These last two procedures remove systematic sources of discrepancy arising between different subjects that are not due to in slice excitation variation. For anatomical comparisons in patients, the color spectroscopic image was superimposed on the grey scale T_2 -weighted image.

The data obtained from phantom acquisitions was

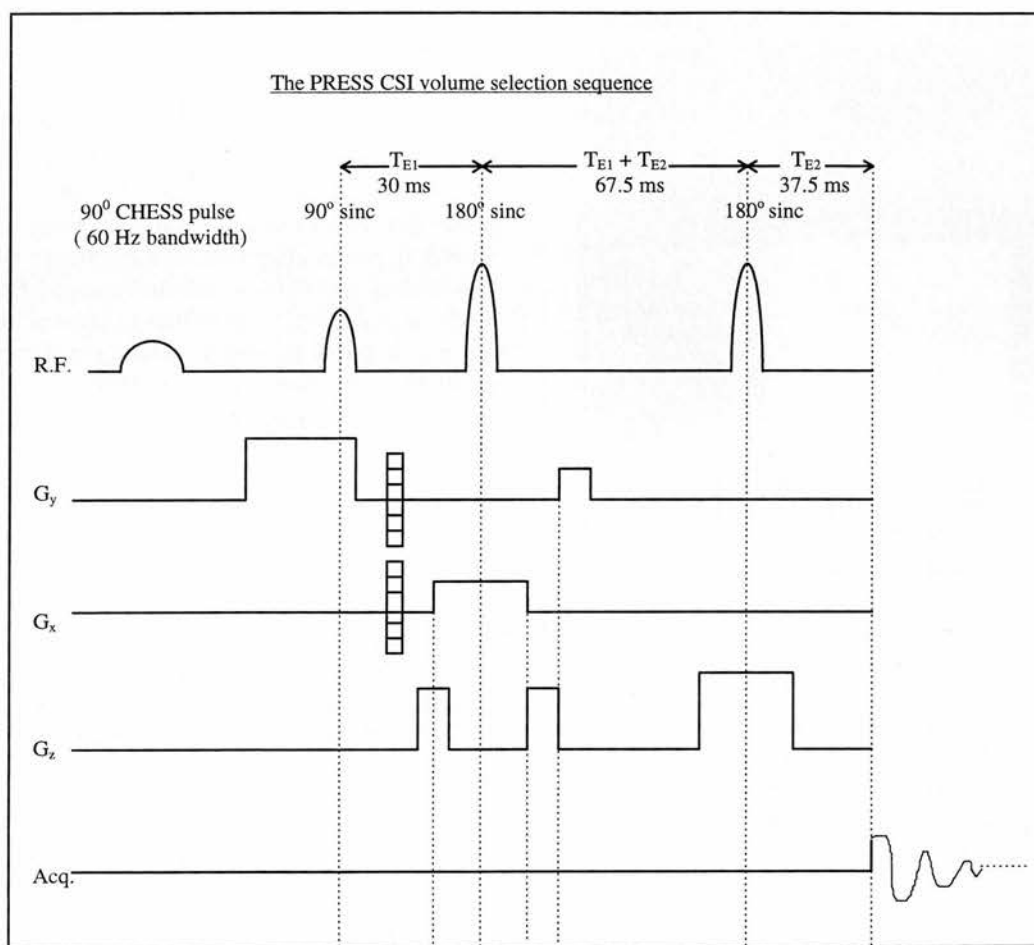


Fig. 1. The PRESS localisation and R.F. excitation pulse sequence. Water suppression is achieved by exciting water protons with a narrow bandwidth (60 Hz) water selective 90° CHES pulse which is subsequently spoiled by the y gradient pulse; the remaining pulses are broad band sinc pulses. These pulses are volume-selected and phase-encoded in the x and y directions and slice-selected in the z direction, by the x , y and z gradient pulses. A total echo time of $TE = 135$ ms was used with a repetition time $TR = 1600$ ms.

processed fully automatically using an automatic phase correction algorithm.¹⁰ An automatic integration was then performed on the real part of the spectrum over user-defined limits for each voxel and the resulting areas were used to construct a 2D map which could be viewed in Matlab® (The Math Works, Inc.)

VOI Localisation-Excitation Profiles

Ideally the VOI prescribed should be a cuboid of uniform magnetisation with in-plane dimensions of n_x by n_y voxels and a thickness of one voxel. The pulses used by the standard manufacturer's SI pulse sequences, in this case PRESS (90° - 180° - 180°) localisation, have sinc waveforms. To investigate the effective spatial magnetisation distribution resulting from such pulses, a water proton density image of the PRESS localised VOI within the phantom (nominal size 75 mm square) was collected.

From this water map, excitation profiles were measured along user-defined lines using the evaluate function in the Numaris operating system of the scanner. In addition a 75-mm square spectroscopic imaging VOI was set up using a background image with a 160-mm FOV. Application of 32×32 phase encoding gave a nominal voxel size of $0.5 \times 0.5 \times 1.0$ cm³. These SI data sets were used to produce acetate, lactate and water chemical shift images of the VOI and its immediate surroundings.

Results and Discussion

The PRESS localised water image of the phantom is shown in Fig. 2. It shows the magnetisation due to the excitation of a 75-mm square, PRESS-localised VOI, within a 240-mm FOV with a pixel matrix of 256, giving a pixel size of 0.94 mm square. From this image, excitation profiles in the y or coronal (90°) and x or sagittal

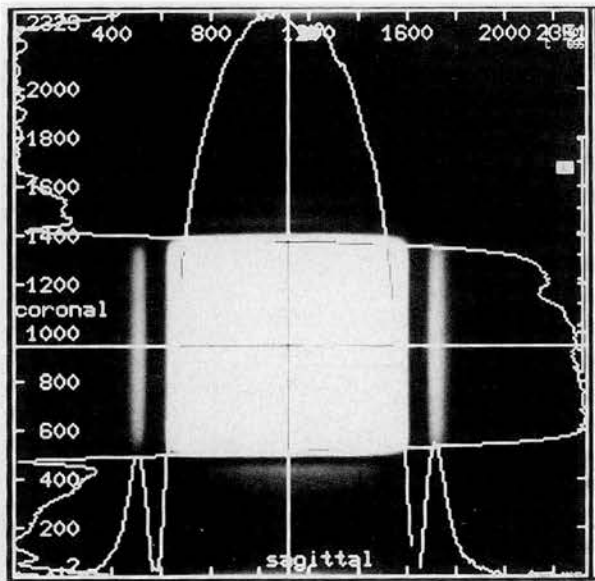


Fig. 2. PRESS water image from a Gd doped water phantom, with the sagittal and coronal excitation profiles calculated from lines across the image.

(180°) directions were calculated by taking the mean pixel intensity from five pixels centred on a user-defined line (see Fig. 2). Shown in Fig. 3 is the water profile

calculated by integrating the area under the spectrum of the SI water reference signal originating from an array of 32×32 voxels with a FOV of 160 mm.

Chemical Shift Artefact and Normalisation

The non-uniformity of Figs. 2–3 show that within-plane normalisation of metabolite peak areas is required if misleading conclusions are to be avoided. Normalisation of the metabolite image grid using the water spectroscopic image was implemented by dividing on a voxel-by-voxel basis (see Fig. 4). These normalisation corrections reveal the problem of chemical shift artefact in SI, with dark and bright fringes at the edge of an otherwise uniform VOI. The effect is most pronounced in the coronal (90°) direction, which is to be expected considering the sharper edges of the profile in that direction. Figure 4 illustrates this effect with the ratio images of the lactate:water profiles.

The theoretical chemical shift artefact can be calculated from the expression for the Larmor frequency ω of a metabolite i , of chemical shift relative to water σ_i , in the presence of a field gradient \mathbf{G} , at a position \mathbf{r} :

$$\omega_i = \gamma(1 - \sigma_i)(B_0 + \mathbf{G} \cdot \mathbf{r}) \quad (1)$$

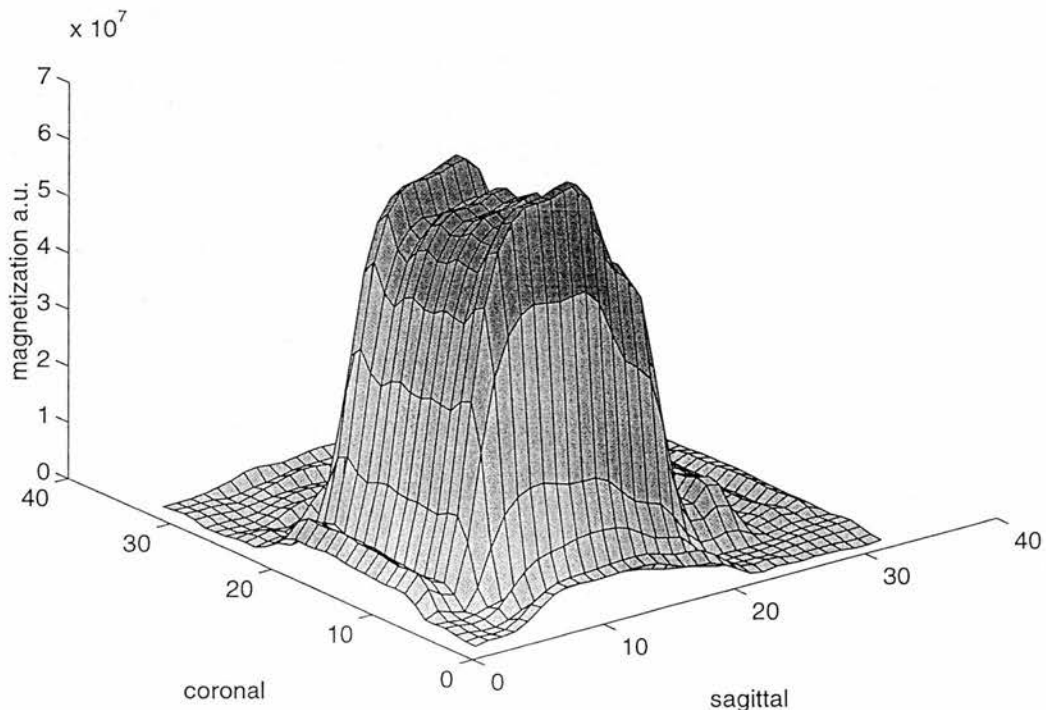


Fig. 3. Excitation profile of a 75 mm \times 75 mm PRESS VOI (160-mm square FOV), obtained by integration of the area under the water peak in the water reference spectrum.

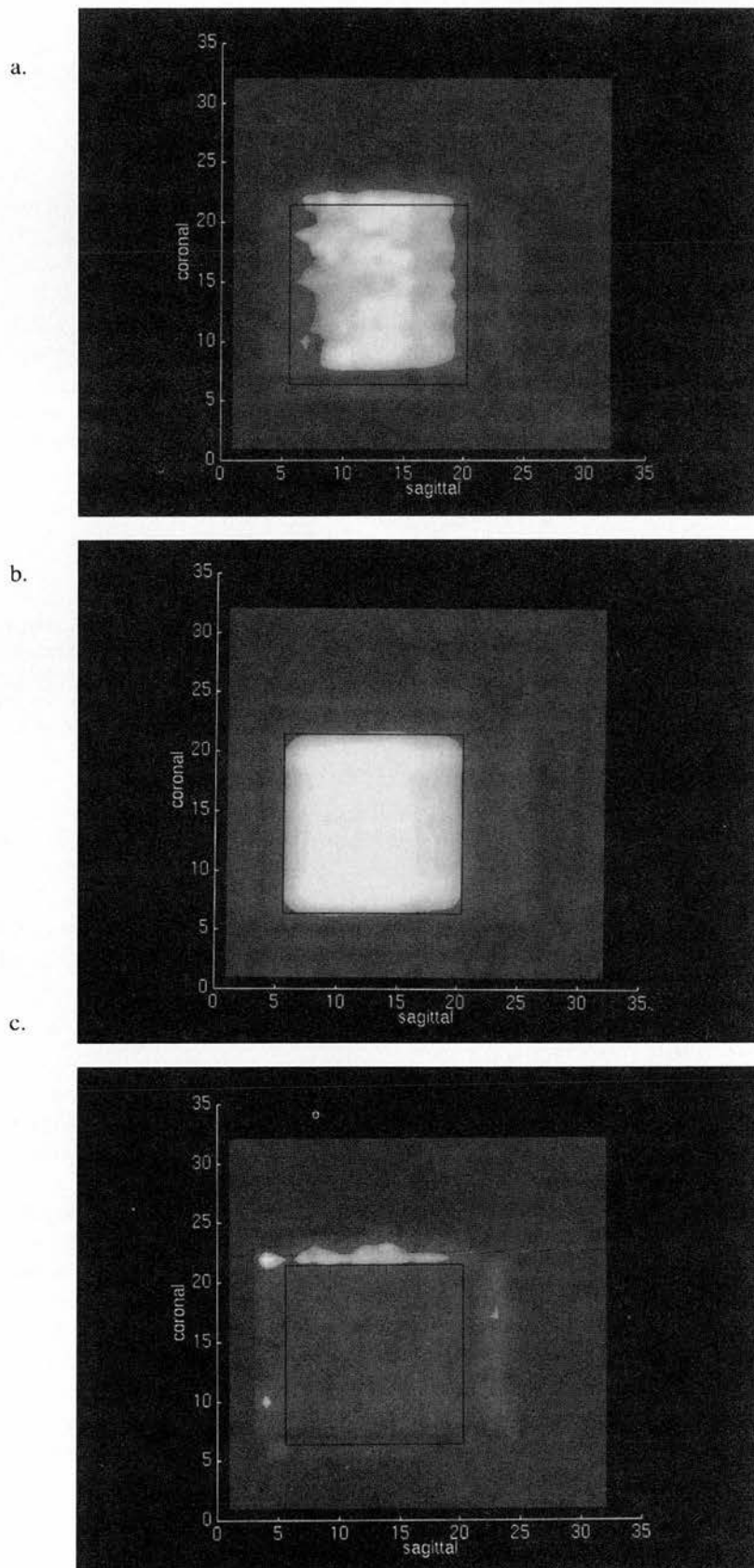


Fig. 4. Normalisation images (a) shows the lactate spectroscopic image from a 32×32 data set with a FOV of 160 mm (32×32 square voxels of edge 5 mm), (b) is the corresponding water reference spectrum image and (c) is the image of the ratio of (a) and (b). Note the uniformity of (c) in the central region with the presence of a bright fringe in the anterior direction and a corresponding dark fringe in the posterior direction. These are due to the chemical shift difference between lactate and water. The square box delineates the position of the edge of the VOI.

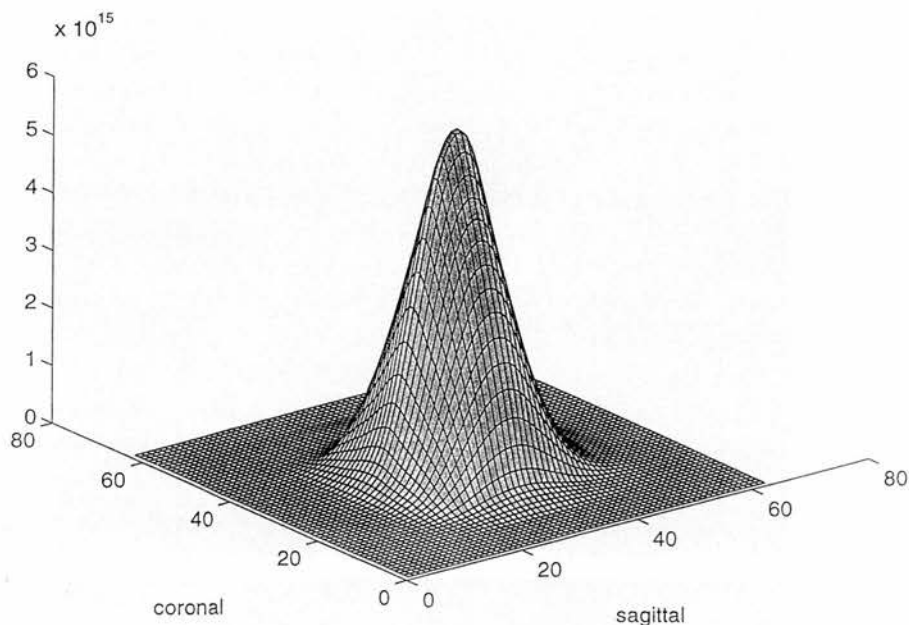


Fig 5. The cross correlation function of the lactate and water images. A 63×63 $[(2N-1) \times (2N-1)]$ matrix grid was formed by the cross correlation of a 32×32 lactate matrix with a 32×32 water matrix. The position of the maximum of this grid indicates the point at which the two data sets overlapped the most. As such, the displacement of the maximum from the centre of the 63×63 array indicates the size and direction of the chemical shift of lactate with respect to water. In this example the maximum was found to be displaced by one voxel from the centre in both the sagittal and coronal directions. with a voxel size of 5 mm this chemical shift is consistent with that of 6.5 mm predicted by theory.

Equation (1) yields an expression for the relative spatial misregistration in the x direction, between the resonance, i and water.

$$\Delta x_i = \left(\frac{B_0 \sigma_i}{\frac{\partial B_0}{\partial x} (1 - \sigma_i)} \right) \approx \frac{\Delta \omega_i}{\gamma \frac{\partial B_0}{\partial x}} \quad (2)$$

So with a field strength of $B_0 = 1.5$ T, gradient strength $\frac{dB}{dx} = 0.8$ mT/m, $\Delta \omega_{lac} = 223$ Hz at 1.5 T then $\Delta x_{lac} = 6.5$ mm. With a voxel resolution of 5 mm in the 160 mm FOV ratio images, the positioning of the bright and dark fringes in Fig. 4. appear consistent with this predicted chemical shift artefact misregistration. To check the direction and size of the chemical shift misregistration in the coronal and sagittal directions, a cross correlation of the water image, $W(x, y)$ and the metabolite image $M(x, y)$ was performed. The resulting cross correlation function $r(\xi, \psi)$ should be centred about a point equal to the chemical shift misregistration of the metabolite as a result of the sagittal and coronal gradients.

The cross correlation function is given by:

$$r(\xi, \psi) = \int_{-\infty}^{\infty} \int_{-\infty}^{\infty} W(x, y) \times M(x + \xi, y + \psi) \cdot dy \cdot dx \quad (3)$$

This integral was implemented on pairs of water and metabolite image matrices using Matlab. A plot of $r(\xi, \psi)$ for a water lactate cross-correlation is illustrated in Fig. 5.

Having accounted for the chemical shift of the metabolite, a normalised image of a VOI from phantom acquisitions has a variation in intensity of less than 20% across its entirety. The existing non-uniformities were found to persist at the edges of the VOI and could be explained by the fact that the shape as well as the position of the VOI profile can differ between metabolites. One cause of discrepancy in the excitation profile between metabolites and water arises from the differences in T_1 relaxation times. This may lead to differential degrees of saturation across the VOI upon application of the subsequent radiofrequency pulse after a time T_R . The distribution of flip angles across a VOI edge depends upon the shape of the excitation pulse and is represented

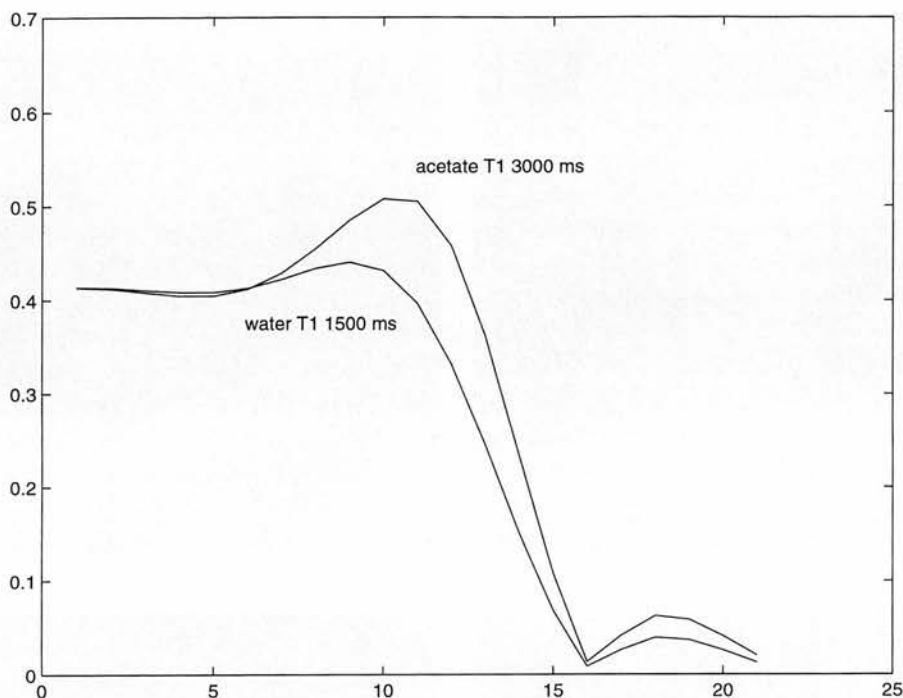


Fig. 6. Simulation of the distribution of magnetisation across the edge of a PRESS VOI localised with a 90° sinc pulse. The simulation was performed for T_1 values of 1500 ms and 3000 ms representing water and acetate in-vitro and TR of 1600 ms. The amplitudes of the plateaux of the profiles have been normalised to the same intensity to enable quantification of the relative overpulsing at the edge of the profile.

in a given direction by the flip angle distribution θ . The shape of the VOI in a given direction is predicted, from the Bloch equations as a function of θ , T_R and T_1 .

$$S(\theta) = \frac{(1 - e^{-\frac{T_R}{T_1}}) \sin \theta}{1 - e^{-\frac{T_R}{T_1}} \cos \theta} \quad (4)$$

Matlab simulations were performed using the spatial distribution of θ across the edges of the coronal sinc pulses (calculated from the time dependence of the sinc pulses using the Cayley-Klein parameters.^{15,19}). A T_R of 1600 ms was used for consistency with our in vivo work with T_1 values of 1500 ms (representing water) and 3000 ms (representing the metabolite acetate). These T_1 values were calculated by integrating the area under the metabolite and water resonances from single voxel PRESS localised spectra at T_R 's of 1600 ms and 3200 ms.¹⁷ Figure 6 shows the results of the simulations. It is clear that there is an 'over pulsing' effect due to incomplete relaxation at the edges of the plateaux of the longer T_1 (acetate) profile. If the plateaux of the water and the acetate profile simulations are normalised to the same intensity then the magnitude of the 'over pulsing' in this

region can be quantified. The result is a water profile that is 25% less intense than the metabolite profile. As such the inconsistencies at the VOI edge can be attributed to differences in T_1 . As a consequence, when normalising in vivo data, a water phantom of T_1 comparable to the T_1 's of metabolites found in vivo (≈ 2000 ms¹⁶) should be used.

A further final possible contribution to non-uniformity in a normalised lactate image results from the J-coupling of the lactate protons. At the edge of a PRESS VOI the distribution of flip angles is found to be non-ideal (Eq. 4¹⁴). As a result the signal from a coupled species, whose signal depends upon protons resonating at different frequencies, will vary in shape at the edges of the VOI.¹⁵ Non-symmetrical doublets will result in the case of lactate, which upon integration may well result in an asymmetric excitation profile.

In-Vivo Image Normalisation

To implement image normalisation a 16×16 water reference data set was taken from a doped phantom acquisition. The VOI was of the same dimensions as that of the SI to be normalised. The phantom was doped with Gd-DTPA at a concentration of 0.1 mM, to give a water T_1 of 2000 ms,¹⁸ comparable with those

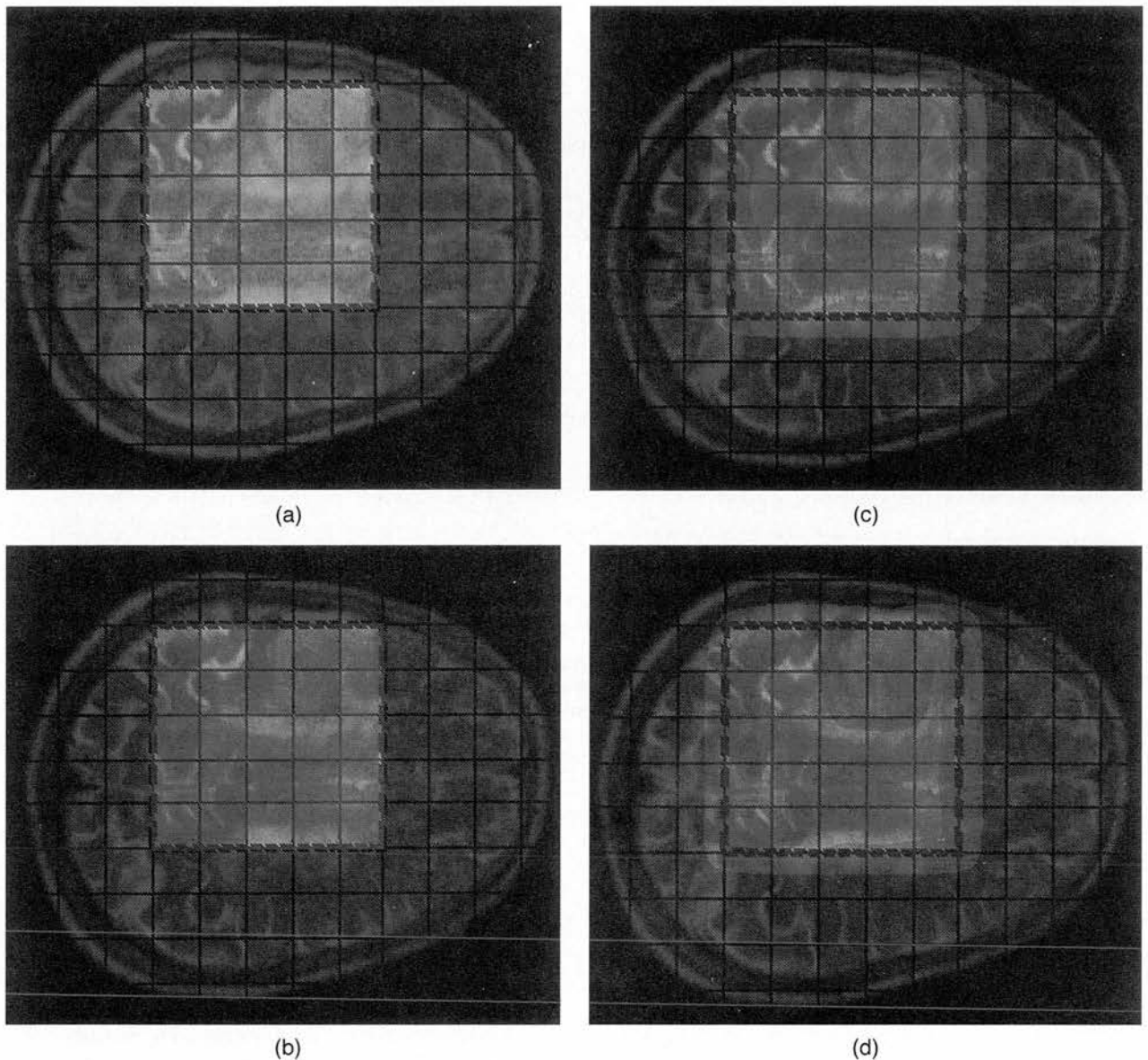


Fig. 7a. NAA image of a patient with an infarct in the right cerebral hemisphere. Superimposed is an edge-detected T_2 -weighted image from the same transverse position. 7b. The image has been normalised with a water reference image from a phantom to account for the spatial distribution of the excitation profile and the chemical shift misregistration of NAA with respect to water. 7c. Interpolated version of b. 7d. Interpolated version of 7b.

of metabolites in healthy tissue at 1.5 T.¹⁶ A user-defined voxel shift was then implemented to align the corners of the two VOI's within the spatial framework of the FOV. This voxel shift is implemented by adding a phase angle in the x and y phase encoding directions prior to the 2D spatial FFT. By prescribing an additional fractional shift to account for the chemical shift misregistration of the specific metabolite, then, images from any of the metabolites can be normalised effectively using a single water image from a VOI of the

same size as that used in vivo. An example of the NAA image from a stroke patient with an infarct in the right cerebral hemisphere is given in Fig. 7, before and after the normalisation procedure. Such images were made for a group of 14 acute stroke patients. Using an interactive region of interest, intensities of the signals from NAA, choline and creatine were calculated from the region covered by the infarct on the T_2 image and from a contra-lateral region. This procedure was implemented on both the normalised and non-normalised

Table 1. Statistical comparisons of metabolite ratios found in infarcted and contralateral regions for non-normalised and normalised sets of metabolite images taken for a group of $n = 14$ stroke patients

	Non-normalised images		Normalised images	
	Infarct:contra	<i>t</i> -test	Infarct:contra	<i>t</i> -test
NAA	0.592	<0.001	0.455	<0.001
Cho	0.984	>0.1	0.757	<0.001
Cr	1.006	>0.1	0.691	<0.001

The mean ratios of the metabolite concentration in the infarcted and contralateral regions are presented together with the *t*-test for significance for difference between the mean intensity found in either hemisphere.

images and the mean intensity in either region calculated. The *t*-test for significant difference between these means, together with the mean ratio of the means, is tabulated in Table 1.

Lipid Contamination

A further consequence of the chemical shift artefact is inadvertent excitation of lipid in the marrow of the skull and subcutaneous layer of the scalp, when placing the VOI. With lipid resonances found in the range 1.5–0.9 ppm ($\Delta\omega = 203$ –242 Hz), which when substituted into Eq. (2) with the gradient strength of 0.8 mT/m, used on our machine, gives $\Delta x_{lip} = 7.1$ mm. Consequently any lipid visible on the transverse magnetic resonance imaging scan used to localise the VOI must be at least 7.1 mm (1/2 a voxel) away from the VOI in the anterior and right hand side directions of the patient. This is because the VOI is positioned assuming it contains only water. Furthermore, additional lipid leakage may result from out of VOI excitation by the side lobes of the PRESS magnetisation profile.

CONCLUSIONS

With a PRESS localisation sequence it is inevitable that chemical shift images will have an intensity proportional to the spatial magnetisation distribution. Specially optimised pulses may well reduce this spatial variation in magnetisation^{11,12,13} but such pulses are often difficult to implement on a clinical system. Corrections for a non-uniform slice excitation will be needed before spectroscopic images can be quantified accurately. Such normalisation procedures will need to be chemical shift-dependent to account for the differences in spatial positioning of a SI VOI as calculated from the magnetisation profiles of different metabolites. The *in vivo* results confirm that the normalisation process has a

significant bearing upon subsequent quantitative measurements made using these spectroscopic images. As such *in vivo* PRESS localised spectroscopic images should be B_1 -normalised prior to any quantitative analysis.

Acknowledgments—The authors thank the Medical Research Council for funding through the Clinical Research Initiative in Neurosciences, Professor W. N. McDicken of the Department of Medical Physics, University of Edinburgh, Martin Connell from the Department of Medical Physics, University of Edinburgh for developing the initial CSI display software, Aad van den Boogart, Biomedical NMR unit, Katholieke Universiteit, Leuven for supplying us with the HLSVD water removal software, and Dr. Joanna Wardlaw, Dr. Robin Sellar, and Jim Cannon from the Department of Clinical Neurosciences, University of Edinburgh for their clinical and technical input.

REFERENCES

1. Marshall, I.; Wardlaw, J.; Cannon, J.; Slattery, J.; Sellar, R.J. Reproducibility of metabolite peak areas in ^1H MRS of brain. *Magn. Reson. Imaging* 14:281–292; 1996.
2. Husted, C.A.; Duijn, J.H.; Matson, G.B.; Maudsley, A.A.; Weiner, M.W. Molar quantitation of *in vivo* proton metabolites in human brain with 3D magnetic resonance spectroscopic imaging. *Magn. Reson. Imaging* 12:661–667; 1994.
3. Duyn, J.H.; Matson, G.B.; Maudsley, A.A.; Hugg, J.W.; Weiner, M.W. Human brain infarction: Proton MR spectroscopy. *Radiology* 183:711–718; 1992.
4. Soher, B.J.; van Zijl, P.C.M.; Duyn, J.H.; Barker, P.B. Quantitative proton spectroscopic imaging of the human brain. *Magn. Reson. Med.* 35: 356–363; 1996.
5. Bottomley, P.A. Spatial localization in NMR spectroscopy *in vivo*. *Ann. NY Acad. Sci.* 508:333–348; 1987.
6. Ordidge, R.J.; Cresshull, I.D. The correction of transient B_0 field shifts allowing for the application of pulsed gradient by phase correction in the time domain. *J. Magn. Reson.* 69:151–155; 1986.
7. Haase, A.; Frahm, J.; Hanicke, W.; Matthaei, D. ^1H NMR chemical shift selective (CHESS) imaging. *Phys. Med. Biol.* 30:341–344; 1985.
8. Pijnappel, W.W.F.; van der Veen, J.W.C. Quantitative analysis of MR signals in the time domain. *Isr. J. of Chem.* 28:249–261; 1988.
9. van den Boogart, A.; van Ormondt, D.; Pijnappel, W.W.F.; de Beer, R.; Ala-Korpela, M. Removal of the water resonance from ^1H magnetic resonance spectra. In: McWhirter, J. A. (Ed.). *Mathematics in Signal Processing III*. Oxford: Clarendon Press, 1994; pp. 175–195.
10. Siegel, M.M. The use of the modified simplex method for automatic phase correction in Fourier-transform nuclear magnetic resonance spectroscopy. *Analytica Chimica Acta* 133:103–108; 1981.
11. Yong, K.; Ryner, L.N.; Thomas, A. Flip angle effects in STEAM and PRESS: SLR vs sinc pulses. In: *Book of abstracts: Third Scientific Meeting of the Society of Magnetic Resonance Medicine*, Vol. 2. Berkeley, CA:SMRM; 1995:1019.

12. Pauly, J.; Le Roux, P.; Nishimura, D.; Macovski, A. Parameter relations for the Shinnar-Le Roux selective pulse design algorithm. *IEEE Trans. Med. Imag.* 10:1: 53–65; 1991.
13. Matson, G.B. An integrated program for amplitude-modulated RF pulse generation and re-mapping with shaped gradients. *Magn. Reson. Imaging* 12:1205–1225; 1994.
14. Hoult, D.I. The solution of the Bloch equations in the presence of a varying B_1 field: An approach to selective pulse analysis. *J. Magn. Reson.* 35:66–86; 1979.
15. Marshall, I., Wild, J.M. Calculations and experimental studies of the lineshape of the lactate doublet in PRESS localised ^1H MRS. *Magn. Reson. Med.* (In press)
16. Wilkinson, I.D.; Paley, M.; Chong, W.K.; Sweeney, B.J.; Shepherd, J.K.; Kendall, B.E.; Hall-Craggs, M.A.; Harrison, M.J.G. Proton spectroscopy in HIV infection: Relaxation times of cerebral metabolites. *Magn. Reson. Imaging* 12:951–957; 1994.
17. Kamada, K.; Houkin, K.; Hida, K.; Matsuzawa, H.; Iwasaki, Y.; Abe, H.; Nakada, T. Localised proton spectroscopy of focal brain pathology in humans: Significant effects of edema on spin-spin relaxation time. *Magn. Reson. Med.* 31:537–540; 1994.
18. Tofts, P.S.; Shuter, B.; Pope, J.M. Ni-DTPA doped agarose gel- a phantom material for Gd-DTPA enhancement measurements. *Magn. Reson. Imaging* 11:127–133; 1993.
19. Wild, J.M.; Marshall, I. Normalisation of metabolite images in ^1H NMR spectroscopic imaging. In: *Book of abstracts: Fifth Scientific Meeting of the Society of Magnetic Resonance Medicine, Vol. 3.* Berkeley, CA:SMRM; 1997: 1457.

Calculations and Experimental Studies of the Lineshape of the Lactate Doublet in PRESS-Localized ^1H MRS

Ian Marshall, James M. Wild

Accurate quantification of NMR metabolites by spectral modeling requires assumed lineshape functions. For singlet resonances, a combination of Lorentzian and Gaussian lineshapes is sufficient, but for weakly J-coupled resonances such as lactate, more complex lineshapes are necessary. In this work, the lactate lineshape is calculated for the PRESS sequence using standard RF pulses, and compared with experimental measurements. A similar comparison is made for PRESS-localized spectroscopic imaging, in which the lineshape varies from voxel to voxel across the field of view. These observations have important implications for the quantification of lactate in experimental and human studies.

Key words: PRESS; lactate; quantification; modeling.

INTRODUCTION

The PRESS sequence (α -t1- β -t1-t2- γ -t2-Acq) (1) is widely used to achieve spatial localization in single voxel ^1H NMR spectroscopy (2-4). In spectroscopic (chemical shift) imaging, PRESS is often used for "inner volume" excitation of brain tissue to avoid contamination of the spectra from peripheral lipids (5). In both cases, the RF pulses α , β , and γ are ideally 90° , 180° , and 180° respectively, and are applied with orthogonal slice selection gradients to define a cuboid volume of interest (VOI). Nonideal slice profiles, equivalent to a variation of flip angle across each dimension of the VOI, lead to a loss of amplitude for singlet resonances (6). Their lineshapes are unaffected, and may be modeled by combined Lorentzian and Gaussian (Voigt) functions (7, 8). For J-coupled resonances, however, the effects are much more complex, and a quantum mechanical or product operator (9) analysis is necessary. An analysis of the PRESS $\alpha_x\beta_x\gamma_x$ sequence for a weakly coupled AX_3 system such as lactate leads to an observable methyl (doublet) signal at the acquisition time of

$$\sigma_s(t_{\text{acq}}) = (k_1 I_{sy} + k_2 I_{sx} + k_3 2I_{sy}I_{1z} + k_4 2I_{sx}I_{1z}) \sin(\alpha_s) \quad [1]$$

where the coefficients k are given in the Appendix. The analysis follows the method of Jung and Lutz for an AX system (10), but is modified for the AX_3 system of lactate (11). Equation [1] represents a linear combination of lineshapes in which the individual components of the doublet are either in-phase (I_{sy} and I_{sx}) or in antiphase

($2I_{sy}I_{1z}$ and $2I_{sx}I_{1z}$) with respect to one another (Fig. 1). In the case of lactate, spin 1 refers to the methine proton whose (quartet) signal appears at approximately 4.2 ppm, and spin s refers to the three equivalent methyl protons (numbered 2, 3, and 4) contributing to the doublet at 1.35 ppm. The chemical shift difference between these two resonances is δ , and leads to different flip angles for the two components (subscripted by 1 for the methine proton and s for the methyl protons) depending on the gradient strength used for spatial localization. The excitation pulse angle α_s affects the amplitude of the complex doublet, whereas nonideal refocusing pulses β_1 , β_s , γ_1 , and γ_s give rise to the antiphase components by a process of polarization transfer between the methyl and methine protons. The refocusing pulses available on many scanners are of the sinc variety, which have fairly poor slice (and therefore flip angle) profiles, and hence some degree of polarization transfer is present (12). Phase correction cannot then be applied to the spectrum to reduce it to the "ideal" in-phase doublet of Fig. 1a, even when the echo time (TE) is a multiple of $1/J$.

In this work, we applied Eq.[1] to predict the lactate doublet lineshape in both single voxel PRESS spectroscopy and spectroscopic (chemical shift) imaging with PRESS localization. We then measured experimental lineshapes using the standard PRESS pulse sequences available on our scanner.

METHOD

Simulations

The coefficients in Eq.[1] were derived analytically for the PRESS sequence ($\alpha_x\beta_x\gamma_x$) available on our scanner (Siemens Magnetom 63SP) as functions of flip angles and timing, taking into account the chemical shift difference between the methyl and methine protons. The VOI was considered as a 3-dimensional array of $40 \times 40 \times 40$ subvoxels, with the flip angles applied along the three directions. The flip angle distribution along each axis was calculated for the Hanning-weighted sinc RF pulse envelopes available on our scanner. A method using the Cayley-Klein parameters to solve the Bloch Equation (13) was implemented in Matlab (The MathWorks Inc, Natick, MA), and was evaluated at 40 sample points across the VOI. The spatial dimensions were scaled such that the flip angles had fallen to half their nominal (center) values at the 10th and 30th sample points. Eq. [1] was then evaluated for each of the 40^3 subvoxels, again using Matlab. Our sequence is asymmetrical, with $t1 = 30$ ms, and the slice selection gradients (2 mT/m for single voxel spectroscopy) lead to a chemical shift of two subvoxels in each direction. We used a coupling constant of $J = 6.9$ Hz ($2/J = 290$ ms). To simulate single voxel spectroscopy, the 40^3 results were summed to yield mean coefficients. A composite lineshape was then calculated from the

MRM 38:415-419 (1997)

From the Department of Medical Physics and Medical Engineering, University of Edinburgh.

Address correspondence to: Ian Marshall, Ph.D., MRI Unit, Western General Hospital, Edinburgh, EH4 2XU, United Kingdom.

Received January 13, 1997; revised March 11, 1997; accepted March 11, 1997.

This work was funded in part by the Medical Research Council's Clinical Research Initiative into acute brain injury.

0740-3194/97 \$3.00

Copyright © 1997 by Williams & Wilkins

All rights of reproduction in any form reserved.

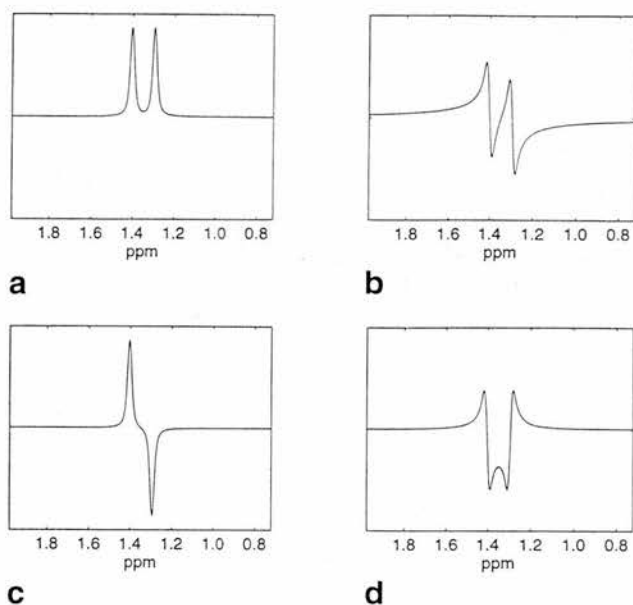


FIG. 1. Lactate methyl doublet basis functions of Eq.[1], with $1/J = 145$ ms, $T_2 = 300$ ms, and Gaussian linebroadening of FWHM = 1 Hz. (a) I_{sy} , the "conventional" or "ideal" absorption mode lineshape; (b) I_{sx} ; (c) $2I_{sy}I_{1z}$; (d) $2I_{sx}I_{1z}$.

basis functions of Fig. 1, using a transverse relaxation time T_2 of 300 ms, and with Gaussian linebroadening of full width at half maximum (FWHM) of 1 Hz to represent susceptibility variations over the VOI (7, 8). The composite lineshapes correspond to the "real" (absorption) mode spectra, which are observed along the negative y -axis on our scanner. In our implementation of spectroscopic imaging, the phase encoding is applied in the α and β directions, while the third direction (corresponding to γ) is unresolved spatially. Thus to simulate the observed spectra, we summed over the 40 subvoxels corresponding to the γ direction. Subvoxels in the α and β directions were grouped to yield the same number of within-VOI voxels as measured experimentally.

In Vitro Spectroscopy

All experiments were conducted on a standard Siemens 1.5T Magnetom 63SP equipped with unshielded gradients of maximum strength 10 mT/m. The standard head coil was used, and the manufacturer's spectroscopy phantom (containing 100 mM acetate and 100 mM lactate) was placed in a saline-filled loading annulus inside the coil. The phantom and coil were positioned at the isocenter of the magnet. Semi-automatic shimming using the linear and Z2 gradients was conducted, based on 3-dimensional field mapping (14). A 24-mm cubical volume of interest (VOI) was localized at the center of the phantom using the scanner's standard PRESS sequence, with a repetition time (TR) of 5s and the recommended echo time (TE) of 135 ms. Four water reference acquisitions were collected, followed by eight acquisitions with CHESS water suppression. Each acquisition consisted of 4096 samples taken at 250- μ s intervals. The experiment was repeated with echo times of 145, 270, and 290 ms. Data processing consisted of time domain phase correc-

tion using the water reference signal to remove the effects of eddy currents (15), mild apodization by a Gaussian window (equivalent FWHM = 0.5 Hz) and Fourier transformation. A further zero-order phase correction of 6° was applied to bring the acetate peak into pure absorption mode. The same processing (including the 6° final phase correction) was applied for each echo time.

Spectroscopic imaging in a transverse plane was conducted using the manufacturer's sequence with PRESS-localized inner volume excitation and an echo time of 135 ms. The sequence was run with a 60×60 mm in-plane VOI (with 0.8 mT/m slice selection gradients) and a thickness of 15 mm (with 3 mT/m slice selection gradient). The FOV was 192 mm, with a 32-by-16 phase encoding matrix giving a voxel size of 6 mm (in the β pulse direction) \times 12 mm (in the α direction) \times 15 mm. The repetition time was 2.5s, thereby giving an acquisition time of 21 min. Both water reference and (CHESS) water-suppressed data sets were acquired. Data processing consisted of 2-dimensional Fourier transformation, phase correction using the water reference data, Gaussian apodization with a FWHM of 0.5Hz, and a final Fourier transformation to the spectral domain.

RESULTS AND DISCUSSION

Figure 2 shows the calculated components of Eq.[1] (see Appendix) for the asymmetrical PRESS sequence used, as a function of TE . The excitation pulse α_s has been set to 90° to maximize the signals. In Fig. 2a, the refocusing pulses have been set to their ideal values of 180° , and the graphs show the behavior predicted by simple theory. Thus at $TE = 145$ ms ($1/J$), I_{sy} attains its maximum value of unity (while the other components are zero), and a pure in-phase doublet corresponding to Fig. 1a is observed. With observation being along the negative y -axis, the doublet is actually inverted. Similarly, at $TE = 290$ ms ($2/J$) an upright in-phase doublet is observed. When TE is $3/2J$ (217.5 ms), only the $2I_{sx}I_{1z}$ component is non-zero, and the antiphase doublet of Fig. 1d is observed. With refocusing pulses of 180° , there are no polarization transfer effects, and the results of Fig. 2a are obtained regardless of the individual values of t_1 and t_2 . Thus the symmetrical PRESS sequence discussed by Jung and Lutz (10) behaves identically under these ideal conditions.

In Fig. 2b, the refocusing pulses have been set to 90° to maximize the polarization transfer between the methine and methyl protons. The behavior of the four components is now a complicated function of TE . The most obvious feature is the sinusoidal modulation at a frequency of $\delta/2$ (89.25 Hz; period 11.2 ms). The amplitude of this modulation as a function of TE is quite different for symmetrical and asymmetrical sequences.

In a real PRESS experiment, the behavior falls between the extremes of Figs. 2a and 2b according to the flip angle profile across the VOI.

The Hanning-weighted sinc waveform used for the 180° RF pulse envelopes is shown in Fig. 3, together with its corresponding flip angle profile. It can be seen that the nominal 180° (π radian) flip angle falls fairly sharply away from the center of the slice. Lengthening the RF

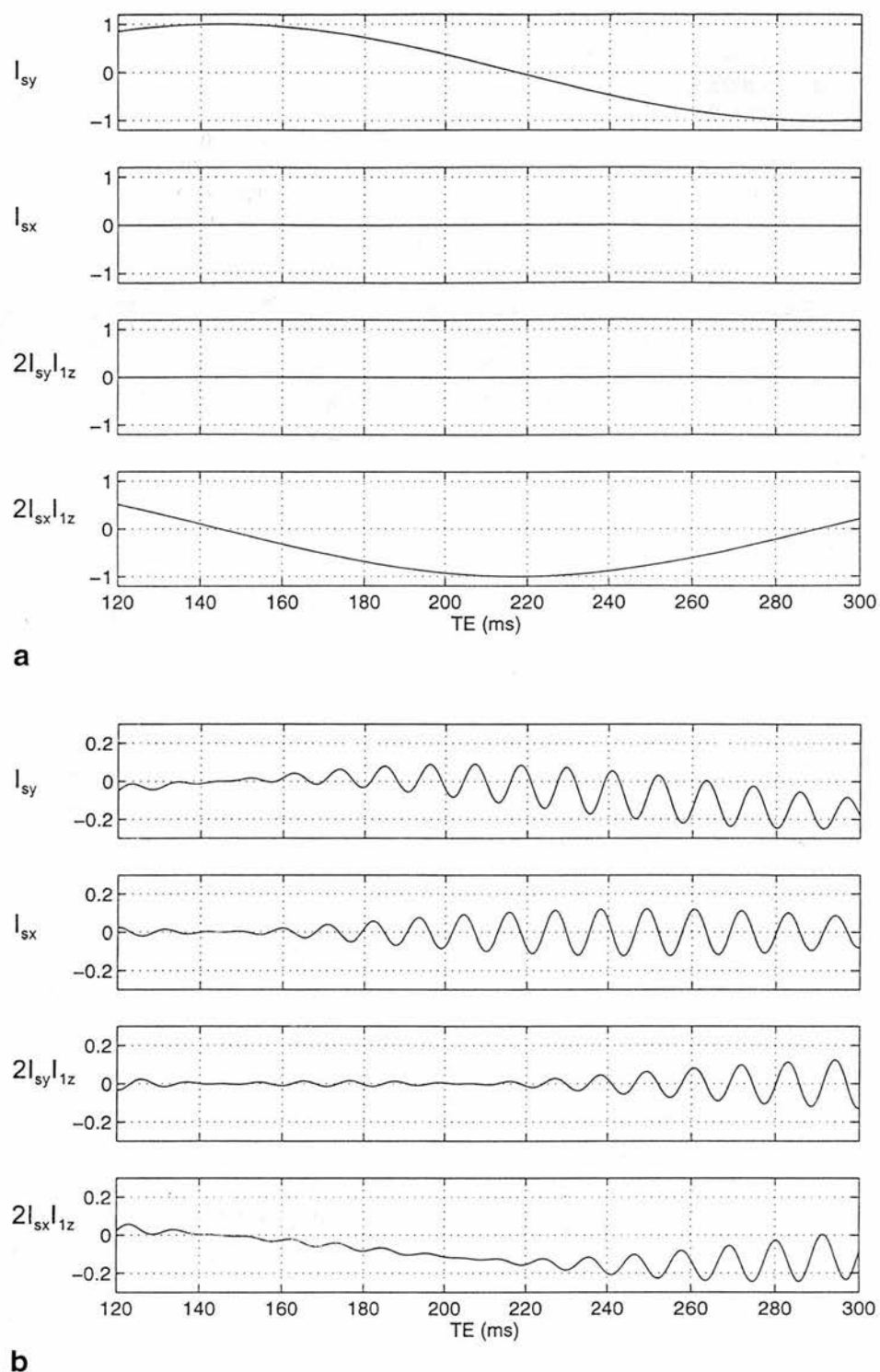


FIG. 2. Behavior of the components of Eq.[1] as a function of echo time TE for the (asymmetrical) PRESS spectroscopic pulse sequence used in this work. (a) With ideal 180° refocusing pulses for β_1 , β_s , γ_1 , and γ_s , the behavior is as expected by simple theory; (b) when the refocusing pulses are all 90° , maximum polarization transfer occurs, and the behavior is a complex function of sequence timing. In a real experiment, the behavior falls between these two extremes according to the flip angle profile across the VOI.

pulse to increase the number of side lobes (i.e., improving the sinc approximation) did not improve the calculated flip angle profile. The poor profile is thus a direct

result of the nonlinearity of the Bloch equations, which becomes important for such large flip angles. Using a value of $J = 6.9$ Hz (i.e., $2/J = 290$ ms), and summing Eq.[1] over all subvoxels gave reasonable agreement with the experimental single voxel spectra for $\delta = 178.5$ Hz (Fig. 4). Calculated spectra for $TE = 135$ and 145 ms do not show as much asymmetry as observed experimentally, but agreement is better at $TE = 270$ and 290 ms. Note the asymmetry and "distorted baselines" compared with the "ideal" doublet of Fig. 1a. The asymmetry arises from the polarization transfer components. Small changes (± 1 Hz) in the value of δ used in the simulations caused significant changes in the appearance of the doublet, especially around 145 and 290 ms. This is because of the modulation effect of the polarization transfer caused by the relatively poor flip angle profile, as demonstrated in Fig. 2b. By contrast, varying $1/J$ in the range 135 to 145 ms had relatively little effect on the lineshape.

Using the same values of J and δ , we calculated the expected appearance of the lactate doublet for a spectroscopic imaging experiment. Summation was conducted over all 40 subvoxels in the γ direction, and subvoxels in the other two directions were grouped to yield a 20×20 array of voxels within the VOI. Each row is simply scaled by $\sin(\alpha_s)$ relative to the central row, whereas along each row the lineshape changes as the angles β_1 and β_s vary. The central row is shown in Fig. 5b, and the corresponding experimental result in Fig. 5a. It can be seen that the main features are predicted well, with the amplitude falling from a maximum at the center of the row towards the noise level at the ends of the row (beyond the edges of the nominal VOI). Small, poorly phased doublets are observed in the transition regions. The asymmetry between the left-hand and right-hand transition re-

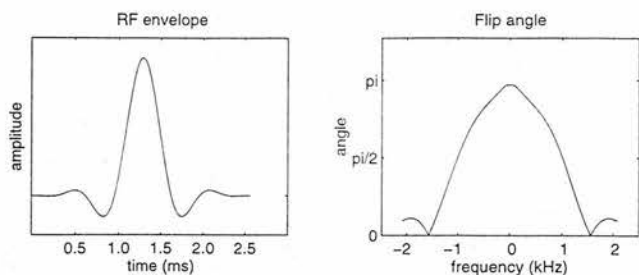


FIG. 3. 180° Hanning-weighted sinc RF pulse waveform as used experimentally, and the corresponding calculated flip angle profile.

gions occurs because of the chemical shift between the methine and methyl protons. Figure 5c shows the calculated spectra obtained when the chemical shift effect is ignored.

Several effects may be responsible for disagreement between the simulated and experimental lineshapes, including inaccurate estimation of δ , imperfect spoiling and out of plane rotation by pulses. We measured the effective δ for the manufacturer's phantom using the HOPE sequence (16), a version of PRESS in which the two refocusing pulses are nominally 90° to maximise the polarization transfer effects (as in Fig. 2b). Fitting the integrated intensity of the lactate doublet for echo times around 290 ms gave $\delta = 178.5(\pm 1.7)$ Hz, which is in excellent agreement with the value we found optimal for matching calculated with experimental lineshapes. However, other sources of error should be considered. Imperfect spoiling would lead to retention of spin components other than those that have been in single quantum states throughout the sequence, and that would therefore have experienced variable amounts of relaxation. Residual eddy current effects may also be significant, especially with unshielded gradient coils as used in this work. A further contribution to the flip angle distribution will be caused by any nonuniformity in head coil RF sensitivity. The use of fairly small VOIs placed at the center of the coil will minimize this effect.

A more complete analysis of the RF pulses shows that the rotations are not exactly about the intended axis. For example, the excitation pulse α_x creates a small amount of x -magnetization M_x in addition to the intended M_y . We are currently investigating these effects.

It is expected that the next generation of MRI scanners will be supplied with numerically optimised RF pulses having significantly better slice profiles than are available on many current machines, particularly for 180° pulses. Alternatives are the use of STEAM localization, with its inherently better 90° refocusing pulses (but only half the signal strength of PRESS), or the use of short echo times to reduce the effects of J-modulation. However, short echo time spectra are complicated by broad macromolecular resonances. Accurate quantification of J-coupled spectra must in general take account of the flip angle variation and timing of localization sequences. Successful spectral modeling will need to include the four basis functions of Fig. 1.

CONCLUSIONS

Calculations and experimental measurements of the lactate doublet lineshape in PRESS spectroscopy show that the lineshape cannot be considered simply as a pair of singlet lineshapes spaced apart by J . A full treatment is necessary for the particular sequence timing and RF pulse envelopes used in order to specify the lineshape. In spectroscopic imaging experiments, the lineshape is also a function of spatial position if PRESS is used for inner volume excitation. These considerations should be taken into account when quantifying lactate by means of spectral modeling. The methods used here may readily be extended to consider other weakly coupled metabolites, and the STEAM localization sequence.

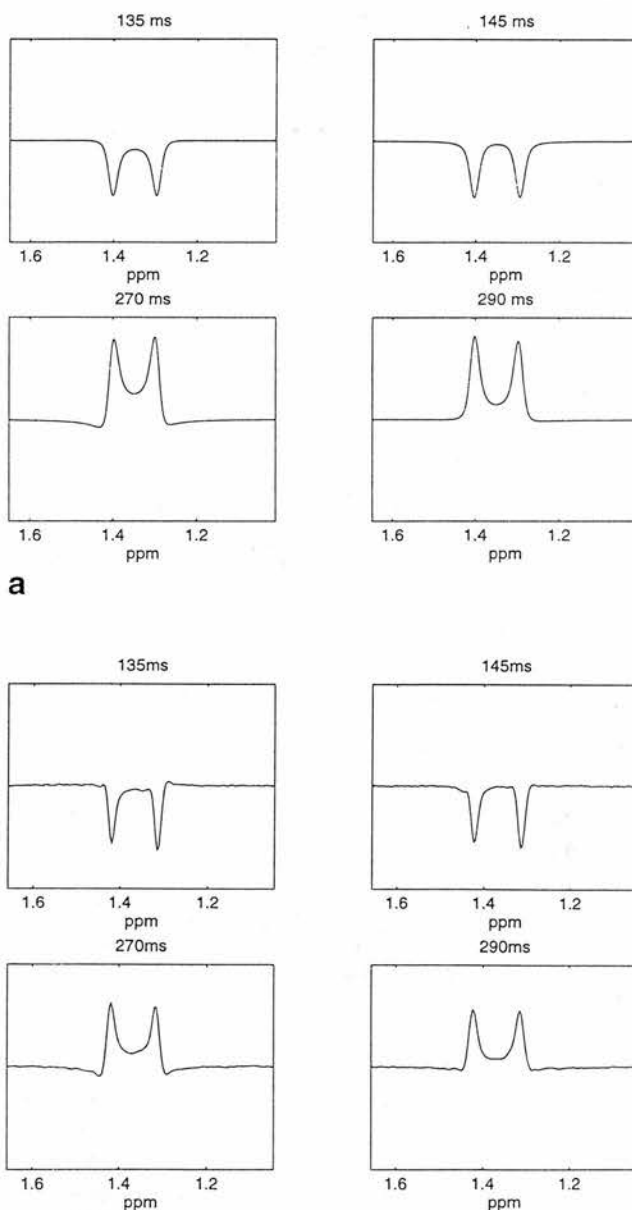


FIG. 4. (a) Calculated and (b) experimental appearance of the lactate doublet for PRESS single voxel spectroscopy with echo times (TE) of 135, 145, 270, and 290 ms.

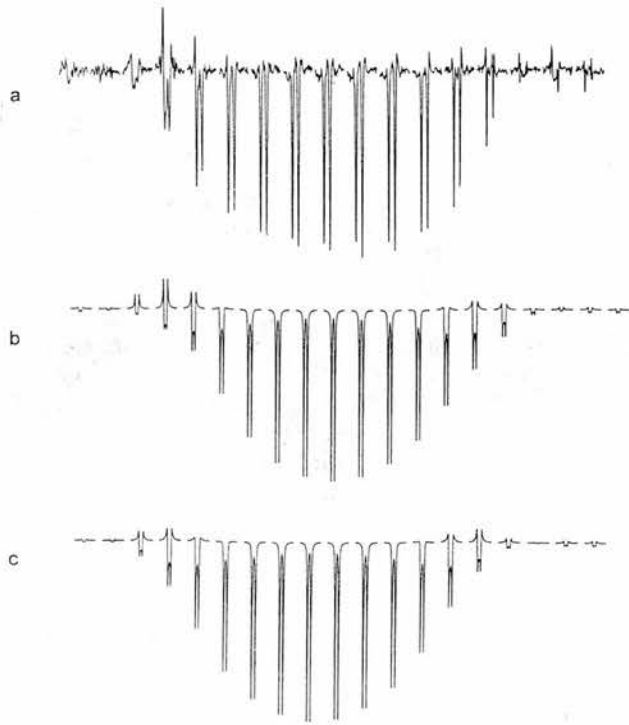


FIG. 5. (a) Experimental appearance of the lactate doublet for the central row of a PRESS-localized spectroscopic imaging experiment with $TE = 135$ ms; (b) corresponding calculated spectra. The flip angles β_1 and β_s decrease from their nominal value of 180° at the center of the VOI towards the edges. Note the asymmetry between the two edges due to the chemical shift effect; (c) calculated spectra neglecting the chemical shift effect.

ACKNOWLEDGMENTS

The authors thank Dr. Michael Bunse for useful discussions.

APPENDIX

The coefficients of Eq.[1] can be calculated by the product operator method (9–11). Assuming ideal spoiler gradients which retain only magnetization that has been in a single quantum state for the entire sequence (the $[-1, 1, -1]$ coherence pathway (17)), the coefficients k are

$$\begin{aligned}
 k_1 &= \frac{1}{4} P \sin(\pi t_1) \sin(\pi t_2) \cos(\pi(t_1 + t_2)) \\
 &\quad \cos(\delta(t_1 + t_2)) \\
 &\quad - \frac{1}{2} A \cos^2(\pi t_2) (1 - \cos(\gamma_s)) \\
 &\quad - \frac{1}{2} A \sin^2(\pi t_2) \cos(\gamma_s) (1 - \cos(\gamma_1)) \\
 &\quad + \frac{1}{2} B \sin(\pi t_2) \cos(\pi t_2) (2\cos(\gamma_s) - 1 - \cos(\gamma_1)\cos(\gamma_s)) \\
 k_2 &= -\frac{1}{4} P \sin(\pi t_1) \sin(\pi t_2) \cos(\pi(t_1 + t_2)) \sin(\delta(t_1 + t_2)) \\
 k_3 &= \frac{1}{4} P \sin(\pi t_1) \cos(\pi t_2) \cos(\pi(t_1 + t_2)) \sin(\delta(t_1 + t_2)) \\
 k_4 &= \frac{1}{4} P \sin(\pi t_1) \cos(\pi t_2) \cos(\pi(t_1 + t_2)) \cos(\delta(t_1 + t_2)) \\
 &\quad + \frac{1}{2} B \sin^2(\pi t_2) (1 - \cos(\gamma_s)) \\
 &\quad + \frac{1}{2} B \cos^2(\pi t_2) \cos(\gamma_s) (1 - \cos(\gamma_1)) \\
 &\quad - \frac{1}{2} A \sin(\pi t_2) \cos(\pi t_2) (2\cos(\gamma_s) - 1 - \cos(\gamma_1)\cos(\gamma_s))
 \end{aligned}$$

where

$$\begin{aligned}
 A &= \frac{1}{2} \cos^2(\pi t_1) (1 - \cos(\beta_s)) + \frac{1}{2} \sin^2(\pi t_1) \cos(\beta_s) \\
 &\quad (1 - \cos(\beta_1)) \\
 B &= \frac{1}{2} \sin(\pi t_1) \cos(\pi t_1) (2\cos(\beta_s) - 1 - \cos(\beta_1)\cos(\beta_s)) \\
 P &= \sin(\beta_1) \sin(\beta_s) \sin(\gamma_1) \sin(\gamma_s)
 \end{aligned}$$

and β and γ are the refocusing pulse flip angles (subscripted by 1 for the methine proton and by s for the methyl protons), t_1 and t_2 are the interpulse timings, J is the magnitude of the coupling between the methine and methyl protons, and δ is the corresponding chemical shift difference. Unlike the AX system, no observable methyl signal is produced by single polarization transfer from the methine proton. Only nontransferred methyl polarization and double polarization transfer components (methyl- β -methine- γ -methyl) contribute to the final methyl signal. The latter components include the factor P in the above expressions.

REFERENCES

1. P. A. Bottomley, Spatial localization in NMR spectroscopy *in vivo*. *Ann. N.Y. Acad. Sci.* **508**, 333–348 (1987).
2. I. D. Wilkinson, M. Paley, W. K. Chong, B. J. Sweeney, J. K. Shepherd, B. E. Kendall, M. A. Hall-Crags, M. J. G. Harrison, Proton spectroscopy in HIV infection: relaxation times of cerebral metabolites. *Magn. Reson. Imaging* **12**, 951–957 (1994).
3. E. B. Cady, Quantitative combined phosphorus and proton PRESS of the brains of newborn human infants. *Magn. Reson. Med.* **33**, 557–563 (1995).
4. D. G. Gadian, N-acetylaspartate and epilepsy. *Magn. Reson. Imaging* **13**, 1193–1195 (1995).
5. N. de Stefano, P. M. Matthews, D. L. Arnold, Reversible decreases in N-acetylaspartate after acute brain injury. *Magn. Reson. Med.* **34**, 721–727 (1995).
6. I. Marshall, J. Wild, J. Wardlaw, Spectral distortion caused by PRESS excitation. British Institute of Radiology meeting on Spectral Localisation, London, June 1996. *Br. J. Radiol.* **69**, 1199 (1996).
7. S. D. Bruce, I. Marshall, J. Higinbotham, P. H. Beswick, The application of a numerical approximation of the Voigt function to synthetically generated MRS data, in "Proc., 13th European Experimental NMR Conference, Paris, May 1996," p. 346.
8. I. Marshall, J. Higinbotham, S. Bruce, A. Freise, Use of Voigt lineshape for quantification of *in vivo* ¹H spectra. *Magn. Reson. Med.* **37**, 651–657 (1997).
9. O. W. Sorensen, G. W. Eich, M. H. Levitt, G. Bodenhausen, R. R. Ernst, Product operator formalism for the description of NMR pulse experiments. *Prog. NMR Spectrosc.* **16**, 163–192 (1983).
10. W.-I. Jung, O. Lutz, Localized double-spin-echo proton spectroscopy of weakly coupled homonuclear spin systems. *J. Magn. Reson.* **96**, 237–251 (1992).
11. M. Bunse, W.-I. Jung, O. Lutz, K. Küper, G. Dietze, Polarization-transfer effects in localized double-spin-echo spectroscopy of weakly coupled homonuclear spin systems. *J. Magn. Reson. A* **114**, 230–237 (1995).
12. F. Schick, T. Nagele, U. Klose, O. Lutz, Lactate quantification by means of PRESS spectroscopy - influence of refocusing pulses and timing scheme. *Magn. Reson. Imaging* **13**, 309–319 (1995).
13. J. Pauly, P. Le Roux, D. Nishimura, A. Macovski, Parameter relations for the Shinnar-Le Roux selective excitation pulse design algorithm. *IEEE Trans. Med. Imaging* **10**, 53–65 (1991).
14. H. Wen, F. A. Jaffer, An *in vivo* automated shimming method taking into account current constraints. *Magn. Reson. Med.* **34**, 898–904 (1995).
15. R. J. Ordidge, I. D. Cresshull, The correction of transient B_0 field shifts following the application of pulsed gradients by phase correction in the time domain. *J. Magn. Reson.* **69**, 151–155 (1986).
16. M. Bunse, W.-I. Jung, F. Schick, G. J. Dietze, O. Lutz, HOPE, a new lactate editing method. *J. Magn. Reson. Series B* **109**, 270–274 (1995).
17. G. J. Barker, T. H. Mareci, Suppression of artifacts in multiple-echo magnetic resonance. *J. Magn. Reson.* **83**, 11–28 (1989).

A Systematic Study of the Lactate Lineshape in PRESS-Localized Proton Spectroscopy

Ian Marshall, James Wild

J-coupled resonances such as lactate exhibit complex behavior in PRESS-localized spectroscopy. Polarization transfer effects due to nonideal slice profiles can lead to substantial errors in quantification unless recognized. In this work, it is shown how these effects can be predicted in a systematic way given the sequence timing and the RF pulse envelopes. Experimental results are presented to highlight the problems of working at the popular echo time of $2/J$.

Key words: PRESS; lactate; quantification; modeling.

INTRODUCTION

The double spin-echo (PRESS) spectroscopic sequence can be represented by $(\alpha-t_1-\beta-t_1-\gamma-t_2-\text{Acq})$ where the RF pulses α , β , and γ are ideally 90, 180, and 180°, respectively. These pulses are applied in the presence of orthogonal slice-selection gradients to localize a volume of interest (VOI). Nonideal slice profiles lead to polarization transfer effects for *J*-coupled resonances, and various authors have studied this phenomenon (1–4). Jung and Lutz (1) gave a theoretical analysis of the weakly coupled AX₃ system, and presented experimental results for lactate (an AX₃ system) with symmetrical PRESS sequences ($t_1 = t_2$) having echo times (TE = $2t_1 + 2t_2$) of multiples of $1/J$. They also compared symmetrical and asymmetrical sequences at TE = $1/J$ and $2/J$. In an experimental study, Schick *et al.* (2) compared lactate spectra acquired with TE around $1/J$ and around $2/J$ using three different RF pulse shapes for spatial localization, and they showed the effect of using different ratios of $t_1 : t_2$. Bunse *et al.* (3) gave an analysis of the weakly coupled AX₃ system subjected to symmetrical PRESS sequences with TE around $(4n - 2)/J$ ($n = 1, 2, \dots$), under which conditions polarization transfer effects are maximized. Experimental results with lactate confirmed the expected behavior. Marshall and Wild (4) gave a theoretical expression for the observable doublet when lactate is subjected to a generalized PRESS sequence, and showed how the doublet lineshape can be calculated given the RF pulse envelopes and the slice-selection gradients. To validate the calculations, they presented experimental results corresponding to asymmetrical sequences.

In this work, we concentrate on the integrated intensity of the lactate doublet lineshape, as this is still the most

popular means of quantification, and, indeed, the only method available on many scanners. By means of surface and line plots, we show systematically the theoretical effects of varying t_1 and t_2 . Experimental results are presented to highlight the problems of working at the popular echo time of $2/J$.

METHOD

A product operator analysis (5) of the PRESS sequence (either $\alpha_x\beta_x\gamma_x$ or $\alpha_x\beta_y\gamma_y$) for a weakly coupled AX₃ system such as lactate leads to an observable methyl (doublet) signal at the acquisition time of

$$\sigma_s(t_{\text{acq}}) = (k_1 I_{sy} + k_2 I_{sx} + k_3 2I_{sy}I_{1z} + k_4 2I_{sx}I_{1z}) \sin(\alpha_s) \quad [1]$$

where the coefficients k have been reported previously (4), but are given in the Appendix for convenience. Equation [1] represents a linear combination of magnetization states in which the individual components of the doublet are either in-phase (I_{sy} and I_{sx}) or in antiphase ($2I_{sy}I_{1z}$ and $2I_{sx}I_{1z}$) with respect to one another. Nonideal refocusing pulses β_1 , β_s , γ_1 , and γ_s give rise to the antiphase components by a process of polarization transfer between the methyl and methine protons.

Simulations

The simulation method was largely as described previously (4), and so will only be summarized here. The coefficients in Eq.[1] were calculated for t_1 and t_2 , each ranging from 0 to 300 ms. The VOI was considered as a three-dimensional array of $40 \times 40 \times 40$ subvoxels (each a 1-mm cube), with the flip angles applied along the three directions. The flip-angle distribution along each axis was calculated for the sinc pulses available on our scanner (Siemens Magnetom 63SP) as shown previously (4), using 2 mT/m slice-selection gradients. The chemical-shift difference δ between the methyl and methine protons is 178.5 Hz, and leads to a displacement of 2.1 mm (two subvoxels) between their respective VOIs, and hence the two groups receive different flip angles. The flip angles had fallen to half their central (nominal) values at 12 mm in each direction, corresponding to an effective experimental VOI of 24-mm dimension. For each combination of t_1 and t_2 , Eq. [1] was evaluated for each of the 40^3 subvoxels, and the results summed to yield mean coefficients. Idealized refocusing pulses of 90 and 180° were also studied. The coupling constant was $J = 6.9$ Hz ($2/J = 290$ ms). Assuming ideal peak area integration (i.e., between infinite limits) or curve fitting, only the I_{sy} state yields a nonzero lineshape integral, and coefficient k_1 then gives the integrated lineshape area. For selected combinations of t_1 and t_2 , composite lineshapes were calculated using basis functions with a

MRM 39:●●●-●●● (1998)

From the Department of Medical Physics and Medical Engineering, University of Edinburgh, Edinburgh, United Kingdom.

Address correspondence to: Ian Marshall, Ph.D., Department of Medical Physics and Medical Engineering, Western General Hospital, Edinburgh, EH4 2XU, United Kingdom.

Received September 23, 1997; revised January 15, 1998; accepted January 15, 1998.

This work was supported in part by the UK Medical Research Council.

0740-3194/98 \$3.00

Copyright © 1998 by Williams & Wilkins

All rights of reproduction in any form reserved.

transverse relaxation time T_2 of 300 ms, and with Gaussian line broadening of full width at half maximum (FWHM) of 1 Hz. Coefficient calculations were carried out using code written in the C language and took several days to run on an UltraSPARC workstation (Sun Microsystems Computer Company, Mountain View, CA). Visualization of results was by Matlab (The Mathworks, Inc., Natick, MA).

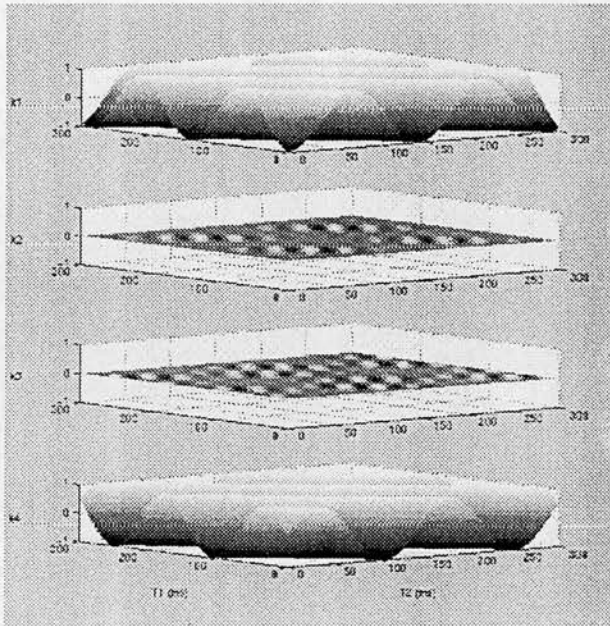
In Vitro Spectroscopy

Experiments were carried out on a Siemens 1.5 T Magnetom 63SP to demonstrate the unwanted polarization transfer effects that occur in symmetrical PRESS sequences around $TE = 2/J$. A phantom containing 100 mM lactate was placed in a saline-filled loading annulus inside the head coil and positioned at the isocenter of the magnet. After shimming, a 24-mm (nominal size) cubical VOI was localized at the center of the phantom using a PRESS sequence with user selectable t_1 and t_2 . Symmetrical sequences (i.e., $t_1 = t_2$) from $TE = 285$ to 292 ms

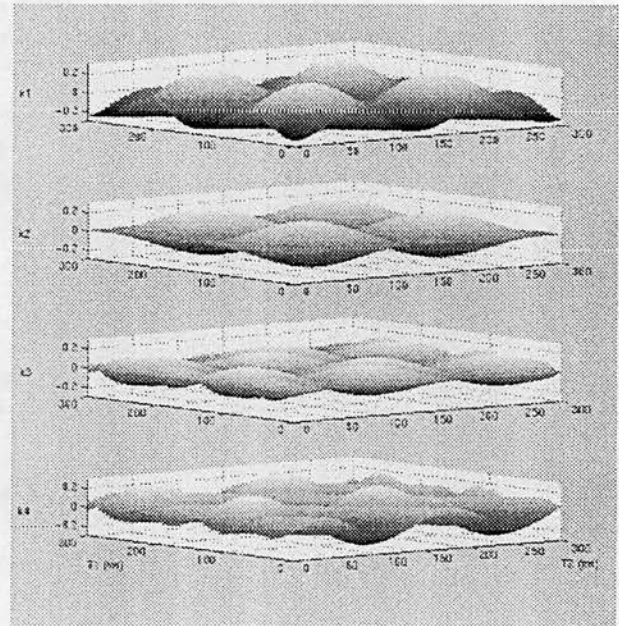
were run, with four water reference acquisitions and eight acquisitions with chemical shift selective (CHESS) water suppression being collected at each TE. Data processing consisted of time domain phase correction (6), removal of residual water components by the Hankel-Lanczos singular value decomposition (HLSVD) method (7), mild apodization by a Gaussian window (equivalent FWHM = 0.5 Hz), and Fourier transformation.

RESULTS AND DISCUSSION

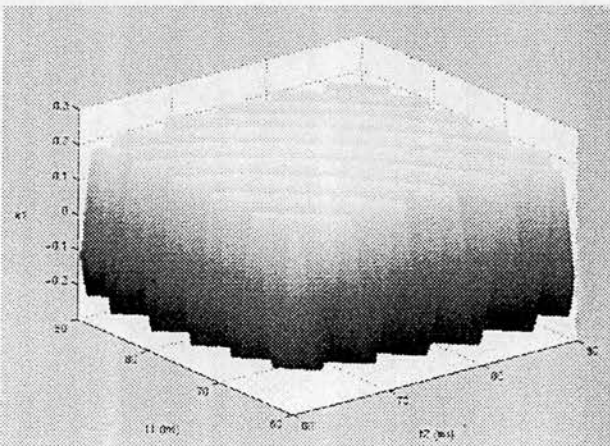
The coefficients k of Eq. [1] are portrayed in Fig. 1 as functions of the sequence timing parameters t_1 and t_2 . In Fig. 1a, the refocusing pulses have been set to their ideal values of 180° , and the coefficients k_2 and k_3 are zero (within computational errors). Coefficients k_1 and k_4 appear as wavelike surfaces of unit amplitude. The "crests" and "troughs" are aligned along lines of constant echo time, with k_4 being out of phase by $\pi/2$ with respect to k_1 . In Fig. 1b, the refocusing pulses have been set to 90° to



a



b



c

FIG. 1. Coefficients k of Eq. [1] as a function of t_1 and t_2 . The echo time TE is $2t_1 + 2t_2$. (a) Refocusing pulses of 180° : from top to bottom, k_1 , k_2 , k_3 , k_4 ; (b) refocusing pulses of 90° ; (c) expanded detail of k_1 with 90° refocusing pulses.

(F_1)

Orig. Op.	OPERATOR:	Session	PROOF:	PE's:	AA's:	COMMENTS	ARTNO:
			D				

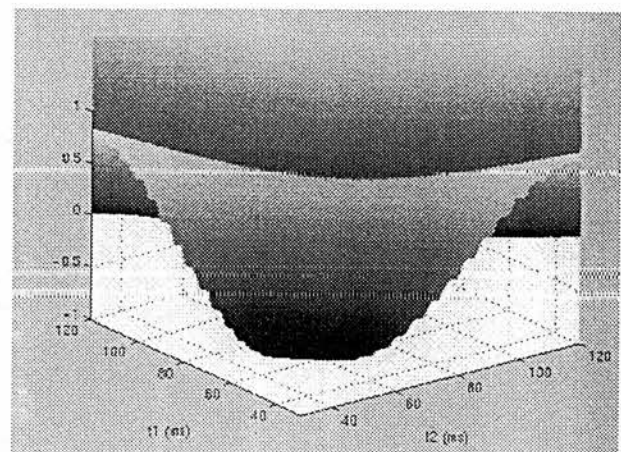
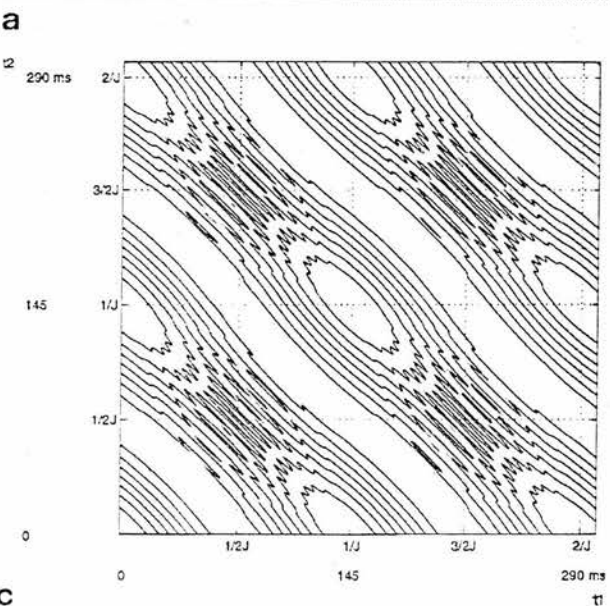
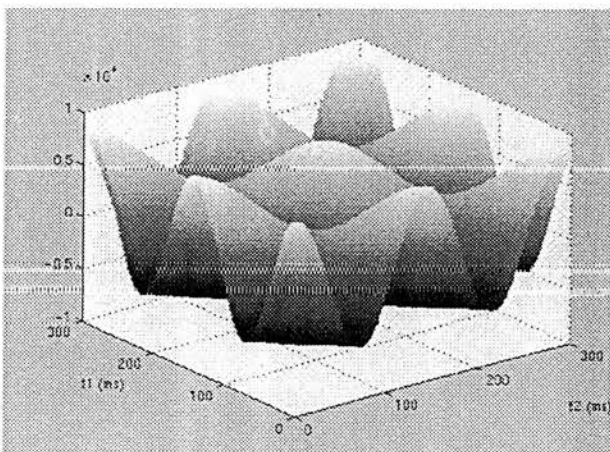
demonstrate the polarization transfer effect. All coefficients are now nonzero and exhibit a complex behavior. In Fig. 1c is shown an enlarged detail of k_1 of Fig. 1b. The "smooth" hump nearest to the viewpoint in Fig. 1b is now revealed to consist of rapid sinusoidal modulations with a period of slightly over 5 ms (in fact 5.6 ms, being equal to $1/\delta$) in $(t_1 + t_2 = TE/2)$. This is the polarization transfer effect.

Basis lineshapes for the methyl doublet were calculated using $1/J = 145$ ms, a spin-spin relaxation time T_2 of 300 ms, and Gaussian line broadening of FWHM of 1 Hz, as described previously (4). Only the pure absorption doublet I_{sy} has a nonzero peak area integral, and so only k_1 need be considered when calculating lineshape areas. All the basis functions contribute to the shape of the doublet, however.

Figure 2a is the central result of this work. It shows the integrated lactate doublet lineshape area (i.e., k_1) arising from a PRESS-localized sequence using Hanning-weighted sinc refocusing pulses of nominal flip angle 180° . The chemical-shift displacement effect of the 2 mT/m slice-selection gradients has been taken into account, as has the polarity of the receiver channels. The lineshape area has been normalized to the theoretical

maximum that occurs for $t_1 = t_2 = 1/J$. The integrated area combines the wavelike features of Fig. 1a with the more complex features of Fig. 1b, as can be seen more clearly in the enlarged detail of Fig. 2b. This shows the polarization transfer modulation superimposed on the gross features of the surface. The integrated lineshape area is presented in Fig. 2c as a contour map that clearly reveals the polarization transfer "fingers" in addition to the gross wavelike features.

Figure 3 shows a section through the integrated lineshape area surface (Fig. 2) corresponding to PRESS sequences with a fixed t_1 of 30 ms. This value was chosen because it corresponds to the standard Siemens PRESS sequence. The range of t_2 is from 0 to 300 ms, yielding echo times from 60 to 660 ms. In an actual sequence, t_2 would have a minimal value somewhat larger than zero to accommodate slice selection and crusher pulses. Several interesting features are evident from Fig. 3; the negative excursions of the area (around $TE = 1/J$ and $3/J$) are smaller than the positive excursions (around $TE = 2/J$ and $4/J$), having values of -0.60 and 0.81, respectively. Thus, neglecting T_2 relaxation, increasing the echo time from 145 to 290 ms would actually *increase* the signal from lactate. In a real experiment in which relaxation



b

FIG. 2. (a) Integrated intensity of the lactate doublet lineshape as a function of t_1 and t_2 , normalized to the theoretical maximum (which occurs for $t_1 = t_2 = 1/J$). PRESS localization with Hanning-weighted sinc refocusing pulses of nominal flip angle 180° , 24-mm VOI, and 2 mT/m localization gradients; (b) detail; (c) plan view with contours.

T

Orig. Op.	OPERATOR:	Session	PROOF:	PE's:	AA's:	COMMENTS	ARTNO:
1st disk, 2nd JHC	shropsha	7	<i>D</i>				036936

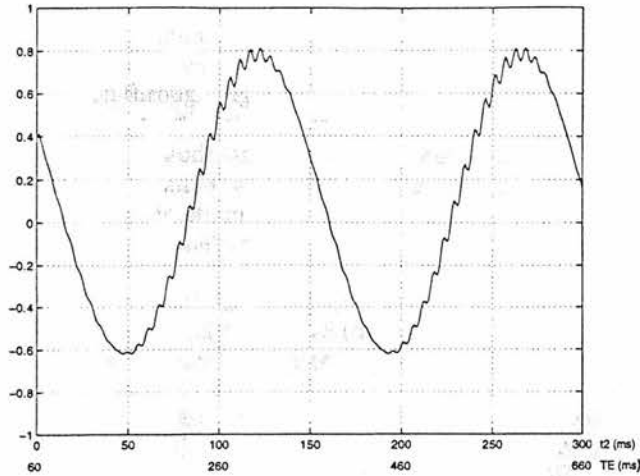


FIG. 3. Section through the surface of Fig. 2 for an asymmetrical PRESS sequence with a fixed t_1 of 30 ms.

occurs, the signal at 290 ms may be larger, smaller, or about the same as that at 145 ms. Polarization transfer modulation is more pronounced as the echo time increases from $1/J$ to $2/J$ than from $2/J$ to $3/J$; i.e., the effect is not symmetrical about $TE = 2/J$. This behavior is repeated from $3/J$. The asymmetries are simply due to the way in which the surface of Fig. 2 is cut, as is most clearly seen by inspection of the contours in Fig. 2c. The polarization transfer effect is most apparent around echo times of $2/J$ and $4/J$, amounting to a 7% difference in signal for slightly different echo times. Even multiples of $1/J$ should, therefore, be avoided if attempting to make quantitative measurements of lactate concentration with this asymmetrical sequence. Under these conditions, the only reliable way of estimating T_2 using the conventional method of making measurements at increasing echo times would be to make measurements at $1/J$, $3/J$, etc. In this way, the worst effects of polarization transfer are avoided, and there is no ambiguity caused by the different peak areas encountered at odd and even multiples of $1/J$.

Figure 4 shows sections through Fig. 2 having fixed echo times of 145 ms ($1/J$) (solid line), 290 ms ($2/J$) (dashed line), and 580 ms ($4/J$) (dashed-dotted line). t_1 and t_2 are varied together such that $TE = 2t_1 + 2t_2$ remains constant. For $TE = 1/J$, the integrated lineshape area is independent of t_1 and t_2 , and has a value of -0.60. This behavior is, in fact, repeated at odd multiples of $1/J$, and corresponds to the flat-bottomed valleys of Fig. 2, most clearly seen in the contour representation of Fig. 2c where they run diagonally from top left to bottom right. The behavior at $TE = 2/J$ is more complex, having the maximal possible value of unity when either t_1 or t_2 is zero. These extreme asymmetrical sequences would not be possible in practice for the reasons discussed above. Physically realizable sequences with nonzero t_1 and t_2 will yield lower area integrals, with the lowest value (of 0.44) occurring for the symmetrical case. The exact value observed around this point is a strong function of the echo time, as we shall see later. Conversely, a symmetrical sequence with $TE = 4/J$ (dashed-dotted line) has the highest possible integrated area. Once again, this value

also occurs for extreme sequences with t_1 or t_2 equal to zero. The lowest area (0.37) occurs when $t_2 = 3t_1$ and vice versa.

Figure 5 shows a section through Fig. 2 for symmetrical PRESS sequences with $t_1 = t_2$. All the features discussed above are present; the gross J modulation, the imbalance of positive and negative areas, and the polarization transfer modulation. With this symmetrical sequence, the polarization transfer effect is symmetrical about $TE = 2/J$, unlike the case of the asymmetrical sequence in Fig. 3. Polarization transfer is most significant around $TE = 2/J$ (i.e., $t_1 = t_2 = 1/2J$), when a small change in TE (of 5.6 ms, equivalent to $1/8$) causes the measured area to change from 0.25 to 0.46 units. This effect is the basis of the HOPE sequence (8) in which the refocusing pulses are nominally 90° and spoiler-gradient pulses are arranged (as in PRESS) to rephase only the double spin echo. PRESS and HOPE sequences are distinguished from stimulated echo acquisition mode (STEAM) sequences (9) in which the spoiler gradients select the stimulated echo while dephasing the double spin echo. Even when the PRESS refocusing pulses are nominally 180° , as here, their nonideal slice profiles cause very significant polarization transfer effects, and the use of such a PRESS sequence cannot be recommended. When TE is an odd multiple of $1/J$, the (inverted) doublet area is much less prone to polarization transfer effects and has a value of approximately 0.6 of the theoretical maximum. Only at echo times of $4m/J$ ($m = 0, 1, \dots$) is the maximal area obtained. $m = 0$ is impractical, although short-echo time sequences are becoming feasible with increased gradient performance. $m = 1$ corresponds to an echo time of 580 ms, which is long enough that significant T_2 decay will have occurred, reducing the available signal strength. Higher values of m are impractical because of excessive T_2 decay.

Examples of doublet lineshapes generated by summation of the results for all 40^3 subvoxels are shown in Fig. 6. The independence of t_1 and t_2 values for an echo time of $1/J$ is

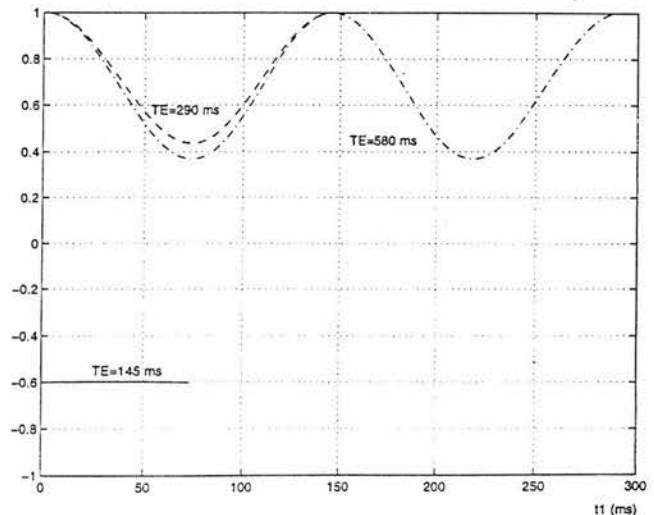


FIG. 4. Sections through the surface of Fig. 2 for fixed echo times of 145 ms ($1/J$) (solid line); (b) 290 ms ($2/J$) (dashed line); (c) 580 ms ($4/J$) (dashed-dotted line).

F5

Copy Query

T

Orig. Op.	OPERATOR:	Session	PROOF:	PE's:	AA's:	COMMENTS	ARTNO:
1st disk, 2nd JHC	shropsha	7					036936

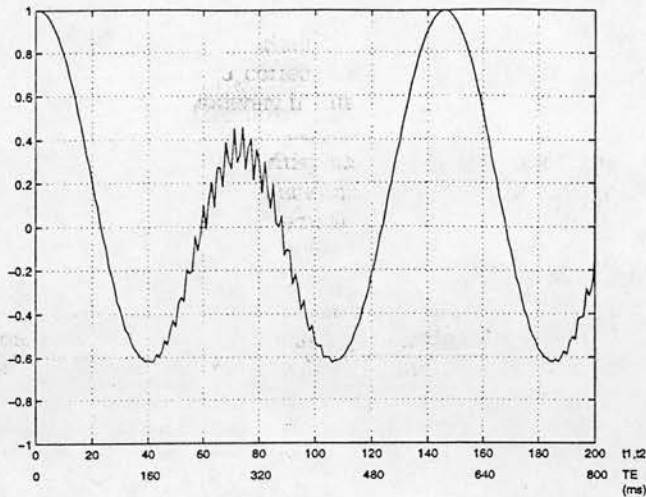


FIG. 5. Section through the surface of Fig. 2 for the symmetrical PRESS sequence ($t_1 = t_2$).

demonstrated by comparison of asymmetrical (Fig. 6a) and symmetrical (Fig. 6c) sequences. Figure 6b shows the lineshape expected from an (asymmetrical) sequence with $TE = 2/J$. The ideal lineshape (maximal area) is achieved only for a symmetrical sequence with $TE = 4/J$ (Fig. 6d).

The polarization transfer modulation of lineshape (and hence integrated area) is shown in Fig. 7. In Fig. 7a, the lineshape has been calculated for symmetrical sequences having echo times of 285 to 292 ms. Corresponding experimental spectra are shown in Fig. 7b. The main features of the calculated lineshapes are confirmed experimentally, notably the increasing depth of the central trough as TE increases, and the highly asymmetric baselines between 287 and 290 ms. The former effect should not be mistaken for increased spectral resolution; it is the result of an increased contribution from the antiphase terms. Several effects may be responsible for the residual differences between the simulated and experimental lineshapes, including inaccurate estimation of δ , imperfect spoiling, out-of-plane rotation by pulses, and eddy currents. The latter may be significant with the unshielded gradient coils used in this work, despite using fairly modest gradient strengths (2 mT/m) and water reference data for phase correction. Increased gradient strengths would reduce the chemical-shift displacement effects but would increase any eddy-current effects. The maximal achievable VOI size would also suffer because of RF amplifier limitations. In fact, simulations with the chemical-shift displacement set to zero (representing infinite gradient strength) gave lineshape integrals of -0.64, 0.82, -0.64, and 1.00, respectively, for the four examples shown in Fig. 6 (compared with the values of -0.60, 0.81, -0.61, and 1.00 that include the effect of 2 mT/m gradients), suggesting that the poor slice profiles have a more significant effect than the use of modest localization gradients. The theoretical calculations do not take account of relaxation effects that may not be insignificant experimentally. A further contribution to the flip-angle distribution will be caused by any nonuniformity in head coil RF sensitivity, but this effect should be minimal with the small, central VOI used.

In calculating the doublet lineshape area, we have assumed ideal integration between infinite limits, so that only the I_{xy} state contributes. This is also correct if lineshape modeling techniques are used. However, if integration is used in practice, it is likely to be restricted in extent by neighboring peaks. The long tails of the antisymmetric dispersion component $2I_{sx}I_{1z}$ will then introduce an error term that increases as the integration width is reduced.

In the derivation of the coefficients k , we have assumed ideal spoiling by gradient pulse pairs placed symmetrically about each of the refocusing pulses. These serve to retain only magnetization that has been in the transverse plane throughout the sequence, leading to the (double) spin echo. The algebra is greatly simplified since all longitudinal magnetization terms can be ignored. If nonideal spoiling is to be investigated, one would have to consider these terms, and also the contribution of spins from outside the selected VOI that experience only one or two of the RF pulses. Many hundred terms would need to be carried through the calculation, making this impractical for manual manipulation, but perhaps amenable to computer algebra systems (10, 11).

The product operator formalism can, in principle, be used to analyze STEAM sequences (12), in which spoiler gradients select the stimulated echo rather than the (double) spin echo. The nomenclature for STEAM is $90^\circ - TE/2 - 90^\circ - TM - 90^\circ - TE/2 - Acq$, with the time interval between the second and third 90° pulses being referred to as the mixing time, TM. During TM, the relevant magnetization is in a longitudinal, zero quantum coherence, state. The echo time, TE, refers to the time during which this magnetization is in the transverse plane. Wilman and Allen (12) presented an analysis of lactate subjected to a STEAM sequence with idealized 90° pulses. In STEAM, the lactate doublet integrated intensity displays

state w.

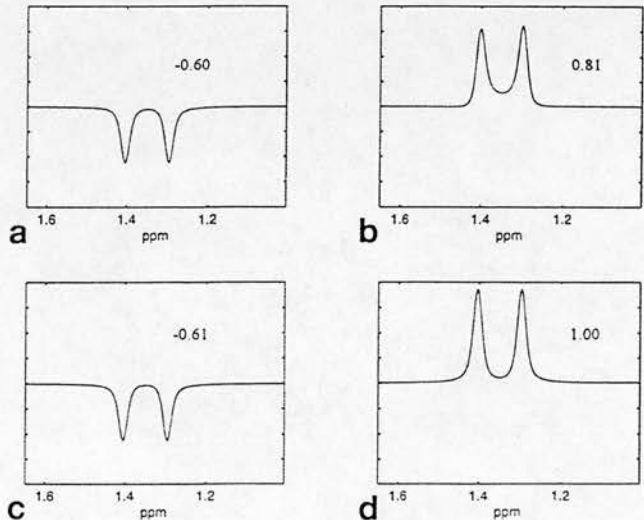


FIG. 6. Examples of calculated PRESS spectra. (a) Asymmetrical sequence with $t_1 = 30$ ms and $TE = 145$ ms; (b) asymmetrical sequence with $t_1 = 30$ ms and $TE = 290$ ms; (c) symmetrical sequence with $TE = 145$ ms; (d) symmetrical sequence with $TE = 580$ ms. The integrated lineshape areas are given relative to the theoretical maximum, which occurs for the symmetrical sequence with $TE = 580$ ms.

T

Orig. Op.	OPERATOR:	Session	PROOF:	PE's:	AA's:	COMMENTS	ARTNO:
1st disk, 2nd JHC	shropsha	7					036936

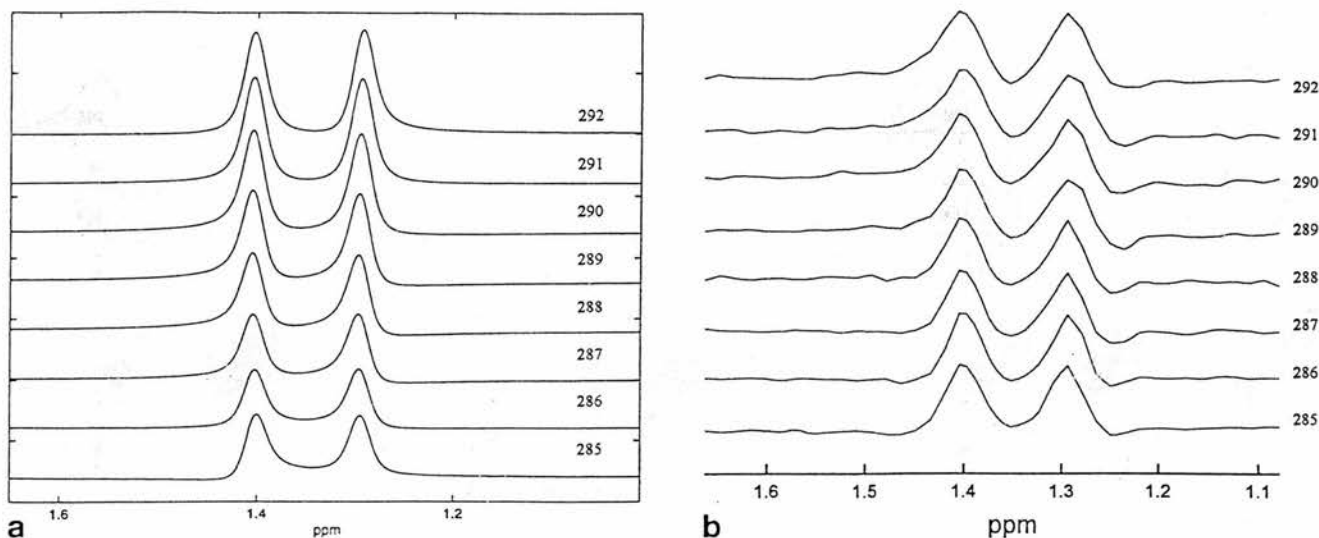


FIG. 7. (a) Series of calculated spectra for symmetrical PRESS sequences around $TE = 290$ ms ($2/J$), showing the polarization transfer modulation caused by imperfect refocusing pulses; (b) corresponding experimental spectra.

~~integrated intensity displays~~ modulations with both TE and TM, of the form $\sin(\delta TE/2)$ and $\sin(\delta TM)$, respectively, compared with the $\sin(\delta(t_1 + t_2)) = \sin(\delta(TE/2))$ for the symmetrical HOPE sequence.

CONCLUSIONS

It is evident that intelligent use of PRESS sequences is needed to avoid the problems highlighted here. Accurate quantification of J -coupled spectra should take account of the flip-angle distribution and the timing of the sequence. In particular, symmetrical PRESS sequences with TE around $2/J$ should be avoided, whereas sequences with TE around $1/J$ and highly asymmetrical sequences are relatively robust. It is expected that the increasing availability of short echo times and numerically optimized slice-selection pulses will alleviate many of the problems of localized spectroscopy.

APPENDIX

The coefficients of Eq.[1] have been reported previously (4) but are repeated here for convenience. Assuming ideal spoiler gradients, and neglecting relaxation effects, they are

$$\begin{aligned}
 k_1 = & 1/4 P \sin(\pi J t_1) \sin(\pi J t_2) \cos(\pi J(t_1 + t_2)) \\
 & \times \cos(\delta(t_1 + t_2)) \\
 & - 1/2 A \cos^2(\pi J t_2) (1 - \cos(\gamma_s)) \\
 & - 1/2 A \sin^2(\pi J t_2) \cos(\gamma_s) (1 - \cos(\gamma_1)) \\
 & + 1/2 B \sin(\pi J t_2) \cos(\pi J t_2) (2\cos(\gamma_s) - 1 \\
 & - \cos(\gamma_1) \cos(\gamma_s)) \quad [A1]
 \end{aligned}$$

$$\begin{aligned}
 k_2 = & -1/4 P \sin(\pi J t_1) \sin(\pi J t_2) \\
 & \times \cos(\pi J(t_1 + t_2)) \sin(\delta(t_1 + t_2)) \quad [A2]
 \end{aligned}$$

$$\begin{aligned}
 k_3 = & 1/4 P \sin(\pi J t_1) \cos(\pi J t_2) \\
 & \times \cos(\pi J(t_1 + t_2)) \sin(\delta(t_1 + t_2)) \quad [A3]
 \end{aligned}$$

$$\begin{aligned}
 k_4 = & 1/4 P \sin(\pi J t_1) \cos(\pi J t_2) \\
 & \times \cos(\pi J(t_1 + t_2)) \cos(\delta(t_1 + t_2)) \\
 & + 1/2 B \sin^2(\pi J t_2) (1 - \cos(\gamma_s)) \\
 & + 1/2 B \cos^2(\pi J t_2) \cos(\gamma_s) (1 - \cos(\gamma_1)) \\
 & - 1/2 A \sin(\pi J t_2) \cos(\pi J t_2) (2\cos(\gamma_s) - 1 \\
 & - \cos(\gamma_1) \cos(\gamma_s)) \quad [A4]
 \end{aligned}$$

where

$$\begin{aligned}
 A = & 1/2 \cos^2(\pi J t_1) (1 - \cos(\beta_s)) \\
 & + 1/2 \sin^2(\pi J t_1) \cos(\beta_s) (1 - \cos(\beta_1)) \quad [A5]
 \end{aligned}$$

$$\begin{aligned}
 B = & 1/2 \sin(\pi J t_1) \cos(\pi J t_1) (2\cos(\beta_s) - 1 \\
 & - \cos(\beta_1) \cos(\beta_s)) \quad [A6]
 \end{aligned}$$

$$P = \sin(\beta_1) \sin(\beta_s) \sin(\gamma_1) \sin(\gamma_s) \quad [A7]$$

and β and γ are the refocusing pulse flip angles (subscripted by 1 for the methine proton and by s for the methyl protons), t_1 and t_2 are the interpulse timings, J is the magnitude of the coupling between the methine and methyl protons, and δ is the corresponding chemical-shift difference.

Orig. Op.	OPERATOR:	Session	PROOF:	PE's:	AA's:	COMMENTS	ARTNO:
1st disk, 2nd JHC	shropsha	8					036936

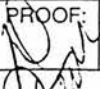
ACKNOWLEDGMENTS

The authors thank Drs. Marzena Arridge and Michael Bunse for useful discussions.

REFERENCES

1. W-I. Jung, O. Lutz, Localized double-spin-echo proton spectroscopy of weakly coupled homonuclear spin systems. *J. Magn. Reson.* **96**, 237-251 (1992).
2. F. Schick, T. Nagele, U. Klose, O. Lutz, Lactate quantification by means of PRESS spectroscopy—influence of refocusing pulses and timing scheme. *Magn. Reson. Imaging* **13**, 309-319 (1995).
3. M. Bunse, W-I. Jung, O. Lutz, K. Küper, G. Dietze, Polarization-transfer effects in localized double-spin-echo spectroscopy of weakly coupled homonuclear spin systems. *J. Magn. Reson. A* **114**, 230-237 (1995).
4. I. Marshall, J. M. Wild, Calculations and experimental studies of the lineshape of the lactate doublet in PRESS-localized ^1H MRS. *Magn. Reson. Med.* **38**, 415-419 (1997).
5. O. W. Sorensen, G. W. Eich, M. H. Levitt, G. Bodenhausen, R. R. Ernst, Product operator formalism for the description of NMR pulse experiments. *Prog. NMR Spectrosc.* **16**, 163-192 (1983).
6. R. J. Ordidge, I. D. Cresshull, The correction of transient B_0 field shifts following the application of pulsed gradients by phase correction in the time domain. *J. Magn. Reson.* **69**, 151-155 (1986).
7. A. van den Boogaart, D. van Ormondt, W. W. F. Pijnappel, R. de Beer, M. Ala-Korpela, Removal of the water resonance from ^1H magnetic resonance spectra. in "Mathematics in Signal Processing, III" (J. G. McWhirter, Ed.), pp. 175-195, Clarendon Press, Oxford, 1994.
8. M. Bunse, W-I. Jung, F. Schick, G. J. Dietze, O. Lutz, HOPE, a new lactate editing method. *J. Magn. Reson. B* **109**, 270-274 (1995).
9. J. Frahm, K.-D. Merboldt, W. Hanicke, Localized proton spectroscopy using stimulated echoes. *J. Magn. Reson.* **72**, 502-508 (1987).
10. R. P. F. Kanter, B. W. Char, A. W. Addison, A computer-algebra application for the description of NMR experiments using the product-operator formalism. *J. Magn. Reson. A* **101**, 23-29 (1993).
11. P. Guntert, N. Schaefer, G. Otting, K. Wuthrich, POMMA: a complete *Mathematica* implementation of the NMR product-operator formalism. *J. Magn. Reson. A* **101**, 103-105 (1993).
12. A. H. Wilman, P. S. Allen, An analytical and experimental evaluation of STEAM versus PRESS for the observation of the lactate doublet. *J. Magn. Reson.* **101**, 102-105 (1993).

T

Orig. Op.	OPERATOR:	Session	PROOF:	PE's:	AA's:	COMMENTS	ARTNO:
1st rnr, 2nd tma(v)	shropsha	8					36936